

PROCEEDINGS OF SPIE



SPIE—The International Society for Optical Engineering

Nonresonant Laser-Matter Interaction (NLMI-10)

Mikhail N. Libenson

Editor

21–23 August 2000

St. Petersburg-Pushkin, Russia

Sponsored by

Russian Foundation for Basic Research

Ministry of Education of the Russian Federation

SPIE—The International Society for Optical Engineering

EOS—European Optical Society

EOARD—U.S. Air Force European Office of Aerospace Research and Development

Organized by

S.I. Vavilov State Optical Institute (Russia)

General Physics Institute, Russian Academy of Sciences

St. Petersburg Institute of Fine Mechanics and Optics (Russia)

SPIE Russia Chapter

St. Petersburg Association of Scientists and Scholars (Russia)

Center TRIZ "Tvorchestvo" (Russia)

DISTRIBUTION STATEMENT A

Approved for Public Release

Distribution Unlimited



Volume 4423

20011113 028

REPORT DOCUMENTATION PAGE

Form Approved OMB No. 0704-0188

Public reporting burden for this collection of information is estimated to average 1 hour per response, including the time for reviewing instructions, searching existing data sources, gathering and maintaining the data needed, and completing and reviewing the collection of information. Send comments regarding this burden estimate or any other aspect of this collection of information, including suggestions for reducing this burden to Washington Headquarters Services, Directorate for Information Operations and Reports, 1215 Jefferson Davis Highway, Suite 1204, Arlington, VA 22202-4302, and to the Office of Management and Budget, Paperwork Reduction Project (0704-0188), Washington, DC 20503.

1. AGENCY USE ONLY (Leave blank)		2. REPORT DATE 2001		3. REPORT TYPE AND DATES COVERED Conference Proceedings	
4. TITLE AND SUBTITLE Nonresonant Laser- Matter Interaction 10				5. FUNDING NUMBERS F61775-00-WF	
6. AUTHOR(S) Conference Committee					
7. PERFORMING ORGANIZATION NAME(S) AND ADDRESS(ES) Scientific Council of the St. Petersburg Association of Scientists and Scholars Universitetskaya naber. 5, office 102 St. Petersburg 199034 Russia				8. PERFORMING ORGANIZATION REPORT NUMBER N/A	
9. SPONSORING/MONITORING AGENCY NAME(S) AND ADDRESS(ES) EOARD PSC 802 BOX 14 FPO 09499-0200				10. SPONSORING/MONITORING AGENCY REPORT NUMBER CSP 00-5058	
11. SUPPLEMENTARY NOTES					
12a. DISTRIBUTION/AVAILABILITY STATEMENT Approved for public release; distribution is unlimited.				12b. DISTRIBUTION CODE A	
13. ABSTRACT (Maximum 200 words) The Final Proceedings for Nonresonant Laser- Matter Interaction 10, 21 August 2000 - 23 August 2000 [Proceedings of SPIE, Vol. 4423] This is an interdisciplinary conference. Topics include structural and phase transitions in condensed matter; laser damage of optical materials and elements; laser-induced surface phenomena; instabilities and self-organization under laser conditioning; and interaction of ultrashort pulses with matter.					
14. SUBJECT TERMS EOARD, laser-induced damage				15. NUMBER OF PAGES 316	
				16. PRICE CODE N/A	
17. SECURITY CLASSIFICATION OF REPORT UNCLASSIFIED	18. SECURITY CLASSIFICATION OF THIS PAGE UNCLASSIFIED	19. SECURITY CLASSIFICATION OF ABSTRACT UNCLASSIFIED	20. LIMITATION OF ABSTRACT UL		

NSN 7540-01-280-5500

Standard Form 298 (Rev. 2-89)
Prescribed by ANSI Std. Z39-18
298-102



PROCEEDINGS OF SPIE

SPIE—The International Society for Optical Engineering

Nonresonant Laser-Matter Interaction (NLMI-10)

Mikhail N. Libenson
Editor

Vitali I. Konov
Mikhail N. Libenson
Chairs

21–23 August 2000
St. Petersburg-Pushkin, Russia

Sponsored by

Russian Foundation for Basic Research
Ministry of Education of the Russian Federation
SPIE—The International Society for Optical Engineering
EOS—European Optical Society
EOARD—U.S. Air Force European Office of Aerospace Research and Development

Organized by

S.I. Vavilov State Optical Institute (Russia)
General Physics Institute, Russian Academy of Sciences
St. Petersburg Institute of Fine Mechanics and Optics (Russia)
SPIE Russia Chapter
St. Petersburg Association of Scientists and Scholars (Russia)
Center TRIZ "Tvorchestvo" (Russia)

In Cooperation with

Association of Scientific Societies of Russia
D.S. Rozhdestvensky Optical Society (Russia)

Published by

SPIE—The International Society for Optical Engineering



Volume 4423

SPIE is an international technical society dedicated to advancing engineering and scientific applications of optical, photonic, imaging, electronic, and optoelectronic technologies.

AQ F02-02-0314



The papers appearing in this book compose the proceedings of the technical conference cited on the cover and title page of this volume. They reflect the authors' opinions and are published as presented, in the interests of timely dissemination. Their inclusion in this publication does not necessarily constitute endorsement by the editors or by SPIE. Papers were selected by the conference program committee to be presented in oral or poster format, and were subject to review by volume editors or program committees.

Please use the following format to cite material from this book:

Author(s), "Title of paper," in *Nonresonant Laser-Matter Interaction (NLMI-10)*, Mikhail N. Libenson, Editor, Proceedings of SPIE Vol. 4423, page numbers (2001).

ISSN 0277-786X
ISBN 0-8194-4130-9

Published by
SPIE—The International Society for Optical Engineering
P.O. Box 10, Bellingham, Washington 98227-0010 USA
Telephone 1 360/676-3290 (Pacific Time) • Fax 1 360/647-1445
<http://www.spie.org/>

Copyright© 2001, The Society of Photo-Optical Instrumentation Engineers.

Copying of material in this book for internal or personal use, or for the internal or personal use of specific clients, beyond the fair use provisions granted by the U.S. Copyright Law is authorized by SPIE subject to payment of copying fees. The Transactional Reporting Service base fee for this volume is \$15.00 per article (or portion thereof), which should be paid directly to the Copyright Clearance Center (CCC), 222 Rosewood Drive, Danvers, MA 01923 USA. Payment may also be made electronically through CCC Online at <http://www.directory.net/copyright/>. Other copying for republication, resale, advertising or promotion, or any form of systematic or multiple reproduction of any material in this book is prohibited except with permission in writing from the publisher. The CCC fee code is 0277-786X/01/\$15.00.

Printed in the United States of America.

Contents

vii	<i>Conference Committees</i>
ix	<i>Introduction</i>

PLENARY PAPER

-
- | | |
|---|--|
| 1 | Nonequilibrium heating and cooling of metals under action of supershort laser pulse
[4423-01]
M. N. Libenson, S.I. Vavilov State Optical Institute (Russia) |
|---|--|

SECTION A LASER-INDUCED PHOTOPHYSICAL AND PHOTOCHEMICAL PROCESSES

- | | |
|----|--|
| 8 | Pulsed-laser deposition of nanometric and micrometric films for optoelectronic applications
[4423-02]
M. L. De Giorgi, L. Elia, M. Fernandez, G. Leggieri, A. Luches, M. Martino, A. Zocco, INFM (Italy) and Univ. degli Studi di Lecce (Italy) |
| 18 | Photoelectrical properties of nonuniform semiconductor under infrared laser radiation
[4423-03]
S. P. Ašmontas, J. Gradauskas, D. Seliuta, Semiconductor Physics Institute (Lithuania); E. Širmulis, Institute of Physics (Lithuania) |
| 28 | Dynamics of 3D representation of interfaces in UV-induced chemical vapor deposition: experiments, modeling, and simulation for silicon nitride thin layers [4423-04]
J. Flicstein, E. Guillonau, France Telecom CNET; J. Marquez, École Nationale Supérieure des Télécommunications (France); L. S. How Kee Chun, Opto+ (France); D. Maisonneuve, France Telecom CNET; C. David, Zh. Zh. Wang, L2M/CNRS (France); J. F. Palmier, J. L. Courant, Opto+ (France) |
| 36 | Modeling of photochemical changes and photodarkening of AsSe films under pulse vacuum ultraviolet radiation [4423-05]
N. A. Kaliteevskaya, R. P. Seisyan, A.F. Ioffe Physico-Technical Institute (Russia) |
| 42 | Optical manipulation of liquid crystals using a two-beam technique [4423-06]
E. Brasselet, T. V. Galstian, Univ. Laval (Canada) |
| 49 | Photostructure transformation effects of layer consisting from CAMC:OMA copolymers under the action of laser irradiation [4423-07]
V. V. Bivol, Ctr. of Optoelectronics (Moldova); V. S. Robu, L. A. Vlad, A. Coban, State Univ. of Moldova; A. M. Prisacari, Ctr. of Optoelectronics (Moldova) |
| 55 | Formation and dynamics of ordered nanometer structures and emission of photons from a rear surface of metal samples at the irradiating of frontal surface by laser pulse [4423-08]
K. B. Abramova, I. P. Shcherbakov, A.F. Ioffe Physico-Technical Institute (Russia) |
| 61 | Infrared laser annealing of nanoporous silicon [4423-09]
V. P. Aksenov, G. N. Mikhailova, General Physics Institute (Russia); J. Boneberg, P. Leiderer, H. J. Muenzer, Univ. of Konstanz (Germany) |

- 65 **Laser annealing of MBE Ge films on the Si substrates** [4423-10]
V. P. Aksenov, G. N. Mikhailova, General Physics Institute (Russia); J. Boneberg, P. Leiderer, H. J. Muenzer, Univ. of Konstanz (Germany)
- 68 **Modification of the surface roughness spectrum by means of power laser radiation** [4423-11]
V. P. Aksenov, G. N. Mikhailova, General Physics Institute (Russia); J. Boneberg, P. Leiderer, H. J. Muenzer, Univ. of Konstanz (Germany)
- 70 **Thermally stimulated luminescence from porous silicon** [4423-12]
V. P. Aksenov, G. N. Mikhailova, General Physics Institute (Russia); J. Boneberg, P. Leiderer, H. J. Muenzer, Univ. of Konstanz (Germany)
- 74 **Formation of 3D dielectric structures by initiating polymerization with the fourth harmonic of an Nd laser** [4423-13]
A. P. Alexandrov, S. V. Muraviov, N. A. Babina, N. M. Bityurin, Institute of Applied Physics (Russia)
- 79 **Radiation action on polymethine dyes prepared on insulating substrates as molecular layers** [4423-14]
A. M. Bonch-Bruevich, E. N. Kaliteevskaya, V. P. Krutyakova, T. K. Razumova, S.I. Vavilov State Optical Institute (Russia)
- 87 **CO₂ laser radiation detection in compensated germanium** [4423-15]
S. Bumelienė, S. P. Ašmontas, Semiconductor Physics Institute (Lithuania); J. Gradauskas, A. Jukna, Semiconductor Physics Institute (Lithuania) and Technical Univ. of Vilnius (Lithuania); J. Paršeliūnas, D. Seliuta, Semiconductor Physics Institute (Lithuania); A. Sužiedėlis, G. Valušis, Semiconductor Physics Institute (Lithuania) and Technical Univ. of Vilnius (Lithuania)
- 91 **Impact of laser and x-ray irradiation on C₆₀ films** [4423-16]
S. O. Kognovitskii, A.F. Ioffe Physico-Technical Institute (Russia); N. V. Kamanina, S.I. Vavilov State Optical Institute (Russia); R. P. Seisyan, M. E. Gaevski, S. I. Nesterov, M. V. Baidakova, M. R. Rymalis, A.F. Ioffe Physico-Technical Institute (Russia)
- 97 **IR laser action on fullerene-doped organic systems** [4423-17]
N. V. Kamanina, S.I. Vavilov State Optical Institute (Russia); I. V. Bagrov, I. M. Belousova, A. P. Zhevlakov, Institute for Laser Physics (Russia)
- 103 **Nonlinear optical properties of *N*-(4-nitrophenyl)-(L)-prolinol doped with fullerenes: mechanisms of optical limiting** [4423-18]
N. V. Kamanina, S.I. Vavilov State Optical Institute (Russia)
- 108 **Laser-induced homogenization of light-diffusing media** [4423-19]
V. L. Komolov, S. G. Przhibel'skii, V. N. Smirnov, S.I. Vavilov State Optical Institute (Russia)
- 115 **New mechanism of laser dry cleaning** [4423-20]
B. S. Luk'yanchuk, Y. W. Zheng, Y. F. Lu, National Univ. of Singapore
- 127 **Peculiarity of CO₂ laser radiation interaction with semiconductor A_{III}B_{VI} compounds** [4423-21]
A. F. Mukhammedgalieva, V. S. Petukhov, B. I. Vasiliev, Moscow State Mining Univ. (Russia)
- 134 **Potential of near- and far-field techniques for the detection of nanoemitters on a laser-illuminated surface** [4423-22]
G. S. Zhdanov, S.I. Vavilov State Optical Institute (Russia)

SECTION B LASER ABLATION

- 141 **Dynamics of subpicosecond laser ablation examined by moments technique** [4423-23]
B. S. Luk'yanchuk, National Univ. of Singapore; S. I. Anisimov, L.D. Landau Institute for Theoretical Physics (Russia); Y. F. Lu, National Univ. of Singapore
- 153 **Microablation of pure metals: laser plasma and crater investigations** [4423-24]
A. F. Semerok, B. Sallé, J.-F. Wagner, CEA Saclay (France); G. Petite, École Polytechnique (France); O. Gobert, P. Meynadier, M. Perdrix, CEA Saclay (France)
- 165 **Time-resolved measurement of ablation from ns-laser-heated aluminum and comparison with simulation** [4423-25]
M. Watanabe, E. Hotta, T. Yabe, Tokyo Institute of Technology (Japan)
- 172 **Pulsed-laser ablation vs. pulsed ion beam evaporation for applications to materials science** [4423-26]
K. Yatsui, M. Hirai, K. Kitajima, T. Suzuki, W. Jiang, Nagaoka Univ. of Technology (Japan)
- 178 **Ablation thresholds of metals with femtosecond laser pulses** [4423-27]
M. Hashida, A. F. Semerok, O. Gobert, CEA Saclay (France); G. Petite, École Polytechnique (France); J.-F. Wagner, CEA Saclay (France)
- 186 **Ablation dynamics of solids heated by femtosecond laser pulses** [4423-28]
B. Rethfeld, K. Sokolowski-Tinten, Univ. Essen (Germany); V. V. Temnov, Univ. Essen (Germany) and Institute of Applied Physics (Russia); S. I. Kudryashov, Univ. Essen (Germany) and M.V. Lomonosov Moscow State Univ. (Russia); J. Bialkowski, Univ. Essen (Germany); A. Cavalleri, Univ. of California/San Diego (USA); D. von der Linde, Univ. Essen (Germany)
- 197 **Model for photothermal laser ablation of polymer-like materials** [4423-29]
N. M. Bityurin, Institute of Applied Physics (Russia)
- 206 **Infrared free-electron laser photoablation of diamond films** [4423-30]
J. Sturmman, Z. Marka, M. M. Albert, R. G. Albridge, J. M. Gilligan, G. Lüpke, S. K. Singh, J. L. Davidson, Vanderbilt Univ. (USA); W. Husinsky, Technische Univ. Wien (Austria); N. H. Tolk, Vanderbilt Univ. (USA)
- 212 **Mechanism of carbon nanotube synthesis by laser ablation** [4423-31]
A. A. Gorbunov, Technische Univ. Dresden (Germany); A. Graff, Institute for Solid State and Materials Research Dresden (Germany); O. Jost, W. Pompe, Technische Univ. Dresden (Germany)
- 218 **Laser ablation of polymers by ultrashort laser pulses (USLP): surface and bulk models** [4423-32]
A. Yu. Malyshev, N. M. Bityurin, Institute of Applied Physics (Russia)
- 226 **Laser ablation of the thin film by thermal tension** [4423-33]
E. A. Shakhno, St. Petersburg Institute of Fine Mechanics and Optics (Russia)
- 232 **Model of laser-induced ablation of solids** [4423-34]
Yu. A. Chivel, L. Ya. Min'ko, Institute of Molecular and Atomic Physics (Belarus)

SECTION C **NONLINEAR OPTICAL PROCESSES AND LASER DAMAGE IN CONDENSED MEDIA**

- 238 **Some electromagnetic aspects of high-power laser interaction with transparent solids**
[4423-35]
V. E. Gruzdev, M. N. Libenson, S.I. Vavilov State Optical Institute (Russia)
- 250 **Nonequilibrium electron and phonon dynamics in solids absorbing a subpicosecond laser pulse** [4423-36]
B. Rethfeld, Univ. Essen (Germany); A. Kaiser, Max-Planck-Institut für Physik komplexer Systeme (Germany); M. Vicanek, G. Simon, Technische Univ. Braunschweig (Germany)
- 262 **Formation of electromagnetic shock waves on optical cycle during propagation of femtosecond laser pulses in transparent solids** [4423-37]
V. E. Gruzdev, A. S. Gruzdeva, S.I. Vavilov State Optical Institute (Russia)
- 274 **Paraxial (2+1)-dimensional self-focusing of extremely short pulses** [4423-38]
M. A. Bakhtin, A. N. Berkovsky, S. A. Kozlov, Yu. A. Shpolyanskiy, St. Petersburg Institute of Fine Mechanics and Optics (Russia)
- 280 **Linear and nonlinear optical tools to measure the dephasing time of localized surface plasmon polaritons** [4423-39]
T. A. Vartanyan, S.I. Vavilov State Optical Institute (Russia); F. Träger, Univ. Kassel (Germany)
- 286 **Spectral, spatial, and polarization characteristics of harmonics generated at interaction of intense laser radiation with aluminum foils** [4423-40]
R. A. Ganeev, NPO Akadempribor (Uzbekistan); J. A. Chakera, M. Raghuramaiah, A. K. Sharma, P. A. Naik, P. D. Gupta, Ctr. for Advanced Technology (India)
- 295 **Nonthermal effects in femtosecond laser damage of transparent materials** [4423-41]
V. E. Gruzdev, A. S. Gruzdeva, S.I. Vavilov State Optical Institute (Russia)
- 307 **Investigation of nonlinear optical parameters of metal composites by Z-scan technique**
[4423-42]
A. I. Rysanyansky, Samarkand State Univ. (Uzbekistan); R. A. Ganeev, Sh. R. Kamalov, NPO Akadempribor (Uzbekistan); M. K. Kodirov, Samarkand State Univ. (Uzbekistan); T. Usmanov, NPO Akadempribor (Uzbekistan)
- 315 *Author Index*

Conference Committees

Honorary Chairs

Alexei M. Bonch-Bruevich, *Corresponding Member*, S.I. Vavilov State Optical Institute/
Russian Academy of Sciences

Alexander M. Prokhorov, *Academician*, General Physics Institute/Russian Academy
of Sciences

Conference Program Committee Chairs

Vitali I. Konov, General Physics Institute (Russia)

Mikhail N. Libenson, S.I. Vavilov State Optical Institute (Russia)

International Program Committee

Sergey I. Anisimov, Russia

Sergey Bagayev, Russia

Mario Bertolotti, Italy

Ian Boyd, UK

Alexander Dement'ev, Lithuania

Jean Dijon, France

Costas Fotakis, Greece

Arthur Guenther, USA

Norbert Kaiser, Germany

Vladimir L. Komolov, Russia

Armando Luches, Italy

Boris S. Luk'yanchuk, Russia

Laslo Nanai, Hungary

Pavel Pashinin, Russia

Guillaume Petite, France

M. J. Soileau, USA

Vadim Veiko, Russia

Kiyoshi Yatsui, Japan

Scientific Secretary of the Conference

Natalie V. Kamanina, S.I. Vavilov State Optical Institute

Section Chairs

- A Laser-Induced Photophysical and Photochemical Processes
Alexei M. Bonch-Bruevich, S.I. Vavilov State Optical Institute (Russia)
Arthur Guenther, Sandia National Laboratories (USA)
Vladimir L. Komolov, S.I. Vavilov State Optical Institute (Russia)
Laslo Nanai, University of Szeged (Hungary)
Natalie V. Kamanina, S.I. Vavilov State Optical Institute (Russia)
Valentin N. Smirnov, S.I. Vavilov State Optical Institute (Russia)
- B Laser Ablation
Mikhail N. Libenson, S.I. Vavilov State Optical Institute (Russia)
Armando Luches, INFN (Italy) and Università degli Studi di Lecce (Italy)
Sergey I. Anisimov, L.D. Landau Institute for Theoretical Physics (Russia)
Kiyoshi Yatsui, Nagaoka University of Technology (Japan)
Galina D. Shandybina, St. Petersburg State Institute of Fine Mechanics
and Optics (Russia)

- C Nonlinear Optical Processes and Laser Damage in Condensed Media
 Boris S. Luk'yanchuk, General Physics Institute (Russia)
 Francesco Michelotti, Università degli Studi di Roma La Sapienza (Italy)
 Tigran A. Vartanyan, S.I. Vavilov State Optical Institute (Russia)
 Norbert Kaiser, Fraunhofer-Institut für Angewandte Optik und Feinmechanik (Germany)
 Anatoliy P. Sukhorukov, M.V. Lomonosov Moscow State University (Russia)

Introduction

The Tenth International Conference on Nonresonant Laser-Matter Interaction (NLMI-10) was held in St. Petersburg (Pushkin) on 21–23 August 2000. Together with the previous International Conference NLMI-9, which was held at the same location in 1996, this jubilee conference carries on at the international level the traditions of the former All-Union conferences on Nonresonant Interaction of Optical Radiation with Matter, which had been held every three years since 1969 in Leningrad. These forums brought together more than 500 participants and always distinguished themselves by their high scientific level, were quite popular in the scientific community of the former USSR, and were well known abroad. They were organized in parallel with the well-known annual Boulder Damage symposia in the U.S. These forums have remarkably complemented each other for the last 30 years. The Eighth All-Union Conference on Nonresonant Interaction of Optical Radiation with Matter (1990) and all the following NLMI conferences were supported by SPIE and its Russia Chapter, including publication of the conferences proceedings in English (Proceedings of SPIE Vols. 1440 and 3093).

More than 100 scientists from 15 countries participated in the NLMI-10 conference. It covered various traditional aspects of the physics of laser heating and destruction of materials, optical damage, laser-induced thermal- and photochemical processes, (including ones at the surface), instabilities, and self-organization during laser-matter interaction. The conference also considered state-of-the-art of experimental and theoretical investigations of the ultrafast processes induced by ultrashort laser pulses in transparent and absorbing condensed media.

The most interest was evoked by the contributions of the leading scientists in laser ablation, especially with short and ultrashort laser pulses. Participants were particularly interested in presentations devoted to the investigation of fundamental mechanisms of laser damage in highly transparent dielectrics, including coupled effects of nonlinear optics and high-power optics.

As it was four years ago, the conference was organized jointly with the Ninth International Conference on Laser-Assisted Microtechnology (LAM-2000), as part of the Second International Symposium on Intensive Laser Actions and their Applications. This combination has proven successful and has allowed us to discuss both fundamental and application problems of laser-matter interaction. It has been decided to hold the next NLMI conference jointly with the LAM conference in St. Petersburg in 2003.

Organization of the conference during such a difficult time for Russian science would have been impossible without financial support from Russian and foreign sponsors. We are grateful to the Russian Foundation for Basic Research for its great support, which allowed many Russian scientists to attend the conference. We are grateful to the Russian Ministry of Education, SPIE and its Russia Chapter, and the European Optical Society (EOS) for their help in the preparation and publication of the conference materials and proceedings. We also thank the U.S. Air Force European Office of Aerospace Research and Development for its contribution to the success of the conference.

Mikhail N. Libenson

Non-equilibrium heating and cooling of metals under action of super-short laser pulse

Mikhail N. Libenson¹

State Research Center "S.I. Vavilov State Optical Institute"

Birzhevaya Liniya 12, St. Petersburg, 199034 Russia

ABSTRACT

It is considered photo-excitation, non-equilibrium heating and thermal after-action induced by super-short laser pulses interacting with metals. It is shown that classical model of thermal laser-induced destruction of metals should be corrected in the case when pulse duration is much less than characteristic time of energy transfer from electrons to the lattice. In particular, possible important role of laser-induced electric-physical processes should be taken into account.

Key words: photo-excitation, non-equilibrium heating, thermalization, laser-induced destruction.

1. INTRODUCTION

Increased attention to laser physics and laser technology connected with femtosecond laser pulses has excited interest to investigation of regulations of action of femtosecond laser pulses on condensed materials. Significant difference of laser action in the case of femtosecond pulses from the case of longer pulses is connected with that pulse duration t_p is smaller (often much smaller) than characteristic time τ of energy transfer from absorbed laser quantum to heat. That means that only intensive photo-excitation of electron sub-system takes place within pulse duration.

This paper is devoted to consideration of non-equilibrium photo-excitation and thermal after-action of super-short laser pulses ($t_p \ll \tau$). Some unusual regularities of those processes are considered for particular case of laser interaction with a metal. Obtained results allow to estimate boundaries of applicability range of well-known two-temperature model of metal heating and damage by short laser pulses^{1, 2}. Attention is also paid to possible important role of laser-induced electro-physical processes in laser destruction of metals.

2. PHOTO-EXCITATION AND THERMALIZATION OF NON-EQUILIBRIUM ELECTRONS

Absorption of laser quanta by free electrons in metal results in growth of kinetic energy of the electrons and transition of their energy distribution from equilibrium one to non-equilibrium one. That well-known feature determines interaction of laser radiation with metals in wide spectral range where there are no inter-band laser-induced transitions. That feature is also a non-evident base for two-temperature model of metal heating by short laser pulses. Together with that it is often assumed that energy thermalization within sub-system of non-equilibrium electrons is so fast that it allows introducing of local electron temperature $T_e(x, t)$ depending on space coordinates and time right from the beginning of absorption of laser radiation. In fact, energy thermalization takes certain time that depends on frequency of electron-electron collision ν_{ee} . Classical value of the frequency is given by expression

$$\nu_{ee}^{cl} = \nu_0 \left(\frac{k_0 T_e}{\varepsilon F} \right)^2. \quad (1)$$

Correct consideration³ shows that real value of collision frequency depends on quantum energy $\hbar\omega$ together with dependence on electron temperature:

¹ Phone: (812) 328-0231, e-mail: mnlbenson@mail.ru

$$\nu_{ee} = \nu_{ee}^{cl}(T_e) \left[1 + \left(\frac{\hbar\omega}{2\pi k_0 T_e} \right)^2 \right]. \quad (2)$$

Here ν_0 is certain constant, k_0 is Boltzmann's constant, ε_F is Fermi energy. Simple calculation shows that value of ν_{ee} is at least 10-30 times more than classical value $\sim 10^{12} \text{ s}^{-1}$ given by (1) for room temperature in the case when laser quantum is more than 1 eV.

Strictly speaking, analysis of dynamical processes should be based on solution to kinetic equation for time-dependent energy-distribution function for electrons subjected to action of laser radiation. Field distribution for those calculations should be obtained in the approximation of weakly anomalous skin-effect because in case of super short laser pulses contribution of surface absorption (A_s) can dominate contribution of bulk absorption (A_v). Bearing that in mind, we can say that obtaining of qualitative description and estimations can be based on diffusion approximation to considered problem. In the framework of that approximation non-equilibrium electrons (with no respect to their energy) are described by integral value of density $n(x,t)$ that varies as a function of time and space (along x -axis for 1D geometry) due to absorption of laser radiation, diffusion and gradual energy thermalization resulting from electron-electron collisions:

$$\frac{\partial n}{\partial t} - D \frac{\partial^2 n}{\partial x^2} = \frac{J}{\delta} \exp\left(-\frac{x}{\delta}\right) - \frac{n}{\langle \tau_{ee} \rangle}. \quad (3)$$

Here $D \sim 100 \text{ cm}^2 \text{ s}^{-1}$ is diffusion constant for electrons in the metal, δ is radiation penetration depth determined only by plasma frequency of free electrons ω_p in the approximation of weak anomalous skin-effect: $\delta = c_0/\omega_p$, c_0 is light speed in vacuum, J is intensity of flux of absorbed laser photons connected with intensity of incident radiation q_0 , absorption coefficient of the metal A and photon energy by the following relation:

$$J = J_0 A = \frac{q_0 A}{\hbar\omega}. \quad (4)$$

What about value $\langle \tau_{ee} \rangle$ (characteristic time of electron-electron collisions averaged over electron energy) – it can be estimated from relation (2) in the first approximation as follows: $\langle \tau_{ee} \rangle \sim 1/\nu_{ee}$.

According to results from theory of skin-effect, there are satisfied the following conditions in considered frequency range

$$\gamma \leq \omega_p \frac{v_F}{c_0} \leq \omega \ll \omega_p \quad (\text{see, for example, } ^4)$$

$$A = A_v + A_s = \frac{2\gamma}{\omega_p} + \frac{3}{4} p \frac{v_F}{c_0}, \quad (5)$$

where γ is full frequency of electron collisions, $0 \leq p \leq 1$ is coefficient of diffusion electron scattering at metal surface, v_F is Fermi speed of electrons. It is well known that main additive contribution into γ results from electron-electron (ν_{ee}) and electron-phonon or electron-ion (ν_{ei}) collisions as well as from electron scattering by defects and impurities (ν_{ed}):

$$\gamma = \nu_{ee}(T_e) + \nu_{ei}(T) + \nu_{ed}. \quad (6)$$

Efficiency of the collisions depends on electron T_e and lattice T temperatures.

Bearing in mind presented above consideration, value of A in (4) should be set to be equal to A_v , while contribution of surface absorption should be included into boundary condition for the problem:

$$-\frac{\partial n}{\partial x}(0,t) = J_0 A_s - j_e, \quad (7)$$

where j_e is "leakage" of electrons connected with external electron emission from metal surface. Coupling of (7) with zero initial condition and condition of solution bounded in bulk metal at large distance from metal surface allows to find space distribution of electron concentration $n(x,t)$. Assuming $J_0 = \text{const}$, one can obtain that $n(x,t)$ grows monotonously in time till it reaches stable distribution with constant value $n(x,\infty) = n(x)$. That constant value is reached really at time $t > 3/\nu_{ee} \sim 10^{-14} - 10^{-13} \text{ s}$. Space distribution $n(x)$ of that steady electron density depends on value of emission current from metal surface. In particular, it can be a curve with maximum of n beneath the metal surface. In the case, when electron emission current from metal surface can be neglected because of any reason, space distribution of electron density is described by function $n(x)$ monotonously decreasing with increasing of coordinate x . Then maximum value of density of non-equilibrium electrons n_0 is reached at metal surface and is given by the following expression:

$$n_0 = J_0 A_v \frac{\tau_{ee}}{\delta + \sqrt{D\tau_{ee}}} + J_0 A_s \sqrt{\frac{\tau_{ee}}{D}}. \quad (8)$$

For example, for $J_0 = 2 \cdot 10^{30} \text{ cm}^{-2} \cdot \text{s}^{-1}$ ($q_0 \sim 10^{11} \text{ W} \cdot \text{cm}^{-2}$ for Nd:YAG laser), $A_v = 5A_s$, $A_s = 0.01$, $\tau_{ee} = 10 \text{ fs}$, $\delta = 0.01 \text{ } \mu\text{m}$, $D = 100 \text{ cm}^2 \cdot \text{s}^{-1}$ one obtains from (8) the following value of electron concentration: $n_0 \sim 7 \cdot 10^{20} \text{ cm}^{-3}$. Such large density of non-equilibrium electrons points at that high level of photo-excitation of the metal can be easily reached at laser intensity typical of femtosecond laser-matter interaction. At the same time, it points at possibility of significant increasing of electronic pressure in irradiated metal.

Thermalization of energy of non-equilibrium electrons results also in gradual growth of electron temperature in time during action of laser pulse while crystal lattice stays practically cold if $t_p \ll \tau$. In the case of 1D geometry, heat conductivity equations for electron and phonon systems, coupled with equation (3), can be written in the following form with taking into account well-known simplifications^{1,2}:

$$c_e \frac{\partial T_e}{\partial t} - \frac{\partial}{\partial x} \left[k_e \frac{\partial T_e}{\partial x} \right] = \frac{n\hbar\omega}{\langle \tau_{ee} \rangle} - g(T_e - T), \quad (9)$$

$$\frac{\partial T}{\partial t} = \frac{T_e - T}{\tau}, \quad \tau = \frac{c_i}{g}. \quad (10)$$

There are denoted specific heats of electron and phonon systems of the metal as c_e and c_i correspondingly, electron thermal conductivity as k_e , electron-phonon coupling constant is denoted as g (it determines rate of energy transfer from electron system to the lattice and value of characteristic time τ).

Equations (3), (9) and (10) coupled with corresponding initial and boundary conditions allow more rigorous consideration of regularities of metal heating by laser super-short laser pulse and specific features of energy "accumulation" in the metal required for subsequent destruction (for example, evaporation) of the metal. It is obvious, that such energy "accumulation" during pulse action can take place only within electron sub-system of the metal (of semiconductor). Leaving detailed analysis of the whole problem (it will be done in other paper), we should point at important feature: if pulse duration satisfies condition $t_p \gg \tau_{ee}$, then laser excitation of electron sub-system becomes mainly thermal, and its adequate description can be based on well-known approximation of electron thermal conductivity. Really, tending of τ_{ee} and D to zero results in merging of equations (3) and (9) into one thermal conductivity equation that takes the following form:

$$c_e(T_e) \frac{\partial T_e}{\partial t} - \frac{\partial}{\partial x} \left[k_e(T_e, T) \frac{\partial T_e}{\partial x} \right] = \frac{q_0 A}{\delta} \exp\left(-\frac{x}{\delta}\right) - g(T_e - T). \quad (11)$$

Together with (10), equation (11) corresponds to two-temperature model of laser heating of a metal^{1,2}. In the case of pulse duration below 1 ps ($t_p < 1 \text{ ps}$) energy transfer to the lattice can be neglected. Then electron sub-system can be considered as thermally isolated.

Starting with paper¹, solution to equation (11) has been analyzed many times (often it is considered as coupled with equation (10)). One of the most detailed analyses of equation (11) can be found in one of recent papers² where solution to (11) is considered with taking into account temperature dependence of $c_e(T_e)$ and $k_e(T_e, T)$. Each dependence is linear function of T_e for the case when $T_e < \varepsilon_F/k_0$ and $T_e \gg T = \text{const}$. Below there are presented two variants of analytical solution to (11) for the case of laser heating of thermally isolated electron sub-system at constant laser intensity $q_0 A = \text{const}$ (see also²). The formulae below present electron temperature T_{e0} at metal surface:

$$f = \frac{2q_0 A \delta}{k_e T_{e0}^0} \left\{ \frac{2\sqrt{a_e t}}{\sqrt{\pi} \delta} + \exp\left(\frac{at}{\delta^2}\right) \Phi\left(\frac{\sqrt{at}}{\delta}\right) - 1 \right\}. \quad (12)$$

where

$$f = \begin{cases} \left(\frac{T_{e0}}{T_{e0}^0} \right)^2 - 1, & \text{for } T_e < \varepsilon_F/2k_0 \end{cases} \quad (13-a)$$

$$f = \begin{cases} 2 \left(\frac{T_{e0}}{T_{e0}^0} - 1 \right), & \text{for constant values of } a_e, c_e, k_e, \end{cases} \quad (13-b)$$

where a_e , k_e are respectively "high-frequency" temperature conductivity and thermal conductivity of electron gas at initial (room) temperature T_e^0 , $\Phi^*(\xi)$ is complementary error function. Temperature dependence of thermo-kinetic constants was not taken into account when obtaining (13-b). It does not result in rough errors as it was shown². Heat deposition in metal can be treated formally as pure surface effect for optical spectrum range starting with pulse duration $t > 10^{-13}$ s, when depth of skin layer is $\delta < (a_e t)^{1/2}$. Then, for $T_{e0} \gg T_e^0$ one can derive from (13-a, b) correspondingly the following asymptotic relations:

$$T_{e0} \approx \left[\frac{2q_0 A t}{c_e (T_e^0) \delta} T_e^0 \right]^{1/2} \sim t^{1/2}, \quad t \ll \delta^2 / a_e, \quad T_{e0} < \varepsilon_F / 2k_0, \quad (14-a)$$

$$T_{e0} \approx \left[\frac{4q_0 A \sqrt{a_e t}}{\sqrt{\pi} k_e} T_e^0 \right]^{1/2} \sim t^{1/4}, \quad t \gg \delta^2 / a_e, \quad T_{e0} < \varepsilon_F / 2k_0, \quad (15-a)$$

$$T_{e0} \approx \frac{q_0 A t}{c_e^* \delta} \sim t, \quad t \ll \delta^2 / a_e^*, \quad (14-b)$$

$$T_{e0} \approx \frac{2q_0 A \sqrt{a_e^* t}}{\sqrt{\pi} k_e^*} \sim t^{1/2}, \quad t \gg \delta^2 / a_e^*, \quad (15-b)$$

where $c_e = c_e^*$, $k_e = k_e^*$, $a_e = a_e^*$ are constants.

Variations of lattice temperature T can be described by simple relaxation equation (10) in the case when lattice thermal conductivity is much smaller than that of electron sub-system. Then space distribution of $T(x, t)$ corresponds to space distribution of electron temperature $T_e(x, t)$ and relation between them can be derived in the following form in the most general case:

$$T(x, t) = \frac{1}{\tau} e^{-\frac{t}{\tau}} \int_0^t T_e(x, t) e^{\frac{t}{\tau}} dt. \quad (16)$$

There are several simplified expressions for variations of lattice temperature (16) corresponding to certain particular cases. To come to particular case, the consideration below is limited by analysis of surface temperature $T(0, t) = T_0(t)$. For example, one can derive the following relation from (16) for early moments $t \ll \tau$.

$$T_0(t) = \frac{1}{\tau} \int_0^t T_{e0}(t) dt. \quad (17)$$

If electron temperature grows according to sub-linear or linear dependence (as it follows from relations (14) and (15), for example) within considered time interval $t > 0$ at the stage of laser-induced heating

$$T_{e0}^h(t) = \mu t^\nu \quad (18)$$

where μ and $0 \leq \nu \leq 1$ are parameters. Then it follows from (18) that by the end of laser pulse ($t = t_p$) electron temperature reaches the following value:

$$T_0^h(t_p) = \frac{t_p}{(\nu+1)\tau} T_{e0}^h(t_p); \quad T_{e0}^h(t_p) = \mu t_p^\nu. \quad (19)$$

Here and below there is introduced superscript "h" at symbol T denoting temperature at the stage of laser-induced heating of the metal in order to distinguish that stage and the stage of laser after-action. It is absolutely clear from (19) that lattice temperature is 100-200 times smaller than electron temperature by the end of laser pulse for typical values of pulse duration $t_p \sim 0.1$ ps and characteristic time of electron-phonon relaxation $\tau \sim 10$ ps. That means that significant thermal effect of laser

action in lattice should be expected after the end of laser pulse. Otherwise, heating of metal surface up to temperature of $T_0^h(t_p) \sim 1000$ K requires overheating of electron sub-system up to $T_{e0}^h(t_p) \sim 100-200$ kK.

3. THERMAL AFTER-ACTION OF LASER PULSE

Now the question is if it is possible growth of lattice temperature at metal surface after end of laser pulse. It may seem like the answer to this question is not difficult: heating after end of laser pulse (referred to as after-heating) is impossible if heat is deposited in metal lattice only during pulse action, and after-heating is possible if heat is deposited even after the end of laser pulse. In fact, there is more complicated but very certain condition determining principal change of character of laser after-action. That condition can be derived rigorously, if one limits consideration only within the case, when the only mechanism of heating (and cooling) is thermal conductivity and all material parameters stay constant with no dependence on temperature. The latter corresponds to linear problem of heat conductivity. Then, under action of "rectangular" laser pulse, after-heating of metal surface takes place within certain time interval after some decreasing of temperature after laser pulse is over if there is at least one point of inflection, on the curve describing metal heating (i.e., temperature growth in time)⁵.

Considering behavior of $T_0(t)$ at large time after the end of laser pulse ($t \gg t_p$), one can derive the following relation from (16):

$$T_0^c(t) = \frac{dT_0^h(t)}{dt} t_p = \frac{t_p}{\tau} [T_{e0}^h(t) - T_0^h(t)]. \quad (20)$$

Here and below superscript "c" point at that considered variations of temperature take place after end of "rectangular" laser pulse. It follows from (20) that the curve, describing metal cooling, has extreme if $T_t'' = 0$ at least at one point at the stage of laser heating. Substituting (16) into (20), one can obtain the following final result:

$$T_0^c(t) = \frac{t_p}{\tau} \left[T_{e0}^h(t) - \frac{1}{\tau} e^{-\frac{t}{\tau}} \int_0^t T_{e0}^h(t) e^{\frac{t}{\tau}} dt \right], \quad (21)$$

where lattice temperature at the stage of after-action is expressed through electron temperature that could be reached by the end of time interval t during laser action. There is one particular, but very important case when electron temperature grows in time according to sub-linear dependence (18) with power $\nu = 1/2$ (see formula 15-b). In that case one can derive the following relation

$$T_0^c(t) = \frac{e^{-\frac{t}{\tau}}}{\tau} \frac{\mu}{2} \int_0^t \frac{e^{\frac{t}{\tau}}}{\sqrt{t}} dt = \frac{\sqrt{\pi}}{2} \sqrt{\frac{t_p}{\tau}} T_{e0}^h(t_p) e^{-\frac{t}{\tau}} \operatorname{erfi} \left(\sqrt{\frac{t}{\tau}} \right), \quad (22)$$

where $\operatorname{erfi}(u) = \frac{2}{\sqrt{\pi}} \int_0^u e^{\xi^2} d\xi$ is table function.

According to (22), lattice temperature at metal surface reaches maximum value for $t = t_0 \approx 0.9\tau$. The value is given by the following formula:

$$T_{0\max}(t_0) \approx 0.48 \sqrt{\frac{t_p}{\tau}} T_{e0}^h(t_p), \quad (23)$$

Assuming $\tau/t_p = 100$ as it was done above, one comes to the following estimations:

$$\frac{T_{0\max}}{T_{e0\max}} \approx 0.048 \text{ and } \frac{T_{0\max}}{T_0^h(t_p)} \approx 7.2. \quad (24)$$

Lattice temperature grows up even after end of very short laser pulse in considered example. That corresponds completely to the mentioned above general principle because in the case, when electron temperature grows as $T_{e0}^h(t) \sim t^{1/2}$, then lattice temperature grows as $T_0^h(t) \sim t^{3/2}$ according to (17). At limiting case of large time ($t \gg \tau$) it follows from (16) that lattice

temperature varies as $T_0^h(t) \sim t^{1/2}$ because electron and lattice temperatures become very similar in that case. It means, that dependence $T_0^h(t)$ has at least one point of inflection.

It should be mentioned well-known example in connection with considered problems. According to it, lattice temperature cannot formally grow up (at least, at metal surface) after end of laser pulse even in spite of intensive heat transfer to the lattice. That can be obtained from considered above equations of thermal conductivity for electron sub-system and the lattice in the case when thermal capacity of electrons is neglected. That corresponds to approximation when fast initial heating of electrons is substituted by sharp step of temperature at initial time moment. Then equation (10), describing mutual variations of two temperatures, has a solution according to which the difference between electron and lattice temperatures θ is maximum at $t = 0$, and all the three functions $T_e(t)$, $T(t)$ and $\theta(t)$ are monotonous. In other words, a maximum of lattice temperature at metal surface is reached by the end of laser pulse and $T(t)$ decreases after the end of laser pulse. Physical reason of such behavior is connected with specific structure of temperature fields within electron and lattice sub-systems. The temperature fields are such that electron thermal conductivity cools metal surface so fast that electron-phonon relaxation can only slow down the process of metal-surface cooling in the case when there is no energy source (laser pulse is over).

4 DISCUSSION AND CONCLUSIONS

Presented consideration allows to obtain several estimations and to come to certain conclusions. First, growth of lattice temperature after end of laser pulse is not very large to provide effective destruction of metal surface. Really, assuming evaporation to be dominating destruction mechanism, one can estimate total thickness h of evaporated surface layer as follows:

$$h = \int_0^\infty V(T_0(t)) dt = s \int_0^\infty \exp\left[-\frac{T_a}{T_0(t)}\right] dt \quad (25)$$

Here it is assumed that speed of evaporation (V) is below sound speed in produced metal vapor (U) and because of that the evaporation speed depends on temperature strongly due to Arrhenius type of the dependence $V(T_0)$. The simplest but quite adequate evaporation model of Frenkel is utilized in (25)¹. The following values are denoted in (25): s is sound speed in the metal, T_a is barrier energy of phase transition liquid-vapor expressed in temperature degrees ($T_a \gg T_0$, $T_0 > T_m$, T_m is melting point). In the framework of this model the most contributions in (25) result from time interval corresponding to temperature close to its maximum value ($t \sim t_0$). Integrating (25) by applying method of saddle points, one comes to the following result:

$$h \approx V(T_{0 \max}) \tau \left(2\pi \frac{T_{0 \max}}{T_a} \right)^{1/2}. \quad (26)$$

Assuming lattice temperature $T_{0 \max}$ to be close to its upper limit ($T_0 \approx T_a/3 \sim 10\text{--}20$ kK, $V \approx 0.05$ s), one can obtain relation $h \approx 0.07 s \tau$ from (26). Thus, thickness of evaporated metal layer is about $h \sim 1$ nm for very typical values of sound speed $s \approx (2\text{--}3)$ km·s⁻¹ and characteristic time of electron-phonon collisions $\tau \sim 10$ ps. Total heat spent for evaporation (with taking into account heat of phase transition L) is about $Q \approx h(L + c_l T_{0 \max}) \sim 10$ mJ·cm⁻², while required laser intensity of incident radiation is about $q_0 \sim (0.1\text{--}1)$ TW·cm⁻² for pulse duration 0.1 ps.

Second, in order to provide such high values of lattice temperature (~ 10 kK), electron temperature at metal surface must reach the value of ~ 200 kK (see, for example, relation (24)). Real value of electron temperature must be at least two times more than obtained estimation because of heat spent for phase transition liquid-vapor. Moreover, attention should be paid to strong positive feedback between heating of electron sub-system and absorption of light resulting from temperature dependence of electron-electron collisions. That effect can give rise to fast thermal instability of the metal and appearing of nonlinear thermal-optical effect in a way similar to that considered in⁶.

To our mind, important conclusion from presented consideration is that existing thermal model of metal heating and destruction by super-short laser pulses is insufficient for correct description. Presented estimations have shown that electron thermal conductivity is very efficient cooling mechanism. It works so effectively and cools metal surface so fast that slowly increasing (within time interval of an order of $\sim \tau$) lattice temperature allows to provide evaporation of metal layer with thickness *a fortiori* smaller than $h \sim s \tau \sim 10$ nm even at large intensity of laser pulse. Taking into account of possible increasing of thickness of evaporated layer due to removal of melted metal by excessive vapor pressure results in no more than 2-3 time increasing of estimated thickness of evaporated metal layer. On the other hand, experimental data⁷ show that 500-fs laser pulse can remove a layer of copper with thickness of several micrometers at laser intensity $q_0 \sim 0.1$ TW·cm⁻².

Some new factors allowing to improve agreement between experimental data and theoretical models can be pointed, after presented above our consideration. The factors are intensive electron emission from metal surface and formation of double electric layer near the surface and appearing of self-consistent quasi-static electric field resulting from electron emission. It has already been pointed at possible important role of electron emission in early paper⁸. Really, at electron temperature $T_{e0} \sim 100$ kK and more, electron emission can result in practically complete dynamical ionization of metal surface leading to change of its structure and, as a consequence, change of destruction mechanism. The role of emission-induced quasi-static electric field cannot be reduced to decreasing of potential barrier for metal evaporation only as it was discussed for a bit different conditions of interaction⁹. Transition from evaporation to surface ionization of the metal can become more important factor for metal destruction. Electrostatic repulsion of ionized atoms at metal surface can be a mechanism of ionization including appearing of specific instabilities of plane ionization front.

5. ACKNOWLEDGEMENTS

The author wishes to thank S.I. Anisimov, V.L. Komolov, E.M. Minaeva, G. Petite, B. Rethfeld, and A.F. Semerok for fruitful discussions at different stages of this research, and V.E. Gruzdev for very important assistance. This work was partially supported by Russian Foundation for Basic Research (grant 00-02-16716a) and INTAS (project97-02-31777).

6. REFERENCES

1. Anisimov S.I., Bonch-Bruевич A.M., El'yashevich M.A., Imas Ya.A., Pavlenko N.A., Romanov G.S. // *Sov. Phys.-Tech. Phys.*, 1967, V. 11, P. 945.
2. Anisimov S.I., Rethfeld B. // *Proceedings of SPIE*, 1997, V. 3093, P. 192.
3. K.P.Gurov, Basics of kinetic theory, Moscow, Nauka, 1966, 351 pages.
4. M.N.Libenson, S.D.Pudkov. // *Sov. Phys. - Technical Physics*, 1977, V. 47, p. 2441.
5. V.L.Komolov, M.N.Libenson, G.D.Shandibina // *Izvestiia Akademii Nauk USSR, Ser. physicheskaiia*, 1985, V. 49, p. 1103.
6. M.N.Libenson // *Sov. Phys. - Technical Physics Letters*, 1979, V. 5, p. 256.
7. Semerok A., Chaléard C., Detalle V., Lacour J.-L., Mauchien P., Meynadier P., Nouvellon C., Sallé B., Palianov P., Perdrix M., Petite G. // *Appl. Surf. Sc.*, 1999, V. 138-139, P. 311.
8. Minaeva E.M., Libenson M.N. // *Proceedings of SPIE*, 1990, V. 1440, P. 63.
9. Golubev O.L. // *Journ. Phys. IV. Coll. C5 suppl. Journ. Phys. III*, 1996, V. 6, P. C5-159.

Pulsed laser deposition of nanometric and micrometric films for optoelectronic applications

M.L. De Giorgi, L. Elia, M. Fernandez, G. Leggieri, A. Luches, M. Martino and A. Zocco
I.N.F.M. and Università di Lecce, Dipartimento di Fisica, 73100 Lecce, Italy

Keywords: laser ablation, thin films, oxides, optoelectronics

Abstract

We ablated Si, SiO and ITO targets in low-pressure O₂ (0.1-5 Pa) with XeCl and KrF laser pulses at fluences of 5-8 J/cm². The films were deposited on Si <100> and glass (BK7) substrates at temperatures of 20-600°C. The substrates were generally set parallel to the target. To reduce droplet deposition, some films were deposited in off-axis configuration or using the so-called "eclipse method", characterized by a shadow mask between target and substrate. Dense, continuous ITO films with resistivity as low as 1.6×10^{-4} Ωcm and a high transparency (80-90%) in the visible region were deposited. Ultra-thin (~6 nm) films were deposited and successfully used as electrodes in optoelectronic devices. Dense, stoichiometric, thick (>2 μm) SiO₂ films were deposited on substrates either at room temperature or heated at moderate temperatures (100-600 °C). Droplet density and surface roughness are kept quite low (~5 nm) by using special deposition configurations. It results that multi-component films like ITO (indium tin oxide) and silica (SiO₂) can be efficiently deposited by using the reactive pulsed laser deposition technique.

1. Introduction

Thin films formed by indium and tin oxide (In₂O₃, ~90%; SnO₂, ~10%), called ITO films, can find applications as transparent conducting electrodes in solar cells, flat-panel displays and for realizing optoelectronic devices, since they present a high electrical conductivity and a high optical transparency in the visible and near-infrared range.¹ Silica (SiO₂) films are among the most used components in microelectronics and optoelectronics, due to their excellent optical and dielectric properties.

The pulsed laser deposition (PLD) method is emerging as a versatile technique. It has been successfully applied to the deposition of thin films of an extremely wide range of materials.² The ability to deposit films with complex compositional profiles at low substrate temperature is a significant advantage of this technique with respect to the traditional ones. When PLD is performed in a low-pressure atmosphere to promote chemical reactions among the ablated species and the ambient gas or vapor, it is called reactive pulsed laser deposition (RPLD). ITO and silicon oxide (SiO_x, 1<x<2) films were already deposited by using the RPLD technique.^{3,4} Our aim was to deposit very thin ITO films and very thick SiO₂ films, to be used in optoelectronic devices. Very thin (a few nm) ITO films are needed in optical commutators. Otherwise the applied electric field could not cross the electrode. In contrast, relatively thick (~2 μm) silica films are needed in integrated optics as buffer layers between a low refractive index optical waveguide and the underlying high refractive index silicon substrate.

In this paper, we present a study of the characteristics of ITO and SiO₂ films deposited by RPLD without a post-deposition anneal. Film properties were measured as a function of the oxygen ambient pressure, of the laser fluence, of the target-to-substrate distance and configuration.

2. Experimental apparatus

Depositions of films were performed in stainless steel vacuum chambers, which were evacuated down to 2×10^{-5} Pa before the introduction of high purity molecular oxygen. The targets were an ITO disc for ITO film deposition, and a Si wafer or a SiO disc for SiO₂ film deposition. They were ablated by using either a XeCl (λ=308 nm) or a KrF (λ=248 nm) excimer laser. The laser pulse length was 30 ns. The laser fluence at the target was 5-8 J/cm². The pulse repetition rates were 10 and 25 Hz, for the XeCl and the KrF laser, respectively. The films were deposited on Si wafers or glass (BK7) plates at temperatures of 20-600 °C.

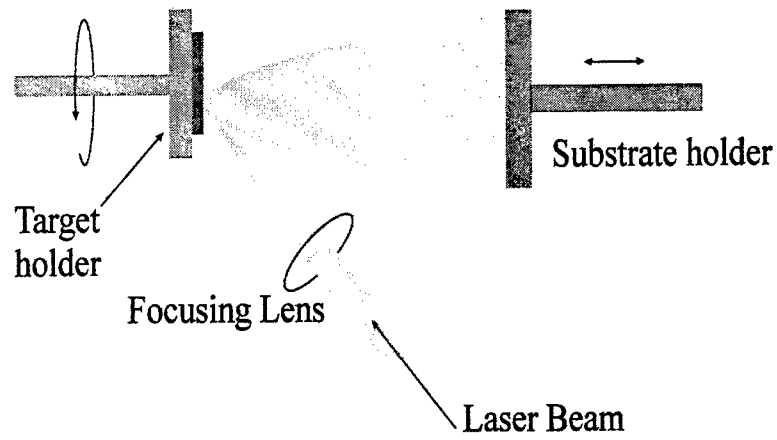


Fig. 1. Deposition system in the on-axis configuration

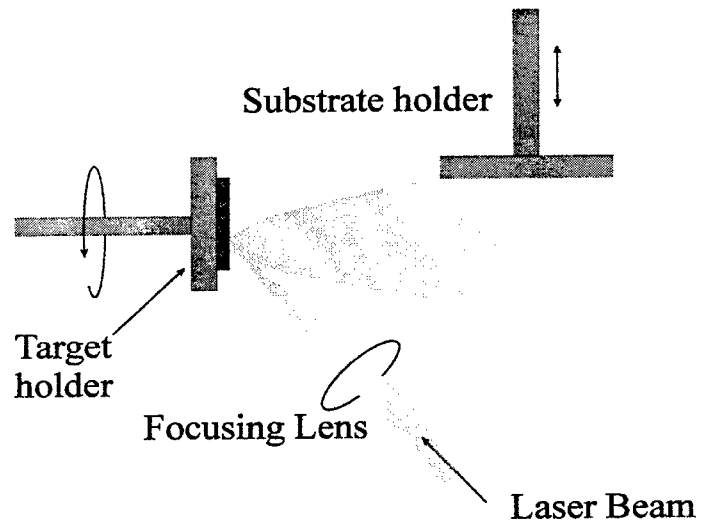


Fig. 2. Deposition system in the off-axis configuration

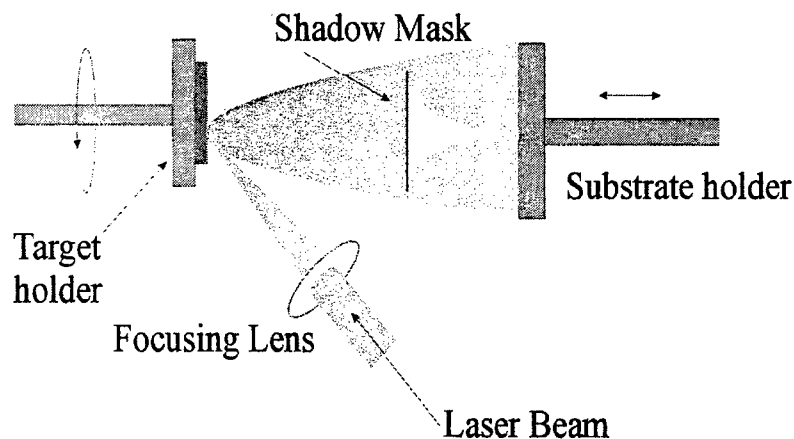


Fig. 3. Deposition system in the eclipse configuration

Besides the traditional on-axis configuration (Fig. 1), where the target and substrate are placed parallel at a certain distance d , some SiO_2 films were deposited in the off-axis configuration⁵ (Fig. 2) or using the “eclipse method”⁶ (Fig. 3), characterized by a shadow mask between target and substrate. Our aim was to reduce droplet deposition, which is the well-known drawback of the PLD technique.

After deposition, the films were analyzed by several diagnostic techniques: atomic force (AFM) and scanning electron microscopy (SEM) were used to evaluate roughness and surface morphology, Rutherford backscattering spectrometry (RBS) with 2 MeV He^+ ions and optical profilometry to evaluate the film thickness, Fourier-transform infrared spectroscopy (FT-IR) to study the chemical structure of the deposited materials. The electrical resistivity of the ITO films was measured with a 4-point resistive probe.

3. Results

3.1 ITO film deposition

ITO films were deposited by using the XeCl laser only. In fact, XeCl laser pulses efficiently ablate the ITO targets. After some tests, it was found that the best set of parameters was: oxygen ambient pressure $p=1$ Pa, laser fluence $F=6$ J/cm², substrate temperature $T=200$ °C. By using these values, ITO films were deposited on BK7 substrates placed at $d=6.3$ cm from the target. Table 1 shows the thickness of the deposited films, as measured with a Sentech FTP 500 optical profilometer.

Table 1: parameters of ITO films deposited by using the XeCl laser

Pulse number	Thickness (nm)	Deposition rate (nm/pulse)
3000	35	0.012
3500	38	0.011
10000	78	0.008
15000	125	0.008

The slow decrease of the ablation rate with increasing successive pulse number is a typical feature of the laser ablation process, due to the slow erosion of the target. The thickness uniformity across the film was found to be within 2-3 nm.

The Transmissivity curve of a typical sample is shown in Fig. 4. The transmissivity in the visible and near infrared range is within 80-90%.

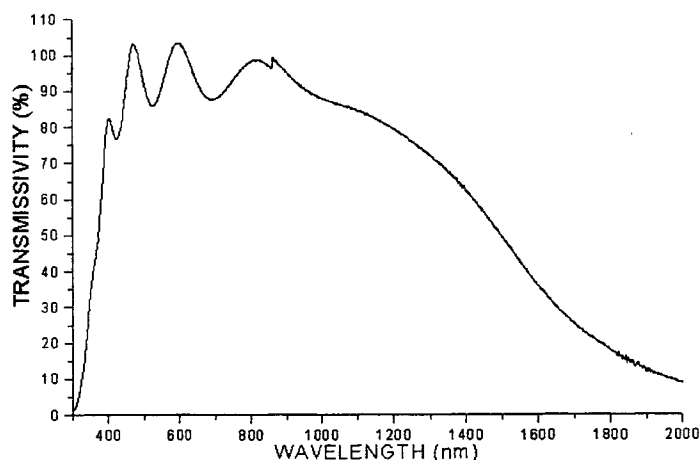


Fig. 4. Transmissivity vs. wavelength of an ITO film, as measured with a single-beam spectrophotometer.

The electrical resistivity of the films was found as low as $1.6 \times 10^{-4} \Omega\text{cm}$, among the best ones in literature. It increases to $2.4 \times 10^{-4} \Omega\text{cm}$ for samples deposited on substrates at room temperature, in otherwise identical experimental conditions. The decrease of the resistivity with increasing substrate temperature can be due to the increasing of the grain size with temperature, thus reducing the grain boundary scattering.³ Resistivity variation across the samples is within $\pm 2\%$, confirming good thickness uniformity of the deposited films.

Once known the deposition rate, very thin ITO films (nominally 6 nm) were deposited with 500 laser pulses. They were successfully used as electrodes in a liquid crystal electro-optic commutator.

3.2 SiO₂ film deposition

The parameters of some SiO₂ films deposited on substrates at room temperature by using a XeCl excimer laser in the traditional on-axis configuration are given in Table 2.

Table 2: parameters of SiO₂ films deposited by using the XeCl excimer laser and the on-axis configuration

Target	Fluence (J/cm ²)	p O ₂ (Pa)	d (mm)	Number of pulses	Thickn. (nm)	Comp.
Si	5	0.1	50	20 000	200	Si ₅ O ₈
SiO	6	0.1	50	20 000	1600	SiO ₂
SiO	6	1	50	80 000	>2000	SiO ₂

As inferred from RBS spectra, stoichiometric SiO_2 films were deposited by ablating SiO targets already at the O_2 ambient pressure of 0.1 Pa. At the same pressure, sub-stoichiometric films (Si_3O_5) were deposited when ablating Si targets.

SEM micrographs show that the film deposited by ablating the Si target contains a high density of droplets with characteristic sizes of a few microns (Fig. 5).

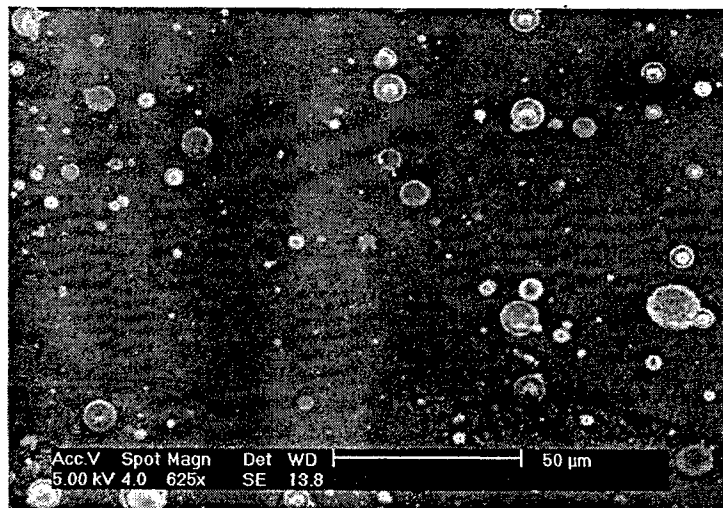


Fig. 5. SEM micrograph of the films deposited by ablating a Si target with XeCl laser pulses in the on-axis configuration

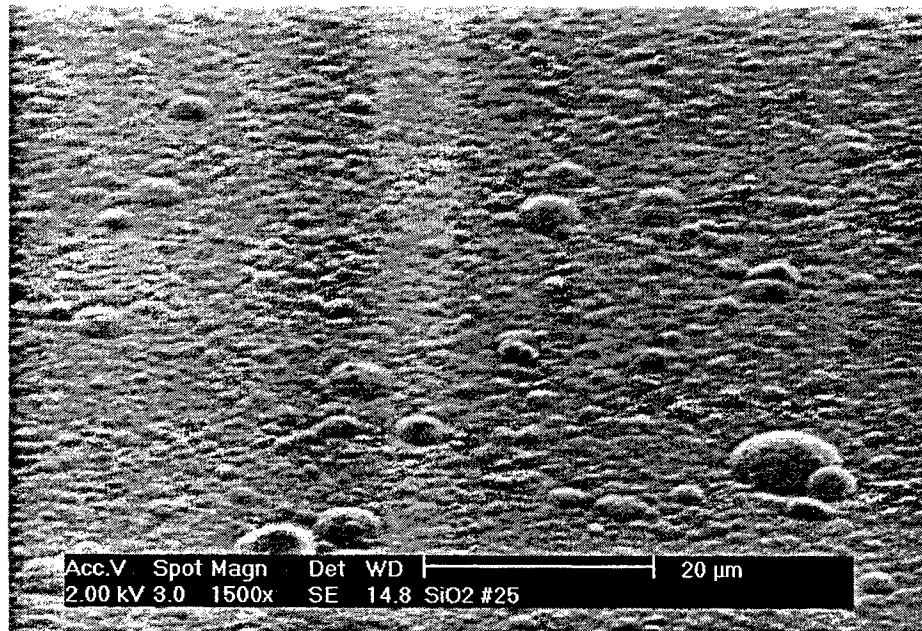


Fig. 6. SEM micrograph of the films deposited by ablating a SiO target with XeCl laser pulses in the on-axis configuration

The deposition rate resulted much higher when SiO targets were ablated, with respect to Si targets. However the surface is still rough and the droplet density is high (Fig. 6).

To try to avoid droplet deposition, we deposited some samples by using the off-axis configuration. The parameters of some SiO₂ films deposited on substrates at room temperature by using a XeCl excimer laser in the off-axis configuration are given in Table 3.

Table 3: parameters of SiO₂ films deposited by using the XeCl excimer laser and the off-axis configuration

Target	Fluence (J/cm ²)	p O ₂ (Pa)	d (mm)	Number of pulses	Thickn. (nm)	Comp.
Si	8	35	20	40 000	1000	SiO ₂
SiO	8	2	20	80 000	>2000	SiO ₂

As inferred from RBS spectra, stoichiometric SiO₂ films were deposited.

SEM micrographs show that samples deposited in the off-axis configuration are generally smoother and with a much lower density of droplets with respect to the ones deposited in the on-axis configuration (Fig. 7).

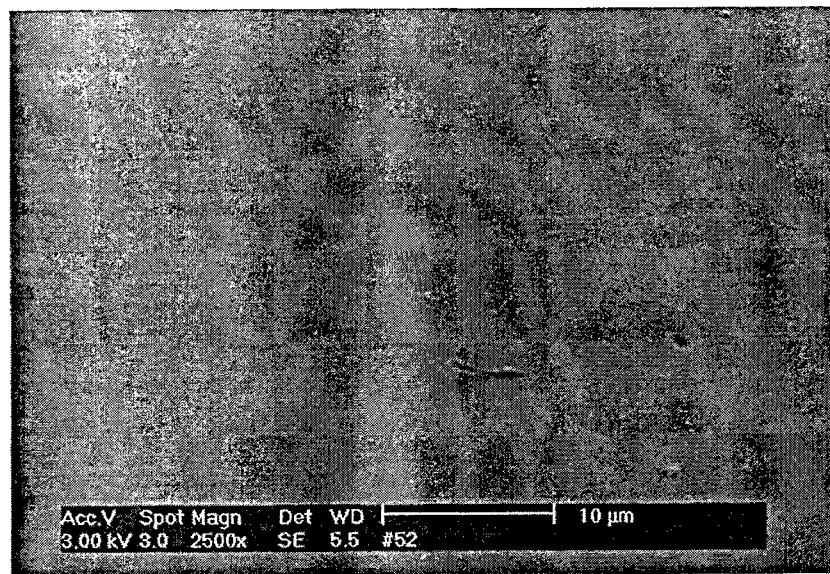


Fig. 7. SEM micrograph of the films deposited by ablating a SiO target with XeCl laser pulses in the off-axis configuration

Some samples seem effectively droplet-free, but it appears that their thickness is not uniform, since it decreases with distance from the target.

Also the samples deposited with the eclipse method are very smooth, but they are uniform in thickness across their whole surface and almost droplet-free, as seen from SEM inspection (Fig. 8).

From AFM inspections, it emerges that the average roughness of the films is higher in the conventional on-axis configuration with respect to the eclipse method (~200 nm against ~50 nm, respectively, in average samples). However, the deposition rate in eclipse configuration is much lower than the one in the traditional on axis configuration (Table 4).

Table 4: parameters of SiO₂ films deposited by using the XeCl excimer laser and the eclipse configuration

Target	Fluence (J/cm ²)	Press. O ₂ (Pa)	d (mm)	Number of pulses	Thickn. (nm)	Comp.
Si	6	10	50	30 000	350	SiO ₂
Si	6	1	50	40 000	570	SiO ₂

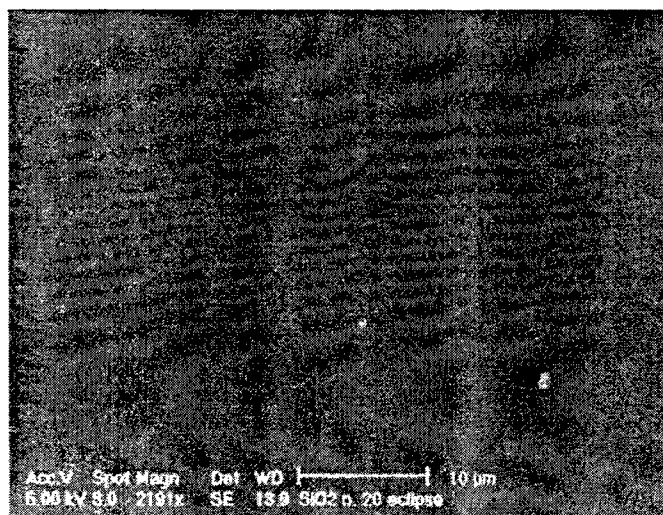


Fig. 8. SEM micrograph of the films deposited by ablating a Si target with XeCl laser pulses in the eclipse configuration

A good compromise between a low smoothness and a reasonable deposition rate is obtained when depositions are performed in a large vacuum chamber, which allows a quite large target-to-substrate distance, in the on-axis configuration. We deposited SiO₂ films by using such an apparatus and a KrF laser (Table 5).

Table 5: parameters of SiO₂ films deposited by using the KrF excimer laser and the on-axis configuration

Target	Temp. (°C)	Fluence (J/cm ²)	Press. O ₂ (Pa)	Tar.-Subs. dist. (mm)	Number of pulses	Thickn. (nm)
Si	20	7	5	80	75 000	1500
Si	20	7	5	120	75 000	700
Si	150	6	5	80	75 000	1900
Si	300	7	5	80	75 000	1800
Si	450	8	5	80	75 000	1800
Si	600	7	5	80	75 000	1850
SiO	150	8.5	1	80	420 000	>2000

SiO₂ films deposited by using the KrF laser beam in a deposition chamber, which allows larger target to substrate distances (80-120 mm), generally show a much lower average roughness (5 to 30 nm) and droplet density with respect to the

samples deposited by using the XeCl laser (Fig. 9). This effect could also be partly due to the moderate (150-600 °C) heating of the substrates.

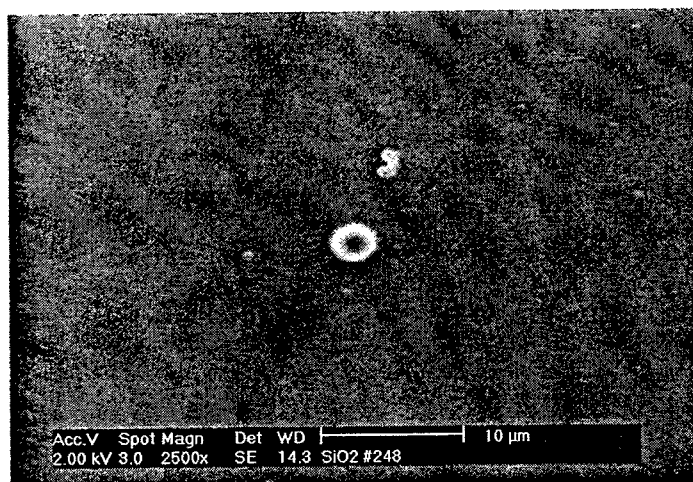


Fig. 9. SEM micrograph of the films deposited by ablating a Si target with KrF laser pulses in the on-line configuration at the O_2 pressure of 5 Pa and at the substrate temperature of 150 °C.

It has to be underlined that RBS spectra always show a good stoichiometry of the deposited films. An example of a RBS spectrum can be seen in Fig. 10.

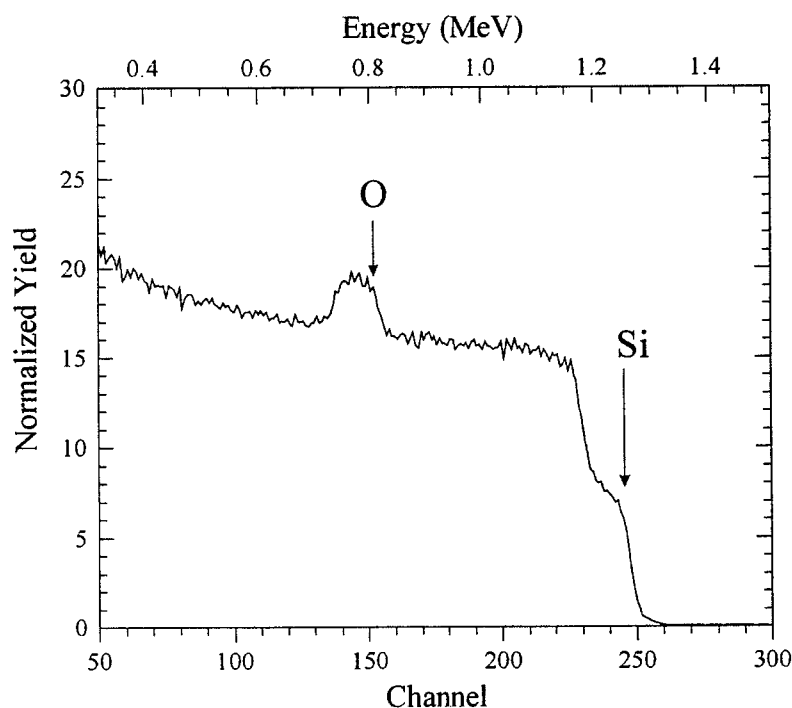


Fig. 10. A typical RBS spectrum of a laser deposited SiO_2 film

However, RBS spectra, while showing the correct ratio between the Si and O atoms in the films, cannot give any information about the chemical links among atoms in the films, due to the high energy (2.2 MeV) of the probing particles (He^+).

Chemical bonds were studied by FT-IR spectroscopy. In the range $400\text{--}4000\text{ cm}^{-1}$ there exist three infrared vibration modes of amorphous or crystalline silicon oxide.⁷ The IR mode at $\sim 450\text{ cm}^{-1}$ is a rocking vibration, in which the oxygen atom motion is out of the Si-O-Si bonding plane; the mode at $\sim 800\text{ cm}^{-1}$ is a bending vibration, with the oxygen atom motion in the Si-O-Si bonding plane; the vibration at $\sim 1075\text{ cm}^{-1}$ is an asymmetric stretching mode, in which the oxygen atom motion is in the Si-O-Si plane and parallel to the line joining two Si atoms.

Figure 11 shows a typical FR-IR spectrum of a laser deposited SiO_2 film, in which the silicon dioxide absorption modes are clearly evident. In the figure, besides the SiO_2 modes, other peaks are clearly apparent. The broad absorption bands around 3350 and 3600 cm^{-1} are usually attributed to O-H stretching modes (from loosely bonded SiOH or adsorbed water).⁸ The small absorption band around 1630 cm^{-1} is attributed to water absorbed in the film.⁹ The absorption band at $\sim 940\text{ cm}^{-1}$ is attributed to a Si-OH bending mode with nonbridging oxygen atoms.⁸ The peaks around 670 , 2325 and 2350 cm^{-1} can be attributed to atmospheric CO_2 . Finally, the absorption band around 1075 cm^{-1} , attributed to the asymmetric stretching mode, shows a pronounced shoulder on the high-wavenumber side, which could be attributed to disorder and/or defects in the silicon dioxide film.¹⁰

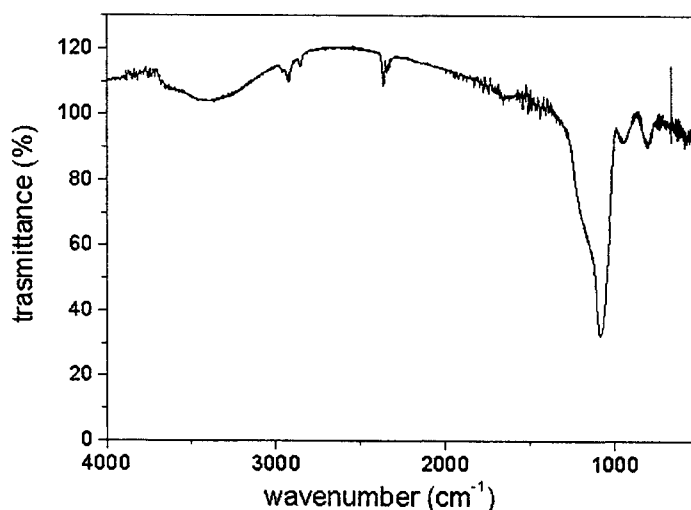


Fig. 11. FT-IR spectrum of the films deposited by ablating a Si target with KrF laser pulses in the on-line configuration at the O_2 pressure of 5 Pa and at the substrate temperature of 150°C .

The FT-IR spectra of the laser deposited films, which clearly show the SiO_2 characteristic absorption features at ~ 450 , 800 and 1075 cm^{-1} , ensure that films are not a mixture of silicon and oxygen, but that the elements are chemically bonded to form silicon dioxide.

4. Conclusions

ITO films were deposited whose quality was found good for optoelectronic applications. We successfully deposited also thick stoichiometric SiO_2 films. It was shown that by using a XeCl excimer laser and the eclipse method it is possible to deposit smooth, almost droplet free SiO_2 films, but at a very low deposition rate ($\sim 10^{-2}\text{ nm/pulse}$). Relatively thick films ($>2\text{ }\mu\text{m}$), with a quite low density of droplets, can be more rapidly obtained by using the KrF excimer laser, a moderate substrate temperature and a relatively large (80-120 mm) substrate-to-target distance.

Acknowledgments

Work supported by INFN under the PAIS project. We thank G. Majni for help in recording RBS spectra.

References

1. H. Kim, A. Piqué, J. S. Horwitz, H. Mattoussi, H. Murata, Z. H. Kafafi, D. B. Chrisey, "Indium tin oxide thin films for organic light-emitting devices", *Appl. Phys. Lett.* 74, p. 3444, 1999.
2. J. S. Horwitz, H. -U. Krebs, K. Mukarami, M. Stuke (Eds.), "Laser Ablation – Proceedings of the 5th International Conference", *Appl. Phys. A* 69 (Suppl.), Springer, 1999.
3. H. Kim, J. S. Horwitz, A. Piqué, C. M. Gilmore, D. B. Chrisey, "Electrical and Optical Properties of Indium Tin Oxide Thin Films Grown by Pulsed Laser Deposition", *Appl. Phys. A* 69, p. S 447, 1999.
4. E. Fogarassy, C. Fuchs, A. Slaoui, S. de Unamuno, J. P. Stoquert, W. Marine, B. Lang, "Low-Temperature Synthesis of Silicon Oxide, Oxynitride, and Nitride Films by Pulsed Excimer Laser Ablation", *J. Appl. Phys.* 76, p. 2612, 1994.
5. N. Inoue, T. Ozaki, T. Monnaka, S. Kashiwabara, R. Fujimoto, "A New Pulsed Laser Deposition Method Using an Aperture Plate", *Jpn. J. Appl. Phys.* 36, p. 704, 1997.
6. K. Kinoshita, H. Ishibashi, T. Kobayashi, "Improved Surface Smoothness of $\text{YBa}_2\text{Cu}_3\text{O}_y$ Films and Related Multilayers by ArF Excimer Laser Deposition with Shadow Mask Eclipse Method", *Jpn. J. Appl. Phys.* 33, p. L417, 1994.
7. T. Hirata, "Evolution of the Infra-Red Vibrational Modes upon Thermal Oxidation of Si Single Crystals", *J. Phys. Chem. Solids* 58, p. 1497, 1998.
8. W.A. Pliskin, "Comparison of Properties of Dielectric Films Deposited by Various Methods", *J. Vac. Sci. Technol.* 14, p. 1064, 1977.
9. A. Slaoui, E. Fogarassy, C. W. White, P. Siffert, "Infrared Characterization of UV Laser-Induced Silicon Oxide Films", *Appl. Phys. Lett.* 53, p. 1832, 1988.
10. P. Lange, "Evidence for Disorder-Induced Vibrational Mode Coupling in Thin Amorphous SiO_2 Films", *J. Appl. Phys.* 66, p. 201, 1989.

Photoelectrical properties of nonuniform semiconductor under infrared laser radiation

S. Ašmontas^{*a}, J. Gradauskas^a, D. Seliuta^a, E. Širmulis^b

^aSemiconductor Physics Institute, A. Goštauto 11, Vilnius 2600, Lithuania

^bInstitute of Physics, A. Goštauto 12, Vilnius 2600, Lithuania

ABSTRACT

Photoelectrical properties of nonuniform semiconductor under infrared laser radiation has been investigated theoretically and experimentally. It is shown that photoemission of hot carriers across the potential barrier and the crystal lattice heating are dominant mechanisms of the photovoltage formation in p-n and l-h junction when laser photon energy less than the semiconductor energy gap. Influence of aluminum arsenide mole fraction in GaAs/Al_xGa_{1-x}As p-n heterojunction on CO₂ laser radiation detection has been studied. It has been established that the photoresponse originating from the free carrier heating depends on the energy band discontinuities in heterojunction. GaAs/Al_xGa_{1-x}As heterojunction with $x \leq 0.2$ is found to be more suitable for infrared detection compared to GaAs homojunction. In metal-semiconductor Schottky contact, photoresponse demonstrates strongly nonlinear (superlinear) dependence on excitation intensity when photon energy is less than Schottky barrier height. We suppose that in this case the photosignal is caused by the multiphoton and multistep electron photoemission across the Schottky barrier.

Key words: infrared detectors, hot carriers, p-n junction, l-h junction, infrared laser, nonlinear photoresponse, photoelectromotive force

1. INTRODUCTION

When nonuniform semiconductor is illuminated with infrared laser radiation the photovoltaic effect is observed. It is known that two mechanisms are dominant in the photovoltage formation. When photon energy $h\nu$ is larger than the forbidden energy gap E_g illumination of semiconductor leads to electron-hole pair generation. In the case of nonuniform semiconductor an ordinary photovoltaic effect occurs due to separation of electrons and holes by internal electric field of inhomogeneity. When light photon energy is smaller than the forbidden energy gap intraband absorption of light by free carriers leads to free carrier heating. The photovoltage appears due to thermoelectromotive force of optically excited hot carriers. In this case the photovoltage polarity is opposite to that of the ordinary photovoltaic effect. The hot carrier photovoltage was observed for the first time in germanium junctions under CO₂ laser radiation¹. Later the hot carrier photovoltage in Si, GaAs, InSb p-n and l-h junctions has been investigated²⁻⁴. Since the hot-carrier energy relaxation time is of the order $10^{-11} \div 10^{-12}$ s devices based on the free carrier heating can be used as fast infrared detectors⁵. In present paper we survey research of the photovoltaic effect arising in nonuniform semiconductor under infrared laser radiation when photon energy is smaller than the energy gap E_g .

2. EXPERIMENTAL DETAILS

The investigated GaAs junctions were made by melting of metal into GaAs substrate or by liquid-phase epitaxial growing of $3 \div 5$ μm layers followed by etching of square mesas (400×400 μm^2). Diameter of the melted contact was around 0.5 mm. Contact size was adjusted to be approximately equal to the laser beam diameter ($200 \div 400$ μm). GaAs/Al_xGa_{1-x}As p-n heterojunctions with different Al concentration x were fabricated using liquid-phase epitaxy. Four types of structures ($x=0, 0.1, 0.2$, and 0.3) have been investigated.

Schottky barrier structures were prepared on n-type monocrystalline silicon wafers of resistivity 1 Ohm-cm. Schottky contacts of 400 μm diameter were formed by deposition of titanium using dc magnetron sputtering followed by thermal

* Correspondence: Email: asmontas@ujpfi.lt; Telephone: 370-2 - 627124; Fax: 370-2-627123

annealing in argon atmosphere. Schottky barrier height ϕ_B determined from the current-voltage (I-V) characteristic was found within the range 0.5 ± 0.6 eV.

Excitation at wavelength $10.6 \mu\text{m}$ was obtained from passively Q-switched CO_2 laser producing 200 ns pulses at repetition rate about 30 Hz. Experiments at wavelengths $2.79 \mu\text{m}$ and $3\div 7 \mu\text{m}$ were performed using nanosecond pulses of erbium (Er:YSGG) laser ($\tau=60$ ns) and picosecond pulses of optical parametrical oscillator PG401DFG ($\tau=15$ ps), respectively. Both of them operated at repetition rate $1\div 2$ Hz. Incident power of the laser beam routinely was varied with neutral Teflon filters. For precise measurements gaseous absorber cell was used. The peak-pulse intensity was measured with germanium photon-drag or pyroelectric photodetector. Epitaxial structures were illuminated from the epi-layer side and the melted junctions and Schottky contacts – from the substrate side. In order to increase excitation intensity the incident light beam was focused on sample surface. Maximum power density was around 10 MW/cm^2 . Temporal behavior of the photosignal and the laser pulse in nanosecond time scale was recorded with digital storage oscilloscope LE'CROY 9360 with sampling rate $5 \cdot 10^9 \text{ s}^{-1}$.

3. RESULTS AND DISCUSSION

3.1 Photoresponse of p-n Junction

When p-n junction is illuminated with CO_2 laser radiation forward current increases due to the free carrier heating. Figure 1 depicts dependence of the photocurrent I_{ph} on bias voltage applied to GaAs p-n junction. It is seen that abrupt increase of the photocurrent takes place when bias voltage "opens" the junction. In reverse bias region magnitude of the photocurrent varies negligibly with external voltage. It has been shown^{3,5} that the negligible variation of the photocurrent at reverse and low forward voltage is caused by recharging of the junction capacitance when it is affected by a short laser pulse (displacement current or capacitive current). Direction of the photocurrent at reverse bias voltage indicates that there is no appreciable change of carrier concentration in GaAs p-n junction under CO_2 laser radiation.

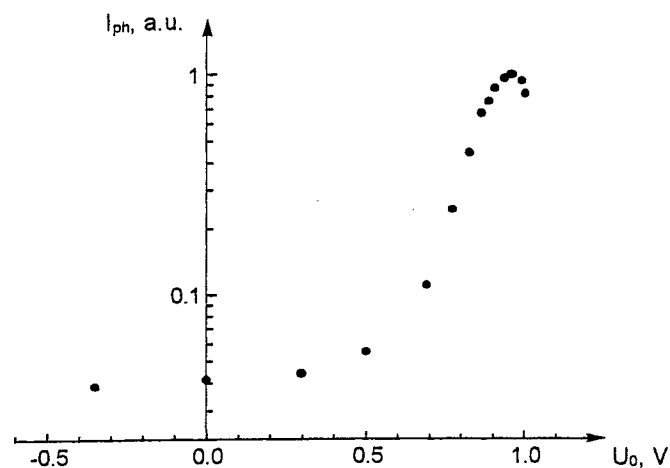


Fig. 1. Photocurrent in GaAs p-n junction versus bias voltage.
 $T_0=300 \text{ K}$

With increasing forward bias p-n junction barrier height is decreased. This results in increase of the hot carrier diffusion across the potential barrier. When the hot-carrier injection current becomes larger than the capacitive current exponential increase of I_{ph} with U_0 is observed. At higher U_0 values the photocurrent reaches maximum and starts to decrease (Fig. 1). It should be noted that the photocurrent reaches maximum at bias value U_m which is close to the p-n junction diffusion potential V_K . In asymmetrical p-n junction, when p-region of the junction is doped much more heavily than n-region:

$p_n \gg n_p$, (1)
the hot-hole photocurrent is given by⁶:

$$j_{ph} = j_{ps} \left\{ \exp \left[\frac{eU_0}{kT_p} + \frac{eV_K}{kT_0} \left(1 + \frac{T_0}{T_p} \right) \right] - 1 \right\} - j_{ps0} \left\{ \exp \left[\frac{eU_0}{kT_0} \right] - 1 \right\}, \quad (2)$$

where $j_{ps0} = eD_p p_n / L_p$ is the saturation current in the dark, j_{ps} is the saturation current under illumination, e is electron charge. D_p and L_p are the diffusion coefficient and the diffusion length of holes, respectively, T_0 is the lattice temperature and T_p is the hot-hole temperature. Value of bias voltage corresponding to the photocurrent maximum U_m can be obtained by differentiating Eq. 2 with respect to U_0 :

$$U_m = V_K - \frac{k T_0 T_p}{e (T_p - T_0)} \ln \frac{T_p j_{ps0}}{T_0 j_{ps}}. \quad (3)$$

At higher values of forward bias ($U_0 > U_m$) the photocurrent starts to decrease in agreement with previous experiments⁵⁻⁷. With further increase of forward bias the potential barrier of p-n junction becomes negligible and the hot-carrier photocurrent disappears. It follows from Eq. 2 that in case when the saturation current of p-n junction does not depend on carrier temperature the photocurrent equals zero at $U_0 = V_K$. Usually small photosignal is observed even at $U_0 \geq V_K$ because of dependence of the carrier mobility, diffusion coefficient and lifetime on temperature.

Measurements of the photocurrent in GaAs/Al_xGa_{1-x}As p-n heterojunctions with different aluminum mole fraction x have shown that increase in x causes shift of the maximum photocurrent voltage U_m towards higher values of forward bias (Fig. 2). The shift originates from increased diffusion potential V_K in heterojunction with respect to homojunction due to energy band discontinuities ΔE_C and ΔE_V (Fig. 3). One should note that potential barriers for electrons and holes are different and increase of U_m in heterostructure is determined by both ΔE_C and ΔE_V . Besides, the shift also depends on electron and hole concentration in p-n heterojunction. We found experimentally that the shift of the maximum voltage U_m is approximately equal to average of quantities ΔE_C and ΔE_V (60 mV for AlAs fraction 0.1).

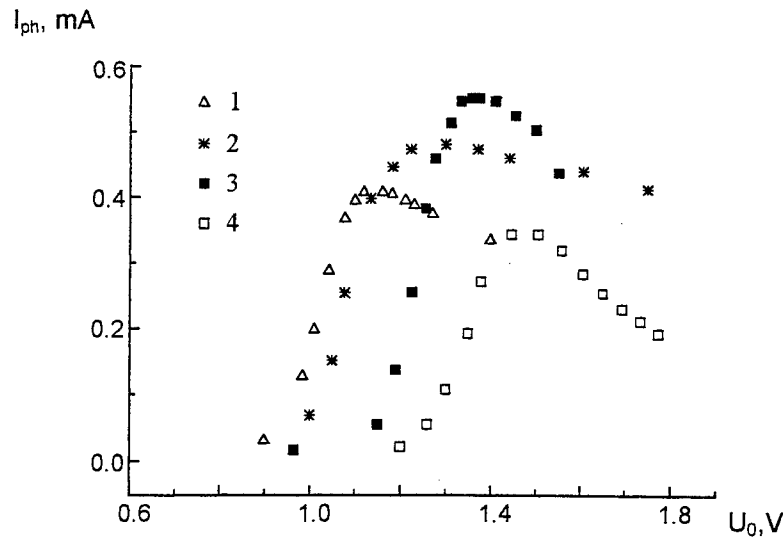


Fig. 2. Photocurrent in GaAs/Al_xGa_{1-x}As p-n heterojunction versus bias voltage. $T_0 = 300$ K. Aluminum concentration x : 1-0, 2-0.1, 3-0.2, 4-0.3.

It is seen from Fig. 2 that magnitude of the photocurrent originating from the free carrier heating depends on the energy band discontinuities to photon energy ratio. When $x \leq 0.2$ maximum value of the photocurrent increases with increasing x . For higher AlAs fraction ($x > 0.2$) the effect is opposite: photocurrent starts to decrease with increasing x . To explain such a behavior of the photocurrent one has to analyze how the energy band discontinuities vary with x . If $x \leq 0.2$ the valence band discontinuity ΔE_V is less than photon energy and the photoexcited holes can overcome the potential barrier. (Note that due to strong asymmetry of doping the hot-electron photocurrent may not be taken into account). When $x = 0.3$ ΔE_V becomes greater than $h\nu$ and major part of hot holes can not overcome the valence band barrier. Therefore, for $x > 0.2$ the photocurrent maximum value decreases with increase in AlAs mole concentration.

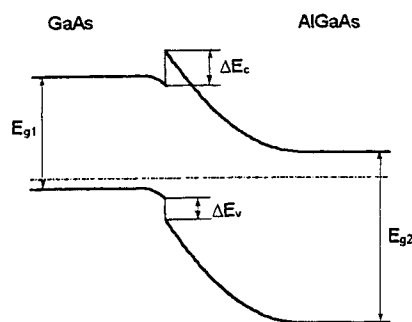


Fig. 3. Energy band diagram of GaAs/AlGaAs p-n heterojunction.

3.2 Photoresponse of l-h Junction

It has been shown in previous section that maximum photocurrent is observed when forward bias voltage is close to V_K and the potential barrier height is much less than that at zero bias. Therefore, for many practical cases in development of infrared detectors and sensors it is more convenient to use l-h (low-high doping) junctions characterised by small potential barrier. Dependence of the photoemf (photovoltage without external bias voltage) in GaAs n-n⁺ and p-p⁺ junctions upon laser intensity is shown in Fig. 4. It should be noted that the photoemf linearly depends on laser intensity. The same dependence has been observed in germanium and silicon l-h junctions^{4,8}. It is also seen from Fig. 4 that the photoresponse in n-n⁺ junction is of the same order of magnitude as that in p-p⁺ junction. It implies that at given excitation intensity the hot-electron temperature is close to the hot-hole temperature.

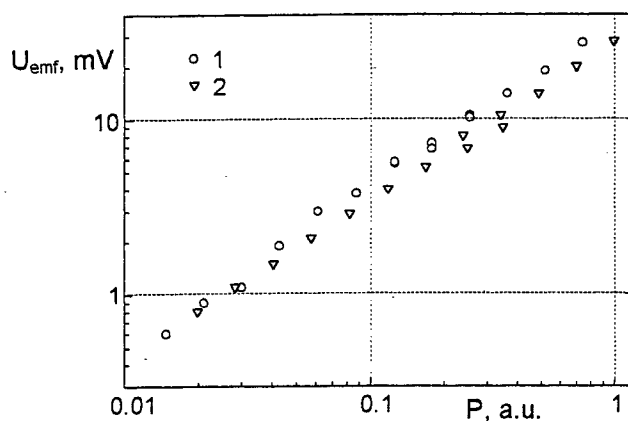


Fig. 4. Photoemf in GaAs l-h junctions versus laser intensity at room temperature. 1 - n-n⁺ junction. 2 - p-p⁺ junction.

It has to be noted that in case of long excitation pulse (duration of hundreds of nanoseconds) the observed photoresponse consists of two components:

$$U_{ph} = U_f + U_T. \quad (4)$$

where U_f is the fast component caused by the free carrier heating and U_T is the slow component caused by the crystal lattice heating.

In order to evaluate U_f and U_T temporal behavior of CO₂ laser intensity has been approximated as:

$$P(t) = P_m \left(\frac{t}{\tau} \right)^4 \exp \left[-4 \left(\frac{t}{\tau} - 1 \right) \right], \quad (5)$$

where I_m is the peak intensity at $t=\tau$, τ is the laser pulse rise time. When the rise time τ is long compared to the hot-carrier energy relaxation time the fast component of the photoemf can be given as:

$$U_f(t) = k_f P(t). \quad (6)$$

The slow component of the photosignal $U_T(t)$ is obtained from relation:

$$\frac{dU_T(t)}{dt} = \frac{\bar{U}_T - U_T(t)}{\tau_T}, \quad (7)$$

where $\bar{U}_T = k_T P(t)$, τ_T is a characteristic decay time of the photoemf.

Solution of Eq. 7 is:

$$U_T = \frac{24 k_T P_m e^4}{\tau_T \tau^4 a^5} \left[\left(1 - ta + \frac{(ta)^2}{2} - \frac{(ta)^3}{6} + \frac{(ta)^4}{24} \right) \times \exp \left(-\frac{4t}{\tau} \right) - \exp \left(-\frac{t}{\tau_T} \right) \right], \quad (8)$$

where $a = 1/\tau_T - 4/\tau$. The coefficients k_T and k_f can be found from the experimental values of the photoemf at $t=\tau$ and $t=t_m$, respectively; t_m is defined by $dU_T/dt=0$ at the moment $t=\tau_m$.

Oscilloscope traces of the laser pulse and the photoresponse pulse in melted GaAs n-n⁺ junction are shown in Fig.5. It is seen that calculated curves are in agreement with experimental traces. Thus, the above approximation allows us to separate and determine both the hot-carrier photovoltage and the thermoelectric effect caused by the crystal lattice heating.

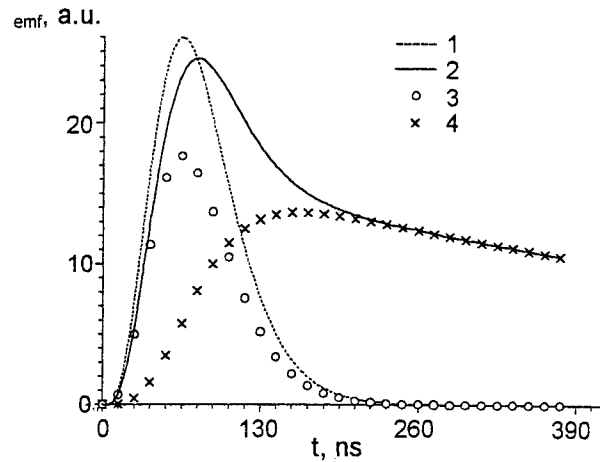


Fig. 5. Experimental traces of CO₂ laser pulse (1) and photoemf pulse in GaAs n-n⁺ junction (2). Calculated traces of the fast component U_f (3) and the thermal component U_T (4).

3.3 Photoresponse of Metal-Semiconductor Schottky Contact

In Schottky contact the photovoltage caused by the electron-hole pair generation and the free-carrier heating may also be observed. However, in metal-semiconductor contact there is an additional photoresponse mechanism - emission of the hot carriers across the Schottky barrier. The latter effect is significant when photon energy is greater than Schottky barrier height and less than the forbidden energy gap.

It is known that linear photoresponse of metal-semiconductor contact rapidly drops down as light wavelength is increased and vanishes when the barrier height exceeds photon energy. The same happens at metal-vacuum boundary: photovoltage disappears when photon energy becomes less than the metal work function. However, it has been found that nonlinear photoeffect may be observed even if the photon energy is several times smaller than the metal work function. Using short powerful laser pulses three-photon⁹, four-photon¹⁰ and five-photon¹¹ photoeffect has been obtained in visible spectral region. In infrared spectral region, Schottky barrier height ϕ_B several times exceeds photon energy, therefore, multiphoton

photoeffect may also be expected. In this research samples have been irradiated at five different excitation wavelengths: 2.79, 3, 5, 7 and 10.6 μm corresponding to ratio of the barrier height over photon energy within the range 2-6. We demonstrate that intense infrared laser excitation gives rise to the photoresponse in Schottky contact even if the photon energy is considerably less than the barrier height.

Current-voltage characteristic of Ti/n-Si Schottky contact (Fig. 6) demonstrates that irradiation gives rise to increase of reverse current which is strongly dependent on light intensity. This means that the photovoltage in Schottky contact appears due to emission of electrons from metal to semiconductor across the potential barrier. In this case polarity of the photosignal is the same as that of the ordinary photovoltaic effect and opposite to that of the hot-carrier photovoltage in p-n and l-h junctions (described above).

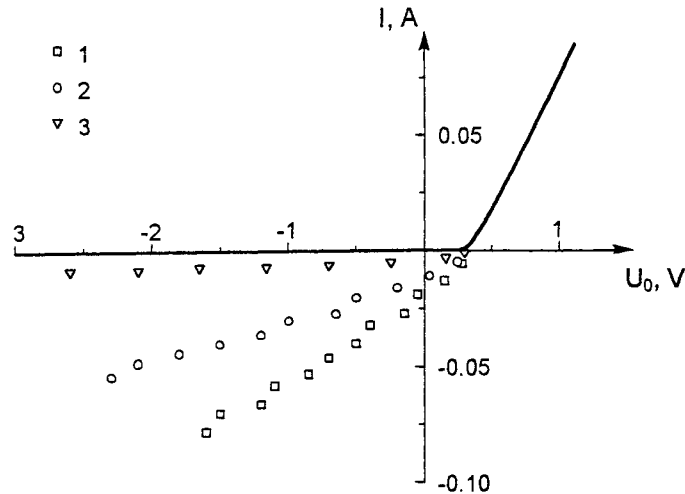
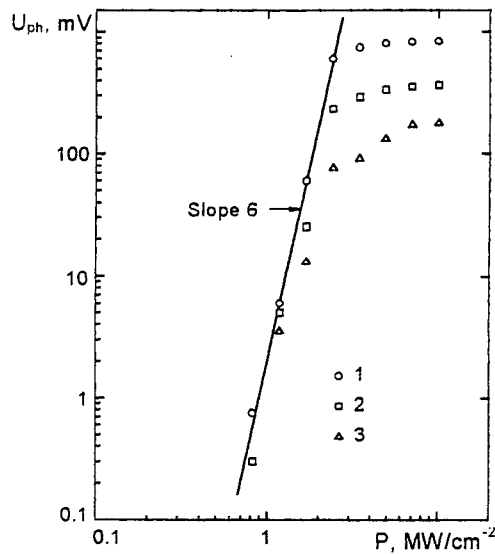


Fig. 6. Current-voltage characteristic of metal-semiconductor contact. Excitation wavelength 10.6 μm . Laser power density, MW/cm^2 : 1 - 10, 2 - 5, 3 - 2.4, solid line - 0.

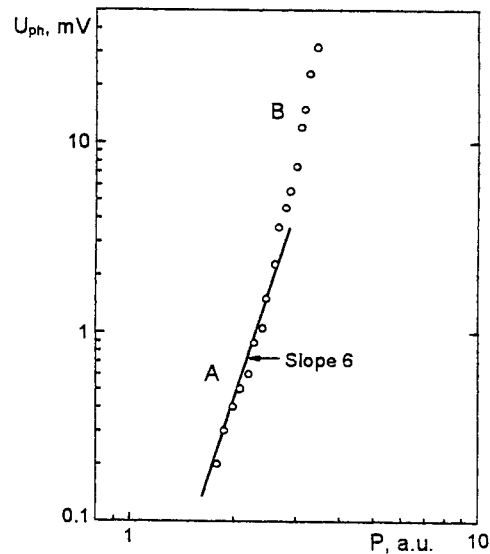
CO_2 laser radiation at wavelength 10.6 μm corresponds to the maximum value of the ratio ($e\phi_B/h\nu = 6$). We found that the photovoltage U_{ph} as a function of laser intensity demonstrates steep superlinear growth followed by decrease in slope and saturation at high light intensities (Fig. 7, a). The photosignal saturation is observed because maximum value of the photovoltage is limited by the junction diffusion potential ϕ_0 . It is seen that magnitude of the photosignal is strongly affected by external bias voltage. Bias dependence of the saturated value of U_{ph} we attribute to ϕ_0 variation with external voltage. One should note that dependence of the emitted charge upon light intensity in log-log scale is linear with the same slope as $U_{ph}(P)$ plot. Besides, the emitted charge is not affected by internal electric field of the junction and dependence $Q(P)$ does not show any saturation at high laser intensities.

More precise measurements of the superlinear part of the characteristic $U_{ph}(P)$ (using gas absorber cell) demonstrate that $U_{ph}(P)$ plot in log-log scale consists of two linear regions with two different slopes (Fig. 7, b). It means that relation between U_{ph} and P is governed by power-law dependence $U_{ph} \propto P^n$ with two different values of n . First region (A) at low values of P is characterised by lower value of n , while at higher intensity values (region B) tendency of increase in slope is observed indicating increased nonlinearity of the photovoltaic effect.

It has been found that at low light intensities (region A) any delay in time between the photosignal pulse and the laser pulse is not observed and the photosignal pulse is narrowed with respect to the laser pulse (Fig. 8). This is related with the nonlinear relation between the photoresponse and the laser intensity. At high light intensities (region B) the photosignal pulse starts to delay with respect to the laser pulse and its width becomes greater than that of the laser pulse. This fact as well as increased value of n in this intensity region suggest thermal origin of the effect. It implies an excessive heating of metal surface followed by thermal generation of electron-hole pairs. Therefore, increase of n in region B is caused by strong (exponential) dependence of the emission current on the metal surface temperature. This is in some agreement with



a



b

Fig. 7. (a) the photovoltage versus CO₂ laser intensity for different bias values: 1 - -0.5V, 2 - 0V, 3 - +0.2V. (b) fragment of the plot in Fig. 2(a) at zero bias voltage. A - low intensity region (photoeffect dominates); B - high intensity region (thermal effect dominates).

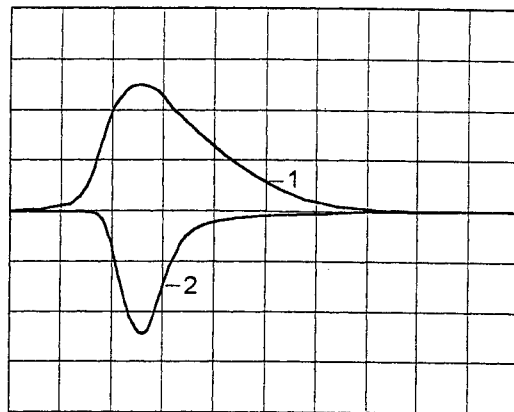


Fig. 8. CO₂ laser pulse trace (1) and the photovoltage pulse trace (2). Vertical axis - in arbitrary units; time scale - 100 ns/div.

nonlinear electron photoemission data obtained for the metal-vacuum interface at high light intensities⁹. In the following we shall consider only the fast photoeffect observed in region A.

The discussed results were obtained at room temperature. At liquid nitrogen temperature we observed nearly twofold increase in magnitude of the signal, however, any variation in slope of the characteristic $U_{ph}(P)$ did not occur.

It is known that the multiphoton effect order is determined by:

$$n = \left[\frac{e\phi_B}{h\nu} + 1 \right], \quad (9)$$

where angle brackets mean integral part of expression.

In the case of CO₂ laser excitation value of the power n obtained from Eq. 9 ($n = 6$) was found to be in agreement with that deduced from the slope of $U_{ph}(P)$ plot in Fig. 7(b), region A. It means that total energy of six quanta is necessary for electron to overcome the potential barrier of metal semiconductor contact but it does not mean that six-photon photoeffect is observed. Experimental data of four-photon and five-photon electron photoemission at metal-vacuum boundary^{10,11} as well as theoretical estimation of the multiphoton excitation rate¹² suggest that probability of pure six-photon effect is extremely small. Therefore, in the investigated range of light intensities the photovoltage value should be by many orders of magnitude less than that observed in our experiments.

Yet it is known that metal-semiconductor interface contains a considerable number of electron energy states distributed within the forbidden energy gap. Therefore, there appears an additional channel of multistep electron excitation via real intermediate states. Let us consider a simplest (second-order) nonlinear process of electron-hole pair generation in semiconductor. In general, the generation rate is given by¹³:

$$g = \frac{N\sigma_1\sigma_2P^2}{\frac{1}{\tau} + (\sigma_1 + \sigma_2)P} + \alpha_2P^2, \quad (10)$$

where the first term represents the two-step generation rate and the second term stands for the two-photon generation rate: N is the number of intermediate energy states per unit volume, τ is the intermediate state life time, $\sigma_{1,2}$ is the light absorption cross-section and α_2 is the two-photon absorption coefficient. It is assumed that electron transition probabilities (valence band - intermediate state and intermediate state - conduction band) are proportional to light intensity with coefficients of proportionality σ_1 and σ_2 , respectively.

It follows from Eq. 10 that at low laser intensities when $\tau^{-1} \gg (\sigma_1 + \sigma_2)P$ both the two-step and the two-photon generation rate are proportional to P^2 . Therefore, the second-power law dependence of the photosignal upon light intensity alone does not identify the physical process. Furthermore, one can show that in the case of n -th order photoeffect the multistep as well as the multiphoton excitation rate (at low intensity levels) are proportional to P^n . Since electron life time in real intermediate state considerably exceeds the one in virtual state probability of the multistep process is much more intense than the multiphoton effect¹⁴ and the difference rapidly grows up as the coefficient of nonlinearity n is increased. Therefore, theoretical value of the photocurrent originating from six-step light absorption^{12,14} is close to that obtained experimentally.

We found that the fast sixth-order photoresponse is not observed in as-fabricated metal-semiconductor contacts and some thermal treatment of samples using powerful laser radiation is necessary in order to obtain the photosignal. To explain these results one should recall that crystal lattice defects at the surface usually create electron energy states. That is why surface state density and distribution are strongly dependent on sample fabrication parameters¹⁵. We assume that initial number of surface energy states is not sufficient for the multistep photoeffect to be measurable. Therefore, heating of metal-semiconductor interface with CO₂ laser pulses at high power density (about 10 MW/cm²) generates additional electronic states and considerably increases the multistep excitation rate. Energy distribution of the interface states in our samples is not known, however, we suppose that the electronic states are distributed quasicontinuously¹⁵ and every virtual state is supported by sufficient number of real interface states. From this we conclude that in case of $\lambda = 10.6 \mu\text{m}$ the six-step electron photoemission is responsible for the observed photovoltage in Ti/n-Si Schottky contact.

Using laser light sources at shorter wavelengths we were able to explore lower-order nonlinear photoeffects. For example, second-order photoeffect was observed for erbium laser excitation ($\lambda = 2.79 \mu\text{m}$) and for parametrical oscillator radiation at wavelength $3 \mu\text{m}$ (Fig. 9). This is in agreement with relation between photon energy and the barrier height: $h\nu < e\phi_B < 2h\nu$. One should note that photosignal pulse duration is less than that of erbium laser pulse and any delay in time between them is not observed. Moreover, similar behavior of U_{ph} versus P (Fig. 9, a and b) is observed despite the difference in laser pulse duration more than three orders of magnitude. It means that in this intensity region thermal effects are not significant.

Third-order photoeffect was observed using pulses of the parametrical oscillator at wavelengths 5 and 7 μm . In this case relation between the Schottky barrier height and photon energy is $2h\nu < e\phi_B < 3h\nu$ and dependence of the photovoltage on laser intensity is close to third-power law (Fig. 10).

To interpret the experimental results in mid-infrared spectral region ($\lambda = 2.79 \div 7 \mu\text{m}$) one has to solve the problem: which process - multistep or multiphoton - is responsible for the observed photovoltage. One should note that, firstly, any thermal treatment of samples is not necessary in this spectral range what speaks in favour of the multiphoton effect. In addition, probability of the two-photon and the three-photon absorption is by many orders of magnitude greater than the six-photon

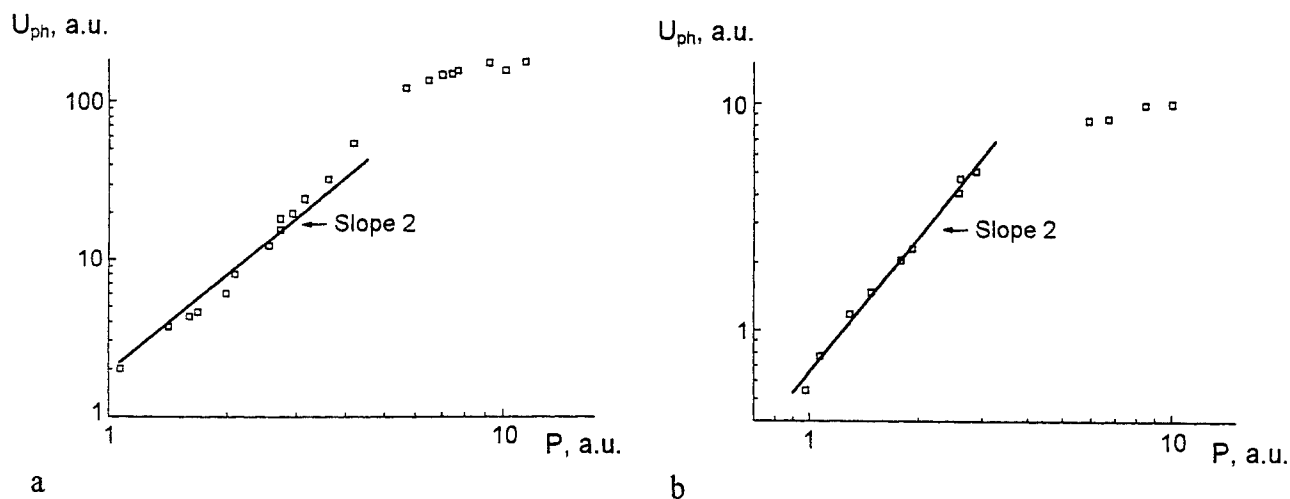


Fig. 9. The photovoltage versus light intensity. Excitation wavelength: (a) - 2.79 μm , (b) - 3 μm .

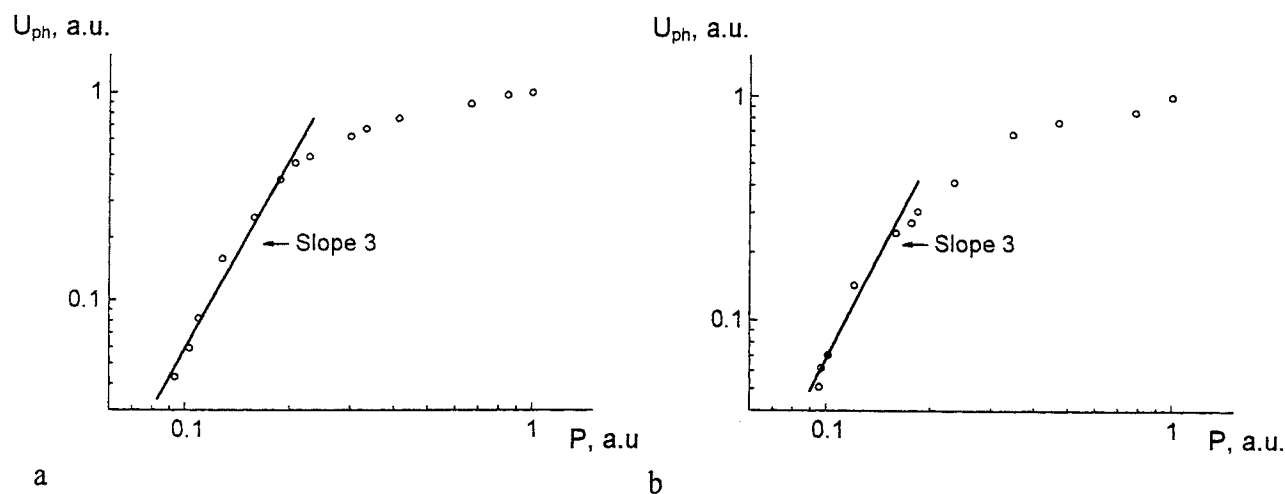


Fig. 10. The photovoltage versus light intensity. Excitation wavelength: (a) - 5 μm , (b) - 7 μm .

effect and, thus, two-photon and three-photon electron photoemission may well be expected within the investigated intensity range. Therefore, we suppose that multi-photon electron photoemission dominates at excitation wavelengths $\lambda=2.79\div 7\mu\text{m}$.

ACKNOWLEDGEMENTS

This work was partly supported by Lithuanian State Science and Education Fund within the framework of "Jutikliai" Programme.

REFERENCES

1. I.Ya.Marmur, Ya.A.Oksman, and A.A.Semenov, "Hot carrier current through p-n junction." *Phys.Tekh.Poluprovodn.* **1**, pp. 2216-2217, 1974 (in Russian).
2. M.Umeno, Y.Sugito, T.Jimbo, H.Hattori, and Y.Amemiya, "Hot photo-carrier and hot electron effects in p-n junctions." *Sol.St.Electron.* **21**, pp. 191-195, 1978.

3. S.Ašmontas, E.Širmulis, and S.Stonys, "Investigation of the photovoltage across germanium p-n junction under pulsed CO₂ laser radiation," *Sov.Phys.-Collection* **24**, pp. 76-87, 1984 (in Russian).
4. S.Ašmontas, E.Maldutis, and E.Širmulis, "CO₂ laser radiation detection by carrier heating in inhomogeneous semiconductors," *Int.J.Optoelectron.* **3**, pp. 263-266, 1988.
5. S.Ašmontas, J.Grauskas, D.Seliuta, A.Sužiedėlis, A.Šilėnas, G.Valušis, "GaAs/AlGaAs heterojunction: a promising detector for infrared radiation," *Proc.: Gallium Arsenide and Related Compounds Application Symposium GAAS'97*, pp. 345-348, Bologna, Italy, 1997.
6. S.Ašmontas, J.Grauskas, D.Seliuta, A.Šilėnas, "Photoemf of hot carriers in non-uniform GaAs," *Proc. SPIE: Optical Organic and Semiconductor Inorganic Materials*, Eds.: E.A.Silinsh, A.Mečvid, A.R.Lūsis, A.O.Ozols, **2968**, pp.104-109, Riga, 1996.
7. M.Lopez Saenz and M.Guerra perez, "The forward biased junction: sensitive detector for far-infrared radiation," *Appl.Phys.Lett.* **68**, pp. 675-677, 1996.
8. S.Ašmontas and E.Širmulis, "The hole heating in silicon by CO₂ laser radiation," *Phys.Tekh.Poluprovodn.* **20**, pp. 2212-2216, 1986.
9. E.M.Logothetis, P.L.Hartman, "Laser-induced electron emission from solids: many-photon photoelectric effects and thermionic emission," *Phys. Rev.*, **184**, pp. 460-474, 1969.
10. J.H.Bechtel, W.L.Smith, and N.Bloembergen, "Four-photon photoemission from tungsten," *Opt. Commun.* **13**, pp. 56-59, 1975.
11. G.Farkas and Z.Gy.Horvath, "Multiphoton electron emission processes induced by different kinds of ultrashort laser pulses," *Opt. Commun.* **12**, pp. 392-395, 1974.
12. F.V.Bunkin and A.M.Prokhorov, "Some peculiarities of laser-mater interaction using short excitation pulses," *Zhurn. Eksp. Teor. Fiz.* **52**, pp. 1610-1615, 1967 (in Russian).
13. D.P. Dvornikov, E. L. Ivchenko, V. V. Pershin, I. D. Jarosheckii, "Effect of the transitions via deep impurity centers to the process of the nonlinear light absorption in semiconductors," *Phys. Tekh. Poluprovodn.* **10**, pp. 2316-2319, 1976 (in Russian).
14. I.V.Lebedev, "Multiphoton ionisation of semiconductors with impurity states," *Optika i Spektrosk.* **33**, pp. 1190-1191, 1972 (in Russian).
15. V.I.Strikha, E.V.Buzaneva, I.A.Radzievskii, *Semiconductor Devices Based on Schottky Contact*, Sov. Radio, Moscow (1974).

Dynamics of 3D representation of interfaces in UV-induced chemical vapor deposition :experiments, modeling and simulation for silicon nitride thin layers

J. Flicstein^{*†}, E. Guillonneau*, J. Marquez****, L. S. How Kee Chun**, D. Maisonneuve*, C. David***, Zh. Zh. Wang***, J. F. Palmier**, J. L. Courant**

France Telecom C.N.E.T.-DTD Laboratoire CDP*, 196, ave. H. Ravera, 92225 Bagneux, France.
*C.N.R.S. URA 250,

**Opto+, Groupement d'Intérêt Economique, Route de Nozay, 91460 Marcoussis,

***C.N.R.S. L2M, Bagneux,

****E.N.S.T. rue Barrault, Paris

ABSTRACT

We study the surface dynamics of silicon nitride films deposited by UV-induced low pressure chemical vapor pressure. Atomic force microscopy measurements show that the surface reaches a scale invariant stationary state coherent with the Kardar-Parisi-Zhang (KPZ) equation. Discrete geometry techniques are oriented to extract morphological characteristics of surface (e.g. roughness) and bulk (e.g. porosity) which corresponds to computer simulated photodeposits. This allows to determine the physical origin of KPZ scaling to be a low value of the surface sticking probability, and connected to the surface concentration of activate charged centers (ACCs), which permits to start the evaluation of the Monte Carlo-molecular dynamics simulator.

Keywords: Thin film deposition; UV-induced chemical vapor deposition; Atomic force microscopy; Heterogeneous photolysis; Monte Carlo-molecular dynamics simulator; surface sticking probability; Heterogeneous nucleation; Surface morphology

1. INTRODUCTION

The dynamics of growing interfaces has become of interest in order to understand the physical processes that determine film quality. Surfaces evolving out of equilibrium, in the absence of instabilities, display time scale invariance i. e. such surfaces are rough. Atomistic simulations of a realistic solid on solid (SOS) model is not only of fundamental interest but also of industrial importance with regard to the control of deposit structure and of film properties. In this respect the dependence with substrate temperature (T) of the roughness and topology of deposited layer is one interesting characteristic to analyze in a 3D representation. Two observations have guided conventional expectations regarding temperature variation. As the processing temperature is usually low in Ultra Violet-induced chemical vapor deposition (UV CVD), this technique has also the advantage to work usually bellow the thermal roughening transition [1,2].

A framework for the study of rough interface dynamics has been the formulation for the surface height $h(\mathbf{r},t)$, where \mathbf{r} denotes a site of 2D substrate, and t is time. Kardar-Parisi-Zhang equation is expected to provide the large scale length dynamics of any surface deposited in an open system [2c]

$$\delta_t h = \nu \nabla^2 h + (\lambda/2)(\nabla h)^2 + \eta(\mathbf{r},t) \quad (1)$$

term I term II term III

[†] Corresponding author: jean.flicstein@rd.francetelecom.fr

In Eq.(1), v and λ are constants. Term I denotes the surface tension. Term II accounts for deposition along normal direction, and term III. accounts for fluctuations in system. Consequently, the root-mean-square (rms) roughness of the deposited layer provides a measure of the deviation from the equilibrium. Analysis of random deposition on face-centered-cubic (fcc) with on top adsorption sites reveals rough deposition at low processing temperature. These observations have led to the concept that the roughness of a deposited film of a given thickness should increase monotonically with decreasing processing temperature. Film structure at higher temperature would then reflect smoothing, and structure at *lower* temperatures would reflect roughening. But it is possible that behavior in photochemical systems can actually be more complicated.

In this paper, we provide a validation of the simulator for the temperature dependence of layer deposition features (for roughness and porosity) as compared with the atomistic model predictions. The contribution herewith is for silicon nitride photodeposition. In the literature, the lateral growth was described as controlled by the diffusion of the material in the gas phase[2]. On the other hand, so far, it has been understood that the vertical growth is mainly governed by the gas phase photolysis [3]. This could be, because all photoproducts arriving on rough side-surfaces are incorporated immediately and it was believed that the surface kinetics does not play an important role in the transport process. However, these observed smooth layers cannot be accounted by the ordinary homogeneous photonucleation. In our present model, for the simulation of photodeposition, we included the heterogeneous photonucleation stage on co-existing UV-induced sites for nucleation (activate charged centers, ACCs).

2. EXPERIMENTAL

A UV light source, in perpendicular configuration, produces a large illuminated substrate area [3]. Precursor molecules (NH_3 , SiH_4) incident on the irradiated photoreaction zone are subjected to localized heterogeneous photolysis. As a consequence, adsorbed photoproducts (adspecies) and volatile photoproducts are obtained. In turn, the adspecies migrate toward centers of nucleation. Amorphous SiN:H films were grown in UV CVD reactor in a range of temperature : 400-650 K. The chamber pressure was in the range : 0.4-3 Torr. The surface morphology was characterized by AFM (Nanoscope III from Digital Instruments, CA) operating in tapping mode at ambient conditions up to 25 °C, with a scale of 10 μm , using silicon nitride cantilevers.

AFM imaging of our silicon nitride shows a deposit. It was observed initially a deposit of small rounded grains 40-60 nm in size (Fig. 1). The grain shape attains a curvature dictated by the boundary energies. The resulted grains morphology is hemiellipsoidal. Following the grain to grain competition and coalescence, film deposition was observed. As deposition proceeds, structures resembling mountains and valleys appears increasing in size. A similar morphology has been reported on silicon oxynitride on films photodeposited by VUV flash lamps [4b].

3. 3. PHYSICO-CHEMICAL MODEL DETAILS AND PARAMETERS

We provide a brief description of our model for silicon nitride deposition on (100) InP to describe irreversible 2D island nucleation and deposition process in UV CVD. The model includes the adsorption site geometry and a referential structure for fcc (100) III-V semiconductors. It is considered concomitant UV photon interaction with the semiconductor surface and precursors. The schematic of our three-dimensional model indicates nine juxtaposed key sequences which can describe the photodeposition process [1,4-5]:

- 1.arrival of precursor(s) flux into the photoreaction volume,
2. precursors are deposited randomly at rate F (monolayers / time) with subsequent adsorption of the precursor(s) onto the substrate,
- 3.heterogeneous photolysis of precursor(s) to produce adspecies *and volatile photoproducts*.
4. isolated adspecies relax to nearest empty nucleation active site and adsorb there ; the encounter of two migrating adspecies irreversibly nucleates a new island ; adspecies impinging on top of layers are stepping down by migration and stabilized incorporation, or desorbing *as volatile photoproducts*,
5. transport of volatile photoproducts out of photoreaction volume,

6. formation of clusters of *adspecies photoproducts* on co-existing photo-induced sites for nucleation (activate charged centers, ACC) and conventional nucleation centers,
7. coalescence of clusters,
8. competition of clusters to produce deposit, and
9. continuous photodeposition, which includes *the stabilized incorporation stage* [12-13].

1. Computational method

A real time Potts-Monte Carlo-Metropolis method is employed here for determination of the events on the substrate surface [6,7]. Time in the Potts model is measured in units of Monte Carlo step (MCS). 1 MCS corresponds to N attempted changes. N is the total number of sites in the system.

The kinetic processes are simulated using an entropic barrier for the *adspecies*, in which the activation energy depends on the configuration of neighboring species. The interaction forces are assumed to be van de Waals-London, with the primary attractive interaction energy falling off as the sixth power of the distance between adsorbates (a). For the fcc lattice, the ratio between distances which separates nn and third-nearest neighbors (nnn) is $2^{1/2}$. So, n and nn interaction energies are among the most conducive parameters in the simulation. Also the sites normalized frequencies (see "**Results and Discussions**"), were checked for Gaussian energy distribution and the results are published elsewhere [4,7c]. Therefore the model includes lattice coordination of SiN:H, species-species interactions out to third-nearest neighbors (nnn), and *adspecies-adspecies* interaction. According to the Monte Carlo algorithm used, the type, site and time of each of the events are chosen with a probability of occurrence that depends on the kinetic rates at each site. For a semi-quantitative analysis of the quality of the depositing layer, we introduced the root mean square (rms) roughness calculated in a square box over all surface sites: Δ (roughness) = $\langle h_i^2 \rangle - \langle h \rangle^2$, expressed in monolayers units, ML. Here h_i is the height of the i th column of the structure. The $\langle \rangle$ denotes an average over all surface sites.

2. Brief description of photolysis reactions.

Heterogeneous photolysis reactions occur on the substrate surface and a global quantum yield is assigned. The flow of precursor is taken to have the photoproduct incorporated in the film. The time increment between incident flow of precursor species onto the substrate surface is $\Delta t_F = (\phi L^2)^{-1}$ where ϕ is the total flow and L the film length, expressed in terms of the number of atomic lattice sites. *Adspecies* migrate from surface site to surface site. Each lattice point may be occupied by a species or a void. The lattice point signifies the position of a particular species in the film below a given site. The lattice sites position is defined by its (x, y, z) coordinates. *Adspecies* are moved from their current surface site with each increment of time. For a specified temperature, *adspecies* are allowed to a specified number of relaxations. Then the number of relaxations is an input parameter. ACCs are continuously created, prior to and during the photolysis and the nucleation, on a III-V substrate. At low luminance, the fractional density of ACCs is small. The fractional density is important in determining the surface morphology. All active nucleation centres have equal probability of photonucleation and equal radial nucleation rate. What is important here is the product of relative generation rate, photolysis and ACCs generation, to surface migration rate. Conversely, in absence of VUV irradiation, a defect free semiconductor surface has a low probability of *adspecies* attachment, which would impose an increase in the critical local supersaturation level, otherwise required to promote photonucleation at the photonucleation threshold. At higher luminance, than this photonucleation threshold, the onset of nucleation occurs, even when the *adspecies* surface density attains a vanishingly small local supersaturation [8]. The statistical probability of the formation of a photolysis end-product is directly related to its co-ordination number. Based on bond energy of dissociation, within the energy minimization calculations [12], we can predict the quality of the deposit.

3. Discrete representation in 3D and topological analysis of simulated depositions.

The information of void and occupied sites in the fcc lattice provided by Monte Carlo-molecular dynamics simulation is organized in function of simulation parameters. Occupied sites are clustered to constitute the bulk, exhibiting rough features at the surface. Voids may be isolated or clustered together forming interconnected pores. In order to count pores, and measure their individual characteristics (size, shape orientation and distribution), they must be isolated in their 3D

representation. An efficient way to do this consist in tracking their discrete 3D boundaries, as first reported by [17] in their cuberille representation, which is the mathematical representation of an fcc grid in terms of points, edges, square faces (facets) and cubes of [19]. Such boundary, or surface extraction, is based on a connectivity analysis of each void site and their void neighbors, when considering the void sites as the foreground and the bulk as background. Connectivity analysis at the site level is the basis for representing topological information at the pore level. Connectivity in the fcc grid is related to neighboring relationships. In 3D image analysis, the equivalent of each site is a voxel (see in Fig. 4, the volume element), considered as a parallelepiped [18]. The nearest neighbor corresponds to the 6-connected neighbors (n), in 3D image processing, the next-nearest neighbor (nn) to the 18-connected neighbors, and the next-to-next nearest neighbor (nnn) to 26-connected neighbors. Each case is characterized, voxels sharing a face, only an edge, or only a vertex, respectively. Fig. 5 is a synoptic diagram of the main elements of these representations, in terms of points, voxels and facets (voxel oriented faces). Our analytic approach consisted in taking advantage of two complementary discrete representations of connected components inside the bulk, V (individual pores); one consists in a facet-based boundary $B_f(V)$, and the other consists in a voxel-based boundary $B_v(V)$. Occupancy is expressed as a binary code associated with each voxel. Each voxel after segmentation bears a unique label corresponding to one identified pore, or to the bulk. This allows for very selective visualization and quantification of structural features. Details of boundary extraction, and morphometrical analysis and visualization using these representations are given in [19, 20].

4. RESULTS AND DISCUSSIONS

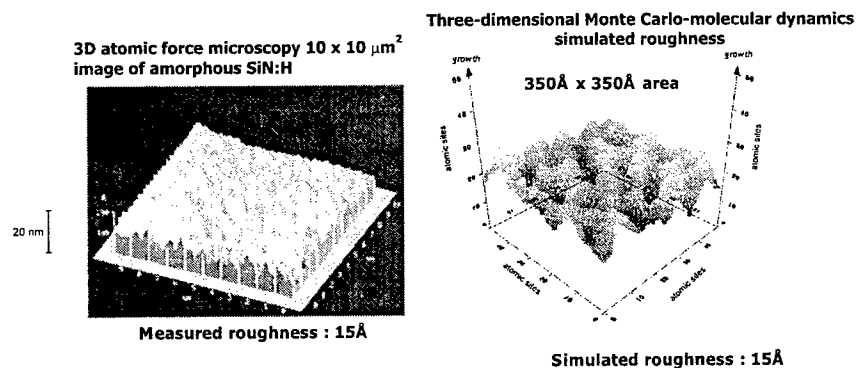


Fig. 1 Comparison between experimental UV photonucleation for SiN:H and simulated nucleation step:
(Left) AFM $10 \times 10 \mu\text{m}^2$ image of amorphous SiN:H films deposited at $T = 550\text{K}$. The vertical bar represents 20 nm.
(Right) Plot of a three-dimensional Monte Carlo-molecular dynamics simulation of roughness in a box. The three axis are, respectively, atomic sites. Various colours are used to distinguish surface atoms at different z co-ordinates.

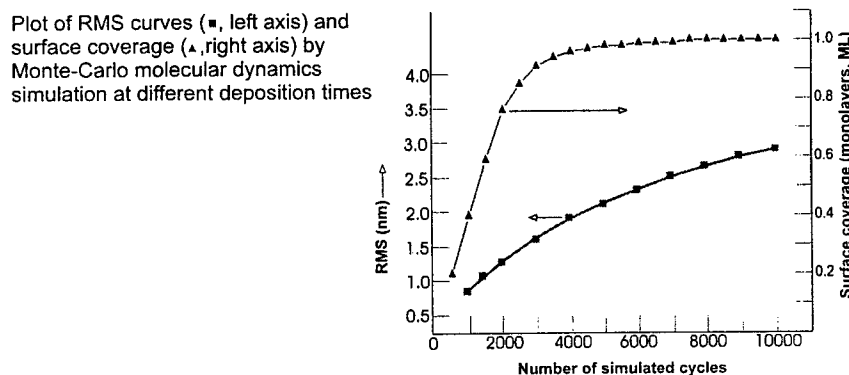


Fig 2. Plot of Root-Mean-Square (RMS) curves (left axis) and surface coverage (right axis) obtained by Monte Carlo-molecular dynamics simulation at different number of simulated cycles
(Left) Three-dimensional temporal evolution of RMS roughness vs number of cycles: during UV photonucleation
(Right) Temporal evolution of expected surface coverage.

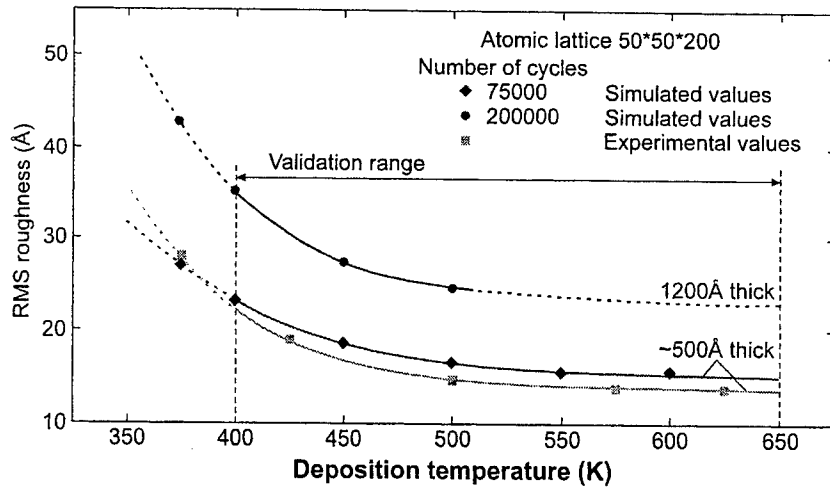


Fig.3 Relative comparison between simulated and experimental roughness values now for larger-scale deposition vs deposition temperature for SiN :H in the validation range of temperature : for 500 Å and, respectively, 1200 Å thick (solid line). The dashed lines are only presenting the expected RMS values.

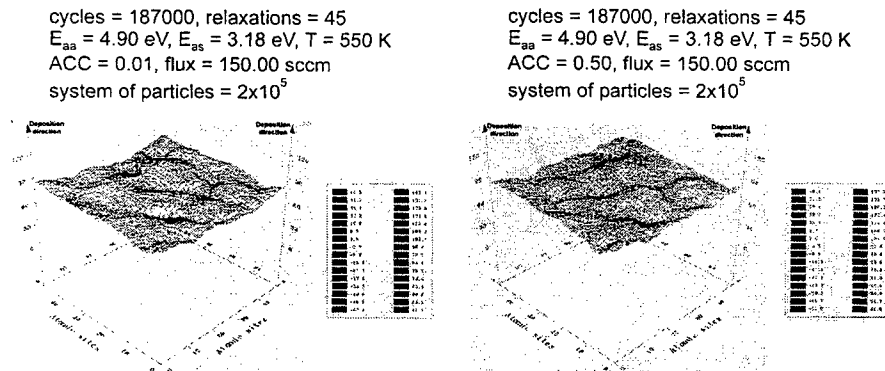


Fig. 4. Large-scale three-dimensional snapshot showing the silicon nitride surface morphology of $1.85 \cdot 10^5$ -particle system deposited at 550 K. Nucleation fractional density occurs at a) 1%, b) 50%. Various colors are used to distinguish surface atoms at different z-coordinates.

In order to compare MC-molecular dynamics simulations and experimental results (see Fig. 1), we have first established the equivalence between the parameters. To this end we have, first, constructed by three-atom adspecies for silicon nitride SiN :H, a box of $50 \times 50 \times 200$ atomic sites, deposited onto the (001) InP substrate. In this box, with constant height, simulation results were obtained. Therefore the validation is restricted to SiN :H_n ($1 \leq n \leq 11$). An average lattice constant of 6.6 Å it is computed from the silicon nitride unit-cell dimensions. In the substrate temperature range, from 400 K to 650 K, the number of cycles of adspecies moves was defined in the simulation. We are considering lateral migration in a succession of columns layers. Other simulation condition, derived from optimum experimental conditions, is a UV luminance of $26 \text{ mW} \cdot \text{cm}^{-2} \cdot \text{sr}$ (at 185 nm wavelength). The concomitant heterogeneous photolysis of NH₃ on the InP substrate is VUV light dependent. The total impinging flow, of the mixture SiH₄/NH₃/N₂ incident on the substrate is 350 sccm. The normalized frequencies for examination of (n), (nn) and (nnn), are $v_n = 81.2 \%$, $v_{nn} = 17.8\%$, $v_{nnn} = 1\%$, respectively. The system was checked with positions centered on the sites and their energies Gaussian distributed [4]. The variance of this Gaussian distribution controls the interaction species-species in the system. We have used a system with constant size in order to be equally affected by finite size. Thus, we have established an equivalence between the simulated and experimental data. We have used a MC-molecular dynamics system with the same size as the experimental one, in order to be equally affected by finite size. Thus we have established an equivalence between the data from MC and experimental conditions. Next, we are aiming to study the evolution of the photonucleation, which starts from the substrate fcc lattice. We performed a set of computational experiments and compared the results of photonucleation, up to $1.6 \cdot 10^4$ iterations. It can

be seen that, in this early growth mode, the photonucleation is clearly displaying low three-dimensional roughness increasing over time (Fig.2, left side). Even during early nucleation, and because a low temperature nucleation, the surface tends to saturate with time (Fig. 2, right side). The peculiarity of the coverage rate is the superposition of the several number of cycles, which are filling the layer. The results of Monte Carlo simulation are validated for the Volmer–Weber modified mode of photonucleation and early photodeposition. In this photonucleation mode, whilst the vertical growth rather than lateral growth dominates in this monolayer, the ACCs fraction influence will increase and rough photonucleation will occur. The shape and the filling morphology (see Fig. 2) of the patterned surfaces are validated by our previously published experimental data [16].

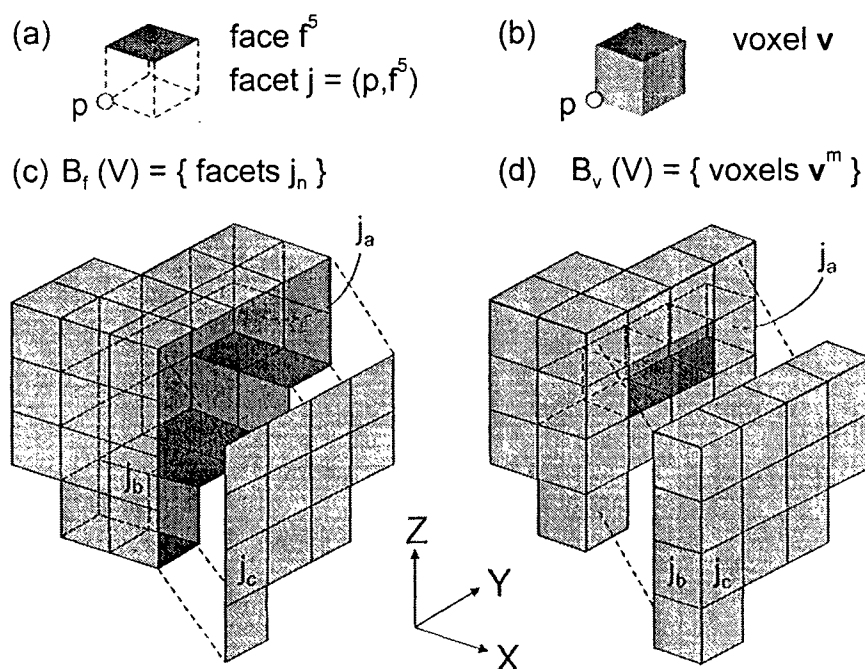
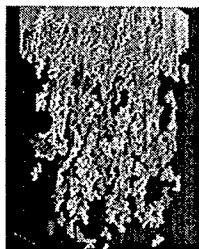


Fig. 5 Synoptic diagram of the main elements of representations of connected components inside the bulk (individual pores), in terms of points, voxels (B_v) and facets (B_f , voxel oriented faces).

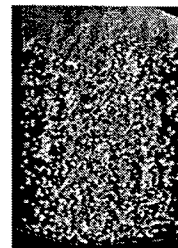
Now, for a semi-quantitative analysis of the quality of the surface, of the depositing layer, we introduced the root mean square roughness (rms) in a square box over all surface sites. Fig. 2(left side) shows the influence of precursor dissociation energy on surface roughness, which displays shifts in the temporal evolution of the rms roughness. The parameters used are the dissociation energy for adspecies-adspecies (E_{aa}) and adspecies-substrate (E_{as}) interactions (aa interaction in all layers (4.9 eV), except the first, as interaction (3.18 eV) [15-16]. The model is defining the deposition rate normal to the substrate. The computed roughness values for ACCs surface fraction (0.2) agrees well (see Fig. 2) with the values measured by Atomic Force Microscopy (AFM). Temporal evolution of the surface roughness showed a transition from rough to smooth deposition at around 450 K (Fig.3). At $T=550$ K adspecies diffusion is more intensive which permits the deposition of high quality material. Comparison of the temporal evolution of the surface roughness, presented in Fig. 4, shows that the steep rms roughness reduction evolution occurs as from a low ACC threshold value of 1%. This evolution is also important in determining the surface filling morphology (Fig. 4). Thus, our large-scale results demonstrate the possibility of obtaining flat and uniform surfaces at low temperatures, even using amorphous layer deposition. This is due to both, enhanced adspecies lateral migration and ACC creation on a bare substrate surface.

Volume of the pore is obtained by counting voxels inside the surface $B_v(V)$. Visualization is performed by displaying of facet elements of $B_f(V)$. selection of specific pores to visualize (the largest, for example) is done by sorting the volume distribution and labeling pores by volume size. Fig. 5 shows the pore distribution in simulation sets corresponding to four photodeposition temperatures, which correspond to the values selected for the range of validation, in Fig. 3. In the validation range , up to 1200 Å, making use of two different experimental techniques, AFM and index of refraction (RI), it was shown that the both characteristics vs temperature for 500 Å are superimposed [22] leading to the same transition temperature :175 °C.

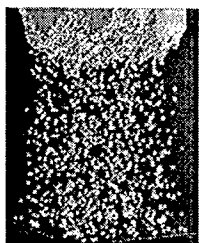
(a) surface and pore distribution at $T=400$ K, with several connected components and 100 Kcycles (about 100 monolayers)



(b) surface shape and pores formed at $T=450$ K



(c) surface shape and pores formed at $T=550$ K



(d) surface shape and pores formed at $T=650$ K

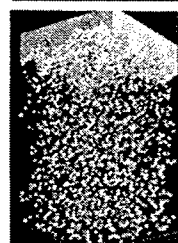


Fig. 6. Typical three-dimensional reconstruction of amorphous SiN :H photodeposition of about 100 ML in function of temperature. Representation of surface shape and pores distribution. Empty space and pores are rendered in opaque colours. The bulk of SiN:H is transparent.

We have found that low pressure Ultra Violet-induced CVD of silicon nitride films is governed by the competition between surface diffusion, lateral growth and shadowing (KPZ behavior), provided that the photonucleation is promoted prior to deposition. We are proposing a new versatile simulator for atomistic photodeposition process with III-V materials. The simulator capability is validated in the mesoscopic-submicron range. Four novel features of the model are included. The essentials are the following : I. The photolysis sequence is restricted to heterogeneous phase. II. Photonucleation priority is developed on activate charge centers (ACCs). III. Coalescence /competition is accounted. IV. Stabilized incorporation insures photodeposition. We have evidenced and identified for SiN:H density a thermal transition. For a thin film 500 Å thick, in a-SiN :H / InP system, this simulator was tested with Atomic Force Microscope and index of refraction results, to be appropriate for both, surface roughness and density. Simultaneously, the resulted porosity transition was evidenced and validated (at 175 °C).

The discrete representation of simulated data allowed to introduce a set of mathematical tools, from 3D imaging domain, in order to interpret connectivity information, at the site level, as topological features. Individual analysis and visualization of each pore was thus possible, making evident changes in their distribution (e.g. in function of temperature). These kind of analysis provides richer information for analysis and visualization, such as pores features and sorting by size and positions; and shall be explored in future works.

5. REFERENCES

- J. C. Rey, Lie-Yea Cheng, J. P. MacVittie, Krishna Saraswat, J. Vac. Sci. Technol. A9,(1991) 1083-1087.
 - J. Flicstein and J. E. Bourée in " *Photochemical processing of electronic materials* ", eds. I. W. Boyd and R. B.Jackman (Academic Press, N. Y., 1992) pp.105-141.
- M. Petitjean, *Thèse, Docteur en Sciences*, Université Paris XI Orsay, 1991.
 - B. Allain, J. Perrin, J. L. Guizot, , *Appl. Surf. Sci.* **3**, pp.205-212, 1989.
 - M. Kardar, G. Parisi, Y.-C. Zhang, *Phys. Rev. Lett* **56**, p.889, 1986.
- J. Flicstein, Y. Vitel, O. Dulac, C. Debauche, Y. I. Nissim, C. Licoppe, *Appl. Surf. Sci.*, **86**, 286-293, 1995.
- J. Flicstein, S. Pata, J. F. Palmier (to be submitted, 1999)
 - J. Flicstein, J. Mba, J.- M. Le Sollicc and J. F. Palmier, Optical properties and modelling of flash VUV induced silicon oxynitride isotropic deposition water and hydroxyl free, *Proc. SPIE.* **3091**, pp.72-82, 1996.
- B. Lewis and J. C. Anderson, " *Nucleation and Growth of Thin Films* ", (Academic Press, London, 1978)
 - J. A. Venables and G. L. Price, in " *Epitaxial Growth* ", J. W. Mathews ed. (Academic Press, London, 1975) pp. 382-436
 - D. Walton, cited in B. Lewis and J. C. Anderson, " *Nucleation and Growth of Thin Films* ", (Academic Press,

London, 1978) p. 498.

d) S. Stoyanov, cited in B. Lewis and J. C. Anderson, *idem* as in c)

6. F. F. Abraham and G. M. White, *J. Appl. Phys.* **41**, pp. 1841-1849, 1970.
7. a) D. E. Kotecki and I. P. Herman, *J. Appl. Phys.* **64**, pp. 4920-4942, 1988.
b) F. Y. Wu, *Rev. Mod. Phys.*, **54**, pp. 235-68, 1982.
c) J. Flicstein, E. Guillonneau, J. Marquez, L. S. How Kee Chun, D. Maisonneuve, C. David, Zh. Zh. Wang, J. F. Palmier, J. L. Courant, *Appl. Surf. Sci.* (accepted, 1999)
8. S. B. Goryachev, in " *Computer Simulation in Materials Science* ", H. O. Kirchner, L. P. Kubin and V. Pontikis eds. (Kluwer ASI series, Dordrechts, 1996) p. 17
9. C. Debauche, *Thèse, Docteur en Sciences*, Université Paris 6 (1993)
10. F. Leblanc, *Thèse, Docteur en Sciences*, Université Paris 7 (1992)
11. Lip Sun How Kee Chun, *Thèse, Docteur en Sciences*, Université Paris XI Orsay, (1997).
12. Z. Yin and F. W. Smith, *J. Vac. Sci. Technol.*, **A9**, pp. 972-977, 1991.
13. P. Quémérais, *J. Phys. (France)*, **4**, pp. 1669-1697, 1994.
14. *Handbook of Physics and Chemistry*, 74 ed. (Rubber Company, London, 1992) sect. 9
15. *JANAF Thermochemical Tables 2nd*. Ed., ed. D. R. Stull and H. Prophet (U.S. GPO, Washington DC, 1971)
16. J. Flicstein, S. Pata, J. M. Le Sollic, L. S. How Kee Chun, J. F. Palmier and J. L. Courant, *Comput. Mater. Sci.* **10**, pp. 116-126, 1998.
17. E. Artzy, G. Frieder and G.T. Herman, *Comput. Graph. Image Proc.* **15**, pp. 1-24, 1981.
18. G.T. Herman, *Geometry of Digital Spaces*, (Boston, Birkhauser, 1998)
19. J. Marquez, *Ph. D. Thesis*, ENST (1998)
20. J. Marquez, I. Bloch, F. Schmitt (to be published, 1999)
21. J. L. Courant, unpublished results
22. J. Flicstein, E. Guillonneau, J. Marquez, L. S. How Kee Chun, D. Maisonneuve, C. David, Zh. Zh. Wang, J. F. Palmier, J. L. Courant (submitted, 1999, *Appl. Surf. Sci.*)

Modeling of photochemical changes and photodarkening of AsSe films under pulse vacuum ultraviolet radiation

N. A. Kaliteevskaya, R.P.Seisyan

A.F.Ioffe Physicotechnical Institute, Politekhnikeskaya 26, St.-Petersburg, Russia.

E-mail: rseis@ffm.ioffe.rssi.ru

ABSTRACT

The theoretical description of photochemical transformation process of glassy chalcogenide semiconductor films (in particular AsSe) has been developed. The effect of pulsed ArF excimer laser radiation ($\lambda=193nm$, $\tau=20ns$) on glassy chalcogenide semiconductor is analyzed. It is found that photochemical transformation of AsSe is characterized by optical sensitivity about $3 cm^3/kJ$ and threshold radiation intensity about $17 kJ/(cm^2 sec)$.

Keywords: vacuum ultraviolet, photoresist, photodarkening, contrast enhancement.

1. INTRODUCTION

Photostimulated transformations in glassy chalcogenide semiconductor (GCS) films are traditionally studied using visible radiation, in particular, as applied to use of GCS as photoresists in microelectronic technology. At the same time, there are important features of photoinduced transformations in GCS under vacuum ultraviolet (VUV) radiation of ArF excimer laser ($\lambda=193nm$) [1]. First of all it is very low laser pulse energy level E_p required for noticeable photostimulated change of optical properties. The changes in the optical properties are accompanied by enhancement of etchability, allowing the use of GCS compounds as highly sensitive inorganic photoresist for VUV laser lithography (threshold exposure $8mJ/cm^2$ for 0.2 μm thick AsSe film in single-pulse regime with $\tau=20ns$ is the record value both for inorganic and organic resists). Thus the printing can be done in "flash-in-fly" regime, without stopping the substrate. The second feature is very high photochromic sensitivity, $\Delta\alpha/\Delta H$, (α is absorption coefficient, $H=E_p \cdot N$ is exposure, N is the number of pulses, E_p is pulse intensity) attained in VUV region of the spectrum, up to $10^6 cm/J$ for $\lambda=193nm$. The studies show that the spectral composition of the radiation has an important influence on the efficiency of the reaction, an indication of the nonthermal nature of the phenomenon.

The very high image contrast was observed in lithography process with GCS as resist. 200nm periodical structure there was obtained by contact lithography using ArF excimer laser radiation [2]. The high quality of image transfer can be connected to some contrast enhancement effect.

The investigation of the photoinduced transformations of AsSe films show that the complete transition of the film material into new state occur under threshold exposure about $30-50 mJ/cm^2$ and further irradiation does not change substantially optical and chemical properties of the film. Besides, it is found that the threshold exposure is decreasing with the increase of pulse intensity.

The photochemical transformation of organic resists consisting of a base resin and photoactive compound (usually inhibitor) can be described by Dill's equations [3].

$$\alpha(z,t) = AM(z,t) + B \quad (1a)$$

$$\frac{\partial I}{\partial z} = -\alpha(z,t)I(z,t) \quad (1b)$$

$$\frac{\partial M(z,t)}{\partial t} = -CM(z,t)I(z,t) \quad (1c),$$

where $M(z,t)$ is a local inhibitor concentration, $\alpha(z,t)$ - local absorption constant, $I(z,t)$ is a local light intensity, C is optical sensitivity, A and B are the constants. In Dill's model the rate of photoinduced transformations is directly proportional to the local light intensity. It means the exposure corresponding to complete formation of image does not depend on light intensity, what apparently is not a case for GHS resists.

2. BASIC EQUATIONS

The Dill's equations (1a-1c) should be modified in order to describe the dependence of the threshold exposure on the light intensity observed for GCS [1]. Let us assume that an irradiation of the film lead to the transition of the material from type 1 to type 2, possessing different optical (e.g. absorption coefficients ρ_1 and ρ_2 for type 1 and type 2 respectively) and chemical (e.g. etchability) properties. The film materials is mixture of type 1 and type 2 materials during the exposure. Therefore, local absorption coefficient can be represented in the form

$$\alpha = \alpha_1 \rho_1 + \alpha_2 \rho_2 = \alpha_2 + (\alpha_1 - \alpha_2) \rho_1 \quad (2a).$$

where ρ_1 and ρ_2 are local relative concentrations of materials type 1 and type 2, thus $\rho_1 + \rho_2 = 1$.

The absorption of light in the film should obey the equation:

$$\frac{\partial I(z,t)}{\partial z} = -\alpha(z,t)I(z,t) \quad (2b).$$

while the photo-induced transformation of the film material can be described by

$$\frac{\partial \rho_1(z,t)}{\partial t} = -f \rho_1(z,t)$$

It is necessary to suggest that the rate of photo-induced transformation should be proportional to the intensity, locally absorbed. On the other hand it is known that the processes of photo-induced transformation are characterized by some threshold intensity. Therefore, function F can be represented in the form

$f = C\alpha(z,t) I(z,t) F(I)$, where $F(I)$ is dimensionless step-like function and sensitivity C has dimensionality $[volume][energy]^{-1}$ and mean the volume of the type 1 material which can be transformed into type 2 by an absorption of the unit of energy. Finally, for the process of photo-induced transformation one can obtain

$$\frac{\partial \rho}{\partial t} = -C\alpha(z,t)I(z,t)F(I)\rho_1 \quad (2c)$$

Equations (4), (5) and (7) together with start and boundary conditions $\rho|_{t=0} = 1$ and $I(t,z=0) = I_0(t)$, where $I_0(t)$ is the intensity of incident light, allows to model of photo-induced transformations of inorganic photoresists.

The exact dependence of the function F on the intensity can be obtained by a development of microscopic theory of photo-induced transformation or by an phenomenological analyze of experimental data, for example photodarkening curves. We will approximate this dependence by an expression

$$F(I) = \frac{1}{2} \left(1 + \tanh \left(\frac{I - I_{th}}{\delta} \right) \right) \quad (4)$$

containing only two fitting parameters: threshold intensity I_{th} and its smearing δ . In case of small δ only upper photoresist layer with thickness z_{th} given by.

$$z_{th} = -\frac{1}{\alpha_1} \ln \left(\frac{I_{th}}{I_0} \right) \quad (5)$$

experiences the transformation into type 2, as it shown on figure 1.

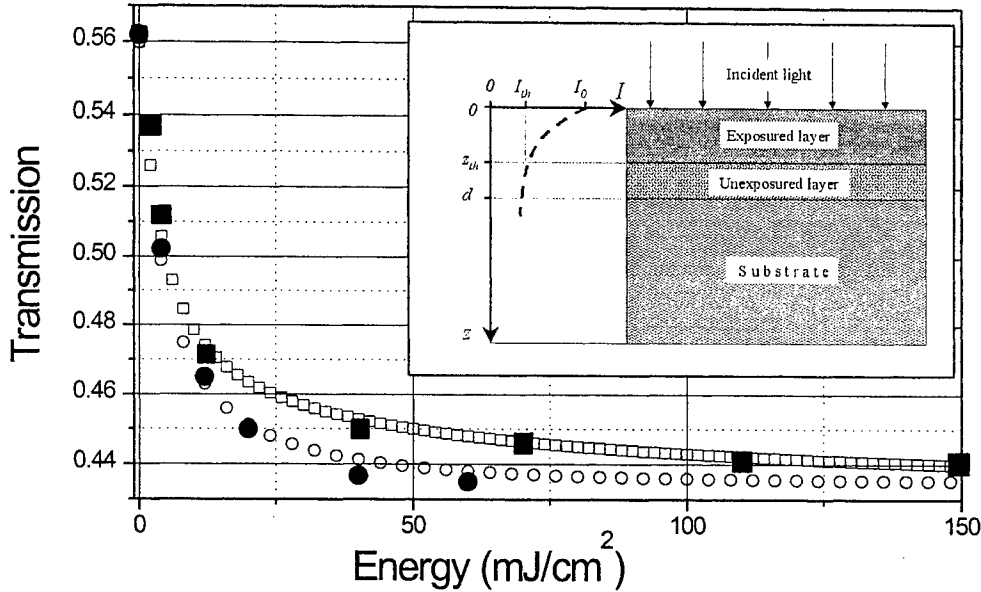


Fig.1. The curves of photodarkening demonstrate the experimental [1](solid symbol) and calculated (open symbol) dependence of transmission coefficient at the probe wavelength 630 nm on the exposure. Circles and squares correspond to pulse energy 2 and 4 mJ/cm², respectively. Inset illustrate the model structure. The intensity profile in photoresist volume. Threshold thickness z_{th} marks the boundary between exposed and unexposed layers.

3. MODELING OF PHOTODARKENING OF AsSe FILMS

Figure1 demonstrates the experimental and calculated dependencies of photodarkening for 200 nm AsSe film irradiated by pulse excimer laser irradiation. The best correspondence of calculated and experimental results can be obtained using the following parameters: $C=3 \cdot 10^{-3} \text{ cm}^3/\text{J}$, $I_{th}=1.7 \cdot 10^4 \text{ J}/(\text{cm}^2 \text{ sec})$, $\delta=8.5 \cdot 10^3 \text{ J}/(\text{cm}^2 \text{ sec})$. The difference between experimental and calculated dependencies can be explained by a deviation of laser temporal shape from Gauss shape, used in calculations.

One can obtain [4], that sensitivity C can be estimated basing on the slope $\delta T/\delta H$ of the photodarkening curves:

$$\delta T/\delta H \approx T_0(\beta_2 - \beta_1)C \quad (6)$$

where T_0 is the transmission coefficient at probe wavelength before irradiation.

4. MODELING OF CONTRAST ENHANCEMENT EFFECT

Let consider how non-linear character of photochemical changes influents the concentration profile of components $\rho_1(z)$ and $\rho_2(z)$ which is produced by exposure. The dissolution velocity depends on component concentrations so the threshold concentration $\rho_{1s}(z)$, which separates soluble ($\rho_1(z) < \rho_{1s}(z)$) and insoluble ($\rho_1(z) > \rho_{1s}(z)$) film areas, should be determined (see Fig.2). The equation system (1) must be resolved to calculate concentration profile in photoresist bulk created during exposure. But advance optimization of process characteristics (for example gradient of concentration profile near threshold concentration and slope of threshold concentration isoline near sample surface) can be analytical done.

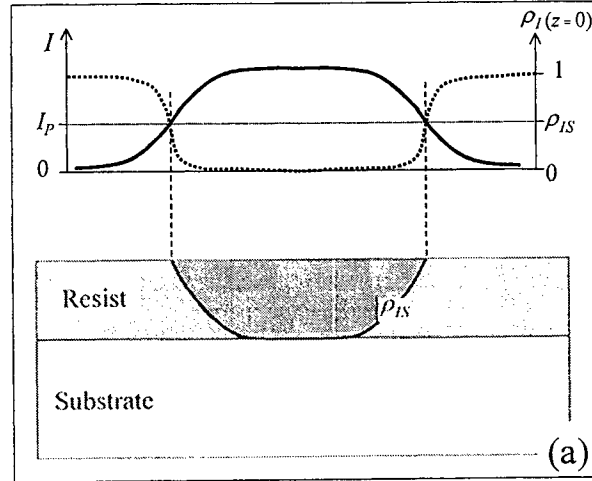


Fig.2. Photoresist on substrate and profile of radiation intensity. Isolines ρ_{1s} separates illuminated and dark areas. Solid line corresponds to spatial profile of intensity and dotted one corresponds to profile of concentration in photoresist bulk.

In case of rectangle pulse with duration T_p and intensity I_p the concentration on the surface after exposure is given by:

$$\rho_1 = [(1 + \gamma) \exp(\alpha_2 C T_p I_p F(I_p)) - \gamma]^{-1} \quad (7).$$

Function $\frac{d\rho_1}{dx}$ should have a maximum near threshold concentration ρ_{1s} to produce high quality image. So the goal is

extreme of function $\frac{d\rho_1}{dx}$.

Let $U = \left. \frac{(\partial \rho_1 / \partial x)}{b} \right|_{\rho=\rho_{1s}}$ (where $b = \frac{1}{I_p} \frac{\partial I_p}{\partial x}$ - relative edge intensity gradient) be a characteristic of contrast enhancement. This dependence can be represented in the form

$$U = (1 + \rho_{1s} \gamma) \rho_{1s} \ln \left(\frac{1/\rho_{1s} + \gamma}{1 + \gamma} \right) \left(1 + \frac{I_p}{F(I_p)} \frac{\partial F(I_p)}{\partial I_p} \right) \quad (8),$$

which has maximal value when the intensity of the pulse obey the equation

$$\exp\left(2\frac{I_p - I_{th}}{\delta}\right)\left(1 - \frac{2I_p}{\delta}\right) + 1 = 0 \quad (9).$$

Fig. 3a-3e demonstrates calculated concentration profiles for different intensity. The spatial profile of radiation is shown on fig.3f by thick solid line. We consider an area near boundary between illuminated and dark areas so intensity is changing from maximum to 0. In each case dose was choose as $\rho_I(x=150)=0.5$. Fig.3c corresponds to optimum intensity $I_p = 0.803I_{th}$. Fig.3a-3b correspond $I_p < 0.803I_{th}$ and fig 3d-3e correspond $I_p > 0.803I_{th}$. It can be seen that width of transition band is minimal when $I_p = 0.803I_{th}$.

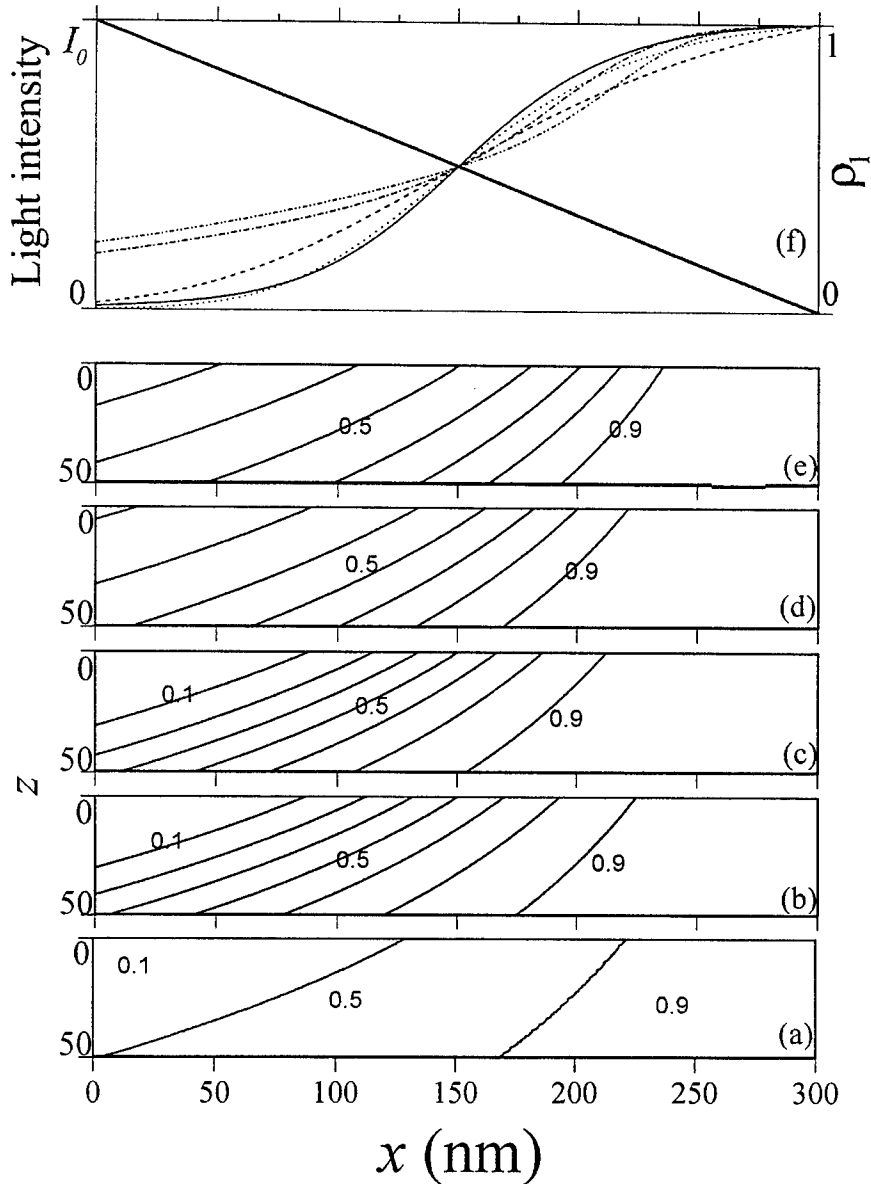


Fig. 3. Calculated concentration profiles for different intensity of radiation: (c) corresponds to optimum intensity $I_p = 0.803I_{th}$; (a-b) correspond $I_p < 0.803I_{th}$ and (d-e) correspond $I_p > 0.803I_{th}$; (f) represents surface concentration $\rho_I = \rho_I(x)$. Thick solid line corresponds to spatial profile of radiation.

Fig. 3f also demonstrate the dependence of surface concentration $\rho_l = \rho_l(x)$. The concentration gradient near boundary is higher than intensity gradient under optimal radiation intensity and dose.

All above is right for rectangle pulse. In other cases the optimal parameter may vary. Anyway they can be determined resolving equation system(1).

5. CONCLUSIONS

The model for theoretical description of photoinduced transformations in GCS has been developed. This model allows to describe satisfactory experimentally obtained dependencies of photodarkening of AsSe films under excimer laser irradiation. Besides, suggested model explains contrast enhancement effect observed for inorganic photoresists.

The high quality image can be produced using optimal radiation intensity and dose for nonlinear photoresist, which have nonlinear dependence on radiation intensity.

6. REFERENCES

1. E.G.Barash, A.Yu.Kabin, V.M.Lyubin, R.P.Seisyan. *Sov. Phys. Tech. Phys.*, **37**(3), 292-296 (1992)
2. L.G.Gladysheva, N.A.Kaliteevskaya, R.P.Seisyan, and D.V.Smirnov, *Tech. Phys. Lett.*, **22**(8), 640-641 (1996)
3. F.H. Dill, W.P. Hornberger, P.S. Hauge, *IEEE Transaction on electron devices*, **ED-22**(7), 445-452 (1995)
4. N.A.Kaliteevskaya, R.P.Seisyan, *Semiconductors*, **34**(7), 857-860 (2000).

Optical manipulation of liquid crystals using a two-beam technique

Etienne Brasselet and Tigran V. Galstian

*Centre d'Optique, Photonique et Laser (COPL)
Université Laval, Québec (Québec) G1K7P4 Canada*

ABSTRACT

The development of techniques of optical manipulation of matter attracts great attention [1]. One of the most interesting mechanisms for such manipulation is the dielectric (non-resonant) light-matter interaction [2]. This point was used by R. Beth, in 1936, to demonstrate an angular manipulation of a birefringent uniform macroscopic object [3]. We have proposed and developed a two-beam technique that is used for the manipulation of nematic liquid crystal (NLC) materials. Pertinent external control parameters, such as the mutual polarization of the two beams, the ratio of the two beams' intensity, the total intensity and the interaction geometry, are pointed out. Effective optical control via the non-resonant angular momentum transfer to the cluster of illuminated molecules is predicted and realized experimentally. In particular, it is shown that quasi-uniform precession regimes may be light-controlled at 100%. Moreover it is shown that the circularly polarized light-induced breakdown of orientational symmetry in non-chiral liquid crystals may result in their macroscopic chiral organization. Stationary, precessing and oscillating chiral modes are observed which may be controlled via the above mentioned external parameters. Consequently, since the non-planar deformations are at the origin of the multistability of the system, it is expected from the theory that some important features of the isothermal light-induced phase transition (first- or second-order, hysteresis width...) should be continuously light-driven, without breaking the circular symmetry of the excitation beams.

We believe that our two-beam technique is not restricted to the field of liquid crystals and may be also applied in biophysics, where living entities should play the role of the non-absorbing and birefringent material.

Keywords: Optical manipulation - Liquid crystals - Dielectric torque - Light angular momentum transfer - Light-induced chirality - Optical multistability - Phase transitions

1. GENERAL BACKGROUND

1.1. Non resonant optical manipulation

In the non-resonant light-matter interaction the dielectric anisotropy may play a crucial role. This point was used by R. Beth, in 1936, to demonstrate an angular manipulation of a birefringent uniform macroscopic object [3]. The situation is more complicated in non-uniform birefringent materials, such as liquid crystals. The non-resonant interaction of light with nematic liquid crystal (NLC) has been investigated extensively for past two decades [4-8]. When a light is normally incident on a homeotropically aligned NLC, a change in the orientational order appears if the intensity is above a threshold. This is the so-called light-induced Fréedericksz transition (LIFT) [4-8], which takes place thanks to the dielectric torque exerted by light on NLC. Depending upon the polarization of the excitation light the LIFT may be first- or second-order. The resulting electromagnetic field and molecular orientational states for the strongly coupled light-NLC system have been studied in details in the case of a single linearly polarized (LP), elliptically or circularly polarized (CP) excitation beams [5,6,8,9].

The aim of this paper is to demonstrate that the use of a two-beam light-matter interaction geometry may dramatically improve the optical control of birefringent materials. In the particular case of non-absorbing NLC, this results in the temporal (Section 2) and spatial (Section 3) manipulation of molecular deformations. The strong coupling between light and NLC allows the experimental observation of new dynamics that are rather well described theoretically (Section 2 and 4).

1.2. Light-matter interaction using a two beam technique

Hereafter we present the two key geometries of our two-beam technique. Namely the co-propagating light-NLC interaction (Fig.1) and counter-propagating one (Fig.2). Let's denote the co-propagating case with $\sigma' = +1$ and the counter-

propagating case with $\sigma' = -1$. The NLC cell is illuminated at normal incidence and the two-beam may be incoherent or coherent, depending of the phenomena under study.

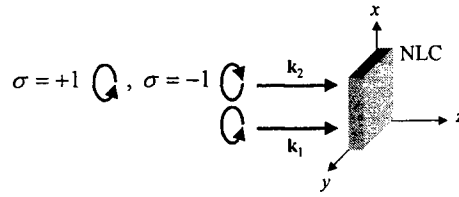


Fig.1: Interaction geometry in the co-propagating case

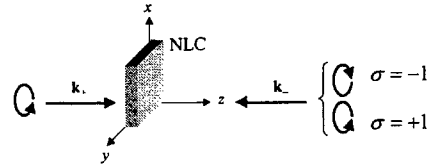


Fig.2: Interaction geometry in the counter-propagating case

Both co- and counter-rotating electric fields of these circularly polarized beams will be considered. In Figs.1-2 we defined with the help of σ , the relative circularity of the two interacting beams in both $\sigma' = \pm 1$ cases. When the two beams' polarization are co-rotating, $\sigma = +1$ and in the counter-rotating case, $\sigma = -1$ (See Figs.1 and 2). The ratio R between the two beam' intensity may be adjustable, hence $R = I_2 / I_1$ when $\sigma' = +1$ and $R = I_- / I_+$ when $\sigma' = -1$. The additional condition $0 \leq R \leq 1$ determines the strongest as the beam indexed by (1) or (+) and the weakest beam as the one indexed by (2) or (-). Finally, the total intensity I_{tot} is also used as a control parameter.

1.3. Physical model and main theoretical results

The theoretical approach, including the twist deformation for the NLC's director \mathbf{n} (local average direction of molecular axes) is done for both $\sigma' = \pm 1$ cases [10]. The light-matter interaction was there considered for normally incident plane waves, impinging on an infinite layer (in the (x, y) plane) of a homeotropically aligned ($\mathbf{n} \parallel \mathbf{e}_z$) cell. The perturbed director \mathbf{n} was described by polar angles θ and φ , as $\mathbf{n} = \mathbf{e}_x \sin \theta \cos \varphi + \mathbf{e}_y \sin \theta \sin \varphi + \mathbf{e}_z \cos \theta$, where θ is the tilt angle between \mathbf{n} and the z axis, φ is the azimuthal angle between the local (\mathbf{n}, z) and (x, z) planes, \mathbf{e}_x , \mathbf{e}_y , and \mathbf{e}_z are unit vectors along the x , y , and z axes (Fig.3).

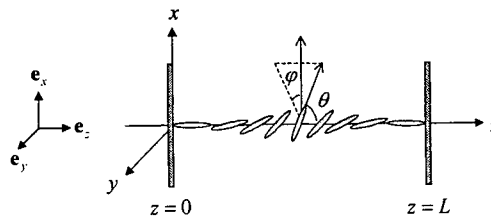


Fig.3 : Definition of the local angles that characterize a reoriented state for the NLC.

The reorientation ($\theta \neq 0$) of the NLC occurs when the total light intensity I_{tot} is above the LIFT threshold I_{th} . In both incoherent [11] and coherent [12] cases, $I_{th} = 2I_{lin}$ where $I_{lin} = 8\pi\epsilon_{\parallel}K_3q^2/(\epsilon_a\epsilon_{\perp})$, $\epsilon_a = \epsilon_{\parallel} - \epsilon_{\perp}$ is the dielectric anisotropy, $q = \pi/L$, L is the cell thickness, K_3 is the elastic constant of bend deformations and γ is the orientational viscosity [13] (whatever are the values of σ and R). Thus, we shall further refer to I_{tot} by means of the total normalized intensity with respect to LIFT threshold intensity, $\tilde{I} = I_{tot} / (2I_{lin})$.

The physical model of excitation was defined using the following dependencies of θ and φ : $\theta = \theta(z)$ and $\varphi = \Omega t + \alpha(z)$, where Ω is the pulsation of the director precession around the z axis and $\alpha(z)$ represents the possible twist of the director deformation. The generalized analytical solution that describes the co- or counter-propagating light-induced deformations is found [10], assuming $\theta^2(z) \ll 1$ when $\theta(z) = \theta_0 \sin(qz)$ is a good approximation, θ_0 is the amplitude of the polar deformation. It will be fruitful to write the solution in the following manner in the incoherent case:

$$\Omega = \frac{1 + \sigma R}{1 + R} f_{\Omega}(\tilde{I}, \Delta) \quad (1)$$

$$T = \frac{1 + \sigma' \sigma R}{1 + R} f_T(\tilde{I}, \Delta), \quad (2)$$

where $f_{T,\Omega}(\tilde{I}, \Delta)$ are functions of materials parameters, \tilde{I} and Δ . The Δ is the total nonlinear phase shift between e - and o -waves after the light passed through the NLC sample, $\Delta \equiv \tilde{L} \theta_0^2$ where $\tilde{L} \equiv (\pi \varepsilon_a \varepsilon_{\perp}^{1/2} L) / (2 \varepsilon_{\parallel} \lambda)$. T is the angle between director orientations near the output and input planes of the cell, $T = \alpha(L) - \alpha(0)$.

For the sake of simplicity let's imagine that in Section 2 and 3 the propagation of light is adiabatic, as in the linear Mauguin regime [13,14]. However, several important differences are present in our case, e.g. the director configuration is coupled to the light field, the phase velocity, and the amplitude of the extraordinary wave are changed along the propagation etc. Thus, during the propagation through the sample, the polarization ellipse of each beam is "attached" to the molecules as shown in Fig.4, where $\mathbf{l}_{\parallel} = (\mathbf{n} - (\mathbf{n} \cdot \mathbf{e}_z) \mathbf{e}_z) / \|\mathbf{n} - (\mathbf{n} \cdot \mathbf{e}_z) \mathbf{e}_z\|$ and $\mathbf{l}_{\perp} = \mathbf{e}_z \times \mathbf{l}_{\parallel}$ are unitary vectors defining respectively the slow and fast local axes of the birefringent slice of NLC located between z and $z + dz$:

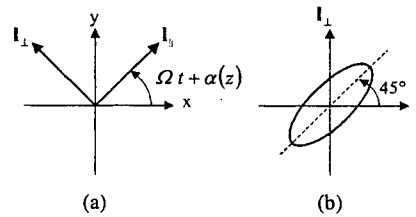


Fig.4 : (a) Slow (\parallel) and fast (\perp) axis of the elementary birefringent slice of NLC between z and $z+dz$.
(b) Polarization ellipse "attached" to the local birefringent axes.

2. OPTICAL TEMPORAL MANIPULATION OF A MOLECULAR CLUSTER

A regular molecular precession regime could be generated by the use of a single circularly polarized beam at the LIFT threshold $\tilde{I} = 1$ [15]. In this case the transferred angular momentum (AM) per photon is $\approx 2\hbar$ ($\Delta \approx \pi$) [10,15,16]. The total AM transferred to matter (that defines its precession rate) cannot be effectively controlled by the total number of photons participating to the AM transfer. Indeed, the total phase shift Δ depends on the \tilde{I} (the total number of photons), moreover dissipation (the viscous torque) increases with the Δ . Another possibility would be the introduction of coherent photons with opposite AM keeping fixed their number. However, the later attempt leads to a breakdown of azimuthal symmetry (the excitation light being then elliptically polarized), creating a preferred reorientation direction and resulting in suppression of regular precession regime.

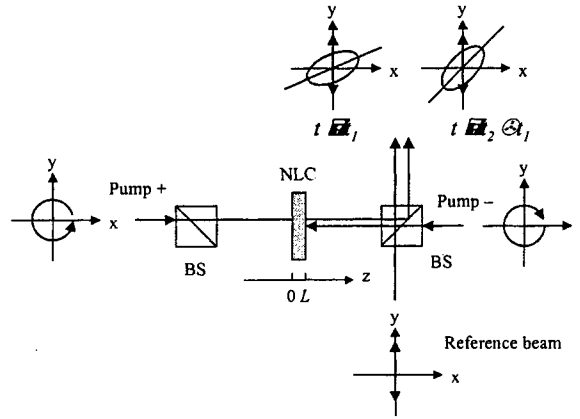


Fig.5 : Experimental set-up allowing the all-optical control of collective molecular precession phenomenon in the counter-propagating case, BS: beamsplitter.

Using two incoherent beams with opposite input AM ($\sigma = -1$), keeping constant \tilde{I} , the molecular precession rate is 100% controllable, simply varying the ratio R of the two beam intensities (see Eq.1 and Fig.6). This is experimentally demonstrated in both co- [17] or counter-propagating geometry [10] (see Fig.5). The precession regime is demonstrated and the precession rate is measured (sign and absolute value) using a simple technique. Namely, the emerging beam from the sample (elliptical) and a reference beam (linear) are simultaneously detected behind a rotating polarizer [10].

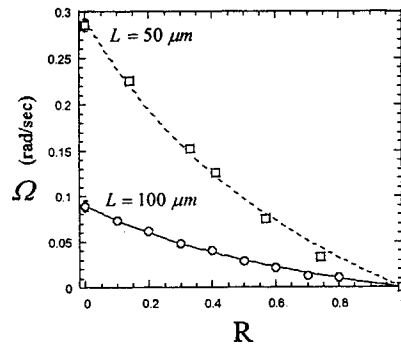


Fig.6 : Demonstration of all-optical temporal manipulation of the reoriented NLC at the LIFT threshold in the counter propagating geometry. Experimental results (circles for $L=100 \mu\text{m}$ and squares for $L=50 \mu\text{m}$) are fitted using Eq.1. Solid line (respectively dashed) is the best fit for $L=100 \mu\text{m}$ (respectively $L=50 \mu\text{m}$).

The intensity dependence of the precession rate depends strongly on the interaction geometry. In the CP LIFT case, the initial quasi-optimal AM transfer condition ($\Delta \approx \pi$) and the dissipation (when Δ increases) together dominate the increase of the total number of photons, when \tilde{I} is increased (slowing down of Ω , Fig.7) [8,10]. The use of two interacting beams allows generating dynamics where the viscous slowing down and AM transfer condition may be compensated by the increasing total intensity (Fig.7) [10]. Thus, the use of a two-beam technique gives an access to several new dynamic regimes of a cluster of NLC molecules that are not observable with a single beam experiment.

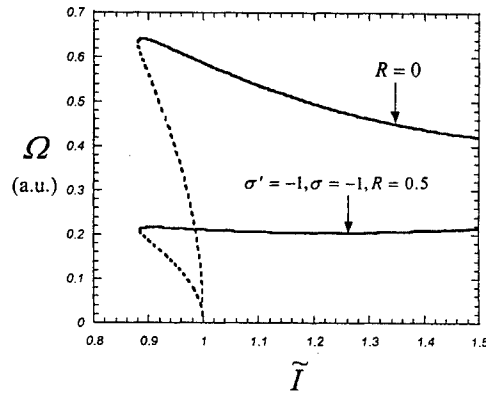
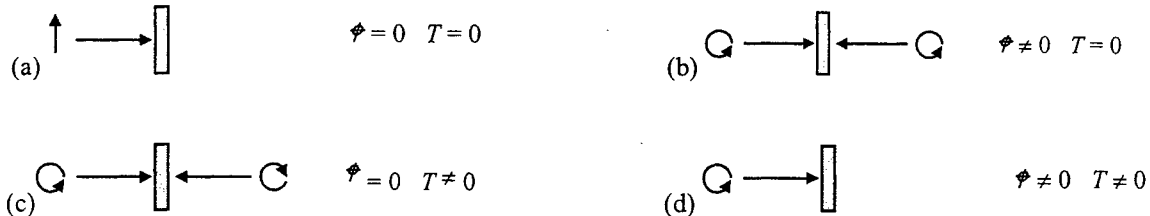


Fig.7 : Comparison of the intensity dependence of the precession rate in a single beam and a two beam interaction geometry.

3. OPTICAL SPATIAL MANIPULATION OF A MOLECULAR CLUSTER

For the sake of simplicity, we shall further refer to the quantity T (introduced in Section 1) as *twist*, keeping in mind that if $T = 0$, the molecular deformation in the volume of NLC is not necessary in-plane ($d\alpha/dz \neq 0$). The analysis of the dependence of T upon the parameters R , σ and σ' (see Eq.2) allows us to predict some important features of LIFT (see Figs.8). For example, the NLC molecules must precess ($\Omega \neq 0$) without twist deformation ($T = 0$) in the case when the LIFT is induced by two counter-propagating beams carrying the same angular momentum ($R = 1, \sigma = 1, \sigma' = -1$, Fig.8b). In contrast, the molecular organization must be twisted ($T \neq 0$), but there should be no precession ($\Omega = 0$) when the LIFT is excited by two counter-propagating beams of the opposed angular momentum ($R = 1, \sigma = -1, \sigma' = -1$, Fig.8c and Fig.9). The use of CP beam ($R = 0$, Fig.8d) should lead to the formation of a twisted molecular deformation, which is precessing around the normal to the cell substrates ($\Omega \neq 0$ and $T \neq 0$). Finally let's recall that the LP LIFT induces a planar and stationary molecular organization ($\Omega = 0, T = 0$) [4-6] (Fig.8a).



Figs.8 : Summary of the various possibilities of spatio-temporal manipulation in the particular case of two incoherent counter-propagating beams.

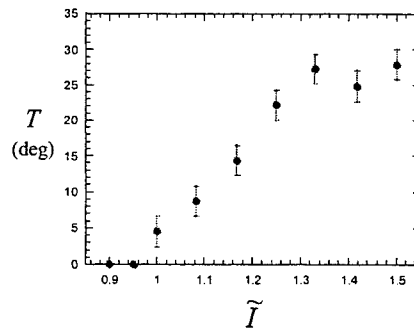


Fig.9 : Total twist angle T versus the normalized intensity in the case of two incoherent counter-propagating beams with opposite AM and equal intensities for $L=80 \mu\text{m}$.

When the LIFT is excited by two counter-propagating beams of the opposed angular momentum ($R = 1, \sigma = -1, \sigma' = -1$, Fig.7c and Fig.8), after the transient regime, the twist is found to be non-zero and constant with time (the precession is absent as predicted above). Thus, we obtained a light-induced and stabilized helicoidal molecular structure from a non-chiral nematic liquid crystal and we can thus speak of light-induced chirality. Note that some theoretical discussion about its possibility was already done in the past [18]. The Fig. (2) shows that the "twisting power" of the total pump field increases with intensity (so with the Δ). For much higher intensity, a transition to a large Δ state (with multiple self-focusing rings [4]) is observed.

The effective control of twisted deformations at fixed total intensity (Eq.2) predict the control of optical bistability without breaking the azimuthal symmetry in the case of two co-propagating beams of opposite input AM. This is not possible in the case of a one beam light-matter interaction geometry. Experimental demonstration of such possibility is currently under study. Thus we expect from our calculations that we could generate a first-order LIFT under azimuthal symmetry whose hysteresis width is all-optically adjustable. Moreover a second-order LIFT may be obtained under the later symmetry when the two-beam intensities are equal.

4. OPTICAL MULTISTABILITY IN NEMATIC LIQUID CRYSTALS : STRONG EXCITATION REGIME

The LP LIFT (in the case of our NLC) is second-order and leads to a unique stable solution for the molecular deformation at a given input intensity [4-7]. On the contrary, theoretical analysis of the first-order [8,16] CP LIFT has shown the possible presence of a multistability for intensities just above the LIFT threshold value and a unique stable solution for much higher intensities [8]. However, the later multistability has never been observed experimentally.

Once again, we show that the control of NLC deformation may be dramatically improved when using a two-beam excitation geometry. Namely, we use a two-beam technique to optically generate and control new spatio-temporal deformation modes in NLC. Thus, a multistability of a light-NLC system is theoretically predicted for light intensities far above the threshold of molecular reorientation. The predicted multistability is observed experimentally. Moreover, it is shown that the discrete-like behavior of orientational states is directly related to the twist (non-planar) deformations. An analysis, that takes into account the contribution of such deformations, is done to propose a physical model explaining the observed confined orientational states. [19]

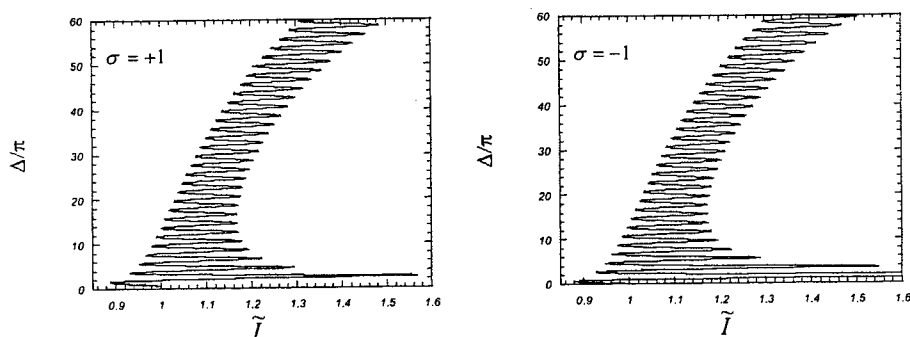


Fig.10 : Calculated total nonlinear phase shift (between the o - and e -waves) versus the normalized intensity obtained for $L=90 \mu\text{m}$, in the case of two co-propagating beams with equal intensities and same input AM ($\sigma=+1$) or opposite input AM ($\sigma=-1$).

5. SUMMARY

Through various examples we have demonstrated that the use of a two-beam technique improves the optical manipulation of a light-NLC system. In particular we obtained an effective control of spatio-temporal molecular deformations. Several demonstrations are made, for the first time to our best knowledge, in the already extensively studied field of liquid crystals optics : a light-driven molecular motor experiment is achieved, a light-induced chirality is obtained in

a initially non-chiral NLC, optical multistability is predicted and observed experimentally, theoretical predictions about a light-driven optical bistability under azimuthal symmetry are done, new dynamics of light-NLC system are observed, etc.

Finally we are convinced that our two-beam technique is not restricted to the field of liquid crystals and may be also applied in all fields of non-resonant optical manipulation and we hope that it will contribute to a better understanding of the light-matter interaction for various materials. Note that in the case of resonant interaction our technique could also be useful, indeed our group recently obtained the optical generation of helicoidal molecular structure in dye doped polymers under the action of helicoidal standing wave (two coherent counter-propagating beams with counter-rotating electric field and equal intensities) [20].

REFERENCES

- [1] C. S. Adams, and E. Riis, *Progress in Quantum Electronics* **21**, 1 (1997).
- [2] A. Ashkin, *Phys. Rev. Lett.* **40**, 729 (1978).
- [3] R. A. Beth, *Phys. Rev.* **50**, 115 (1936).
- [4] S. D. Durbin, S. M. Arakelian, and Y. R. Shen, *Phys. Rev. Lett.* **47**, 1411 (1981).
- [5] B. Ya Zel'dovich, N. V. Tabiryan, and Yu. S. Chilingaryan, *Zh. Eksp. Teor. Fiz* **81**, 72 (1981) [*Sov. Phys. JETP* **54**, 1, 32 (1981)]; B. Ya Zel'dovich and N. V. Tabiryan, *Zh. Eksp. Teor. Fiz* **82**, 1126 (1982) [*Sov. Phys. JETP* **55**, 656 (1982)]; N. V. Tabiryan, A. V. Sukhov, and B. Ya Zel'dovich, *Mol. Cryst. Liq. Cryst.* **136**, 1 (1986).
- [6] A. S. Zolot'ko, V. F. Kitaeva, N. N. Sobolev, and A. P. Sukhorukov, *Zh. Eksp. Teor. Fiz* **81**, 933 (1981) [*Sov. Phys. JETP* **54**, 496 (1981)]; A. S. Zolot'ko, V. F. Kitaeva, N. N. Sobolev, and L. Csillag, *Pis'ma Zh. Eksp. Teor. Fiz* **34**, 5, 263 (1981) [*JETP Lett.*, **34**, 5, 250 (1981)].
- [7] H. L. Ong, *Phys. Rev. A* **28**, 2393 (1983).
- [8] L. Marruci, G. Abbate, S. Ferraiuolo, P. Maddalena, and E. Santamato, *Phys. Rev. A* **46**, 4859 (1992).
- [9] E. Santamato, G. Abbate, P. Maddalena, L. Marruci, and Y. R. Shen, *Phys. Rev. Lett.* **64**, 1377 (1990).
- [10] E. Brasselet and T. V. Galstian, *Optical control of molecular orientational dynamics in LC*, to be published.
- [11] T. V. Galstian, A. A. Yesayan, and V. Drnoyan, *Phys. Rev. E* **58**, 4605 (1998);
- [12] E. Brasselet and T. V. Galstian, *Fréedericksz transition in NLC under coherent interaction of counter-propagating light waves*, to be published.
- [13] P. G. de Gennes, and J. Prost, *The Physics of Liquid Crystals* (Clarendon Press, Oxford, 1993), 2nd ed..
- [14] C. Mauguin, *Phys. Z.*, **12**, 1011 (1911).
- [15] E. Santamato, B. Daino, M. Romangoli, M. Settembre, and Y. R. Shen, *Phys. Rev. Lett.* **57**, 2423 (1986).
- [16] A. S. Zolot'ko, and A. P. Sukhorukov, *Pis'ma Zh. Eksp. Teor. Fiz* **52**, 1, 707 (1990) [*JETP Lett.* **52**, 1, 63 (1990)]. [17] T. V. Galstian, and V. Drnoyan, *Phys. Rev. Lett.* **78**, 2760 (1997).
- [18] S. M. Arakelyan, Private communication.
- [19] E. Brasselet and T. V. Galstian, *Optical multistability and confined orientational states in nematic liquid crystals: Strong excitation regime*, to be published
- [20] R. Birabassov, T. Galstian, *Holographic reflection gratings in dye-doped polymer materials*, 2000 International Conference on Applications of Photonic Technology (ICAPT2000), June 12-16, Québec City, Canada.

Photostructure transformation effects of layer consisting from CAMC:OMA copolymers under the action of laser irradiation

V. Bivol, V. Robu*, L. Vlad*, A. Coban*, A. Prisacari

Center of Optoelectronics of Academy of Sciences of Moldova Republic
1 Academiei Str., MD-2028, Chisinau, Moldova Republic

* State University of Moldova Republic

ABSTRACT

The photochemical method of image recording of carbazole - containing polymeric layers (f.e. PVC and its copolymers or poly -N - epoxypropylcarbazole, containing under 10% of photochemical cross-linking agents at the range of calcogen - derivatives of methane and etc.) attributes to well-known methods of image recording.

The carbazolalkylmethacrylate (CAMC) copolymer with octylmethacrylate (OMA) photoplastic carries has been investigated in details on the purpose to enlarge the image photographic characteristics of carbasolalkylmethacrylate. The photopolymer layers were made by pouring from solutions.

The structure of CAMC is 1:1 and contains OMA varying from 0 to 50mol%. There were additionally added about 5-16% iodophorm CHI_3 for photo-cross-linking of given copolymer layers. The best results of macromolecular photo-cross-linking in UV-rays were obtained with 60-70mol% CAMC containing copolymers. It can be connected with good flexibility of polymeric macromolecules. Optimal concentration of iodophorm was about 8-10%.

It has been used a coherent laser beam with $\lambda=420$ nm for holographic images recording (Ne-Cd-lazer). There were obtained holographic gratings with resolution 1500 mm^{-1} and diffraction efficiency 23%. This material has photographic sensitivity $10^3 \text{ m}^2/\text{J}$ that allows using the explored copolymers for elaboration of a new optic media for holographic images recording.

Keywords: copolymer, layer, image, registration, cross-linking, recording, laser, holography, resolution, diffraction efficiency.

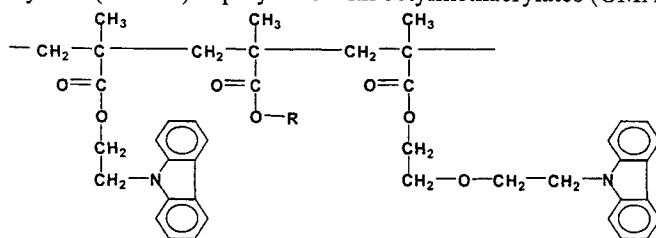
1. INTRODUCTION

Recently special attention was given to the problem of holographic registration of images and information with the purpose of a solution of various scientific and technical problems, as well as for protection of important documents from falsification. For solution of the given problem occupied reliefs-graphic methods of registration of holograms with application of inorganic semiconductors or organic photoconductors (PC) from carbazol-containing polymers sensitized by electron-donor additives the special place in the scientific and technical literature [1 – 4]. On photopolymer PC-layers from carbazol-containing polymers of the polyepoxypropylcarbazol type or vinylcarbazol with oktylmethacrylate copolymers the holographic images with good diffraction efficiency 10-12 %, resolution up to 500 mm^{-1} and photographic sensitivity $10^{-5} - 10^{-6} \text{ J/sm}^2$ were obtained by the photothermoplastic method of the recording [4].

With the purpose of improving of the photographic characteristics, in particular the diffraction efficiency and the resolution, as well as for simplification of the process of production we studied and proposed photopolymer layers from carbazol-containing compositions with 4-10 % of the cross-linking agents capable to photostructurization. The possibility of using of the obtained mediums for registration of holographic images with better photographic characteristics is investigated.

2. EXPERIMENTS AND RESULTS

Carbazolylalkylmethacrylates (CAMC) copolymers with octylmethacrylates (OMA) of the common formula



containing about 60 mol % of carbazolyl links were obtained by a method of radical polymerization in a tholuen solution. Polyepoxypropylcarbazol (PEPC) is commercially available. The given photopolymer was synthesised from N-epoxypropylcarbazol by cation or anion polymerization methods.

For preparation of the samples mediums the solutions of above indicated CAMC and PEPC copolymers added with 0-10 % of iodophorm CHI_3 or other cross-linking agents were prepared. The photopolymer layers were applied both on transparent poly(ethylenethereftalat) films and on rigid substrates from an optical glass. The thickness of the samples ranged from 1,0 μm to 20,0 μm . The samples were dried up on air and then in a drying camber at $T^\circ \sim 40^\circ\text{C}$ within 24 hours.

The samples of carriers for photothermoplastic registration were prepared from tholuen solutions sensitized by electron-acceptor additions by deposition on metalized poly(ethylenethereftalat) films with transparency $\sim 90\%$.

2.1. Sensitometric investigations

It is known [5, 6] that photo-chemical transformations in carbazol-containing polymers at the presence of cross-linking agents like iodophorm CHI_3 occur according to the ion-radical mechanism with formation at the issue of spatially – cross-linked structures, that allows to use them for registration of information. In the given part of work the sensitometric characteristics (photo-sensitivity, coefficient of visibility and other parameters) in dependence from the concentration of CHI_3 in a photoconducting layers and from their thickness, from the kind of radiation etc were investigated. The trial study was carried out on PC-layers from PEPC taken as an analogy and from CAMC:OMA copolymers. The layers were exposed to ultra-violet light with incident energy $E = 10 - 20 \text{ mW}/\text{sm}^2$ and also to white light (mercury-quartz lamp PRK-4 and 500 W incandescent lamp as sources). The photo-structural transformations were observed visually as modification of colour of the PC-layers and through losing of solubility of the irradiated areas. Quantitatively, the photo-structural modifications are well seen in the spectra of visible region.

The maximum of visible absorption spectra (Fig.1) is observed in the interval 630-650 nm. As follows from Figure 1 in a defined time $t = 30 \text{ s}$ the intensity of absorption becomes constant and corresponds to a full cross-linking of the PC-layers.

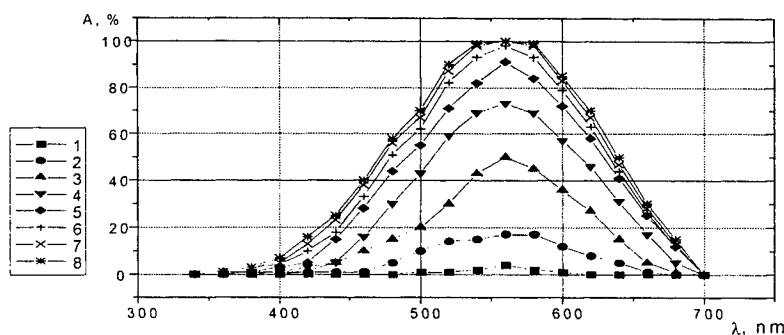


Fig. 1. Modification of the absorption intensity with the time of exposure of the layers:
1 - 0 s; 2 - 5 s; 3 - 10 s; 4 - 15 s; 5 - 20 s; 6 - 25 s; 7 - 30 s; 8 - 40 s;

The investigation of the polymeric composition influence on structural photo-cross-linking in dependence on carbazolic nucleus concentration (as CAMC-1 and CAMC-2) in polymers represents a great interest. There are investigated the process activation of layers photo-cross-linking with different additives (f.e. chloranyl etc.).

It was shown the layers photo-cross-linking acceleration in dependence on increasing of chloranyl (ClAn) concentration (1-2%) in polymeric compositions (CAMC-1:CAMC-2 (50:50mol%) was called as poly-CAMC, CAMC:OMA). The time of layers full photo-cross-linking regresses from 30-35 minutes to 18-20 minutes in the case of poly-CAMC (Fig.2) and CAMC:OMA(Fig.3) with UV-irradiation.

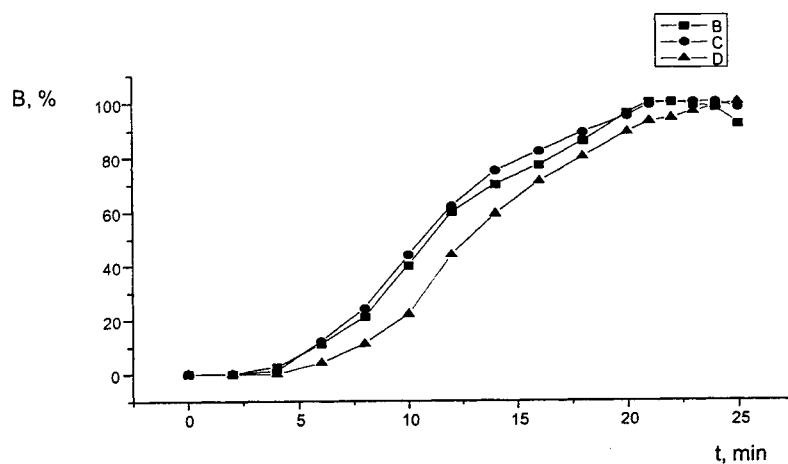


Fig. 2. Dependence of photo-structurization of layers with the time of UV-irradiation:
 B – CAMC1:2(50:50)+10%CHI₃+1%ClAn;
 C – CAMC1:2(50:50)+10%CHI₃+2%ClAn;
 D – CAMC1:2(50:50)+10%CHI₃.

In the case of laser irradiation the photo-cross-linking time is about 3-5 min. The optimal concentration in photopolymer layers is about 2% as we can see from Fig.2, Fig.3 and especially from Fig.4.

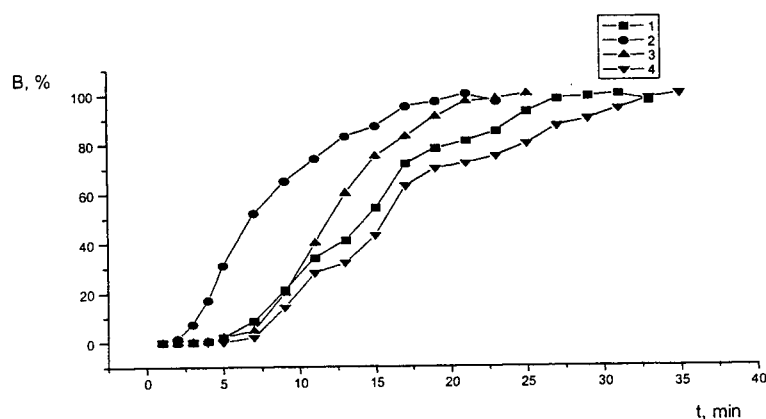


Fig.3. Dependence of photo-structurization of layers with the time of UV-irradiation:
 1 – CAMC:OMA (60:40)+10%CHI₃+1%ClAn;
 2 – CAMC:OMA (60:40)+10%CHI₃+2%ClAn;
 3 – CAMC:OMA (60:40)+10%CHI₃+3%ClAn;
 4 – CAMC:OMA(60:40)+10%CHI₃.

With the following increasing of chloranyl concentration the photo-cross-linking process became less as we can see from Fig.4. It can be connected with carbasol nucleus isolation. Such effect we have observed in the case of OMA concentration increasing in the CAMC:OMA copolymers.

The increasing of OMA plastifier component concentration always results to the layers photo-cross-linking time increasing. The increasing of OMA molar concentration in copolymer layers from 0 to 40mol% results to the layers photo-cross-linking time increasing more than for 15 minutes.

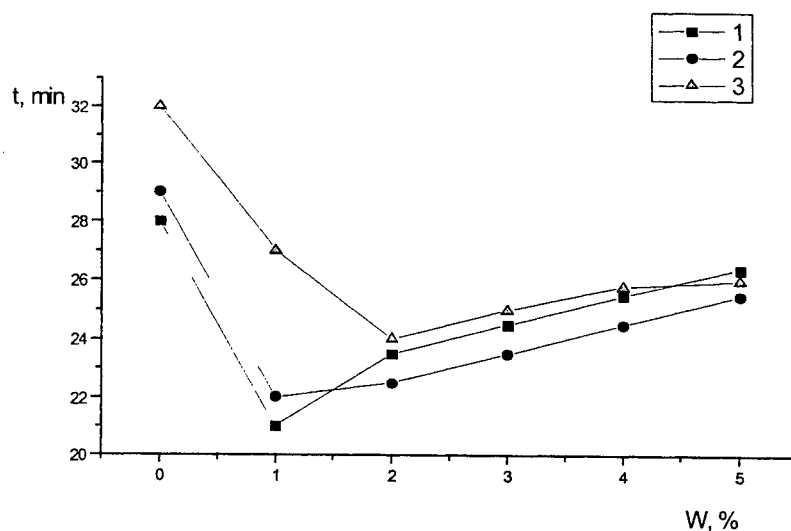


Fig.4. Dependence of the complete photo-structurization of the CAMC-layers with different OMA concentration on the concentration of ClAn:

- 1 - CAMC (1:2) (50:50);
- 2 - CAMC:OMA (80:20);
- 3 - CAMC:OMA (60:40).

2.2. Holography investigations

To obtain good holograms on the PC-polymer layers an installation on the base of 1W CW Argon - Ion laser and 20 mW He-Cd laser was mounted. An iris diaphragm was placed intra-cavity to select single mode output from Argon-Ion laser (type LG-106). This regime allows us to increase the length of coherence and, as a consequence, to obtain good holographic scene with the depth of definition up to 15 sm. The laser power in single mode output was 200 mW on wavelength $\lambda=0,49 \mu\text{m}$ for Argon-Ion laser and 15 mW on wavelength $\lambda=0,42 \mu\text{m}$ for He-Cd laser.

Optical set-up of the experimental holographic installation is presented in Fig. 5 and consists of: 1 - He-Cd laser; 2 - mirrors; 3 - PC-polymer layer; 4 - collimator system; 5 - He-Ne laser; 6 - photo-detector; 7 - optical power meter and transformation system; 8 - computer system; 9 - beam splitter.

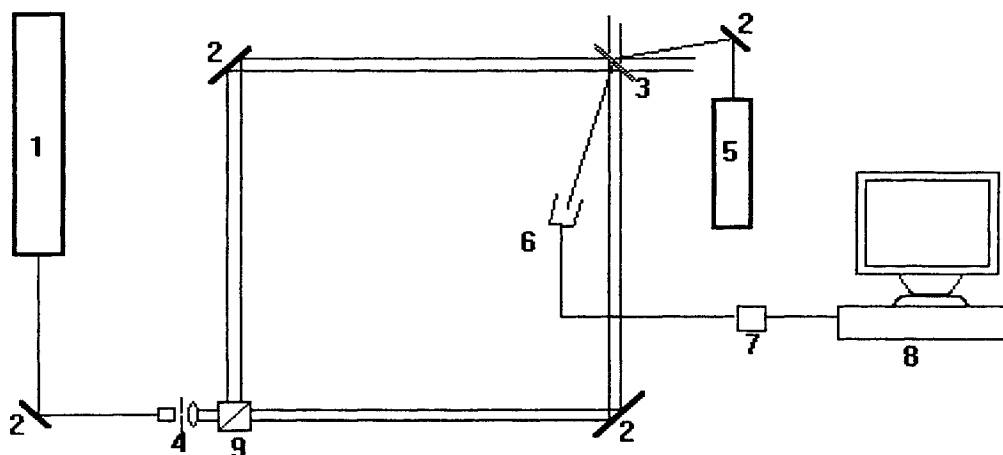


Fig. 7. Optical setup:

1 - He-Cd laser; 2 - mirrors; 3 - PC polymer layer; 4 - collimator system;
5 - He-Ne laser; 6 - photo-detector; 7 - optical power meter and transformation
system; 8 - computer system; 9 - beam splitter.

The experimental results on reflection hologram recording have shown that the resolution of the holographic monolayer based on PEPC and CAMC:OMA photoconductor polymer layers is no less than 2000 mm^{-1} . The maximum of the diffraction efficiency of the reflection holograms is 1,5 % at the layer thickness of 5-6 μm . The following chemical treatment permits to increase the diffraction efficiency up to 20 %.

For the layers capable to photostructurization made from copolymers of carbazol-containing compositions with 4-10 % of cross-linking agents and with 1-2% of HlAn, the dependence of diffraction efficiency of registered diffraction gratings on the time of exposition was investigated. The registration of diffraction gratings was carried out at spatial frequencies 1500 mm^{-1} . The results of measurements are shown in a Table 1.

Table 1

1 – PEPC+8%CHI₃+1%HlAn samples; 2, 3 – PEPC+8%CHI₃+2%HlAn samples;
4, 5 – poly-CAMC+8%CHI₃+2%HlAn samples; 6 – CAMC:OMA (80:20)+8%CHI₃+2%HlAn samples;
7 – CAMC:OMA (60:40)+8%CHI₃+2%HlAn samples;

$N_{\text{sampl.}}$	$n, \mu\text{m}$	$\eta_{\text{IR}} + \eta_{\text{I'R}}, \%$	$\eta_{\text{IT}} + \eta_{\text{I'T}}, \%$	$t_{\text{expos}}, \text{min}$	$t_{\text{treat}}, \text{s}$
1	5-6	1,5	2,7	4	10
2	5-6	1,8	3,5	4	10
3	5-6	2,2	15,3	8	10
4	5-6	5,4	3,1	4	10
5	5-6	23,0	12,0	8	10
6	5-6	19,6	10,3	8	10
7	5-6	16,3	8,2	8	30

$$\lambda=0,42 \mu\text{m}; W=7 \text{ mW}; \nu=1500 \text{ mm}^{-1},$$

It is seen from the table that the diffraction efficiency of the poly-CAMC-layers with 2% of HlAn increases up to 23 % with the exposition time up to 8 min.

3. CONCLUSION

1. The photopolymer layers capable to photostructurization from carbazol-containing compositions with 4-10 % of the cross-linking agents are offered.
2. The contents of carbazol-containing copolymers has an influence at all photo-cross-linking process.
3. The increasing of carbazolic component in carbazolyalkylmethacrylate copolymers reduces the full photo-cross-linking time more than for 25%.
4. The optimum concentration of sewing component CHI_3 in PEPC and CEM:OMA PC-layers is 8-10%.
5. The activator presence (f.e. chloranyl – 1-2%) accelerates the photo-cross-linking process.
6. The obtained layers are examined with the aim of registration holographic images with improved photographic characteristics.
7. The diffraction efficiency of the registered diffraction gratings reaches 23 % with increasing of exposure time up to 8 min.

REFERENCES

1. Kuvshinskii N.G., Nahodkin N.G., Lamko I.N. *Fundamentalnie osnovi opticheskoi pamiati i sredi*. Kiev, v.18, p.15-34, 1987.
2. Vannikov A.V., Grishina A.D. *Fotochimia polimernih kompleksov*. M., "Nauka", 1984.
3. N.Barba, G.Dragalina, S.Robu. *Compusi coordinativi si polimeri. Sinteza si utilizarea*. Chisinau, "Stiinta", p.69, 1991.
4. Kartujanski A.L. *Perspectives and possibilities of unsilver photoography*, Leningrad, 1988 (Rus).
5. Колнинов О., Милинчук В. и др. *Высокомолекулярные соединения*. Т.22, №9, 1980, с.2042.
6. Милинчук В. *"Макрорадикалы"*, Москва, 1989.

Formation and dynamics of ordered nanometer structures and emission of photons from a rear surface of metal samples at the irradiating of frontal surface by laser pulse.

K.B. Abramova, I.P. Shcherbakov

Ioffe Physico-Technical Institute RAS St. Petersburg, Russia; E-mail: abramova.mhd@pop.ioffe.rssi.ru

With the help of tunnel microscopy it was carried out the experimental research of the form and quantity of defects formed on the back surface of Cu, Ag and Au samples, at irradiating their frontal surface by laser pulses. The correlation between quantity of defects arising on a rear surface of metal and intensity of its luminescence was observed. The offered mechanism of generation of emission, and also capability of research of the emergence of mobile dislocations on a surface of metal with the help of mechanoluminescence are discussed.

key words: metal target, rear surface, nanometer structure, luminescence, tunnel microscopy

Introduction.

In formation of physical properties of solid the important role is played by defects of a crystalline structure. Among them large value have the one-dimensional defects - dislocations, which appearance results, in particular, in change of the energy spectrum of crystal determining many physical properties of a solid. The optical measurements bear the direct information on optical transitions in crystal and, therefore, their research gives information about features of dislocations in a solid.

For present work the interest is represented with research, directed on study correlation between the emergence of mobile dislocations on a metal surface and emission of photons at loading. In [1,2,3] it is shown, that at deformation of noble metal samples (Cu, Ag and Au) on their surface the submicrodefects as prisms with an apex angle equal $\sim 70^\circ$ will be derivated. It is known [4], that Cu, Ag and Au have CFC - lattice, in which the angle between planes of easy glide

(111) and $(11\bar{1}) \gg 70.5^\circ$. Therefore, it is natural to consider that these defects will arise due to emergence of mobile dislocations on a metal surface [2,3]. By release of energy, accumulated in dislocation nuclei, at their emergence on a metal surface under the action of stress fields in [5,6] were explained the results of experiments [7], in which the emission of photons accompanying the destruction of metal samples was registered. Later it was shown, that the similar emission accompanies also deformation of metals, including loading with the help of the laser pulse [8,9]. Experimentally are investigated temporary and spectral characteristic of emission from various metals. It is shown, that at deformation and destruction in spectral characteristic of emission there are certain bands of luminescence depending on an electron structure of metal surface, and the emission begins, when the stresses in a sample are close to a yield point [10,11].

According to the theory [5,6,12] the intensity of a mechanoluminescence is described by the formula

$$I = \eta \langle \hbar \omega \rangle g_0 \exp(-\alpha t) \quad (1)$$

Where η - probability of an emission recombination, $\langle \hbar \omega \rangle$ - mean energy of quantum, α - constant depending on metal properties, t - time, g_0 - speed of holes generation.

$$g_0 = \frac{P_b \varepsilon}{a b} \quad (2)$$

Where $\dot{\epsilon}$ - speed of change of deformation, P_h - probability of formation of a hole, a - lattice parameter, b - Burgers vector.

From the adduced formulas it is evident, that the intensity of mechanoluminescence depends on several parameters, but all of them are constant for the given metal, the elimination is made only with quantity of speed of deformation change, expression for which has a form

$$\dot{\epsilon} = N_d b v_d \quad (3)$$

Where N_d, v_d accordingly concentration of mobile dislocations and speed of their motion. Experimentally is confirmed, that under all other equal conditions the intensity of luminescence is the more, the more is application velocity of the load and the is more, than more is initial density of dislocations in a researched sample [8,13,14]

In [14] at research of mechanoluminescence arising on the rear surface of a metal sample at irradiation the frontal surface by laser pulses of the same power was revealed, that with increase of number of irradiating laser pulses, the intensity of a mechanoluminescence decreases. The supposition was stated, that the decreasing of intensity of mechanoluminescence, is caused by gradual decreasing the number of dislocations during irradiation, which are capable to emerge on a surface of a metal sample.

The present work continues a cycle of these researches. If the mechanoluminescence is really connected with an emergence of mobile dislocations on a sample surface, then must be observed the correlation between mechanoluminescence intensity and change of dislocation quantity on a surface at irradiating metal samples by several pulses. The present work is delivered with the purpose of check of this supposition, and also for research of capabilities, which will allow to establish the regularities of dislocations motion with the help of registration of emission.

Experimental technique.

The profiles of surfaces of copper samples by cleanness 99,96 %, silver - cleanness 99,99 % and gold - cleanness 99,99 %, thickness 0.1- 0.5 mm, area 30 x 30 mm were investigated.

The changes of a relief of a surface were registered with the help of scanning tunnel profilometer DTP-1 developed in a scientific research institute of physics LSU and made by the production co-operative "ERA".

For the control of the resolution and the stability of the device was used a diffraction lattice on arsenid hallium, on which surface the layer of gold was spray-coated. The measuring edges were produced from a tungsten wire by electrochemical etching. Their form was evaluated on images of most minor defects on topograms.

In a profilometer a measuring edge capable moving perpendicularly surfaces, no more than on 1 μ m. To delete microirregularities exceeding 1 μ m, the samples were polished with diamond pastes, then were washed out by acetone and spirit.

Chemical structure of a surface before and after researches was checked with the help of Auger - spectrometer LH-10. It appeared, that the researched surfaces are covered with a layer of oxide by a thickness of $\sim 1,5 \div 2$ nm. To level distortion, which could arise because of availability of this layer, it was investigated the form and sizes of defects exceeding 5 nm.

At condensation of water vapors of air on researching surface of metals the electrolyte will generate on a researched surface, in which there is an ionic current eliminating a capability of obtaining the profile of a surface. To suppress this phenomenon, a sample was covered by a hood from polyurethane, through which dry nitrogen was purged.

For registration of luminescence the investigated surface was placed at a distance $r_1 = 3$ cm from entrance window with a radius 0.3cm of the photomultiplier FEU - 136, sensitive to radiation in the range of wavelengths 300 - 800 nm and working in analog mode in a complex with the digital storing oscillograph.

For creation of mechanical stresses the frontal surface of a plate was irradiated by pulses of the laser with the following parameters: duration - 1.5 ms, energy in a mode of free generation - 24 J, wavelength 1.06 μ m. The diameter of light beam ranging from 2 up to 8 mm. The power of light dropping on a surface of a plate, was varied with the help of neutral light filters, selecting its size such, that the irradiated spot on the frontal surface of a sample did not fail, but the intensity of luminescence of the rear surface was sufficient for reliable registration. In experiments in present article, the energy entered in a sample for one pulse was $P \approx 2J \approx 0.2P_{thr}$.

Results of measurements.

The evolution of a topography of a rear surface of silver at irradiation of its frontal surface by laser pulses of the same power, depending on number of irradiating laser pulses is shown on Fig. 1. On (Fig. 1a) the topogram of a rear surface of a silver sample after a polishing of a surface by diamond paste is shown. One can see on it the grooves located under an angle $\approx 30^\circ$ to the X-axis, depth $\approx 20\text{nm}$, width $200 - 300\text{ nm}$ and length $\approx 2\text{ }\mu\text{m}$. One wall of defects is perpendicular surface, and the opposite makes with it an angle $\approx 30^\circ$. It is known, that such orientation of walls forms at a mechanical polishing of samples [2,4]. After effect of single laser pulse by power $P_1 \approx 0.2P_{\text{thr}}$ on the frontal surface, the groove has disappeared (Fig. 1b). On a surface of a sample the defects looking like cavities and ledges are visible. The depth (altitude) of these defects varies from 15nm up to 30nm , and cross sizes from 50nm up to 200nm . Effect of the second of laser pulse the same power results that the number of defects which are looking like cavities and ledges is increased, and the distance between defects decreases. The depth (altitude) of these defects also varies from 15nm up to 30nm , and cross sizes from 50nm up to 200nm . (Fig. 1c). The similar change of a submicrorelief of a rear surface is observed and after irradiation by the third laser pulse of the same power: the further increase of number of defects which are looking like cavities and ledges happens, and the distance between defects continues decreasing. Again appearing defects have the same form and sizes, as in the previous cases. (Fig. 1d). In all three cases again appearing defects look like a print of a prism, which three walls are approximately perpendicular to the surfaces of a sample, and the fourth makes with it the angle $\approx 30^\circ$. An apex angle of a defect $\approx 70^\circ$. The similar topograms are obtained in experiments with copper and gold samples. It means [2,3], that the defects were generated due to displacement of bands of a material caused by moving of trains of boundary dislocations.

As it was written above, the irradiation energy of samples was chosen sufficient for excitation of luminescence of a researched surface. From a comparison of appropriate oscillograms one can see, that the intensity of excited emission decreases from a pulse to a pulse.

Discussion of results.

As evident from a comparison of topograms (Fig. 1) at the first loading the grooves generated at a polishing disappear, as though they are smoothed, however from results described in [3] follows, that it does not excite luminescence and in this case does not represent interest. It is important that after each loading of a sample the changes of a submicrorelief of a researched surface take place, and these changes are not random: there are cavities and ledges of the identical sizes and identical form which are looking like a print of a prism, i.e. the defects generated by moving of dislocations appear on a surface. The obtained topograms allow not only to establish the form and sizes of generated defects, but also to calculate their number N on each topogram, and therefore quantity of defects ΔN generated as a result of first, second, etc. loading. On (Fig. 2) is shown the relation of number of defects, which are looking like a print of a prism, generated as a result of series loading, from number of loading (the curve 1). There is submitted relation of intensity of a luminescence pulse (curve 2) the same samples from number of loading. As evident from figure the relations are similar.

Conclusions.

The results of performed experiments show, that cyclical loading of metal samples by the laser pulses of the same power not destroying an irradiated surface, can result in change of a submicrorelief and excitation of luminescence of a rear surface. Thus the form and the sizes of formed defects are constant. At each consequent irradiation the intensity of luminescence decreases, the duration of emission decreases a little, the total number of defects from irradiation to irradiation grows, but at each consequent irradiation the number of defects, again generated on a surface, decreases. The form of defects, doubtlessly, speaks that they were generated due to an emergence of trains of mobile dislocations on a surface. The decreasing of number of dislocations which have emerged on a surface at cyclical loading, apparently, is connected with decreasing of quantity of dislocations in the surface layer of metal, the attaching energy of which is less, then the brought. Earlier it is established that the increase of energy of an irradiating pulse of the laser at repeated loading results in increase of intensity of photon emission [14]. Therefore, it is necessary to expect increase of number of formed defects on a surface. The preservation of the duration of a luminescence pulse means an invariance in circumscribed conditions the speed of motion of dislocations going out on a surface.

So it is shown, that the intensity of a mechanoluminescence directly depends on number of dislocations, which have emerged on a surface of a metal sample. At cyclical loading of a sample the quantity of dislocations which have

emerged on a surface gradually decreases from loading to unloading. The performed researches visually show, that the dislocation mechanism of luminescence excitation is realized, and allow to speak about capability studying of dislocations motion in the surface layer of metal with the help of mechanoluminescence.

**The work is made at support RFFI grant № 97- 02-18097
and FCP "Integration" the project A0142/KO854.**

References.

1. Vettegren V.I., Gilyarov V.L., Rakhimov S.N., Svetlov V.N. Phys. Solid State. 1997. V.40. № 4. P.668 - 671.
2. Vettegren V.I., Rakhimov S.N., Svetlov V.N. Phys. Solid State. V.40. № 12. p.2180-2183.
3. Abramova K.B., Vettegren V.I., Shcherbakov I.P., Rakhimov S.Sh., Svetlov V.N. Zh. Tekh. Fiz. (Tech. Phys.). 1999. V.69. № 12. P. 102-104. Technol. 1996. 31. Vol. 4. P.495 - 500.
4. Novikov I.I. Defects of a crystalline structure of metals. Metallurgy, M. 1975.200p-s.
5. Molotskii M.I. // Phys. Solid State. 1978. V.20. № 6. P.1651- 1656.
6. Molotskii M.I. Sov. Scien. Rev. 1989 V.13 Part 3. P.1-84.
7. Abramova K.B., Valitskyi V.P., Zlatin N.A., Peregood B.P., Pukhonto I.Ya., Fedichkina Z.V. (Sov. Phys.) JETP. 1976. V.71. N 11. P.1873-1879.
8. Abramova K.B., Shcherbakov I.P. Zh. Tekh. Fiz. (Tech. Phys.). V.64. № 9. P.76-90.
9. Kondyrev A.M., Shcherbakov I.P., Abramova K.B., Chmel A.E Zh. Tekh. Fiz. (Tech. Phys.). 1992. V.62. № 1. P.206-208.
10. Abramova K.B., Shcherbakov I.P., Semenov A.A., Rusakov A.I. The Phys. Solid State. 1998. V.40. № 6. P.957
11. K.B.Abramova, A.I.Rusakov, A.A.Semenov, I.P.Shcherbakov. J.Appl. Phys. 2000. Vol. 87. № 6. P.3132-3135.
12. Chandra B.R., Ryan M.S., Seema R Simon, Ansari M.H. // Cryst. Res. Technol. 1996. 31. Vol. 4. P.495 - 500.
13. Abramova K.B., Pakhomov A.B., Peregood B.P., Shcherbakov I.P. Zh. Tekh. Fiz. (Tech. Phys.).1986. V.56 №5, P.978-981
14. Abramova K.B., Shcherbakov I.P., Pukhonto I.Ya., Kondyrev A.M. // the Zh. Tekh. Fiz. (Tech. Phys.). 1996. V.66. № 5. P.190 - 196.

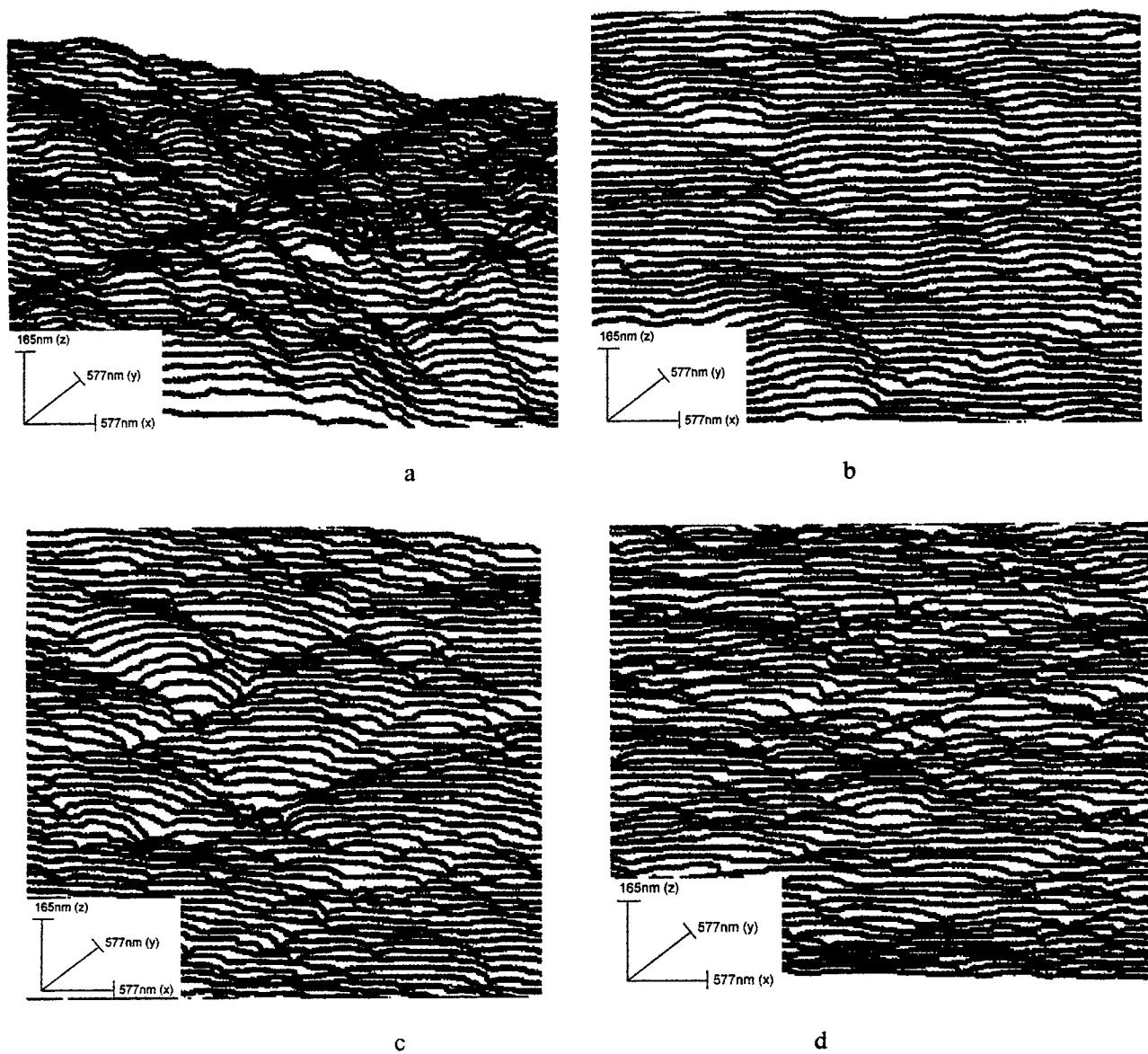


Fig.1. Topograms of a surface of a silver sample. a – a surface of a sample after a polishing, b - after the first loading, c - after the second, d - after the third.

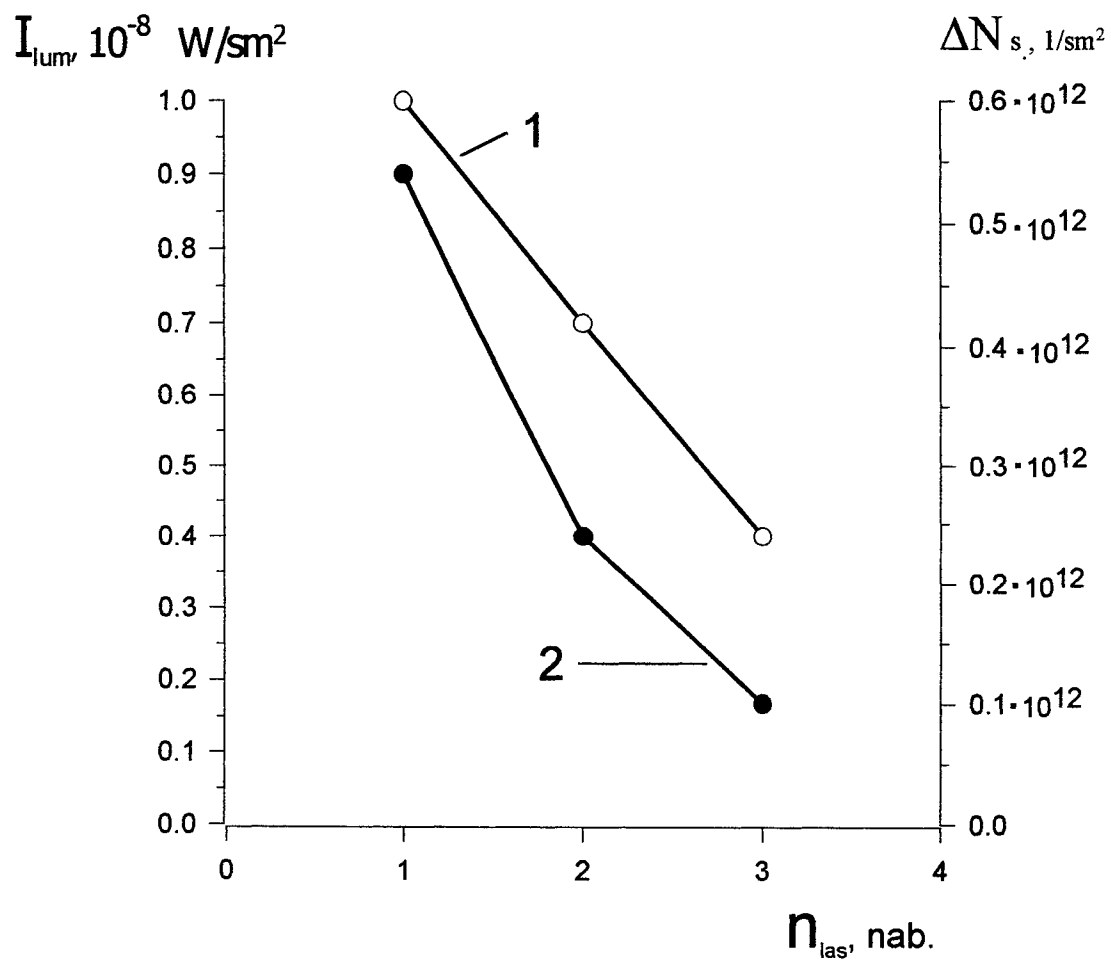


Fig.2. Relations of number of the appeared defects on a surface of a sample (1) and intensity of photons emission (2) from number of loading.

Infrared laser annealing of nanoporous silicon

V. P. Aksenov¹, G.N. Mikhailova¹, J. Boneberg², P. Leiderer², H. J. Muenzer²

¹ General Physics Institute, Vavilov str. 38, 117942, Moscow, Russia

²Department of Physics, University of Konstanz, D-78434 Konstanz, Germany

ABSTRACT

We have investigated the correlation of photoluminescence (PL) properties with certain etching conditions and laser annealing of porous silicon (PS). We used the optical second-harmonic generation (SHG) and photoluminescence methods for studies of IR laser annealing of porous silicon. We observed that IR illumination by series of laser pulses causes decreasing of SH signal and increasing of luminescence efficiency for PS samples.

Keywords: laser annealing, second harmonic generation, porous silicon

1. INTRODUCTION

The mechanisms of luminescence of porous silicon have been extensively studied by many groups.[1-3]. Nevertheless, existing experimental data are still insufficient to select any specific model for the phenomenon of strong luminescence of porous Si. We have shown the correlation between photoluminescence peculiarities and certain etching conditions and annealing. We have investigated the dependence of the PL intensity for both the laser annealed and etched samples.

It is well known that the PL intensity of PS is quenched by thermal annealing in the temperature range of 400-450 °C [13]. The decrease of PL intensity depends on the thermal annealing duration. A low threshold energy of PL degradation indicates that the thermal induced degradation of PS photoluminescence is the result of thermodesorption from the surface of porous silicon. The experimental results show that PL degradation in porous silicon is related to the formation of recombination centers associated with Si dangling bonds.

1.1 Theory of SHG in PS

SHG arises from the non-linear polarization $P(2\omega)$ induced by an incident laser field $E(\omega)$. For centrosymmetric materials such as Si, bulk dipole fields are forbidden and only the much smaller, higher order, bulk fields contribute [4]. Surface states dominate in the dipolar response from clean Si(001) and Si(111) surfaces for 1064nm excitation [5-8], while strain localized at the interface appears to be responsible for a resonance at 375nm for Si(001) and Si(111) [8,9]. When using these excitation conditions, the bulk higher order contributions can be neglected.

For PS the lack of long-range order is important in assessing the possible surface contribution. The material has structure on the scale of 2-8 nm, leading to substantial cancellation of the dipolar SH signal, because within the coherence length of the SHG process [10] the material has a mesoscopic centre of symmetry. Thus PS would not be expected to possess a large SH signal even with its huge surface area, but it may have a signal which can be used for characterization purposes. In-plane isotropy is expected, which suggests polarization rotation, as used in Langmuir-Blodgett monolayer studies [12], as the best approach. With in-plane isotropy the p- and s-components of the reflected SH intensity are equations (1,2) for a linearly polarized incident wave at frequency ω and the field vector making an angle α to the plane of incidence,

$$I_{2\omega}^p = c \left| \left[(f_1 \chi_{zxx} + f_2 \chi_{zzz} + f_3 \chi_{xxz}) \cos^2 \alpha + f_4 \chi_{zxx} \sin^2 \alpha \right] E(\omega)^2 \right|^2 \quad (1)$$

$$I_{2\omega}^s = c \left| \left[(f_5 \chi_{xxz} \sin(2\alpha)) \right] E(\omega)^2 \right|^2 \quad (2)$$

where χ_{ijk} is the second-order non-linear susceptibility tensor component reflecting the structure and symmetry properties of the surface or interface, f_i is a Fresnel factor, z is the surface normal, x - z is the plane of incidence and c is a collection of

constants. From Eqs. (1) and (2) it can be seen that the shape of the intensity curve for p-polarized SH output depends on χ_{zzz} , χ_{zxz} and χ_{xxz} , while the shape depends only on χ_{xxz} for s-polarized output.

2. EXPERIMENTAL SETUP

Porous silicon samples were prepared by anodic etching of n-type ($0.5 \Omega \text{ cm}$) Si (100) wafers with an $\text{HF}:\text{C}_2\text{H}_5\text{OH}$ (1:1) solution at current densities of 20 mA cm^{-2} . We used 1064 nm excitation for SHG experiments from porous silicon and 532 nm from Q-switched YAG-laser for PL experiments. The pulse duration was 10 ns at 10 Hz repetition rate. The laser pulse energy was maintained below 100 mJ/cm^2 to avoid damage. A red-sensitive photomultiplier, and Tektronics digitizer were used to record the PL decay.

3. RESULTS AND DISCUSSIONS

PS samples were irradiated in air by IR laser radiation (wavelength 1064 nm, energy 20–100 mJ/cm^2 , duration of pulse 10 ns). Fig. 1 shows the variation in p-polarized SH intensity with input polarization angle α for PS using surface-state-sensitive 1064 nm excitation with energy 10 mJ/cm^2 . The relative sizes of the signals are uncorrected for any change in SH beam cross-section due to scattering in the PS. When the sample was rotated by 45° about the z axis, no change was observed in SH signals obtained from either PS consistent with in-plane isotropy.

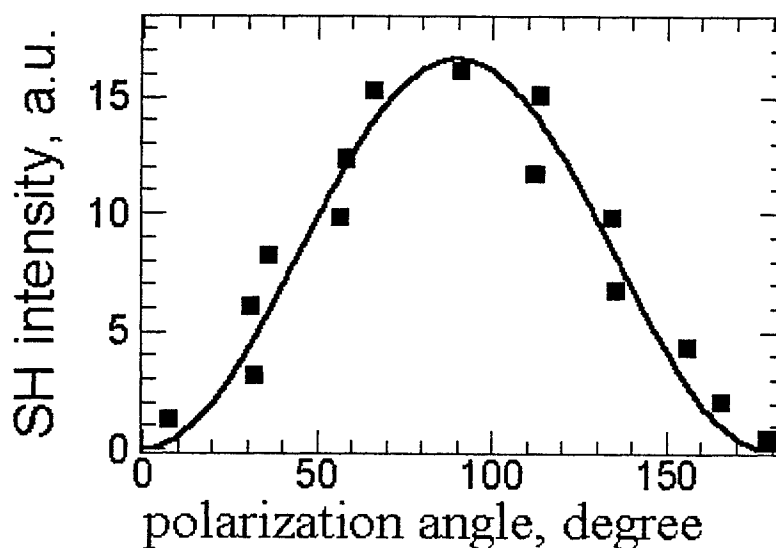


Fig. 1. Variation in p-polarized SH intensity as a function of input linear polarization angle α for PS using 1064 nm excitation.

For series of IR laser pulses with $E=100 \text{ mJ/cm}^2$ catastrophic decreasing signal of SHG for nanoporous PS sample with a diameter of quantum wires equaled 2-4 nm were observed that represented on Fig. 2. Increasing of PL intensity and decay of PL time constant were observed for annealed nanoporous samples with decreased SHG -Fig.3. The decay of PL time constant increased from 25 μs to 32 μs (Fig. 3.).

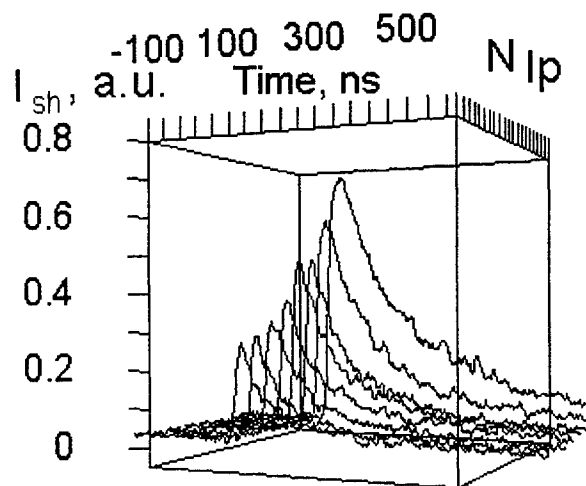


Fig. 2. Room temperature SHG for porous silicon. The sample was excited by 1064 nm radiation of YAG laser with a energy density of 100 mJ/cm². The curves represent: as signal SHG degradate under illumination of series of laser pulses. The temporal behavior of the signal was determined by the time response of the photomultiplier.

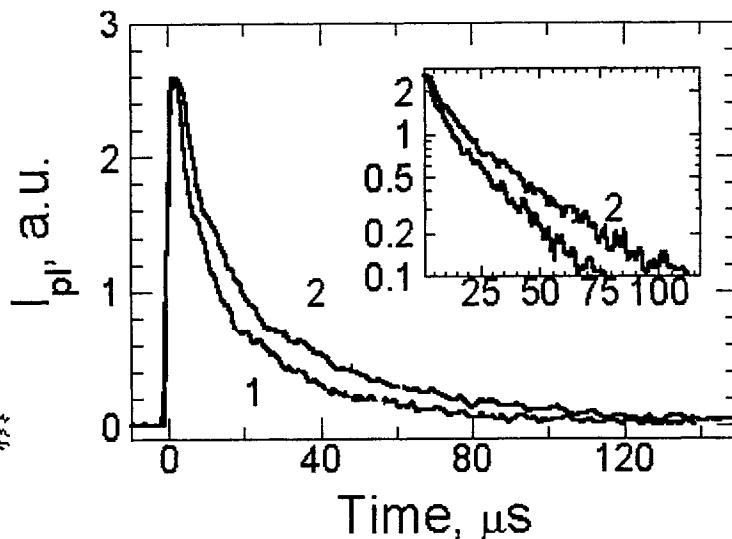


Fig. 3. The kinetics of room temperature integrated PL (600 nm – 850 nm) of the nanoporous PS sample. Plots of PL kinetics before (curve 1) and after IR annealing (curve 2) are shown. Inset: PL kinetics at the same conditions.

For series of IR laser pulses with $E=100$ mJ/cm² decreasing and growth signal of SHG for nanoporous PS sample with a diameter of quantum wires is equal 10-15 nm were observed as presented on Fig. 4. For this annealed nanoporous samples decreasing of PL intensity and decay PL time constant were observed -Fig.3. The decay PL time constant decreased from 26 μs to 17 μs Fig. 5.

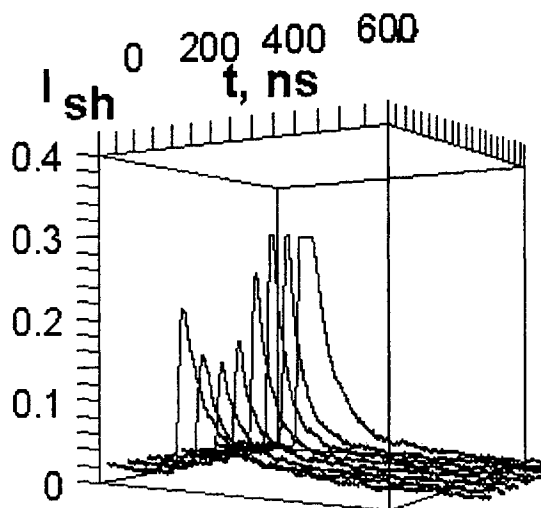


Fig. 4. Room temperature SHG for porous silicon. The sample was excited by 1064 nm radiation of YAG laser with a power density of 100 mJ/cm². The curves represent growth of signal SHG after a degradation under illumination of series of laser pulses.

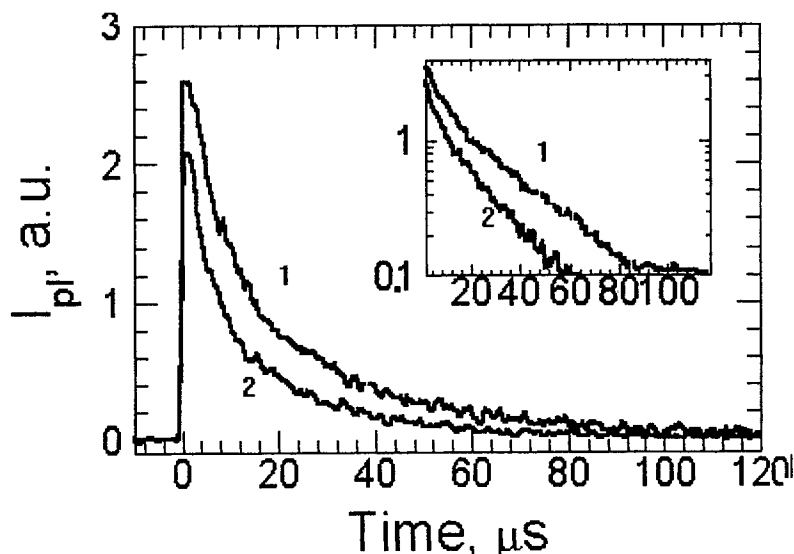


Fig. 5. The kinetics of room temperature integrated PL (600 nm – 850 nm) of the nanoporous PS sample. Plots of PL kinetics before (curve 1) and after IR annealing (curve 2) are shown.

It is well known that the PL intensity of PS is quenched by thermal annealing in the temperature range of 400-450°C [13]. The decrease of PL intensity depends on the thermal annealing duration. The experimental results show that PL degradation in porous silicon is related to the formation of recombination centers associated with Si dangling bonds. It is known also that hydrogen plays an important role in the photoluminescence process. Desorption of hydrogen from the porous silicon surface layer was correlated with decreasing of the photoluminescence intensity and increasing of SH signal.

In contrast with thermal annealing where we have thermodesorption from the surface in porous silicon and the process is determined by annealing duration, IR laser annealing cleans and makes active Si dangling bonds and H adsorption disrupts the surface states. As a result SH signal damps dramatically and nonradiative recombination channels remove. The luminescence time constant of the annealed material increased: it suggests that H absorption of the surface of PS remove nonradiative recombination channels. These observations indicate that the electronic properties of the surface of the porous Si play a key role in obtaining of the efficient luminescence from this material.

It is possible that the growth of signal SHG after degradate under illumination of series of IR laser pulses (Fig. 4) is related with deficit of H in PS sample.

4. CONCLUSION

To summarize, we have investigated the correlation between optical properties and etching conditions, laser annealing of porous Si. We have found the correlation between the PL intensity and the SHG intensity for laser annealed PS. The luminescence time constant of the annealed material is found to be increased at decreasing of the signal of SH, that suggests the desorption of the surface of PS and removing of the nonradiative recombination channels.

5. ACKNOWLEDGMENTS

The authors gratefully acknowledge the financial support by the Deutsche Forschungsgemeinschaft (DFG) and the Russian Foundation for Basic Research (RFFI) (grant N 96-00089).

6. REFERENCES

1. A. Uhler, *Bell Sys. Tech. J.* **35**, 333 (1956).
2. T. Canham, *Apple. Pays. Lett.* **57**, 1046 (1990).
3. K.Y.Lo, J.T.Due, *IEEE Photonics Tech. Lett.* **5**, 651 (1993).
4. T.F. Heinz, in H.E. Ponath and G.I. Stegeman (eds) *Nonlinear Surface Electromagnetic Phenomena*, Elsevier, Amsterdam, 1991, p.353.
5. U.Hofer, L. Li and T.F.Heinz, *Rhys. Rev.* **B45**, 9485 (1992).
6. R.W.J.Hollering, et al. *J. Vac. Sci. Technol.* **A8**, 3997 (1990).
7. M. Cavanagh, J.R. Power, J. F. McGilp, H. Munderb, M. G. Berger, *Thin Solid Films* **255**, 146 (1995)
8. J. R. Power and J. F. McGilp, *Surf. Sci.*, **287-288**, 708 (1993).
9. W. Daum, H.-J. Krause, U. Reichel and H. Ibach, *Phys. Rev. Lett.* **71**, 1234 (1993).
10. V. Mizrahi and J. E. Sipe, *J. Opt. Soc. Am.* **B5**, 660 (1988).
11. Ò. G. Zhang, Ñ. H. Zhang and G. Ê. Wong, *J. Opt. Sos. Am.* **A7**, 902 (1990).
12. Z.-R. Tang and J. F. McGilp, *J. Phys.: Condens. Matter.* **4**, 7965 (1992).
13. N. Hady Zoubir, M. Vergnat, T. Delatour, A. Burneau, and Ph. de Donato, *Appl. Phys. Lett.* **65**, 82 (1994).

Laser annealing of MBE Ge films on the Si substrates

V. P. Aksenov¹, G.N. Mikhailova¹, J. Boneberg², P. Leiderer², H. J. Muenzer²

¹ General Physics Institute, Vavilov str. 38, 117942, Moscow, Russia

²Department of Physics, University of Konstanz, D-78434 Konstanz, Germany

ABSTRACT

We report the studies of process of laser annealing of island Ge films on the Si substrates. Based on the time-resolved reflectivity measurements, we obtained the data concerning melting, the dissolution and the resolidification of Ge thin films on the Si after laser annealing with nanosecond laser pulse. We observed periodic melting of the interface Ge-Si under an illumination by series of laser pulses that connected with the peculiarity of the solution Ge in Si.

Keywords: laser annealing, island film Ge on the Si, molecular beam epitaxy, time-resolved surface reflectivity measurements

1. INTRODUCTION

A heteroepitaxy of spontaneously forming quantum dots has become quite popular recently. This is a relatively straightforward method for producing of nanoscale features, which compared to lithographic methods, and presents exciting technological opportunities. This technique exploits the strain-driven layer-to-island transition in lattice mismatched semiconductor systems to produce remarkably uniform size distributions of nanoscale three-dimensional islands.

An island growth has become an important topic of current research both experimentally and theoretically due to low-dimensional carrier confinement effects expected [1]. Material systems with high lattice mismatch such as Ge on the Si (001) exhibit a growth mode transition from two-dimensional layer-by-layer growth to three-dimensional island growth beyond a critical layer thickness. Ge on the Si (001) shows an enhancement of optical features [2].

At the large deviation from equilibrium phase transformations have gained considerable attraction since the discovery of the unique properties of metallic glasses. Metallic glasses are formed at quench rates of about 10^6 K s^{-1} (depending on alloy). Melting of thin films on the non-reactive substrates by pulsed laser annealing allows to examine nucleation and solidification phenomena at even higher quench rates [3,4]. By optical reflection with nanosecond time resolution we studied the dynamics of laser melting and solidification of the MBE Ge films of 10-nm-thick grown directly on the Si (001) substrates.

The interaction of laser pulses with strongly absorbing media has been of great interest in the eighties. A large part of this activity is motivated by the technological necessity of annealing of ion-implanted surface layers of silicon in such a manner that steep gradients in the impurity doping profiles are maintained [5-8]. The processes occurring during the rapid temperature quench of a thin liquid layer are interesting also from the fundamental point of view, for example with respect to the process which limit the velocity of dissolution of the liquid layers.

In this work we report on laser-induced melting, dissolution and solidification of thin films of Ge on the Si, investigated by optical reflection measurements with nanosecond time resolution.

2. EXPERIMENTAL SETUP

The laser action produced by 532 nm pulse frequency doubled radiation from Q-switched YAG-laser. The pulse duration was 10 ns. The laser pulse energy was 10 mJ/cm^2 - 150 mJ/cm^2 . The laser pulse incident nearly perpendicular upon the surface was only mildly focused to a spot diameter of about 3-mm. For the measurement of the reflectivity we used p-polarized continuous wave (CW) He-Ne laser ($\lambda=633 \text{ nm}$, 7 mW) with an angle of incidence of 45° . The laser was focused to diameter of 20 μm on the surface so that the variation in the pulse laser beam intensity across the diameter of the test laser could be neglected. The reflected light was detected by pin diode (risetime less than 1 ns) and registered by fast digital storage oscilloscope.

Samples were prepared using standard molecular beam epitaxy techniques. Atomic force microscope analyses were performed on Ge islands on the Si. It shown that coherently strained islands had a base width of about 170 nm and a height of 10-20 nm. These parameters remain constant over a wide range of temperatures and are independent on the presence of facets or dislocations. Optical measurements appear very suitable for these studies, because the reflection and transmission

properties differ strongly from the corresponding phase, and in addition in each phase also depend on the temperature. Beginning from the crystalline Si at 300 K, e.g., reflection coefficient R (at $\lambda=632.8$ nm and perpendicular incidence) increases from 36% to a value of 42% at melting temperature. Upon the appearance of the liquid phase, which is metallic one, R jumps up to 70%, and then slowly decreases again as the temperature is raised further.

3. RESULTS AND DISCUSSION

We studied the dynamics of laser melting and solidification of the MBE Ge films of 10-nm-thick grown directly on the Si(001) substrates by optical reflection with nanosecond time resolution. We observed a particularity of a dissolution of the liquid film of Ge at energy density of 100 mJ/cm².

The Ge/Si faceting [9,10] observed for the MBE Ge film on the Si substrate can be caused by a solid-state diffusion process or melting of interfacial Ge layer and subsequent alloying with the Si substrate. This phenomenon is associated with extensive confinement of threading dislocations near the Ge/Si interface. We have the Ge film and alloy Ge/Si. The experimental results are divided into three regions, depending on the energy density of the annealing laser: heating of the solid Ge film, partial melting and complete melting of the Ge film, melting of Ge/Si alloy layer.

Fig. 1. shows the time resolved reflectivity for the wavelength 633 nm during laser annealing of the island Ge films on the Si substrate with different energy densities of the laser pulse. The intense laser generation of the electron-hole plasma in the crystal Ge decreases the dielectric constant of layer and decreases reflectivity. The reflectivity changes due to heating of the solid phase have time delay near 120-150 ns ($E=35-45$ mJ/cm²) with respect of the excitation pulse. We conclude that phonon system of Ge-film has a weak bond with Si substrate. Upon melting of the Ge film an increase of the reflectivity is observed; that is an evidence of a transition to the metallic phase ($E=45$ mJ/cm²).

Fig. 2. shows the reflectivity curves for an energy density $E>50$ mJ/cm². We connect this increasing of the reflectivity with partial melting of Ge/Si alloy layers produced in the process of molecular beam epitaxy of Ge at the Si substrate. The dissolution of the liquid Ge produce the dense network of dislocations observed near the interface and decreased the temperature of melting Ge/Si alloy.

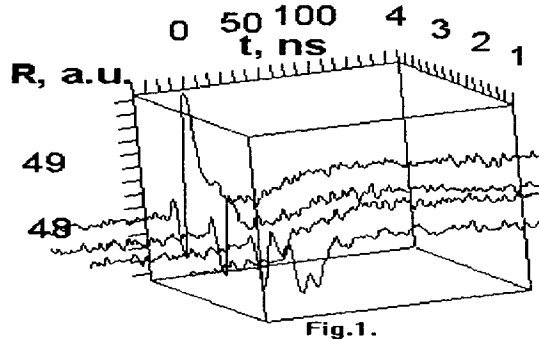


Fig.1.

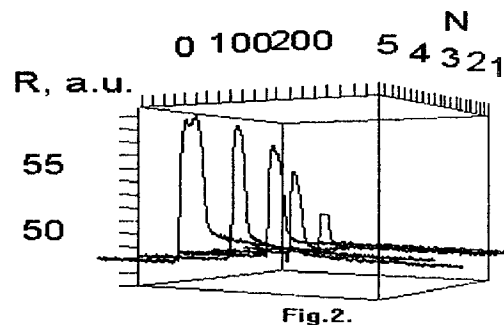


Fig.2.

Fig. 1. Time-resolved reflectivity - R at 633 nm- of thin Ge film ($d=10$ nm) on the Si substrates at an energy density: 1- $E=28$ mJ/cm²; 2- $E=35$ mJ/cm²; 3- $E=40$ mJ/cm²; 4- $E=45$ mJ/cm².

Fig.2. Time-resolved reflectivity - R at 633 nm- of thin Ge film ($d=10$ nm) on the Si substrates at an energy density: 1- $E=55$ mJ/cm²; 2- $E=68$ mJ/cm²; 3- $E=78$ mJ/cm²; 4- $E=90$ mJ/cm²; 5- $E=105$ mJ/cm².

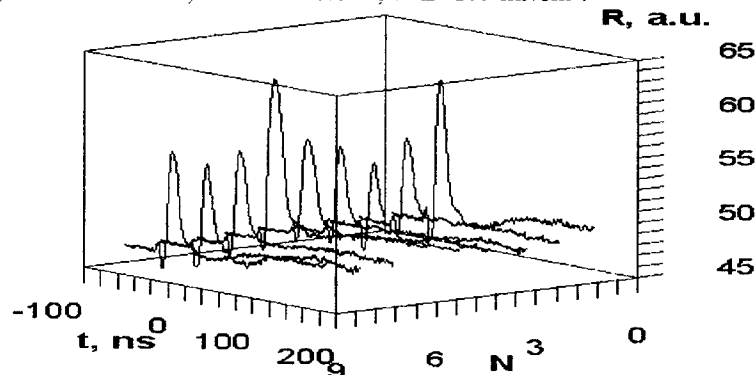


Fig. 3.

Fig. 3. Fig.1. Time-resolved reflectivity -R at 633 nm- of thin Ge film ($d=10$ nm) on the Si substrates at an energy density $E=100$ mJ/cm² for the sequence of the laser pulses.

We observed the particularity of the dissolution of liquid film Ge in the Si for case of partial melting of a Ge/Si interface at density of energy 100-120 mJ/ cm². Figure 3 shows the reflected light amplitudes for the sequence of pulses with $E=100$ mJ/ cm² from the structure. Under effect of three-four laser pulses, process of dissolution liquid Ge in alloy Ge/Si decreases the temperature of melting an alloy and the following laser pulse melts the complete volume of alloy. The periodic process continued toward to the complete dissolution of the Ge film.

ACKNOWLEDGMENTS

The authors gratefully acknowledge the financial support by the Deutsche Forschungsgemeinschaft (DFG) and the Russian Foundation for Basic Research (RFFI) (grant N 96-00089).

References

1. A.I.Yakimov, V.A.Markov, A.V.Dvurechenskii, and O.P.Pchelyakov, J. Phys. Condens. Matter. 6, 2573 (1994).
2. R.Apetz, L. Vescan, A. Hartman, C. Dieker, and H.Luth, Appl. Phys. Lett. 66, 445 (1995).
3. S.R.Stiffler, M.O.Thompson and P.S. Peercy, Phys.Rev. B, 43, 9851 (1991).
4. J.Boneberg, J.Nedelcu, H.Bender and P.Leiderer, Mater.Sci. Engin. A 173, 347 (1993).
5. Laser-Solid Interaction and Laser Processing, ed. by S. D .Ferris, H. J. Leamy. and J. M. Poate (AIP, New York 1979).
6. Laser and Electron Beam Processing of Materials, ed. by C. W. White and P. S. Peercy (Academic Press, New York 1990).
7. Laser and Electron-Beam Solid Interaction and Material Processing, ed. by J. F. Gibbons, L. D. Hess, and T. W. Sigmon (North-Holland, Amsterdam 1981).
8. A.E.Bell: RCA Rev. 40, 295 (1979)
9. M. Gorill, L. Vescan, K. Schmidt, S. Mesters, and H. Luth, Appl. Phys. Lett. 71, 410 (1997).
10. D. P. Malta, J. B.Posthill, R. J. Markunas, and T. P. Humphreys, Appl. Phys. Lett. 71, 410 (1997).

The modification of the surface roughness spectrum by means of power laser radiation

V. P. Aksenov¹, G.N. Mikhailova¹, J. Boneberg², P. Leiderer², H. J. Muenzer²

¹ General Physics Institute, Vavilov str. 38, 117942, Moscow, Russia

² Department of Physics, University of Konstanz, D-78434 Konstanz, Germany

We study the periodic damage structures that can be produced on the rough-surface of semiconductors when they are irradiated with a single beam of intense laser radiation. We observed a formation of periodic surface structures for porous Si (PS) with microscopic surface roughness. In the case of more strong rough Ge (for Ge samples with hand polished surface) we observed an opposite effect to ripple formation: i.e an effective destruction of resonance Fourier components of the random disturbed surface.

Keywords: laser annealing, surface plasmon, diffraction, periodic surface structures

1. INTRODUCTION

It has been known for several years that laser annealing and damage may be accompanied by formation of periodic surface structures or "ripples" on the surface of various metals, semiconductors, and insulators [1-12]. It is generally considered that the pattern takes place from inhomogeneous energy deposition associated with the interference of the incident beam with a diffracted surface wave, which comes from scattering of incident wave off a grating-like structure on the surface. The surface plasmon for metals and liquid semiconductors, "radiation remnants" for insulators are considered as the surface waves in this case. The modulation of the incident power - and in turn, the strength of the grating may grow, depending upon the exact nature of the grating, leading to an exponential growth or positive feedback regime similar to small-scale self-focusing in dielectrics. Only the Fourier component of the initial random disturbance which diffracts light almost exactly along the surface grows, and the strength of the initial grating is unimportant since exponential growth processes can start from noise. We note that significant positive feedback has to occur in less than the pulse duration.

Recent observation of visible photoluminescence [13] and electroluminescence [14,15] from porous silicon samples at room temperature has prompted a great interest in this material. This interest persisted due to its potential application in micro- and optoelectronics. In view of device applications, the attention is currently focused on the enhancement of the optical and electro-optical properties of PS samples. Porous semiconductors allow to analyze of the fundamental properties of photon-exciton coupling [16] and have consequences for the performance of nonlinear optical devices [17] and laser devices they decrease as the radiative emission lifetime and lead to strong unidirectionality of the emitted light.

The aim of the present work is to extend studies of the PS. We propose to study the formation of periodic surface structures on PS layer, produced by an anodization process on silicon wafer. The refractive index of PS is determined by its porosity, which depends only on the current density of electrochemical process once other etching parameters are kept fixed; the anodization time determined the layer width. We study the laser action on the rough-surface of semiconductors such as porous Si and Ge. We observed a formation of resonance periodic surface structures (scattered laser light along the surface) for porous Si with microscopic surface roughness. In the case of more strong rough we observed an opposite effect to ripple formation: i.e an effective destruction of resonance Fourier components of the random disturbed surface..

2. EXPERIMENTAL

The microporous Si samples are prepared by electrochemical etching of n-type (0.5 $\Omega\cdot\text{cm}$), (100)-oriented Si wafers. The electrolyte is 1:1 mixture of pure $\text{C}_2\text{H}_5\text{OH}$ and concentrated HF. Typical thickness of the porous Si layer are 2-5 μm .

The samples were annealed by pulses of linearly polarized light (532nm or 1064 nm) from Q-switched YAG-laser. The pulse duration was 10 ns at 10 Hz repetition rate. The laser pulse energy was 10 mJ/cm^2 -150 mJ/cm^2 . Although we have looked at the actual damage features, we have found that considerably more information can be gleaned from studying the Fourier transform of the damage by viewing the far field reflection of a 460-nm Ar laser beam normally incident on the damaged region [8].

3. RESULTS AND DISCUSSIONS

3.1. Germanium Samples

The growth of the "ripples" on the germanium surface was well studied in the eighties. We observed decreasing of the intensity of the diffuse back scattering test light for diffraction angles region, which correspond to resonance gratings after action of the series laser pulses. The simplest explanation for destruction of resonance surface gratings for case rough-surface of Ge would be that for high roughness we have many random phase sources of generation surface waves. The "distracted" interference produced the effective transformation of the roughness spectrum.

3.2. Porous Silicon Samples

The lower level of the diffraction of green laser beam was observed for PS samples with respect to Ge samples. For 532-nm excitation by *p*-polarized light at near-normal incidence on PS layer surface, the well known periodic damage consists of two superimposed sets of fringes perpendicular to the polarization with spacing of $d=0.53/(1\pm\sin\theta)$ μm where θ is the angle of incidence. The ripples with a spacing of $d=0.53/\cos\theta$ μm were observed for $\theta>35^\circ$. For 1064-nm excitation of PS, the ripples formation was observed with spacing $d=1.06/(n\pm\sin\theta)$ μm where n is the refractive index of PS, that is determined by porosity of PS ($n=1.5$ - 2.2 for PS with porosity 40%-60%)

ACKNOWLEDGMENTS

The authors gratefully acknowledges the financial support by the Deutsche Forschungsgemeinschaft (DFG) and the Russian Foundation for Basic Research (RFFI) (grant N 96-00089).

References

1. D.C.Emmony, R.P.Howson, and L.J.Willis, Appl. Phys.Lett. 23,598(1973)
2. N.R.Isenor, Appl.Phys.Lett. 31, 148 (1977)
3. H. J. Leamy, G. A. Rozgonyi, T. T. Sheng, and G.K.. Celler, Appl. Phys. Lett. 32, 535 (1978).
4. G. N. Maracas, G. L. Harris, C. A. Lee, and R. A. McFarlane, Appl. Phys. Lett. 33, 453 (1978).
5. M.Oron and O. Sorenson. Appl. Phys. Lett. 35, 782 (1979).
6. P.A. Temple and M. J Soileau, IEEE J. Quantum Electron. QE-17, 2067 (1981)
7. A. K. Jain, V. N. Kulkarni, D. K. Sood, and J. S. Uppal, J. Appl. Phys. 52, 4882 (1981)
8. V.P.Aksenov and B.G.Zhurkin, Doklady Akademii nauk, v.265, 1365(1982)
9. J. F Young, J. E. Sipe, J. S. Preston, and H. M. van Driel, Appl. Phys. Lett. 41, 261 (1982).
10. P. M. Fauchet and A. E. Siegman, Appl.Phys. Lett. 40, 824 (1982)
11. F. Keilmann and Y. H. Bai, Appl. Phys. A29, 9 (1982)
12. D. J. Ehrlich, S. R. J. Brueck and J. Y. Tsao, Appl. Phys. Lett. 41, 630 (1982)
13. L. T. Canham, Appl. Phys. Lett. 57, 1046 (1990)
14. P. Steiner, E. Kozlowski, and W. Lang, Appl. Phys. Lett. 63, 2700 (1993)
15. L. Pavesi, M. Ceschini, G. Mariotto, E. Zanghellini, O. Bisi, M. Anderie, L. Calliari, and M. Fodrizzi, J.Appl. Phys. 75, 1118 (1994)
16. C. Weisbuch, M. Nishioka, A. Ishikawa, and Y.Arakawa, Phys. Rev. Lett. 69, 3314 (1992)
17. T. Rivera, F. R. Ladan, A. Izrael, R. Kuszelewicz, and J. I. Oudar, Appl. Phys. Lett. 64, 869 (1994)

Thermally Stimulated Luminescence from Porous Silicon

V. P. Aksenov¹, G.N. Mikhailova¹, J. Boneberg², P. Leiderer², H. J. Muenzer²

¹ General Physics Institute, Vavilov str. 38, 117942, Moscow, Russia

² Department of Physics, University of Konstanz, D-78434 Konstanz, Germany

ABSTRACT

The time-resolved evolution of the cloud of the porous silicon (PS) particles produced by laser ablation is studied *in situ* by the analysis of the kinetics of photoluminescence (PL) signal. The cloud of the nanometer-sized silicon crystallites had the high enhancement of luminescence quantum efficiency (QE) in the red region of spectra. The slow PL kinetics component, which is due to the localized carriers, decays on a millisecond time scale.

We observed high intensity of laser ablation process for light excited PS. We also study the emission of photons from remnants of porous silicon after laser ablation of PS sample. The red light generation was observed in this case of excitation of PS. Time-resolved experiments on the luminescence show that likely there are large lifetime phonons in quantum silicon wires.

Keywords: laser ablation, luminescence, nanocrystallites, porous silicon

1. INTRODUCTION

There is currently intense interest in the optical and electronic properties of nanometer-sized semiconductor crystallites. The study of quantum size effects in nanometer crystallites made from direct-gap semiconductors such as CdSe [1], CuCl [2] etc. reveals that with a decrease in the crystallite size, the band gap energy increases and the excited electronic states become discrete with high oscillator strength. Recently, a great of research effort has been focused on indirect-gap semiconductor crystallites made from Si [3,4] or Ge [5]. However, in spite of many theoretical and experimental studies the mechanism of the visible photoluminescence from porous Si and Si nanometer-sized crystallites it still remains unclear.

With a large surface-to-volume ratio in nanometer-sized crystallites, the surface effects become more enhanced with decreasing the size of nanometer-sized crystallites. The presence of the crystallite surface as a boundary and a source of surface states makes crystallites different from epitaxial low-dimensional structures [1], and the surface effects as well as the quantum confinement effects control the optical and electronic properties of nanometer-sized crystallites [1,2]. There is a strong dependence of photoluminescence spectra and lifetime of e-h pairs on silicon wires diameter [5]. These two effects also complicate the mechanism of the broad visible PL in electrochemically etched porous Si [6]. Time-resolved PL studies in porous Si [7-10] indicate that the recombination processes are complex and the PL in electrochemically etched porous Si exhibits nonexponential behavior. The broad PL spectrum and nonexponential slow PL decay suggest that the disorder-induced localized states plays an important role in the radiative recombination process [7-10].

In the following we use experimental technique to study the kinetics of the photoluminescence of PS and PL of the cloud of the damaged silicon wires produced by laser ablation of porous silicon.

The aim of this letter is the experimental investigation of QE and kinetics of the photoluminescence of isolated nanocrystallites of PS; changes in the electronic properties of Si nanocrystals as a function of particle size.

2. EXPERIMENTAL

The laser ablation of porous silicon was produced by 532 nm or 1064 nm-pulses radiation from Q-switched YAG-laser in the atmosphere. The pulse duration was 10 ns. The laser pulse energy was 100 mJ/cm² - 150 mJ/cm². A red-sensitive photomultiplier, and a Tektronics digitizer were used to record the PL decay. Sensitive avalanche photodiode was used for

recording IR PL (1.2-1.6 μm) decay from PS. The microporous Si samples were prepared by electrochemical etching of n-type ($0.5 \Omega\text{-cm}$), (100)-oriented Si wafers. The electrolyte is 1:1 mixture of pure $\text{C}_2\text{H}_5\text{OH}$ and concentrated aqueous HF. Typical thickness of the porous Si layer are 2-5 μm . Nanoporous silicon layers were prepared from boron doped p-type (100) silicon of $12 \Omega\text{ cm}$ resistivity by electrochemical etching in the electrolyte $\text{H}_2\text{O} : \text{HF} : \text{C}_2\text{H}_5\text{OH} = 1:1:2$. We used etching regime with average current density of 14 mA/cm^2 and etching time of 20 min.

3. RESULTS AND DISCUSSIONS

We study the emission of photons from a cloud of porous silicon after laser ablation of PS sample. High efficiency of light generation was observed in case of PS ablation produced by 532 nm laser pulse. The dominant sample responses were increasing of PL intensity and increasing of decay PL constant by several times in comparison with the usual laser excitation represented on Fig.1. Increasing of luminescence of the cloud of the porous silicon particles produced by laser ablation is connected with gigantic effective emitted surface of system.

Figure 1 shows typical PL kinetics for the cloud PS nanocrystallites and for PS sample.

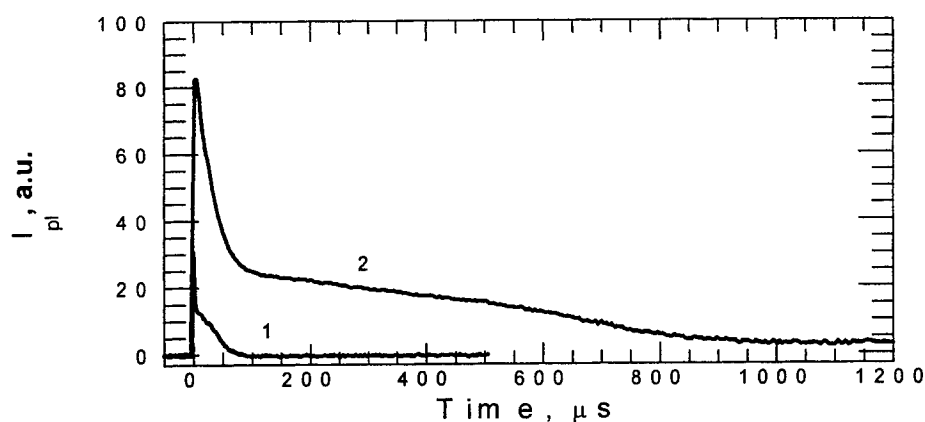


Fig. 1. The temporal behavior of the PL signal detected at red range of spectra: curve 1 – before ablation excitation pulse (530 nm has energy 60 mJ/cm^2); curve 2 – regime of ablation, $E=150 \text{ mJ/cm}^2$.

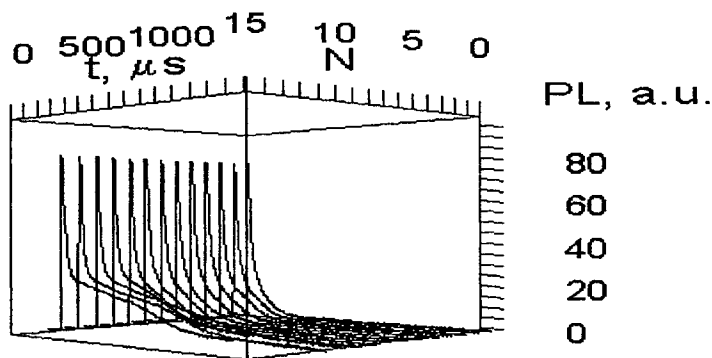


Fig. 2. The temporal behavior of the optical signal detected at red range of spectra for series excitation pulses.

A damage of PS layer after each laser pulse and decreasing of the PL intensity from PS observed are shown in Fig. 2.

The temporal behavior of the optical signal detected at the red range of spectra for several samples of PS are shown in Fig. 3. Decreasing of the decay constant with increasing of silicon wires diameter was observed. There is a strong dependence of lifetime of e-h pairs on the silicon wires diameter.

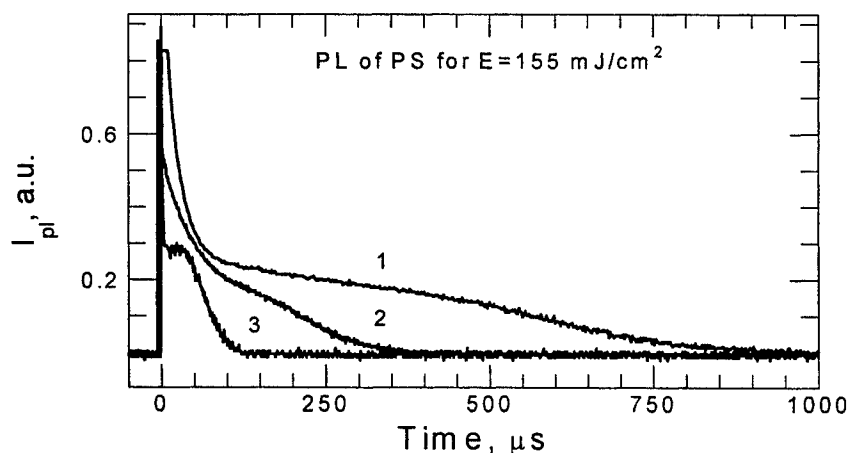


Fig. 3. Temporal behavior of the optical signal detected at red range of spectra for different samples of PS: 1 – nanoporous silicon wires diameter near 2-4 nm; 2 – $d=8-12$ nm; 3 – $d=15-20$ nm. Increasing of silicon wires diameter in PS results in decreasing of PL decay time constant.

The laser ablation of porous silicon produced by 1064 nm-pulses radiation with energy $E=400$ mJ/cm² had low velocity of etching and low excitation of PS. A efficient excitation of PS by IR laser spark was very low. Addition of synchronized 532 nm pulse with $E=10$ mJ/cm² high increased excitation of PS and the velocity of etching of PS. It likely was connected with photo-induced free carrier absorption of IR radiation and decreasing of bonds of excited PS wires. In this case we have the effective laser ablation of excited states in PS.

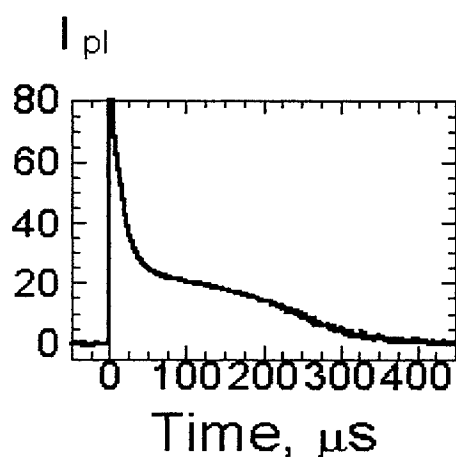


Fig. 4. The temporal behavior of the optical signal detected at red range of spectra (600-850 nm). Excitation pulse with 530 nm has energy 100 mJ/cm².

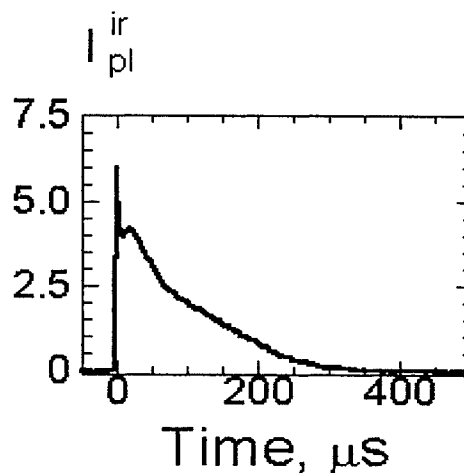


Fig.5. The temporal response of the emitted visible light detected (1200 nm-1600 nm).

We also study the emission of photons from remnants of porous silicon wires after laser ablation of PS sample. The same kinetics of PL signal was detected for emitted photons with energies up to 1.2-1.6 μ m in this case (Fig. 4. and Fig. 5.). These results show that the light emission is not directly related to heating. The energy cannot diffuse along the surface, because the Si wires are spatially isolated. The main relaxation mechanism is coupling to the phonon branches of the Si wires. A very important mechanism of excitation of e-h pairs is connected with processes of destruction the silicon wires by a laser spark. Time-resolved experiments on the luminescence in IR and red region of spectra show that likely there are large lifetime

phonons in the quantum silicon wires [11]. We have observed thermally stimulated luminescence with large time constant from porous silicon heated by laser spark.

4. CONCLUSION

We have observed high QE of luminescence with large time constant from the cloud of the porous silicon nanometer-sized particles produced by laser ablation of PS. High efficiency of light generation was observed in this case of excitation of PS.

5. ACKNOWLEDGMENTS

The authors gratefully acknowledge the financial support by the Deutsche Forschungsgemeinschaft (DFG) and the Russian Foundation for Basic Research (RFFI) (grant N 96-00089).

6. REFERENCES

1. M. G. Bawendi et al. *Rhys. Rev. Lett.* **65**, 1623 (1990); M.G. Bawendi, W. L. Wilson, P. J. Carroll, and L. E. Brus, *J. Chem. Phys.* **96**, 949 (1990).
2. T. Itoh et al., *J. Lumin.* **41**, 235 (1995).
3. T. Canham, *Appl. Phys. Lett.* **57**, 1046 (1990); A. G. Gullis and T. Canham, *Nature* **353**, 335 (1991).
4. V. Lehmann and U. Gosele, *Appl. Phys. Lett.* **58**, 856 (1991).
5. Y. Maeda et al., *Appl. Phys. Lett.* **59**, 3168 (1991); Y. Kanemitsu et al., *ibid.* **61**, 2178 (1992).
6. Y. Kanemitsu et al., *Phys. Rev.* **B48**, 2827 (1993).
7. J. C. Vial et al., *Phys. Rev.* **B45**, 14171 (1992).
8. N. Ookubo et al., *Appl. Phys. Lett.* **61**, 640 (1992).
9. M. Kondo, *J. Non-Cryst. Solids* **164-166**, 941 (1993).
10. P. D. J. Calcot et al., *Phys. Condens. Matter.* **5**, L91 (1993).
11. J. Diener, M. Ben-Chorin, D. I Kovalev, S. D. Ganichev, and F. Koch, *Phys. Rev.* **B52**, 8617 (1995).

Formation of 3D dielectric structures by initiating polymerization with the fourth harmonic of a Nd laser

Alexander P. Alexandrov*, Sergey V. Muraviov, Nadezhda A. Babina, Nikita M. Bityurin*
Institute of Applied Physics, RAS, 603600, Nizhnii Novgorod, Russia

ABSTRACT

We studied the process of formation of 3D polymer structures by initiating polymerization with laser radiation. Polymers based on such monomers as methyl methacrylate (MMA) and ethyleneglycolmonomethacrylate (EGM) were investigated. Polymerization was initiated by the fourth harmonic radiation of a Q-switched Nd:YAP laser ($\lambda=270$ nm) without any specially introduced initiator. Initiation is provided by the direct photolysis of monomers. At this wavelength the absorption of monomers is significantly higher than the absorption of corresponding polymer. It results in bleaching of the media during polymerization.

Keywords: laser photopolymerization, three-dimensional structure, microfabrication technology

1. INTRODUCTION

Recently the microfabrication technology that uses laser photopolymerization has been extensively studied¹⁻³. Microfabrication technology has been employed in 3D waveguide technologies⁴, photofabrication of three-dimensional photonic crystals^{5,6}, 3D optical data storage⁷.

3D objects are reported to be formed due to initiation of radical polymerization during two-photon photolysis of a specially introduced initiator⁶. Viscous mixtures of oligomer and monomer are used as initial material. The polymerization process is localized in the bulk of the material by focusing laser radiation.

In many works, however, single-photon-absorbed polymerization has been used. The localization of the polymerization process is also achieved by focusing.

In this paper we discuss the possibility of creating polymer structures based on polymethyl methacrylate. Instead of introducing a special initiator, it appeared to be possible to use direct photolysis of monomer by ultraviolet radiation to produce radicals for radical polymerization.

The formation of 3D structures with single-photon initiation is limited by the penetration depth of radiation³. However, for the PMMA-MMA system the absorption spectrum of polymer has short-wave shift relative to the absorption spectrum of corresponding monomer. It results in bleaching of the media by initiating laser radiation while monomer is converting to polymer. We realized the regime of running front of polymerization when the length of polymerized structure significantly exceeds the initial penetration depth.

2. MATERIALS AND METHODS

Investigations of polymerization kinetics were carried out in a simple split cuvette comprising two quartz windows and a Teflon layer 50-500 μm in thickness between them. Initial objects were viscous solution of polymethyl methacrylate (PMMA) in methyl methacrylate (MMA) with polymer concentration 50 and 20 percent by mass. Further in these experiments we used another monomer – ethylene glycol monomethacrylate (EGM) with admixture of ethylene glycol dimethacrylate (EGDM). For simplicity we shall call this monomer "EGM". Polymerization was carried out for viscous solution of PMMA in EGM, for prepolymer of EGM, and for original monomer EGM.

* Correspondence: E-mail: bit@appl.sci.nnov.ru, phone: +7-8312-384389, FAX: +7-8312-363792

Employing EGM in our experiment is connected with the fact that the polymer, synthesized from this monomer, is cross-linked, and it is not soluble in monomer. This property permits one to separate the polymer from the reaction mixture very easily.

Initiation was made by the fourth harmonic radiation of a Q-switched Nd:YAP laser ($\lambda=270$ nm) with pulse duration of 15 ns, repetition rate 10 Hz, and beam divergence $3 \cdot 10^{-3}$.

The degree of polymerization was controlled through alteration of transmission of the reaction mixture at the wavelength of 270 nm. It is known from the literature that ϵ for monomer (MMA) at $\lambda=270$ nm is 50 mole/(l*cm), a value much exceeding the polymer absorption. This was confirmed by further measurements.

3. RESULTS AND DISCUSSIONS

Figure 1 displays the transmission spectrum of the initial solution of PMMA in MMA (50/50) in a cuvette 60 μ m in thickness before (a) and after (b) laser irradiation.

Figure 2 shows similar plots for monomer EGM and a corresponding polymer for the layer 600 μ m in thickness.

The bleaching of the medium as a result of the conversion of monomer to polymer is evident. For EGM the penetration depth of initiating radiation in the monomer ($\lambda=270$ nm) is approximately 40 μ m (attenuation by a factor of e), but as a result of polymerization the penetration depth is 600 μ m.

Figure 3 shows the transmission of the medium at $\lambda=270$ nm vs irradiation dose at pulse fluence $F=3.6$ mJ/cm².

This kinetic curve is characterized by:

- ♦ the presence of the induction period which is approximately 0.1 of the total dose of irradiation;
- ♦ a region of polymerization kinetics with almost constant rate;
- ♦ a region of saturation.

The induction period at the beginning of the reaction is connected with the competition of reactions of radicals being formed with the monomer and dissolved oxygen. The saturation region corresponds to the end of polymerization.

Figure 4 displays kinetic curves (conversion vs irradiation dose) for $F=10$ mJ/cm² and $F=60$ mJ/cm².

It is evident that at increasing energy of initiating radiation the polymerization kinetics changes significantly. However, a characteristic feature is that the polymerization process finishes at approximately the same total irradiation dose of 60-70 J/cm².

It is clear that the increase in radiation energy is directly proportional to a decrease in irradiation time before the end of polymerization. For $F=10$ mJ/cm² the required time is 10 min, whereas for $F=60$ mJ/cm² this time is 2.0 min.

Based on these results we choose conditions and regimes for formation of 3D polymer structures.

Our experiments were carried out using specially designed rectangular cuvettes that allow observing and controlling the structure growth.

The cuvette was filled either by pure monomer EGM or by a solution of PMMA in this monomer. The cuvette was irradiated from bottom through the quartz base by the fourth harmonic radiation focused by a lens with a focal distance of 25 mm. A binocular microscope was arranged aside to perform visual control.

After polymerization, an unbound monomer was washed away with solvent.

The obtained structure was visualized in the digital photography system (microscope – CCD camera – computer).

An example of one of such synthesized structures is given in Fig. 5. The characteristic size of this structure is 400 x 400 μ m. The length of the structure 10 times exceeds the initial laser radiation penetration depth.

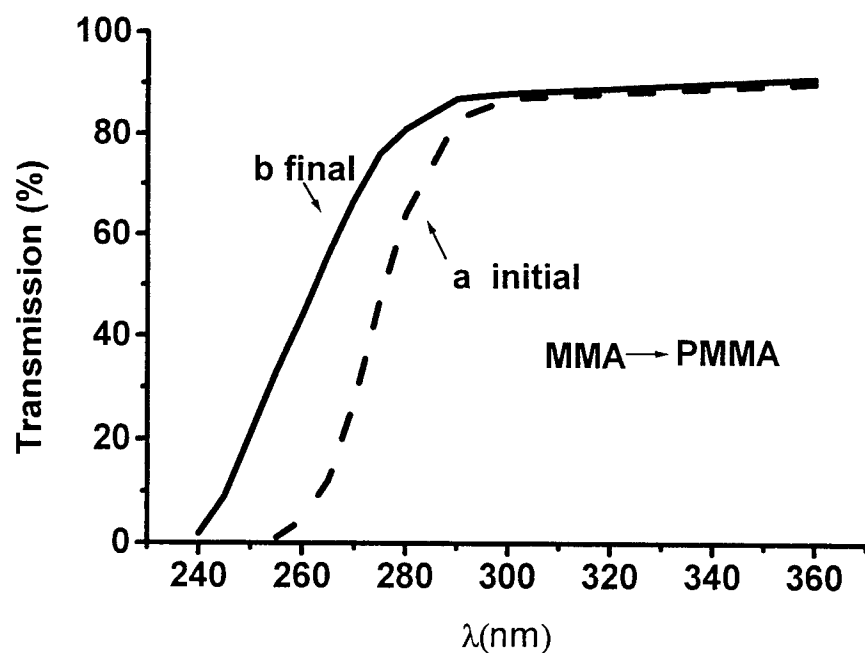


Fig.1 Transmission spectrum of the cuvette filled with a solution of PMMA in MMA with the concentration 50/50. The cuvette is 60 μm in thickness. a – before and b – after polymerization.

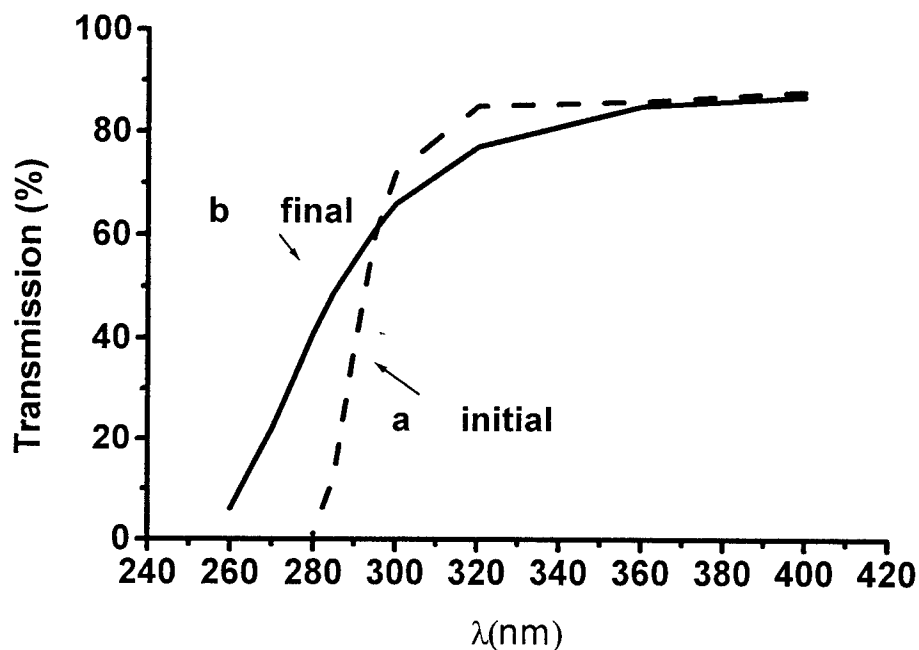


Fig.2 Transmission spectrum of the cuvette with the EGM monomer, the cuvette is 600 μm in thickness. a – before and b – after polymerization.

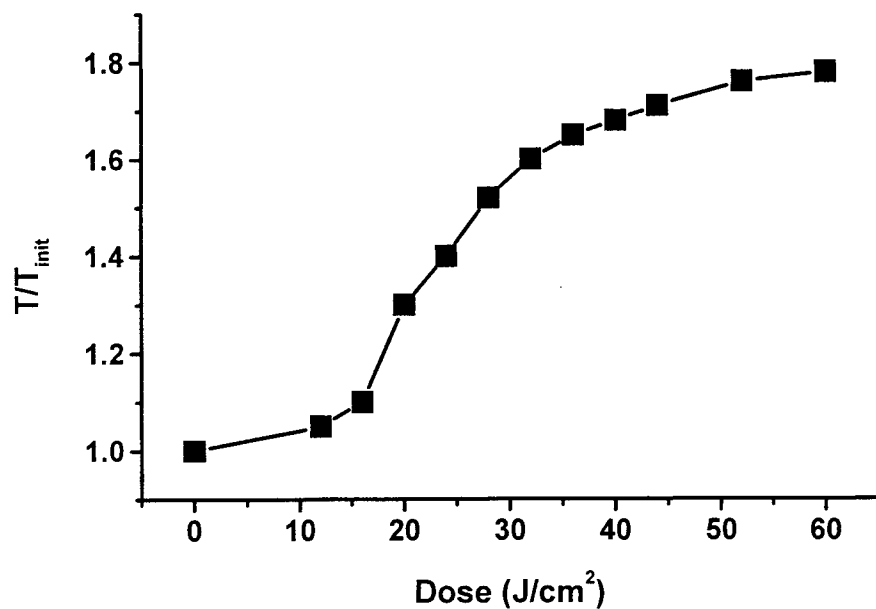


Fig.3. Relative transmission (T/T_{init}) of the cuvette with the solution of PMMA in MMA (50/50) vs irradiation dose, T_{init} - is the initial transmission. Pulse fluence $F=3.1mJ/cm^2$.

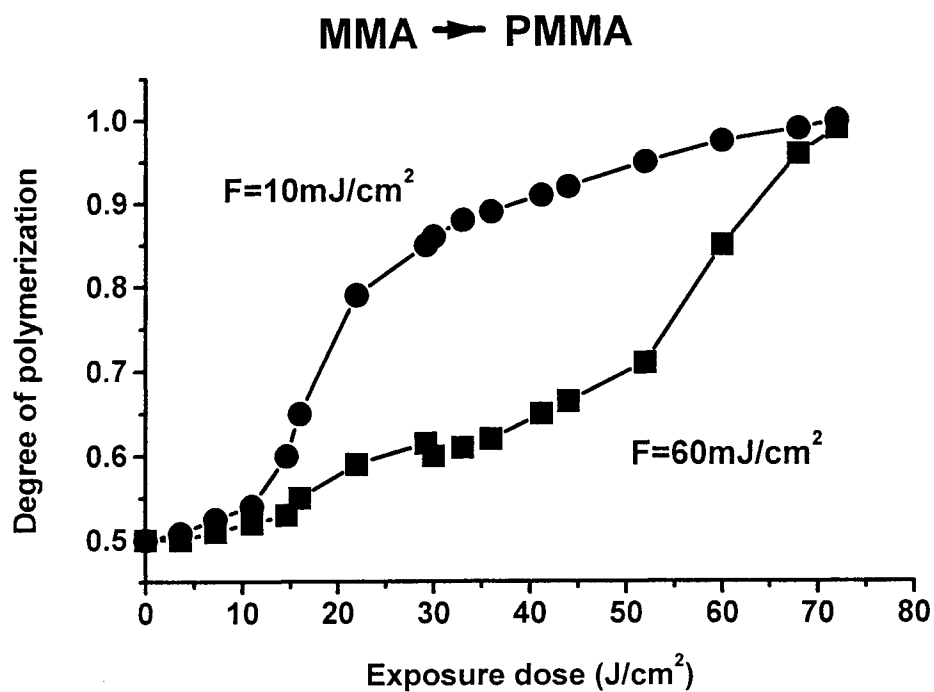


Fig.4. Degree of polymerization vs irradiation dose. a - $F = 10 mJ/cm^2$, b - $F = 60 mJ/cm^2$.

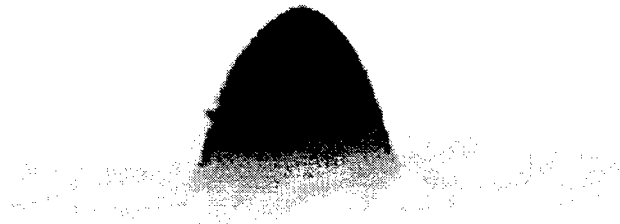


Fig.5. Polymer structure synthesized from the monomer EGM at laser irradiation dose $75\text{J}/\text{cm}^2$.

4. CONCLUSIONS

It is shown that polymerization in the studied mixtures using radiation with $\lambda=270\text{ nm}$ is carried out without any specially introduced initiator in the regime of bleaching of the reaction medium. This allows polymerization of layers whose thickness is much more than the penetration depth of initiating radiation.

Using the suggested technique a cylindrical structure $400\text{ }\mu\text{m}$ in diameter and $400\text{ }\mu\text{m}$ in length was synthesized. With appropriate focusing it is possible to obtain structures with diameter less than $100\text{ }\mu\text{m}$.

REFERENCES

1. Shoji Maruo, Osamu Nakamura and Satoshi Kawata, Three-dimensional with two-photon-absorbed photopolymerization, *Optics letters*, Vol. 22, N2, pp. 132 - 134, 1997.
2. Shoji Maruo and Koji Ikuta, Three-dimensional microfabrication by use of single-photon-absorbed polymerization, *Appl. Phys. Lett.*, Vol.76, N 19, pp. 2656-2658, 2000.
3. Katsumi Yamaguchi and Takechi Nakamoto, Micro fabrication by UV laser photopolymerization, *Memoirs of the School of Engineering*, Nagoya University, Vol. 50, N 1/2, pp. 33-82, 1999.
4. Mukesh P. Joshi, Haridas E. Pudavar, J. Swiatkiewiz, P.N. Prasad and B. A. Reianhardt, Three-dimensional optical circuitry using two-photon-assisted polymerization, *Appl. Phys. Lett.*, Vol. 74, N 2, pp. 170-172, 1999.
5. Satoru Shoji and Satoshi Kawata, Photofabrication of three-dimensional photonic crystals by multibeam laser interference into a photopolymerizable resin, *Appl. Phys. Lett.*, Vol. 76, N 19, pp. 2668-2670, 2000.
6. Hong-Bo Sun, Shigeki Matsuo and Hiroaki Misawa, Three-dimensional photonic crystal structures achieved with two-photon-absorption photopolymerization of resin, *Appl. Phys. Lett.*, Vol. 74, N 6, pp. 786-788, 1999.
7. Brian H. Cumpston, Sundaravel P. Ananthavel, Stephen Barlow, Daniel L. Dyer, Jeffrey E. Ehrlich, Lael L. Erskine, Ahmed A. Heikal, Stephen M. Kuebler, I.-Y. Sandy Lee, Dianne McCord-Maughon, Jinqi Qin, Harald Roedel, Mariacristina Rumi, Xiang-Li Wu, Seth R. Marber and Joseph W. Perry. Two-photon polymerization initiators for three-dimensional optical data storage and microfabrication. *Nature* (London) Vol. 398, P. 51-54, 1999.

Radiation Action on Polymethine Dyes Prepared on Insulating Substrates as Molecular Layers

A. M. Bonch-Bruevich, E. N. Kaliteevskaya, V. P. Krutyakova, and T. K. Razumova

Vavilov State Optical Institute, St. Petersburg, Russia

ABSTRACT

Action of the resonance radiation of varied power on polymethine dyes coated as submono- and thicker layers onto glass and quartz was studied. Effect of the dye structure on the optical properties of molecular layers was explored. The layer absorption spectra within 320-1000 nm were measured for dicarbocyanine dyes differing in chemical structures and electronic symmetries. The absorption spectra of dye layers contain a few maxima, whose relative intensity is a function of the dye concentration on a surface, and are considerably broader than the solution spectra, irrespective of molecular symmetry. Irreversible transformation of the dye absorption spectra was studied under the action of resonance laser radiation of varied power and on heating in the dark. The heating and the pulsed laser irradiation of low power and energy lead mainly to the optical density redistribution among different spectral maxima. At high-power irradiation, the optical density redistribution is accompanied by the considerable decrease in the optical density. Simultaneously, the extinction coefficient of the layer increased in the short-wave edge of the absorption spectrum (400-500 nm), i.e., outside the dye absorption band, indicative of dye destruction via irreversible photooxidation. It is concluded that the dye layer contains a few types of absorption centers: two types of monomers, dimers, and probably, J-aggregates. The interaction with a substrate affects the symmetry of electronic density distribution in a dye molecule, whereas the irradiation and heating of a layer result in the destruction of dye and affect the relative amount of various absorption centers.

Keywords: polymethine dyes, molecular layers, monomer, dimer, aggregate, laser photodestruction, thermal destruction.

1. INTRODUCTION

Organic dye layers on insulating substrates and Langmuir-Blodgett (LB) films are studied for a long time.¹ Now thin dye layers have found a wide range of high technology applications, including dichroic color filters for liquid crystal displays, field effect transistors for optoelectronic switches, and solar photovoltaic cells.² Most of the dye functions are based on collective properties, such as photoconductivity,³ energy transfer,⁴ and specific absorption or reflections of light,⁵ i.e., they are determined by layer morphology. In the majority of works, the method of second harmonic generation was used allowing probing of molecular orientation with respect to the substrate surface.⁶ It was shown that the S_0-S_1 transition dipole moment of cationic dye is inclined to insulating surface. The destruction of layers under the action of single-pulse laser radiation was studied by the same method in Ref. 7 and photoisomerization and evaporation were concluded to be responsible for the decrease in the second harmonic signal.

Recently, advanced microscopic techniques, such as tunneling and atomic force microscopy, are used providing high spatial resolution, to probe morphology of molecular layers, crystalline phase, in particular. According to the UV, visible, and IR spectroscopy data,⁸ molecular orientation, relative domain concentration, and morphology of LB films vary after a few hours of preparation. The formation of crystalline phase from the amorphous phase in a symmetric monocarbocyanine dye layer at different temperatures was studied in Ref. 9. The fact that the dye spectrum is considerably broader for amorphous layer than for solution was explained by higher inhomogeneous broadening of the dye layer spectrum.

We study effect of the symmetry of intramolecular electronic density distribution on spectral properties of molecular dye layers, the interaction of dye layers with laser radiation of varied power, and behavior of dye layers on heating in the dark.

2. EXPERIMENTAL

Long-conjugated polymethine dyes, symmetric and asymmetric dicarbocyanines, were used after recrystallization and drying. Spectrally pure acetone and ethyl alcohol were solvents. Molecular layers were spin coated from dye solutions in polar solvents containing solely monomeric forms. The absorption spectra of layers were recorded on a SF-9 and Perkin-Elmer Lambda 9 spectrophotometers (scan rate 1 nm). To probe low-density layers, a sandwich assembly containing a few layers coated under similar conditions was used. The temperature measurements were performed in a thermostated oven controlled to within 1°C with a thermometer.

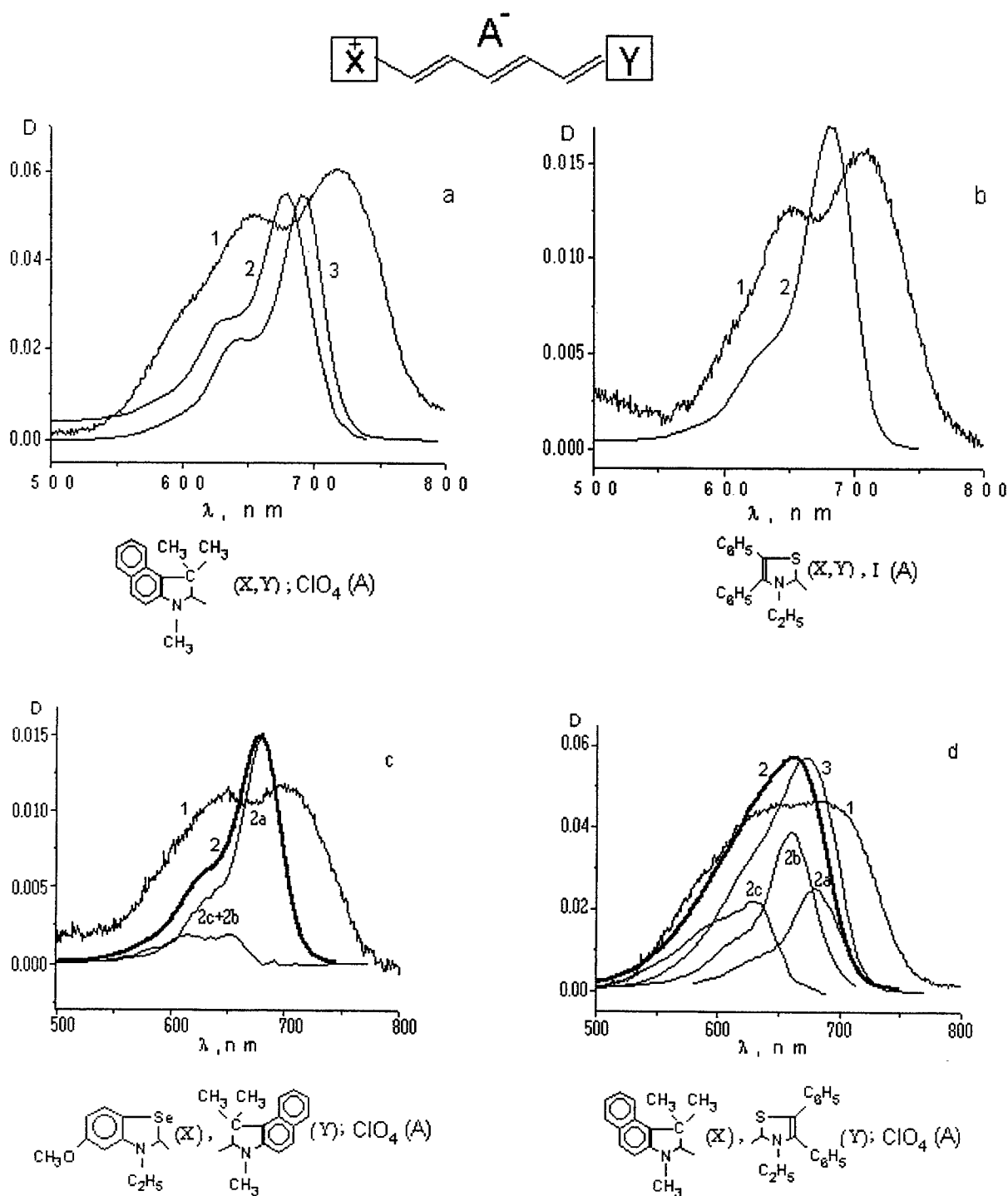


Fig 1. The structural formulas of polymethine dyes along with their absorption spectra corresponding to (1) molecular layers on glass and (2) ethanol and (3) methylene chloride solutions. (a) SPD1, $\Phi_{01} = \Phi_{02} = 45^\circ$; (b) SPD2, $\Phi_{01} = \Phi_{02} = 65^\circ$; (c) APD1, $\Phi_{01} = 53^\circ$; $\Phi_{02} = 45^\circ$; (d) APD2, $\Phi_{01} = 45^\circ$, $\Phi_{02} = 65^\circ$. The spectra 2a, 2b, and 2c in Figs. 1c,d are separated from spectrum 2 and correspond to the three equilibrium stereoisomers. (2a) all-trans isomer. The spectrum 1d is taken from a 10-layer sandwich based on 5 substrates

Excitation source was a Rb-laser delivering ~ 17 nm Q-switched pulses at $\lambda = 694$ nm with up to 400 mJ maximal energy. To measure the pulse energy, a photoelement calibrated against the IMO-1 energy-measuring device was used in set with a RC circuit

Separation of the layer absorption spectrum onto single components was performed by fitting the single component spectrum to the sum of the two Gaussian profiles similar in width (0-0 or 0-1 transitions). The following procedure was used: the spectra of layers containing the minimal number of species (photodestructured layers and those coated from the least concentrated solution) were used to derive the Gaussian profile parameters for the spectra of the corresponding monomers. Then, the spectra of aggregated species were derived from the spectra of layers coated from strongly concentrated solutions using these parameters.

3. THE ABSORPTION SPECTRA OF POLYMETHINE DYES OF DIFFERENT STRUCTURE

The structural formulas of symmetric and asymmetric polymethine dyes (SPD1, 2 and APD1, 2) bearing heterocyclic end groups of various electron donating ability (Φ_0) are shown in Fig. 1 together with the absorption spectra of dye solutions and molecular layers on Crown-8-grade glass. Similar spectra were observed for a few of symmetric and asymmetric dicarbocyanines differing in symmetries and Φ_0 values on glass and fused quartz. As seen from Fig.1, the spectra of dye layers are considerably broader than of dye solutions and have more than one maximum. Similar broadening of the absorption spectra was also observed for one of monocarbocyanine layer on quartz in.⁸

The change in the coating conditions, including solution concentration and volume, solvent type, and substrate temperature, changes the spectral width, the ratio of the maxima, and the maxima positions in the layer spectrum. The normalized absorption spectra of SPD1 layers with the various maximum optical density (D_{\max}), which were coated from variously concentrated solutions characterized by the maximum absorption coefficient k_{\max} , are demonstrated in Fig. 2.

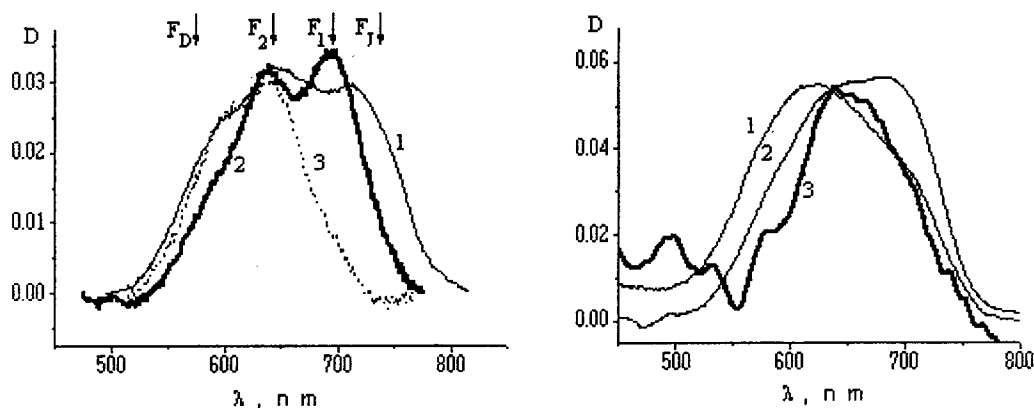


Fig. 2. The absorption spectra of SPD1 layers of various density (D) spin coated onto glass from ethanol solutions of varied concentration (k_{\max}). (1) $k_{\max} = 600 \text{ cm}^{-1}$, $D_{\max} = 0.031$, (2) $k_{\max} = 100 \text{ cm}^{-1}$, $D_{\max} = 0.0085$, and (3) $k_{\max} = 68 \text{ cm}^{-1}$, $D_{\max} = 0.0025$. The spectra 2 and 3 are normalized to spectrum 1 at $\lambda = 640 \text{ nm}$. The spectrum 3 is recorded on a 3-layer sandwich.

Fig. 3. The absorption spectra of APD2 layers of various density (D) spin coated onto glass from acetone (1,3) and ethanol (2) solutions of varied concentration (k_{\max}). (1) $k_{\max} = 240 \text{ cm}^{-1}$, $D_{\max} = 0.055$, (2) $k_{\max} = 80 \text{ cm}^{-1}$, $D_{\max} = 0.0055$, and (3) $k_{\max} = 8 \text{ cm}^{-1}$, $D_{\max} = 0.0045$. The spectra 2 and 3 are normalized to spectrum 1 at $\lambda = 640 \text{ nm}$. The spectrum 2 is taken from a 10-layer sandwich.

A low-density spectrum consists of the main band around ~ 645 nm that is blue-shifted with respect to the all-trans monomer maximum responsible for the spectrum of SPD1 solution and has shoulder at the long wavelength edge. For layers coated under identical conditions, the relative intensity of the shoulder markedly varies from sample to sample, which suggests presence of the second longer-wave component. At medium D_{\max} , the band intensities of these two components are close and the spectral parameters corresponding to identical deposition conditions are similar. The maximum of the long-wave component is close to the all-trans monomer maximum in the spectrum of dye in low polarity methylene chloride (around 698

and 690 nm, respectively). The high-density spectrum is broader in both directions, the maxima of the spectral envelope are shifted toward long and short waves and their ratio is changed. Similar transformations were also observed for APD2 (Fig. 3). The results obtained show that with increasing molecular concentration on the surface the number of different species F_i contributing to the absorption spectrum of SPD1 layer increases to at least 4 as maximum (Fig. 2).

4. ACTION OF INTENSE LASER RADIATION

The effect of pulsed laser radiation of varied average intensity (I_{av}) and total energy density (E_{Σ}) on SPD1 layers is demonstrated in Fig. 4. As seen, the action of power radiation with the large E_{Σ} value results in the destruction of the layer and the decrease in the band density within 520-800 nm. The optical density within 400-480 nm increases simultaneously, indicative of dye destruction via irreversible photooxidation.¹⁰ In the process, the photodestruction yield of various destructing species is different (Fig. 4a). The highest resistance to irradiation is exhibited by the F_1 species whose absorption maximum is close to the all-trans monomer in solution, i.e., to the excitation wavelength. At the same time, the band density around 645 nm that is due to the F_2 species decreases considerably. In the process, the most long-wave band due to F_j species and the most short-wave band due to F_D species that does not absorb exciting radiation disappear virtually completely.

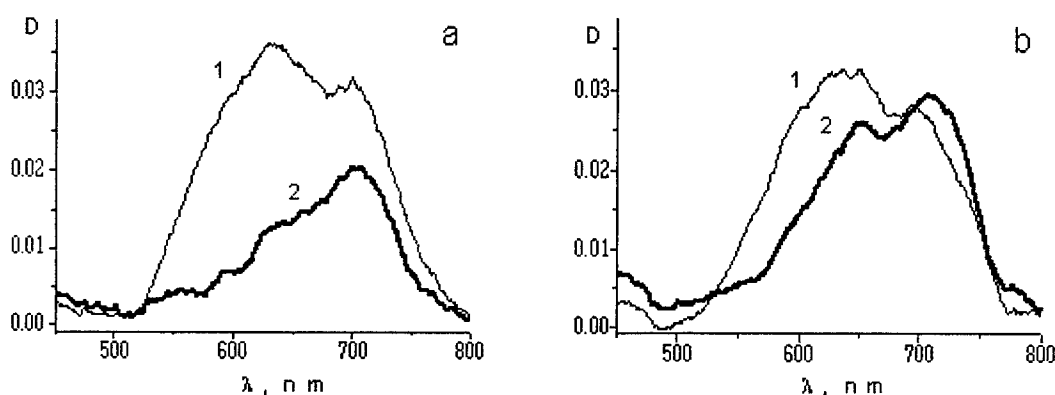


Fig. 4. Transformation of the absorption spectrum of SPD1 layer on glass under the action of 694-nm single pulse laser radiation. (1) before irradiation and (2) after irradiation with (a) $I_{av} = 9 \cdot 10^{25}$ photon/cm²s and a total energy density in 5 pulses $E_{\Sigma} = 3.1$ J/cm² and (b) $I_{av} = 3 \cdot 10^{25}$ photon/cm²s and $E_{\Sigma} = 0.88$ J/cm² in 5 pulses

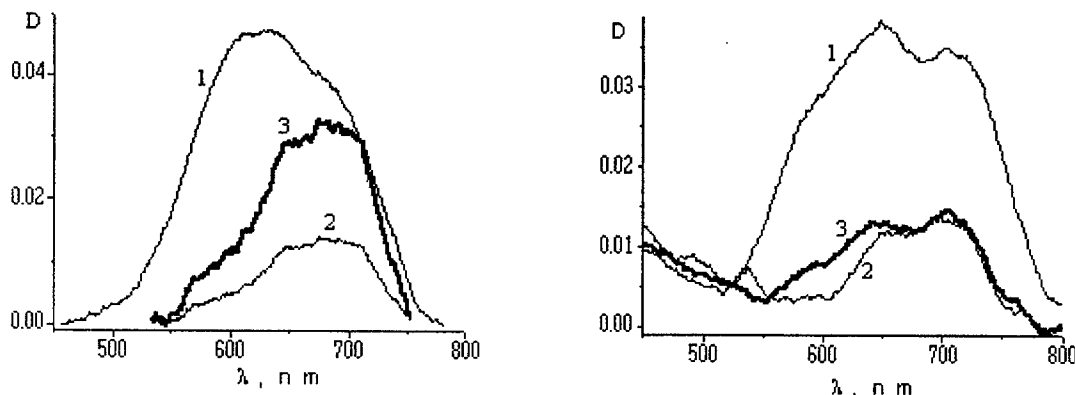


Fig. 5. Transformation of the absorption spectrum of APD2 layer on glass under the action of 694-nm single-pulse laser radiation. (1) before irradiation and (2) after irradiation with $I_{av} = 1.1 \cdot 10^{26}$ photon/cm²s and $E_{\Sigma} = 8.1$ J/cm² in 14 pulses. (3) spectrum 2 normalized to spectrum 1 at $\lambda = 705$ nm.

Fig. 6. Transformation of the absorption spectrum of SPD1 layer on glass. (1) before irradiation and after (2) 15 min and (3) 19 days of storage following 694 nm single-pulse laser irradiation with $I_{av} = 1.1 \cdot 10^{26}$ photon/cm²s and $E_{\Sigma} = 5.2$ J/cm² in 8 pulses.

Closely matched results were also obtained for APD2 layers (Fig. 5). The transformation of the layer spectrum following laser action was also observed (Fig. 6). The F_D concentration in the SPD1 layer stored for a long time in the dark at room temperature increases considerably.

At lower I_{av} and E_Σ the character of the spectral transformations varies: the optical density of the SPD1 spectrum changes inconsiderably so that the intensity of the F_1 band increases, whereas that of the F_D band decreases (Fig. 4b).

As known, absorption of light results in the photodestruction of a dye. However, the heating induced by nonradiative dissipation of the absorbed energy can also affect dye destruction. For this reason, we performed the temperature studies on dye layers.

5. TEMPERATURE STUDIES

Effect of 1-h heating at $+190^\circ\text{C}$ on the SPD1 layer spectrum is demonstrated in Fig. 7. After heating, the F_D band disappears, whereas the intensity of the absorption maximum around 698 nm increases. Subsequent storage in the dark at room temperature caused the F_D and F_j band intensities to be increased slightly.

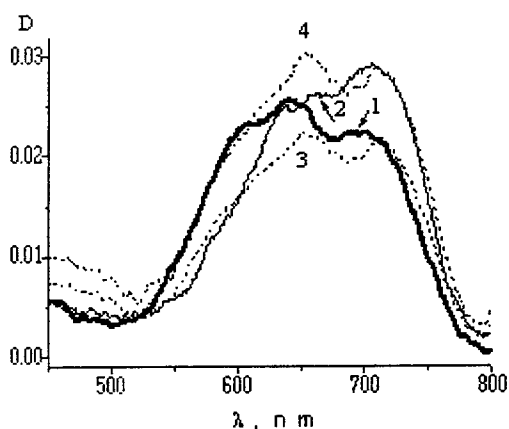


Fig. 7. Temperature transformation of the absorption spectrum of SPD1 layer coated from ethanol solution with $k_{\max} = 600 \text{ cm}^{-1}$ onto glass substrate. (1) initial layer and layer stored for (2) 15 min and (3) 2 days following 1h heating at $+190^\circ\text{C}$. (4) spectrum 3 normalized to spectrum 2 at $\lambda = 705 \text{ nm}$.

6. DISCUSSION

Comparison of the layer spectra with different optical densities along with study of the laser radiation effect allows single components to be separated from the layer spectra. Such separation for SPD1 and APD2 is demonstrated in Figs. 8 and 9, respectively. The spectral widths of these components' spectra ($w_{0.0} \approx 1000\text{-}1500 \text{ cm}^{-1}$) are broader than of the SPD1 spectrum in methylene chloride ($w_{0.0} \approx 600 \text{ cm}^{-1}$). For monomeric species this result may be explained by growth of the inhomogeneous broadening of the layer spectrum.

At low concentrations of the initial solution, the optical density of the F_2 band is considerably higher than of the F_1 band. This implies that layer starts covering from F_2 species. The above result and the fact that the F_1 spectrum resembles the spectrum in solution indicate these both species to be monomers. The fact that the F_1 band appears solely in the high-density spectra suggests that this species is aggregated dye, probably J-aggregate. Also, the position and the increase in the relative intensity with surface concentration allow the F_D band to be assigned to dimeric form.

Using these assumptions, we calculated the surface concentration of the layer species. The oscillation forces (f) were assumed to be close for monomeric forms and J-aggregates and lower by approximately 1.7-fold (1.5 - 2-fold on the average¹¹) for dimers. For spectra 1, 2, and 3 from Fig. 2 the calculated surface concentration (N_{SF_i}) and the total coefficient of substrate coverage (K_Σ) with dye monolayers are listed in Table. The limiting angle (φ_i) of the transition dipole moment inclination to the substrate surface was estimated by assuming $K_{F_{1,2}} = 1$, where $K_{F_{1,2}}$ is coverage of F_1 and F_2 monomers in the layer coated from the $k_{\max} = 600 \text{ cm}^{-1}$ solution. The calculations used experimental data and the following equations:

$$K_\Sigma = K_{F_1} + K_{F_2} + K_{FD} + K_{FJ}$$

$$K_{F_i} = \alpha N_{\text{SF}_i} S_{\text{mFi}}, \quad N_{\text{SF}_i} = 2.3 D_{\text{maxFi}} / \sigma_{\text{max}} \cos^2 \varphi_i$$

$$S_{\text{mFi}} = S_{\text{m}} \cos \varphi_i + S_{\text{mL}} \sin \varphi_i, \quad \sigma_{\text{maxFi}} = 1.5 \sigma_{\text{max sol}} Q_{\text{sol}} / Q_{\text{Fi}}$$

Here, N_{SFi} is surface concentration of F_i species, D_{maxFi} is the maximum density within the F_i band; α is the number of the monomers incorporated into the F_i species; S_{mFi} is the substrate area occupied by monomers incorporated into the F_i species; $S_{\text{m||}}$ is the projection area of molecule onto the end groups' plane; $S_{\text{m\perp}}$ is the projection area of molecule onto the plane normal to the major axis; $Q_{\text{sol}} / Q_{\text{Fi}}$ is the ratio of the areas normalized to the long-wave maximum of the solution and the F_i absorption spectra; the coefficient 1.5 in the equation for calculating the absorption cross section σ_{maxFi} of F_i from the absorption cross section of solution accounts for the difference in possible molecular orientations in the solution (3D-medium) and in the layer (2D-medium). For SPD1, $S_{\text{m||}} \approx 1.6 \text{ nm}^2$, $S_{\text{m\perp}} \approx 0.36 \text{ nm}^2$ (as estimated from the Van der Waals radii) and $\sigma_{\text{max sol}} = 0.067 \text{ nm}^2$. In calculation of K_{mFi} we used $\alpha=1$ for $F_{1,2}$ и $\alpha=2$ for F_D . The lower limit of the K_{Σ} value for spectrum 1 in Fig. 2 was calculated by assuming that for F_j aggregates $\alpha=4$, $\phi_i = 0^\circ$ and $S_{\text{mFi}} = 1.6 \text{ nm}^2$.

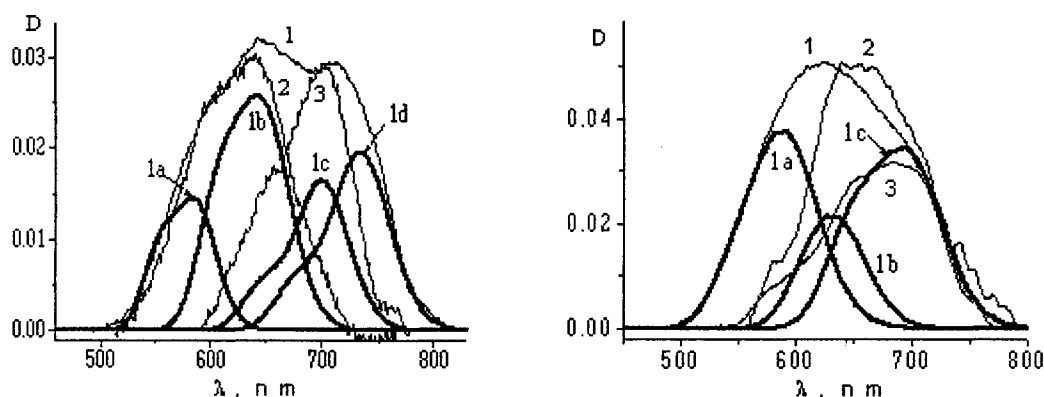


Fig. 8. The absorption spectrum of SPD1 layer and its separation onto single-species spectra. (1) $k_{\text{max}} = 600$ and (2) 68 cm^{-1} . (3) spectrum 1 after irradiation (694-nm Q-switched pulses, $I_{\text{av}} = 1 \cdot 10^{26} \text{ photon/cm}^2 \text{ s}$, the total energy density in 11 pulses $E_{\Sigma} = 8.1 \text{ J/cm}^2$). The single components separated from spectrum 1 are due to F_D (1a), F_2 (1b), F_1 (1c), and F_j (1d) species. $\chi^2 = 2.5 \cdot 10^{-7}$. The spectra 2 and 3 are normalized to spectrum 1 at $\lambda = 590$ and 705 nm , respectively.

Fig. 9. The absorption spectrum of APD2 layer and its separation onto single-species spectra. (1) $k_{\text{max}} = 240$ and (2) 8 cm^{-1} . (3) spectrum 1 after irradiation (694-nm Q-switched pulses, $I_{\text{av}} = 1.1 \cdot 10^{26} \text{ photon/cm}^2 \text{ s}$, the total energy density in 13 pulses $E_{\Sigma} = 10.6 \text{ J/cm}^2$). The single components separated from spectrum 1 are due to F_D (1a), F_2 (1b), and F_1 (1c) species. $\chi^2 = 5.9 \cdot 10^{-7}$. The spectra 2 and 3 are normalized to spectrum 1 at $\lambda = 715 \text{ nm}$.

Table. The calculated surface concentration of the species in the SPD1 layers and the total coefficient of substrate coverage with molecular monolayers

Spectrum in Fig. 2	$k_{\text{max}} \text{ cm}^{-1}$	$D_{\text{max}}^*)$	K_{Σ}	$N_{\text{SFi}}, \text{ nm}^{-2}$			
				F_1	F_2	F_D	F_j
1	600	0.031	≥ 6	0.62	0.62	0.62	0.37
2	100	0.009	0.93	0.23	0.18	0.084	0
3	68	0.0025	0.27	0.01	0.06	0.05	0
			$\phi_i, \text{ deg}$	22	21	2	
			$S_{\text{mFi}}, \text{ nm}^2$	1.62	1.62	1.62	

*) the maximal optical density of the layer spectrum.

The table data show that with growing initial solution concentration, the surface concentration of F_D and F_j species in the layer increases and the more considerable increase is observed for F_j species. The F_j band is present virtually solely in spectrum 1 at the maximal K_{Σ} value. This indicates that the degree of aggregation into F_j species is considerably higher than

into F_D ones. At low concentrations of the initial solution and $K_\Sigma \ll 1$ the surface concentration of F_2 species markedly exceeds that of F_1 ones.

The destruction of F_D with temperature is accompanied by growing of the F_1 and F_2 surface concentrations. The growth of the F_1 surface concentration was also observed under the action of single-pulse laser radiation with low I_{av} и E_Σ . This shows that the F_1 and F_2 species are incorporated into the F_D aggregates. At the same time, at higher I_{av} and E_Σ , the F_1 and F_D bands disappear and the surface concentration of monomers decreases. In the process, the photodestruction yield is considerably higher for F_2 than for F_1 . The destruction of highly aggregated species F_1 can be of photo- or thermal origin. The thermal destruction is due to the heating of layer via nonradiative dissipation of the absorbed radiation energy. Evidently, the destruction of the F_D species not absorbing laser radiation is of thermal origin. The aggregate destruction in a layer should increase the surface concentration of monomers, in line with the observations at low I_{av} and E_Σ . However, under the action of radiation the photodestruction of absorbing monomers also occurs, which should result in the decrease of their concentration. Evidently, the resulting change in the surface concentration of the F_1 and F_2 monomers depends on competition between these processes. The process of the increase in the monomer concentration dominates at low E_Σ values, whereas that of the decrease in the monomer concentration, at high E_Σ values.

After the layer was stored in the dark at room temperature, the F_D species partially recovered, whereas the highly aggregated species F_1 did not recover, which is explained by considerable decrease in the monomer concentration owing to photodestruction.

As seen from Fig. 2, apart from the monomer bands, the band due to the F_D aggregates can also be revealed in the layer spectrum even at low concentrations of the initial solution and $N_{SF_1} \ll 1$ (spectrum 3). This fact indicates that molecules cover film as islands, where single-layer monomers F_2 , two-layer dimers F_D , and all-trans isomers F_1 may be present.

We have made two suggestions about the nature of the F_2 monomers:

1. The F_2 monomer is a stereoisomeric species different from all-trans isomer F_1 . This species has spectrum shorter-wave shifted with respect to that of all-trans isomer and the higher photodestruction yield. The increase in the equilibrium concentration of such species in a layer is governed by the interaction of molecule with substrate, which results in the distortion of molecular electronic symmetry. This assumption is corroborated by the fact that several equilibrium isomeric species with close concentrations can simultaneously exist in solutions of highly asymmetric APD.¹² For example, in solution of APD2 bearing end groups strongly differing in electron donating abilities ($\Delta\Phi_0=20^0$) the three isomeric species coexist. In this case, the species responsible for the shorter-wave band peaked at 659 nm, rather than all-trans isomers responsible for the 681 nm band, have the maximal concentration in polar solution (Fig. 1d). The similarity of the spectral properties of SPD and APD layers also shows that variations of the molecular electronic symmetry upon interaction with substrate essentially affect spectral properties of the dye layers (Fig. 1).
2. The F_2 monomer is similar to the all-trans monomer F_1 , but the molecular arrangement in a layer is different, namely, the F_2 monomers are arranged within the first layer interacting with substrate, which results in the shift of the dye absorption spectrum and affects the photodestruction yield, whereas the F_1 monomers are arranged within the second layer where this interaction is considerably weaker.¹³

The difference between the two-layer assembly of weakly interacting F_1 and F_2 monomers and the dimeric layer of strongly interacting monomers can be explained by incorporation of water molecules into the dimer.¹⁴ Then, the low rate of the dimer reduction in a destructed layer stored in the dark is reasonable, because the recovery of monomers to dimers requires water molecules that had left a layer after heating. The water can be incorporated into the layer solely from the air. In the literature, suggestions were made that water also facilitates attachment of dye molecules to the substrate surface.¹⁵ This fact can explain why under irradiation or heating the F_2 monomers from the first layer are destructed considerably higher than the F_2 monomers from the second layer.

7. CONCLUSION

1. The spectral parameters of symmetric and asymmetric dicarbocyanine polymethine dyes change in a similar manner upon transition from solution to layer on insulating surface, which is explained by the distortion of electronic symmetry upon dye-substrate interaction.
2. The spectra of dicarbocyanine polymethine layer with the monomeric layer coverage $K_\Sigma \leq 1$ are determined by arrangement of dye molecules into one or two-layer islands. The two-layer islands may include both two weakly interacting monomeric layers differing in the spectral properties and dimeric layer.

3. As surface concentration increases, the more aggregated species possessing the higher degree of aggregation are formed apart from dimers. The layers with high surface concentration contain two monomeric species, dimeric species, and, probably, J-aggregates. The concentration ratio of these species depends on the coating conditions, including concentration and volume of the initial solution, solvent type, and substrate temperature. Prolonged heating causes aggregates to destruct and the number of monomeric species to increase.
4. The action of single pulse monochromatic laser radiation results in the destruction of monomeric and aggregated species, including those not absorbing exciting radiation. The destruction is due to the photodecay of absorbing monomeric species and thermal destruction of aggregated species (dimers and J-aggregates).
5. The number of monomeric species changes depending on the ratio of the growth rate of monomer concentration owing to aggregate decay and the rate of photodecay of the monomers. This ratio depends on the initial concentrations of monomers and aggregates and on the excitation conditions including total energy density, the number of acting pulses, and the pulse energy and power. The number of monomeric species increases at low total energy density and radiation power and decreases when these parameters are high. The photodestruction rate of the monomers of the first layer is considerably higher than of the second layer.
6. In a destructed layer stored for a long time in the dark, the dimeric species partially recover probably due to the recovery of equilibrium water concentration in the layer.

8. ACKNOWLEDGEMENT

The work was financially supported by the Russian Fund for Fundamental Research (grant no.99-02-18223). We thank Dr. E.P Shchelkina who synthesized the dyes studied.

9. REFERENCES

1. A.N. Terenin, "Fotonika molecul krasitelei" (Photonics of Dye Molecules), Leningrad: Nauka, 1967, pp. 190-193.
2. J.D. Wright, "Molecular Crystals," Cambridge: Cambridge Univ. Press, 1995.
3. K. Law, *J. Chem. Phys.*, **93**, pp. 449-486, 1993.
4. De Boer, S. and D.A. Wierma, *Chem. Phys. Lett.*, **165**, pp. 45-53, 1990.
5. J. Fabian, H. Nakazumi, and M. Matsuoka, *Chem. Rev.*, **92**, pp. 1197-1226, 1992.
6. D.J. Campbell, D.A. Yiggins, and R.M.J. Corn, *Phys. Chem.*, **94**, pp. 3681-3689, 1990.
7. St.R. Meech and K. Yoshiharta, *J. Phys. Chem.*, **94**, pp. 4913-4920, 1990.
8. M. Shinichi, I. Keiji, and O. Yukihiro, *J. Chem. Phys.*, **104**, pp. 1183-1190, 2000.
9. J. Tao, G. Mao, and L. Daehne, *J. Am. Chem. Soc.*, **121**, pp. 3475-3485, 1999.
10. E.N. Kaliteevskaya and T.K. Razumova, *Opt. Spektrosk.*, **48**, pp. 290-295, 1980.
11. Ref 1, p. 183.
12. T.K. Razumova, A.N. Tarnovskii, and E.P. Shchelkina, *Opt. Spectrosc. (USSR)*, **72**, pp. 1102-1114, 1992.
13. Ref 1, pp. 486-487.
14. Ref 1, p. 184.
15. Ref 1, p. 191.

CO₂ laser radiation detection in compensated germanium

S. Bumelienė^a, S. Ašmontas^a, J. Gradauskas^{a,b}, A. Jukna^{a,b},
J. Paršeliūnas^a, D. Seliuta^a, A. Sužiedėlis^{a,b}, G. Valušis^{a,b}

^a Semiconductor Physics Institute, A. Goštauto 11, Vilnius LT-2600, Lithuania

^b Gediminas' Technical University of Vilnius, Saulėtekio av.11, 2054 Vilnius, Lithuania

ABSTRACT

We report the results of experimental study of infrared radiation detection in a bulk of compensated germanium. Au or Ni with deep levels in the forbidden energy gap was used as compensating impurities. In spite of great difference in their activation energies the change of electrical resistance of the samples under CO₂ laser illumination indicated the similar rise of carrier density in the valence band which can not be explained only by means of direct hole activation from these levels. The DC measurements have shown the activation character of the electrical conductivity of compensated semiconductors. Evaluation of spatial quantity of in-homogenates in compensated semiconductors confirmed the importance of energetic bands bending due to the existence of ionised impurities complexes for infrared detection.

Keywords: CO₂ laser radiation detection, carrier heating, deep levels in semiconductors.

1. INTRODUCTION

Various devices based on the carrier heating by electromagnetic radiation are successfully used for infrared and microwave detection using non-uniform *l-h* junctions¹. A special attention is paid to *p*-type germanium due to its wide application in microwave¹ and infrared² detection, as well as in the point of view of basic physics³. Microwave detection in the *l-h* junctions of *p*-type germanium compensated with Au impurities has shown the restriction of the dynamic range due to the field dependencies of hole energy relaxation time, hole mobility and hole capture cross-section in this material⁴. On the other hand it is well known that germanium with several impurities is being widely used as an infrared light photodetector⁵. The infrared detection in the bulk of germanium compensated with gold revealed the predomination of hole activation from Au levels by CO₂ laser illumination over the carrier heating at low temperatures⁴. In this paper we report experimental investigation of CO₂ laser radiation detection peculiarities in *p*-Ge compensated with Au or Ni impurities having levels of different depth.

2. SAMPLES AND EXPERIMENTAL TECHNIQUE

We used *p*-type germanium compensated with gold or nickel impurities, the concentration of which was in the order of $(1,5\div3)\cdot 10^{15} \text{ cm}^{-3}$. The *p-p*⁺ junctions were made on the ends of dumb-bell-shaped samples by alloying indium contacts in vacuum. The DC measurements were performed using nanosecond duration pulses of low repetition rate to avoid crystal lattice heating. As a source of infrared radiation the Q-switched CO₂ laser with operation wavelength 10.6 μm, pulse duration 150 ns, and repetition rate 40 Hz was used. Maximum power density was of about 1.20 MW/cm². The central narrow part of the sample was illuminated for registration of electrical resistance change under influence of CO₂ laser radiation. The measurements at cryogenic temperatures were made in liquid nitrogen vapour surroundings. In the case of these low temperature measurements the optical cryostat was used.

3. EXPERIMENTAL RESULTS AND DISCUSSION

The measurements of temperature dependence of electrical resistance of the samples have shown the position of energetic levels ΔE_A of compensating acceptors in germanium with respect to the top of valence band as can be seen in Fig. 1. The value of ΔE_A was derived in temperature range where the electrical resistance change resulted mainly from carrier density change with the temperature. Non-exponential behaviour of the presented curves at higher temperatures can be explained by the exhaustion of deep impurity levels before the beginning of the intervalley generation. The sublinear run of the electrical resistance of the samples of germanium compensated with Ni impurities in low temperature range we attribute to peculiarities of high value electrical resistance measurement technique because the nickel level ($\Delta E_A = 0,22 \text{ eV}$) is deeper than the gold one ($\Delta E_A = 0,15 \text{ eV}$) (Fig. 1).

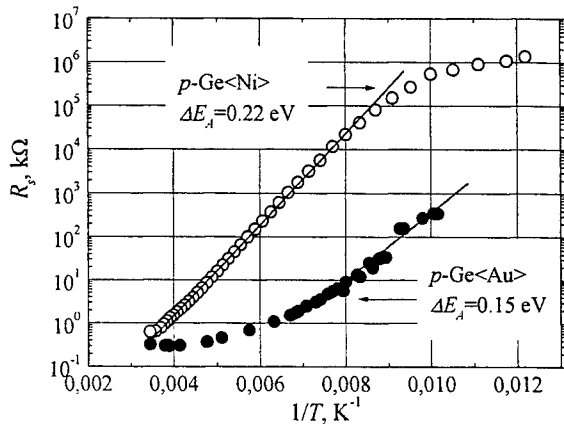


Fig. 1. Temperature dependencies of electrical resistance of compensated germanium samples

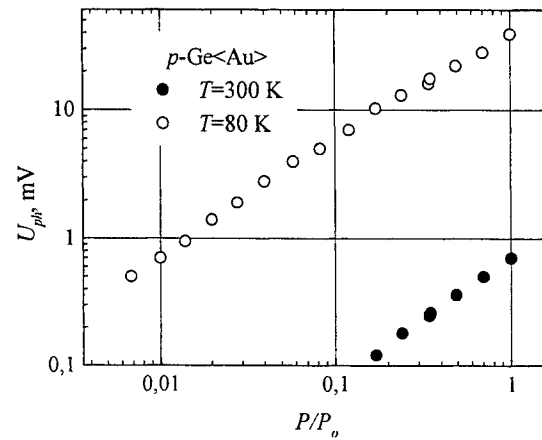


Fig. 2. The dependence of photo-voltage arising in p^+ - p -Ge<Au> contact on laser illumination intensity

The photo-voltage arising on the ends of the p -Ge samples compensated with Au impurities linearly depends on laser illumination intensity as can be seen from Fig.2. However, whereas, at room temperature the polarity of photo-voltage corresponds to the decrease of electrical conductivity of p -Ge under laser illumination, then at liquid nitrogen temperature the polarity of photo-voltage indicates the increase of the conductivity. In first case we associate this with carrier mobility decrease due to the hole heating by laser illumination, while in the second one the increased conductivity can be explained by competitive action of carrier density increase under laser illumination.

We measured the temperature dependence of electrical resistance change under influence of CO_2 laser radiation of the samples of germanium compensated with gold or nickel impurities (see Fig. 3). The results were quite different in comparison with these of non-compensated germanium where the decrease of the resistance followed the energy dependence of hole mobility. In p -Ge<Au> the increase of the electrical resistance was observed at room temperature,

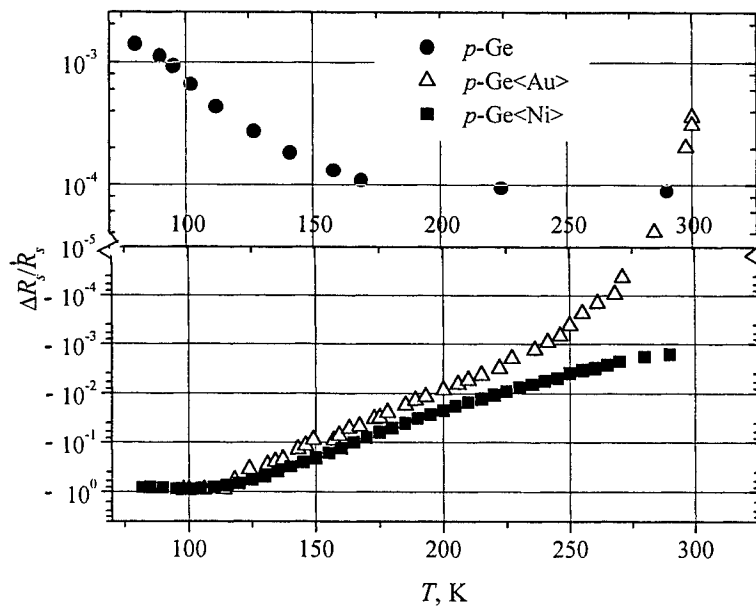


Fig. 3. The temperature dependence of relative electrical resistance change of pure and compensated germanium under CO_2 laser illumination.

meanwhile at lower temperatures the photoresistance have decreased. In the case of compensating impurity of Ni the resistance decreased under IR illumination over all measured temperature range. It is worth to note that in spite of very different depth of level of Au and Ni impurities the temperature dependence of sample photoconductivity is similar in both cases of investigated impurities in the temperature range lower than room temperature (Fig. 3). On the other hand, the energy of the quantum of CO₂ laser light is sufficiently smaller in comparison with activation energy of the investigated impurities. Meanwhile, the electrical resistance change measurements under influence of microwave radiation have shown no carrier density increase in measured temperature range as can be seen from Fig. 4 for germanium compensated with Au impurities.

The change of the compensated germanium resistance under CO₂ laser illumination can be explained by the concentration effects, which predominated over the carrier heating ones. On the one hand, the hole mobility decreases at increasing charge carrier energy, meanwhile the free hole concentration rises due to the energy dependence of the capture cross section of attractive Au or Ni recombination centres⁶. However the observed decrease of the resistance of the sample with the energy of CO₂ laser radiation can not be explained by the hole capture diminution due to the insignificance of the latter effect. On the other hand the hole concentration increase can not be sufficient intensive due to direct hole activation from impurity levels to valence band. So we explain the observed phenomena by the competition of charge carrier heating effects and free hole concentration increase due to the presence of random potential of the energetic bands in compensated germanium.

As a background for the ideology from the point of view of existence of random inhomogenates we used the works^{7,8}, where the main features of the highly compensated or disordered semiconductors were determined. Because the current-voltage (*I-V*) characteristics of such semiconductors are described by a law

$$I \sim \exp\left[-\left(E_a - \alpha E^{1/2}\right)/kT\right] \quad (1)$$

where E_a - the activation energy of electrical conductivity, α - the parameter of the inhomogeneity, E - the electric field strength, k - the Boltzmann constant, T - the lattice temperature, we have measured those characteristics at different lattice temperatures. The figure 5 shows the *I-V* characteristics of germanium compensated with Au impurities, while in the Fig. 6 are depicted the *I-V* ones of Ni compensated germanium.

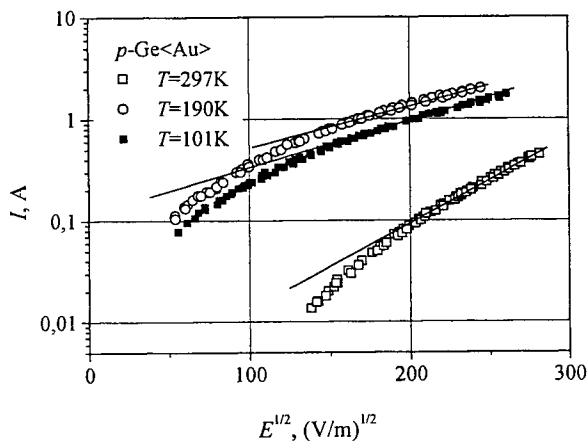


Fig. 5. The *I-V* characteristic of the Au compensated germanium

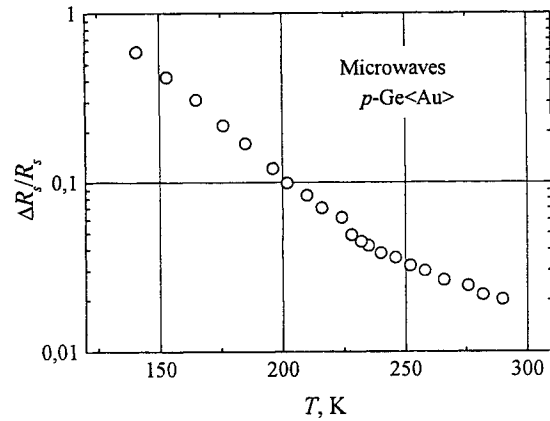


Fig. 4. The temperature dependence of relative electrical resistance change of compensated germanium in microwave electric field

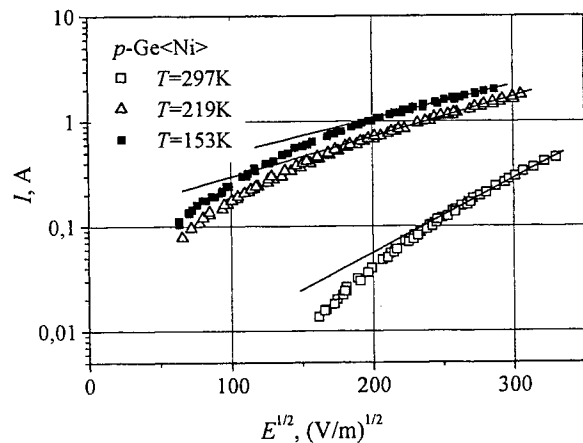


Fig. 6. The *I-V* characteristic of the Ni compensated germanium

We have found that the electrical conductivity has an activation character, and these characteristics are very similar to that of the disordered material⁸ or highly compensated semiconductors^{9,10}. Such findings suggested the idea that the inhomogeneities can play an important role in the phenomena of infrared detection in compensated germanium.

Evaluation of the parameter of the inhomogeneity α at different lattice temperature from eq. (1) have shown its slight temperature dependence in the case of $p\text{-Ge}\langle\text{Au}\rangle$, while in germanium compensated with Ni impurities this parameter was nearly temperature independent. The parameter α is related with energetical and spatial quantity of inhomogeneity⁷

$$\alpha = (0.25eaV_0)^{1/2}, \quad (2)$$

where e is electron charge, a denotes the length of inhomogeneity, and V_0 is the fluctuation magnitude of random potential. Taking into consideration the fluctuation magnitude equal to the CO_2 laser quantum energy value $V_0 = 0,11 \text{ eV}$, we have that the holes feel inhomogeneities which lengths are of the order of $1 \mu\text{m}$, for both $p\text{-Ge}\langle\text{Au}\rangle$ and $p\text{-Ge}\langle\text{Ni}\rangle$ samples at low temperatures. At room temperature the spatial value of random inhomogeneity in germanium compensated with Au impurities was a little higher which resulted in slighter distortion of valence band edge, thus in predomination of hole heating effects over the activation processes from deep Au level as can be seen from Fig. 3.

4. CONCLUSIONS

The investigation of the detection of CO_2 laser infrared radiation in a bulk of compensated germanium offers us the following conclusions:

- ❖ the electrical resistance change of the samples revealed the hole concentration increase in germanium compensated with Ni impurities in temperature range from room to liquid nitrogen temperature, while in the case of germanium compensated with Au impurities the hole concentration increase was observed in lower than 275K temperature range;
- ❖ the hole concentration increase under CO_2 laser radiation can be explained by means of both charge carrier heating effects and the distortion of valence band edge due to the presence of the complexes of compensating impurities, i.e. the percolation character of electrical conductivity take place in the investigated germanium compensated with Au and Ni impurities;
- ❖ the temperature dependence of the spatial value of random inhomogeneities have been observed only in the case of germanium compensated with Au: the length of the inhomogeneity which feel the heated holes rises with temperature increase. As a result at room temperature a slighter distortion of valence band edge occurs and the predomination of hole heating over their activation from Au level takes place.

5. REFERENCES

1. S. Ašmontas, *Electrogradient Phenomena in Semiconductors*, Mokslas, Vilnius, pp. 184 (1984) (in Russian).
2. S. Ašmontas, E. Maldutis and E. Širmulis, "CO₂ laser radiation detection by carrier heating in inhomogeneous semiconductors", *Int. Journ. Optoelectronics*, Vol. 3, No. 3, pp. 263-266, (1988).
3. S. Ašmontas, J. Gradauskas, A. Sužiedėlis, G. Valušis, "Features of thermoelectromotive force in Au/ $p\text{-Ge}$ junctions", *IEEE Issue, Proc of XVI Intern. Conf. on Thermoelectrics*, pp. 753-756 (1997).
4. S. Ašmontas, S. Bumelienė, J. Gradauskas, A. Sužiedėlis, G. Valušis, "Microwave and infrared detection in compensated germanium", *Lithuanian Journ. Phys.*, Vol. 40, No. 1-3, pp. 47-50 (2000).
5. S.M. Sze, *Physics of Semiconductor Devices*, A Wiley Interscience Publication John&Sons, New York. Chichester. Brisbane. Toronto. Singapore, pp.455 (1981) (in Russian).
6. V.N. Abakumov, V.I. Perel, I.N. Yassievich, *Nonradiation Rekombination in Semiconductors*, Institut of nuclear physics RAC, C-Peterburg, pp. 385 (1997) (in Russian).
7. B.I. Schlovskii, "Percolation conductivity in strong electric fields", *Soviet Physics - Fiz. Techn. Poluprovodn.*, Vol. 13, No 1, pp.93-97 (1979).
8. A.Y. Vul, S.V. Kidalov, "Influence of nonhomogeneous doping impurities distribution for the photoelectric characteristic of resistivity structures based on solid solution $\text{GaAs}_{1-x}\text{Sb}_x$ ", *Soviet Physics - Fiz. Techn. Poluprovodn.*, Vol. 21, No 5, pp. 804-809 (1987).
9. S. Ašmontas, A. Skučienė, "Electrical properties of compensated n-InP", *Proc. 8th Symp. on Ultrafast Phenomena in Semiconductors*, pp.205-208, (1992).
10. S. Ašmontas, S. Dedulevičius, Ž. Kancleris, L. Subačius, G. Valušis, "Investigation of hot electron relaxation in electric fields in compensated $\text{InSb}\langle\text{Cr}\rangle$ ", *Lithuanian Journ. of Phys.*, Vol. 32, No 3, pp.425-433 (1992).

Impact of laser and X-ray irradiation on C₆₀-films.

S.O. Kognovitskii, N.V. Kamanina *, R.P. Seisyan, M.E. Gaevski,
S.I. Nesterov, M.V. Baidakova, M.R. Rymalis

Ioffe Physico-Technical Institute, RAS, St. Petersburg, Russia

* S.I. Vavilov State Optical Institute, St. Petersburg, Russia

E-mail: kogn@spectr.ioffe.rssi.ru

ABSTRACT

The modification of C₆₀-film structure under laser and X-ray irradiation has been investigated. The wide spectral and dose ranges of irradiation have been applied: from visible light to hard X-ray, and from low to high intensity, when the optical nonlinear effects appear. The structure changes (including the polymerization) manifesting close to nonlinear threshold have been found. They have exhibited the nonreversible effect contribution to the nonlinear parameters of initial C₆₀-films. The dependence of C₆₀-film structure modification on irradiation wavelength has been demonstrated by the photoluminescence and transmission spectral measurements, the solubility controlling, and data of X-ray diffractometry as well. The contribution of X-ray and a secondary electron flow to polymerization of the C₆₀-film has been determined [1]. The information about C₆₀-film modification may be used for optical limiting devices and for the development of UV and X-ray resists.

Keywords: fullerenes, X-ray irradiation, thin films

1. C₆₀-FILMS

Films were deposited on Au-, GaAs-, and Si-substrates (100) by a vacuum evaporate method from high-pure C₆₀-powder. Thickness of the films was varied from 300 to 600 nm. From an electron-spectroscopic analysis, a surface layer of the film (with thickness about 50 nm) became 20 molar percent saturated with oxygen due to an influence of air in several days.

Equilibrium solid state of fullerene at temperature below 260K is the crystal with simple cubic lattice (symmetry "sc") and with a very weak van der Waals linkage between fullerene molecules. Fullerenes and the linkage between them are drastically changed under an impact of electromagnetic or electron beams. The influence of these beams causes the transitions of fullerenes to excited triplet states, in which the molecules enter into chemical reactions between themselves. As a result, polymer complexes from fullerene molecules or polymer clusters, which are products of fullerene deep photochemical destruction, are generated. Carbon based material obtained is characterized by a high chemical and mechanical strength. The polymerization processes are accelerated in atmospheric oxygen.

2. INFLUENCE OF VISIBLE LASER IRRADIATION ON FULLERENE FILMS

Characteristics of the laser irradiation used in this experiments are: wavelength $\lambda_{ex} = 532$ nm, pulsewidth $\tau = 15$ ns, incident energy density $P = 0.075\text{--}2$ J/cm². The optical nonlinearity of the pure fullerene film on the glass substrate was demonstrated. Optical nonlinear threshold was found at energy density of incident light pulse of about 1.6 J/cm² at room temperature $T=300$ K. The optical limiting effect (Fig.1) was found at a higher energy density. Optical breakdown of C₆₀-film was shown at energy density of about 2 J/cm².

The significant content of C₆₀-film was found insoluble in toluene after irradiation with energy density $P \geq 0.2$ J/cm². This fact indicate that the nonreversible effects contribute to the optical limiting. That is confirmed by luminescence measurements of C₆₀-films (fig.2). Changing of luminescence spectra demonstrates the redistribution of the density of different type excitonic X-traps in solid fullerenes (photo-induced or intrinsic, for example, polymer complexes) [2-5].

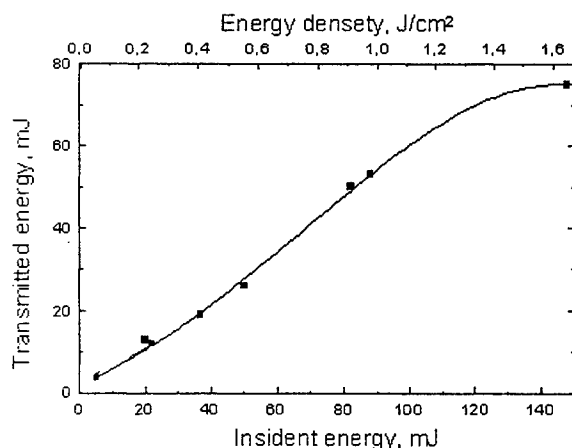


Fig.1. The optical limiting effect of pure fullerene film on glass substrate.

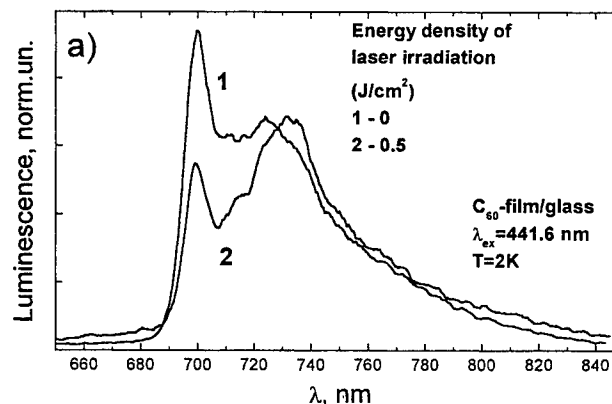


Fig.2. Photoluminescence spectra of initial C_{60} -films on glass substrate (1) and after laser irradiation (2).

It was found that resonances in the transmission spectra remain unchanged. That fact shows that electron transitions of single C_{60} -molecules in irradiating films remain unchanged too.

The effect of the visible laser modification of fullerene film allowed to write the hologram image with spatial frequency $\Lambda = 100 \text{ mm}^{-1}$ on C_{60} -film at incident energy density $P = 0.28 \text{ J/cm}^2$ successfully.

3. INFLUENCE OF POWERFUL ULTRAVIOLET IRRADIATION ON FULLERENE FILMS.

The photo-ablation effect under powerful ultraviolet irradiation is easily realized due to very weak van der Waals linkage between fullerene molecules.

Therefore this effect may be applied to creation of submicron structures from fullerene films and change their geometric parameters. Pointed technological method holds the great promise because it is characterized by relative simplicity and requires no adding chemical or plasma etching.

In the present work, the C_{60} films were irradiated by a powerful pulse ultraviolet KrF-excimer laser with wavelength of 248 nm. The pulsewidth was about 15 ns. The energy density was $W = 0.34 \text{ J/cm}^2$ in the center of unfocused light beam at the single pulse.

As a result, a surface layer of the film (with thickness about 35 nm) was undergone to photo-ablation whereas a deeper layer of the film (with thickness of about 100 nm) suffered a structure modification due to the polymerization and the destruction of fullerenes. The modified film part was characterized by elastically and mechanical robustness. In the case of small film thickness, all film (on depth) was polymerized (see on Fig.3).

On the data derived from ellipsometry (by Dr. T.L. Makarova), the optical density decreased in the film part exposed by an UV laser:

$n' = 1.3$ for polymerized part,

$n = 1.95$ for initial film at wavelength 632.8 nm.

The changes in luminescence and reflection spectra were investigated in visible wavelength range at polymerization by excimer laser light. Both increasing FWHM and decreasing amplitude of both the «red» luminescence line (1.71 eV) and the resonance peculiarity (2.02 eV) in the reflection spectrum were found. This fact is due to a decrease in quantity of non-

destroyed fullerenes and due to an increase in the damping of electron states of the fullerene crystal caused by scattering on polymerized fullerene clusters.

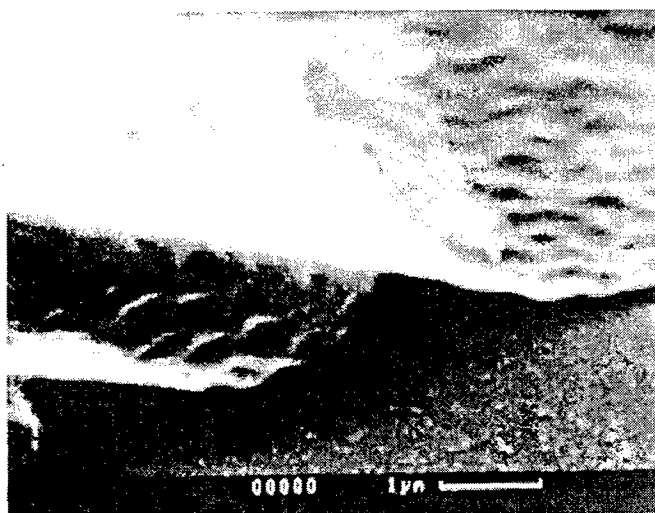


Fig. 3. Electron image of C₆₀-film polymerized by single UV pulse of excimer laser ($W=1.2\text{J}/\text{cm}^2$) into air atmosphere.

4. FABRICATION ONE-DIMENSION SUBMICRON STRUCTURES FROM FULLERENE FILMS BY UV PHOTO-ABLATION.

Essentially inhomogeneous spatial distribution of UV light intensity may induce the inhomogeneous efficiency of photo-ablation along surface fullerene film and lead to creation of geometrical submicron structures from fullerenes films.

The traditional methods of inhomogeneous distribution formation of light intensity, such as photo-sweep and interference of several intersect beams, are applied. Because the coherence length of the excimer laser used was about several millimeters the interference was realized between incidence irradiation and reflecting or scattering on objects located close to film surface.

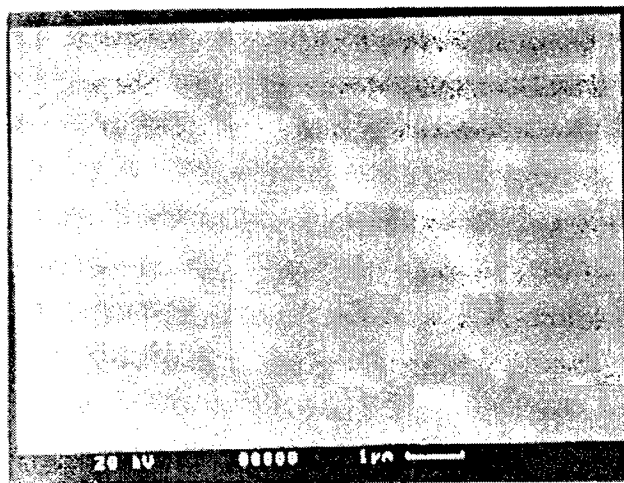


Fig. 4. SEM-image of sinusoidal geometrical grating fabricating on surface of the flat C₆₀-film by an UV pulse of the excimer laser into air atmosphere due photo-ablation.

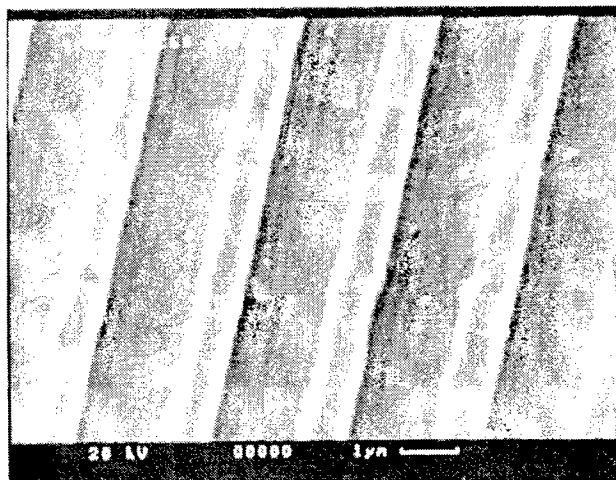


Fig.5. SEM-image of array of carbon-based wires formed on walls of triangular-type big grating as a result of photo-ablation.

The reflection from a miniature aluminum mirror located nearer than 0.5 mm from film surface was used. In this experiment the XeCl excimer laser with wavelength 308 nm, $t(\text{pulse})=10$ ns and $W=0.25$ J/cm² was applied. By this manner the sinusoidal geometrical grating was fabricated (Fig.4.).

To realize interference of incident and scattering UV light the surface triangular-type big grating made on corrugated GaAs substrate was used. The grating had the period of 2.6 μm and the height of 0.5 μm . The GaAs grating was coated by the fullerene film with thickness of 100 nm. The sample was exposed by the XeCl laser with $W=0.23$ J/cm². The inhomogeneous periodical distribution of light intensity appeared close to the grating surface. That led to forming the nanowires with the width of 150 nm from the fullerene film on the grating walls (Fig.5.).

In the present work, a new interesting process of the photo-ablation was confirmed under interference incident and surface electromagnetic wave excited on the fullerene film (with thickness of 100 nm) near deep split by KrF laser. This process resulted in the formation sinusoidal geometrical grating on fullerene film surface with period about 170 nm (Fig.6). Found effect pointed on performing condition for existing surface waves on fullerene film:

$$\text{Re}(\epsilon_{\text{C60-film}}(V_{\text{ex}}, E_{\text{ex}}, T)) < -\text{Re}(\epsilon_{\text{env}}(V_{\text{ex}}, E_{\text{ex}}, T)) .$$

The detected effect of “writing” of surface electromagnetic wave may be used for determination of optical parameters of fullerene films (for example, $\text{Re}(\epsilon_{\text{C60-film}})$ and $\text{Im}(\epsilon_{\text{C60-film}})$).

Hence, the capacity of fullerene crystal easy to reproduce distribution of light intensity near its surface was demonstrated. The method of fabrication of one-dimension surface submicron structures on the fullerene films using the photo-ablation effect in inhomogeneous distributing electromagnetic field was proposed. This effect may be used for optical writing information and holographic recording.

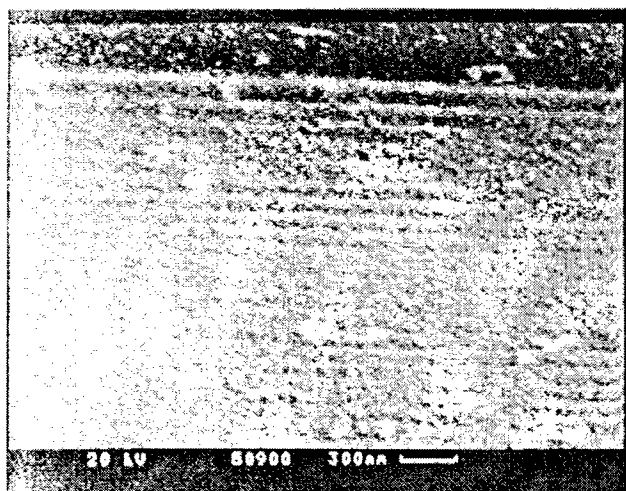


Fig. 6. SEM-image of sinusoidal geometrical grating fabricating on surface of the flat C₆₀-film due photo-ablation under interference of UV incident and surface electromagnetic wave.

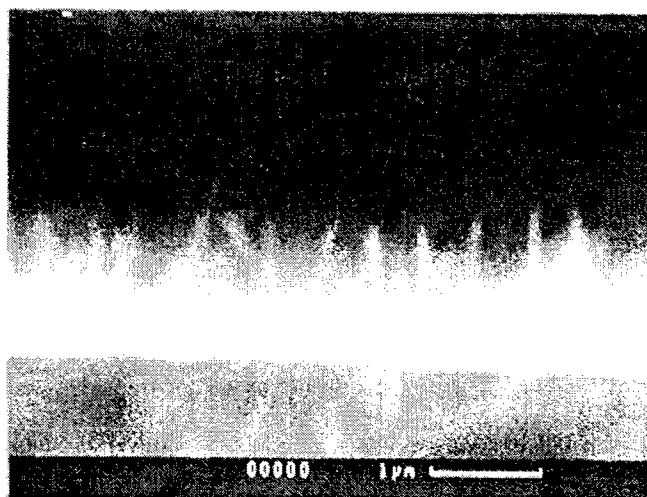


Fig.7. SEM-image of self-organizing vertical standing carbon nanotubes.

The formation of nanotubes at a power UV irradiation of the C₆₀ film was found. The fullerene film with thickness of 500 nm was exposed by 6 pulses of KrF excimer laser with integral energy density about 2 J/cm². Moreover the sample was acted upon by argon plasma at the sparing regime. As a result of the combined influence of laser light and plasma, the vertical standing needle-type nanotubes self-organized (Fig.7). Their height reached 2 μm , diameter was about 70 nm. Probably, these nanotubes are multilayer carbon nanotubes.

5. EXPOSURE THE C₆₀-FILMS BY X-RAY IRRADIATION

The conventional Dmax/RC RIGAKU diffractometer with copper radiation ($\lambda=1.542 \text{ \AA}$) was used for exposure the C₆₀-films by X-ray irradiation. In the experiments the tube voltage of about 50 kV was applied with the current of 150mA. The samples were located close to the output window of the X-ray source.

It was found that irradiation of the C₆₀-film by X-ray induced drastic structural changes. The part of the film became insoluble in the toluene after X-ray irradiation due to formation of the polymer type complexes from C₆₀ molecules or (and) their fragments. Both the thickness of this part and character of structure modifications depended on the irradiation dose. The structural changes influenced the luminescence spectra of the C₆₀-film. The form of luminescence spectra also strongly depended on the X-ray dose (Fig.8). The strong dependence of the spectra on the solid fullerene structure showed that the qualitative different optical centers (like polymer complexes) induced at different X-ray dose played the main role in the forming luminescence. This fact was confirmed by the qualitative invariability of luminescence spectra after treatment of film by solvent (toluene). By this means, the luminescence irradiation of X-ray deposited fullerene film was due to insoluble fullerene based complexes.

Described changes are due to the impact of X-ray and are not connected with influence of secondary electrons bearing by X-ray. That follows from qualitative invariability of luminescence spectra at different substrate medium (Ti and glass) possessing different possibility of secondary electrons bearing. The direct impact by incident beam of electron leads to the qualitative variant luminescence spectra changes (Fig.9) in comparison with the X-ray action.

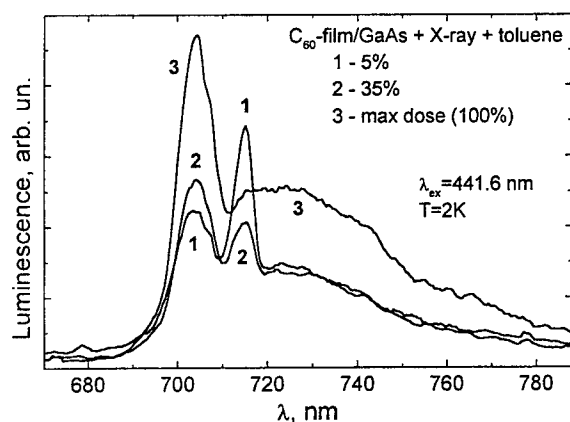


Fig.8. Luminescence spectra of C₆₀-film at different X-ray dose.

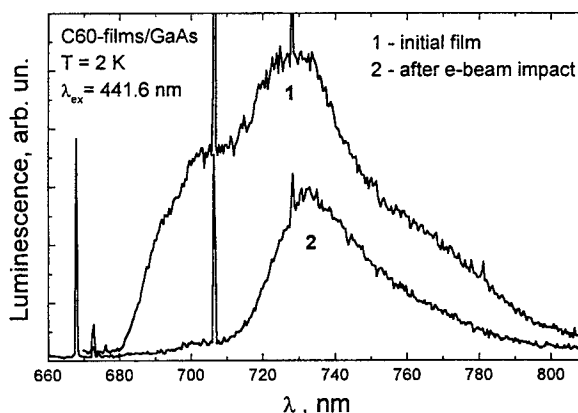


Fig.9. Luminescence spectra of both initial C₆₀-film and after electron beam impact.

6. ACKNOWLEDGMENTS.

The authors are grateful to Prof. S.G. Konnikov, Prof. R.P. Seisyan, and Prof. N.S. Averkiev for useful discussion, Dr. V.M. Busov and Dr. A.V. Naschekin for help at microscopic studies of structures, Dr. I.P. Smirnova for help in the sample fabrication. The work was supported by the Russian Foundation for Basic research (project No. 98-02-18117) and Russian State Scientific-Technical Program («Actual direction of condensed medium physics. Fullerenes and atomic clusters», 1998, project «Beam-2. Photon», N 3-7-98 (99030)).

7. REFERENCES

1. H. Kramer, R. Baumann, J. Bargon, J. Hormes, H. Zumaque-Diaz, G.A. Kohring, "Molecular nanostructures", *Proc. Int. Winterschool on Electronic Properties of Novel Materials*, 1-8 March 1997, Kirchberg, Austria. pp. 537-540, 1997.
2. U.D. Venkateswaran, M.G. Schall, P. Zhou, P.C. Eklund, *Solid State Commun.*, **96**, pp. 951-955, 1995.

3. U.D. Venkateswaran, D. Sanzi, A.M. Rao, P.C. Eklund, L. Marques, J.-L. Hodeau, M. Nunez-Regueiro, *Phys. Rev. B*, **57**, pp. R3193-R3196, 1998.
4. V. Capozzi, M. Santoro, G. Celentano, H. Berger, G.F. Lorusso, *J. of Luminescence*, **76-77**, pp. 395-398, 1998.
5. W. Guss, J. Feldmann, E.O. Gobel, C. Taliani, H. Mohn, W. Muller, P. Haussler, H.-U. ter Meer, *Phys. Rev. Lett.*, **72**, pp. 2644-2647, 1994.

IR laser action on fullerene-doped organic systems

N.V.Kamanina^{a*}, I.V.Bagrov^b, I.M.Belousova^b, A.P.Zhevlakov^b

^a Vavilov State Optical Institute, 12 Birzhevaya Line, St. Petersburg, 199034, Russia

^b Institute for Laser Physics, 14 Birzhevaya Line, St. Petersburg, 199034, Russia

ABSTRACT

An optical limiting of the laser radiation over IR range in organic compounds based on polyimide has been studied. The non-linear transmission at a wavelength of 1315 nm as well as spectral properties of the compounds have been investigated. The results obtained have been explained by the donor-acceptor interaction mechanism that affects nonlinear-optical properties of organic molecules. The fullerene-doped polyimide structures have been determined to be effective optical limiting materials for attenuating a power density of more than $2 \text{ J}\cdot\text{cm}^{-2}$ in the IR range.

Keywords: optical limiting, IR laser irradiation, polyimide, fullerene

1. INTRODUCTION

It is well known, a thermal effect, reverse saturable absorption (RSA), two-photon and free-carrier absorption, nonlinear refraction and laser induced scattering are applied in the fullerene-doped structures to explain the optical limiting (OL) effect in them [1-3]. Specially, the RSA effect has been studied as a basic mechanism that is included in theoretical and experimental OL considerations in the visible spectral range. It is caused by the following fact [4,5]. The OL properties in the visible spectral range are determined by the efficient population of a triplet state with a higher absorption cross-section than that of the ground state. For pulsewidth less than the lifetime of the triplet state, the triplet state will act as an accumulation site. For example, the limiting action of C_{60} solution will be most effective for pulses shorter than the triplet state lifetime of $40 \mu\text{s}$ [5]. In this case, the population of the triplet state T_1 increases as the incident energy increases. RSA, and therefore OL are realized due to the transition from T_n to T_1 . Both kinetics of population and destruction of the excitation levels, which take place in OL, are well described by the six-level system [3,6]. The OL effect in the organic systems over the visible spectral range was revealed in polymethacrylate doped with C_{60} [5,7], in bicyanovinylpyridine- C_{60} compounds [8], in polysilane- C_{60} structures [9]. Enhancement of photoconductivity in the fullerene-doped systems based on polyvinylcarbazole was observed in papers [10,11]. The effect of fullerene doping on the spectral properties of 2-cyclooctylamino-5-nitropyridine was shown in Ref. [12]. The first OL results for these compounds were received in paper [13]. Peculiarities of the OL effect in the visible spectral range in polyimide systems doped with fullerenes C_{60} and C_{70} were investigated in the papers [14,15]. It was shown that the Förster mechanism could be included to explain the OL effect for multicomponent systems consisted of fullerenes and dyes [15] and it was underlined the reinforcement of donor-acceptor interaction in them.

In the present paper the OL effect in the IR spectral range have been studied both in the fullerene-doped polyimide solution and in thin films. The polyimide compounds have been considered as effective systems for eyes and sensors protection over the broad spectral range, including IR.

2. EXPERIMENT

In our experiments, 0.5-1% solutions of photosensitive polyimide 6B (which chemical formula was described in the paper [16]) in chloroform were used. Fullerene C_{60} was applied as sensitizers. Malachite green was used as an additional impurity. The fullerene concentration was varied from 0.5 to 5 wt.%, the dye concentration was 1 wt.%. The $1 \mu\text{m}$ thick fullerene-doped polyimide films were prepared by spin-coating of the 5-6.5% polyimide solution in 1,1,2,2-tetrachloroethane on a glass substrate. The fullerene C_{70} concentration was varied from 0.1 to 0.5 wt.% in this case. Fullerene-doped non-photosensitive polyimide 81A was investigated as a possible matrix with a high laser strength for OL applications.

* E-mail: kamanin@ffm.ioffe.rssi.ru

The experimental setup for the OL investigations in the IR spectral range is presented in the Fig.1. A dependence of the transmission on an input energy was measured with a use of a photodissociation iodine laser with a wavelength of 1315 nm. The laser was pumped by a nonmagnetic coaxial Xe lamp, which an interior quartz tube was filled in by components of a laser mixture: $n\text{-C}_3\text{F}_7\text{I}$ (RI) and SF_6 . Partial pressure of $n\text{-C}_3\text{F}_7\text{I}$ (RI) and SF_6 was 35 and 500 mm of Hg, respectively. The diameter and length of the active zone were 0.8 cm and 50 cm, respectively. The pumping and laser pulsewidth was 8 μs and 50 ns, respectively. A spot on the sample surface was 2 mm. The input energy was measured with a calorimeter. The energy transmitted through a set of filters and the sample was measured with a pyroelectric photometer.

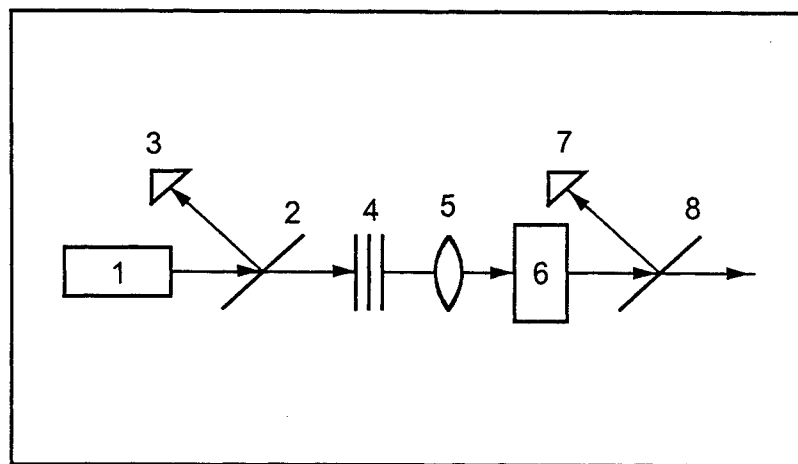


Fig.1. Experimental setup. 1 – photodissociation iodine laser; 2, 8 – beam splitters; 3, 7 – photodetectors; 4 – light filters; 5 – a lens; and 6 – sample.

The low-power transmission for photosensitive polyimide 6B was about 0.85 at wavelength of 1315 nm, while the one for non-photosensitive polyimide 81A was about 0.75. Spectroscopic measurements were carried out with a Perkin-Elmer Lambda 9 instrument in the wavelength range 200-3000 nm.

3. RESULTS AND DISCUSSION

The dependence of the output energy density (W_{out}) on the input energy density (W_{in}) is shown in Fig. 2 for the 1% solutions of photosensitive polyimide 6B in chloroform. Nonlinear transmission was observed for all sensitized samples. In the doped polyimide with 1 wt.% of C_{60} the 2.5-fold attenuation of the incident beam was measured at W_{in} of more than $1.0 \text{ J}\cdot\text{cm}^{-2}$. The polyimide system doped with 5 wt.% of C_{60} showed the near-linear transmission up to W_{in} of $0.65\text{-}0.75 \text{ J}\cdot\text{cm}^{-2}$ and the transmission saturation above W_{in} of $1.1\text{-}1.2 \text{ J}\cdot\text{cm}^{-2}$. The attenuation of the incident beam for this compound was observed at $1.25 \text{ J}\cdot\text{cm}^{-2}$ and exceeded at least by the factor of 3-4. The less OL effect was observed in the 0.5% solutions of polyimide in chloroform with 5 wt.% of C_{60} . No peculiarities were determined in the polyimide-chloroform system with 1 wt.% of C_{60} . For comparison, the large OL effect was found in the polyimide-chloroform solution simultaneously doped with C_{60} and the malachite green dye. In this case the 5.5-6-fold attenuation of the incident beam was observed at W_{in} of $1.5 \text{ J}\cdot\text{cm}^{-2}$. The system kept the essential laser strength up to the input energy density of $2.5 \text{ J}\cdot\text{cm}^{-2}$.

It should be noticed that weak scattering was observed in the doped polyimide-chloroform solutions. This result was determined by the cluster formation causing fluctuations of the solution density. The fluctuations resulted in irregular irradiation absorption along the beam diameter.

The dependence of the output energy density (W_{out}) on the input energy density (W_{in}) is shown in Fig. 3 for the thin C_{70} -doped polyimide 6B films. The OL effect was observed for all fullerene-doped films at W_{in} of more than $0.3\text{-}0.4 \text{ J}\cdot\text{cm}^{-2}$, corresponding to the attenuation of laser energy density by the factor of 1.3-3.0 that depended on the fullerene concentration in the photosensitive polyimide matrix. Therefore, the difference in transmission between samples 1 and 2 was determined by the fullerene concentration. However, the result was caused not only by a higher fullerene concentration, but by a

possible complex formation between a donor fragment of a polyimide molecule and fullerene as well. Really, the drastic attenuation of laser energy density by the factor of 9-12 for the polyimide films with 0.5 wt% of C_{70} at W_{in} of 0.6-0.8 $J \cdot cm^{-2}$ was caused when the new complex was activated.

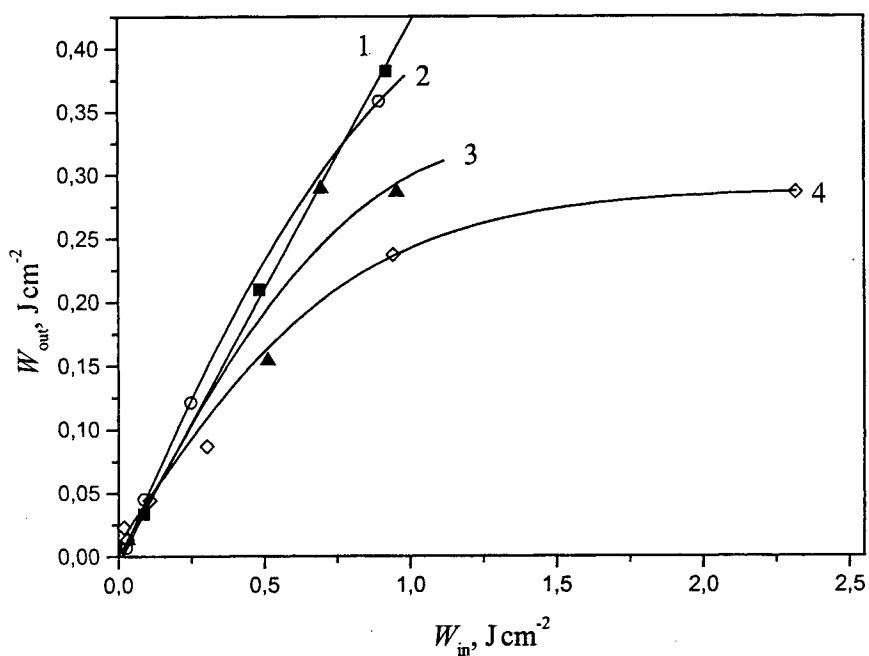


Fig.2. Dependence of W_{out} on W_{in} for the polyimide 6B – chloroform solutions with the C_{60} concentration: 1 – 0 wt.%; 2 – 1 wt.%; 3 – 5 wt.%; and 4 – 1 wt.% of C_{60} and 1 wt.% of malachite green.

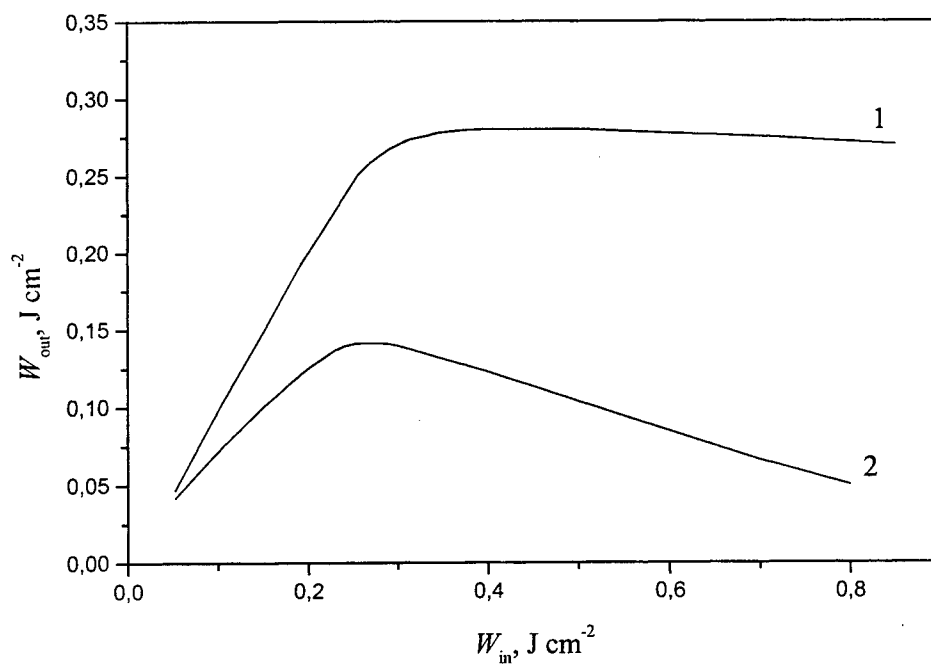


Fig.3. Dependence of W_{out} on W_{in} in films: (1) polyimide 6B with the 0.2 wt.% of fullerene C_{70} and (2) polyimide 6B with 0.5 wt.% of fullerene C_{70} .

The following evidences can be used. Electron affinity of fullerene is ~ 2.65 eV, that is more than the one for acceptor fragments of most organic molecules. It is well known that the monomeric links of polyimides are intramolecular donor-acceptor complexes with the charge transfer between the donor (triphenylamine) and acceptor (diimide) molecular fragments, which can be changed using various dopant molecules. The acceptor diimide fragment is of electron affinity of about 1.12–1.46 eV that is twice less than the one of fullerene. Interest in the investigation on physical-chemical properties of fullerene-doped systems is generated, among other things, by unique ability of fullerenes to influence the initial donor-acceptor interaction. The high electron affinity of fullerene suggests that ones are able to sensitize efficiently the organic molecules creating new complexes with their donor fragments. It should be noticed that the simple model for the intramolecular transfer of an injected electron into C_{60} and C_{70} was proposed from the concept of orbital interaction [17]. In our case the additional condition for the transfer is the arrangement of the molecular planes in parallel, that provides the largest overlapping the electron densities of the molecular orbitals. The C_{60} and C_{70} molecules are spherical or rugby-ball in shape, respectively. On exciting, triphenylamine molecule experiences a conformational transformation, changing from the neutral tetrahedral form to the ionized planar one [18]. This effect along with less dimensions of the triphenylamine molecule (0.5 nm) than those of the fullerene molecule (0.7–0.8 nm) allow the arrangement of their molecular planes to be expected in parallel. From the previous results [14,15,18] one can say that fullerenes provoke the creation of reverse saturable absorption materials based on polyimide with the high absorption cross section. The absorption cross section of donor-acceptor complex of fullerene with donor polyimide 6B fragment (triphenylamine) was recently estimated in the paper [18]. It is really about 300 times more than the one of intramolecular polyimide complexes. Therefore the fullerenes are more effective acceptors for the system studied. Moreover, the carriers become free after the charge transfer to the fullerene molecules, where the surface charge is delocalized [9]. Thus the reinforcement of donor-acceptor interaction in the films investigated because of the free-carrier absorption influence the OL effect in the IR spectral range for fullerene-doped structures.

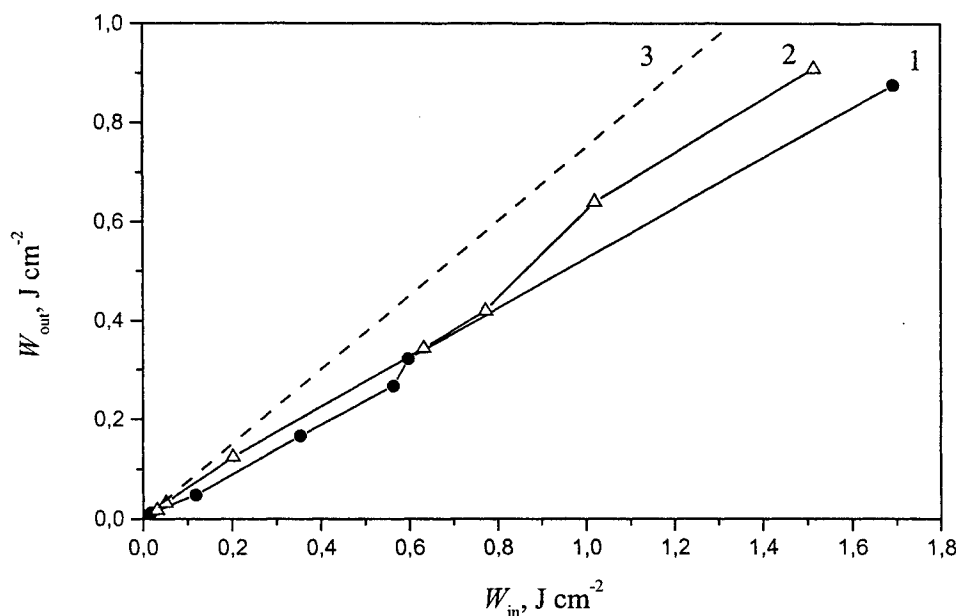


Fig.4. Dependence of W_{out} on W_{in} in films: (1) polyimide 81A with the 1 wt.% of fullerene C_{60} and (2) polyimide 81A with 1 wt.% of fullerene C_{70} . (3) – a low-power transmission for non-photosensitive polyimide 81A.

It should be noticed that the peculiarities of the OL effect in the fullerene-dye-doped polyimide-chloroform solution do not also contradict with the evidence for the complex formation mentioned above. Because the malachite green electron affinity is ~ 1.6 eV [19], it can be possible to create the complex with polyimide donor fragment and to be the effective donor for fullerenes as well. The most optical limiting observed in the polyimide-chloroform solution doped with fullerene and dyes simultaneously (Fig. 2, curve 4) presents this case. Recently, it has been shown that since the absorption spectrum of the fullerene-polyimide system is overlapped with the fluorescence spectrum of malachite green [15] resonance conditions are fulfilled in the polyimide-dye-fullerene structure in the visible spectral range. Overlapping the electron shells of the dye and the fullerene molecules provides the favorable conditions for the charge transfer complex formation as the result of the

free electron exchange between donor (dye) and acceptor (fullerene). It causes the spectral changes in the IR range and explains the OL peculiarities in that. Moreover, the dye introduction makes the process complicated. The OL investigation allows multi-step interaction to be revealed in the multi-component system. The interaction involves, among other processes, the intramolecular complex formation both in polyimide and between dye and triphenylamine as well as the complex formation both between fullerene and triphenylamine and between fullerene (as acceptor) and dye (as donor). In the last case the reverse saturable absorption effect is likely to be additionally described by the Förster mechanism [20]. Therefore, the Förster mechanism should be included in the OL peculiarities in the IR spectral range for photosensitive polyimide systems.

The dependence of W_{out} on W_{in} for fullerene-doped non-photosensitive polyimide 81A at $\lambda=1315$ nm is shown in Fig.4. As seen from this figure, there are no OL peculiarities for the fullerene-doped structure, while the dopant concentration is 2-5 times more than that for the fullerene-doped polyimide 6B (Fig.3, curves 1 and 2). Therefore, the processes observed in the fullerene-doped non-photosensitive polyimide films are not associated with reinforcement of the intramolecular donor-acceptor interaction, which is caused by the fullerene introduction in the photosensitive polyimide 6B. Thus, to reveal nonlinear properties in organic materials, the carrier transfer mechanism is to manifest itself in the molecules sensitized by fullerenes. Therefore the OL effect has not been found for non-photosensitive polyimide 81A in the IR spectral range, because the complex formation does not take place there. However, OL is likely to be observed at more fullerene concentration than that is applied in current experiments or is to be revealed at larger intense laser beams, when IR-active vibrational modes of fullerene are activated [21].

4. CONCLUSION

In conclusion, the optical limiting effect over IR spectral range in both fullerene-doped polyimide 6B solutions and thin films as well as in the multicomponent systems consisted of fullerenes and dyes has been detected. The peculiarities observed have been explained by reverse saturable absorption mechanism and reinforcement of the donor-acceptor interaction. It has been shown that the Förster approach could be applied for the OL explanation in the multicomponent structures. The results obtained have testified that the fullerene-doped polyimide 6B structures could be applied as effective optical limiting materials for attenuating a power density of more than $2 \text{ J}\cdot\text{cm}^{-2}$ in the IR spectral range.

No optical limiting effect has been found in the fullerene-doped non-photosensitive polyimide 81A structures in the IR spectral range for laser beam power densities and fullerene concentration, which were used in the experiments. These results do not contradict with the idea about importance of donor-acceptor interaction mechanism for nonlinear-optical properties existence in the π -conjugated organic compounds.

5. ACKNOWLEDGEMENTS

The authors would like to thank Prof. B.V.Kotov, Dr. V.I. Berendyaev and Dr. N.A.Vasilenko (Karpov Research Physical-Chemical Institute, Moscow, Russia) for their help in the work. This work was supported by Russian National Program "Optoelectronic and Laser Technologies" and International Grant ISTC Project 145 "Optical barrier".

6. REFERENCES

1. L.W. Tutt, T.F. Boggess "A review of optical limiting mechanisms and devices using organics, fullerenes, semiconductors and other materials," *Prog. Quant. Electron.* **17**, pp. 299-338, 1993.
2. L.W. Tutt and A. Kost, "Optical limiting performance of C_{60} and C_{70} solutions," *Nature* **356**, pp. 225-226, 1992.
3. S. Couris, E. Koudoumas, A.A. Ruth, and S. Leach, "Concentration and wavelength dependence of the effective third-order susceptibility and optical limiting of C_{60} in toluene solution," *J. Phys. B: At. Mol. Opt. Phys.* **28**, pp. 4537-4554, 1995.
4. A.V. Eletsii and B.M. Smirnov, "Fullerenes and structures of carbon," *Usp. Fiz. Nauk* **165**, pp. 977-1009, 1995 [in Russian].
5. V.P. Belousov, I.M. Belousova, V.P. Budtov, V.V. Danilov, O.B. Danilov, A.G. Kalintsev, and A.A. Mak, "Fullerenes: Structural, physical-chemical, and nonlinear optical properties," *J. Opt. Technol.* **64**, pp. 1081-1109, 1997.

6. H. Hoshi, N. Nakamura, Y. Maruyama, T. Nakagawa, S. Suzuki, H. Shiromaru, and Y. Achiba, "Optical second- and third-harmonic generations in C_{60} film," *Jap. J. Appl. Phys., Part 2* **30**, pp. L1397-L1398, 1991.
7. A. Kost, L. Tutt, M.B. Klein, T.K. Dougherty, and W.E. Elias, "Optical limiting with C_{60} in polymethyl methacrylate," *Opt. Lett.* **18**, pp. 334-336, 1993.
8. M. Ouyang, K.Z. Wang, H.X. Zhang, Z.Q. Xue, C.H. Huang, D. Qiang, "Study of a novel C_{60} -2,6-bis(2,2-bicyanovinyl)pyridine complex thin film", *Appl. Phys. Lett.* **68**, pp. 2441-2443, 1996.
9. K. Hosoda, K. Tada, M. Ishikawa, and K. Yoshino, "Effect of C_{60} doping on electrical and optical properties of poly [(disilanylene) oligophenylenes]," *Jpn. J. Appl. Phys., Part 2* **36**, pp. L372-L375, 1997.
10. Y. Wang, N. Herron, J. Casper. "Bucky ball and quantum dot doped polymers: a new class of optoelectronic materials," *Mater. Sci. Eng. B* **19**, pp. 61-66, 1993.
11. A. Itaya, I. Sizzuki, Y. Tsuboi, and H. Miyasaka. "Photoinduced electron transfer processes of C_{60} -doped poly(N-vinylcarbazole) films as revealed by picosecond laser photolysis," *J. Phys. Chem. B* **101**, pp. 5118-5123, 1997.
12. N. Kamanina, A. Barrientos, A. Leyderman, Y. Cui, V. Vikhnin and M. Vlasse, "Effect of fullerene doping on the absorption edge shift in COANP," *Molecular Mater.* **13**, pp. 275-280, 2000.
13. N. V. Kamanina, L. N. Kaporskii, Alex Leyderman, and Alfonso Barrientos, "The effect of optical attenuation of laser radiation in a fullerene-containing COANP-polyimide system," *Tech. Phys. Lett.* **26**, pp. 279-281, 2000.
14. N.V. Kamanina, L.N. Kaporskii, and B.V. Kotov, "Absorption spectra and optical limiting of the fullerene-polyimide system," *Opt. Commun.* **152**, pp. 280-282, 1998.
15. N.V. Kamanina, "Reverse saturable absorption in fullerene-containing polyimides. Applicability of the Förster model," *Opt. Commun.* **162**, pp. 228-232, 1999.
16. P. I. Dubenskov, T. S. Zhuravleva, A. V. Vannikov, N. A. Vasilenko, E. V. Lamskaya, V. I. Berendyaev, "Photoconductive properties of some soluble aromatic polyimides," *Vysokomol. Soedin. A*, **30**, pp. 1211-1217, 1988 [in Russian].
17. M. Okada, K. Okahara, K. Tanaka, T. Yamabe, "A remark on intramolecular transfer of an injected electron in C_{60} and C_{70} ," *Fullerene Science and Technology* **4**, pp. 167-176, 1996.
18. Y. A. Cherkasov, N. V. Kamanina, E. L. Alexandrova, V. I. Berendyaev, N. A. Vasilenko, and B. V. Kotov, "Polyimides: New properties of xerographic, thermoplastic, and liquid-crystal structures," *Proceed. of SPIE* **3471**, pp. 254-260, 1998.
19. F. Gutman and L. E. Lyons, *Organic Semiconductors*, J. Wiley & Sons, New York, 1967.
20. T. Förster, "Transfer mechanisms of electronic excitation," *Disc. Farad. Soc.*, **27**, pp. 7-17, 1959.
21. K. Lee, R.A.J. Janssen, N.S. Sariciftci, and A.J. Heeger, "Direct evidence of photoinduced electron transfer in conducting-polymer- C_{60} composites by infrared photoexcitation spectroscopy," *Phys. Rev. B*, **49**, pp. 5781-5784, 1994.

Nonlinear optical properties of *N*-(4-nitrophenyl)-(L)-prolinol doped with fullerenes: Mechanisms of optical limiting

Natalie V. Kamanina*

S.I. Vavilov State Optical Institute, 12 Birzhevaya Line, St. Petersburg 199034, Russia

ABSTRACT

The non-linear transmission of the laser radiation (532 nm and 337 nm) in the fullerene-containing *N*-(4-nitrophenyl)-(L)-prolinol (NPP) films has been investigated. Optical limiting of the laser radiation has been observed in the UV and visible spectral regions. The results obtained have been explained by reverse saturable absorption, two-photon and carrier-free absorption, and charge transfer complex formation.

Keywords: nonlinear optical properties, *N*-(4-nitrophenyl)-(L)-prolinol, fullerenes, optical limiting

1. INTRODUCTION

An influence of fullerenes on properties of various materials is being studied intensively.^{1,2} New materials are involved in the investigations,³⁻⁷ which generate both general and practical interest. The capability of fullerenes to modify optical properties of materials occupies a prominent place in the investigations,⁶⁻⁹ because it holds the greatest promise for device applications,^{2,5,9} in particular, for protection of eyes and devices against laser radiation.³ A search for materials, which limits the laser radiation to good advantage, has shown good potentialities of π -conjugated organic systems.¹⁰ A fullerene introduction in the systems has allowed effective optical limiters to be developed.^{3,11,12}

N-(4-nitrophenyl)-(L)-prolinol (NPP) falls in the π -conjugated organic systems. NPP is of high nonlinear optical characteristics, which are comparable to those for KDP and LiNiO₃.¹³⁻¹⁵ Moreover, it is transparent in the wavelength range 480–2000 nm,¹³ and its dielectric properties change with temperature.¹⁵

In the present paper the effect of C₆₀ and C₇₀ doping on an absorption spectrum and transmission of NPP has been investigated. Mechanisms explained optical limiting effect have been discussed.

2. EXPERIMENT

2–3 μ m thick films of 3 percent fullerene-containing NPP solution in tetrachloroethane were investigated. Non-photosensitive polyimide 81A was used as a film-forming base. The fullerene (C₆₀ or C₇₀) concentration in dry NPP was 1 wt.%. The relationship between the NPP solution and the film-forming base was 2:1. The films were formed on glass substrates.

Absorption spectra of pure and fullerene-doped NPP and polyimide 81A were investigated by means of Perkin-Elmer Lambda 9 spectrometer in the wavelength range 200–3000 nm.

Transmission of laser radiation was investigated using the second harmonic ($\lambda = 532$ nm) of a pulsed Nd-YAG laser (a pulsewidth of 15 ns, a laser spot of 3–3.5 mm) and a quasi-continuous nitrogen-laser ($\lambda = 337$ nm, a repetition frequency of 1 kHz, a pulsewidth of 10 ns, a laser spot of 3.5 mm) in visible and UV ranges, respectively. The dependence of an output energy (E_{out}) on an input energy (E_{in}) was measured. E_{in} was varied using a set of light filters.

* E-mail: kamanin@ffm.ioffe.rssi.ru

3. RESULTS AND DISCUSSION

The fullerene introduction into NPP causes absorption changes of the NPP film in both UV and IR regions, while no dramatic changes are observed in the wavelength range 500-2500 nm. The absorption spectra are shown in Fig.1a and 1b for the UV and IR regions, respectively. The absorption shift in the UV region is indicative of electron structure changes. The fullerene introduction is likely to arrange macromolecules, resulting the shift because of a decrease in a scattering angle.¹⁶

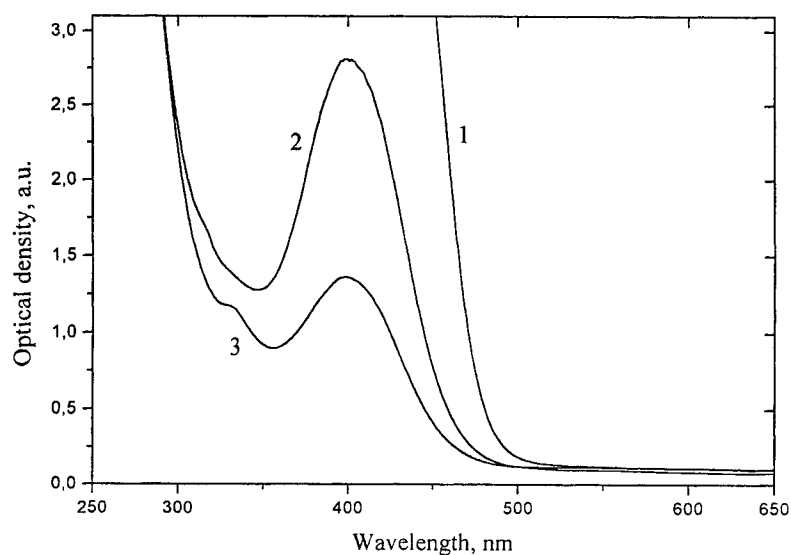


Fig. 1a. UV absorption spectra of a pure NPP film (1), NPP with 1 wt.% C₇₀ (2), and NPP with 1 wt.% C₆₀ (3).

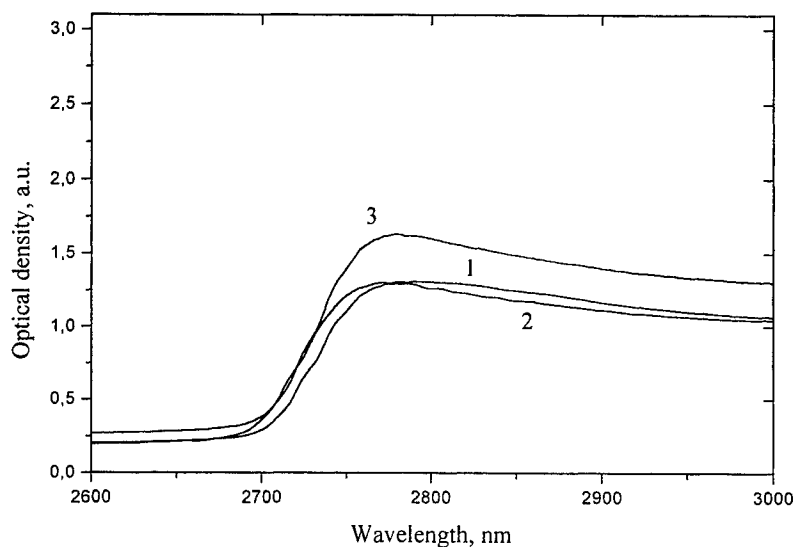


Fig. 1b. IR absorption spectra of a pure NPP film (1), NPP with 1 wt.% C₇₀ (2), and NPP with 1 wt.% C₆₀ (3).

The IR spectral changes are possible caused by a donor-acceptor complex formation between an NPP donor fragment and fullerene, because of more electron affinity of fullerene. An NPP acceptor fragment is a NO₂ group, which is bound to the donor fragment through the benzene ring. For a separate NO₂ molecule or radical, electron affinity is 2.3 eV, while the NO₂ group bound to the benzene ring has electron affinity of only 0.54 eV,¹⁷ i.e. it is smaller than the one of fullerene (2.65 eV).

Moreover, electrons are delocalized at the fullerenes clusters⁷, therefore photoconductivity could increase drastically. Really, dark and photoconductivities of fullerene-doped NPP structures at bias voltage of 65-70 V were one order of magnitude more than those for the fullerene-free systems. The spectral and photoconductive peculiarities observed have provoked interest in the transmission investigations of the NPP films.

The dependence of the output energy (E_{out}) on the input energy (E_{in}) under the 532 nm laser radiation is shown in Fig. 2. The absorption is observed to increase for the C_{60} -NPP film as E_{in} increases due to reverse saturable absorption effect. This effect is determined by a population increase of fullerene excited states. Because the laser pulsewidth (τ_p) of 15 ns is longer than a time of singlet-triplet interaction (1.2 ns),¹⁸ the triplet state accumulates the excited states.

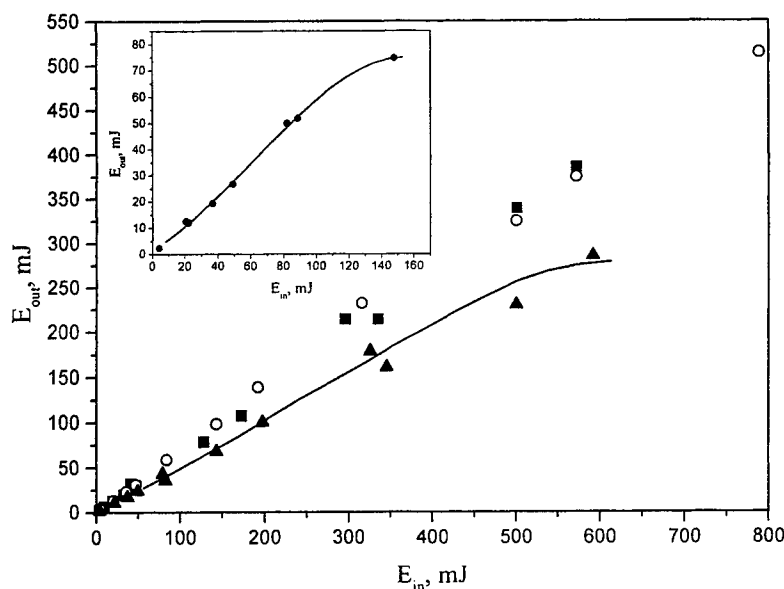


Fig. 2. The dependence of the output energy (E_{out}) on the input energy (E_{in}) at $\lambda=532$ nm for films of pure NPP (■), NPP with 1 wt.% C_{70} (○), and NPP with 1 wt.% C_{60} (▲); in the inset, E_{out} vs E_{in} for a pure C_{60} film.

It should be noticed that the optical limiting levels of the C_{60} -NPP and pure C_{60} films are close together. However, the C_{60} -NPP film is of more laser strength. It should be mentioned that the little increase in absorption at $\lambda=532$ nm is caused by two photon absorption mechanism because resonance line of fullerene C_{60} is 565 nm, that is close to laser irradiation wavelength, 532 nm.

The dependence of E_{out} on E_{in} under the 337 nm laser radiation is shown in Fig. 3. The drastic attenuation of the laser radiation is observed. The absorption saturation begins at E_{in} of 65-70 mW followed by a clarification. The clarification is likely to be caused by both ablation of the films and laser-induced changes in photorefraction. It should be noticed that this effect is not observed in the pure NPP films.

The C_{60} and C_{70} introduction into NPP allowed, for the first time, transmission of NPP to be controlled in UV and blue regions. Therefore, fullerenes are a promising sensitizer for NPP in these spectral regions.

4. CONCLUSION

The non-linear transmission of the laser radiation (532 nm and 337 nm) has been investigated in the fullerene-containing *N*-(4-nitrophenyl)-(*L*)-prolinol films. The processes observed in the NPP films are associated with reverse saturable absorption, two-photon absorption, free-carrier absorption, and charge transfer complex formation. The last mechanism can reinforce or reconstruct the intramolecular donor-acceptor interaction that is caused by the fullerene introduction. Therefore, the carrier transfer in the fullerene-containing materials is possible not only between the intramolecular fragments, but between donor fragment of photosensitive molecules and fullerenes as well.

The investigations have shown that the films hold much promise for their optical device applications. The non-linear optical properties of the NPP films doped with C_{60} or C_{70} stimulate research on recording of phase and amplitude holograms in them.

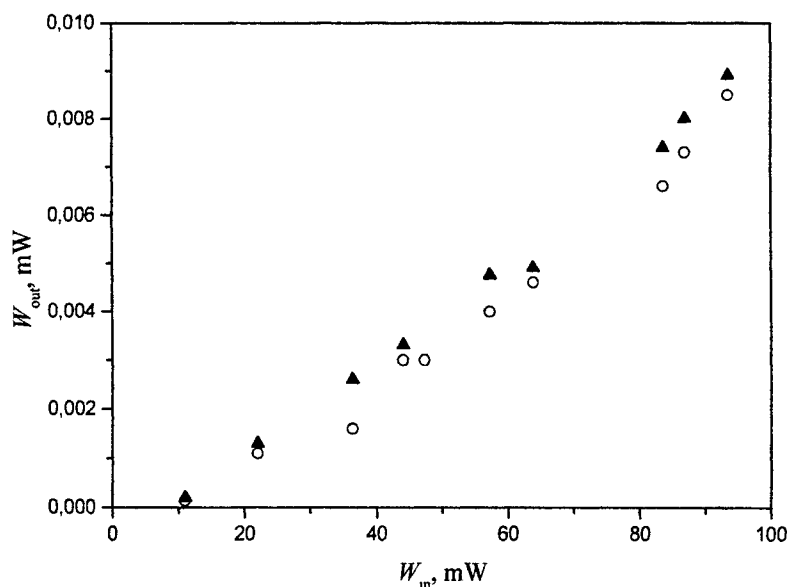


Fig. 3. The dependence of the output power (W_{out}) on the input power (W_{in}) at $\lambda=337$ nm for films of NPP with 1 wt.% C_{70} (○) and NPP with 1 wt.% C_{60} (▲).

5. ACKNOWLEDGEMENTS

The author wishes to thank Prof. B.V. Kotov, Dr. N.A. Vasilenko (Karpov Research Physical-Chemical Institute, Moscow, Russia), Dr. S.O. Kognovitsky (Ioffe Physico-Technical Institute, St. Petersburg, Russia), Dr. A. Leyderman and Dr. A. Barrientos (University of Puerto-Rico, Mayagüez, PR, USA), Dr. L.N. Kaporskii (Vavilov State Optical Institute, St. Petersburg, Russia) for their help in this study. This work was partially supported by the Russian National Program "Optoelectronic and Laser Technologies".

6. REFERENCES

1. S.M. Silence, C.A. Walsh, J.C. Scott, and W.E. Moerner, " C_{60} sensitization of a photorefractive polymer," *Appl. Phys. Lett.* **61**, pp. 2967-2969, 1992.
2. Y. Wang, N. Herron, and J. Casper, "Bucky ball and quantum dot doped polymers: A new class of optoelectronic materials," *Mater. Sci. Eng.* **B19**, pp. 61-66, 1993.
3. A. Kost, L. Tutt, M.B. Klein, T.K. Dougherty, and W.E. Elias, "Optical limiting with C_{60} in polymethyl methacrylate," *Opt. Lett.* **18**, pp. 334-336, 1993.
4. K. Lee, R.A.J. Janssen, N.S. Sariciftci, and A.J. Heeger, "Direct evidence of photoinduced electron transfer in conducting-polymer- C_{60} composites by infrared photoexcitation spectroscopy," *Phys. Rev.* **B49**, pp. 5781-5784, 1994.
5. M. Ouyang, K.Z. Wang, H.X. Zhang, and Z.Q. Xue, "Study of a novel C_{60} -2,6-bis(2,2-bicyanovinyl)pyridine complex thin film," *Appl. Phys. Lett.* **68**, pp. 2441-2443, 1996.
6. K. Lee, E.K. Miller, N.S. Sariciftci, J.C. Hummelen, F. Wudl, and A.J. Heeger, "Photoinduced absorption and photoinduced reflectance in conducting polymer/methanofullerene films: Nonlinear-optical changes in the complex index of refraction," *Phys. Rev.* **B54**, pp. 10525-10529, 1996.
7. K. Hosoda, R. Tada, M. Ishikawa and K. Yoshino, "Effect of C_{60} doping on electrical and optical properties of poly[(disilanylene)oligophenylenes]," *Jpn. J. Appl. Phys. Part 2* **36**, pp. L372-L375, 1997.

8. Z. Lu, S.H. Goh, S.Y. Lee, X. Sun, and W. Ji, "Synthesis, characterization and nonlinear optical properties of copolymers of benzylaminofullerene with methyl methacrylate or ethyl methacrylate," *Polymer* **40**, pp. 2863-2867, 1999.
9. N.V. Kamanina, N.M. Kozhevnikov, and N.A. Vasilenko, "Comparative investigations on dynamic characteristics of optically addressed liquid crystal spatial light modulators with photosensitive layers based on polyimide doped with dyes and fullerenes," *Proceed. SPIE* **3633**, pp. 122-128, 1999.
10. M. Albota, D. Beljonne, J.-L. Brédas, J. E. Ehrlich, J.-Y. Fu, A.A. Heikal, S. Hess, T. Kogej, M.D. Levin, S.R. Marder, D. McCord-Maughon, J.W. Perry, H. Röckel, M. Rumi, G. Subramaniam, W.W. Webb, X.-L. Wu, and C. Xu, "Design of Organic Molecules with Large Two-Photon Absorption Cross Sections," *Science* **281**, pp. 1653-1656, 1998.
11. N.V. Kamanina, L.N. Kaporskii, and B.V. Kotov, "Absorption spectra and optical limiting of the fullerene-polyimide system," *Opt. Commun.* **152**, pp. 280-282, 1998.
12. N.V. Kamanina, "Reverse saturable absorption in fullerene-containing polyimides. Applicability of the Förster model," *Opt. Commun.* **162**, pp. 228-232, 1999.
13. J. Zyss, J.F. Nicoud, and M. Coquillay, "Chirality and hydrogen bonding in molecular crystals for phase-matched second-harmonic generation: N-(4-nitrophenyl)-(L)-prolinol (NPP)," *J. Chem. Phys.* **81**, pp. 4160-4167, 1984.
14. G. Lahajnar, I. Zupančič, R. Blinc, A. Zidanšek, R. Kind, and M. Ehrensperger, "NMR self-diffusion study of organic glasses: COANP, MBANP, PNP, NPP," *Z. Phys.* **B95**, pp. 243-247, 1994.
15. Y. Cui, J. Wu, N. Kamanina, A. Pasaje, A. Leyderman, A. Barrientos, M. Vlasse and B.G. Penn, "Dielectric study of dynamics of organic glasses," *J. Phys. D: Appl. Phys.* **32**, pp. 3215-3221, 1999.
16. J.T. Foley and E. Wolf, "Frequency shift of spectral lines generated by scattering from space-time fluctuations," *Phys. Rev. A* **40**, pp. 588-598, 1989.
17. L.V. Gurvich, G.V. Karachevtsev, V.N. Kondrat'ev, Yu.A. Lebedev, V.A. Medvedev, V.K. Potapov, and Yu.S. Khodeev, *Energies of Chemical Bond Breaking, Ionization Potentials And Electron Affinity*, Nauka, Moscow, 1974 [in Russian].
18. V.P. Belousov, I.M. Belousova, V.P. Budtov, V.V. Danilov, O.B. Danilov, A.G. Kalintsev, and A.A. Mak, "Fullerenes: Structural, physical-chemical, and nonlinear optical properties," *J. Opt. Technol.* **64**, pp. 1081-1109, 1997.

Laser-Induced Homogenization of the Light-Diffusing Media

Vladimir L. Komolov, Sergey G. Przhibel'skii, Valentin N. Smirnov
Vavilov State Optical Institute, 12 Birzhevaya Line, St. Petersburg, 199034, Russia
Phone, fax: +7 (812) 108 5737; e-mail: komolov@mail.ru

ABSTRACT

We discuss different manifestations of the laser-induced homogenization (LIH) in the light-diffusing media - an abrupt decrease of the light diffusion in condensed media under the intensive light action. The key mechanisms of the LIH are discussed including the avalanche-like ones. We present the results of the simplest model, describing the LIH arising upon melting of a solid, when the abrupt drop of the light scattering occurs due to homogenization of optical properties of the medium.

Keywords: laser-matter interaction, light diffusion, feedback, extinction coefficient, scattering, melting

1. INTRODUCTION

The problem of propagation of radiation in media with the strong scattering remains one of the basic problems in optics. It is far from a final stage both in theory and in experiment in spite of long-term investigations. The specific feature of light beam propagation in the light-diffusing medium is the essential changes of its geometry due to the multiple scattering of the light. The significant distortion of both angular and temporal radiation parameters restricts strongly the possibility of light action on the objects inside such media¹. At the same time the necessity of such action arises in a lot of applications. We can say for example about interaction of light with tissues, polymers, amorphous and polycrystalline materials etc.

The theory of light beam propagation in light-diffusing media had been developed rather completely within the frameworks of parabolic approximation of transfer equations^{2,3}. But for proper description of the nonlinear propagation one has to take into account the dependencies of medium parameters on the local intensity of radiation that makes the complete description of light propagation very difficult. In the present paper we tested several effects of light - medium interaction based on the simple models that don't require the cumbersome calculations of radiation field distributions.

In the present paper we predict the possibility of the essential changes of light scattering in condensed media when the light intensity exceeds some characteristic values. The experimental confirmation of predicted effects can essentially improve our knowledge of the light-diffusing media behavior in intense light fields and may be useful for some practical applications.

Our consideration is valid for the medium with the known law of extinction dependence on the light intensity. We assume that the light-diffusion is due to the local inhomogeneity of the medium and the extinction decrease is caused by the medium homogenization. Therefore the effects under consideration are called the Laser-Induced Homogenization (LIH).

In the present paper we restrict ourselves by analyzing the simplest but not the only process results to LIH - the melting of the optically inhomogeneous light-diffusing solid material. There is a wide set of such solids that become "transparent" in liquid phase for example paraffins, fats, etc. Among of the inorganic substances that demonstrates LIH-effect one can see the polycrystalline and powder material where the light-diffusing and often the absorption too are due to the processes at the grain boundaries^{4,5}. In the latest case the medium transition to the liquid phase is accompanied by the strong reduction both the scattering and the absorption of the material.

2. STATEMENT OF PROBLEM

For the correct description of the light propagation on the light-diffusing media one have to take into account the feedback between radiation and medium parameters. In the present paper a simple method for description of some processes in light-diffusing medium is offered and realized. This method is valid for the media with isotropic scattering with small values of main free path of the photon. This method permit to describe the light beam propagation as diffusion process determined by the extinction coefficient of the medium.

Let the monochromatic light beam to propagate along X-axis in the semi-infinite medium with extinction coefficient β and absorption coefficient α . Let us assume that this light cause the media heating and when the temperature achieves the melting point, T_M , the scattering coefficient α_s falls to zero value.

The light intensity $I(x)$ below melting point ($T < T_M$) attenuates according to Bouguer law

$$I(x) = I_0 \cdot \exp(-\beta \cdot x) \quad (1)$$

Above the melting point ($T > T_M$) the scattering vanishes and light can penetrate to the greater depth:

$$I(x) = I_0 \cdot \exp(-\alpha \cdot x) \quad (2)$$

Thus the boundary of the area where the scattering is absent, $X = X_M$, moves following the movement of melting isotherm: $X_M = X(T_M)$. The scheme of space dependencies of extinction coefficient β , temperature T and light intensity I for the two time moments ($t_2 > t_1$) is shown at the Figure 1.

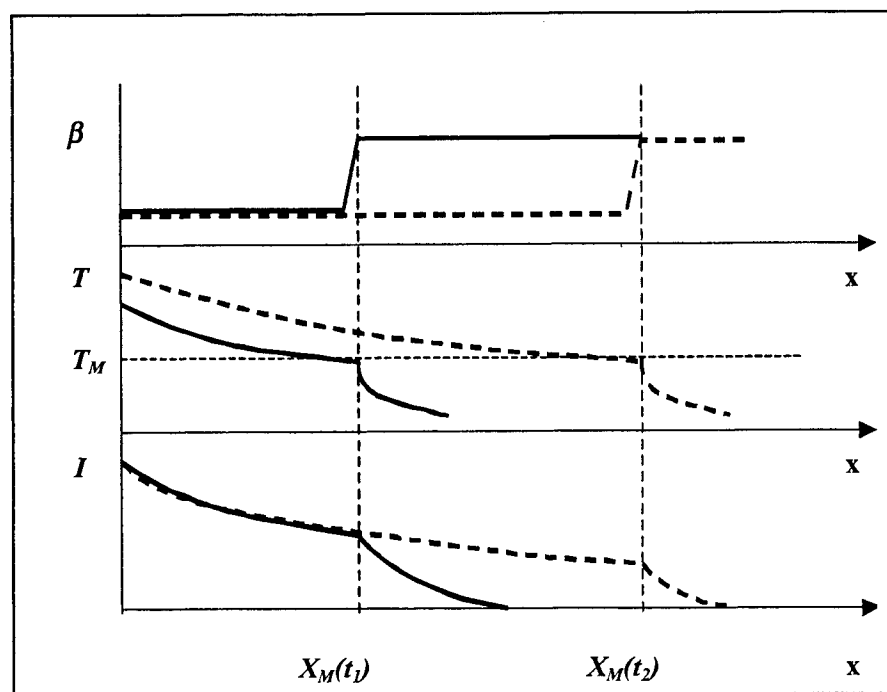


Figure 1. The coordinate dependencies of extinction, temperature and light intensity for two different time moments.

In this approach the light propagation description bases on the solution of the heat equations for the medium that change it aggregate state. In general this equations have the following form:

$$\begin{cases} \frac{\partial T_1}{\partial t} = a \cdot \frac{\partial^2 T_1}{\partial x^2} + \frac{\alpha \cdot I_0 \cdot \exp(-\alpha \cdot x)}{\rho \cdot c} & T_1 > T_M \\ \frac{\partial T_2}{\partial t} = a \cdot \frac{\partial^2 T_2}{\partial x^2} + \frac{\alpha \cdot I(X_M) \cdot \exp(-\beta \cdot x)}{\rho \cdot c} & T_2 < T_M \end{cases} \quad (3)$$

for the melt (area 1) and solid (area 2) phases accordingly. $T_1(t=0) = T_2(t=0) = T_0$. At the boundary $X = X_M(t)$ we have the following conditions:

$$\begin{cases} T_1 = T_2 = T_M \end{cases} \quad (4a)$$

$$\begin{cases} k \left(\frac{\partial T_2}{\partial x} - \frac{\partial T_1}{\partial x} \right) = L \rho \cdot \frac{dX_M}{dt}, \text{ where } L - \text{heat of melting} \end{cases} \quad (4b)$$

Unfortunately the nonlinear equations (3),(4) can not be solved analytically for the general case and the numerical computation results are not demonstrative enough. That is why we shall construct some physically clear but the approximate estimations to illustrate the main features of LIH.

3. STEADY-STATE SOLUTIONS

To construct some base for further conclusions we'll choose the special set of the boundary conditions which allows the steady-state solution for Eq.3. It is easy to see that steady-state regimes can be realized when one fixes the temperature at the external boundary of the medium: $T(x=0) = T_0$

Under such boundary conditions the melting zone arises *inside* of solid and in general case there are the three areas with different optical parameters exists in the medium. At the low intensity levels when the melting can not occurs the steady-state temperature field defined by the equation:

$$\frac{d^2 T}{dx^2} = -Q \cdot \exp(-\beta \cdot x); \quad T|_{x=0} = T_0; \quad T|_{x \rightarrow \infty} < \infty, \quad Q \equiv \frac{\alpha \cdot I_0}{k} \quad (5)$$

is given by the following simple expression:

$$T(x) = T_0 + \frac{Q}{\beta^2} [1 - \exp(-\beta \cdot x)] \quad (6)$$

With the intensity growth the melting zone arises inside the material and its optical properties differs essentially from that in the solid phase. However under the above mentioned boundary conditions the steady-state temperature profile still exists and is given by the following equations:

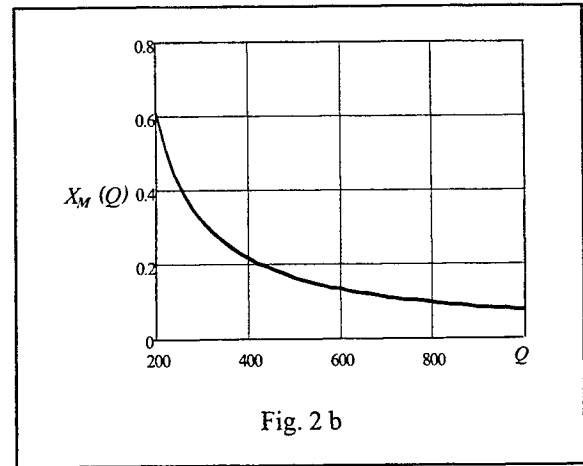
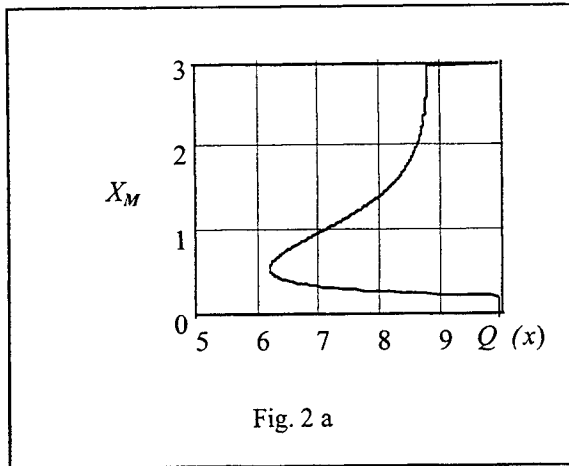
$$\begin{cases} \frac{d^2 T_1}{dx^2} = -Q \cdot \exp(-\beta \cdot x) & ; \\ \frac{d^2 T_2}{dx^2} = -Q \cdot \exp(-\beta \cdot X_M) \cdot \exp[-\alpha(x - X_M)] \end{cases} \quad (7)$$

$$T|_{x=0} = T_0; \quad T|_{x \rightarrow \infty} < \infty, \quad \text{at } x = X_M: \quad T_1 = T_2; \quad \frac{dT_1}{dx} = \frac{dT_2}{dx}$$

The solution of Eq.7 permits to create the expression that defines the stationary position of the front edge of melting zone X_M in dependence on light flow intensity I_0 :

$$\frac{T_M - T_0}{Q} = \frac{1}{\beta^2} [1 - \exp(-\beta \cdot X_M)] + X_M \left(\frac{1}{\alpha} - \frac{1}{\beta} \right) \exp(-\beta \cdot X_M) \quad (8)$$

It should be noted that in the certain range of intensities I (or Q that is the same) the Eq.8 permits the existence of **two** solutions (see Fig.2a). One of this solutions is unstable and it disappears with the light flow growth. We shall discuss the physical nature of this solutions below. The typical dependence of the **stable** steady position X_M on the light intensity is shown at the Fig.2b.



4. DYNAMICS OF LIH DEVELOPMENT

To analyze the occurrence and temporary development of LIH processes we shall use the solution of the simplest "basic" non-stationary problem - the heating of the medium without melting with zero initial and boundary conditions:

$$\frac{1}{a} \frac{\partial T}{\partial t} = \frac{\partial^2 T}{\partial x^2} + Q \cdot \exp(-\beta x); \quad T|_{t=0} = 0; \quad T|_{x=0} = 0; \quad T|_{x \rightarrow \infty} < \infty \quad (9)$$

The solution of Eq.9 using standard procedure gives the following expression for the temperature:

$$T(x, t) = \frac{Q}{\beta^2} \left\{ e^{-\beta \cdot x} \left(e^{a \cdot \beta^2 t} - 1 \right) + \Phi^* \left(\frac{x}{2\sqrt{at}} \right) - \frac{1}{2} e^{a \beta^2 t} \left[e^{-\beta \cdot x} \Phi^* \left(\frac{x}{2\sqrt{at}} - \beta \sqrt{at} \right) + e^{\beta \cdot x} \Phi^* \left(\frac{x}{2\sqrt{at}} + \beta \sqrt{at} \right) \right] \right\} \quad (10)$$

where $\Phi^*(x) = \frac{2}{\sqrt{\pi}} \int_x^\infty e^{-\xi^2} d\xi$.

The typical temperature profiles (normalized to the temperature value in maximum) for two time moments are presented at the Fig. 3. The characteristic feature of this profiles is the very slow movement of the temperature maximum from the surface due to the small penetration depth of the radiation inside the light-diffusing medium. Just this smooth maximum is responsible for the unstable stationary solution occurrence. The things is that the melt arising near T_M causes the scattering reduction of the medium near X_M . It results to the small growth of the light flow and thus to slight temperature increase nearby X_M . It results in heat flow occurrence directed towards the surface that acts on the medium already heated almost up to the melting point. In this case even slightly changes of optical parameters in melting phase results in

the strong feedback between the speed of isotherm $T = T_M$ movement towards the surface and the local light intensity in corresponding cross-section ($x = X_0$). Arising instability of temperature distribution leads to the jump-like movement of the melting front towards surface up to its stable position.

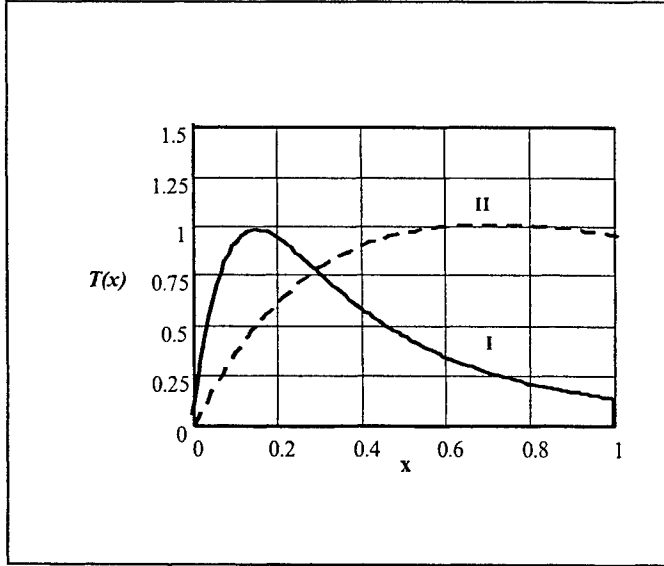


Fig. 3. Typical temperature profiles for two different time moments ($t_{II} = 200 t_I$) (arbitrary units)

As for the movement of the second (back) melting boundary it can be estimated from the following simple consideration. Far from the place of heat allocation the temperature profile can be approximated by the expression $T(x, t) = T_0 + T_* \exp(-x^2 / 4t)$, where T_* is the difference between the maximal and initial (T_0) temperatures. At the melting boundary $T(X_M, t) = T_M$. This expression defines the boundary position $X_M(t) = 2\sqrt{t \cdot \ln(T_* / T_{*m})}$, that moves with the speed $v(t) = \sqrt{\ln(T_* / T_{*m}) / t}$. The heat flow from the melt towards boundary is $-\frac{\partial T}{\partial x} \Big|_{X_M=0} = T_{*m} \sqrt{\ln(T_* / T_{*m})}$. This quantity is just the *moving boundary condition* that is

necessary for solution constructing in the “far” zone (where the medium remains solid). As the “left” and “right” gradients difference decreases as $\sim t^{-1/2}$ one should neglect the derivative jump. In this case the boundary movement results in the same solution for “far” zone as without any melting. Note that for this case the speed of the back front movement is rather small for inside the medium with the small light penetration depth it is completely defined by the slow heat conduction processes.

The LIH behavior for the media in which melting is accompanied by the reduction not only the scattering but absorption is absolutely different from the above mentioned case. The example of such medium may be any polycrystal in which both scattering and absorption are stipulated by the processes at the grain boundaries. The estimations of melting front movement for the solids of this type are given below. We assume for simplicity that extinction coefficient becomes zero just when the melting temperature is reached. Then far from the front surface of solid we have the temperature profile that is stationary in the coordinates linked with the moving boundary and it is given by the following equation:

$$\left\{ \begin{array}{l} v \cdot \frac{dT}{dy} + a \cdot \frac{d^2 T}{dy^2} = -Q \cdot \exp(-\beta y), \quad \text{where } y = x - vt \\ \text{with the boundary condition} \\ -k \frac{dT}{dy} \Big|_{y=0} = \rho \cdot L \cdot v \end{array} \right. \quad (11)$$

When the movement is quick one can neglect the second order derivative:

$$\begin{cases} \frac{dT}{dy} = -\frac{Q}{v} \cdot \exp(-\beta y), & \text{where } y = x - vt \\ \left. \frac{dT}{dy} \right|_{y=0} = -\frac{\rho \cdot L \cdot v}{k} = -\frac{Q}{v} \Rightarrow Qk = \rho \cdot L \cdot v^2, \end{cases} \quad (12)$$

$$\text{or } v = \sqrt{\frac{Qk}{\rho L}} = \sqrt{\frac{\alpha I_0}{\rho L}}$$

Thus the temperature is given by the expression:

$$T - T_m = \frac{Q}{v} \cdot \beta \cdot \left(e^{-\beta \cdot y} - 1 \right) \quad (13)$$

So for the systems that are transparent in the melting phase on the contrary of the slow movement of the LIH front due to the heat conduction the self-congruent LIH regime with the high-speed melting front movement can be realized.

One can improve the above estimations taking into account the thermal conductivity processes i.e. solving the complete Eq. 11. Then the temperature would be given by:

$$T = \frac{a}{v} \left[\frac{\rho \cdot L \cdot v}{k} - \frac{Q}{(v - a\beta)} \right] \cdot e^{-\frac{v}{a} \cdot y} + \frac{Q}{(v - a\beta) \cdot \beta} \cdot e^{-\beta \cdot y} \quad (14)$$

and the front velocity value is determined by the conditions at the LIH boundary:

$$\frac{a}{v} \left[\frac{\rho \cdot L \cdot v}{k} - \frac{Q}{(v - a\beta)} \right] + \frac{Q}{(v - a\beta) \cdot \beta} = T_M \quad (15)$$

5. PRINCIPAL RESULTS AND CONCLUSIONS

We shall list the main results of our analysis of some features of thermal-type LIH behavior. It has been shown that:

- Under the thermal-type LIH the homogenization of material may be reached in the inner area of the solid not touching the front boundary of irradiated medium.
- The metastable state can be observed for the irradiated scattering medium. The transition from this state to the low-scattering occurs by jump resulting from sporadic fluctuation.
- For the media where homogenization is accompanied by absorption decrease the self-congruent LIH regime with the high-speed melting front movement can be realized. The LIH front velocity in this case is determined by the radiation intensity.

Finally we shall emphasize that we discuss the thermal model of LIH only as the simple example that shows clearly the principal features of this effect. The other form of LIH can arise in materials where the changes of scattering are due to the proper changes of the space correlation functions of the medium polarizability⁶. The examples of such media are polymers or the liquid crystals where the scattering is caused by the chaotic orientation of long polymer chains or crystallites correspondingly. The transparence of this media results not from the aggregate state changes and can arise as the lower levels of radiation energy.

This work is supported by the Russian Foundation for Basic Research (project No 00-02-16830).

6. REFERENCES

1. Zege E.P., Ivanov A.P., Katsev I.L. The Image Transfer in the Scattering Medium, Minsk, "Nauka i Tekhnika", 1985. (in Russian)
2. Apresyan L.A., Kravtsov Yu.A. The Theory of Radiative Transfer. Statistical and wave aspects. Moscow, "Nauka", 1983. (in Russian)
3. Radiative Transfer in Scattering and Absorbing Atmospheres: Standard Computational procedures, Edited by J. Lenoble, A. DEEPAK Publishing, 1985, USA.
4. Wiersma D.S., van Albada M.P., van Tiggelen B.A., Lagendijk A. Phys. Rev. Lett., 1995, v. 74, pp. 4193-4196.
5. Wiersma D.S., Bartolini P., Lagendijk A., Righini R. Nature, 1997, v.390, pp. 671-673.
6. Eskin V.E. Light Scattering in the Polymer Solutions, Moscow, "Nauka", 1973. (in Russian)

A new mechanism of laser dry cleaning

B. S. Luk'yanchuk *, Y. W. Zheng, Y. F. Lu

Laser Microprocessing Laboratory, Data Storage Institute and Department of Electrical Engineering
National University of Singapore, Singapore 119260

ABSTRACT

The dry laser cleaning arises due to thermal expansion of the substrate and/or particle, when the corresponding acceleration (breaking) force produces work sufficient to overcome the adhesion energy. The previous examinations of the dry cleaning were done for two mechanisms: 1) expansion of absorbing particle on the transparent substrate and 2) expansion (thermal deformation) of the absorbing substrate with non-absorbing particle. Nevertheless using model with conventional mechanism based on the 1D surface expansion, one can find (for the smooth laser pulse) threshold fluence by the order of magnitude higher than experimental one. In the present paper, we discuss the new mechanism for situation when the particle is heated due to thermal contact with substrate, and additional thermodetachment effect, caused by optical enhancement. It is shown that these effects can be responsible for relatively small threshold fluence for laser cleaning of SiO₂ particles (with size 0.5-1.0 μm) from the surface of Si by ns-excimer laser pulse.

Keywords: Laser Cleaning, Modelling, Dry Cleaning

1. INTRODUCTION

Pulsed laser cleaning demonstrates a great sensitivity of the cleaning efficiency to the optical properties of the particle and substrate, as well as to the temporal shape and other characteristics of the laser pulse. The initial step in laser cleaning is the absorption of laser light. The material optical properties influence the distribution of absorbed energy, which can be rather complex. To analyze the typical situation for laser cleaning conventional Mie theory [1-5] is insufficient and one should solve the more complex problem "particle on the surface" [6-9]. For example, in the case of an absorbing substrate and a transparent particle the latter works as a focusing lens [10-14]. The distribution of the absorbed intensity varies strongly with the particle size (radius), a , and radiation wavelength, λ . If one considers the particle as a perfect sphere, then a common size parameter, $q = 2\pi a n/\lambda$ arises within the Mie theory. Particle extinction versus this parameter shows oscillations, caused by optical resonance [12, 15]. To understand this and some other optical effects in laser cleaning a special examination should be done for near-field distribution of absorbed and scattered laser energy [11-14].

The next step in the analysis of dry laser cleaning is related to thermal expansion of the substrate and/or particle, where the acceleration (breaking) force produces work sufficient to overcome the adhesion energy. Although the mechanism of dry laser cleaning related to the thermal expansion of materials is commonly accepted, some details of this mechanism need clarification. Depending on the duration of the laser pulse, optical properties and geometry, one can distinguish two limiting cases: 1) Quasistatic expansion, where one can neglect the formation of an acoustic wave, and 2) Short laser pulse irradiation accompanied by acoustic wave generation [16]. In the quasistatic regime to the best of our knowledge, the previous examinations of the dry cleaning (see, e.g. [12, 17] and Refs. therein) were done for two mechanisms: 1) expansion of absorbing particles on the transparent substrates and 2) expansion (thermal deformation) of the absorbing substrate with non-absorbing particles (see in Fig. 1). In the present paper, we discuss a new mechanism when the particle is heated due to thermal contact with the substrate, and analyze the effects caused by optical enhancement.

* Corresponding author: boris@dsi.nus.edu.sg. On leave Wave Research Center at General Physics Institute of Russian Academy of Sciences, 117942 Moscow, Russia

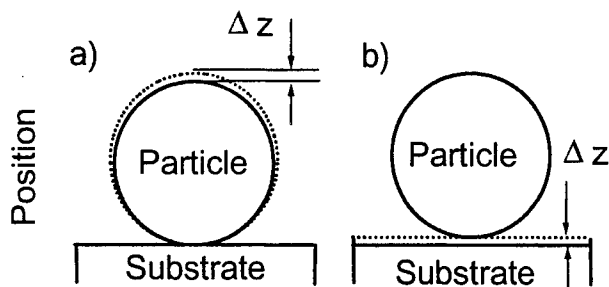


Fig.1. Schematic for two conventional mechanisms of the particle and substrate deformations: a) absorbing particle and transparent substrate; b) transparent particle and absorbing substrate.

The thermal expansion of material is given by $\Delta z = \alpha T L$, where α is the linear thermal expansion coefficient, T is the temperature rise, and L is the characteristic length of the heated material. In the case of thermally thin particle $L \approx R$, where R is the radius of the particle. On the other hand, for an absorbing substrate $L \approx \delta$, where δ is the absorption coefficient. For strongly absorbing substrate δ is very big, typically $\delta \ll R$. Thus, if the heat from the substrate can be efficiently transferred to the particle, one would expect additional acceleration force due to the particle deformation. Also, if the particle works as near-field focusing lens [10-14] it may strongly increase the cleaning efficiency.

2. THEORETICAL MODEL FOR THE SUBSTRATE EXPANSION

Here we discuss briefly the conventional model for dry cleaning, which permits an estimation of the threshold fluence for particle removal. For dry laser cleaning, particles can be ejected from particulate-contaminated surfaces by short-pulse laser irradiation due to fast thermal expansion of the particle and/or solid surfaces. The following will focus on the necessary steps in modeling of laser cleaning which include modelling of adhesion, thermal expansion of substrate and criteria of particle removal.

The particle is attracted to the surface by the Van der Waals force, which occurs due to dipole interactions. If one considers the particle as a deformed sphere, then, according to Hamaker [18] the attraction force is given by

$$F = \frac{\langle \omega \rangle R}{8\pi h^2} + \frac{\langle \omega \rangle a^2}{8\pi h^3}, \quad (1)$$

where R is the radius of the particle, h the separation distance ($h \approx 4 \text{ \AA}$), and a the radius of contact. The Lifshitz constant $\langle \omega \rangle$ is related to Hamaker constant, A , by $A = \frac{3}{4\pi} \langle \omega \rangle$. The Hamaker constant depends on the properties of the particle, substrate and medium.

The attraction force (1) is very big, it is sufficient to say that the maximal pressure within the range of "a point contact" is, typically, 10 Kbar and higher [19]. It is clear that this high loading leads to elastic or even plastic deformation of the material. Analyses of these deformations as well as the general problem of adherence are still under discussion, see, e.g. [20].

A first examination of the pressure distribution within the contact area was done by H. Hertz in 1882, this distribution follows a parabolic law, see the analysis of the Hertz solution, for example, in § 9 of the book [21]. Using this distribution, Derjaguin [22] found the relation between the radius of contact, a , and loading force, P , for spherical particle:

$$a^3 = \frac{3}{4} \frac{P R}{E^*}, \quad \frac{1}{E^*} = \left(\frac{1 - \sigma_1^2}{E_1} + \frac{1 - \sigma_2^2}{E_2} \right), \quad P = \frac{\langle \omega \rangle R}{8\pi h^2}. \quad (2)$$

where $\sigma_{1,2}$ and $E_{1,2}$ are the Poisson coefficients and Young's modulus for the particle and substrate, the effective loading force due to adhesion is presented by the first term in (1). The adhesion-induced deformations are quite complex, and some other

factors (adhesion forces outside the area of contact, etc.) should be taken into account to describe well the experimental data. At present, two models of adhesion are commonly accepted: Derjaguin-Miller-Toropov (DMT) model for "hard" materials [23, 24] and Johnson-Kendall-Roberts (JKR) model for "soft" materials [25, 26]. The transition between the two models was also discussed [27, 28].

The distance between the center of the spherical particle and the substrate surface for nondeformed materials is given by $z_s = R + h$. Due to deformation of materials under the action of an external load and adhesion force this distance will be $z_s' < z_s$. The variation $\delta = z_s - z_s'$ is called deformation parameter. If no other load is exerted on the particle, the initial deformation parameter δ_0 is expressed in the DMT theory as

$$\delta_0 = \frac{1}{8} \left(\frac{9 R \langle \omega \rangle^2}{2 \pi^2 h^4 E^{*2}} \right)^{1/3}. \quad (3)$$

The elastic repelling force, F_e , and energy of the deformation, W_e , are expressed by

$$F_e = \frac{4}{3} E^* \sqrt{R \delta_0^3}, \quad W_e = \frac{8}{15} E^* \sqrt{R \delta_0^5}. \quad (4)$$

When the substrate expands, the position of the substrate surface, z_s , varies with time, $z_s = z_s(t)$, $z_s(0) = 0$. The particle dislocation is a function of time t , say $f(t)$. Then the running deformation parameter, $\delta(t)$ at time t can be expressed as

$$\delta(t) = z_s(t) - f(t) + \delta_0. \quad (5)$$

The acceleration due to the elastic force (4) can be expressed as [10]:

$$\frac{4}{3} \pi R^3 \rho_0 \frac{d^2 f}{dt^2} = \frac{4}{3} \sqrt{R} E^* [\delta(t)^{3/2} - \delta_0^{3/2}], \quad (6)$$

where ρ_0 is the density of the particle. The initial conditions for Eq. (6) are

$$\left. \frac{df}{dt} \right|_{t=0} = 0, \quad f|_{t=0} = 0. \quad (7)$$

To find the surface position, $z_s(t)$, we use solution $T = T(z, t)$ of 1D heat equation. From this solution one can estimate the surface position by

$$z_s(t) = \alpha_T \int_0^\infty T(z, t) dz. \quad (8)$$

Because of the energy conservation, one can write the condition

$$(1 - R_s) \int_0^t I(t_1) dt_1 = c \rho \int_0^\infty T(z, t) dz, \quad (9)$$

here c and ρ are respectively heat capacity and density of the heated substrate, R_s is reflectivity of the surface. We consider the smooth pulse shape, typical for excimer laser pulse [29]

$$I(t) = I_0 \frac{t}{\tau} \exp\left[-\frac{t}{\tau}\right]. \quad (10)$$

The laser fluence is given by $\Phi = I_0 \tau$, and pulse duration at the full width at half-maximum $t_p \approx 2.446 \tau$. From the equations (8)-(10) one can estimate the surface position, $z_s(t)$, by

$$z_s(t) = \frac{\alpha_T \Phi (1 - R_s)}{c \rho} \left[1 - \left(1 + \frac{t}{\tau} \right) e^{-t/\tau} \right]. \quad (11)$$

For the rectangular laser pulse with the pulse duration τ , a similar dependence is given by

$$z_s(t) = \frac{\alpha_T \Phi (1 - R_s)}{c \rho} \left[\frac{t}{\tau} \Theta_H\left(1 - \frac{t}{\tau}\right) + \Theta_H\left(\frac{t}{\tau} - 1\right) \right], \quad (12)$$

here $\Theta_H(x)$ is the unit step function (the Heaviside function). Rectangular pulse corresponds to constant expansion velocity. This case was examined in [30]. The 1D model has natural restriction, related to absence of inward motion of the surface during cooling stage. To take into account this effect one should use the 3D thermo-elastic model. Effects related to temperature dependencies of parameters (solution of non-linear heat equation) can also play an important role. Nevertheless, because of its simplicity, the derived model can be used for the preliminary estimations.

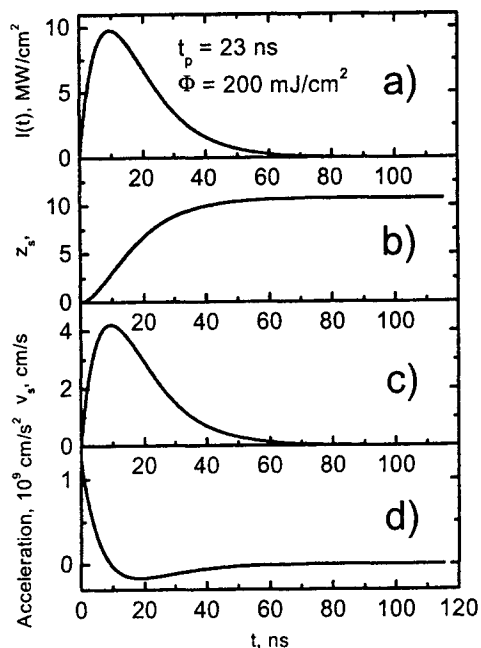
In Fig. 2 we present an example of the surface expansion for a smooth laser pulse. Constant parameters of material, which have been used on the calculations, are of the same order of magnitude as parameters for Si (see Table 1). One can see that characteristic acceleration of the surface reaches 10^9 cm/s^2 at a laser fluence of 200 mJ/cm^2 and pulse duration $t_p = 23 \text{ ns}$. These values are close to that found experimentally in [31].

Integration of equation (6) shows that the particle performs an oscillatory motion (compressive-tensile motion). The driving force for this motion is the "push", produced by accelerated surface during substrate thermal expansion. It is convenient to present this oscillatory motion of the particle as a phase trajectory on the plane $\{v, \delta\}$, where $v = df/dt$ is the particle velocity, see in Fig. 3. The characteristic period of oscillations, T , in Fig. 3a consists $\approx 10 \text{ ns}$ (frequency $\omega = 2\pi/T \approx 6 \cdot 10^8 \text{ s}^{-1}$). This frequency is significantly smaller than the Eigenfrequency of the particle sound vibrations, $\omega_p \approx \pi c / R \approx 3 \cdot 10^{10} \text{ s}^{-1}$, (see Problem 3, to § 22 in [21]).

This oscillatory motion is highly interesting and many problems immediately arise. We did not find in the literature any examination of these problems for laser cleaning. Meanwhile, there are many important consequences, which permit to suggest new ways to improve the laser cleaning efficiency. In fact, the most important problem is the oscillation damping. It means that more realistic equation of motion (compare to Equation (6)) should include terms proportional to the particle velocity. The two damping mechanisms seem to be of great importance. The first one is related to emission of sound (see Problem 4, to § 22 in [21]). Another mechanism is related to plastic deformation of the material [17] (in fact, this mechanism was mentioned in the Problem 1 to § 9 in [21]).

Although the heating process happens only within a short time interval, it determines both the kinetic energy and the elastic potential energy necessary to overcome the adhesion force. The condition for the particle removal can be written from the simple energetic consideration given in [30]:

$$\frac{8}{15} E^* \sqrt{R \delta(t)^5} + \frac{4}{3} \pi R^3 \frac{\rho_0 v^2}{2} \geq \frac{1}{2} P \delta(t) + \frac{\langle \omega \rangle R}{8\pi h}. \quad (13)$$



Parameter	Value
Absorption coefficient, α , cm^{-1}	$1.5 \cdot 10^6$
Heat capacity, c , J/g K	0.83
Density, ρ , g/cm^3	2.5
Thermal expansion, α_T , K^{-1}	$2.7 \cdot 10^{-6}$
Young modulus, E , dynes/cm^2	$6.0 \cdot 10^{11}$
Poisson coefficient, ν	0.3
Hamaker constant, A , erg	$7.5 \cdot 10^{-13}$

Table 1. Parameters which have been used in calculations.

Fig. 2. Laser pulse shape (a), and characteristics of the substrate thermal expansion: Position of the surface (b); Surface velocity (c); Surface acceleration (d). Laser fluence 200 mJ/cm^2 , duration of laser pulse 23 ns.

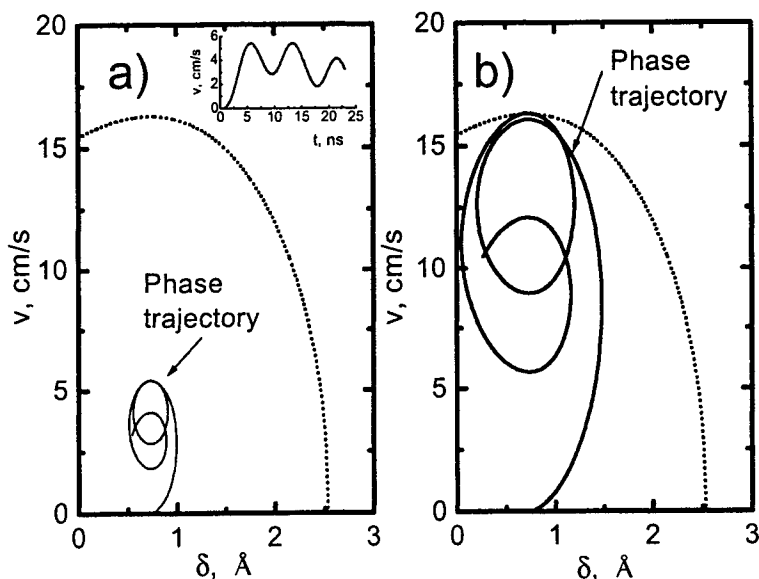


Fig. 3. Phase trajectories of the particle with size $2r = 1 \mu\text{m}$, resulting from the laser pulse ($t_p = 23 \text{ ns}$) action onto the absorbing surface: a) Laser fluence $= 250 \text{ mJ/cm}^2$; b) fluence $= 765 \text{ mJ/cm}^2$. Dotted curves present energy criteria (13), removal of the particle occurs when the phase trajectory arises above the curve. Initial point for the phase trajectories (at $t = 0$) corresponds to coordinates: $\delta_0 = 0.73 \text{ Å}$ and $v = 0$. The final point corresponds to the moment $t = t_p$. Pay attention that condition for the particle removal is reached not for the first, but for the second oscillation. The insertion in a) shows the particle velocity versus time (period of oscillations is $\approx 10 \text{ ns}$).

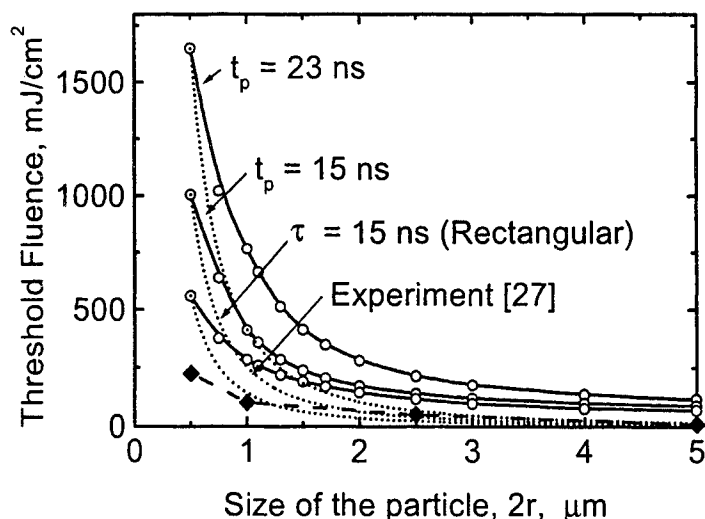


Fig. 4. Threshold fluence for laser cleaning versus size of particle for different laser pulse duration. Two pulse shapes are examined: rectangular pulse ($\tau = 15$ ns) and smooth excimer pulse with $t_p = 23$ and 15 ns. Diamonds show experimental points, found in [27], for dry laser cleaning with KrF excimer laser (smooth pulse, $t_p = 23$ ns). The dotted lines present the dependence $\tau_{th} \propto R^{-2}$ [28].

The first term in the left side of the equation is the elastic deformation potential energy, the second term is the kinetic energy of the particle. The first item in the right side presents the work done by adhesion force (2), the second item is the adhesion energy of the "point contact". For the first term we use approximation of the DMT-theory which shows that the adhesion force is rapidly reduced to $P/2$ with $\geq 0.1h$. Condition (13) can be presented as some border on the plane $\{v, \tau\}$, see in Fig. 3. One can see that with a small fluence particle phase trajectory does not cross the bifurcation curve (13), while starting with some fluence one fulfill condition for the particle removal. It is not necessary that the particle removal occurs during the first vibration of the particle. Depending on the pulse shape, the particle may perform a few vibrations before removal. For example in Fig. 3 b, the removal of the particle occurs during the second oscillation motion. The characteristic frequency of vibration $\propto R^{-3/2}$ increases for smaller particles. Probably, this effect can be used for the diagnostics of the size distribution function of polluting particles.

In Fig. 4 one can see the result of examination of the threshold fluence on the pulse duration and particle size. This picture presents the main tendencies in dry laser cleaning. First, the small particles are more difficult to be removed than the big particles. Second, the threshold fluence is smaller for a shorter laser pulse. Third, the cleaning effect strongly depends on the pulse shape. The rectangular pulse has significant advantages compared to a smooth excimer pulse. We should mention that the dependence $\tau_{th} \propto R^{-2}$, which follows from the simplified consideration [32] does not agree with both experimental and the present theoretical consideration.

Comparing the theoretical and experimental [10, 30] results one can say that the mechanism, related to the thermal expansion of substrate is insufficient to explain the experimental cleaning efficiency. This discrepancy can be evidently seen also from Fig. 7 in paper [30], where theoretical calculations were performed for rectangular laser pulse. Thus, a new, more efficient mechanism should be considered to explain the dry cleaning efficiency.

Instead of the energy criterion in the form (13) one can use simplified energy criterion [29]:

$$\frac{4}{3} \pi R^3 \frac{\rho_0 v^2}{2} \geq \frac{\langle \omega \rangle R}{8 \pi h}. \quad (14)$$

Criterion (14) at typical conditions coincides with (13) with accuracy $\approx 5\%$. For example, with smooth pulse, $t_p = 23$ ns and particle with radius $r = 0.5 \mu\text{m}$ using (13) one find the threshold fluence 765 mJ/cm^2 (see in Fig. 4), while criterion (14) yields 725 mJ/cm^2 .

In the majority of papers related to laser cleaning, another criterion for the particle removal is used, namely the "force criterion" (the corresponding force, related to the particle acceleration, should exceed the force of Van der Waals attraction). This approximation holds for sufficiently long laser pulses. We have to mention that this criterion needs negative accelerations (see in [31]).

3. THERMAL CONTACT AND THE PARTICLE EXPANSION

Considering in the previous paragraph the mechanism of laser cleaning related to thermal expansion of a substrate, we at the same time neglected the effect of the particle heating. Meanwhile, the surface of silicon with typical laser fluences is heated up to a few hundred Kelvin, and part of this thermal energy will transfer into the particle through the thermal contact with radius a , see equation (2). The heat transfer through the Van der Waals layer (separation distance h) arises due to dissipation of electromagnetic fluctuations [33], the same fluctuations are responsible for the Van der Waals force between two contacted solids [34, 35]. Although we did not find the theory of the thermal contact in the literature (e.g. calculation of the thermal resistance of the van der Waals layer, etc.) we shall consider this contact sufficiently efficient.

For the first estimation, we can consider that the particle temperature in region of contact is the same as the substrate temperature. Additionally we consider that the back influence of the particle onto the substrate is negligible (that is because of very efficient radial heat conduction through particle).

It is easy to estimate the upper limit of the expected effect of the particle expansion. For the thermally thin particle its temperature, T_p , will be the same, as a substrate surface temperature, $T_s(t)$. Thus, the thermal expansion of the particle is given by quantity by the order of

$$\delta_p(t) = \tau_p R T_s(t), \quad (15)$$

where τ_p is the linear thermal expansion coefficient for the particle.

The value of T_s can be estimated from the solution of 1D linear heat equation,

$$T_s(t) = (1 - R_s) \frac{\alpha \chi}{\kappa} \int_0^t dt_1 I(t - t_1) e^{-\alpha^2 \chi t_1} \operatorname{erfc}[\alpha \sqrt{\chi t_1}], \quad (16)$$

where κ and χ are, correspondingly, the heat conductivity and the heat diffusivity of substrate, pulse shape is given by formula (10).

Then we add $\delta_p(t)$ value to $\delta(t)$ in (5), to find the threshold fluence (initial condition (7) is $f'(t=0) = \delta_p'(t=0)$).

Although the thermal expansion coefficient for SiO_2 is small, $\alpha_{Tp} = 5 \cdot 10^{-7} \text{ K}^{-1}$, thus, the deformation caused by the particle is smaller than that for the substrate (see in Fig. 5a) it produces comparable expansion velocity, (see in Fig. 5b).

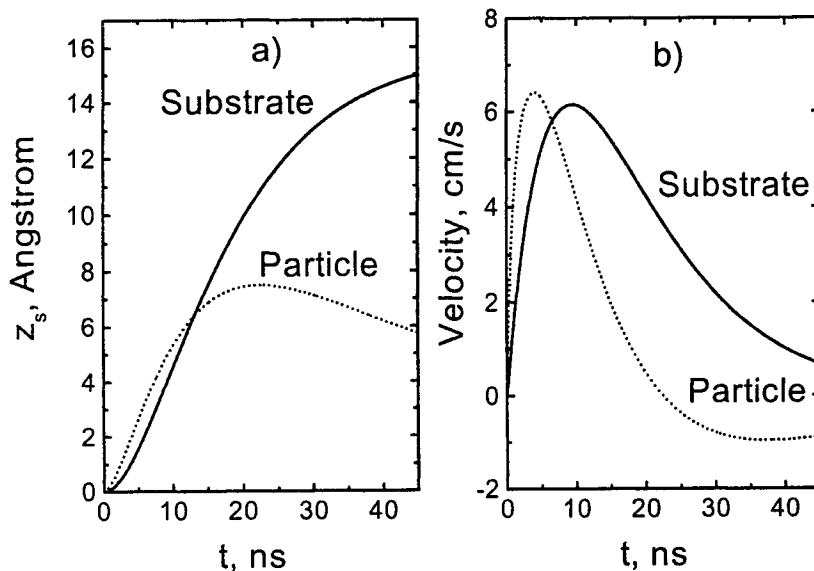


Fig. 5. a) The deformations caused by Si substrate and SiO_2 particle with size $r = 0.5 \mu\text{m}$ at laser fluence $\Phi = 365 \text{ mJ/cm}^2$. b) The corresponding expansion velocities.

In result the threshold fluence is reduced approximately twice due to the influence of the thermal contact. It is equal to 790 mJ/cm^2 (for $r = 0.25 \text{ }\mu\text{m}$) and 365 mJ/cm^2 (for $r = 0.5 \text{ }\mu\text{m}$). Although it is closer to experimental data in Fig. 4, one can say that the thermal contact, by itself, is still insufficient to explain the low threshold fluence. Some speculations can be done with respect to thermal expansion coefficient, probably, small amorphous SiO_2 particles have a higher α_p value than the bulk material.

4. 3D-EFFECTS AND OTHER MECHANISMS OF LASER CLEANING ENHANCEMENT

Another enhancement effect in laser cleaning is related to the near-field focusing effect produced by the particle. In the previous examination we neglected the influence of the transparent particle onto the laser intensity distribution on the substrate surface. Nevertheless, the theoretical investigations [10-12] and recent experiments [13, 14] show that the particle-laser interaction produces non-uniform near field light intensity distribution around the particle-substrate contacting point. For KrF excimer (248 nm) irradiating on Si substrate contaminated with $1.0 \text{ }\mu\text{m}$ spherical silica particle, the "enhanced" near field light intensity can be assumed as the simplest Gaussian distribution, with a beam radius of about $0.05 \text{ }\mu\text{m}$ [12]. In such circumstance we solve the 3D nonlinear, non-stationary heat equation with finite difference method.

We assume the near-field light intensity can be fitted by the simplest Gaussian distribution:

$$I(r, t) = I(t) e^{-r^2/r_0^2}, \quad (17)$$

where r_0 is the radius of Gaussian beam, and $I(t)$ is the pulse shape, given by equation (10). Figure 6 is the comparison of the near-field light intensity, found in [12] (after light scattering by $1.0 \text{ }\mu\text{m}$ silica particle) with the fitting Gaussian spatial profile (17). It is found that the main lobe of the "true" field fits well to the Gaussian beam. Since the magnitude of the side lobe is an order less the main lobe, their contribution to the thermal expansion can be ignored.

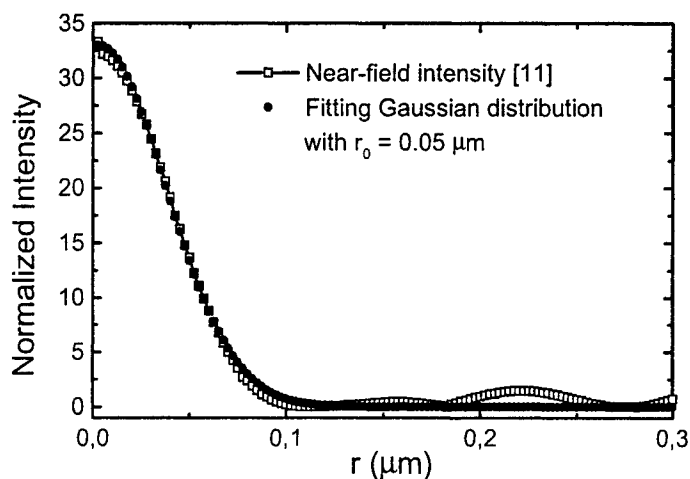


Fig. 6. Light intensity profile of the "true" near-field intensity distribution [12] and its best fitting by Gaussian function.

For the nonlinear heat equation, the heat capacity c , heat conductivity κ , and absorptivity $R(T_s)$ are functions of the temperature. At the same time we consider the constant density, (take into account variations of the density one should consider more complex hydrodynamic equations). These dependencies are fitted on the basis of previous experimental data. For thermal conductivity of $\kappa(T) = k/(T - T_k)$ [36], where $k = 299 \text{ W cm}^{-1} \text{ K}$, $T_k = 99 \text{ K}$. The reflectivity is $R(T) = R_0 + 4.29 \times 10^{-5} T$,

where T is in Kelvin and R_0 is a constant dependent on the wavelength of the laser used [36, 37]. For KrF excimer laser, $R_0 = 0.66$. The heat capacity is $c(T) = 1.99 + 2.54 \times 10^{-4} T - 3.68 \times 10^{-4} T^{-2}$ [38, 39].

A numerical solution of the nonlinear 3D heat equation was done with finite difference method [40]. We adapt a non-uniform space nodal structure with respect to both r and z coordinates, e.g., $r_i = 2 r_0 / i(i+1)$. Although the nodal truncation error is proportional to the distance from the center, the influence of these nodes to the particle movement under thermal expansion is less important since they are far away from the contacting point.

To verify the accuracy of numerical calculation, we compare the numerical solution of the linear 3D temperature profile with the analytical solution of the heat equation with constant parameters. The analytical solution is given by (see, e.g. [29]):

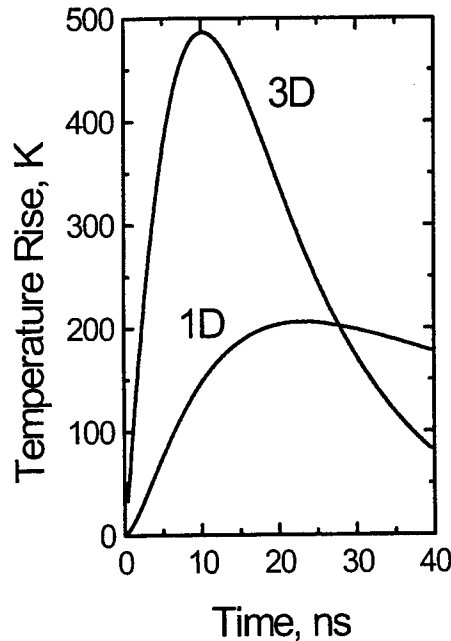
$$T(r, z, t) = \frac{(1-R)\alpha\chi_0^2}{2\kappa} \int_0^t dt_1 I(t-t_1) e^{-\frac{r^2}{r_0^2 + 4\chi t_1}} F(z, t_1), \quad (18)$$

where $\chi = \kappa / cp$ is the thermal diffusivity, and F -function is given by

$$F(z, t) = e^{\alpha^2 \chi t} \left\{ e^{\alpha z} \operatorname{erfc}[\alpha \sqrt{\chi t} + \frac{z}{2\sqrt{\chi t}}] + e^{-\alpha z} \operatorname{erfc}[\alpha \sqrt{\chi t} - \frac{z}{2\sqrt{\chi t}}] \right\}. \quad (19)$$

The node number was 40×40 for space divisions in radial and z direction, and 10^6 for time division. The calculating time by finite difference solver was about 15 minutes on DEC workstation. Thus calculated result has deviation less than 0.3% to analytical solution (18).

Then we use the finite difference solver to find characteristic temperature rise in Si substrate. Examples of calculations are shown in Fig. 7. One can see from the figure that the enhanced near-field intensity can produce faster and higher temperature rise at the contacting spot, than 1D solution, which has been used in the preliminary consideration. It is clear that this effect facilitates particle removal.



The inhomogeneous heating of the target leads to displacement of the target different parts with respect to their initial positions, which results in the internal stress formation. Another reason for the stress formation is an external force. The vector of displacement, $\mathbf{u} = \mathbf{u}(r, z, t)$, characterizes the displacement of the matter. The equation for the displacement is given by the thermoelasticity theory [21, 41]:

$$\rho \mathbf{u} = \frac{E}{2(1+\sigma)} \Delta \mathbf{u} + \frac{E}{2(1+\sigma)(1-2\sigma)} \operatorname{grad} \operatorname{div} \mathbf{u} - \frac{\alpha_T E}{3(1-2\sigma)} \operatorname{grad} T, \quad (20)$$

where σ is the Poisson's ratio, E is the Young's modulus, and α_T is the volume thermal expansion coefficient.

One can consider the potential deformations, where vector \mathbf{u} can be presented in the form $\mathbf{u} = \operatorname{grad} A$, where A is scalar potential of displacement. The equation (20) is reduced to the simple equation for scalar potential. The problem is, however, that the deformations of an elastic medium bounded by a plane are non-potential, in general (see § 8 in [21]).

Fig. 7. Temperature rise at the central point calculated with enhanced light intensity (3D) and uniform light intensity (1D). Parameters of the laser pulse, $t_p = 10$ ns, $\Phi = 100$ mJ/cm². After interacting with 1.0 μm particle, the Poynting vector in z direction at the central point (enhanced fluence) is about 3.25 J/cm², $r_0 = 0.05 \mu\text{m}$.

Since the size r_0 of optically enhanced region is very small, the radial temperature distribution established very fast, $r_0^2 / \approx 0.1$ ns for $r_0 \approx 10^{-5}$ cm. It means that one can use the quasi-static solution of (20) for the problem with ns-laser pulses. For a static case, the general solution of (20) for the cylindrical geometry is given in terms of Youngdahl functions [42]. For the cylindrically symmetric case $\theta = 0$, while for other functions one can write the equations [42, 43]:

$$\Delta\Omega = \frac{1}{2(1-\sigma)} \left[-\frac{\partial^2 \Psi}{\partial z^2} + 2(1+\nu)\alpha T \right], \quad \Delta\Psi = \frac{\partial^2 \Psi}{\partial r^2} + \frac{1}{r} \frac{\partial \Psi}{\partial r} + \frac{\partial^2 \Psi}{\partial z^2} = 0. \quad (21)$$

One may consider the unloaded surface, i.e. boundary condition on the surface: $\sigma_{ik} n_k n_i = 0$ [21], where n_k is the unit normal vector to the surface. Considering the small deformations, one can find

$$\sigma_{zz}|_{z=0} = 0, \quad \sigma_{rz}|_{z=0} = 0, \quad (22)$$

and the trivial conditions at infinity, $\sigma_{ik} \rightarrow 0$, when r or z tends to infinity.

The given quasi-stationary problem was solved in [43] for the Gaussian beam profile. It is represented by integrals containing the Bessel functions; we do not write out here appropriate bulky formulas. Let's note only, that these formulas are written out in such kind, that they contain factor T_{\max} , representing established temperature in the center, and the effective radius size r_0 . Both quantities can be found from the calculations. Instead of T_{\max} one can use the solution of a nonlinear heat equation. The example of such calculation for z -component of a displacement vector is shown in Fig. 8. One can see from the figure that the typical expansion velocity in this case one order of magnitude faster than values found from 1D problem (see in Fig. 2 and Fig. 5). This permits to consider that mainly the optical enhancement effect is responsible for a rather small threshold in experiments [10, 30].

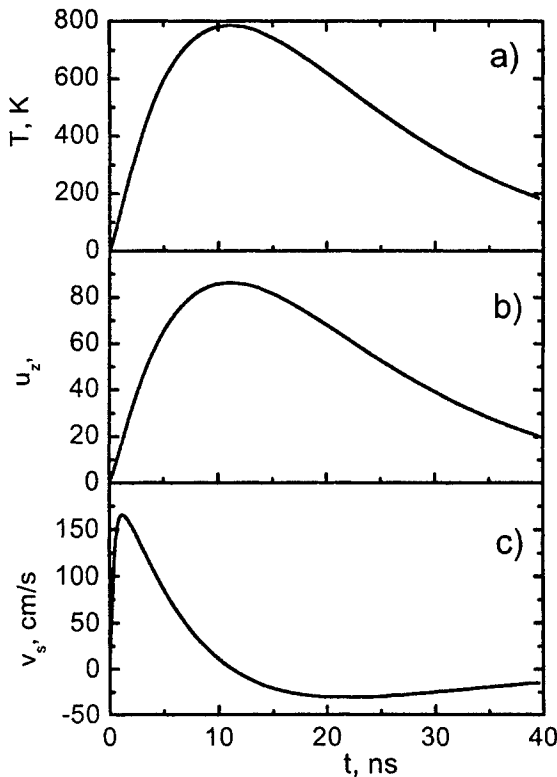


Fig. 8. The dynamics of the heating and the substrate surface deformation at the beam center (i. e. under the particle). Calculations take into account the optical enhancement effect. Duration of the laser pulse, $t_p = 10$ ns, the effective radius $r_0 = 0.2 \mu m$, and the enhanced fluence is about $6 J/cm^2$: (a) dynamics of the temperature change found from the numerical solution of the nonlinear heat equation; (b) deformation of a substrate and (c) the appropriate expansion velocity. The values $E = 1.13 \cdot 10^{12}$ dynes/cm² and $\alpha_T = 4 \cdot 10^{-6} K^{-1}$, distinguished from the given in the Table 1 were used in calculations.

5. CONCLUSION

The calculation of the particle ejection during laser cleaning with ns-laser pulse is done for conventional model, based on the idea of 1D surface expansion. It is shown that this "conventional" model can not explain relatively small threshold fluence for the small particles: calculated threshold fluence by the order of magnitude higher than experimental one. Thus, a new mechanism should be suggested to explain experimental data.

We analyzed the "most probable" two candidates for new mechanisms. One is related to the thermal contact effect, when particle is heated additionally by heated substrate surface. This mechanism can decrease the calculated threshold approximately twice.

Another mechanism is related to the influence of the particles onto the distribution of laser intensity. Our examination shows that "enhanced" near-field light intensity yields sufficient expansion velocity to explain experimental effect. More radical step was suggested in [13], where the authors consider that with shorter laser pulse the dry laser etching effect can be explained by local substrate evaporation. Although it needs further clarification, we consider that suggested mechanisms may be reasonable alternative to 1D surface expansion. Results of the recent paper [44] also do not confirm 1D thermal expansion mechanism. Authors consider that the realistic model should include effects of absorption in particulate.

Some interesting problem arises with the particle dynamics. According to our calculations the particle performs the oscillatory motion (typical frequency $\approx 6 \cdot 10^8 \text{ s}^{-1}$), induced by cleaning laser pulse. This allows, in principal, strong resonance enhancement of the cleaning efficiency with the help of additional low-power source of the corresponding frequency. The main problem here is related to the oscillations damping, which needs a further clarification. Some analysis of these effects was done in [45].

ACKNOWLEDGEMENTS

We wish to thank Prof. S. Anisimov, Dr. N. Arnold, Dr. M. Mosbacher and Prof. D. Kane for discussions. B. L. is thankful to people in Data Storage Institute at National University of Singapore for their hospitality during his visit in Singapore and to the Russian Basic Research Foundation (grant 98-02-16104) for financial support.

REFERENCES

- [1] J. A. Stratton: *Electromagnetic Theory*, (McGraw-Hill, New York & London, 1941)
- [2] M. Kerker: *The scattering of Light*, (Academic Press, New York & London, 1969)
- [3] H. C. Van de Hulst: *Light Scattering by Small Particles*, (Dower Publ., New York, 1981)
- [4] C. E. Bohren, D. R. Huffman: *Absorption and Scattering of Light by Small Particles*, (John Wiley & Sons, 1983).
- [5] M. Born, E. Wolf: *Principles of Optics*, 7-th Edition, (Cambridge University Press, 1999)
- [6] P. A. Bobbert, J. Vlieger: *Physica A*, vol. 137, 209 (1986)
- [7] P. A. Bobbert, J. Vlieger, R. Greef: *Physica A*, vol. 137, 243 (1986)
- [8] G. L. Wojcik, D. K. Vaughan, L. K. Galbraith: *Proc. SPIE*, vol. 777, 21 (1987)
- [9] M. I. Mishenko, J. W. Hovenier, L. D. Travis (Eds.): *Light Scattering by Nonspherical Particles*, (Academic Press, 2000)
- [10] Y. F. Lu, Y. W. Zheng, W. D. Song: *J. Appl. Phys.* 87, 1534 (2000)
- [11] P. Leiderer, J. Boneberg, V. Dobler, M. Mosbacher, H. -J. Münzer, N. Chaoui, J. Siegel, J. Solis, C. N. Afonso, T. Fourier, G. Schrems, D. Bäuerle: *Proc. SPIE*, vol. 4065, 249 (2000)
- [12] B. S. Luk'yanchuk, Y. W. Zheng, Y. F. Lu: *Proc. SPIE*, vol. 4065, 576 (2000)
- [13] M. Mosbacher, H. -J. Münzer, J. Zimmermann, J. Solis, J. Boneberg, P. Leiderer: *Appl. Phys. A* (2000) –in press
- [14] Y. F. Lu, L. Zhang, W. D. Song, Y. W. Zheng, B. S. Luk'yanchuk: *JETP Letters*, vol. 72, issue 9, 658 (2000)
- [15] See e.g. Section 4 "Optical Resonances" in "Selected Papers on Light Scattering", Ed. by M. Kerker, *Proc. SPIE*, vol. 951 (Part One), (1989)
- [16] A. A. Kolomenskii, H. A. Schuessler, V. G. Mikhalevich, A. A. Maznev: *J. Appl. Phys.* 84, 2404 (1998)
- [17] Y. F. Lu, W. D. Song, Y. Zhang, Y. W. Zheng: *Proc. SPIE*, vol. 3618, 278 (1999)
- [18] H. C. Hamaker: *Physica*, 4 (10), 1058 (1937)

- [19] R. A. Bowling, In: K. L. Mittal (Ed.): *Particles on the Surfaces I. Detection, Adhesion, and Removal*, (Plenum Press, N.Y. & London, 1988), p. 77
- [20] D. S. Rimai, L. P. DeMejio, K. L. Mittal (Eds.): *Fundamentals of Adhesion and Interfaces*, (VSP, Utrecht, Netherlands, 1995)
- [21] L. D. Landau, E. M. Lifshitz: *Theory of Elasticity*, (Pergamon Press, 1975)
- [22] B. V. Derjaguin: *Kolloid Z.*, **69**, 155 (1934)
- [23] B. V. Derjaguin, V. M. Muller, Yu. P. Toporov: *Journal of Colloid and Interface Science*, **53**, 314 (1975); **73**, 293 (1980)
- [24] V. M. Muller, V. S. Yushchenko, B. V. Derjaguin: *Journal of Colloid and Interface Science*, **77**, 91 (1980); **92**, 92 (1983).
- [25] K. L. Johnson, K. Kendall, A. D. Roberts: *Proc. Roy. Soc.*, **A 324**, 301 (1971)
- [26] K. L. Johnson, In: "*Theoretical and Applied Mechanics*", Ed. by W. T. Koiter, p.133 (North-Holland 1976)
- [27] D. Maugis: *Journal of Colloid and Interface Science*, **150**, 243 (1992)
- [28] D. Maugis, B. Gauthier-Manuel: In Ref. [30], p. 49
- [29] D. Bäuerle: *Laser Processing and Chemistry*, 3rd Edition, (Springer-Verlag, Berlin 2000)
- [30] Y. F. Lu, Y. W. Zheng, W. D. Song: *Appl. Phys. A* **68**, 569 (1999)
- [31] V. Dobler, R. Oltra, J. P. Boquillon, M. Mosbacher, J. Boneberg, P. Leiderer: *Appl. Phys. A* **69** [Suppl], S335 (1999)
- [32] W. Zapka, W. Ziemlich, A. C. Tam: *Appl. Phys. Lett.* **58**, 2217 (1991)
- [33] L. D. Landau, E. M. Lifshitz: *Electrodynamics of Continuous Media*, § 90 (Pergamon Press, 1980).
- [34] E. M. Lifshitz, L. P. Pitaevsky: *Statistical Physics*, Part 2, §§ 80-82 (Pergamon Press, 1980)
- [35] A. A. Abrikosov, L. P. Gorkov, I. E. Dzyaloshinski: *Methods of Quantum Field Theory in Statistical Physics*, (Prentice-Hall, Englewood Cliffs, New Jersey, 1965)
- [36] J. E. Moody, R. H. Hendel: *J. Appl. Phys.* **48**, 3895 (1997)
- [37] G. E. Jr. Jellison, F. A. Modine: *Phys. Rev. B* **27**, 7466 (1983)
- [38] I. S. Grigoriev, E. Z. Meilikhov (Editors): *Handbook of Physical Quantities*, (CRC Press, Boca Raton, 1997)
- [39] O. Madelung (Editor): "*Semiconductors-Basic Data*" (2nd Edition), (Springer, Singapore, 1996)
- [40] M. Necati Ozisik: "*Heat Conduction*", (New York, Wiley, 1993)
- [41] I. S. Sokolnikoff: *Mathematical Theory of Elasticity*, (McGraw-Hill, 1956)
- [42] C. K. Youngdahl: *Int. J. Engng Sci.*, **7**, 61 (1969)
- [43] L. P. Welsh, J. A. Tuchman, I. P. Herman: *J. Appl. Phys.*, **64**, 6274 (1988)
- [44] D. R. Halfpenny, D. M. Kane: *J. Appl. Phys.* **86**, 6641 (1999)
- [45] N. Arnold, to be published

SOME PECULARITY OF CO₂ - LASER RADIATION INTERACTION WITH SEMICONDUCTOR A_{II} B_{VI} COMPOUNDS

A.F. Mukhammedgalieva, V. S. Petukhov, B. I. Vasiliev
Moskow State Mining university ,
Physical institute of Russian Academy of sciences

1. INTRODUCTION

Under the impact of powerful laser radiation in semiconductors occur processes, essentially changing their properties. For instance, in [1] was observed annealing of ion-implanted silicon, vastly improving quality of semiconductor devices, made from it. In [2] was observed laser-stimulated diffusion of impurity atoms on the direction to surface, and in [3], on the contrary, deep into of semiconductor. In [4] an increase a velocity of chemical reactions on semiconductor surface under the influence of laser radiation was observed. In the present work spectra of radiation reflection of low power continuous CO₂-laser from the surface of monocrystals of semiconductor A_{II} B_{VI} compounds previously irradiated by powerful pulses of CO₂-laser were investigated.

2. EXPERIMENT

Samples were cut out from monocrystals CdS, CdSe and ZnSe - ZnS as plates, oriented in perpendicular optical axis *c* planes. Monocrystals CdS have low resistance with specific resistivity less than $4 \cdot 10^3 \Omega \cdot \text{cm}$, monocrystals CdSe have resistivity more than $10^6 \Omega \cdot \text{cm}$, resistivity of solid solution ZnSe - ZnS monocrystals specially was not checked, due to phenomenon of selfcompensation they always have high resistivity. One plate of solid solution ZnSe - ZnS was etched in HCl solution before getting a dim surface on Se-side of the plate, and then was carefully washed out in distilled water and was dried.

Installation for an irradiation semiconductor monocrystals was mounted on an optical table, in which threading holes to make rigid fastening of all optical elements were provided. Optical installation scheme is presented on a Fig.1. Powerful pulsed CO₂-laser 1 generated a pulses by time duration 100 ns at the frequency $1046,85 \text{ cm}^{-1}$. It was possible to control energy in a pulse by selection of filter 2. Part of laser radiation energy of the pulse was reflected from light splitting plate 4 and fell into calorimeter 3, and part of them going through collecting lens 5 and calibrated diaphragm 6, got to the semiconductor monocrystal plate 7. Gauss distribution of energy in the beam was provided by means of changing an arrangement of lens 5 and diaphragms 6 concerning a plane of a target 7, therewith the mutually unequivocal conformity of indications of calorimeter 3 and other same calorimeter placed after the diaphragm 6 instead of monocrystal plate 7 was established. In such way it was possible exactly to define energy in each pulse during experiment. By numerous experiences an optimum density of energy on surfaces of semiconductor monocrystals was established. It means, that if laser pulses left imprints at surfaces of samples, the samples themselves did not yet break-down as a result of thermotensions, caused by these pulses. This density of energy has equal 5 J/cm^2 . Laser beam left on the surface of sample the imprint by diameter 1,5 mm, which area was insufficient for the subsequent study of reflection. Such irradiation an area of monocrystal plate by series of six pulses was impressed, moreover there imprints settled down in two rows with a step of 4 mm. Such geometry of irradiating surface has appeared most convenient for the subsequent study of reflection of CO₂-laser radiation from a surface of semiconductors.

Optical installation scheme on study a reflection of laser radiation from a surface of semiconductors is presented on a Fig. 2. Gasdischarging tube 2 of low power continuous CO₂-laser was placed between the concave long focused mirror 1 and diffraction lattice 3, forming resonator of the laser. The tuning of frequency of laser generations was realized by turn of the diffraction lattice 3 around vertical axis. Measurement of power of laser radiation falling on the sample 7 was made by calorimeter 6 on the splitting reflection of laser radiation by plainly parallel germanium plate 5. The radiation reflected from the sample fell into calorimeter 8. Diaphragm 9 and calorimeter 10 are necessary for the preliminary tuning the optical system and determination of mutual unequivocal conformity between falling on the sample and reflected from the germanium plate powers of laser radiation. Beam of light from low-power HeNe-laser 11, reflected from a glass plate 12, rigidly mounted on the back of the holder of diffraction lattice 3, give on a scale 13 light label, which allow to adjust exactly CO₂-laser on one or another generation line.

3. RESULTS OF MEASUREMENTS AND DISCUSSION

The frequency of continuous CO₂-laser was tuned within a range from 1029,44 up to 1060,61 cm⁻¹. Thereby the power of generation varied from 0,17 up to 1,25 W.

On a Fig. 3 the spectrum of reflection from polished surface of the monocrystal plate of cadmium sulfide cut out along a basic plane is presented. At the reflection spectrum of irradiated sample the appreciable rise is observed on the frequency, close to generation frequency of the powerful pulsed CO₂-laser. Such rise is not observed at reflection from nearby nonirradiating area of the monocrystal. The monocrystal plate of cadmium selenide cut out parallel of the base plane and polished on the both sides was irradiated with precisely same power density radiation and with the same frequency. The spectrum of reflection from the surface of the monocrystal CdSe is presented on a Fig. 4. The rise is here also observed on the nonirradiated surface of the monocrystal at the frequency of the laser impact. Difference in reflection spectra from monocrystals CdS and CdSe seemed unexplained until have compared electrophysical parameters of samples: CdS had resistivity $4 \cdot 10^3 \Omega \cdot \text{cm}$, but CdSe $\sim 10^6 \Omega \cdot \text{cm}$. Obviously, the radiation of the pulsed CO₂-laser being absorbed on free carriers in the cadmium sulfide caused spatially modulated break-down of the structure in the crystalline lattice CdS, while under the same level of the power density it passed unabsorbedly through the high resistive monocrystal plate of CdSe caused not damages of the crystalline lattice. The selectivity of reflection of the low power CO₂-laser radiation is caused by strict spatial periodicity of structural break-down in the crystal CdS, caused by powerful pulsed CO₂-laser radiation. The selectivity of reflection of the low power CO₂-laser radiation in CdSe is caused by own oscillations of crystalline lattice of this semiconductor, as far as the rise is observed at reflection from nonirradiated surface area of the monocrystal.

Two monocrystal plates of solid solution ZnSe-ZnS, one of them was glance, but other - dim, both undoubtedly with high resistivity because of phenomena of selfcompensation, which possesses this compound, have been irradiated by powerful pulsed CO₂-laser for finding out of influence of quality of surface on the discovered effect. For this aim their spectra of reflection were recorded by means of low power continuous CO₂-laser. As expected, through the glance plate the laser pulses passed not causing appreciable changes on the irradiated surface and in spectra of reflection, but on etched in HCl surfaces visible imprint of laser beam and distinctive rise in spectra of reflection on the frequency of laser impact were observed. It may be seen at a Fig. 5, where the spectra of reflection of the CO₂-laser radiation from irradiated and nonirradiated surfaces of etched in HCl monocrystal plate ZnSe - ZnS are presented, near to frequency of laser impact on the irradiated surface area ZnSe - ZnS such effect of selective reflection as from low-resistance monocrystal CdS is observed.

4. CONCLUSION

As a result of the carried out researches the rise in spectra of reflection from semiconductor monocrystals near the frequency of generation of the powerful laser by which these monocrystals previously were irradiated was found . This phenomenon is explained by spatial periodicity of structure of an inprint of a laser beam.

REFERENCES

1. Demireva D., Ziffudin L., Barbova M. - Semicond. Sci. Technol., 1998, v.13, No 11, p. 1290 - 1293.
2. White C. W., Narayan T., Young R. T. - Science, 1979, v. 204, p. 461 - 468.
3. White C. W., Narayan T., Appleton B. R. e. a. - J. Appl. Phys. - 1979, v. 50, No 4, p.2967 -2969.
4. Osgood R. M., Sanchez R. A., Erlich D. T. e. a. - Appl. Phys. Letters, 1982, v. 40, No 5, p. 391 - 395.

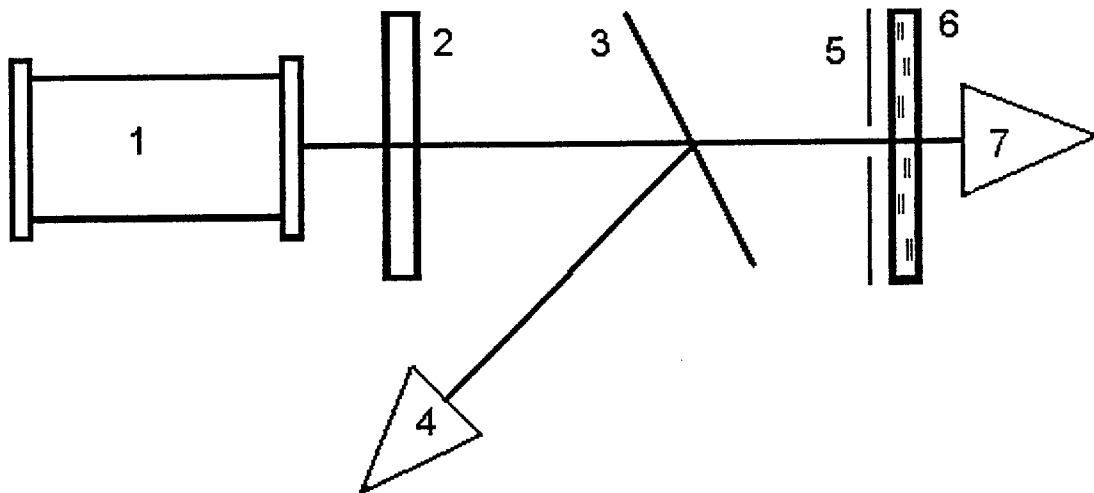


Fig. 1. Optical installation scheme for irradiation of semiconductor monocrystals by high power laser pulses

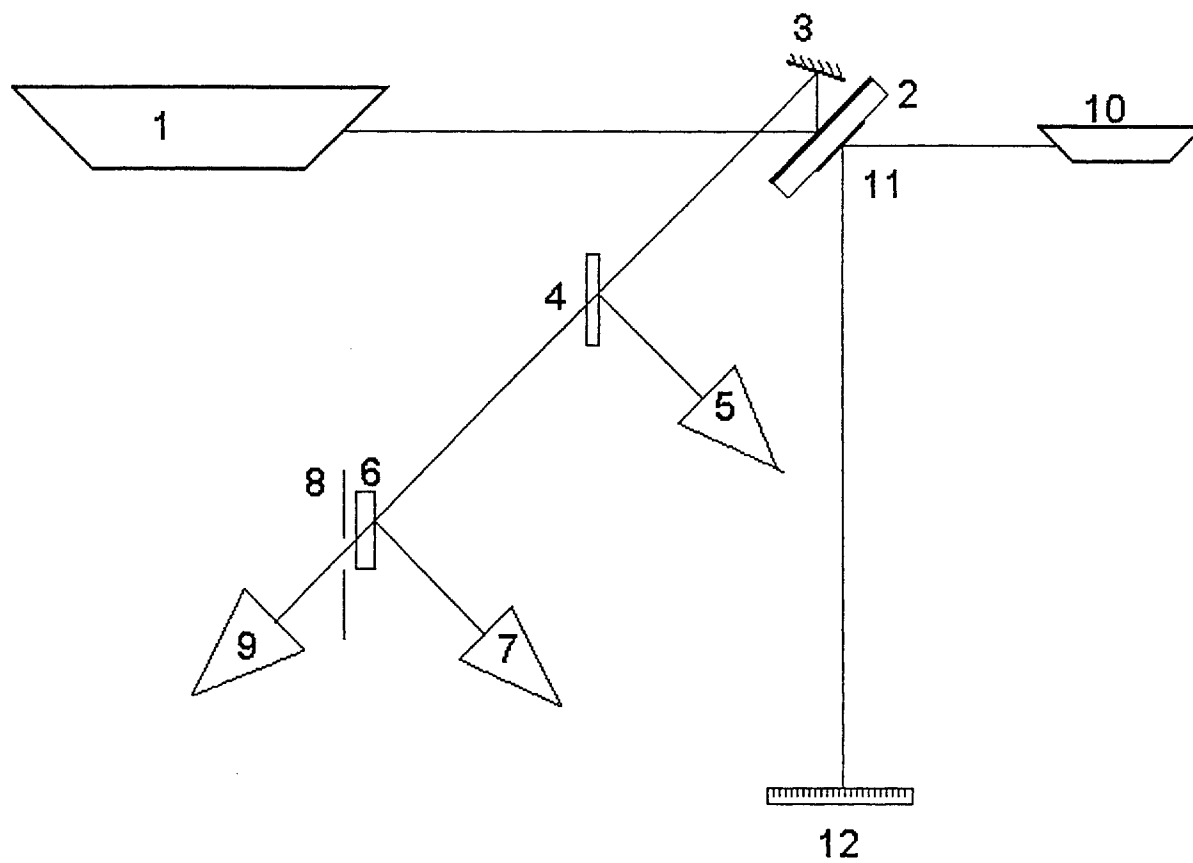


Fig. 2. Optical installation scheme on study a reflection of laser radiation from a surface of semiconductors

Fig. 3. Spectra of reflection CO₂-laser radiation from monocrystal CdS

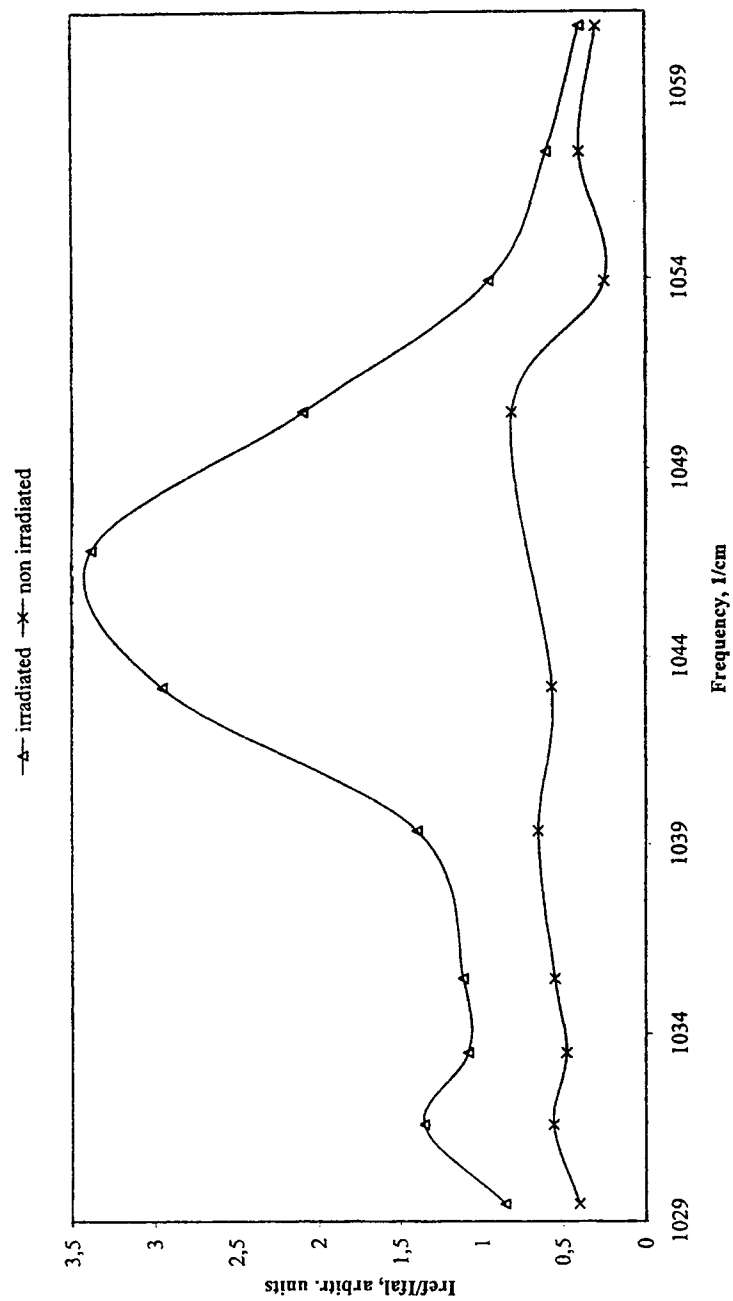


Fig. 4. Spectra of reflection CO_2 -laser radiation from monocrystal CdSe

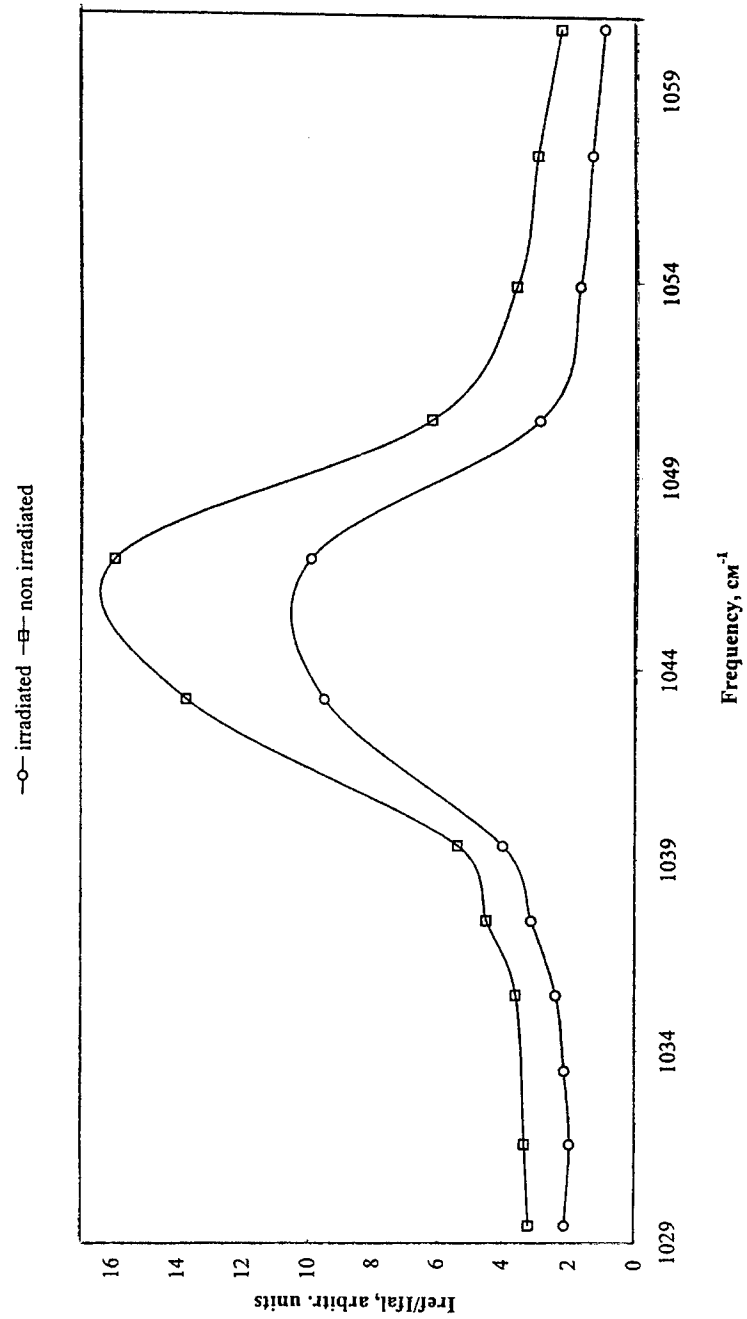
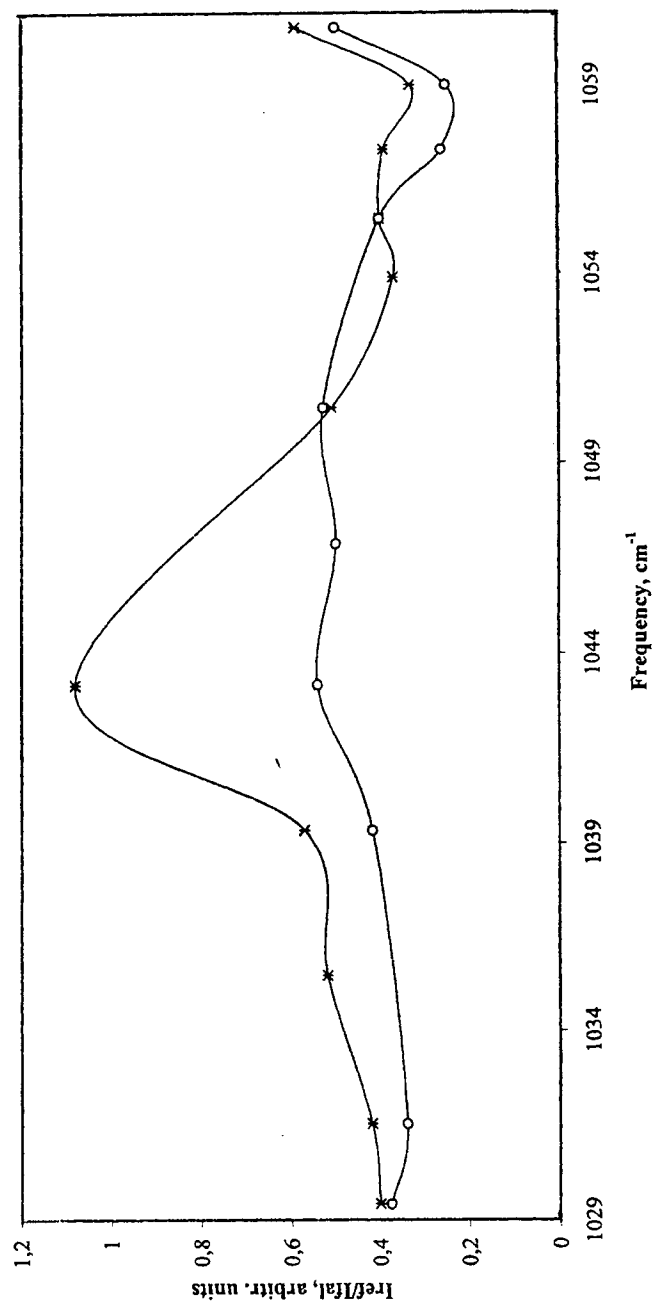


Fig. 5. Spectra of reflection CO_2 -laser radiation from etched in HCl surface
of monocrystal ZnSe-ZnS
—*— irradiated —○— non irradiated



POTENTIALS OF NEAR- AND FAR-FIELD TECHNIQUES FOR THE DETECTION OF NANOEMITTERS ON LASER ILLUMINATED SURFACE.

G.S. Zhdanov

*S.I. Vavilov State Optical Institute
12, Birzhevaya Liniya, 199034, St. Petersburg, Russia
e-mail : rendez@solaris.ru*

ABSTRACT

A simple technique for density determination of nm-sized light-emitting areas on a flat surface such as those produced by quantum dots (QDs) is proposed. The method is based on the measurements of luminescence intensity fluctuations at the center of inhomogeneously broadened spectral band from a sample illuminated through a series of masks with apertures in the 0.1 - 1 μm range. The fluctuation amplitudes depend crucially on the number of emitters involved. As shown by simulation the latter may be established with better than 100% accuracy as well as the averaged surface density. With aperture diameter as small as $\sim 0,2 \lambda$ in-depth discrimination of QDs in the aperture near-field is possible.

Keywords : quantum dots, photoluminescence, inhomogeneous broadening

I. INTRODUCTION

Considerable research efforts are aimed at mapping and characterization of nm-sized inhomogeneities in solids with optical techniques. Due to quantum confinement effect optical transitions in nano-crystallites are very sensitive to their size and shape, so that these can be spectroscopically discriminated [1]. Of particular interest are semiconductor quantum dots (QDs) which are essentially artificial "solid-state atoms" produced by controllable intermixing of two or more materials with different compositions and band structures [2,3]. The spacial confinement of electrons and holes leads to a discrete energy level structure. Resulting concentration of the oscillator strength and tunability of transition frequencies make QDs very attractive for both basic research and technological applications. On the other hand, ensemble of QDs is an ideal model in analyzing clusters of the same size but with less predictable properties.

A crucial problem in QDs spectroscopy is to separate features related to single QDs from composite spectra. Given the typical QDs surface density $n_s \sim 10^{10} \text{cm}^{-2}$ [3] the regime of single dot spectroscopy can be reached by using techniques with submicrometer spatial resolution. In recent years, considerable progress has been achieved in near-field optics, allowing resolution well below the diffraction limit [4]. In the near-field scanning optical microscope (NSOM) a tapered optical probe, usually with a small aperture at the apex, scans a specimen at a distance of several nanometers. Using NSOM in combination with high-resolution spectrometer Hess et al. [5] demonstrated a series of sharp peaks in conventionally broadened luminescence spectra of quantum wells. These peaks were attributed to one or several overlapping QDs. Surprisingly, comparable results were obtained later with much simpler far-field micro-photoluminescence (μ -PL) techniques [6-10]. Regarding the species under investigation special growth conditions for low QD density were applied, or active areas in the sub- μm range were selected by mesa etching or metal shadow masks.

The transformation of a broadened band into discrete peaks proceeds through intermediate stages with different degree of spectrum profile roughening. Recently, some simulations were reported [11,12] aimed at determination of QDs density from experimental spectra related to these stages. However, no details of the spectra treatment to obtain quantitative data were given, and the results seem to predict trends rather than absolute numbers.

In this letter we address particularly a version of μ -PL technique with extended capabilities to extract QDs density from luminescence spectra. A key feature is that instead of one several masks with aperture diameters in the 0.1-1 μm range are deposited on various parts of a flat specimen with macroscopically uniform properties. The lack of adjustment facilities compared to those of NSOM is not essentially detrimental due to statistical averaging of data. The smallest aperture size as well as in NSOM is determined by intensity limitations rather than technological reasons. A series of masks with down to 0.16 μm aperture diameter have been prepared and probed for transmission reproducibility.

The evolution of spectral band profile with the number N of QDs involved is calculated and the results are compared to simulations with each dot being responsible for one or several peaks of variable amplitudes. Intensity fluctuations at the band center are shown to be a measure of N with tens percent accuracy. Collecting spectra through different apertures provides an opportunity to observe various stages of band disintegration with the same specimen, thus making interpretation of the results more reliable. The appearance of satellite spectral lines and their effect on accuracy of QDs number measurements are discussed. In the last paragraph an issue of QDs discrimination by their position in the near-field of a subwavelength aperture is considered. With apertures approaching 0.1 μm in diameter nearly exponential decrease of luminescence intensity with QDs distance from the surface is expected.

2. ROUGHENING OF SPECTRAL BAND PROFILE : THEORY AND SIMULATION.

QD luminescence results from generation of electron-hole pairs by photons with an energy E_e followed by radiative decay of excitons and emission of photons with a different energy E . At first let us assume that just one sharp spectral line with typical FWHM (full width at half maximum) $\Gamma_{\text{hom}} \leq 100 \mu\text{eV}$ [10] may be assigned to each QD.

Luminescence band produced by a large number N of QDs which may be treated as nm-sized spheres of slightly different radii R is inhomogeneously broadened to FWHM $\Gamma_{\text{het}} \sim 1\text{-}10 \text{ meV}$ [5-7].

Following the approach [11] we may relate the broadened band intensity profile $S(E)$ to distribution functions $f(E)$ and $f(R)$

$$S(E) = A\alpha(E_e, E)f(E) = A\alpha(E_e, E)f(R)(dE/dR)^{-1} \quad (1)$$

where $\alpha(E_e, E)$ is the absorption factor; the constant A includes the quantum yield and may be chosen to satisfy normalization condition. The $E(R)$ functional dependence arises from the increase of the energy gap E_g between conduction and valence bands in a small particle compared to that E_{g0} in the bulk material

$$E_g = (\gamma/R^\nu) + E_{g0} \quad (2)$$

where $\nu \leq 2$ [1].

As seen from eqs. (1) and (2), $S(E)$ is a function of several variables which are characteristic for a particular system. Measured profiles, however, resemble each other being always bell-shaped (e.g. [5,7,11]), so that they may be approximated by normal distribution function

$$S(E) = (1/\sigma\sqrt{2\pi}) \exp[-(E-E_0)^2/2\sigma^2] \quad (3)$$

with maximum at $E = E_0$ and standard deviation σ , or

$$S(u) = (1/\sqrt{2\pi}) \exp(-u^2/2)$$

where $u = (E - E_0) / \sigma$. The Gaussian $S(E)$ plot apparently results from contributions of several independent factors. To follow the evolution of $S(E)$ with decreasing number N of QDs we have performed simulations assuming that all lines fall into the $E_0 - 3\sigma \leq E \leq E_0 + 3\sigma$ interval divided into $2m$ narrower intervals or bins of $2\Gamma_{\text{hom}}$ FWHM so that lines from two neighbour bins might be easily resolved. Experimental data for

$\Gamma_{het}, \Gamma_{hom}$ quoted above indicate that $\Gamma_{het}/\Gamma_{hom} \approx 50$ or $m=30$ is a good choice. With bin indices increasing from the center to the both sides ($j = \pm 1, \pm 2, \dots, \pm m$) the probability p_j of finding one of the equally intensive lines in the j -bin is easily obtained from eq.(3)

$$p_j = \int_{v_j}^{v_{j+1}} S(u) du = (1/2) [\text{erf}(v_{j+1}) - \text{erf}(v_j)] \quad (4)$$

where $v_j = |j|/10$ and $\text{erf}(x)$ is the error integral [13]. The scatter of measured numbers x_j of lines in each bin around the mean numbers μ_j depends on N . By distributing N lines at random among $2m$ bins weighted as p_j in eq.(4) we call "a success" falling out of a line in the j -bin and "a failure" that in any of another bins as by binominal distribution. The mean and standart deviation of the binominal distribution are given by [13]

$$\mu_j = Np_j, \quad \sigma_j = [Np_j(1-p_j)]^{1/2} \quad (5)$$

As can be seen from eq.(4), for q bins closest to the center numbers p_j differ only slightly. If, for example, $q=10$ $p_j \approx p \equiv (1/q) \sum p_j$ for any j such that $|j| \leq 5$ with an accuracy of several percent. Within this error, assuming that correlation of "successes" for any of q bins might be neglected (as by $N \rightarrow \infty$) we shall regard the measured numbers x_j of lines in q bins as a result of q successive attempts for the j -bin using the apparent relation of mean values and standart deviations for sample and parent distributions

$$\sigma_\Sigma / \langle x \rangle \approx \sigma_j / \mu_j \quad (6)$$

or, more correctly [13]

$$\langle x \rangle = \mu_j \pm (\sigma_j / \sqrt{q}), \quad \sigma_\Sigma = \sigma_j [1 \pm (1/\sqrt{2q})] \quad (7)$$

To simplify an analysis of spectra we replace σ_Σ by

$$\Delta x = x_{\max} - x_{\min} = \sigma_\Sigma \omega(q) \quad (8)$$

where x_{\max}, x_{\min} are the extremal numbers measured in any of the q bins and $\omega(q)$ can be substituted from tables[14]. Dropping indices j and combining eqs.(5)-(8) we come to the final result

$$\begin{aligned} N \pm \delta N &= [(\langle x \rangle / \Delta x) \omega(q)]^2 [(1-p)/p] [1 \pm (2/q)^{1/2}] [1 + (2/Np)^{1/2}] = \\ &= 2,43 \cdot 10^2 (\langle x \rangle / \Delta x)^2 [1 \pm 0,45 (1+7,2/\sqrt{N})] \end{aligned} \quad (9)$$

where $p=3,8 \cdot 10^{-2}, q=10, \omega(q)=3,1$.

The last step is to replace the number of lines x_j by measured intensities S_j which are assumed to increase linearly with x_j , leading to

$$(\langle x \rangle / \Delta x) \approx (S_{\max} + S_{\min}) / [2(S_{\max} - S_{\min})] \quad (10)$$

where S_{\max}, S_{\min} are the highest peak and the lowest dip near the spectrum center.

The simulated spectra for $N=2 \cdot 10^2$ and $N=1 \cdot 10^3$ are displayed in Fig.1. The predicted increase of intensity fluctuations with decreasing N is evident. To check the validity of the approach to give quantitative data we performed eight simulations with $N=2 \cdot 10^2$ and found the averaged number of dots from eqs. (9),(10) $N_{cal} = (2,6 \pm 0,5)10^2$ to be in fair agreement with the correct number as well as with expected variations $\delta N = \pm 0,7 \cdot 10^2$ and $\delta N = \pm 0,2 \cdot 10^2$ for 1 and 8 averaged spectra accordingly.

In the foregoing discussion linear increase of luminescence intensity with the number of dots irrespective of their energy was assumed with $S(E)=f(E)$ as a result. To be more realistic we should introduce weighting factor $w(E)$ so that $S(E)=w(E)f(E)$.

Since now $S(E_0) = w(E_0)f(E_0) > f(E_0)$ the number N of dots involved in the formation of the spectrum center and defined by eq.(9) appears smaller then the real number N_e . Introducing the correction factor ε we obtain

$$N_{\varepsilon} = N\varepsilon = (N/q) \sum_{j=-q/2}^{j=q/2} w(E_j) \quad , \quad \varepsilon > 1$$

Assuming that luminescence efficiency of dots increases as R^3 and substituting $v=1,5$ in eq.(2) we have estimated ε for ensemble of QDs with a typical ratio $\Delta R/R=0,1$. It is shown that maximum of $f(E)$ plot is shifted relative to E_0 by only 2-3 bins, leading to $\varepsilon \approx 1.05$, which means that the resulting effect may be neglected. In a less probable case with $\Delta R/R = 1$ N_{ε} might be several times larger than N .

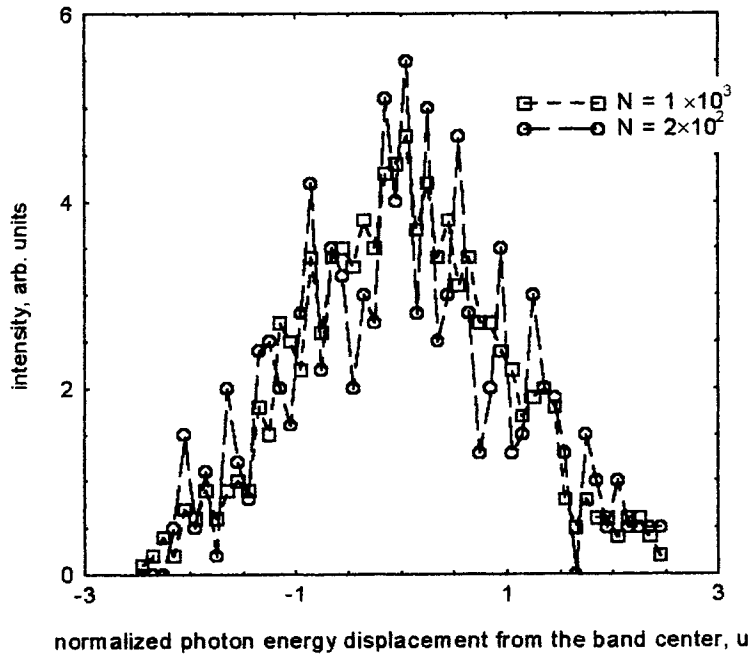


Fig.1. Simulated spectra for two different dot numbers $N=2 \cdot 10^2$ and $N=1 \cdot 10^3$. Gaussian distribution of luminescence intensity was assumed. The amplitude of fluctuations at the center was used as a measure of N . Similar intensity profiles might be expected by illuminating specimen with QDs density of $2 \cdot 10^{10} \text{ cm}^{-2}$ through apertures of $0.5 \mu\text{m}$ and $1.3 \mu\text{m}$ radii accordingly.

3. SATELLITE LINES.

With increasing excitation power transitions caused by decomposition of biexcitons and multiexciton complexes as well as by relaxation from higher excited states become more pronounced leading to appearance of a series of lines in single QDs spectra [6,10]. At first sight, the enhancement of the number of lines within a broadened band might lead to profile smoothing. In fact, this is not the case. Let the compound spectrum $S(E)$ be produced by overlapping of L unresolved bands $S_i(E)$ each corresponding to transitions at energies around E_i . Then

$$S(E) = \sum_i C_i S_i(E) \quad , \quad S(E_0) = \sum_i C_i S_i(E_i + \Delta E_i)$$

with C_i accounting for different contributions from constituents to the total intensity and $\Delta E_i = E_0 - E_i$. Assuming for simplicity C_i and $S_i(E)$ being independent on i we obtain

$$S(E_0)/S_i(E_i) = (1/L) \sum \exp [-(1/2)(\Delta E_i/\sigma_i)^2] = \eta \leq 1 \quad (11)$$

where η denotes the intensity maxima ratio and exponentials result from Gaussian $S_i(E)$ plots with σ_i as standard deviations. It follows from eqs.(3),(11) that

$$\sigma/\sigma_I = 1/\eta \geq 1$$

If bin (or pixel) width determined by Γ_{hom} is fixed and σ increases the number of lines per bin decreases so that corrected number N_{η} of QDs is given by

$$N_{\eta} = N\eta$$

where N is defined by eq. (9).

Of particular interest for QDs spectroscopy is the case when discrete lines are resolved. A crucial issue is whether all of the lines belong to a single QD or if a number of QDs are involved [5-10]. This issue might be approached by comparing spectra collected through equisized apertures from various areas.

Let us consider QDs distributed in a random way as those produced by interfacial steps [5,6]. The number \tilde{N} of observed lines is given by $\tilde{N} = LN$ where L is the average number of lines per 1 QD and N is the number of QDs which is assumed to obey Poisson distribution with mean $\langle N \rangle$ and standard deviation $\langle N \rangle^{1/2}$ [13]. For aperture radii a being the same all over the mask the scatter of measured results is defined by

$$\delta\tilde{N}/\langle\tilde{N}\rangle = \delta N/\langle N \rangle = \langle N^{-1/2} \rangle, \quad \text{while with variable } a$$

$$\delta\tilde{N}/\langle\tilde{N}\rangle = [(1/\langle N \rangle) + (2\delta a/a)^2]^{1/2} = [(L/\langle\tilde{N}\rangle) + (2\delta a/a)^2]^{1/2} \quad (12)$$

Plots of $(\delta\tilde{N}/\langle\tilde{N}\rangle)$ as a function of L from eq.(12) for $\tilde{N} = 16$ are displayed in Fig.2. Essentially, contribution of L to fluctuations of \tilde{N} drops with increase of both $(\delta a/a)$ and \tilde{N} . The most favorable conditions are offered by NSOM since all the spectra are excited or collected through the same aperture. With μ -PL techniques uncontrollable variations of aperture size are inevitable. The simplest way to probe them is to measure transmission efficiencies of various apertures in a mask. We have carried out such measurements with a series of masks containing apertures of various diameter determined by calibrated latex spheres. Typical results for apertures with nominal diameter $0.51 \mu\text{m}$ are displayed in Fig.3. Assuming transmission to increase linearly with aperture area we obtained $(\delta a/a)=0.12$. As can be seen from Fig.2 the difference in signal fluctuations for various L is expected to be 3 times smaller in this case than with $a = \text{const}$.

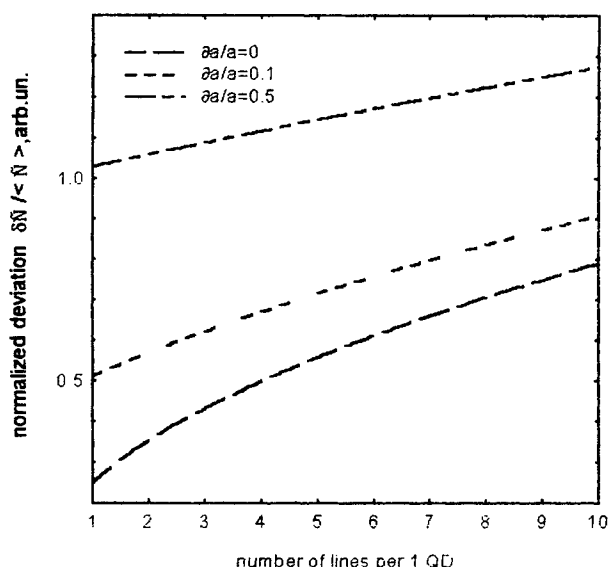


Fig.2 Normalized deviation of the measured number \tilde{N} of lines from the average $\langle\tilde{N}\rangle$ as a function of the number L of those produced by 1 QD(from eq.(12)).

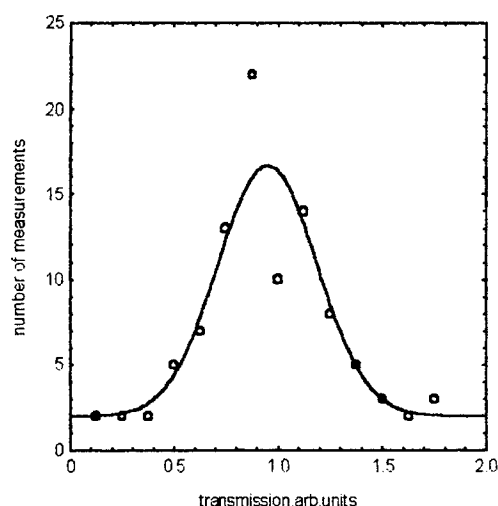


Fig.3 . Distribution of transmission efficiencies of apertures in a mask with nominal aperture diameter $0.51 \mu\text{m}$

4. NEAR- AND FAR-FIELD CONTRIBUTIONS TO EXCITATION INTENSITY.

It was tacitly assumed so far that all emission centers are positioned on the specimen surface. With increasing distance z from the surface excitation intensity decreases due to divergence of the light beam which is especially important for apertures of subwavelength dimensions. The radiation emanating from the aperture of radius $a \ll \lambda$ with λ being the excitation wavelength stays collimated in the near-field and spreads out in the far-field. The rigorous solution of the near-field problem is possible only for some special cases so that reasonable approximations are to be sought for. As shown by Bethe [15] transmission of a small aperture measured in the far-field is reduced by a factor of $\sim (ka)^2$ with $k=2\pi/\lambda$ denoting the wave number. As a result, near- and far-field constituents at $z=0$ may be sought as $I_{n0} = I_0 [1 - (\xi ka)^2]$, $I_{f0} = I_0 (\xi ka)^2$ where I_0 is the total intensity and $\xi \sim 1$ is the fitting parameter. Grober et al. [16] described the optical field generated by a small aperture as analytical expansion over a complete set of optical modes and confirmed the expected exponential decay $I_z = I_0 \exp(-z/a)$ for apertures up to $a \approx 0.1\lambda$. In the range $a < z < \lambda$ the lateral extension of field increases approximately as z .

Combining these results and assuming $\xi = 1$ we obtain for $z \leq \lambda$

$$(I_z/I_0) = [1 - (ka)^2] \exp(-z/a) + k^2 a^4 / (a+z)^2, \quad ka \leq 1 \quad (13)$$

$$(I_z/I_0) = (a/(a+z))^2, \quad ka > 1 \quad (14)$$

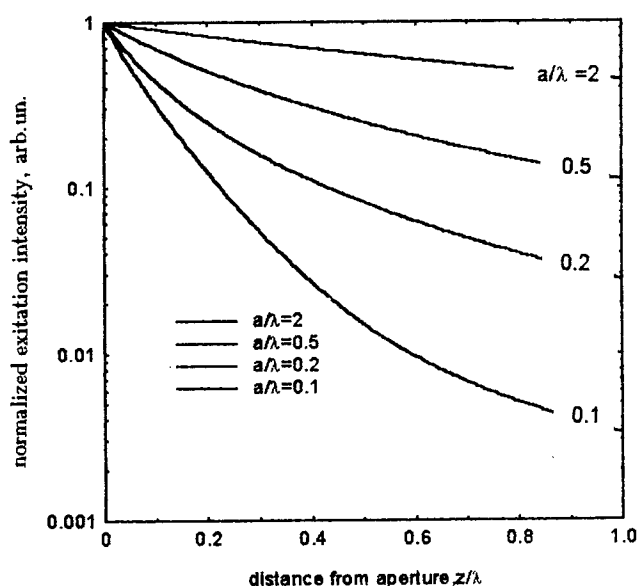


Fig.4. Normalized excitation intensity I_z/I_0 as a function of normalized distance z/λ from the aperture (from eq.(13),(14)).

Plots of I_z/I_0 as a function of z/λ according to eqs. (13), (14) are shown in Fig.4. Divergence of curves for different a/λ makes it possible to probe in-depth distribution of QDs. Essential (up to 2 orders of magnitude) discrepancy of luminescence intensities collected through different apertures from those predicted by transmission far-field measurements might be indicative that emission centers are mainly concentrated beyond the near-field range of the smallest aperture.

5.CONCLUSION.

We have considered several issues pertaining to determination of QDs density from roughening of the luminescence spectrum profile. A correlation has been established between the intensity fluctuations at the center of the inhomogeneously broadened band and the number of QDs selected by an aperture. The capability of the proposed technique to give quantitative data has been proved by simulation.

Collecting spectra through a series of masks with different aperture diameters allows one to follow successive stages of broadened band disintegration with the same specimen which is impossible with conventional NSOM techniques although aperture diameters might be comparable in both cases. On the other hand, inevitable fluctuations of aperture diameters deteriorate the reliability of data extracted from different areas in the mask if those were not statistically averaged.

With aperture radius approaching 0.1λ QDs in-depth analysis might be possible for flat specimen as in NSOM due to exponential decrease of electromagnetic field intensity with increasing distance from the aperture.

REFERENCES

1. S.Veprec, "Electronic and mechanical properties of nanocrystallites by approach to molecular dimensions", *Thin Solid Films* **297**, pp. 145-153, 1997
2. L.L.Chang, L. Esaki, "Semiconductor quantum heterostructures", *Phys.Today* **45**, pp. 36-43, 1992
3. D. Bimberg, M. Grundbaum, N.N. Ledentsov, "Quantum dot heterostructures", Wiley, Chichester, 1999
4. E.Betzig, J.K.Trautman, "Near-field optics: Microscopy, spectroscopy and surface modification beyond the diffraction limit", *Science* **257**, pp. 189-195, 1992
5. H.F.Hess, E.Betzig, T.D.Harris, L.N. Pfeifer, K.W. West, "Near-field spectroscopy of the quantum constituents of a luminescent system", *Science* **264**, pp. 1740-1745, 1994
6. K.Brunner, G.Abstreiter, G.Bohm G.Trankle, G.Weimann, "Sharp-line photoluminescence and two-photon absorption of zero-dimensional biexcitons in a GaAs/AlGaAs structure", *Phys.Rev.Lett.* **73**, pp.1138-1141, 1994
7. D.Gammon, E.S.Snow, D.S.Katzer "Excited state spectroscopy of excitons in single quantum dots", *Appl.Phys.Lett.* **67**, pp.2391-2393, 1995
8. D.Hessman, F.Castrillo, M.E.Pistol, C.Pryor, L.Samuelson, "Excited states of individual quantum dots studied by photoluminescence spectroscopy", *Appl.Phys.Lett.* **69**, pp. 749-751, 1996
9. H.Htoon, H.Yu, D.Kulik, J.W.Keto, O.Baklenov, A.L.Holmes, B.G.Streetman, C.K.Shih, "Quantum dots at the nanometer scale : Interdot carrier shuffling and multiparticle states", *Phys.Rev.B* **60**, pp. 11026-11029, 1999
10. A.Zrenner, F.Findeis, E. Beham, M. Markmann, G.Bohm, G. Abstreiter, "Spectroscopy of single self-assembled quantum dots", *J. Luminescence* **87-89**, pp.35-39, 2000
11. I.Yamakawa, M.Ichida, S.V. Sorokin, A.A. Toropov, A.N.Titkov, S.V.Ivanov, A.Nakamura, "Cathodoluminescence and photoluminescence decay behaviors of CdSe dots embedded in ZnSe", *J.Luminescence* **87-89**, pp. 384-386, 2000
12. K.Edamatsu, T.Itoh, S. Hashimoto, B.P. Zhang, Y.Segawa, "Micro-photoluminescence spectroscopy of CuCl quantum dots in thin NaCl crystals", *J.Luminescence* **87-89**, pp.387-389, 2000
13. J.R.Taylor "An introduction to error analysis", Univ.Science Books, Mill Valley, Calif., 1982
14. J.S. Milton, J.C. Arnold, " Probability and statistics in the engineering and computing sciences", McGraw-Hill, N.-Y., 1986
15. H.A.Bethe, "Theory of diffraction by small holes", *Phys.Rev.* **66**, pp. 163-182, 1944
16. R.D.Grober, T. Rutherford, T.D. Harris, " Model approximation of the electromagnetic field of a near- field optical probe", *Appl. Opt.* **35**, pp. 3488-3495, 1996

Dynamics of Subpicosecond Laser Ablation, Examined by Moments Technique

B. S. Luk'yanchuk ^{a*}, S. I. Anisimov ^b, Y. F. Lu ^a

^a Laser Microprocessing Laboratory, Data Storage Institute and Department of Electrical Engineering
National University of Singapore, Singapore 119260

^b L. D. Landau Institute for Theoretical Physics, Russian Academy of Sciences, 117940 Moscow, Russia

ABSTRACT

The interaction of subpicosecond laser pulses with metals is studied theoretically using phenomenological two-temperature model. A semi-analytical approach to a quantitative analysis of electron and lattice temperatures is presented. Using the nonstationary averaging technique (moment's technique) the coupled system of nonlinear heat equations for electron and lattice temperatures is transformed into the set of four ordinary differential equations. Resulting system is convenient for the fast analysis of nonstationary laser heating and laser ablation with ultrashort laser pulses.

Keywords: subpicosecond laser ablation, two-temperature model, moment's technique

1. INTRODUCTION

Femtosecond laser ablation is attractive for micromachining applications [1, 2]. Meanwhile, the mechanisms, which eventually lead to material removal, are still under discussions and a complete understanding of the involved phenomena is lacking. The problem contains a number of essential peculiarities related to energy absorption, specific optical and thermodynamic properties of the solid, electron-phonon coupling, ejection mechanism, and the plume expansion dynamics. With femtosecond ablation of metals the basic problem refers to electron-phonon interaction and hot electron phenomena in condensed matter. The basic idea of the transient nonequilibrium phenomena in electron gas and lattice was suggested more than 30 years ago [3-5]. Nevertheless the direct measurements of necessary characteristics with femtosecond temporal resolution are very difficult [6-10]. Thus, reasonable analysis of physical mechanisms involved in femtosecond laser ablation should be done on the basis of theoretical analysis of experimental data.

Recently the dynamics of the electron-phonon coupling were studied on the basis of the kinetic equation [11]. This study confirms the basic ideas of two-temperature model and permits to calculate the electron-phonon coupling constant and some other characteristics through the microscopic characteristics of metals. Thus, models become more and more detailed and numerical calculations call for more and more powerful computers.

At the same time, to analyze numerous effects in subpicosecond laser ablation it is useful to develop semianalytical method of "intermediate power", which should be flexible, applicable for the quantitative analysis of experimental data and using a PC. In fact, a similar problem is actual for nanosecond laser ablation, where reliable analysis was recently developed on the basis of the nonstationary averaging (moments technique) to solve the nonlinear heat equation [12-14]. This model was applied to different materials, including metals and polymers. This model permitted, for example, to solve the problem, related to the mechanism of UV laser ablation of polyimide, which was the subject of many speculations. Calculations clearly show that the ablation at 248, 308 and 351 nm wavelengths is purely thermal (with common activation energy 1.55 eV), while for the ablation with 193 nm experimental results strongly deviate from the thermal model [12]. A similar effect was found for laser ablation of metals with respect to laser pulse duration. With nanosecond laser pulses ablation of indium follows satisfactorily to purely thermal mechanism, while for subpicosecond pulses experimental results deviate from purely thermal [13]. We believe that the deviations are related to electron-phonon coupling effect.

The main motivation for the present paper was to develop a similar moment's technique to solve the nonstationary two-temperature phenomenological model.

* Corresponding author: boris@dsi.nus.edu.sg. On leave Wave Research Center at General Physics Institute of Russian Academy of Sciences, 117942 Moscow, Russia, lukyanch@kapella.gpi.ru

2. The two-temperature model.

The two-temperature model describes the energy transport inside a metal through two coupled equations for the electron temperature T_e and the lattice (phonon) temperature T_i :

$$c_e \frac{\partial T_e}{\partial t} = c_e v \frac{\partial T_e}{\partial z} + \frac{\partial}{\partial z} \left(\kappa_e \frac{\partial T_e}{\partial z} \right) + Q - \mu (T_e - T_i), \quad (1)$$

$$c_i \frac{\partial T_i}{\partial t} = c_i v \frac{\partial T_i}{\partial z} + \frac{\partial}{\partial z} \left(\kappa_i \frac{\partial T_i}{\partial z} \right) + \mu (T_e - T_i), \quad (2)$$

where c_e and c_i are the volumetric heat capacities [J/cm³ K] of electrons and lattice, respectively. The parameters κ_e and κ_i are the electron and lattice heat conductivities, the parameter $\mu = c_e / \tau$, related to the electron-phonon coupling constant, describes the energy exchange rate [W/cm³ K] between the electron and lattice subsystems (τ is characteristic time for electron cooling). The heat source term Q describes the energy release in the electron subsystem:

$$Q = -\frac{\partial I}{\partial z} = \alpha I, \quad I(0, t) = I_s(t), \quad (3)$$

where α is absorption coefficient and I_s is the value of the absorbed intensity on the surface of metal (at $z = 0$). The value of $I_s(t) = I(t) A$ depends on laser pulse shape $I(t)$ and the surface absorptivity $A = 1 - R$ (here R is the reflectivity). For the ultrashort laser pulse the plasma-vapor plume does not influence the absorption of laser radiation. We consider the smooth pulse shape in the following form

$$I(t) = I_0 \frac{t}{t_\ell} \exp\left(-\frac{t}{t_\ell}\right). \quad (4)$$

The laser fluence is given by $\Phi = I_0 t_\ell$ and pulse duration at the full width at half maximum is $t_p \approx 2.446 t_\ell$.

The heat equations (1) and (2) are written in the reference frame fixed with the ablation front, $v = v(t)$ is the ablation rate changing during the pulse and after pulse end. This definition is slightly different from the standard definition of two-temperature model (e.g. [15, 16]), where some small terms in (1), (2) are omitted. Nevertheless we will use this form, because it is convenient for the further analysis.

One should define the boundary conditions. Two of them present fluxes of the energies on the surface $z = 0$:

$$-\kappa_e \frac{\partial T_e}{\partial z} \Big|_{z=0} = J_e, \quad (5)$$

where

$$J_e = -b_0 (T_\infty + T_{es})^2 \exp\left[-\frac{T_u}{T_\infty + T_{es}}\right], \quad (\text{Richardson law}), \quad (6)$$

and the heat flux caused by the ablation

$$-\kappa_i \frac{\partial T_i}{\partial z} \Big|_{z=0} = J_i = -\rho v L, \quad (7)$$

where L is the latent heat of evaporation, ρ is the density of a solid, $T_\infty = 300$ K is the initial temperature.

Two other boundary conditions (at $z = \infty$) and the initial conditions (at $t = 0$) are trivial:

$$T_e \Big|_{z=\infty} = T_i \Big|_{z=\infty} = T_e \Big|_{t=0} = T_i \Big|_{t=0} = 0. \quad (8)$$

We shall use additional index "s" to indicate temperatures at the surface $z = 0$, i.e. $T_e \Big|_{z=0} = T_{es}$, $T_i \Big|_{z=0} = T_{is}$. The value T_{es} enters into the Richardson law (6), while the quantity T_{is} defines the ablation rate

$$v = v_0 \cdot \exp\left[-\frac{T_a}{T_\infty + T_{is}}\right]. \quad (9)$$

To provide the model, which permits to analyze experimental data, one should take into account the temperature dependencies of the coefficients $c_e, c_i, \kappa_e, \kappa_i, A, \alpha$ and μ . For example, the electronic heat capacity varies linearly with electronic temperature, $c_e = \beta T_e$. Although lattice heat capacity c_i is practically constant above the Debye temperature T_D , nevertheless one can include into the value latent heat of fusion or any other phase transition, thus, the effective value of c_i depends on the lattice temperature T_i (and T_e for the case of nonequilibrium phase transition). The same refers to the electron thermal conductivity κ_e , which depends on both temperatures T_e and T_i [10, 16]. The reflectivity R and absorption coefficient α also depend, in general, on both temperatures T_e and T_i . In semiconductors R varies linearly with electronic temperature T_e [10].

At least a part of these temperature dependent parameters can be treated by the moment's technique the same way as in [12-14]. Nevertheless we start with the simplest analysis where we consider all the coefficients as constants. This permits us to examine the problem of coupled equations by moment's technique. The important part of the analysis is to outline the so called "fast" and "slow" variables. The "fast" variables can be adiabatically excluded which leads to simplification of the resulting system of the ordinary differential equations. This model permits to analyze the qualitative role of different parameters, which is important for the preliminary analysis of experimental data.

In conclusion, one should say that the two-temperature model (1), (2) is derived under the assumption that the classical Fourier law describes the electron and phonon energy transports. It is applicable for times, which are longer than characteristic relaxation time τ_e within the electron gas. This time depends on the electronic temperature (i.e. the laser fluence). It typically comprises a few hundred fs [10]. In turn, the assumption, related to diffusional transport of electronic energy in (1) assumes that characteristic variations of the electronic temperature arise in the spatial scales larger than the electron mean free part ℓ_e . For shorter scales the electron transport is "mostly ballistic". The value $\ell_e \approx v_F \tau_e$ (v_F is the Fermi velocity of electrons) varies through the order of magnitude for different metals. For example, for Ni ℓ_e comprises a few tens of nm, while for Au its comprises a few hundred nm [17, 18].

When the relaxation time, τ , tends to zero ($\mu \rightarrow \infty$), the two-temperature model (1), (2) transfers into the conventional model of thermal evaporation [4] with a common temperature of solid $T = T_i \equiv T_e$:

$$c \frac{\partial T}{\partial t} = c v \frac{\partial T}{\partial z} + \frac{\partial}{\partial z} \left(\kappa \frac{\partial T}{\partial z} \right) + Q, \quad (10)$$

The values $c = c_e + c_i$ and $\kappa = \kappa_e + \kappa_i$ present the total heat capacity and heat conductivity of the solid.

3. Stationary evaporation wave in two-temperature model.

Before starting the examination of dynamic regimes of heating and ablation we have to analyze the stationary ablation regime with constant intensity, $I_s = \text{const}$. It corresponds to the situation, where the time derivatives in the left-hand side of equations (1) and (2) are identically equal to zero. Stationary evaporation wave presents a solution, which is attractor of the problem. Thus, this solution is important for general behavior of the problem.

We search for the stationary temperature distributions $T_e(z)$ and $T_i(z)$ in the following form:

$$T_e = T_{e1} e^{-p_1 z} - \frac{\alpha T_{es} + (p_1 - \alpha) T_{e1} - J_e / \kappa_e}{p_2 - \alpha} e^{-p_2 z} + \frac{p_2 T_{es} - (p_2 - p_1) T_{e1} - J_e / \kappa_e}{p_2 - \alpha} e^{-\alpha z}, \quad (11)$$

$$T_i = T_{i1} e^{-p_1 z} - \frac{\alpha T_{is} + (p_1 - \alpha) T_{i1} - J_i / \kappa_i}{p_2 - \alpha} e^{-p_2 z} + \frac{p_2 T_{is} - (p_2 - p_1) T_{i1} - J_i / \kappa_i}{p_2 - \alpha} e^{-\alpha z}. \quad (12)$$

where $T_{es} = T_e|_{z=0}$ and $T_{is} = T_i|_{z=0}$ are the surface temperatures, and the values T_{e1} and T_{i1} are some unknown characteristic temperatures. Distributions (11), (12) automatically fulfil the boundary conditions at $z = 0$ and $z = \infty$.

Substituting (11) and (12) into the heat equations one can find equations for unknown quantities. Characteristic exponents $p_1 = 1/\ell_1$ and $p_2 = 1/\ell_2$ are the roots of dispersion equation:

$$\Pi(p) \equiv a_3 p^3 - a_2 p^2 + a_1 p + a_0 = 0, \quad p = 1/\ell, \quad (13)$$

where

$$a_3 = \kappa_e \kappa_i, \quad a_2 = (c_i \kappa_e + c_e \kappa_i) v, \quad a_1 = c_e c_i v^2 - \mu (\kappa_e + \kappa_i), \quad a_0 = (c_e + c_i) v \mu.$$

Two roots of cubic equation (13) with positive real parts are used as p_1 and p_2 . In the paper [16] the equivalent dispersion equation has been written in a slightly different form (some terms are considered to be small and thus omitted). To demonstrate the behavior of the roots we use a set of parameters, typical for metals (for example, Al [19]). This set of parameters is presented in Table 1.

Table 1. Parameters, which had been used in calculations

Parameter	Value
Heat capacity c_e (electronic), [J/cm ³ K]	0.04035
Heat capacity c_i (lattice), [J/cm ³ K]	2.43
Heat conductivity κ_e (electronic), [W/cm K]	2.37
Heat conductivity κ_i (lattice), [W/cm K]	1
Time τ , ($\mu = c_e \tau$) [ps]	1
Density ρ , [g/cm ³]	2.688
Latent heat of evaporation L , [J/g K]	10860
Preexponent v_0 in (9), [cm/s]	414000
Activation energy T_a in (9), [K]	35240
Work function T_u in (6), [K]	49300
Richardson constant b_0 in (6) [W/cm ² K ²]	120.4
Initial temperature T_∞ , [K]	300
Absorption coefficient α , [cm ⁻¹]	$1.516 \cdot 10^5$
Absorptivity A	1

The biggest root $p_1 = 1/\ell_1$ (for given set of parameters it is real and positive) is presented by G. Cardano formula

$$p_1 = \frac{1}{3a_3} \left[a_2 + \left(\frac{g + \sqrt{g^2 + 4b^3}}{2} \right)^{1/3} - b \left(\frac{2}{g + \sqrt{g^2 + 4b^3}} \right)^{1/3} \right], \quad (14)$$

where

$$g = 2a_2^3 - 9a_1a_2a_3 - 27a_0a_3^2, \quad b = 3a_1a_3 - a_2^2.$$

Two other roots of dispersion equation (13), which contain the factors $1 \pm i\sqrt{3}$, are also real for the given set of parameters. One root is positive and another is negative. The positive root $p_2 = 1/\ell_2$ is defined as

$$p_2 = \frac{1}{3a_3} \left[a_2 - \frac{1+i\sqrt{3}}{2} \left(\frac{g + \sqrt{g^2 + 4b^3}}{2} \right)^{1/3} + b \frac{1-i\sqrt{3}}{2} \left(\frac{2}{g + \sqrt{g^2 + 4b^3}} \right)^{1/3} \right]. \quad (15)$$

These roots obey the relations $p_1 \gg p_2 > 0$.

According to (13) the roots of equation (13) depend on one variable parameter, ν (or parameter T_{es} in accordance with equation (9)). In Fig. 1 the inverse values ℓ_1 and ℓ_2 are shown as functions of the ablation rate, ν and the surface lattice temperature T_{es} .

With relaxation time, τ , tends to zero ($\mu \rightarrow \infty$) one can find that the root ℓ_1 also tends to zero, while the root ℓ_2 tends to limited value, which corresponds to thermal length in conventional surface evaporation model:

$$\ell_1|_{\mu \rightarrow \infty} \approx \frac{1}{\sqrt{\mu}} \sqrt{\frac{\kappa_e + \kappa_i}{\kappa_e \kappa_i}} \rightarrow 0, \quad \ell_2|_{\mu \rightarrow \infty} = \frac{\chi}{\nu}, \quad (16)$$

where $\chi = \frac{\kappa_e + \kappa_i}{c_e + c_i}$ is the heat diffusivity of a solid. Thus, one can say that the length ℓ_2 is the characteristic thermal penetration depth, while the length ℓ_1 controls the electronic temperature distribution near the surface.

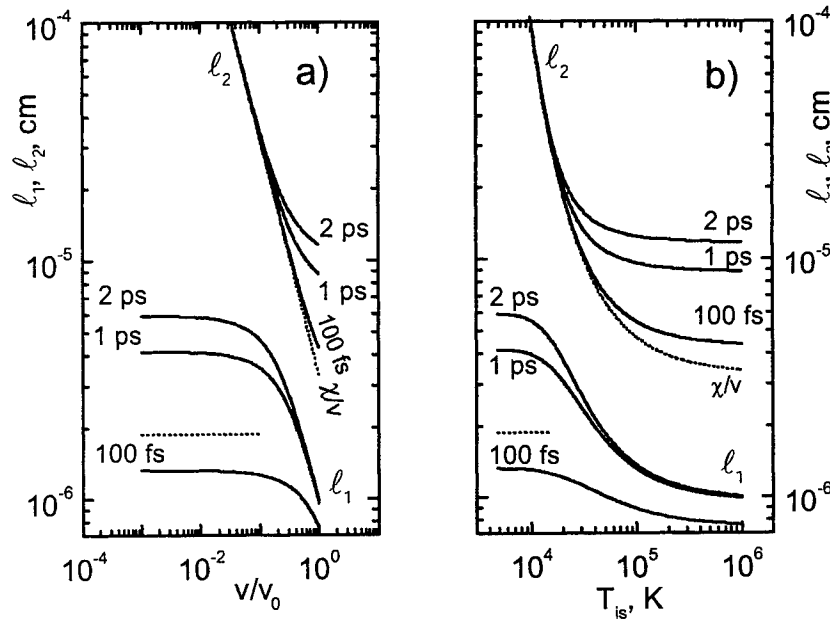


Fig. 1. Characteristic lengths ℓ_1 and ℓ_2 are shown as functions of the ablation rate, ν (a) and the surface lattice temperature T_{es} (b). The parameters, which have been used in calculations, are given in Table 1. The curves are presented for three different values of relaxation time $\tau = 2$ ps, 1 ps and 100 fs. Asymptotic values (16) are shown by dot lines (ℓ_1 calculate for $\tau = 100$ fs). One can see that with small temperatures ℓ_2 is close to their asymptotic "thermal" value, while ℓ_1 is practically constant.

If one introduce, for brevity, coefficients a_i and b_i in distributions (11), (12):

$$T_e(z) = a_1 \exp\left[-\frac{z}{\ell_1}\right] + a_2 \exp\left[-\frac{z}{\ell_2}\right] + a_q \exp[-\alpha z], \quad (17)$$

$$T_i(z) = b_1 \exp\left[-\frac{z}{\ell_1}\right] + b_2 \exp\left[-\frac{z}{\ell_2}\right] + b_q \exp[-\alpha z]. \quad (18)$$

then unknown coefficients a_i and b_i can be found from algebraic equations. For example:

$$a_q = -q \frac{c_e \nu \alpha - \alpha^2 \kappa_i + \mu}{\Pi(\alpha)}, \quad b_q = -q \frac{\mu}{\Pi(\alpha)}, \quad (19)$$

where $\Pi(\alpha) = a_3 \alpha^3 - a_2 \alpha^2 + a_1 \alpha + a_0$.

In Fig. 2 the different characteristics are shown as a function of laser intensity, I_s . Calculations are performed for relaxation time $\tau = 1$ ps and parameters, given in Table 1.

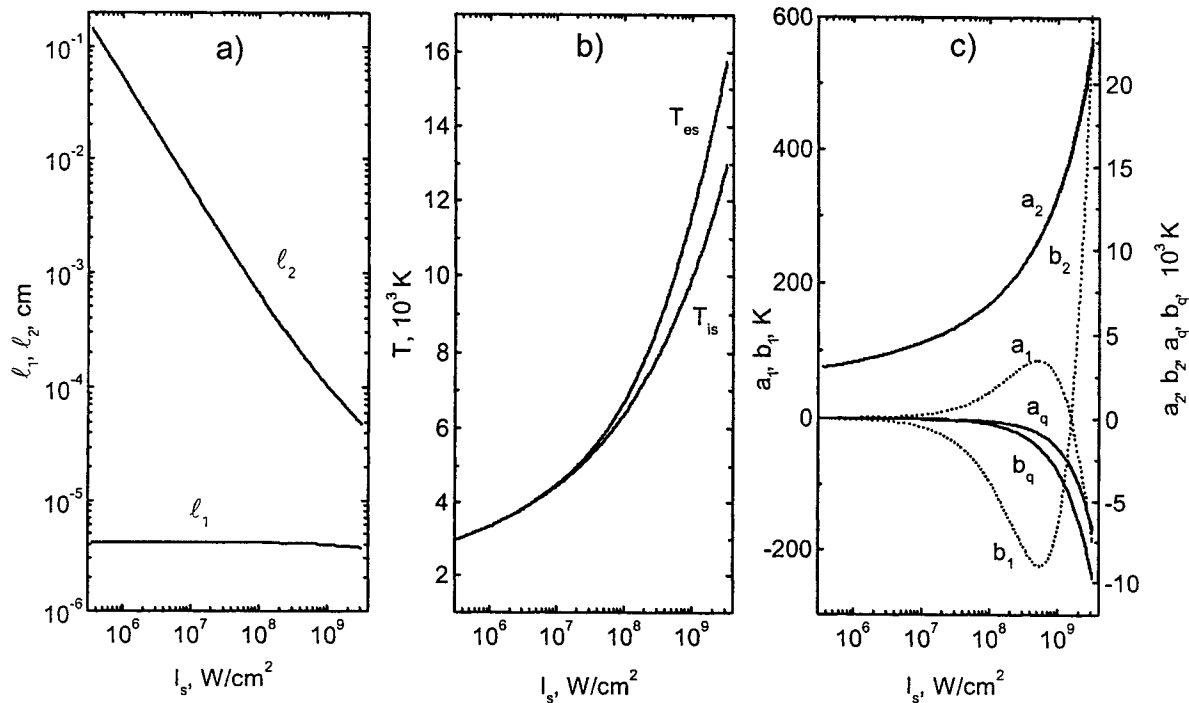


Fig. 2. Different parameters of stationary evaporation wave as functions of laser intensity: a) characteristic lengths ℓ_1 and ℓ_2 ; b) surface temperatures T_{es} and T_{is} ; c) coefficients a_i and b_i in formulae (17), (18) (a_1 and b_1 are shown by dots – left scale). $a_2 > b_2$, but in the scale of the figure they practically coincide.

The typical stationary temperature distributions versus z coordinate are shown in Fig. 3. One can see from Fig. 3 and Fig. 2b that with increase of the intensity the electronic temperature breaks away the lattice temperature. The qualitative variation occurs at intensity $I_s > I_{crit}$, where the coefficients a_1 and b_1 change signs. At $I_s > I_{crit}$ the flux $J_i > J_e$ (see Fig. 4), which means that the heat losses at the surface are caused mainly by latent heat of evaporation. At $I_s > I_{crit}$ the situation is opposite, cooling of the surface is caused by the emission of electrons. For the given example $I_{crit} \approx 1.5 \cdot 10^9 \text{ W/cm}^2$.

In the given examples surface electron temperature everywhere is higher, than the lattice temperature, thus, the stationary ablation is accompanied by nonequilibrium emission of hot electrons. This phenomena is much more pronounced in nonstationary processes with short (ps) laser pulses [20, 21] or even ultrashort (fs) laser pulses, where non-thermalized electron gas may be observed [6-9].

Calculations show that at some set of parameters one can find a situation, where the surface electron temperature is lower than the lattice temperature, although inside the material one has a conventional situation with "hot electrons".

One can see from the stationary solution, that the terms proportional to $\exp[-z/\ell_1]$ do not play an important role in temperature distributions. The corresponding amplitudes a_1 and b_1 are typically two orders of magnitude lower than characteristic surface temperatures T_{es} and T_{is} (see in Fig. 2). The role of these terms is important for the values of the surface gradient of the temperatures. At the same time too big gradients are damped due to ballistic electron transport.

Thus, during the analysis of non-stationary heating, we neglect the effects, which lead to big gradients at the scale $z < \ell_1 \ll \alpha^{-1}$ (it is, typically, $z \approx 100 - 300 \text{ \AA}$). Careful treatment of this scale needs for the model modification, destined for the inclusion of ballistic transport of electrons.

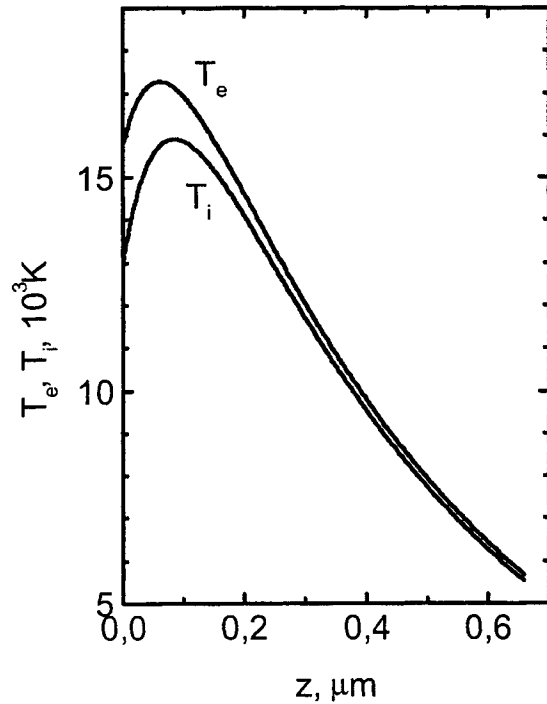


Fig. 3. Stationary temperature distributions versus z coordinate for the parameters, given in Table 1 and $I_s = 3.2 \cdot 10^9 \text{ W/cm}^2$.

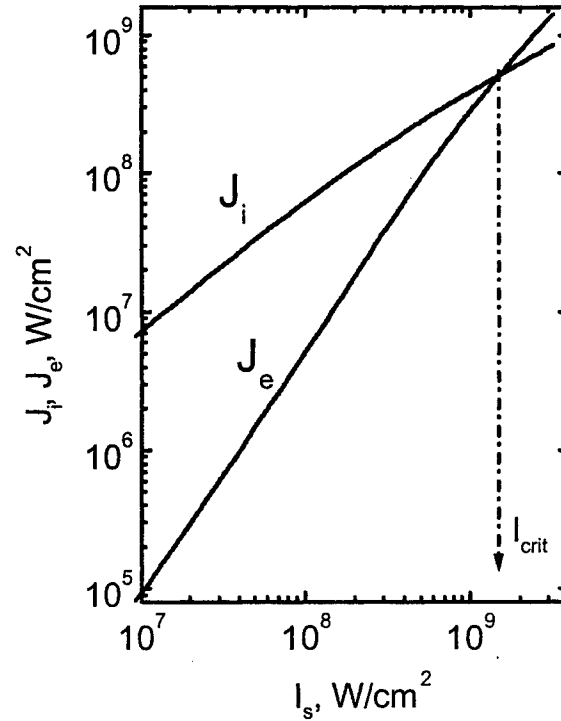


Fig. 4. Fluxes of energy, J_e and J_i (see (6), (7)), versus laser radiation intensity I_s . $I_{\text{crit}} \approx 1.5 \cdot 10^9 \text{ W/cm}^2$.

4. Application of the moment's technique to solve the two-temperature model.

The main problem, related to the non-stationary effects in laser heating and ablation with ultrashort laser pulse, is a great difference between the characteristic times of heating of electrons and lattice. Thus, ablation, typically, starts when the laser pulse is finished. In the time scale comparable with the laser pulse duration and characteristic time of electron cooling two-temperature model can be simplified, namely, the terms $\nu \nabla T_{e,i}$, related to ablation, can be omitted. If one additionally neglects the phonon component of the thermal conductivity, then, simplified two-temperature model is reduced to [15]:

$$c_e \frac{\partial T_e}{\partial t} = \frac{\partial}{\partial z} \left(\kappa_e \frac{\partial T_e}{\partial z} \right) + Q - \mu (T_e - T_i), \quad (20)$$

$$c_i \frac{\partial T_i}{\partial t} = \mu (T_e - T_i). \quad (21)$$

In fact, both the qualitative examination [15] and numerical calculations [6, 7, 22] were performed for simplified model (20), (21). Meanwhile to examine laser ablation one should take into account omitted terms $\nu \nabla T_{e,i}$. It leads to the necessity of solving non-stationary two-temperature model (1), (2), which, in turn, needs large calculation time. Thus, late stage of the process was not satisfactorily theoretically examined.

At the same time, it can be done using the non-stationary averaging technique (principles of this technique see e.g. [23, 24]). This technique is close to Galerkin technique, nevertheless it has some physical advantages. Namely, the moments can be chosen in such a way that corresponding differential equations express some conservation laws [12]. Practical

examples of this technique to solve different problems are presented in [24, 25]. Recently, the nanosecond laser ablation was treated successfully by this method [12-14].

An important part of the moment's technique is to choose the trial solution in a "good form". Here we set the trial solution for the temperatures $T_e(z, t)$ and $T_i(z, t)$ in the following form:

$$T_e = \frac{1}{1 - \alpha \ell_e} \left[\left(T_{es} - \frac{\ell_e}{\kappa_e} J_e \right) e^{-\alpha z} - \left(T_{es} \alpha \ell_e - \frac{\ell_e}{\kappa_e} J_e \right) e^{-z/\ell_e} \right], \quad (22)$$

$$T_i = \frac{1}{1 - \alpha \ell_i} \left[\left(T_{is} - \frac{\ell_i}{\kappa_i} J_i \right) e^{-\alpha z} - \left(T_{is} \alpha \ell_i - \frac{\ell_i}{\kappa_i} J_i \right) e^{-z/\ell_i} \right]. \quad (23)$$

This form satisfies boundary conditions (5)-(8) at $z = 0$ and $z = \infty$. Trial solutions (22), (23) contain four unknown functions: two characteristic surface temperatures $T_{es}(t)$, $T_{is}(t)$, and two characteristic lengths $\ell_e(t)$, $\ell_i(t)$. In fact, more detailed consideration should include additional exponents and preexponential terms to obtain correct transfer to the stationary solutions (11), (12). Nevertheless we omitted these terms by the reasons discussed above.

According to the method, we introduce four moments of the electronic and lattice temperatures:

$$M_0 = \int_0^\infty T_e dz, \quad M_1 = \int_0^\infty T_e z dz, \quad (24)$$

$$N_0 = \int_0^\infty T_i dz, \quad N_1 = \int_0^\infty T_i z dz. \quad (25)$$

Integrating (1) and (2), one can easily find four ordinary differential equations for the moments:

$$\begin{aligned} c_e \frac{dM_0}{dt} &= -c_e v T_{es} + J_e + I_s - \mu (M_0 - N_0), \\ c_e \frac{dM_1}{dt} &= -c_e v M_0 + \kappa_e T_{es} + \frac{I_s}{\alpha} - \mu (M_1 - N_1), \end{aligned} \quad (26)$$

$$\begin{aligned} c_i \frac{dN_0}{dt} &= -c_i v T_{is} + J_i + \mu (M_0 - N_0), \\ c_i \frac{dN_1}{dt} &= -c_i v N_0 + \kappa_i T_{is} + \mu (M_1 - N_1). \end{aligned} \quad (27)$$

The further work is just to substitute (22), (23) into (23)-(27) to find the differential equations for unknown quantities $T_{es}(t)$, $T_{is}(t)$ and $\ell_e(t)$, $\ell_i(t)$. Because the fluxes J_e and J_i depend on corresponding surface temperatures (see (6), (7), (9)), the resulting equations lead to the bulky mathematical formulas. Nevertheless, the advantage of high level software like "Mathematica" [26], permits to formulate problem for computer calculations directly in the initial form (22)-(27). Integration of the resulting equations can be done very fast, all the pictures below were calculated approximately for a few second with PC Pentium 300 MHz.

In Fig. 5 dynamics of laser heating is shown for the laser pulse with the shape, given by formula (4) with the pulse duration $t_p = 1$ ps, and laser fluence $\Phi = 0.15$ J/cm². Other parameters are given in Table 1. One can see in the figure that the electronic temperature T_e breaks away from the lattice temperature during the laser pulse. The electron temperature reaches its maximum at $t = 1.8$ ps. The characteristic time of heating of the phonon subsystem is approximately $c_i / \mu \gg c_e / \mu = \tau$. In the given example the maximum of the phonon temperature is reached at $t \approx 27.2$ ps. The characteristic scales ℓ_e and ℓ_i increase with time approximately as $\propto \sqrt{t}$. At large time the difference between ℓ_e and ℓ_i becomes negligible. However, at $t \approx 100$ ps $\ell_e > \ell_i$ since $\kappa_e > \kappa_i$.

In Fig. 6 the fluxes of electrons and heavy particles are presented. One can see that each flux reaches its maximum at the maximum of corresponding temperature. In Fig. 7 we present the maximal temperatures of electrons and lattice as functions of laser fluence for laser pulse with $t_p = 1$ ps.

We see thus, that the moment's method gives the results that agree with other methods. Note, however, that the moments method permits to continue calculation to great times that is important for the analysis of ablation since this process is completed typically in nanosecond time scale. It can be seen from Fig. 8 where the thickness of ablated material is shown as a function of time. Finally, the total thickness of the ablated material versus laser fluence is shown in Fig. 9.

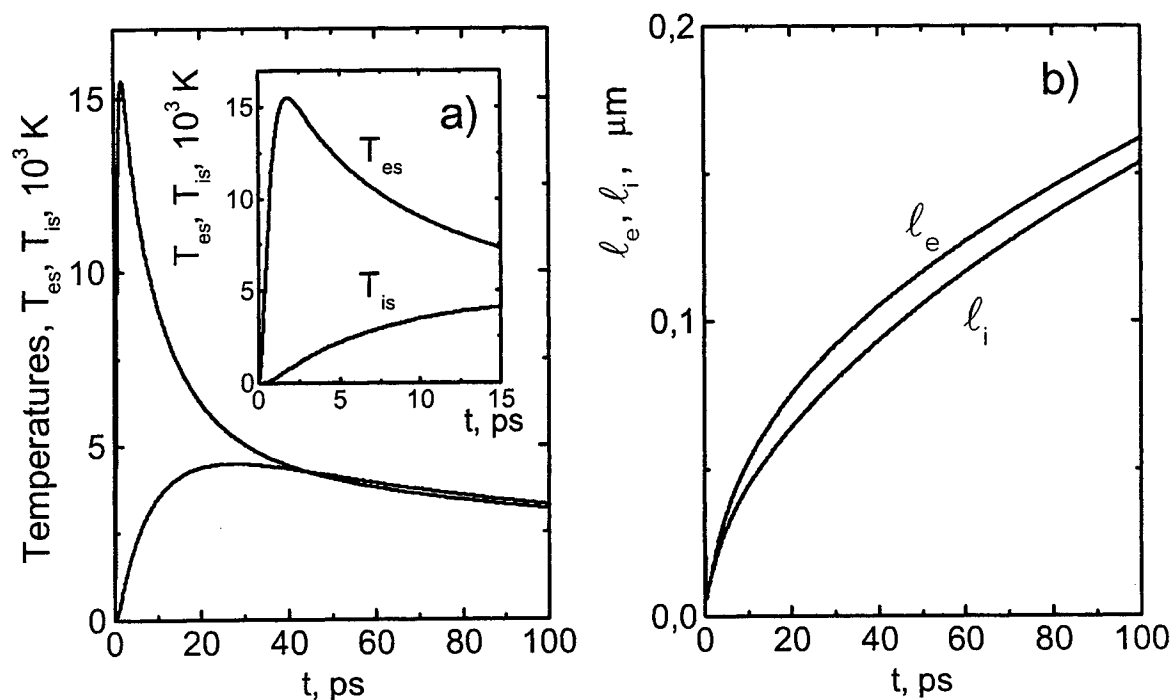


Fig. 5. Dynamics of laser heating with the pulse duration $t_p = 1$ ps, and laser fluence $\Phi = 0.15$ J/cm². a) The surface temperatures T_{es} and T_{is} . Insertion shows the initial stage of the process. b) The characteristic lengths $\ell_e(t), \ell_i(t)$ for electronic and phonon temperature distributions.

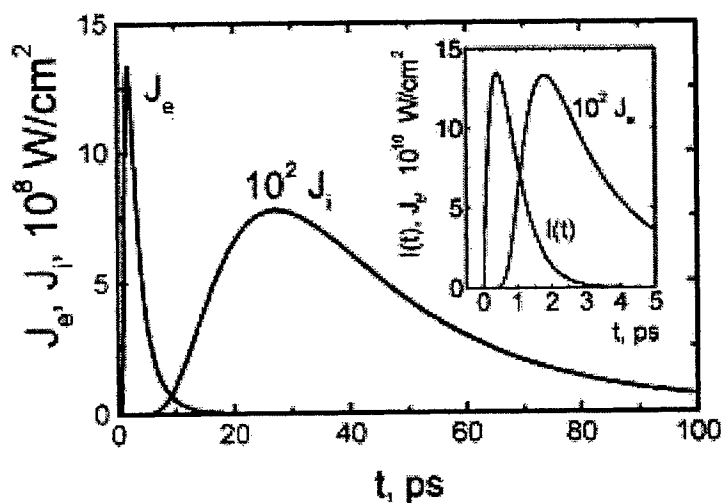


Fig. 6. The fluxes of electrons and heavy particles for laser heating with the pulse duration $t_p = 1$ ps, and laser fluence $\Phi = 0.15$ J/cm². The insertion presents the pulse shape and the electron's flux.

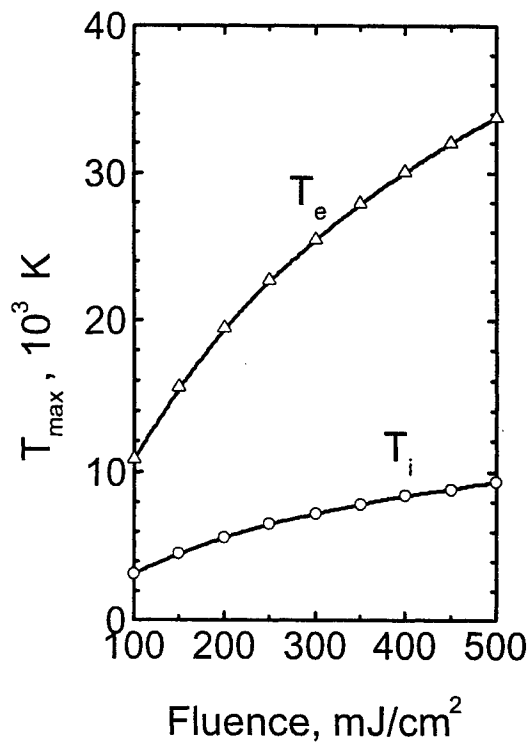


Fig. 7. The maximal temperatures of electrons and lattice as functions of laser fluence for laser pulse with $t_p = 1$ ps. Parameters are given in Table 1.

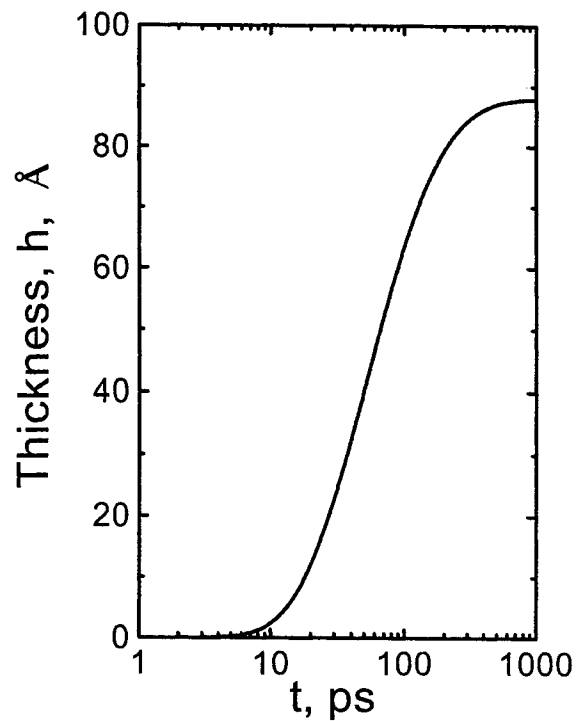


Fig. 8. Dynamics of laser ablation for laser pulse with $t_p = 1$ ps and fluence $\Phi = 500$ mJ/cm². Other parameters are given in Table 1.

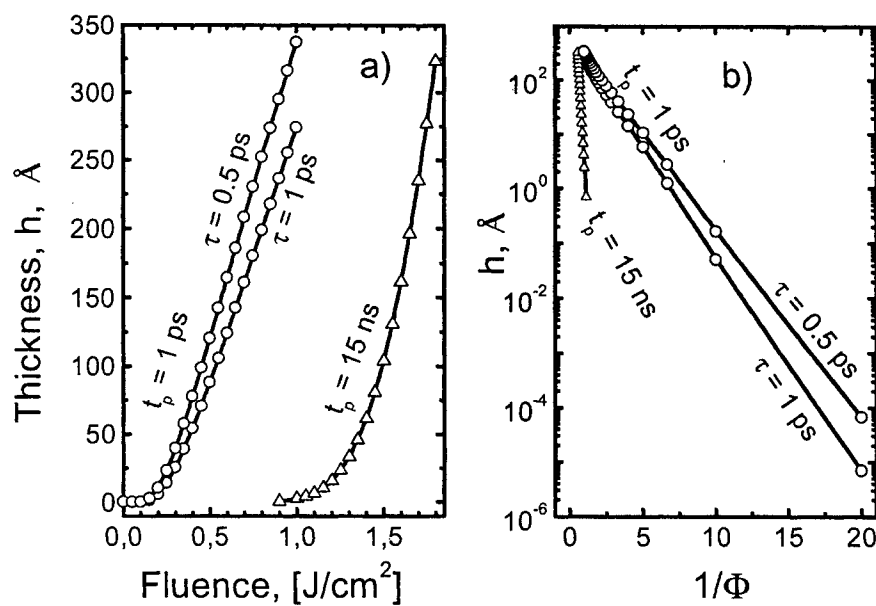


Fig. 9. Ablation rate (total thickness of the ablated material per laser pulse). Two curves with duration of laser pulse $t_p = 1$ ps are shown and one curve with $t_p = 15$ ns. The short laser pulses are calculated with two relaxation times $\tau = 0.5$ and 1 ps. Long laser pulse is calculated with $\tau \leq 1$ ps. Other parameters are given in Table 1. Figure a) presents picture in "normal" coordinates, while Figure b) shows the same curve in "Arrhenius coordinates": $\log[h] = f[1/\Phi]$.

From Fig. 9 one can see the typical effects in ablation kinetics. With long (ns) laser pulse kinetics of ablation is insensitive for relaxation time; all curves with $\tau \leq 1$ ps coincide and follow purely thermal model [12] with one common temperature. For short (ps) laser pulse kinetic curves are sensitive to relaxation time. Situation with $\tau \rightarrow 0$, which corresponds to purely thermal model, yields too fast ablation compare to those, which can be seen experimentally, (see e.g. discussion in [13]). From Fig. 9 one can see well known effect when the threshold fluence becomes lower for shorter pulse [1]. Thus, the given moment's equations present of by correct way qualitative effects of two-temperature model. Calculations are very fast, which permits to use this model for the analysis of experimental data. The necessary step, related to thermal dependencies of different parameters is not difficult. We shall discuss it in a separate paper.

5. CONCLUSION

The purpose of this work was to propose a fast and convenient method of solving of the equations of phenomenological two-temperature model. The advantage of the method proposed is a possibility to study long time behavior, which appears to be difficult with finite difference numerical methods. The method permits to simulate characteristics, which are directly measured in experiments. It is of a great importance for the analysis of experimental data.

ACKNOWLEDGEMENTS

We wish to thank N. Arnold, L. Falkovsky and B. Rethfeld for discussions. B. L. is thankful to people in Data Storage Institute at National University of Singapore for their hospitality during his visit in Singapore. This paper was done (in part) under financial support of the Russian Basic Research Foundation.

REFERENCES

- [1] D. Bäuerle, *Laser Processing and Chemistry*, 2 Ed., Springer-Verlag, Berlin, 1996
- [2] R. Russo, D. Geohegan, K. Murakami, R. Haglund (Eds.), *Laser Ablation*, Proc. E-MRS, North-Holland, Amsterdam, 1998
- [3] S. I. Anisimov, A. M. Bonch-Bruевич, M. A. El'yashevich, Ya. A. Imas, N. A. Pavlenko, G. S. Romanov, "Effect of the powerful light fluxes on metals", *Sov. Phys. - Tech. Phys.*, **11**, 945 (1967)
- [4] S. I. Anisimov, Ya. A. Imas, G. S. Romanov, Yu. V. Khodyko, *Action of High-Power Radiation on Metals*, National Technical Information Service, Springfield, VA, 1971
- [5] S. I. Anisimov, B. L. Kapeliovich, T. L. Perel'man, "Electron emission from metal surfaces exposed to ultrashort laser pulses", *JETP*, **39**, 375 (1974)
- [6] J. G. Fujimoto, J. M. Liu, E. P. Ippen, N. Blombergen, "Femtosecond laser interaction with metallic tungsten and nonequilibrium electron and lattice temperatures", *Phys. Rev. Lett.* **53**, 1873 (1984).
- [7] X. Y. Wang, D. M. Riffle, Y.-S. Lee, M. C. Downer, "Time-resolved electron-temperature measurement in a highly excited gold target using femtosecond thermionic emission", *Phys. Rev. B* **50**, 8016 (1994)
- [8] C.-K. Sun, F. Vallée, L. H. Acioli, E. P. Ippen, J. G. Fujimoto, "Femtosecond-tunable measurement of electron thermalization in gold", *Phys. Rev. B* **50**, 15337 (1994)
- [9] R. Groeneveld, H. Sprik, A. Lagendijk, "Femtosecond spectroscopy of electron-electron and electron-phonon energy relaxation in Ag and Au", *Phys. Rev. B* **51**, 11433 (1995)
- [10] J. Hohlfeld, J. G. Müller, S. -S. Wellershoff, E. Matthias, "Time-resolved thermorefectivity of thin gold films and its dependence on film thickness", *Appl. Phys. B* **64**, 387 (1997)
- [11] L. A. Falkovsky, E. G. Mishenko, "Electron-lattice kinetics of metals heated by ultrashort laser pulses", *JETP*, vol. **88**, 84 (1999)
- [12] N. Arnold, B. Luk'yanchuk, N. Biturin, "A fast quantitative modeling of ns laser ablation based on nonstationary averaging technique", *Appl. Surf. Sci.*, vol. **127-129**, 184 (1998)
- [13] N. Arnold, B. Luk'yanchuk, N. Biturin, D. Bäuerle, "Nonstationary effects in laser ablation of Indium: Calculations based on spatial moments technique", *Laser Physics*, vol. **8**, 47 (1998)
- [14] N. Arnold, B. Luk'yanchuk, N. Biturin, D. Bäuerle, "A fast quantitative modeling of ns laser ablation based on nonstationary averaging technique (spatial moments technique)", *Proc. SPIE*, vol. **3343**, 484 (1998)

- [15] S. I. Anisimov, V. A. Khokhlov, *Instabilities in Laser-Matter Interaction*, CRC Press, Boca Raton, 1995
- [16] S. I. Anisimov, B. Rethfeld, "On the theory of ultrashort laser pulse interaction with a metal", *Izvestia Akademii Nauk (Fiz.)*, vol. **61**, 1642 (1997)
- [17] J. Güdde, J. Hohlfeld, J. G. Müller, E. Matthias, "Damage threshold dependence on electron-phonon coupling in Au and Ni films", *Appl. Surf. Sci.* vol. **127-129**, 40, (1998)
- [18] S.-S. Wellershoff, J. Hohlfeld, J. Güdde, E. Matthias, "The role of electron-phonon coupling in femtosecond laser damage of metals", *Appl. Phys. A* **69** [Suppl.], S99 (1999)
- [19] B. Rethfeld, A. Kaiser, M. Vicanek, G. Simon, "Femtosecond laser-induced heating of electron gas in aluminium", *Appl. Phys. A* **69** [Suppl.], S109 (1999)
- [20] S. I. Anisimov, V. A. Bendinsky, G. Farkas, "Nonlinear photoelectric emission from metals induced by a laser radiation", *Sov. Phys. Uspekhi* **20**, 467 (1977)
- [21] M. G. Agranat, A. A. Benditsky, G. M. Gandel'man, A. G. Devyatkov, P. S. Kondratenko, B. I. Makshantsev, G. I. Rukman, B. M. Stepanov, "Noninertial radiation from metals in interaction with ultrashort pulses of coherent infrared radiation", *JETP Lett.* **30**, 167 (1979)
- [22] S. I. Anisimov, B. I. Makshantsev, A. V. Barsukov, "Metal surface heating by picosecond laser pulses", *Opt. and Acoust. Rev.*, **1**, 251 (1991)
- [23] A. A. Samarsky, V. A. Galaktionov, S. P. Kurdyumov, A. P. Mikhailov, *Regimes with sharpening for the problems of quasi-linear parabolic equations*, Moscow, Nauka, 1985 (In Russian)
- [24] D. Zwillinger, *Handbook of Differential Equations*, Academic Press, Boston, 1989
- [25] N. V. Karlov, N. A. Kirichenko, B. S. Luk'yanchuk, *Laser Thermochemistry. Fundamentals and Applications*, Cambridge International Science Publishing, Cambridge, UK, 2000
- [26] S. Wolfram, *Mathematica*, 4-th Edition (Wolfram Media / Cambridge University Press 1999)

Microablation of Pure Metals: Laser Plasma and Crater Investigations

A. Semerok¹, B. Sallé, J.-F. Wagner, G. Petite*, O. Gobert**, P. Meynadier**,
M. Perdrix**,

CEA Saclay, DPE/SPCP/LSLA, Bât.391, 91191 Gif sur Yvette cedex, France

* Ecole Polytechnique, DSM/DRECAM/LSI, 91128 Palaiseau cedex, France

** CEA Saclay, DSM/DRECAM/SPAM, Bât.522, 91191 Gif sur Yvette cedex, France

ABSTRACT

Crater shapes and plasma plume expansion in the interaction of femtosecond (70 fs), picosecond (20 ps) and nanosecond (6 ns) laser pulses (wavelengths- 800 nm; 400 nm and 266 nm for femtosecond Ti-Al₂O₃ laser ; 1064 nm, 532 nm and 266 nm for nanosecond and picosecond Nd-YAG lasers; mode- nearly TEM₀₀; waist diameter- of the order of 10 μ m) with various pure metals in air and noble gases at atmospheric pressure were studied. The craters formed at the surfaces were measured by an optical microscope profilometer with 0.01 μ m depth and 0.5 μ m lateral resolutions. The measurements of laser plasma expansion were carried out with ICCD camera with 3 μ m spatial and 1 ns temporal resolutions. These measurements were made in 0-100 ns time delay range and at different wavelengths in 200-850 nm optical spectral range. Laser ablation efficiencies, crater profiles, plasma plume shapes at different time delays, rates of plasma expansion in both longitudinal and transversal directions to the laser beam were obtained. Experimental results were analyzed from the point of view of different theoretical models of laser beam interaction with plasma and metals. The laser pulse duration range used in our study was of particular interest, as it includes the characteristic time of electron-phonon relaxation in solids, that is, of the order of one picosecond. Thus, we could study the different regimes of laser ablation without (for fs pulses) and with (for ns pulses) laser beam/plasma plume interaction. It was found that for nanosecond pulses the laser beam absorption, as well as its scattering and reflection in plasma, were the limiting factors for efficient laser ablation and precise material processing with sharply focused laser beams.

Keywords: laser ablation, metal samples, laser plasma, ablation efficiency, surface microanalysis.

1. INTRODUCTION

Modern industry technologies and nuclear industry, in particular, have been seeking for simple reliable methods for solid matter composition analysis and elemental surface mapping. Laser Ablation Optical Emission Spectroscopy (LA-OES) seems an appropriate and attractive method for this kind of microanalysis. The measurements can be carried out in-situ at atmospheric pressure with a wide variety of metal samples without any special pre-treatment of target matter. This looks especially advantageous for radioactive matter microanalysis. The analytical signal of LA-OES method is represented by the spectral line intensity of exited atoms or ions of plasma. The accuracy of the method is determined by the analytical signal value that is associated directly with the number of ablated particles. This number is very low at laser microablation. To make the analytical signal value higher, it is necessary to increase the laser fluence at microablation measurements in the range of 10 – 1000 J/cm². To make the measurements as accurate as possible, it is also important to know the analytical performance of laser ablation (ablation efficiency, crater parameters, plasma plume expansion) and the mechanisms of sharply focused laser pulse/target surface interaction. The interaction is a complex process involving heating, melting, evaporation, excitation, and ionization. It depends on laser beam parameters (pulse duration, energy, wavelength, angular divergence, spot size), the physical properties of solid matter, surrounding environment composition, and pressure. The interaction process results in a crater formation on the target surface and the creation of microplasma above it. This plasma, being composed of electrons, excited atoms and ions, defines the analytical performance of laser ablation and can be analyzed to determine the target composition. The laser pulse interaction with the near-surface plasma and the surrounding gas can affect the laser beam distribution on the target surface resulting in decreasing spatial resolution and efficiency of the

¹ A.S. (correspondence): Tel. : +33(1)69086557, FAX : +33(1)69087738, Email : asemerek@cea.fr

method. Thus, the description of crater parameters (diameter, depth, volume and shape) and plasma plume expansion is seen as an interesting method of studying certain physical mechanisms of laser ablation to obtain the optimal parameters of LA-OES. The investigation of crater parameters and microplasma expansion in the interaction of laser pulses (70 fs - 6 ns pulse duration, 1064 nm, 800 nm, 532 nm, 400 nm and 266 nm wavelength) with pure metals was the aim of this work. Various regimes of laser ablation in this range of laser pulse duration can be studied. They are defined by the characteristic time of electron-phonon interaction in solid matters (of the order of 1 ps) and correspond to the ablation with laser/plasma interaction (for ns/ps pulses) and without it (for fs pulses). Laser/plasma and laser/air interaction process can change significantly both the laser beam intensity distribution on the solid surface and the laser plume expansion features. The laser plasma limiting effects at laser microablation were also under study in this work.

2. EXPERIMENTS

The experiments were carried out with three different lasers in air, nitrogen and noble gases (Ar, Ne, Kr, He) at atmospheric pressure. A set of metal samples (Cu, Al, Fe, Ni, Mo and Pb) with various matter parameters (Table 1) was chosen to study the effect of matter properties on laser ablation process. The target surfaces were polished to facilitate the localization of microcraters and to increase the accuracy of crater parameter measurements. The roughness values were determined as a mean root square value on the zone of $100\mu\text{m} \times 100\mu\text{m}$ and are $1.74\mu\text{m}$ (Pb), $0.91\mu\text{m}$ (Al), $0.078\mu\text{m}$ (Cu), $0.077\mu\text{m}$ (Fe), $0.15\mu\text{m}$ (Ni) and $0.26\mu\text{m}$ (Mo). High roughness values of Pb, Al, Mo and Ni resulted from imperfect surface flatness rather than from surface micrometric ripples. Microcrater localization and characterization were made sufficiently easy with such rough metal surfaces.

The ns pulse experiments were performed with a Nd-YAG laser (Quantel Compact YG 585) with 6 ns (FWHM) pulse duration emitting on the first (1064 nm), second (532 nm) or fourth (266 nm) harmonic. The commercial version of this type of lasers has a multimode beam structure, but for most of our nanosecond experiments the Gaussian beam intensity distribution was obtained with a diaphragm being installed inside the resonator cavity. The laser beams were focused by a 100 mm lens (the Gaussian beam) or by an optical microscope objective of focal length $F=24\text{ mm}$ (the multimode beam) at normal incidence to the sample surface. Intensity distribution of the focused beams in waist was measured by a CCD camera with an optical objective and was found to be close to the Gaussian distribution for the laser with a diaphragm inside resonator cavity. The waist diameters were $10\mu\text{m}$ (FWHM of intensity distribution) for 1064 nm and 532 nm, and $6\mu\text{m}$ for 266 nm. The laser beam energy was varied in $0.01\text{ mJ} \leq E \leq 4\text{ mJ}$ range ($10\text{ J/cm}^2 \leq F \leq 4500\text{ J/cm}^2$).

For the picosecond experiments, we used a Nd-YAG laser (laboratory-made equipment) with a Sagnac resonator with an intracavity extraction of a single pulse. The output of the oscillator was amplified and spatially filtered giving the yield of 70 mJ per pulse at 1064 nm with 25 ps duration. The fundamental frequency was doubled by a KDP crystal and separated from the second harmonic by a dichroic mirror. At 532 nm, the pulse duration was of 18 ps. The intensity of second harmonic was adjusted in 0.05 - 20 mJ range by changing the polarization of the beam at 1064 nm with a quarter-wave plate located before the KDP crystal. The energy of the second harmonic was monitored by the fast photodiode-scope system. The second harmonic was also doubled by the KDP crystal. At 266 nm the pulse duration was of 13 ps. The ps laser beams were focused onto the targets by a 100 mm quartz lens. The diameter (FWHM) and the radiation intensity distribution in the beam waist of the second harmonic (1064 nm and 532 nm) were measured by a CCD camera with an objective ($\times 66$ magnification). 90% of radiation were of the Gaussian distribution with $d \approx 20\mu\text{m}$ (FWHM) for 1064 nm and $d \approx 9.5\mu\text{m}$ (FWHM) for 532 nm, while 10% of the beam were distributed more or less uniformly on the spot of a $50\mu\text{m}$ diameter. This diffused part of the beam was probably resulting from the non-uniformities of the optical elements and diffusion scattering on their surfaces. To measure the beam diameter on the fourth harmonic (266 nm), we used the method of "punching a hole" on a thin $12\mu\text{m}$ Al foil by a focused laser beam and evaluating the transmission of the very same beam, but having been attenuated. The holes of different diameters may be punched by changing the radiation energy and pulse number. By comparing the transmission coefficient with the hole diameter, we may determine the type of intensity distribution and measure the beam diameter. The waist diameter of the fourth harmonic obtained by this method was found to be $d_{4\omega} \approx 6.5\mu\text{m}$ (FWHM). It should be noted, that similar to the fundamental and second harmonics, approximately 20% of radiation were in a diffused part of the beam and were distributed on the spot of a $50\mu\text{m}$ diameter.

The femtosecond experiments were performed with a Ti-Al₂O₃ laser emitting on the first (800 nm), second (400 nm) or third (266 nm) harmonic. The laser beams with wavelengths of 800 nm or 400 nm were focused by a 150 mm lens at normal incidence to the metal sample surface. A 200 mm lens was used for 266 nm laser beam. The waist diameters were found to

be close to 10 μm (FWHM of the intensity distribution) for all laser beams. The laser pulse duration was of 70 fs, but could also be adjusted in 70 fs - 10 ps range by an appropriate choice of the distance between the pulse compressor gratings. The temporal contrast of 70 fs laser pulses on 800 nm was sufficiently high with more than 70% pulse energy being in a fs pulse. The laser energy was varied in 2 $\mu\text{J} \leq E \leq 800 \mu\text{J}$ range ($2 \text{ J/cm}^2 \leq F \leq 800 \text{ J/cm}^2$) by a quarter wave plate with polarizer.

The craters formed at the surfaces were studied with an optical microscope profilometer (MicroXam Phase Shift Technology, USA) of 0.5 μm lateral and 0.01 μm longitudinal resolutions. The laser plasma images were obtained by an intensified gated CCD camera (Hamamatsu C4346-01) with 3 ns gate time. At the first stage of the laser plasma expansion, the time delay with 1 ns step was applied. A microscope objective of 40 \times magnification was used for the laser plasma imaging with 3 μm lateral resolution. Thus, laser plasma expansion was measured with 3 μm spatial and 1 ns time resolutions. These measurements were performed in 0–100 ns time delay range and at different wavelengths in 200–850 nm optical spectral range. Other objectives of 12.5 \times and 2.5 \times magnifications were used for laser plasma imaging at the time delay range of 40 - 500 ns and 500 - 1000 ns, where plasma dimensions reached up to 1000 μm . The ablation efficiency can be defined either as a ratio of crater depth to laser fluence or as a ratio of ablated matter volume to laser pulse energy. For analytical applications, the latter definition is more preferable, as the energy distribution of the sharply focused laser beam on the target surface after surface plasma creation is perturbed and not known. The most pronounced intensity distribution deviations due to the laser beam/plasma interaction are to be expected at nanosecond pulses when the surface plasma may expand to the height value comparable to the laser beam diameter. It is necessary to point out that if the laser beam profile is the same as the one of the crater, then the two above mentioned definitions of ablation efficiency may be regarded identical.

3. EXPERIMENTAL RESULTS

Crater shapes obtained in our experiments were found to depend on laser beam diameter, laser pulse duration, energy, wavelength, target, and environmental conditions. Fig.1 gives the typical crater profiles with parameters that were used for crater description (diameter at the surface level – D_m , diameter at half-height – $D_{0.5}$, depth – h , volume – V , and convexity height – δ). In general, the crater profiles were not identical to the spatial distribution of laser intensity (Fig. 2-4). Only with the low energy, the crater shape was observed to coincide with the laser intensity distribution of fs pulses (of any wavelength) and ns/ps pulses for the second and fourth harmonics (Fig. 3). For the high pulse energies, the crater shapes differed significantly from the intensity distribution on the target. Crater shape broadening was accompanied by crater profile changes. In some cases, the central area of the crater was observed to be less ablated than the neighboring zone around the crater center. Besides, we observed the formation of either an additional wide shallow crater of 50 μm diameter or several circle-shaped craters framing the main crater. Such deformations of the crater shape were clearly defined at ablation in noble gases (Ar, Kr) with low ionization potential and for 1064 nm pulses. With ns and ps laser pulses, on the target surface along the crater boundary we observed formation of a convexity, the height of which depended on a target matter, pulse duration, energy, and pulse number. The convexity was more important for ns pulses. With the pulse energy or pulse number increase, the ratio of the convexity height (δ) to the crater depth (h) decreased. The convexity height was less important for short wavelength (226 nm) than for infrared pulses (1064 nm). For fs pulses (of any wavelength), the crater profiles were observed without any convexity formation (Fig. 2). It should be noted that the best crater parameters (crater shapes, crater surface roughness, absence of convexity, maximal depth per pulse) were obtained with a femtosecond laser. The crater diameters $D_{0.5}$ and D_m were mainly determined by the laser beam diameter, but depended on pulse energy, laser wavelength, and target matter as well. For both ps and ns pulses with low energy on 1064 nm, the crater diameters $D_{0.5}$ were smaller than laser beam diameter (Fig. 4). At higher energies, the crater diameters were found to be larger than those of the laser beam for all wavelengths and pulse durations. Fig. 5 gives the dependencies of crater diameters $D_{0.5}$ and D_m on the incident laser energy (532 nm, 6 ns) for copper. In 0.01–1 mJ range, the surface diameter was observed to increase significantly from initial 10–15 μm to about 50 μm . For the energies higher than 1 mJ, the diameter reached approximately the same value of around 50 μm . For 532 nm ns pulses, crater diameter $D_{0.5}$ demonstrated a particular behavior with the laser pulse energy. It increased from 10 μm at 0.01 mJ up to 20 μm at 0.1 mJ. Then, it fell to a constant value of around 18 μm . From 0.2 mJ and upwards, the profile of the crater suffered crucial changes - a large shallow area of erosion (additional crater) could be observed to appear around the main deep crater (Fig. 4 and Fig. 6). In our experiments with ns/ps (532 nm, 266 nm) and fs (of any wavelength) lasers, the crater depth and volume were observed to increase with laser fluence and energy, respectively (Fig. 7 and Fig. 8). The crater behavior of copper targets was similar to all metal samples under investigation. The differences observed were attributed to ablation efficiencies. For 532 nm 6 ns laser beam, they were found to be 5000 $\mu\text{m}^3/\text{mJ}$, 2000 $\mu\text{m}^3/\text{mJ}$ and 6000 $\mu\text{m}^3/\text{mJ}$ for Al, Cu and Pb, respectively. In the low energy range of 0.01–0.06 mJ, the ablation efficiency for copper was the same for all ns-laser wavelengths (Fig. 9). With the pulse energies higher

than 0.06 mJ, the ablation was more efficient for short wavelengths. Ablation efficiency of multimode ns laser beam was found to be higher than monomode ns laser ablation efficiency, and its value for 266 nm and 532 nm pulses was of the same order as the one for femtosecond laser. Crater depth and volume dependencies on ps laser energy were similar to the ones on ns pulses. The difference lay in ablation efficiency value that was obtained higher for 532 nm and 266 nm nanosecond pulses in 0.1-1.0 mJ energy range. For 1064 nm laser pulses, ablation efficiency was the same for both ns and ps lasers. The craters formed with different Ti-Al₂O₃ laser pulse durations of 70 fs-2 ps were of the similar profile. No convexity was observed on the target surface around the crater. The crater depth per pulse versus laser pulse duration is shown on Fig. 10. No significant changes of crater depth were observed in 70-800 fs range. For higher pulse durations, the crater depth decreased with laser pulse duration increase. The same behavior was observed for crater volume versus laser pulse duration. Fs laser ablation efficiency of Cu target (2000 $\mu\text{m}^3/\text{mJ}$) was found to be independent of the laser wavelength for 70 fs pulses (Fig. 11).

The plasma expansion was studied with copper, aluminum and lead targets for ns, ps and fs laser pulses. The plasma dimensions were measured at the maximum plasma plume intensity divided by 10. This intensity level was considered as the plasma plume boundary. For Cu target and 532 nm nanosecond laser pulses at low energy ($E < 0.1$ mJ, $F < 100$ J/cm²), the ablated vapor escapes the surface with fast expansion in the normal direction away from the target. At the end of the laser pulse (15 ns delay), the plasma comes unstuck from the surface and takes a shape of a "mushroom". An intense plasma core is found near the surface with the maximum plasma intensity being observed at a certain distance from the surface. Then, the intensity decreases until it reaches its minimum. It begins to increase again until the maximum is reached at a distance of around 75 μm above the sample surface. For longer delay times, the emission near the surface disappears, and the plasma volume is not found to evolve any more. This kind of plasma behavior is observed in 0.01-0.4 mJ energy range (10-400 J/cm² fluence range). At 1 mJ energy ($F = 1000$ J/cm²), the rate of the plasma expansion is higher. An additional cone-shaped plume is detected in this case. The formation of this cone-shaped plume is observed for plasmas created with energies higher than 0.4 mJ ($F = 400$ J/cm²). For short delay times (0-20 ns), highly intense bubbles can be seen in the plume on the laser beam path. The width of these bubbles is measured to be close to the laser beam diameter (10 μm). With a 515 nm filter that cuts off the laser wavelength, the plasma obtained at 1 mJ does not produce intense bubbles. A similar observation was made with the filters being transmitted in the ranges of $250 < \lambda < 400$ nm and $600 < \lambda < 800$ nm. Thus, we may conclude that the bubbles are not associated with a larger concentration of the excited atoms in these areas, but they are rather attributed to diffusion of the laser beam by the plasma. The behavior of the ns laser plasma obtained at 1064 nm was similar to the one obtained at 532 nm. But the fluences, when the plasma form was suffering changes, were different. For 1064 nm, we observed the creation of a cone-shaped plasma at the fluences higher than 200 J/cm² and the bubble production at the fluences higher than 600 J/cm². This bubble production was accompanied by an additional crater formation (Fig. 6) and by decrease in ablation efficiency. Neither bubble production, nor cone-shaped plasma were observed with 266 nm ns laser pulses in 0.001-0.15 energy range. Plasma shapes were hemispherical up to the maximal energy ($E = 0.15$ mJ, $F = 600$ J/cm²) applied in our experiments. No qualitative changes in the plasma shape were observed with different gases (Ar, Kr, He, N₂) either. The temporal evolution of longitudinal dimension of plasmas created by 532 nm ns laser on aluminum, copper and lead samples at 1 mJ is presented on Fig. 12. The plasma begins to grow very quickly during the first 50 ns and the expansion rate is not found to depend on the ablated matter. It reaches the maximum extension at 500 ns delay, then no changes are observed. The most efficiently ablated matter (Pb) was observed to have the largest plasma volume. With the energy increase, the initial expansion rate and the maximum plasma volume dimension are observed to grow (Fig. 13). Nevertheless, the temporal evolution of plasma dimensions is found to be the same for all the energies. With 532 nm laser beam in 0.1-1 mJ low energy range, the plasma shapes obtained with Cu target were identical for both ps and ns lasers. But the plasma expansion velocity was observed to be different. For ps laser, it was found to be 3×10^4 m/s and independent of laser pulse energy, laser wavelength, and environmental conditions (air, Ar, Kr, He, N₂). For different pulse durations and wavelengths of a Ti-Al₂O₃ laser, the plasma demonstrated a similar spatial evolution. The temporal evolution of plasma longitudinal dimension is given on Fig. 14. Plasma transversal dimension had the same temporal evolution. During the first nanoseconds, the ablated matter escaped the surface with a fast expansion in the normal direction away from the target. The initial rates of expansion did not depend significantly on the laser pulse duration. Longitudinal and transversal rates of expansion for 20 μJ laser pulses were found to be about 4.6×10^5 cm/s and 3×10^5 cm/s, respectively. Those values were close to the sound velocity in copper target. From 25 ns delay and upwards, the plasma volume was not found to evolve any more, but it depended on the laser pulse duration. Nonlinear 800 nm fs laser beam/air interaction was observed for the fluences higher than 50 J/cm². This interaction was manifested by visible light generation in the waist zone and by more important angular divergence of the visible light. Nonlinear pulse/air interaction was accompanied by an important crater broadening.

Environmental effect on laser ablation and laser plasma properties was studied with Cu target and ns/ps lasers. A jet of Ar, He, Ne, Kr, Xe, or N₂ gases was provided to the zone of laser/target interaction. Laser plasma plumes obtained with nitrogen were identical to those in air. Thus, nitrogen, being the main component of air, may be considered responsible for the laser plasma characteristics. With the noble gases, the correlation between the ionization potentials and plasma expansion was observed. At the Cu target ablation by the fundamental frequency of ns Nd-YAG laser with He (having the highest ionization potential of 24.6 eV), the plasma shapes were observed to be of a hemispherical shape in the whole energy range of 0.04 - 20 mJ ($10 \text{ J/cm}^2 \leq F \leq 5000 \text{ J/cm}^2$). With Ar and Ne ablation experiments with the energies higher than 0.6 mJ ($F=150 \text{ J/cm}^2$), the plasma was found to be cone-shaped. With the energies of the order of 20 mJ ($F=5000 \text{ J/cm}^2$), the plasma was of a stretched shape with bubbled structure. Fig. 16 gives the rate of plasma expansion in Ar, Ne and He for three different laser energies. The ablation efficiency with these gases was identical for low laser pulse energies. With the energy increase, the ablation efficiency was found to decrease initially for Ar, and then for Ne, while for He its value remained constant (Fig. 17).

4. DISCUSSION

Laser ablation is a complex multi-parameter process that is impossible to be described with one particular model. Depending on specific parameters of laser beam/target matter interaction, various models seem appropriate to be applied. The experimental results allow to find out the interdependence of the ablation rate and efficiency with the parameters of laser beam/target interaction and to compare the results with different theoretical models of laser ablation. The ablation efficiency was determined as the ratio of the ablation rate h ($\mu\text{m/pulse}$) to the laser energy fluence F (J/cm^2). Ablation efficiency can be roughly estimated by the energy balance expressed by: $h = \kappa F(c\rho\Delta T + \lambda\rho + \chi\rho)^{-1}$, where κ - surface absorptivity, ΔT - temperature change, ρ - matter density, c - specific heat capacity, λ and χ - melting and evaporation heat values of the target, respectively. This approach does not take into account many phenomena accompanying laser ablation process and, thus, affecting the ablation properties. Ablation rate estimated by this expression is higher than the one obtained experimentally. Moreover, ablation efficiency and rate were found to depend on the pulse duration, beam spot size, environmental condition, laser fluence and wavelength. Table 2 gives the ablation efficiencies for various targets and interaction parameters in low fluence range $1\text{-}10 \text{ J/cm}^2$.

For the applied range of laser pulse duration and fluence, two ablation regimes can be distinguished: below 1 ps, when a non-thermal, non stationary laser beam/target interaction takes place and above 1 ps, when laser beam/target interaction is being accompanied by a thermal process resulting in laser plasma creation¹. Laser beam/plasma interaction plays a crucial role in laser ablation and in laser microablation, in particular. At laser microablation, not only plasma shielding, but laser beam/plasma refraction as well affect the ablation properties. In general, ablation efficiency was found to decrease with the increase of the laser fluence. For the 4th harmonic (266 nm) of Nd-YAG ns and ps lasers, ablation efficiency was higher than the one for fundamental and second harmonics (1064 and 532 nm). This can be explained by higher surface absorptivity and by lower plasma attenuation due to inverse Bremsstrahlung^{2,3} and one photon photoionization⁴. For ultraviolet radiation, inverse Bremsstrahlung absorption is usually regarded fundamental in the laser beam parameter range under study. But we think that the photoionization should not be excluded from consideration, as the plasma temperature at the initial stages of laser beam / target interaction may be as high as 10 eV. In this case, the excited level population will be sufficient for one photon ionization. Higher laser ablation efficiency was obtained with smaller Nd-YAG laser beam spots. The increase of the ablation efficiency with the reducing of the laser beam spot is explained by a faster expansion of the near-surface plasma for a smaller laser beam spot^{2,5,6}. This results in a lower absorption of the laser beam in plasma. To determine the ablation rate of ns ablation, the model⁷ looks attractive as it gave rather good values of ablation rate with a KrF laser beam (spot diameter of $150 \mu\text{m}$)⁸. In this model the ablation rate was expressed as:

$$h(\mu\text{m}) \cong 2.66\Psi^{9/8}\rho^{-1}(\text{g/cm}^3)\text{A}^{-1}(\text{a.m.u.})^{1/4}\text{I}^{1/2}(\text{W/cm}^2)\lambda^{-1/2}(\text{cm})\tau^{3/4}(\text{sec}),$$
 where $\Psi = 0.5\text{A}(\text{a.m.u.})[Z^2(Z+1)]^{1/3}$; A - atomic mass; Z - the charge state of the ions (we supposed that $Z=1$, i.e. the ions are single-ionized); ρ - the target density; I - the laser beam intensity; λ - the laser wavelength and τ - the laser pulse duration. The above expression was deduced from the theoretical model suggested in^{9,10,11} followed by its further developing in^{12,13}. This model is based on three fundamental assumptions: a) heated layer thickness at the end of the laser pulse is much higher than the laser optical absorption depth; b) laser intensity is several times stronger than the ablation threshold intensity; c) plasma expansion is one-dimensional during the laser beam / target interaction. The principal assumption to obtain the expression for ablation rate was that the plasma is sufficient to transmit only 1/3 of the incident ablation energy down to the surface. Despite the fact that our KrF laser experiments did not correspond exactly to one-dimensional plasma expansion and were performed at

atmospheric pressure, the theoretical ablation rate was found to be in a reasonable agreement with the experimental data. For the Nd-YAG laser experiments with the beam spot being reduced to 10 μm , the assumption of one-dimensional plasma expansion was found not to be valid at all. For this case, the theoretical ablation rate was significantly lower (of the order of 10 times) than the experimental results.

The fs laser ablation efficiency (with the pulse duration less than 800 fs) was found to be independent of the pulse duration. It can be explained within the framework of the fs-laser ablation model¹⁴. The ablation rate in this model is characterized by the efficient penetration depth $l = \alpha^{-1}$ and can be expressed by^{15, 16} $L = \alpha^{-1} \ln(F/F_{th})$, where α - optical absorption or heat penetration coefficient, F_{th} - ablation threshold fluence. For short laser pulses, the ablation rate is determined by the optical absorption coefficient that is independent of laser pulse duration. With pulse duration longer than 800 fs, the penetration depth is determined by heat penetration: $\alpha = (D\tau)^{-0.5}$, where D - coefficient of thermal diffusion. In this case, ablation rate decreases as $(\tau)^{-0.5}$ with pulse duration increase. Thus, this model can quantitatively explain the experimentally observed ablation rate relation with Ti-Al₂O₃ laser pulse duration in 70 fs – 2 ps range.

The experimentally obtained ablation rates were higher for ns pulses than those for ps pulses (10 - 20 ps). This can be explained by more important ps plasma absorption. During ps pulse duration, ablated matter (plasma) has not enough time to escape the interaction zone and is still found near the target surface. Its shielding property is, probably, more important than the one in case of ns ablation. The linear dependence of the ablation rate on the pulse number, when crater depths are smaller than their diameters, testifies to the fact that the plasma expansion does not suffer any changes with the crater depth growth. The rippled crater profile can be explained either by surface wave generation¹⁷ or by condensation of ablated matter on the crater surface^{1, 18}. The condensation is of a higher value at atmospheric pressure. The air particles prevent the ablated matter from escaping the target surface far away. During the initial stages of expansion, the velocity of mass center of plasma particles may be higher than the particle thermal velocities. Then, the velocity of mass center of plasma particles decreases and laser plasma volume begins to expand in all directions with the thermal velocity. The more plasma is close to the target surface, the more ablated matter condensates on the target surface.

Knowing the properties of the target matter (Table 1), we tried to establish the matter properties/ablation rate correlation. A sufficiently good agreement was found with the melting point temperature (Fig. 15). This was an unexpected result, because normally the laser plasma temperature near the target surface significantly exceeds not only the melting point temperature, but the boiling point temperature as well. It seems that an important role in the crater formation should be attributed to the processes dealing with plasma / target interaction (liquid matter ejection).

Knowing the plasma dimension curve slope (Fig. 13), the longitudinal and transversal expansion velocities can be deduced at the beginning of the expansion (Table 3). For $E < 0.4$ mJ, the longitudinal expansion velocity is observed to be lower than the transversal one. Above 0.4 mJ where the plasma is cone-shaped, the longitudinal velocity becomes higher than the transversal one. Additional experiments with the incident angle of 45° demonstrated that this cone-shaped plume follows the direction of the Nd-YAG laser beam even though the plasma near the sample expands in the normal direction to the target. This observation implies that the cone-shaped plume is initiated by the plasma absorption of the laser light resulting in a laser supported ionization wave in air. The plasma plume expansion velocity v_p can be simulated by the "absorption wave" model¹⁹. In this model, the energy balance can be described as²⁰: $I \cong \beta \sigma T^4 + v_p(cT + E_i)$, where β - a coefficient of plasma grayness, σ - the Stephan-Boltzmann constant, I ($\text{W}\cdot\text{cm}^{-2}$) - laser intensity, c ($\text{J}\cdot\text{cm}^{-3}\cdot\text{K}^{-1}$) - specific thermal capacity of air, T (K) - temperature of plasma and E_i - specific ionization energy of air. The energy of ionization (E_i) and the thermal capacity (c) should be evaluated with taking into account the degree of ionization (it is about 3 for the plasma temperature $T \approx 10^5$ K²¹) and the contribution of free electrons and chemical reactions in air. This makes the numerical evaluation of v_p very difficult. With high plasma temperatures ($T \cong 10^5 - 3 \times 10^5$ K) and high laser intensities ($10 - 100$ GW/cm^2), the velocity of the plasma plume expansion can be estimated from the kinetic theory of electron ionization²¹ $v_{exp} \cong CkT_e(8kT_e/\pi m)^{1/2}N^{2/3}$, where T_e - temperature of electrons in plasma (approximately equal to T), m - the mass of electron, N - the concentration of atoms in initial gas, C - a constant about $(0.7 - 0.85) \times 10^{-17}$ cm^2/eV . The value of v_p in this case is about 10^6 cm/s. This is in a sufficiently good agreement with experimental data (Table 3). But there are no grounds to consider this model universal, as the optical properties of plasma can suffer significant changes during laser/plasma interaction. For solid matter surface temperature $T > 1\text{eV}$, the crater growth velocity may be determined by the Frenkel expression²²: $v_c(T) \cong v_s \exp(-E_0/kT)$, where v_s - a velocity close to the sound velocity in solid matter; E_0 - the energy of atom bond in solid matter; kT - the plasma particles energy. In this case, the plasma expansion velocity has at least to be

equal to or higher than the crater growth velocity. Thus, for ablation regime without plasma absorption wave (laser energies $0.01 \leq E \leq 0.4$ mJ), the plasma expansion can be estimated by the Frenkel formula. Table 4 compares the experimental values of the maximum longitudinal dimensions of copper plasma for different energies with the theoretical data. The maximum height reached by the plasma front was evaluated by the following expression²³: $R_{\max} \approx 0.39 \times (\eta E / P_0)^{1/3}$, where P_0 – the pressure of ambient gas, η – the ratio of the plasma plume energy to that of the laser. The experimental results are in good agreement with theoretical values for $\eta = 0.25$ and laser energies below 0.4 mJ.

The experimentally obtained crater broadening and its profile changes with the laser pulse energy increase can be attributed to the strong scattering and refraction of the laser beam in plasma. Thus, our experiments, analogously to the results in²⁴, demonstrated that the diffusion and refraction by plasma plume play a decisive role in laser intensity distribution on the solid surface resulting in crater broadening and its profile changes.

5. CONCLUSIONS

Taking into account the ablation efficiency dependence on a laser pulse duration and wavelength, we can conclude that the best ablation efficiency was obtained with a fs laser. It is in good agreement with the results of literature^{25, 26}. This could be explained by a shorter laser pulse duration compared to a typical time (of a few ps) of electron-phonon collisions in solid matter. Two different regimes of laser-target interaction could be defined as:

1) a fs regime, where a laser pulse terminates before the energy is completely redistributed in the solid matter^{27, 28}. It is likely that the energy is deposited in the matter without laser / plasma interaction resulting in a better ablation efficiency than the one in the ps and ns regimes.

2) a ps / ns regime, where the pulse duration is of the same order or longer than the energy relaxation time. In this case, the irradiated volume heating is fast enough to vaporize the surface during the laser pulse, and plasma shielding can occur. The main result obtained in this case is a better efficiency with a ns pulse than with a ps pulse for the same wavelength and laser beam spots. To explain this higher efficiency for a ns case, the following phenomena in the laser / matter interaction process should be taken into account:

- the hydrodynamic motion of ablated matter and vaporization front propagation during the laser pulse. The ablation should be considered as a dynamic process because the vaporization front moves into the solid matter during the pulse and this velocity is limited by the sound velocity of solid matter. Hence, both the ablated depth and the volume is found to increase with the laser pulse duration²⁸

- laser pulse energy absorption in a dense near-surface plasma. Two main processes responsible for plasma absorption are the following: 1) Inverse Bremsstrahlung that depends on electron density and laser wavelength and 2) photoionization that depends on atomic density, laser photon energy, and intensity I^m for m-photons ionization. For a sufficiently hot and dense plasma with an important excited level population, a one - photon photoionization absorption may be dominant⁴. With the ps pulse, both the laser intensity and the plasma particle density are higher than those for the ns pulse case. Thus, we can conclude that for ps pulses, the plasma absorption is higher and, consequently, the ablation efficiency is lower.

The experimental studies of crater profile and plasma expansion at the interaction of the sharply focused nanosecond laser beam with metal samples demonstrated with certainty the plasma limiting effects on laser microablation. This was revealed not only by the decrease in crater depth growth with laser energy increase, but by the crater broadening and its profile changes as well. The experimentally obtained velocities of plasma plume expansion and the dimensions of the laser plasma plume may be described sufficiently well within the framework of the Frenkel expression²² and the shock wave²³ models.

ACKNOWLEDGMENTS

The authors would like to acknowledge Prof. M. Libenson and Dr. N. Arnold for the fruitful discussions on the results, and LSLA laboratory personnel for the technical support provided for this experimental work.

REFERENCES

- 1 D. Von der Linde, K. Sokolowski-Tinten, J. Bialkowski, "Laser-solid interaction in the femtosecond time regime", *Appl. Surf. Sci.* **109- 110**, pp. 1-10 (1997).
- 2 D. Bäuerl, *Laser Processing and Chemistry*, Springer-Verlag, Berlin Heidelberg New-York (1996).

- 3 C. Geertsen, A. Briand, F. Chartier, J.-L. Lacour, P. Mauchien and S. Sjöström, "Comparison between infrared and ultraviolet laser ablation at atmospheric pressure-implication for solid sampling inductively coupled plasma spectroscopy", *J. Analit. Atom. Spectr.*, **9**, pp. 17-22 (1994).
- 4 J. J. Chang and B. E. Warner, "Laser-plasma interaction during visible-laser ablation of metals", *Appl. Phys. Lett.*, **69**, pp. 473-475 (1996).
- 5 M. Eyett and D. Bäuerl, "Influence of the beam spot size on ablation rates in pulsed-laser processing", *Appl. Phys. Lett.*, **51**, pp. 2054-2055 (1987).
- 6 B. Wolff-Rottke, J. Ihlemann, H. Schmidt and A. Scholl, "Influence of the laser-spot diameter on photo-ablation rates", *Appl. Phys.*, **A60**, pp. 13-17 (1995).
- 7 R. W. Dreyfus, C. Phipps and A. Vertes, "Extending laser fusion concepts into the lower power ($\leq 1 \text{ GW/cm}^2$) microelectronics arena", *Proceeding of the International Conference COLA'93* (1993).
- 8 B. Sallé, C. Chaléard, V. Detalle, J.L. Lacour, P. Mauchien, C. Nouvellon, A. Semerok, "Laser ablation efficiency of metal samples with UV Laser nanosecond pulses", *Appl. Surf. Science*, **138-139**, pp. 302-305 (1999).
- 9 A. Caruso, B. Bertolli and P. Giupponi, *Nuovo Cimento*, **45**, p. 176 (1966).
- 10 I. V. Nemchinov, "Solid-state motion of radiation-heated vapors of a material in the presence of lateral spreading flow", *J. Appl. Math. Mech.*, **31**, pp. 320-339 (1967).
- 11 R. E. Kidder, "Application of lasers to the production of high-temperature and high-pressure plasma", *Nucl. Fusion*, **8**, pp. 3-12 (1968).
- 12 R. E. Kidder, *Proceeding of the International School of Physics "Enrico Fermi"*, course XLVIII, pp. 306-352, Eds P. Caldirola and H. Knoepfel, Academic, New York London (1971).
- 13 C. R. Phipps, T. P. Turner, R. F. Harrison, G. W. York, W. S. Osborne, K. C. Spicochi and T. R. King, "Impulse coupling to targets in vacuum by KrF, HF, CO₂ single-pulse lasers", *J. Appl. Phys.*, **63**, pp. 1083-1096 (1988).
- 14 S.I. Anisimov, B. Rethfeld, "On the theory of ultrashort laser pulse interaction with metal", *SPIE Proceedings* **3093**, pp. 192-203 (1996).
- 15 S. Preuss, A. Demchuk, M. Stuke, "Sub-picosecond UV laser ablation of metals" *Appl. Phys.* **A61**, pp.33-37 (1995).
- 16 B. N. Chichkov, C. Momma, S. Nolte, F. von. Alvensleben, A. Tunnermann, "Femtosecond, picosecond and nanosecond laser ablation of solids" *Appl. Phys.*, **A63**, pp.109-115 (1996).
- 17 A.M. Prokhorov, V.I. Konov, I. Ursu and I.N. Mihailescu, "Laser Heating of Metals", Hilger (1990).
- 18 R. Kelly and A. Miotello, "Laser-pulse sputtering of atoms and molecules, Part II. Recondensation effects", *Nucl. Instr. and Meth. in Phys. Research*, **B91**, pp. 682-691 (1994).
- 19 E. A. Berchenko, A. P. Sobolev, B. T. Fedyushin, "Propagation of laser-absorption waves in a gas", *Sov. J. Quant. Electr.*, **9**, pp. 907-908 (1979).
- 20 L. J. Radziemski, D. A. Cremer, "Laser Induced Plasmas and Applications", Marcel Dekker New York (1989).
- 21 Ya. Zeldovich and Yu. Raizer, "Physics of Shock Waves and of High-Temperature Hydrodynamic Effects", Academic Press, N.-Y.-London (1966).
- 22 Y. I. Frenkel, "Kinetic Theory of Liquids", Dover Publications, Inc., New York (1955).
- 23 N. Arnold, J. Gruber, J. Heitz, "Spherical expansion of the vapor plume into ambient gas: an analytical model", *Appl. Phys. A* **69**, pp. S87-S93 (1999).
- 24 A. M. Bonch-Bruевич, O. I. Kakabushkin, L. N. Kaporskii, V. S. Salyadinov, "Anisotropy in the scattering of light by the plasma of a laser spark", *Sov. Tech. Phys. Lett.*, **66**, pp. 289-290 (1980).
- 25 T.V. Kononenko, S.V. Garnov, S.M. Klimentov, V.I. Konov, E.N. Loubnin, F. Dausinger, A. Raiber, C. Taut, *Applied Surface Science*, **109/110**, p. 48 (1997).
- 26 C. Momma, B.N. Chichkov, S. Nolte, F. Von Alvensleben, A. Tunnermann, H. Welling, B. Wellegehausen, *Optics Communications*, **129**, p. 134 (1996).
- 27 D. Von Der Linde, K. Sokolowski-Tinten, J. Bialkowski, *Applied Surface Science*, **109/110**, p. 1 (1997).
- 28 C.R.Phipps, T.P.Turner, R.F.Harrison, G.W.York,W.Z.Ozborne, G.K.Anderson, X.F.Corlis, L.C.Haynes, H.S.Steele, K.C.Spicochi, *J.Appl.Phys.*, **64**, p. 1083 (1988).
- 29 R. C. Weast and M. J. Astle, *CRS Handbook of Chemistry and Physics*, CRS Press, Inc., Boca Raton, Florida, 1992.

Table 1. Thermal and photophysical properties of targets for ambient pressure and temperature²⁹.

	Al	Cu	Fe	Ni	Pb	Mo
Thermal conductivity k (Wcm ⁻¹ K ⁻¹)	2.37	4.01	0.802	0.9	0.353	1.38
Potential of ionization (eV)	5.986	7.726	7.87	7.6	7.42	7.099
Melting point temperature (K)	933	1358	1809	1726	601	2890
Boiling point temperature (K)	2793	2836	3135	3005	2023	4912
Heat of evaporation (kJmol ⁻¹)	293.4	300.3	349.6	378	178	598
Heat of fusion (kJmol ⁻¹)	10.79	13.05	13.80	17.4	4.8	32
Heat capacity C_p (J g ⁻¹ K ⁻¹)	0.9	0.38	0.44	0.44	0.1	0.25
Atomic number	13	29	26	28	82	42
Atomic mass (a.m.u.)	26.98	63.55	55.85	59	207	95.94
Density ρ (g cm ⁻³)	2.7	8.96	7.86	8.9	11.4	10.2
Hardness (mean value)	2.45	2.75	4.5	4	1.5	

Table 2. Ablation efficiency in 10⁸ μm^3 /J. Laser pulse energies are in 10-100 μJ range (low fluence range 1-10 J/cm²).

	70 fs Ti-Al ₂ O ₃ laser	ps Nd - YAG laser			TEM ₀₀ Nd-YAG ns laser			multimode Nd - YAG	ns laser
	800 nm 400 nm 266 nm	1064 nm 20 μm	532 nm 10 μm	266 nm 7 μm	1064 nm 20 μm	532 nm 10 μm	266 nm 8 μm	532 nm 8 μm	266 nm 8 μm
Cu	0.03	0.004	0.009	0.028	0.02	0.02	0.02	0.031	0.065
Al	0.05	0.010	0.040	0.057	0.05	0.05	0.06	0.124	0.293
Fe	0.01	0.0045	0.004	0.006	0.009		0.01	0.015	0.031
Ni	0.014	0.006	0.007	0.009	0.007		0.03		
Pb	0.125	0.020	0.125	0.213	0.06	0.06	0.09	0.186	0.457
Mo	0.008	0.003	0.007	0.005	0.006		0.014		

Table 3. Longitudinal and transversal velocities of copper plasma versus the incident laser energy.

Energy mJ	Longitudinal velocity cm / s	Transversal velocity cm / s
0.01	2.3×10^5	3.6×10^5
0.04	4.4×10^5	5.0×10^5
0.1	4.6×10^5	5.7×10^5
0.2	6.0×10^5	8.3×10^5
0.4	9.4×10^5	8.5×10^5
1	1.4×10^6	1.1×10^6
2	2.0×10^6	1.4×10^6
4	2.7×10^6	1.6×10^6

Table 4. Experimental h_{exp} and theoretical h_{theor} longitudinal dimensions of copper plasma for different energies at 532 nm.

Energy mJ	H_{exp} μm	H_{theor} μm
0.01	125	114
0.04	168	181
0.1	217	246
0.2	290	310
0.4	258	390
1	644	529
2	>550	667
4	>620	840

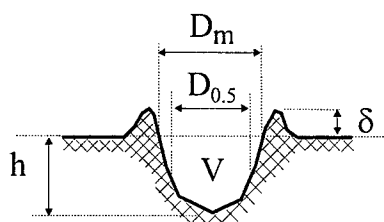


Fig. 1. Crater spatial characteristics.

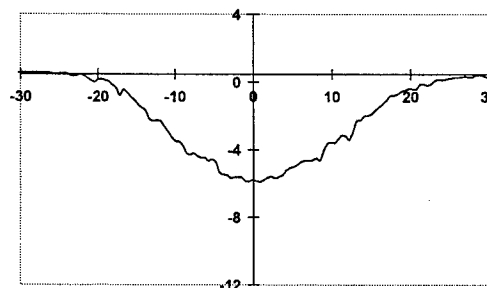


Fig. 2. Cu crater obtained with fs laser (400 nm, 150 fs) after 10 laser pulses.

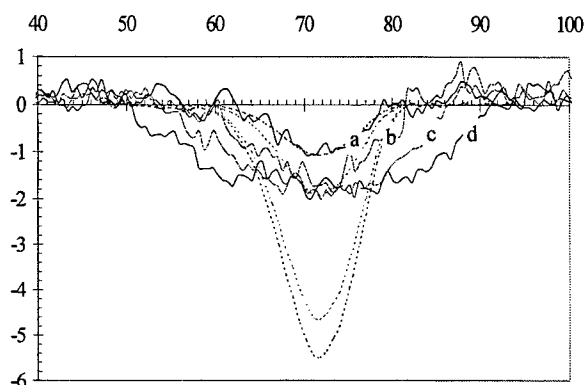


Fig. 3. Craters in Cu (solid lines) at different ps laser (532 nm) pulse energies (a- 0.28mJ, b- 0.5 mJ, c- 1.21 mJ and d- 1.43 mJ). Laser waist diameter - 9.5 μm (FWHM). Dotted lines - intensity distribution of the above energies. For the pulse energy $E = 0.28$ mJ, the intensity distribution amplitude is chosen for the best matching with the crater shape. Reference scales are in μm .

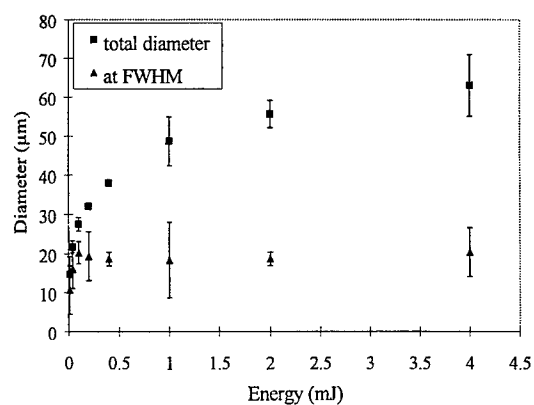


Fig. 5. Dependence of crater diameter on incident laser energy for copper (532 nm, 6 ns, one pulse).

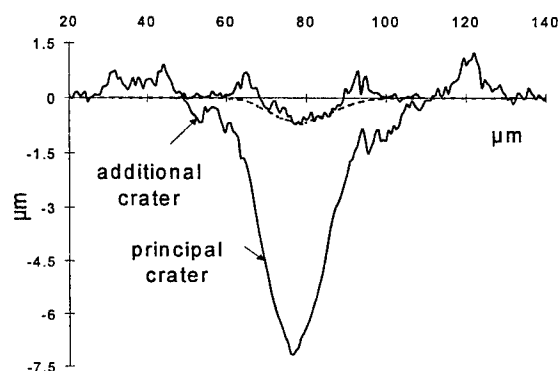


Fig. 4. Craters in Cu obtained after one ns laser pulse at 1064 nm with 20 mJ and 0.1 mJ energy. Dotted line - laser intensity distribution.

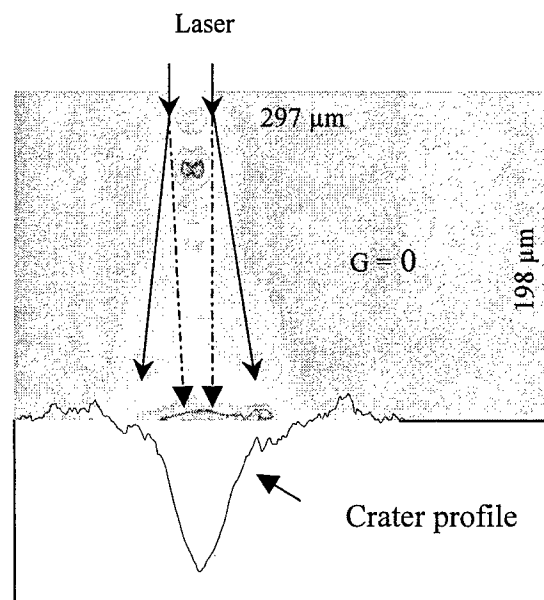


Fig. 6. Bubbles formation accompanied by crater broadening (20 mJ, 1064 nm, 6 ns, air).

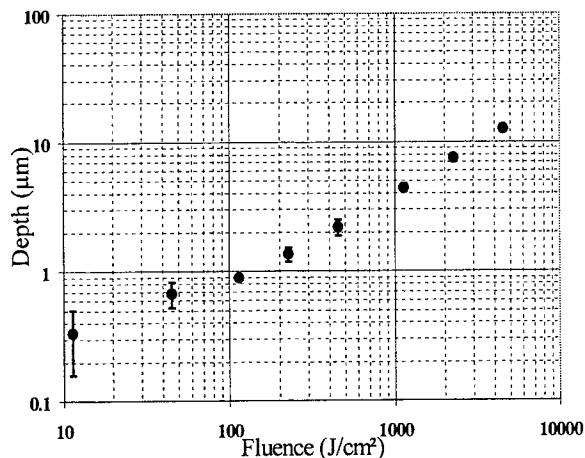


Fig. 7. Dependence of crater depth on laser fluence for copper after one shot (532 nm, 6 ns).

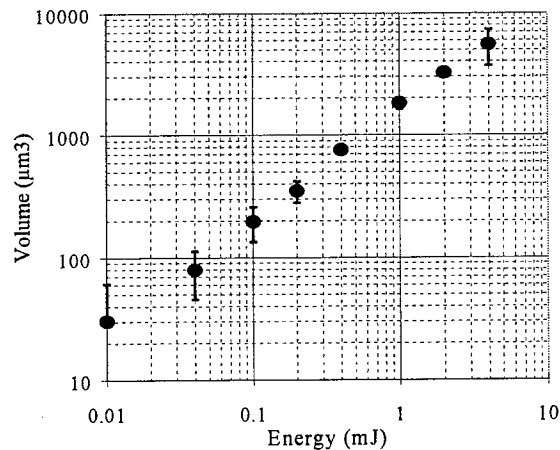


Fig. 8. Dependence of crater volume on laser energy for copper (532 nm, 6 ns).

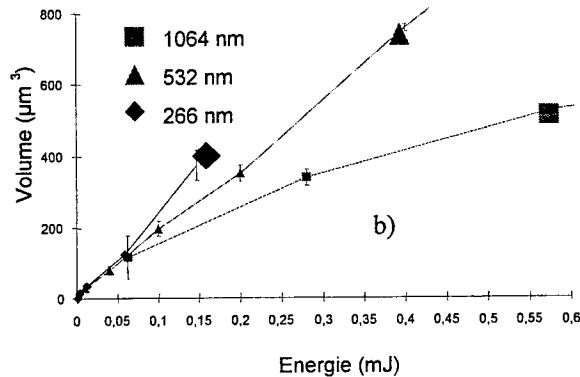
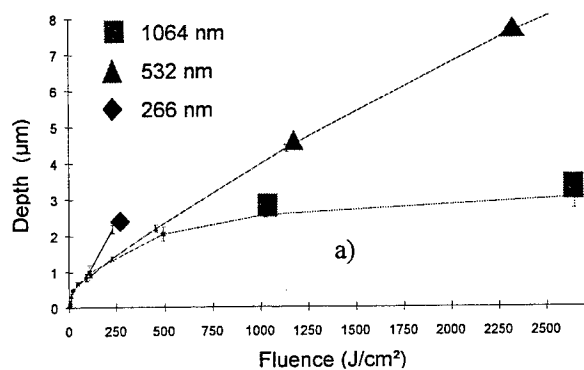


Fig. 9. Cu crater depth (a) and volume (b) as a function of ns laser fluence and energy, respectively, for 1064, 532 and 266 nm. Beam diameter is 10 μm .

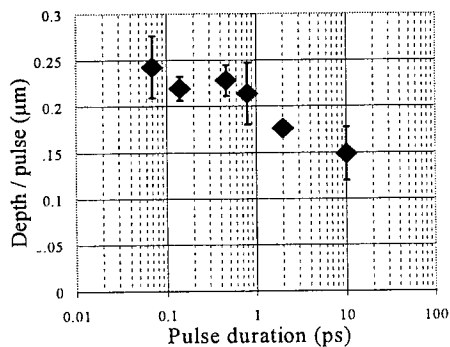


Fig. 10. Laser ablation efficiency for different pulse durations of Ti:Al₂O₃ laser. Target - Cu, wavelength - 800 nm, energy - 20 μJ .

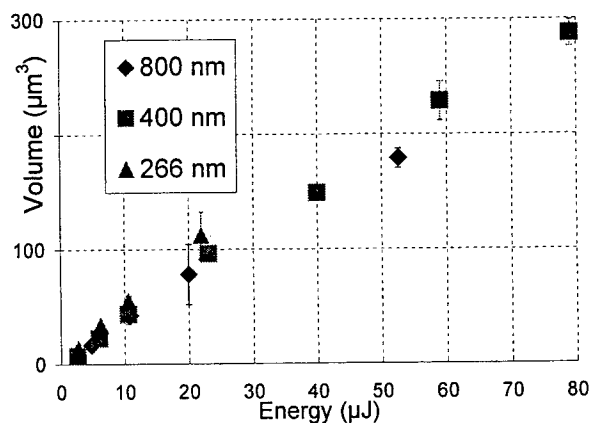


Fig. 11. Cu ablation efficiency for 800, 400 and 266 nm 70 fs laser pulses.

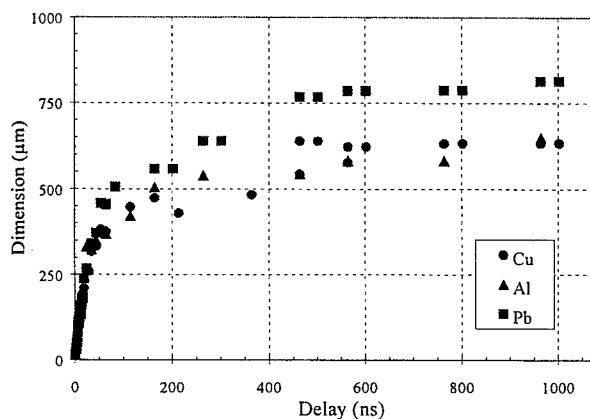


Fig. 12. Temporal evolution of longitudinal dimension of plasma created on aluminum, copper and lead for 1 mJ, 532 nm.

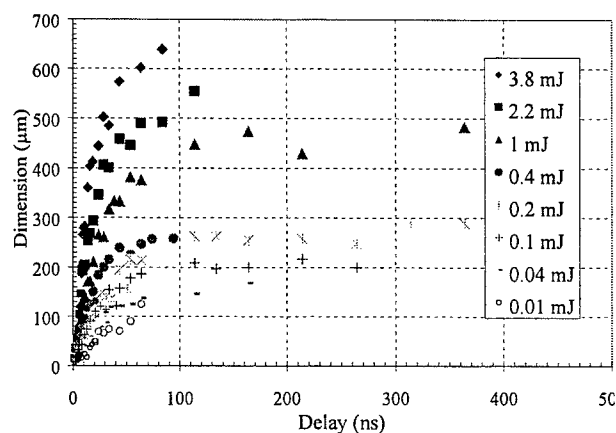


Fig. 13. Temporal evolution of the longitudinal copper plasma dimension for 0.01- 4 mJ energies. (532 nm)

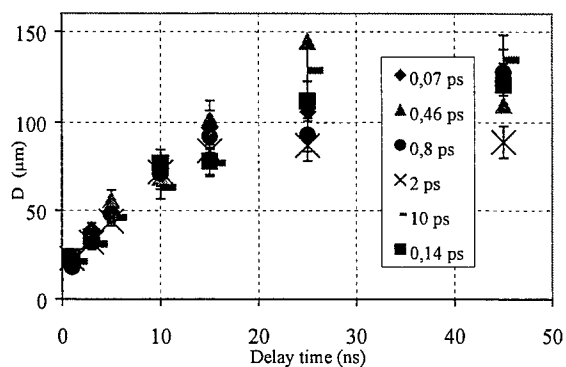


Fig. 14. Temporal evolution of the longitudinal copper plasma dimension obtained with different 800 nm pulse durations. Laser pulse energy – 20 μJ .

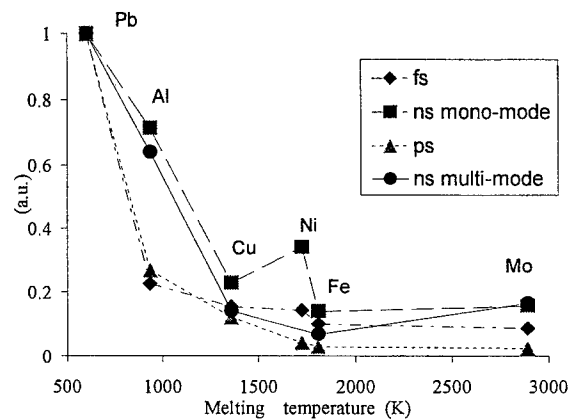


Fig. 15. Crater volume / melting temperature correlation (266 nm, 6 μJ , 7 - 8 μm beam diameter).

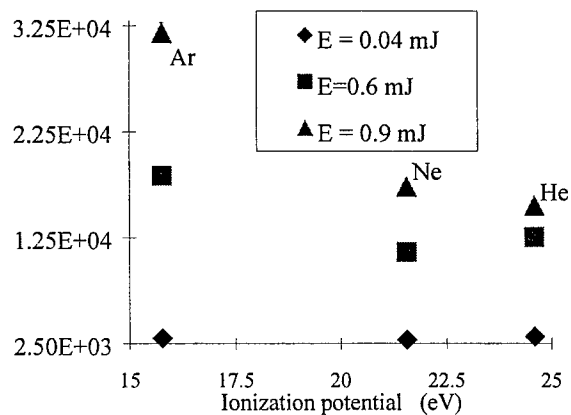


Fig. 16. Longitudinal plasma expansion velocity in different gases (Cu, 1064 nm).

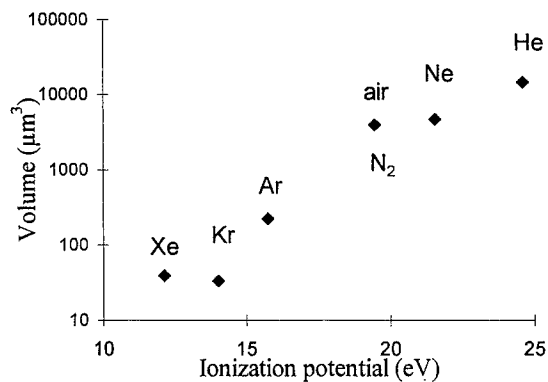


Fig. 17. Cu crater ablated volume after one laser shot (20 mJ, 1064 nm).

Time-resolved measurement of ablation from ns-laser-heated aluminum and comparison with simulation

M. Watanabe^a, E. Hotta^a and T. Yabe^b

^a Department of Energy Sciences, Tokyo Institute of Technology,
4259 Nagatsuta, Midori-ku, Yokohama 226-8502, Japan

^b Department of Mechanical Sciences and Engineering, Tokyo Institute of Technology,
2-12-1 O-okayama, Meguro-ku, Tokyo 152-8552, Japan

ABSTRACT

An experimental and numerical study was conducted on ablation from ns-laser heated aluminum. The goal of present study is to clarify the laser ablation phenomena.

In experiments, a YAG laser of 650mJ in 4-7nsec was used to perpendicularly illuminate an aluminum target. Time-resolved measurements were conducted using high-speed camera system. Also, a numerical simulation was conducted using CIP(Cubic-Interpolated Pseudoparticle Propagation) method.

The experimental results of time-resolved measurements indicate that the target surface itself is melting until late after the laser irradiation. The SEM pictures of the irradiated target surface are showing the generation of many minute protrusions. These protrusions near the part that laser is irradiated are facing toward the laser beam path and those of the surroundings are facing toward circumference. It is found by numerical simulation that this is due to the appearance of the critical point just after the laser irradiation. Since the laser beam goes around the critical point, the damaged part expands toward circumference.

Keywords: Laser ablation, High-speed photograph, CIP method, Critical point

1. INTRODUCTION

Laser beam can locally generate high energy condition with plasma formation. When a pulsed laser beam is focused on a solid target, ablation plasma is generated near the surface of the target. This kind of technology with beam-material interaction has been applied to many industrial fields, for example, inertial confinement fusion, laser processing, laser-triggered switch, X-ray source for lithography and microscopes, deposition of a superconducting thin film and so on¹⁻³. However, compared with the widely applicable investigation, the physical process of the ablation is still not clarified.

In order to clarify the process of laser ablation, it is necessary to understand the initial stage of various processes involved during the laser-target interaction, such as evaporation, plasma formation, hydrodynamics and its subsequent expansion.

Recently, the hydrodynamic simulation of laser ablation has shown some very interesting results. Yabe et al.^{4,5} raised a question on whether a formation of crater on the target is finished during laser pulse. If this crater could be created during laser pulse, the cutting speed should be much larger than the speeds of sound wave and elastic wave inside target material.

Their report pointed out a possibility that the crater of target was formed well after the laser-pulse ended. However, there is no experimental verification concerning this delay. Therefore, our experiments aim to measure this delay by time-resolved observation of ablation plasma.

In this paper, time-resolved measurements of ablation from ns-laser heated aluminum were conducted using high-speed camera system. Also, a numerical simulation was conducted using CIP(Cubic-Interpolated Pseudoparticle Propagation) method⁴.

2. EXPERIMENT

Time-resolved measurement of ablation plasma was conducted by using a high-speed camera system (IMACON 468, DRS Hadrand Ltd.). Figure 1 shows a schematic diagram of the experimental setup. The laser used is a Q-switched Nd-YAG laser, the wavelength and the pulse width of which are 1064nm and 4-7ns, respectively. The target was made of aluminum and mounted perpendicular to laser beam in target chamber. The target surface was freshened up in each shot. The target chamber can be evacuated to a pressure better than 5×10^{-5} Torr. The laser was focused to the target with a diameter of about $100 \mu\text{m}$, giving a peak irradiance of $1.7 \times 10^{12} \text{ W/cm}^2$ at an energy of 650mJ.

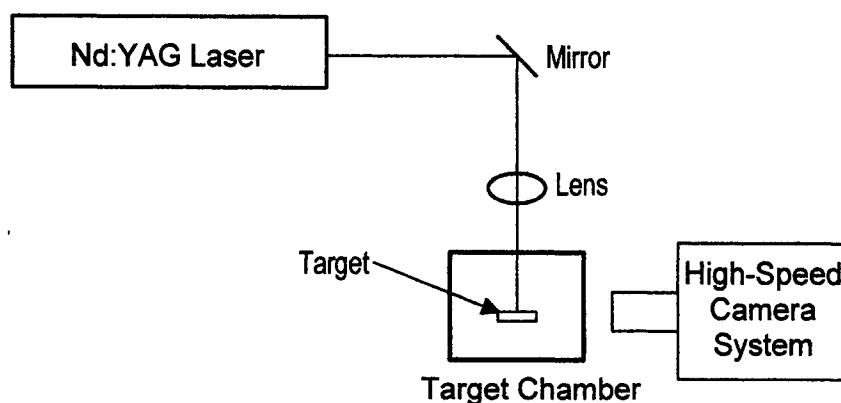


Figure 1. Schematic diagram of laser ablation experiment.

3. NUMERICAL SIMULATION

To numerically simulate the laser ablation phenomena, the CIP method developed by Yabe et al. was applied to the axisymmetric hydrodynamic equations including thermal conduction, viscosity, elastic-plastic effect, equation of state and laser energy deposition. This method is so convenient that it can simulate a dynamic phase transition from metal to vapor. For the initial condition, the laser parameters of Nd-YAG laser were used.

4. RESULTS AND DISCUSSION

Figures 2(a)-(h) show the side-on framing photographs of laser ablation plasma taken by visible light emitted from plasma plume. Although the light emissions were integrated along the direction of observation, we can qualitatively guess the time sequential formation of the ablation plasma. Exposure time is 10ns for every photograph. The time just after the laser irradiation is chosen as the origin of time, as shown in Fig. 2(a).

When the laser beam is irradiated, plasma accompanied by a very strong radiation grows from the target surface in the vertical direction of the target, as shown in Fig. 2(b)-(d). Figures 3(a)-(c) are the side-on framing photographs taken in the narrower range of the vicinity of the target surface by using a microscope. In Fig. 3(a), a very strong plasma is produced by the laser pulse. Although the generated plasma expands from the target, the strongest part still stays near the target surface, as shown in Fig. 3(b)-(c).

Furthermore, the plasma plume spreads over in wide angle from vertical direction, as time proceeds. From Fig. 2(e) and 2(f), it is seen that the strong radiation is remaining near the target surface. This indicates that the target surface itself is melting until late after the laser irradiation. This agrees with the numerical results obtained by Yabe et al.^[5]. After this, the radiation of the outside part is remaining its brightness stronger than that of the central part, as shown in Fig. 2(g)-(h).

We observe a crater generated by a single laser shot. Figure 4(a) and (b) show photographs obtained by 3D Profile Microscope (VK-8500, KEYENCE CORPORATION) with the magnification of 10 times and 50 times. It is found that a mark, the diameter of which is about 1 mm, is made on the target surface by laser irradiation. The diameter of the generated

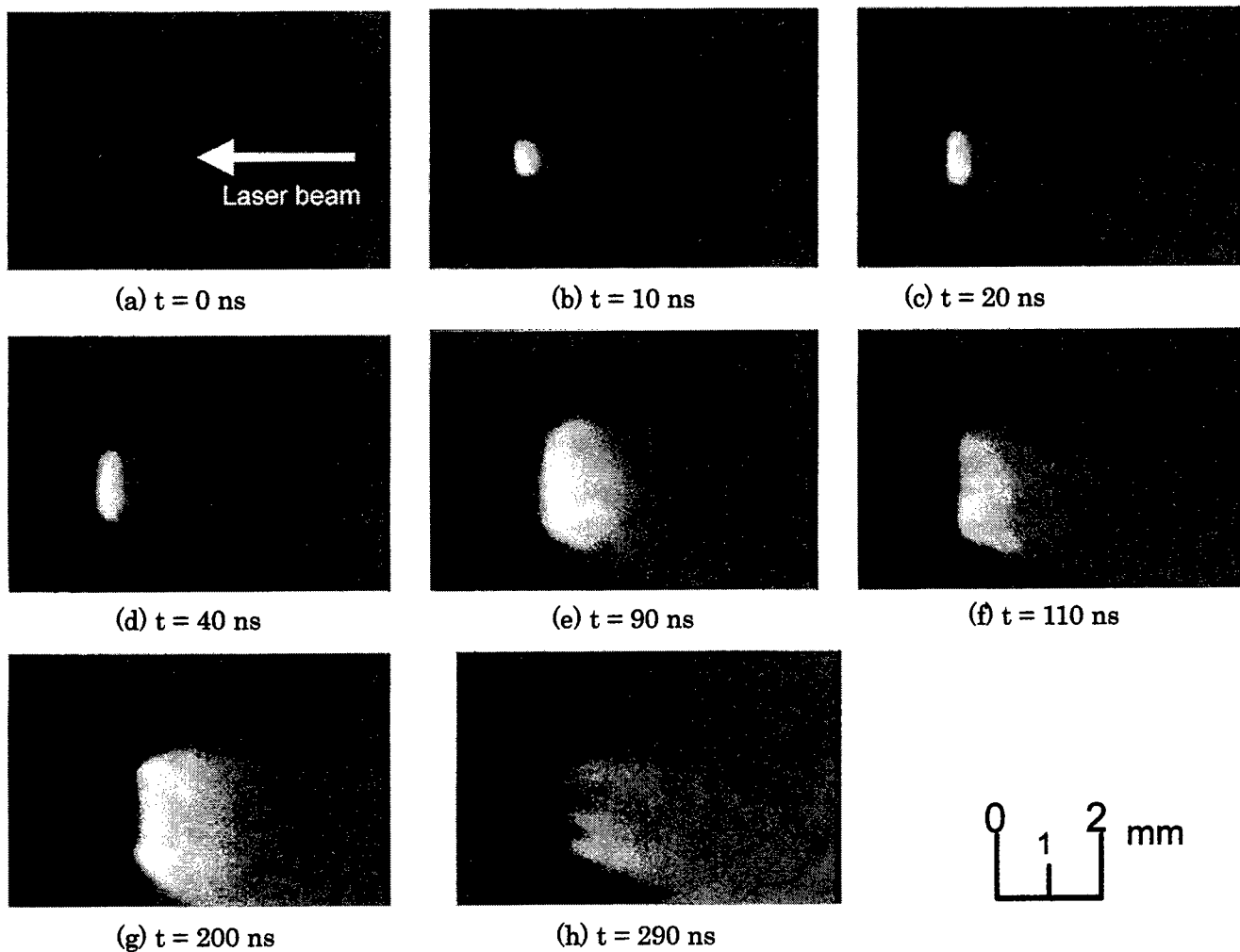


Figure 2. Side-on framing photographs

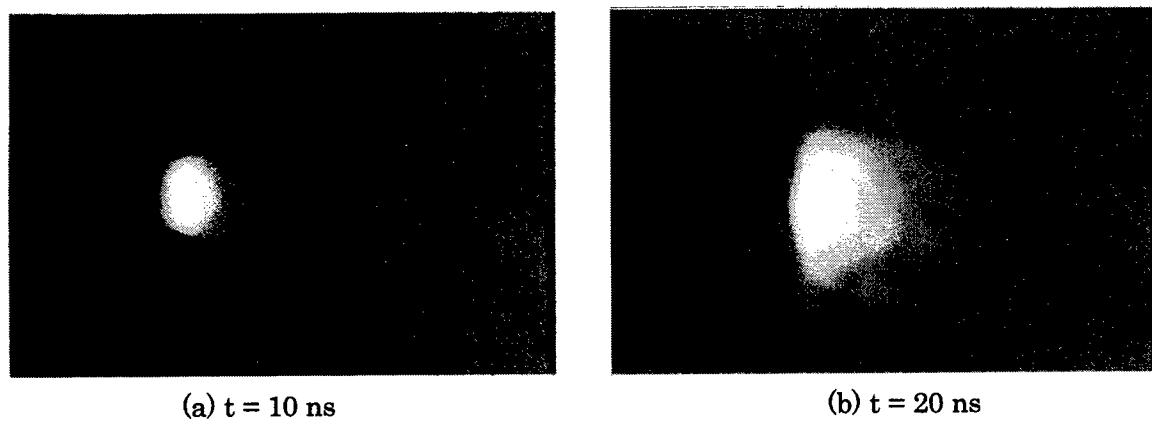
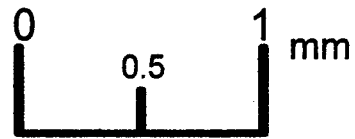
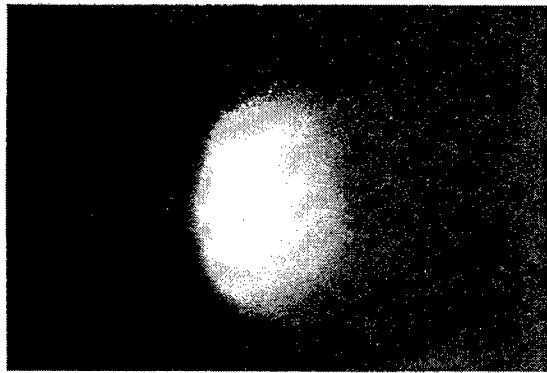
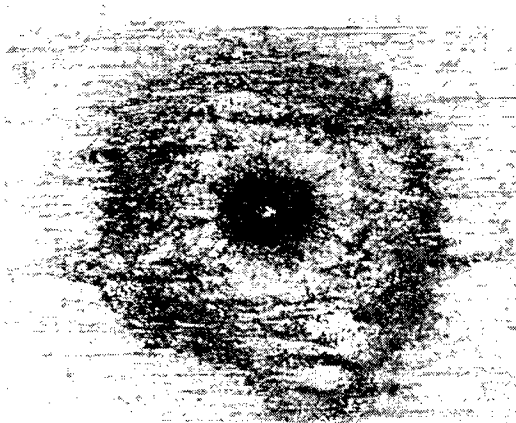


Figure 3. Side-on framing photographs



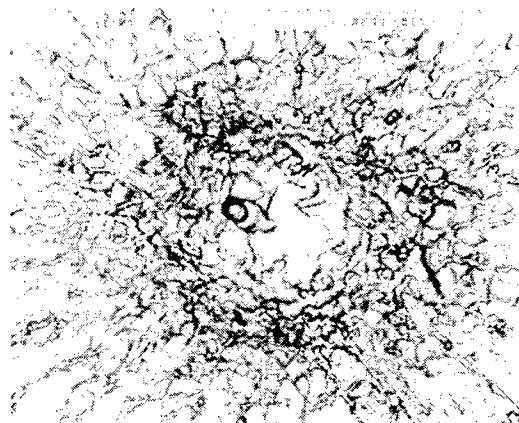
(c) $t = 40 \text{ ns}$

Figure 3. Side-on framing photographs taken in the narrower range



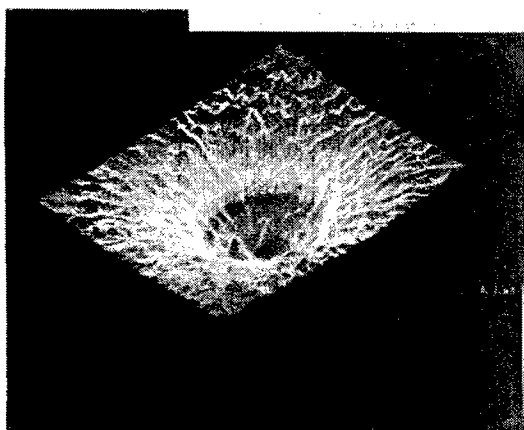
$500 \mu\text{m}$

(a)



$100 \mu\text{m}$

(b)



(c)

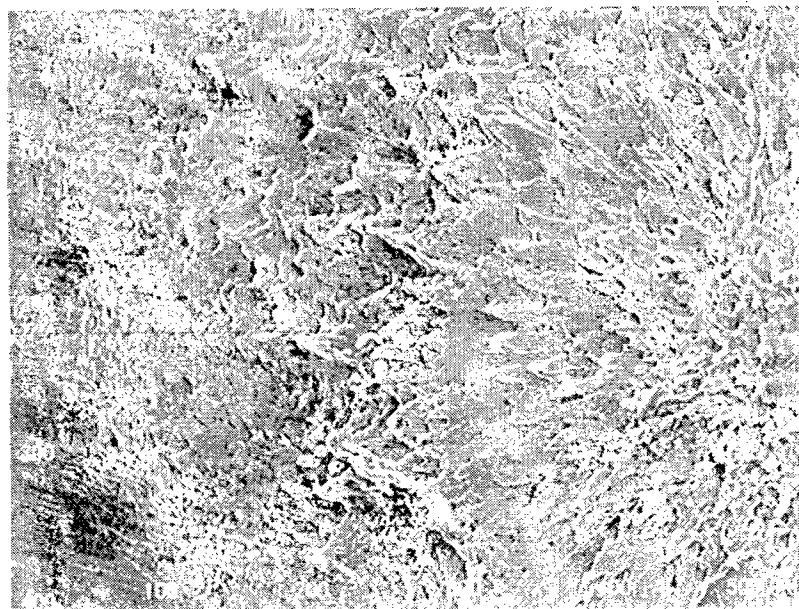
Figure 4. Crater configuration observed by using microscope

crater is about $250\mu\text{m}$ and the depth is about $43\mu\text{m}$. The central part of the crater is showing a sharp heat change, as shown in Fig.4(b). Also, the crater is created in a corn form of the angle of 45 degrees as shown in Fig.4(c). This angle is in accord with the dispersive direction of the plasma plume shown in Fig.2(g).

The photograph shown in Fig. 5 is taken at the central part of the crater by using Scanning electron microscope. We can find many minute protrusions around the center part of the crater. These protrusions near the part where laser is irradiated are facing toward the laser beam direction. However, the surroundings are facing toward circumference.

Figures 6 (a)-(c) show the density contours obtained by numerical simulation. The figures are being enlarged 5 times toward laser incidence, to make it easy to understand phenomena. At the center point, a deep crater is formed. The ablation plasma grows in the vertical direction of the target. Then the plasma plume spreads over in wide angle from vertical direction, as time proceeds. Finally, the mark of the laser irradiation is widely spread. This agrees well with the experimental results. Furthermore, the filamentation shown in Fig. 6(c) is similar to the experimental result as shown in Fig.2(e). From these numerical results, we can find the following interesting phenomena. Figure 7(a)-(d) show the density and temperature contours during laser irradiation. Just after the laser beam reaches at the target surface, a critical point is generated. Once the critical point is formed, the laser beam cannot reach the crater part of the target. The laser beam and thermal conduction that go around the critical point heat the outside part of the crater and generate a next critical point. Because the generation of the critical point continuously spreads to the circumferential direction, the mark of the laser irradiation becomes much larger in comparison with the diameter of focused laser beam. The many protrusions around the crater shown in Fig.5 seem to be generated by these phenomena.

Figure 8 shows the final crater configuration obtained both by the experiment and the numerical simulation. Good agreements in the diameter and depth of the crater are obtained between the experimental and numerical results.



200 μm

Figure 5. SEM photograph

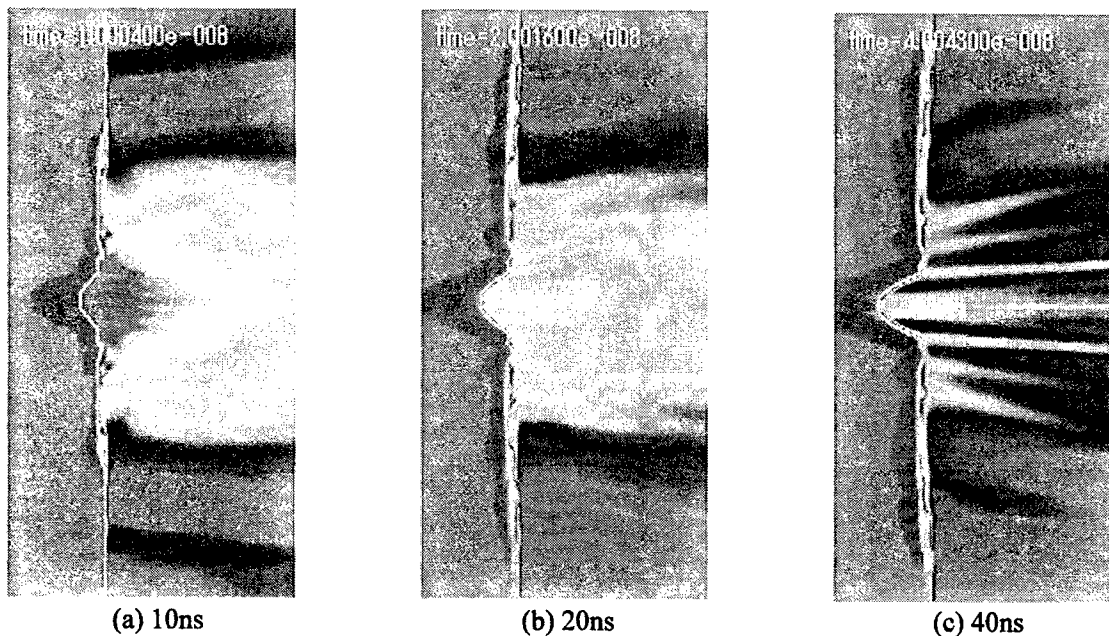


Figure 6. Density contours

5. CONCLUSIONS

Experimental and numerical studies were conducted on ablation from ns-laser heated aluminum. Results obtained are summarized as follows,

- (1) The experimental results of time-resolved measurements show that the target surface itself is melting well after the laser irradiation.
- (2) There are many minute protrusions on the surface of the crater. The protrusions near the part where laser is irradiated are facing toward the laser beam direction and the surroundings are facing toward circumference.
- (3) Just after the laser irradiation, a critical point appears far from the target surface. Since the laser beam and heat wave go around this point, the damaged part expands toward circumference.

6. REFERENCE

1. J. C. Miller and D. B. Geohegan (eds.), *Laser Ablation*, AIP, 1994.
2. R. C. Elton, *X-ray Laser*, Academic Press, 1990.
3. I. Fukushi, M. Watanabe, E. Hotta, A. Okino and K. Ko, *Characteristics of Laser-Triggered Vacuum Switch*, Proc. XIXth Int. Symp. on Discharges and Electrical Insulation in Vacuum, 2, pp.511-514, 2000.
4. T.Yabe Y.Zhang, and F.Xiao, Lecture Note in Physics, Springer , pp.439-457, 1998.
5. T. Yabe, H. Daido, T. Aoki, E. Matsunaga and K. Arisawa, *Anomalous Crater Formation in Pulsed-Laser-Illuminated Aluminum Slab and Debris Distribution*, Research Rep. NIFS-417, 1996.

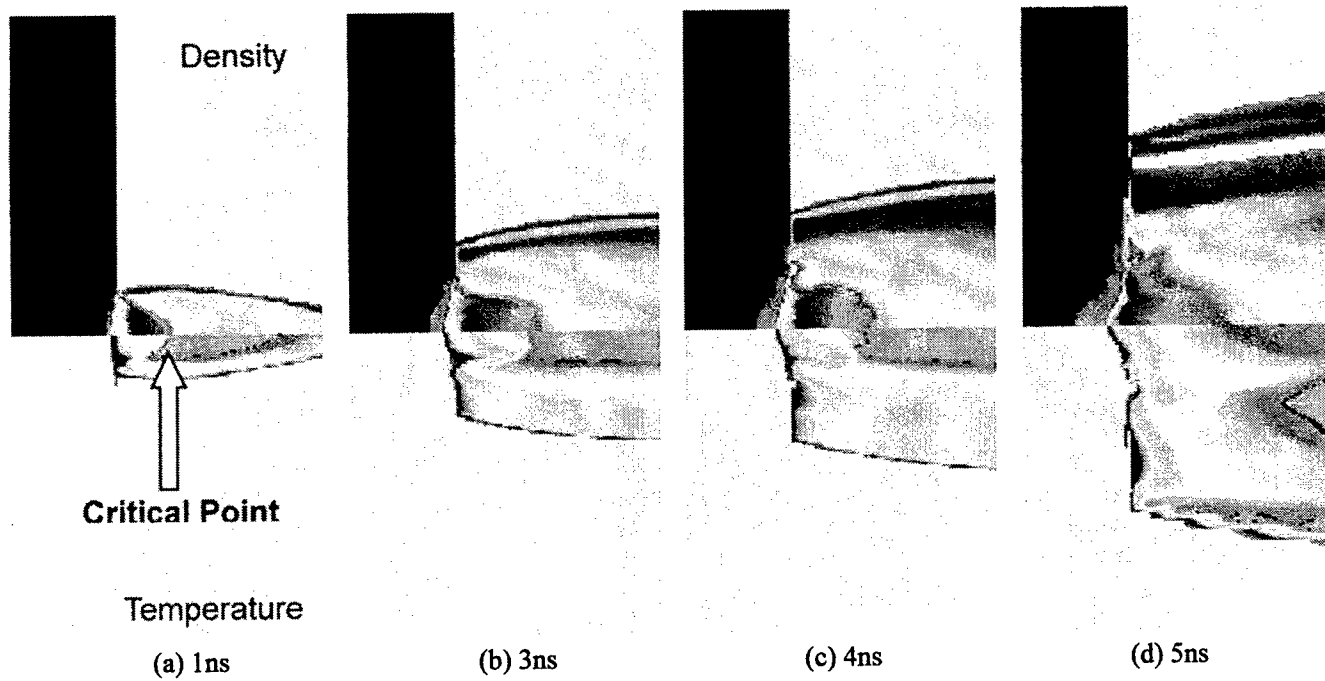


Figure 7. Density and temperature contours just after laser irradiation.

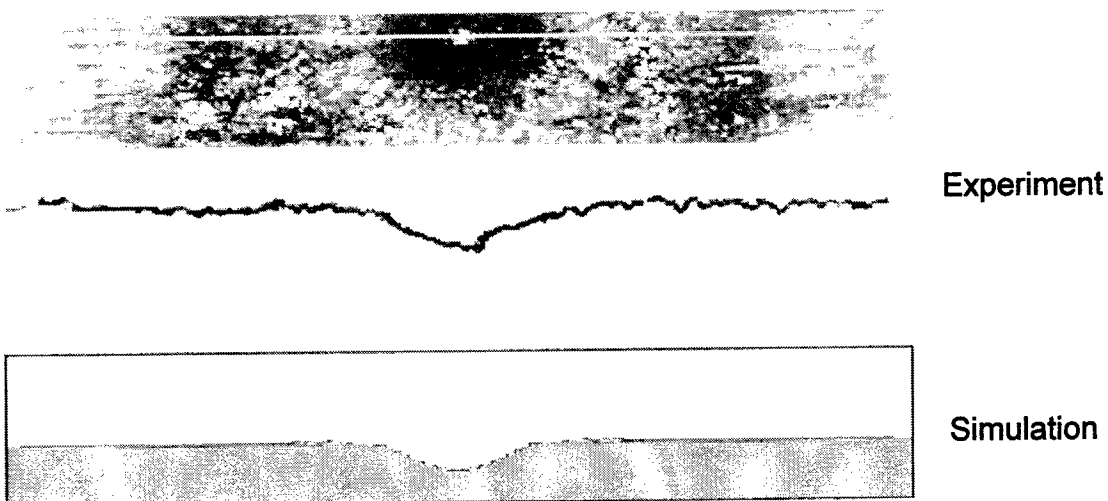


Figure 8. Comparison of the generated crater between experiment and numerical simulation.

Pulsed Laser Ablation vs Pulsed Ion Beam Evaporation for the Applications to Materials Science

K. Yatsui, M. Hirai, K. Kitajima, T. Suzuki, and W. Jiang

Extreme Energy-Density Research Institute, Nagaoka University of Technology,
Nagaoka, Niigata 940-2188, Japan

ABSTRACT

Applications of ablation plasma to materials science have been carried out using pulsed laser ablation and pulsed ion beam evaporation. Although basic idea is similar each other, the energy absorption mechanism of the two processes differs a lot, yielding big difference such as in the preparation of thin films. Compared with the pulsed laser ablation, the pulsed ion beam ablation has an advantage of higher plasma density inherent to huge energy density on targets. Two examples will be shown for the preparation of hard films, for example (Cr,Al)N films by pulsed laser ablation and B₄C films by pulsed ion beam evaporation.

1. INTRODUCTION

If an intense pulsed laser beam is irradiated on solid targets, its energy is deposited on the surface, yielding high energy density per unit area. When the energy deposited exceeds the energy required for the rotation, vibration, excitation and ionization of the target, high density plasma will be produced, which is called by ablation plasma. Such the pulsed laser ablation (PLA) plasma has been successfully applied for the preparation of thin films, or the synthesis of nanosize powders by the rapid cooling with the surrounding gas molecules. The preparation of fullerenes has been demonstrated as well.

With the PLA, however, it has been found that there exist several drawbacks. On the surface of the thin films prepared, there were a lot of droplets, yielding poor morphology. It takes a long time to prepare the films, on the order of an hour. There exists mismatch of the composition ratio between the original target and the film prepared, hence giving poor stoichiometry.

To use the ablation plasma produced by intense pulsed light ion beam represented by proton, on the other hand, has been successfully demonstrated by the present authors in 1988 to prepare thin films of ZnS, which was named by pulsed ion beam evaporation (IBE).¹⁾ High density ablation plasma has been easily achieved by the pulsed ion beam interaction with targets, for example on the order of n (plasma density) $\sim 10^{20} \text{ cm}^{-3}$.²⁾ Compared with the preparation by PLA, the IBE is characterized and summarized as follows.^{1,3-7)}

- a. Since the energy absorption by IBE is classical in the interaction with targets, there is no reflection with the target, while the reflection on target cannot be neglected with PLA.
- b. The energy absorption process is nonlinear for PLA, and the energy conversion efficiency from the electric power to laser is considerably low, being on the order of several percentage. On the other hand, the conversion efficiency of the ion beam is very high on the order of 50 %, hence being inexpensive compared with PLA.
- c. The plasma density is sufficiently high so that the local thermodynamic equilibrium (LTE) is always satisfied, not only near the target but also nearby the substrate. In PLA, on the other hand, the LTE is only satisfied near the target, but not near the substrate.
- d. Due to high density plasma, the instantaneous deposition rate is extremely high, being on the order of several cm/s.
- e. Due to high density plasma, the deposition is available even with the backside or masked configuration, where the substrate is placed just behind the target holder or in the masked plate so that the ablation plasma is not able to hit the substrate directly. Therefore, the films prepared are free from droplets.
- f. The pulse width is short compared with the thermal conduction time, and hence the adiabatic expansion of the high density ablation plasma into vacuum takes place. Therefore, the preparation is available even without heating the

substrate. Hence it is basically a low temperature process.

- g. Since the preparation is carried out in a very short time duration, typically by one shot, good stoichiometry can be available due to the less interaction of the ablation plasma with the impurities.
- h. The preparation is available even in a vacuum by IBE.

After our first preparation of thin films in 1988, we have succeeded in the preparation of various kinds of thin films of YBaCuO, ITO, ZrO₂, C, BN, BaTiO₃, (Ba,Sr)TiO₃, and apatite. Furthermore, from the above features, the synthesis of ultrafine nanosize powders such as of Al₂O₃, AlN, TiO₂, and TiN has been successfully demonstrated by IBE as well,⁷⁻¹¹⁾ where the high density ablation plasma is rapidly cooled by the interaction with molecules of the background gas. By use of analytic modeling of the IBE including beam-target interaction, the beam expansion into vacuum, and the growth of powders due to coagulation, we have succeeded in the understanding to synthesize the powders. In addition, the production of fullerenes and its higher orders has been demonstrated by IBE by use of graphite target.¹²⁾

For the preparation of thin films, the IBE is much more superior than PLA to need higher energy density and/or plasma density, or larger area because the achievement of the energy density is available from several J/cm² to several kJ/cm². If necessary, the ion beam has been found to be focused very tightly to 360 μ m in diameter.

2. BASIC PROCESS^{4,5)}

The physical process of the pulsed ablation plasma can be divided into two phases. The first phase is the beam-driven expansion during the pulse width, which includes the beam-target interaction, the evaporation of the target, and the interaction of the evaporation material with the incident beam. After the beam pulse, an adiabatic expansion takes place into vacuum, hence yielding the preparation of the thin films.

Basic equations governing the ablation process are the equations of continuity, momentum, energy, and the state. One-dimensional hydrodynamic equations can be used for this purpose. The only difference between PLA and IBE exists in the equation of energy. For IBE, the time derivative of the mass of the evaporated material per unit area can be assumed to be zero, whereas it can be given by a constant for PLA.

Using the above idea, the basic physics governing the ion beam ablation plasma has been well understood from the comparison between the experiment and the simulation.

3. PREPARATION OF THIN FILMS OF (Cr,Al)N BY PLA

The preparation of (Cr_{1-x},Al_x)N film is very interesting from a viewpoint of wear-protective coatings with higher oxidation resistance at high temperatures¹³⁾. The coating may provide an alternative instead of CrN coatings used conventionally. The preparation of thin films was tried by physical vapor deposition (PVD).

In the equilibrium Cr-Al-N ternary-phase diagram, Cr, Al and N can not be soluble in AlN and CrN. Previous studies on the microstructure and the metastable phases in (Cr_{1-x},Al_x)N films prepared by physical vapor deposition (PVD) were mainly discussed on the Al content in the films. The microstructure of the (Cr_{1-x},Al_x)N films prepared by PLD was studied in the present paper.

A PLD system by Nd:YAG laser was used to prepare (Cr_{1-x},Al_x)N films to ablate Cr and Al. The parameters of the laser were 355 nm (3 ω), 7 nsec, and 10Hz. Base pressure of the chamber was 5 \times 10⁻⁶ Torr. The substrate was heated up to 400°C. The films were prepared on Si (111) wafer by ablated plasma of Cr and Al at a pressure of 50 mTorr of nitrogen. The chemical bonding was measured by FT-IR, while the microhardness by Vickers hardness tester at the load of 5 gf.

Figure 1 shows the FT-IR spectra, where the film was prepared at d_{T-S} = 40 mm, and p_N = 50 mTorr. The composition of Al to metal (Cr + Al) in the films was measured by EDX and RBS. The (Cr_{1-x},Al_x)N films, where x is below 0.75, show the peaks associated with Cr-N bonding. The (Cr_{0.10},Al_{0.90})N and AlN films indicate the presence of Al-N binding.

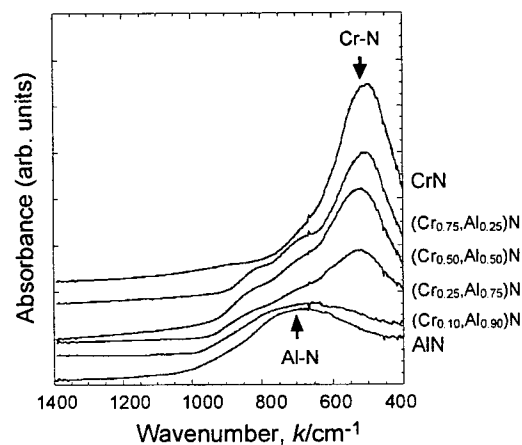


Fig. 1 FT-IR spectra of (Cr_{1-x},Al) films prepared at 40 mTorr (N₂) and 400°C of substrate temperature.

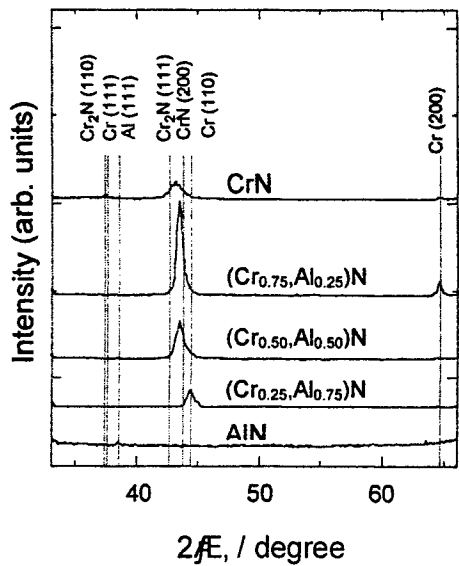


Fig.2 XRD patterns of $(\text{Cr}_{1-x}\text{Al}_x)\text{N}$ films prepared at 40 mTorr (N_2) and 400°C of substrate temperature

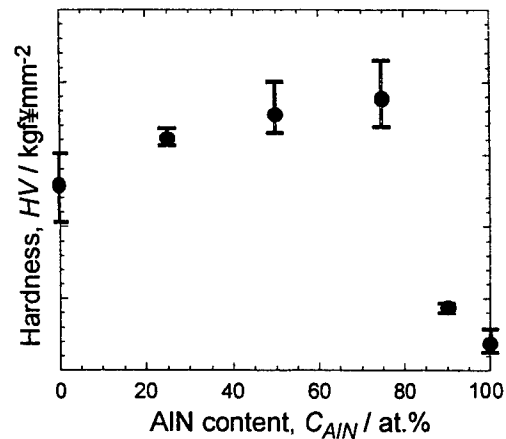


Fig.3 Microhardness of $(\text{Cr}_{1-x}\text{Al}_x)\text{N}$ films as a function of content of AlN

The phase of the $(\text{Cr}_{1-x}\text{Al}_x)\text{N}$ films for various x values was studied by XRD. Typical XRD patterns for $x = 0.10, 0.25, 0.50$ and 0.75 are shown in Fig. 2. The composition of Al to metal (Cr + Al) was measured by EDX and RBS.

The XRD patterns of the films for $x = 0.10 \sim 0.75$ show a single-phase B1-NaCl structure, like CrN. The AlN film appears as amorphous. With increasing x , the peak is shifted to higher 2θ , smaller lattice parameter. The lattice parameters of the B1-single phase of $(\text{Cr}_{1-x}\text{Al}_x)\text{N}$ films decreases with increasing AlN content, probably due to Al substituting with Cr in CrN lattice.

It is predicted that the critical solubility of AlN into CrN with B1 structure is 77 atomic percent¹³⁾. The experimental results show that it is B1 structure for CrN below 77 at. % AlN, and that it changes to B4 structure for AlN above 77 at. % AlN. Taking into account the accuracy of EDX measurement, this prediction of AlN solubility limit into CrN (77 at. %) shows a good agreement with the experimental results (75 at.%) from the viewpoint of the limit of AlN solved.

Figure 3 shows the microhardness of the $(\text{Cr}_{1-x}\text{Al}_x)\text{N}$ films for various x values. The hardness increases with x up to about 0.75, and then decreases.

Although the increase in the hardness caused by substitution of Al atom with Cr atom in B1 type CrN lattice was reported¹⁴⁾, the hardening mechanism was not clear. One idea is associated with the solution hardening. Here, we consider the hardening mechanism from a viewpoint of mechanical property.

The bulk modulus B (GPa) is expressed by and It is expressed as $B = 1761 \cdot d^{-3.5}$, where d is the nearest neighbor distance (\AA) of AB compounds with tetrahedral coordinate¹⁵⁾. With decreasing the interatomic distance, the potential to affect the atoms increases; in other words, the bonding strength between A and B is increased. Although there are some problems to apply this to Cr-Al-N directly because of neglecting the effects of d electrons, bulk modulus increases with decreasing interatomic distance. The decrease in the interatomic distance was reported by Al substitute to Cr into the CrN lattice.¹⁶⁾ Thus the hardening of Cr-Al-N pseudobinary films can be interpreted by the increase in the bulk moduli.

4. PREPARATION OF THIN FILMS OF B_4C BY IBE¹⁷⁾

Boron carbide (B_4C) is known as one of materials by its hardness, wear resistant and stability at high temperature. It can be applied, for example, for coating material for cutting tools. The preparation of thin films of B_4C , therefore, seems to be very interesting in wide applications in the industries. As far as the authors know, furthermore, no results have been reported on the preparation of thin films of crystallized B_4C .

We have experimentally tried to prepare the B_4C films by using IBE, where high-density ablation plasma is deposited on the target placed nearby the target. The experiment has been carried out on the intense, pulsed, light-ion beam generator, "ETIGO-II".¹⁸⁾

Figure 4 shows the schematic of the experimental arrangement. A magnetically insulated ion diode (MID) has been used in the experiment. It consists of an anode covered by polyethylene sheet on the surface as the ion source and a cathode with a vane structure, through which the ion beam can be extracted. The cathode serves as one-turn theta-pinch coil to produce transverse magnetic field as well. The target was placed at the geometrically focusing point of the ion beam. Specifically, it is possible to produce the following maximum output of the pulsed power; beam voltage ~ 3 MV, current ~ 460 kA, pulse width ~ 50 ns, power ~ 1.4 TW, and energy ~ 70 kJ. Experimentally, however, we have typically operated at the beam voltage $\sim (0.8 \sim 1)$ MV, which typically yields the energy density of the ion beam to be $50 \sim 100$ J/cm².

Various configurations have been studied such as front side (FS), back side (BS) and mask side (MS), where the substrate is placed in front of the target, back side, and mask side, respectively. The experiments were carried out by d_{AT} (distance between anode and target) ~ 190 mm, d_{TS} (distance between target and substrate) ~ 70 mm (FS), 77 mm (BS) and 92 mm (MS), number of shots ~ 20 or 50 , T_s (substrate temperature) \sim R.T., and p (pressure) $\sim 10^{-4}$ Torr.

To study the chemical coupling, we have analyzed the film by FT-IR (Fourier transform infrared analysis). Figure 5 shows a typical data of FT-IR, where the thickness of the films were 1 μ m for FS by 20 shots, 700 nm for BS (50 shots) and 400 nm for MS (50 shots), respectively. We see the presence of the absorption peaks¹⁹⁾ associated with B-C stretching bond at $1,085$ cm⁻¹ and the vibration of B₁₂ cluster-to-B₁₂ cluster at $1,380$ cm⁻¹.

The crystallization of the films has been studied by XRD measurements, the data of which are shown in Fig. 6(a) and Fig. 6 (b). Clearly, we see the presence of the highly crystallized B₄C thin films not only by FS but also by MS, compared with the JCPDS data. By BS, on the other hand, the films seem to be amorphous due to the lack of the crystallization. This may be understood that the plasma density of the ablation plasma is very high not only by FS but also MS, and that correspondingly migration actively takes place near the substrate. On the other hand, by BS the plasma density is quite low and migration does not take place, and furthermore the thickness of the film is too thin.

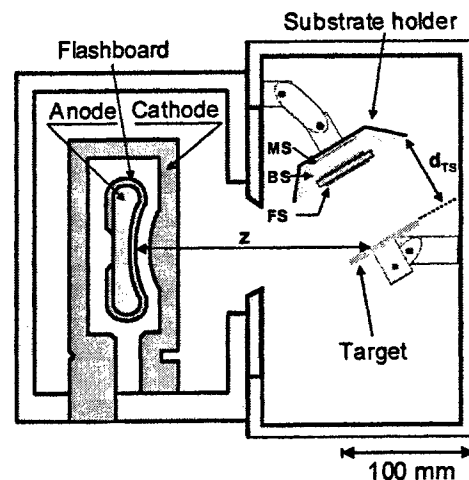


Fig. 4 Outline of experimental setup

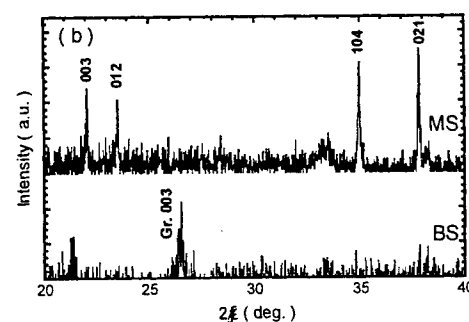


Fig. 5 FT-IR spectra, where DS, MS, and BS correspond to front side, mask side and back side, respectively.

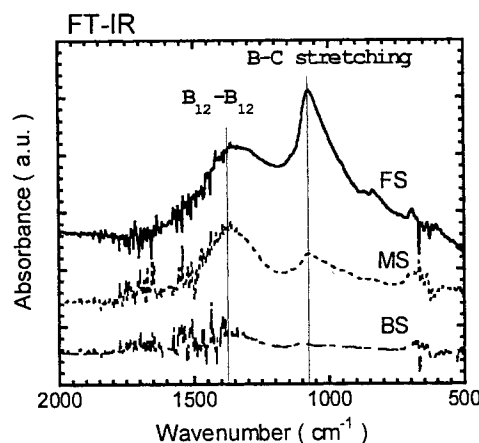
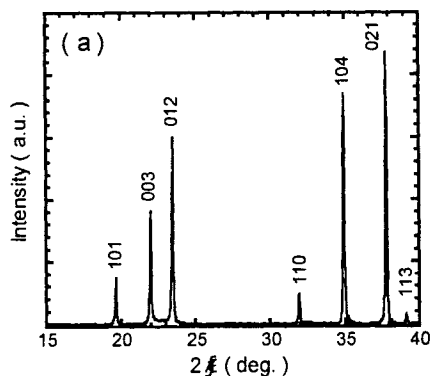


Fig. 6 XRD data of B₄C films prepared by (a) FS, and (b) MS and BS

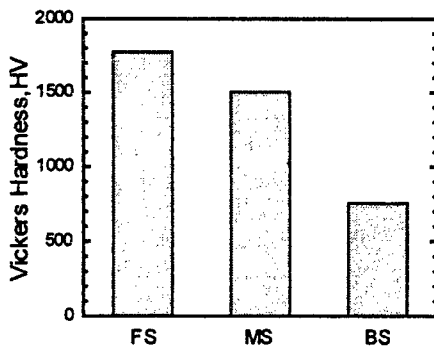


Fig. 7 Vickers hardness of B₄C films prepared by different configurations.

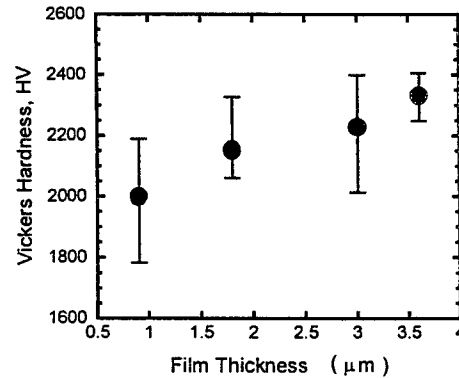


Fig. 8 Vickers hardness of B₄C films as a function of films thickness.

In addition, Vickers hardness has been measured, the data of which is typically shown in Fig. 7. The maximum hardness has been achieved as HV ~ 1,800 by FS, which is much larger than those by MS (1500) and BS (800). Using SEM, we have also studied the morphology of the surface of these films. The surface by FS has been observed to be rough, while those of BS and MS pretty smooth.

Figure 8 shows Vickers hardness of the film prepared by FS as a function of the film thickness, where the films are 0.9 μm (10 shots); 1.8 μm (20 shots); 3.0 μm (30 shots); and 3.6 μm (40 shots) thick. We have found from Fig. 8 that the hardness increases with increasing film thickness, and that the maximum hardness is achieved by HV ~ 2,300 for 3.6 μm thick film prepared by 40 shots.

5. CONCLUDING REMARKS

The (Cr_{1-x}, Al_x)N films have been successfully prepared by PLA. The (Cr_{1-x}, Al_x)N films for $x = 0.25 \sim 0.75$ atomic percent was found to be a metastable single-phase B1-NaCl structure. With increasing Al content, the films are found to be amorphous. Experimentally, AlN solubility limit has been found to be 77 at.% AlN, being in a reasonable agreement with the theoretical estimate of 75 at.% AlN. The hardness increases with x up to 0.75, and decreases rapidly due to the presence of amorphous structure. The hardness resulting from Al solved into CrN lattice seems to be due to the decrease in the lattice parameters.

Furthermore, for the first time as far as we know, we have succeeded in the preparation of the crystallized thin films of B₄C by ion beam evaporation. Vickers hardness increases with increasing film thickness, and the maximum value achieved has been observed to be HV ~ 2,300.

Though the basic idea for the preparation of thin films by the ablation plasma are similar between PLA and IBE, the energy absorption process is considerably different. The IBE by pulsed ion beam seems to be more convenient required the achievement of high density plasma because both the energy conversion efficiency and the density of the ablation plasma are very high. *In situ* preparation is available, without heating the substrate, even in a vacuum. No annealing is required as well, because the substrate is heated by a huge heat flux by the irradiation of the intense pulsed ion beam. Wide applications might be expected by IBE together with the development of pulsed power technology, particularly associated with highly repetitive pulsed power machines.

REFERENCES

1. Y. Shimotori, et al., *J. Appl. Phys.*, **63**, 968 (1988).
2. K. Yatsui, et al., *Laser Interaction & Rel. Plas. Pheno.* (Plenum Press, 1992), 567.
3. K. Yatsui, *Laser & Part. Beams* **7**, 733 (1989).
4. X. D. Kang, et al., *Jpn. J. Appl. Phys.*, **33**, 1155 (1994).

5. K. Yatsui, et al., *Phys. Plasmas* **1**, 1730 (1994).
6. T. Sonegawa, et al., *Appl. Phys. Letters* **69**, 2193 (1996).
7. K. Yatsui, et al., *Jpn. J. Appl. Phys.*, **36**, 4928 (1997).
8. K. Yatsui, et al., *Appl. Phys. Letters* **67**, 1214 (1995).
9. Y. Nakagawa, et al., *J. Mater. Sci.*, **33**, 529 (1998).
10. Q. Zhu, et al., *J. Appl. Phys.*, **86**, 5279 (1999).
11. K. Yatsui, et al., *J. Nanoparticle Res.*, **2**, 75 (2000).
12. S. Kurashima, et al., *Proc. National Inst. for Fusion Sci.* (1999) 19.
13. Y. Makino, *Mater. Sci. and Tech.*, **A192/193**, 77 (1995).
14. Sugishima, et al., *Surface & Coating Tech.*, **97**, 590 (1997).
15. M. L. Cohen, *Phys. Rev.*, **B32**, 7988 (1985).
16. J. Vetter, et al., *Surface & Coating Tech.*, **98**, 1223 (1998).
17. K. Kitajima, et al., *Proc. 13th Int'l Conf. High-Power Particle Beams*, 299 (2000).
18. Tokuchi, et al., *Proc. 2nd Int'l Symp. ICF Res. by High-Power Beams*, (1986) p. 430.
19. T. Hu, et al., *Thin Solid Films* **332**, 80 (1998).

ABLATION THRESHOLDS OF METALS WITH FEMTOSECOND LASER PULSES

M. Hashida*, A. Semerok, O. Gobert^a, G. Petite^b, J.-F. Wagner

CEA Saclay, DPE/SPCP/LSLA, Bât.391, 91191 Gif sur Yvette Cedex, France

^a CEA Saclay, DSM/DRECAM/SPAM, Bât.522, 91191 Gif sur Yvette Cedex, France

^b Ecole Polytechnique, DSM/DRECAM/LSI, 91128 Gif sur Yvette cedex, France

ABSTRACT

The laser ablation threshold experiments were performed on pure metals (Cu, Al, Fe, Zn, Ni, Pb, Mo) with the fs Gaussian laser beam (800 nm wavelength, 70 fs pulse width, 0.01 – 28 J/cm² fluence range) focused to 41.5mm spot diameter (at 1/e intensity level) onto metal surfaces. Three different ablation thresholds were distinguished. The multi-shot ablation threshold for Cu with 70 fs pulse was found to be 0.018 J/cm² and of one order of magnitude lower than that one observed previously. In the fluence range of 0.018 – 0.2 J/cm² the ablation rate was ≈ 0.01 nm/pulse. The threshold dependence on the pulse duration was demonstrated in the range of 70 fs – 5 ps for Cu. As the laser pulse width increased, the ablation threshold had the tendency to be higher. The ablation rate dependence on laser fluence for the other metals under study in our experiments with 70 fs was similar to that of Cu.

Keywords: Ablation threshold, femtosecond laser, metal target, ablation rate.

1. INTRODUCTION

Laser ablation can be used for various applications such as, for example, diagnostics of target composition¹, microstructure processing, removal of small space debris and radioactive surface cleaning²⁻³. For further improvement of these technologies and to make them more accurate, a knowledge of laser ablation mechanisms is important. The laser ablation with short pulses may be categorized by two different regimes distinguished by the characteristic time of electron-phonon interaction in metals. When the laser pulse width is shorter than the characteristic time (τ_{e-p} of several ps),^{4,6} the ablation threshold is smaller than that of a longer pulse and the ablation rate is modified efficiently. A large amount of both experimental and theoretical works on laser ablation with ultra short laser pulses has been done until recently⁷⁻²¹. However, the process of controlled ablation of matter has not been clearly understood and needs further investigation. As the knowledge of ablation threshold allows to explain better the physical mechanisms of short pulse laser ablation, it was the purpose of our study to investigate the ablation threshold of various metal samples with sub- ps laser pulses.

The ablation threshold was determined by two different methods. The first one was to study the ablation rate dependence on the laser fluence. In this case, the ablation rate L can be expressed by^{19,20}:

$$L = \frac{1}{\alpha} \ln \left(\frac{F}{F_{th}} \right)$$

where α - optical absorption or heat penetration coefficient, F - laser fluence. The ablation threshold (F_{th}) was determined by the laser fluence where the ablation rate was suffering rapid changes. The second method was applied to study the crater surface diameter dependence on the laser fluence. In this case, for the crater diameter (Γ) obtained with the Gaussian laser beam with the diameter (a), the ablation threshold can be expressed by:

$$F_{th} = F \exp \left\{ - \left(\frac{\Gamma}{a} \right)^2 \right\}$$

The ablation threshold can be roughly estimated by the laser fluence (F) resulting in the minimal crater diameter. To obtain

*Correspondence: Email:hashida @ile.osaka-u.ac.jp; WWW:http//; Telephone +33-1-69-08-6557; Fax +33-1-69-08-7738

the ablation threshold measurements with the precision of less than 15%, the crater diameter should be $F \leq 0.59 a$.

The ablation thresholds, ablation rates and crater shapes for metallic targets with short pulse laser are reported in this paper.

2. EXPERIMENTS

For the ablation experiment with metal samples, we used the ultra short laser system LUCA (CEA Saclay, France). The experimental parameters are summarized in Table 1. Fig.1 presents the experimental setup for ablation threshold measurement. The fs laser beam was guided to the target with three mirrors and a quartz lens ($f=100$ mm) focusing the beam perpendicularly onto the metal target surface. A near Gaussian beam profile was verified by measuring a laser intensity distribution on the surface position with a SPIRICON beam analyzer. On the target surface, the Gaussian laser beam took the shape of an ellipse with horizontal and vertical width of $41.5\mu\text{m}$ and $65.7\mu\text{m}$, respectively, at the intensity $1/e$ height. Thus, the efficient area of interaction was of $2.14 \times 10^{-5} \text{ cm}^2$. The laser energy was varied from $0.21\mu\text{J}$ to $600\mu\text{J}$ with an attenuator (quarter waveplate and polarizer). The maximum fluence on target surface was of 28 J/cm^2 . The energy stability was kept $\leq \pm 5\%$ during our experiments in atmospheric pressure at room temperature with pure metals. The laser repetition rate was of 20Hz . An electromechanical shutter was used to choose the desired number of laser shots for crater production. To determine the ablation threshold precisely, the diameter of the laser beam on the target surface should be kept of the constant value in moving the target under study or replacing the target by another sample. To keep the conditions of laser beam/target surface interaction the same, special adjustment was made to move the target in the direction parallel to its surface. For this purpose, a Michelson interferometer, comprising reference mirror, mirror M4 and target surface, was used in our experiment. The experimental set up comprised a He-Ne laser beam for optical scheme and target adjustment. The target could be easily placed in a desired laser beam diameter spot within $\pm 5\%$ precision. The craters obtained were measured with an optical microscope profilometer (MicroXam-Phase Shift Technology) with lateral resolution of $0.5\mu\text{m}$ and depth resolution of $0.01\mu\text{m}$.

Table 1 Experimental parameters for the ablation threshold measurements

Metal sample	Cu, Al, Fe, Zn, Ni, Pb, Mo
size	5x5 cm
thickness	~1 cm
surface roughness	~30 nm (RMS)
Laser wavelength	800 nm
spot size	$41.5\mu\text{m} \times 65.7\mu\text{m}$
energy	$0.21 \sim 600\mu\text{J}$ ($10 \text{ mJ/cm}^2 \sim 28 \text{ J/cm}^2$)
energy stability	< 5%
pulse width	70fs ~ 5ps
Pulse width stability	2% (RMS)
repetition rate	20Hz

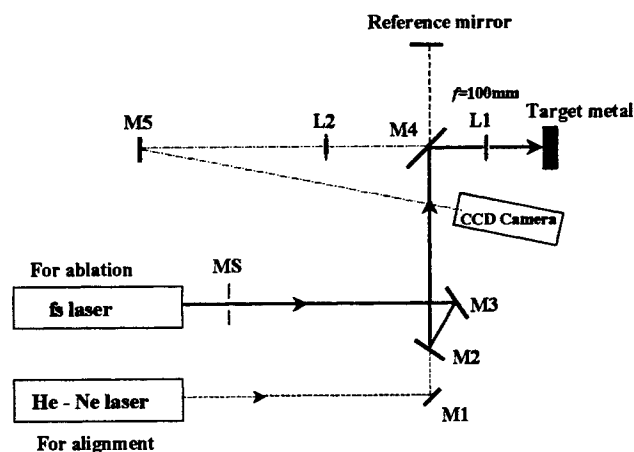


Fig.1 Experimental setup for the ablation threshold measurements. M: mirror, L: lens, MS: electromechanical shutter

The experiment was performed with a different number of laser shots. Fig. 2(a) and 2(b) show the increase of the crater depth for Cu sample. The ablation rate was defined as the crater depth per one laser shot. In this experiment, the ablation rates were $0.33 \mu\text{m/pulse}$ and 0.0093 nm/pulse for the laser fluence 13.4 J/cm^2 and 0.073 J/cm^2 , respectively. The inaccuracy of measurements was due to the crater structure with small spikes. Fig. 3 shows the ablation rate dependence on the laser fluence. Each ablation rate was obtained knowing the crater depth dependence on number of laser shots. The number of laser shots, that could result in the ablation depth detectable with a microscope profilometer, was 1-128 shots for

$F > 4 \text{ J/cm}^2$ and > 128 shots for $F < 4 \text{ J/cm}^2$. In the laser fluence range of $0.018 - 0.1 \text{ J/cm}^2$, the crater depth per pulse was so low that it was necessary to make 144000 laser shots to determine the ablation rate. For the low fluence range, the ablation threshold was found to be 0.018 J/cm^2 . The ablation rates were $\approx 0.01 \text{ nm/pulse}$ in the fluence range of $0.018 - 0.2 \text{ J/cm}^2$. The ablation rate was changing at the fluence of 0.18 J/cm^2 and 1.0 J/cm^2 . These fluence values seem to be another ablation thresholds.

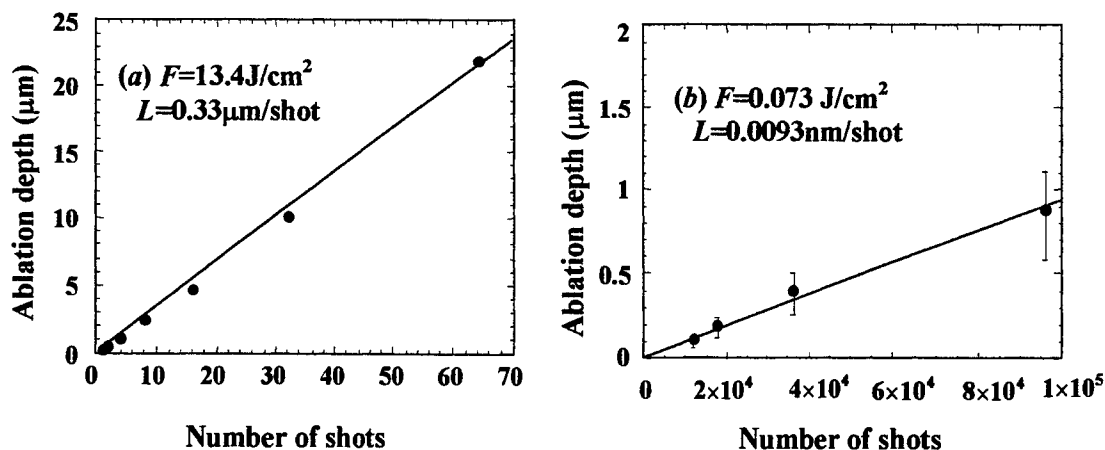


Fig. 2. Ablation depth obtained with Cu by multi laser shots for 70 fs laser pulse.

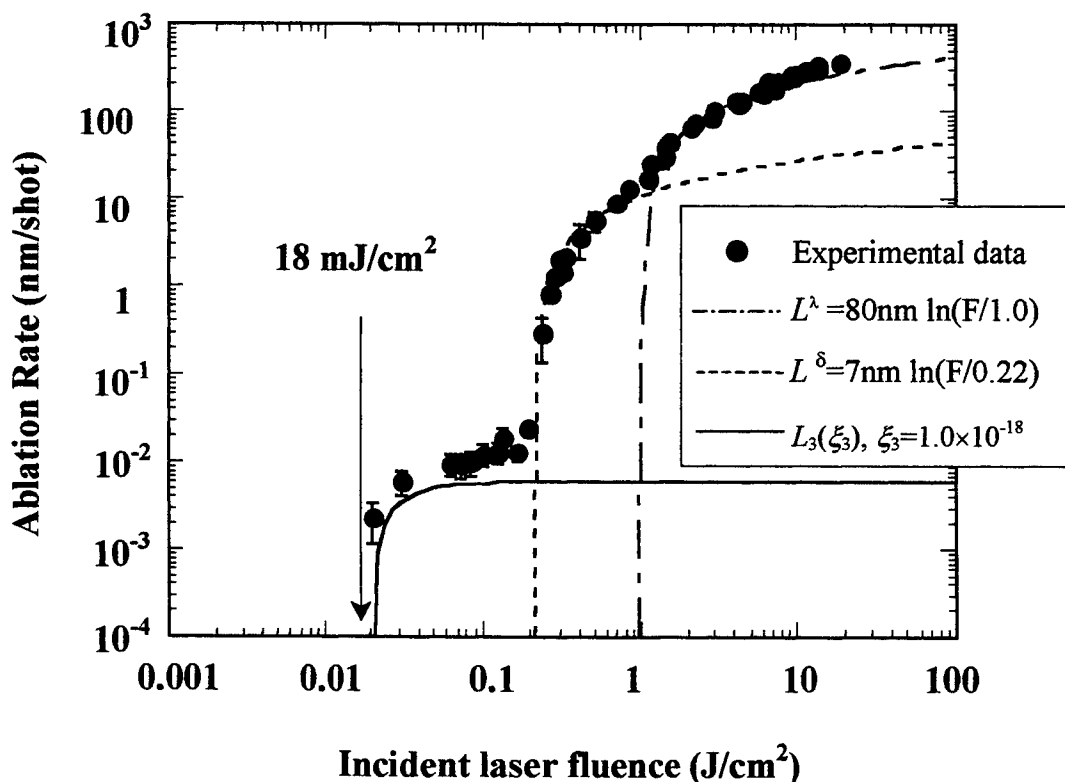


Fig. 3. Dependence of the Cu ablation rate on incident laser fluence with 70 fs pulse. The dotted and dashed-dotted curves are the calculated ablation rates based on a thermal model (logarithmic dependence). The solid curve is the calculated ablation rate obtained with the assumption of a three-photon absorption.

Fig. 4 shows typical crater profiles for Cu sample at different laser fluence values. The horizontal central section of the crater profiles was always used to determine the ablation threshold because the horizontal profile of the laser beam was in a fairly good agreement with the Gaussian shape. At each fluence, the crater profile was very reproducible. The profiles of the craters in Fig. 4(d)–4(f) were quite different from the laser beam profile and demonstrated a sharp peak in the center of a crater. At the fluence of 262 mJ/cm^2 , the diameter of the crater on a sample surface was of $13 \text{ }\mu\text{m}$. This diameter value was much smaller than that of the laser beam. Fig. 5 illustrates the dependence of surface crater diameter on incident laser fluence. Crater diameter values demonstrate two different dependencies with minimum diameters of $14 \text{ }\mu\text{m}$ and $24 \text{ }\mu\text{m}$ for the laser fluence of 0.02 J/cm^2 and 0.25 J/cm^2 , respectively. From the interpolation of these two dependencies to $\Gamma = 0$, the ablation thresholds were estimated as $F_{th}=0.018 \text{ J/cm}^2$ and $F_{th}=0.18 \text{ J/cm}^2$, respectively. The obtained ablation threshold values were equal to the thresholds obtained by the ablation rate dependence on laser fluence. Fig. 6 presents the diameter of the sharp peak (Fig. 4 d–f) that is assumed to be produced by the contribution of ablation with another threshold. The minimum diameter ($\Gamma=10 \text{ }\mu\text{m}$) of such sharp peaks gives the threshold fluence $F_{th}=0.250 \text{ J/cm}^2$.

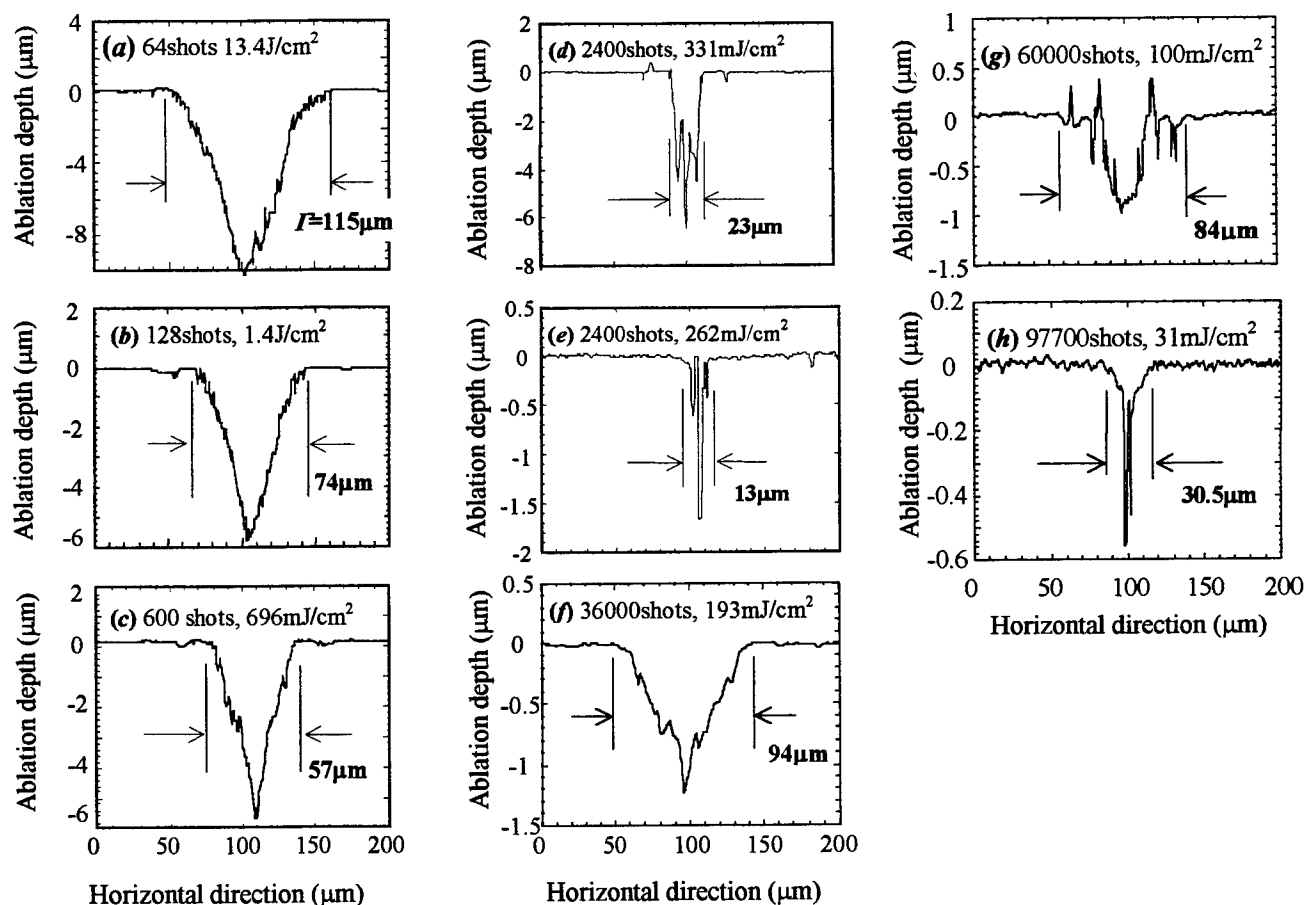


Fig. 4 Typical Cu crater profiles at different laser fluence with 70 fs.

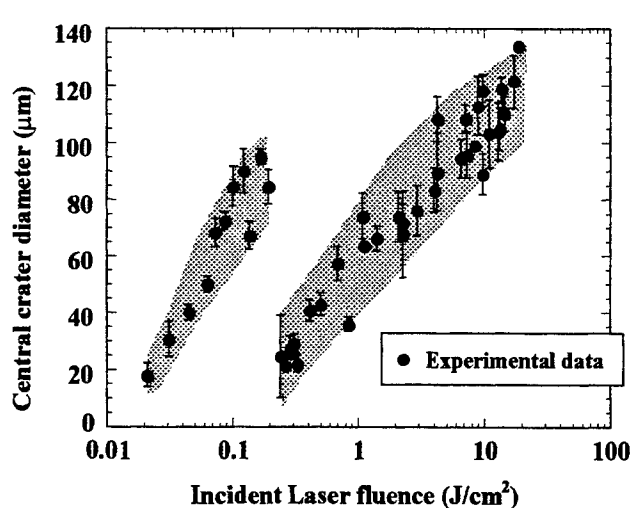


Fig.5 Dependence of the Cu crater diameter on incident laser fluence with 70fs.

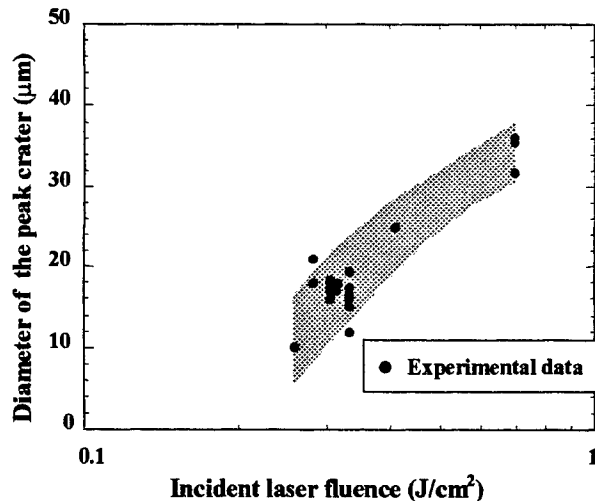


Fig. 6 Dependence of the Cu crater diameter on incident laser fluence with 70fs.

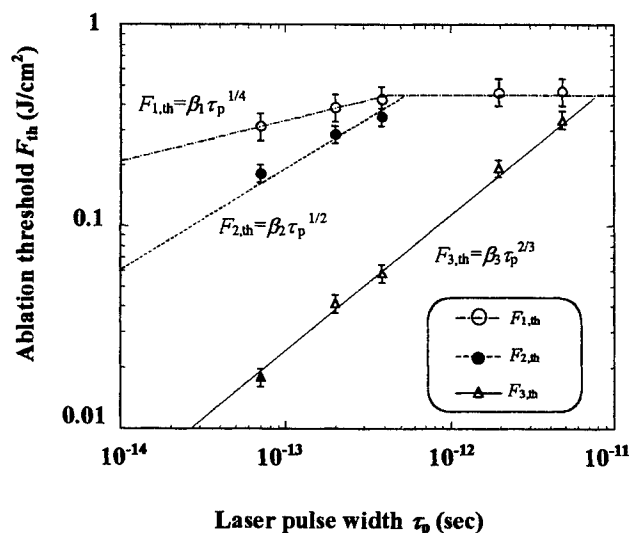


Fig. 7. Dependence of the ablation threshold on incident laser pulse width

Fig.7 gives the pulse width dependencies of the three obtained ablation thresholds ($F_{1,th}$, $F_{2,th}$, and $F_{3,th}$). The ablation thresholds $F_{2,th}$ and $F_{3,th}$ were determined by two different methods mentioned above and were found to be of the same value. With the pulse width longer than 2 ps, the ablation threshold $F_{1,th}$ could not be easily distinguished from $F_{2,th}$ as their values were almost the same. However, the ablation threshold was considered to be $F_{1,th}$ because the ablation rates in the fluence range above $F_{1,th}$ were quantitatively identical to those of the shorter pulse. The ablation threshold $F_{1,th}$ was saturated to 0.450 J/cm² at the pulse width of 4 ps. The lines of Fig. 7 were determined by the method of the least square fitting applied to the results obtained for each threshold. The fitting lines show that the dependencies are $F_{1,th} = \beta_1 \tau_p^{1/4}$, $F_{2,th} = \beta_2 \tau_p^{1/2}$, and $F_{3,th} = \beta_3 \tau_p^{2/3}$, respectively. Fig. 8 summarizes the experimental results of the ablation rate dependence of different metals (Fe, Ni, Pb, Mo, Zn, and Al) for 70 fs pulse. For all the metals under study in our experiments with 70 fs, the ablation thresholds ($F_{1,th}$, $F_{2,th}$, and $F_{3,th}$) were obtained with these two methods. The ablation rate lower than one atomic layer was observed near $F_{3,th}$.

3. DISCUSSION

The dependence of the ablation rate for Cu can be expressed by two different logarithmic functions²¹: $L = \delta \ln(F/F_{th}^{\delta})$ and $L = \lambda \ln(F/F_{th}^{\lambda})$, where $F_{th}^{\delta} = 0.14 \text{ J/cm}^2$ and $F_{th}^{\lambda} = 0.46 \text{ J/cm}^2$. They were characterized by the optical penetration depth ($\delta = 10 \text{ nm}$) and the electronic thermal conduction ($\lambda = 80 \text{ nm}$), respectively. This treatment of the ablation rate was used to analyze our experimental results. Fig. 3 presents the best fitting of the calculated dependencies of the ablation rate with the experimental results obtained with $\delta = 7 \text{ nm}$ and $F_{th}^{\delta} = 0.22 \text{ J/cm}^2$ for medium fluence regime, $\lambda = 80 \text{ nm}$ and $F_{th}^{\lambda} = 1.0 \text{ J/cm}^2$ for high fluence regime, respectively. For other metals under study, the calculation was done by adjusting δ , F_{th}^{δ} , λ , and F_{th}^{λ} . The experimental results and the calculated values of ablation thresholds were found to be different as ~ 1.5 for $F_{2,th}$ and F_{th}^{δ} and ~ 4 for $F_{1,th}$ and F_{th}^{λ} , respectively. Besides, with the ablation thresholds experimentally observed, the calculated dependencies of the ablation rate were not found to be in agreement with the experimental results in a wide range of laser fluences.

The multi-shot ablation threshold $F_{3,th} = 0.018 \text{ J/cm}^2$ (Fig.3) in our experiments was of one order of magnitude lower than $F_{2,th}$. The obtained ablation rates near $F_{3,th}$ could not be explained by the logarithmic dependence based on a thermal model as the ablation rate was less than one atomic layer in our experiments.

It was also reported in²¹ that for the pulses longer than 1 ps, the absence of the first logarithmic regime $L = \delta \ln(F/F_{th}^{\delta})$ results from the electronic heat diffusion during the laser pulse. However, the analytical relation between the ablation threshold and the pulse width was not presented. The results of our work might suggest the pulse width dependence on the ablation thresholds be explained by the process of m -photon absorption²². For m -photon absorption and incident laser pulse $I(0,t)$ of a rectangular shape, the ablation rate L_m can be analytically obtained and expressed as:

$$L_m = \frac{1}{(m-1)\xi_m} \left\{ \left(\frac{E_{TH}}{\tau_p \xi_m} \right)^{\frac{1-m}{m}} - \left(\frac{F}{\tau_p} \right)^{\frac{1-m}{m}} \right\} \quad (1)$$

$m \geq 2$

,where ξ_m - m -photon absorption coefficient, E_{TH} - ablation threshold energy per unit volume, F - incident laser fluence, τ_p - incident laser pulse width. The threshold fluence dependence on laser pulse width can be obtained from Eq.(1) at the condition of $L_m = 0$:

$$F_{th} = \left(\frac{E_{TH}}{\xi_m} \right)^{\frac{1}{m}} \tau_p^{\frac{m-1}{m}} = \beta_m \tau_p^{\frac{m-1}{m}} \quad (2)$$

The ablation threshold values obtained experimentally (Fig.7) were in good agreement with the function of $\beta_1 \tau_p^{1/4}$ for $F_{1,th}$, $\beta_2 \tau_p^{1/2}$ for $F_{2,th}$, $\beta_3 \tau_p^{2/3}$ for $F_{3,th}$. Thus, the ablation thresholds of $F_{3,th}$ and $F_{2,th}$ may be resulting from 3-photon and 2-photon absorption process, respectively. To explain the observed ablation rate dependence with the ablation threshold of $F_{3,th}$, the ablation rate L was calculated with the assumption that the ablation is resulting from 3-photon absorption process. The absorption coefficients of m -photon absorption (ξ_m) for Cu are not known. ξ_3 was determined by the parameter β_3 , obtained by the best fitting with experimental data, and $E_{TH} = 1840 \text{ J/cm}^3$ for Cu at room temperature²³. The calculated ablation rate with $\xi_3 = 1.0 \times 10^{-18} \text{ cm}^3/\text{W}^2$ is shown as a solid curve in Fig.3. It was in agreement of the factor of two with experimental results. The ablation rate of $F_{2,th}$ was calculated analogously. However, the calculated ablation rates are of two order of magnitude lower than the experimental ones. For other metals under study, the calculation of the ablation rate of $F_{3,th}$ was done by adjusting ξ_3 . The calculated results are shown in Fig.8.

Unexpectedly we found that the ablation rate dependence on the laser fluence can be well enough approximated by superposition of three different curves for all metals under study in our experiments:

$$\begin{aligned} L_3 &= \kappa_3^{-1} \ln(F/F_{3,th}) && \text{in low fluence regime,} \\ L_2 &= \kappa_2^{-1} [\ln(F/F_{2,th})]^2 && \text{in medium fluence regime,} \\ L_1 &= \kappa_1^{-1} [\ln(F/F_{1,th})]^3 && \text{in high fluence regime,} \end{aligned}$$

The reasonable explication of the fact that the curves are in a fairly good agreement with the experimental results has not been found yet.

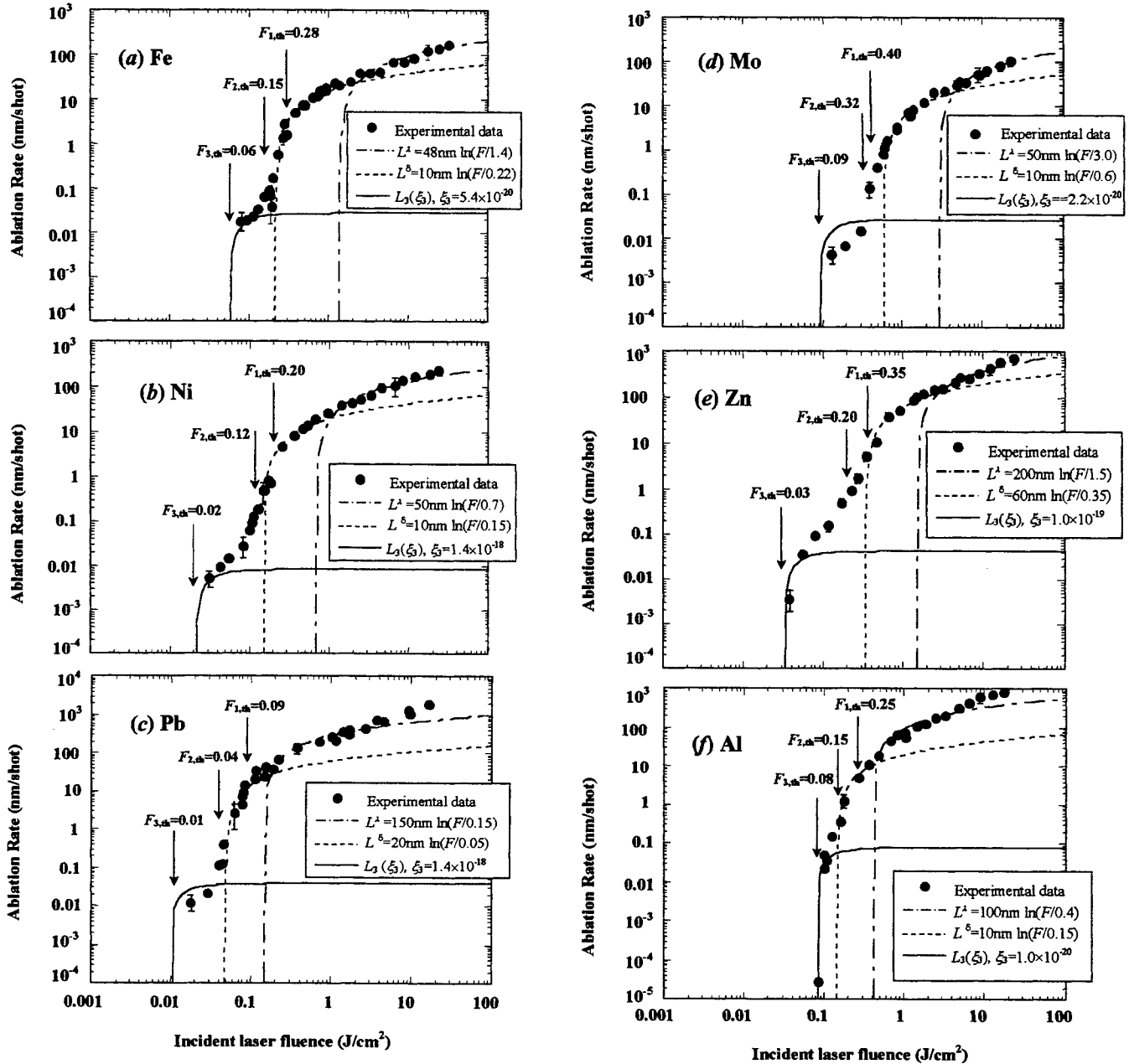


Fig. 8. Dependence of the ablation rate on incident laser fluence with 70 fs pulse. The dotted and dashed-dotted curves are the calculated ablation rates based on a thermal model (logarithmic dependence). The solid curve is the calculated ablation rate obtained with the assumption of a three-photon absorption. $F_{1,th}$, $F_{2,th}$, and $F_{3,th}$ are the ablation threshold obtained experimentally in high, medium, and low fluence regime, respectively.

4. CONCLUSION

Three ablation thresholds were determined in the experiments with fs laser pulses and pure metal samples. The pulse width dependencies of the ablation thresholds were obtained for Cu sample. They were found to be in good agreement with the functions of $\beta_1 \tau_p^{1/4}$ for $F_{1,th}$, $\beta_2 \tau_p^{1/2}$ for $F_{2,th}$, $\beta_3 \tau_p^{2/3}$ for $F_{3,th}$. Experimental results were analyzed within the framework of thermal laser ablation model that could not explain sufficiently well the obtained results. The ablation model with multi-

photon absorption was applied to explain some particular features of ablation rate with low energy pulses.

ACKNOWLEDGEMENTS

The authors would like to acknowledge the technical assistance of SPAM and LSLA laboratories, CEA Saclay, France. One of the authors, M.H., would like to acknowledge the Institute for Laser Technology, Japan for partial financial support of his participation in NLMI-10 conference.

REFERENCES

1. C. Geertsen, J. L. Lacour, P. Mauchien, L. Pierrard, "Evaluation of laser ablation optical emission sepectrometry for microanalysis in aluminium samples" *Spectrochim. Act.* **B 51** (1996) pp. 1403-1416
2. M. L. Sentis, P. Delaporte, W. Marine *et al*, "Cleaning of large area by excimer laser ablation" *Proceedings of SPIE* **3887** (1999)
3. X. Liu and G. Mourou, "Ultrashort laser pulses takes precision machining" *Laser Focus World*, August (1997) pp. 101-118
4. S.D.Bronson, A.Kazeroonian, J.S.Moodera, D.W.Face, T.K.Cheng, "Femtosecond Room-Temperature Measurement of the Electron-Phonon coupling Constant λ in mettalic superconductors", *Phys. Rev. Lett.* **64** (1990) pp. 2172-2175
5. G. L. Eesley, "Generation of nonequilibrium electron and lattice temperatures in copper by picosecond laser pulses", *Phys. Rev.* **B 33** (1986) pp. 2144-2151
6. M.I. Kaganov, I.M. Lifshitz, and L.V. Tanatarov, "Relaxation between electrons and the crystalline lattice", *Sov. Phys. JETP* **4** (1957) pp.173-178
7. H. Strehlow, "Heating of opaque surface by picosecond laser pulses", *Appl. Phys. A* **65** (1977) pp.355-360
8. P. P. Pronko, S. K. Dutta, D. Du, and R. K. Singh, "Thermophysical effects in laser processing of materials with picosecond and femtosecond pulses", *J. Appl. Phys.* **78** (1995) pp. 6233-6240
9. P.P. Pronko, S.K. Dutta, J. Squier, J.V. Rudd, D. Du, G. Mourou, "Machning of sub-micron holes using a femtosecond laser at 800nm" *Opt. Commun.* **114** (1995) pp. 106-110
10. S. Preuss, E. Matthias, M. Stuke, "Sub-picosecond UV-laser ablation of Ni films: strong fluence reduction and thickness-independent removal", *Appl. Phys.* **A59** (1994) pp. 79 -82
11. B.C. Stuart, M.D. Feit, S. Herman, A.M. Rubenchik, B.W. Shore, and M.D. Perry, "Optical ablation by high-power short-pulse lasers", *J. Opt. Soc. Am.* **B13** (1996) pp. 459-468
12. P. Simon, J. Ihlemann, "Ablation of submicron structures on metals and semiconductors by femtosecond UV-laser pulses", *Appl. Surf. Sci.* **109/110** (1997) pp. 25-29
13. K. Sokolowski-Tinten, J. Bialkowski, A. Cavalleri, D. von der Linde, A. Oparin, J.Meyer-ter-Vern, S.I. Anisimov, "Transient states of matter during short pulse laser ablation", *Phys. Rev. Lett.* **81** (1998) pp. 224-227
14. H.E. Elsayed-Ali, T.B. Norris, M.A. Pessot, and G.A. Mourou, "Time-resolved obsevation of electron-phonon relaxation in copper" *Phys. Rev. Lett.* **58** (1987) pp. 1212-1215
15. W.S. Fann, R. Storz and H.W.K. Tom, J. Bokor, "Electron thermalization in gold" *Phys. Rev.* **B46** (1992-II) pp. 13592-13595
16. S.S. Wellershoff, J. Gudde, J. Hohlfeld, J.G. Muller, E. Matthias, "The role of electron-phonon coupling in femtosecond laser damage of metals" (1998) *SPIE*
17. J. Gudde, J. Hohlfeld, J.G. Muller, E. Mattias, "Damage threshold dependence on electron-phonon coupling in Au and Ni films" *Appl. Surf. Sci.* **127-129** (1998) pp. 40-45
18. S.I.Anisimov, N.A. Inogamov, A.M. Opartin, B. Rethfeld, T.Yabe, M. Ogawa, V.E. Fortov, "Pulsed laser evaporation: equation-of-state effects" *Appl. Phys.* **A69** (1999) pp. 617-620
19. S. Preuss, A. Demchuk, M. Stuke, "Sub-picosecond UV laser ablation of metals" *Appl. Phys. A* **61** (1995) pp. 33-37
20. B. N. Chichkov, C. Momma, S. Nolte, F. von Alvensleben, A. Tunnermann, "Femtosecond, picosecond and nanosecond laser ablation of solids" *Appl. Phys.* **A63** (1996) pp. 109-115
21. S. Nolte, C. Momma, H. Jacobs, and A. Tunnermann, B.N. Chichkov, B. Wellegehausen, and H. Welling, "Ablation of metals by ultrashort laser pulses" *J. Opt. Soc. Am.* **B14** (1997) pp. 2716-2722
22. S. Preuss, M. Spath, Y. Zhang, and M. Stuke, "Time resolved dynamics of subpicosecond laser ablation" *Appl. Phys. Lett.* **62** (1993) pp. 3049-3051
23. *CRC handbook of Chemistry and Physics, 68th ed.*, edited by R. C. Weast, (CRC press, 1987-1988) pp. E-379

Ablation dynamics of solids heated by femtosecond laser pulses

B. Rethfeld^a, K. Sokolowski-Tinten^a, V.V. Temnov^{a,b}, S.I. Kudryashov^{a,c},
J. Bialkowski^a, A. Cavalleri^d and D. von der Linde^a

^a Institut für Laser- und Plasmaphysik, Universität Essen, D-45117 Essen, Germany

^b Institute of Applied Physics, 603600 Nizhnij Novgorod, Ulyanova St. 46, Russia

^c Chemical faculty of the Moscow State University, Moscow, Russia

^d Department of Chemistry and Biochemistry, University of California,
San Diego, La Jolla, CA 92093-0339, USA

ABSTRACT

Ultrafast time resolved microscopy of femtosecond laser irradiated surfaces reveals a universal feature of the ablating surface on nanosecond time scale. All investigated materials show rings in the ablation zone, which were identified as an interference pattern (Newton fringes). Optically sharp surfaces occur during expansion of the heated material as a result of anomalous hydrodynamic expansion effects. Experimentally, the rings are observed within a certain fluence range which strongly depends on material parameters. The lower limit of this fluence range is the ablation threshold. We predict a fluence ratio between the upper and the lower fluence limit approximately equal to the ratio of critical temperature to boiling temperature at normal pressure. This estimate is experimentally confirmed on different materials (Si, graphite, Au, Al).

Keywords: femtosecond laser pulses, ablation, time-resolved microscopy, equation of state, phase transition

1. INTRODUCTION

Irradiation of solid surfaces with intense laser pulses can lead to removal of material, called ablation. Short pulse laser ablation is of great interest for technological applications and also for the fundamental physics. Using subpicosecond laser pulses for ablation, the initial energy deposition, lattice heating and eventual material transport are temporally separated. The energy is deposited on a timescale of typically 100 fs, given by the pulse duration. After this time the main part of energy resides in the electron subsystem.¹ Subsequently, energy is transferred to the lattice by electron-phonon coupling mechanisms, leading to lattice heating on a time scale of a few picoseconds. Actual removal of material takes place after lattice heating on a time scale determined by the speed of sound, approximately 10^{-10} to 10^{-9} s.

Thus, for femtosecond laser-induced ablation, the laser pulse does not interact with the ablating material. Another important feature of short pulse laser ablation is the fact that matter passes through highly nonequilibrium states before ablation is completed. In addition to nonequilibrium of electronic and vibrational degrees of freedom, states of very high pressure and temperature can be reached on pico- to nanosecond timescales.

In this article we focus on an effect that occurs when highly pressurized, heated material expands into vacuum and transforms into a gaseous state. Time resolved microscopy, described in the next section, reveals a universal feature of the ablating surface observed for a wide variety of metals and semiconductors near the ablation threshold. All materials show interference rings on a nanosecond time scale, leading to the conclusion that sharp density gradients occur during expansion. This type of density profile can be explained by an anomalous hydrodynamic behavior which occurs during expansion when the laser-heated material crosses the boundary of the two-phase region. The experimental observation and theoretical explanation are described in section 3. Our hypotheses on the nature of the fluence limits where these phenomena can be observed are supported by the experimental data in section 4.

E-mail correspondence to brf@ilp.physik.uni-essen.de

2. TIME RESOLVED MICROSCOPY

Time resolved microscopy is a powerful tool to study transient states of matter. The technique has been introduced by Downer et al. in 1985.² It combines ultrafast pump-probe techniques with optical microscopy, thus achieving high temporal *and* spatial resolution. Our experimental setup is shown schematically in Fig. 1.

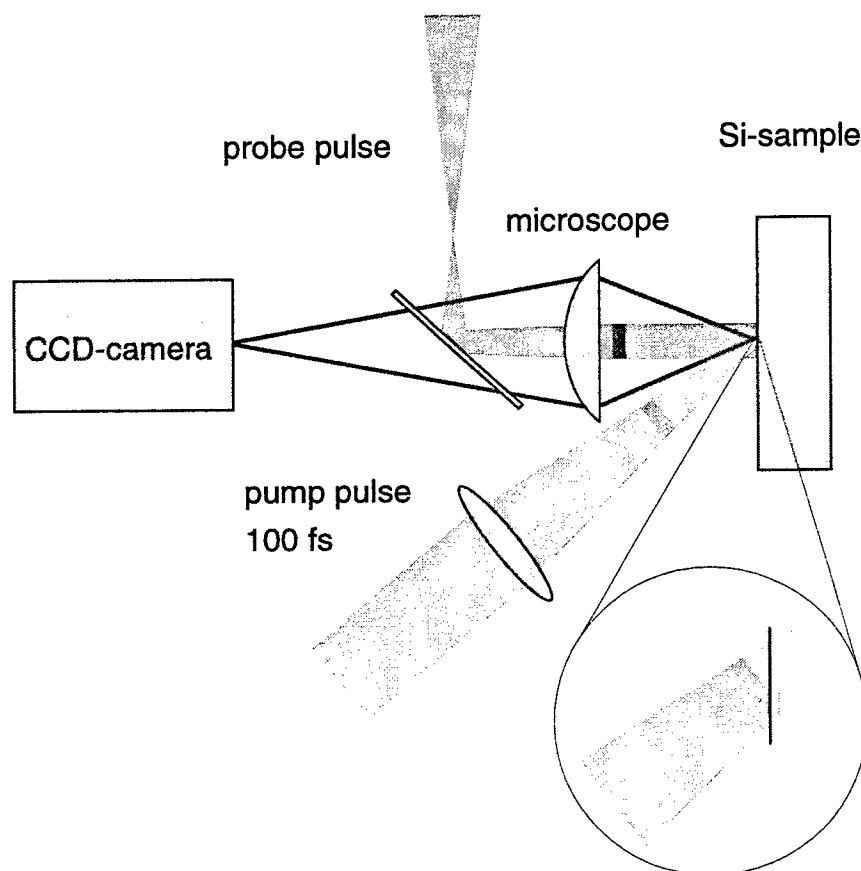


Figure 1. Experimental set-up for time-resolved optical microscopy. The insert shows how the pump pulse sweeps across the surface of the sample.

An intense pump pulse excites the sample and initiates ablation. A second weak probe pulse serves as an illumination of the optical microscope. This illuminating pulse can be delayed with respect to the pump pulse. Thus snapshot pictures of the irradiated surface can be taken at different moments. This technique permits monitoring of all stages of the evolution of the ablation process, from the deposition of the laser energy at early stages to the formation of the final surface morphology. The temporal resolution is given by the duration of the probe pulse, while the spatial resolution is determined by the properties of the optical microscope, in our case approx. $2\ \mu\text{m}$. Using a laser pulse with an approximately Gaussian intensity distribution as a pump pulse, this method also provides information on the fluence dependence of the examined processes in a single snapshot picture.

In the experiments laser pulses of 120 fs duration at 620 nm were used both for pump and probe. The reflected probe light picked up by the microscope was recorded with a CCD-camera.

3. NEWTON FRINGE PHENOMENON AS EQUATION-OF-STATE EFFECT

3.1. Experimental observation

Fig. 2 shows a sequence of time-resolved optical micrographs viewed in normal direction. These pictures represent the time evolution of the reflectivity of a silicon surface after the laser excitation. The peak fluence of the pump pulse was $F_{\max} = 0.47 \text{ J/cm}^2$, approx. 1.5 times the ablation threshold $F_{\text{th}} = 0.32 \text{ J/cm}^2$. The sequence in Fig. 2 covers the entire period from the deposition of laser energy to the appearance of final surface modification. The numbers in each frame indicate the delay time between pump and probe in the center of the beams. Since the pump pulse is incident at an angle of 45° on the surface, the actual time delay depends on the spatial coordinate. The pump pulse sweeps across the surface from left to right; in the first frame in Fig. 2 (0.1 ps) the left edge of the pump pulse is just touching the surface. The elliptical shape of the reflectivity pattern at later times simply reflects the oblique angle of incidence.

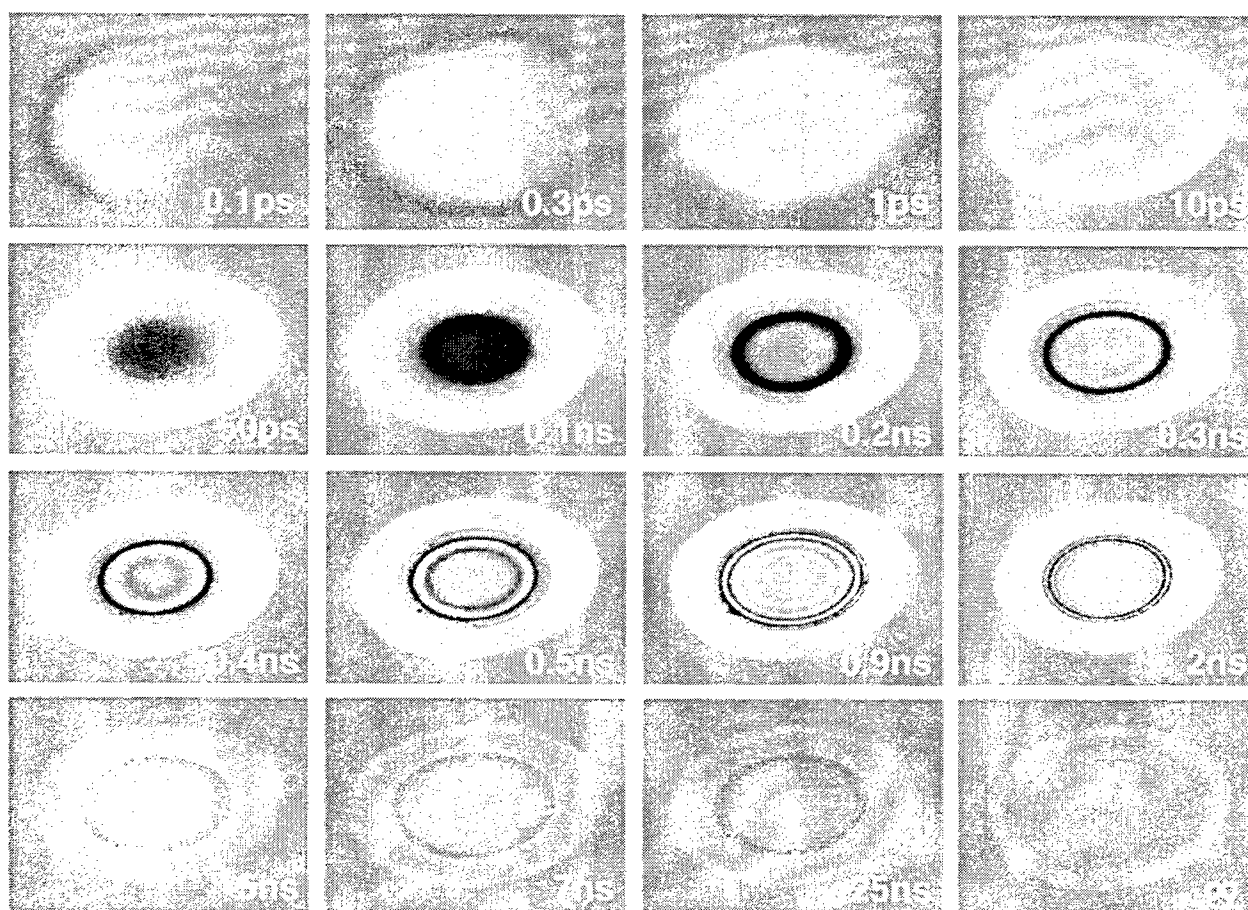


Figure 2. Snapshots of the ablating surface with 120 fs resolution. Pump fluence was 0.47 J/cm^2 , frame size is $300 \mu\text{m} \times 200 \mu\text{m}$.

The large increase in the optical reflectivity observed in the first few hundred femtoseconds indicates an ultrafast solid-to-liquid phase transition. This process is known to occur in covalently bonded semiconductors³⁻⁵ and is caused by an instability of the lattice after strong electronic excitation.^{6,7} After a few picoseconds the reflectivity starts

to decrease in the center of the irradiated zone, marking the onset of ablation. This zone develops into a structure of bright and dark rings. The number of rings increases as time proceeds. After a few nanoseconds this spatial modulation of reflectivity vanishes and resolidification sets in. The last picture shows the final changes of the surface morphology. The sharp ring in the inner part represents the boundary of the area where ablation has occurred. Moreover, the comparison of the final image with the transient pictures shows that this area is identical to the area where the bright and dark rings occurred.

The striking observation of a system of narrow dark and bright rings on ablating surfaces was made on all materials investigated so far. Fig. 3 shows examples of different materials. The transient ring structure represents an universal phenomenon associated with the ablation of absorbing materials.

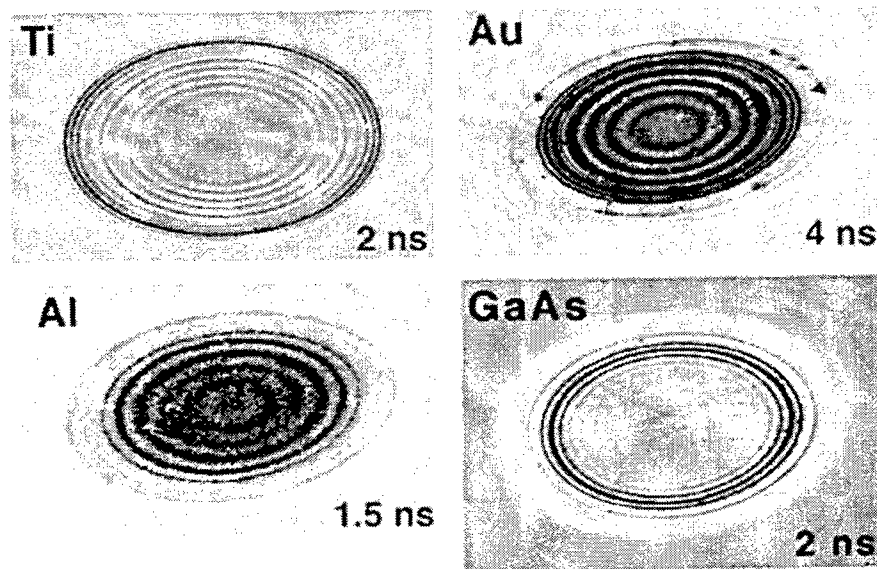


Figure 3. Transient ring structure on different materials. The maximum fluence in the center of the ablating region was for titanium $F_{\max} = 0.31 \text{ J/cm}^2 = 2.38 F_{\text{th}}$, for gold $F_{\max} = 1.2 \text{ J/cm}^2 = 4.29 F_{\text{th}}$, for aluminum $F_{\max} = 1.2 \text{ J/cm}^2 = 2.31 F_{\text{th}}$, and for gallium arsenide $F_{\max} = 0.47 \text{ J/cm}^2 = 2.14 F_{\text{th}}$.

To prove that the ring structure is an interference pattern experiments were performed with different probe wavelengths.^{8,9} From the observed wavelength dependence of the ring spacing the ring structure could be clearly identified as an interference phenomenon (Newton fringes).

Two basic requirements must be satisfied to explain the observed interference patterns and the high contrast in terms of an expanding layer of ablating material: (1) The ablation process must lead to the formation of a pair of optically sharp interfaces containing the ablating material. The optical density must drop sharply across this layers over a distance much smaller than the wavelength. (2) The absorption in the ablating layer must be weak.

In the following sections we show that these requirements are fulfilled due to equation-of-state effects during free expansion of pressurized matter into vacuum.^{10,11}

3.2. Self-similar rarefaction wave

Consider a uniform semi-infinite layer of material with a density equal to normal solid density ρ_0 , and a temperature of the order of the critical temperature of the material. Because the initial rapid laser excitation can be viewed as

isochoric heating this describes approximately the situation at the beginning of the expansion of the laser-heated material.

The expansion is fast in comparison with the time scale of heat conduction and can thus be considered as an adiabatic process. The flow is described by the equations of gas dynamics

$$\begin{aligned}\frac{\partial \rho}{\partial t} + \frac{\partial}{\partial x}(\rho u) &= 0 \\ \frac{\partial u}{\partial t} + u \frac{\partial}{\partial x} u &= -\frac{1}{\rho} \frac{\partial p}{\partial x},\end{aligned}\tag{1}$$

where ρ is the density, and p is the pressure of the material which expands in x direction with the mass velocity u . The set of equations (1) is completed by the equation of the isentrope $S(p, \rho) = \text{const}$, which we take in the form $p = p(\rho)$. This equation system can be transformed into an implicit equation for the density profile being dependent on the spatial coordinate, more precisely on the self-similar coordinate x/t ^{11,12}:

$$\frac{x}{t}(\rho) = -c_s(\rho) + \int_{\rho}^{\rho_0} c_s(\rho') \frac{d\rho'}{\rho'}.\tag{2}$$

Here, $c_s(\rho) = \sqrt{(\partial p / \partial \rho)_S}$ is the local sound velocity, which is the key parameter in the following discussion.

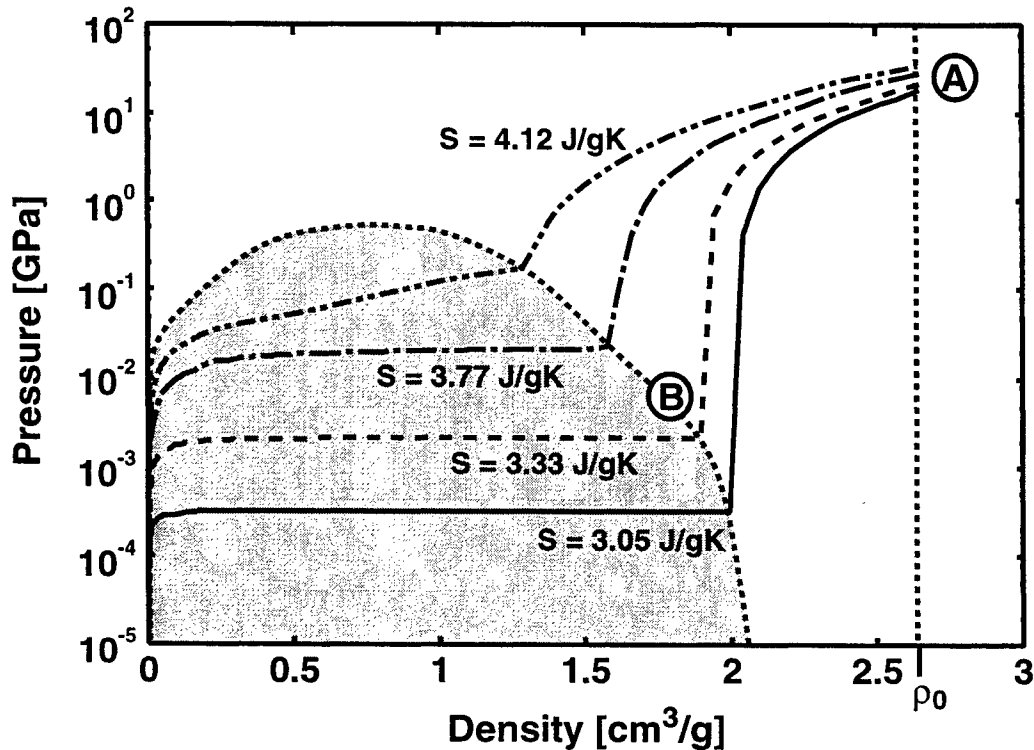


Figure 4. Phase diagram of aluminum with four isentropes and the isochore with solid-state density. The two-phase region (liquid-gas) is shaded.

As an example we consider the phase-diagram of aluminium. Fig. 4 shows the pressure-versus-density diagram, together with four isentropes, taken from the tabulated equation-of-state data of aluminium which were constructed

by the methods developed in Refs. 13,14. After the initial rapid isochoric heating by laser excitation (vertical dotted line), the material is in a state marked by the letter A. Expansion occurs along the isentrope, for example the one marked by the dashed line. The square root of the slope of the isentrope is the sound velocity which enters equation (2). Outside the two-phase region (coexistence of liquid and gas phase, shaded area) the sound velocity has a high, approximately constant value of the order of $\sim 10^4$ m/s. Under these conditions the expansion leads to an approximately exponential $\rho(x/t)$ -profile, according to equation (2). However, the sound velocity decreases sharply¹² when the isentrope enters the two-phase-region. As shown in Fig. 4 there is a distinct kink of the isentrope at point B on the binodal line. The strong drop of the sound velocity by several orders of magnitude causes a jump in $x/t(\rho)$ in eq. (2) and thus a plateau of constant density $\rho(x/t)$. More importantly, the low value of sound velocity x/t in eq. (2) stays nearly constant with decreasing ρ . For the $\rho(x/t)$ profile this leads to a steep, step-like density gradient.

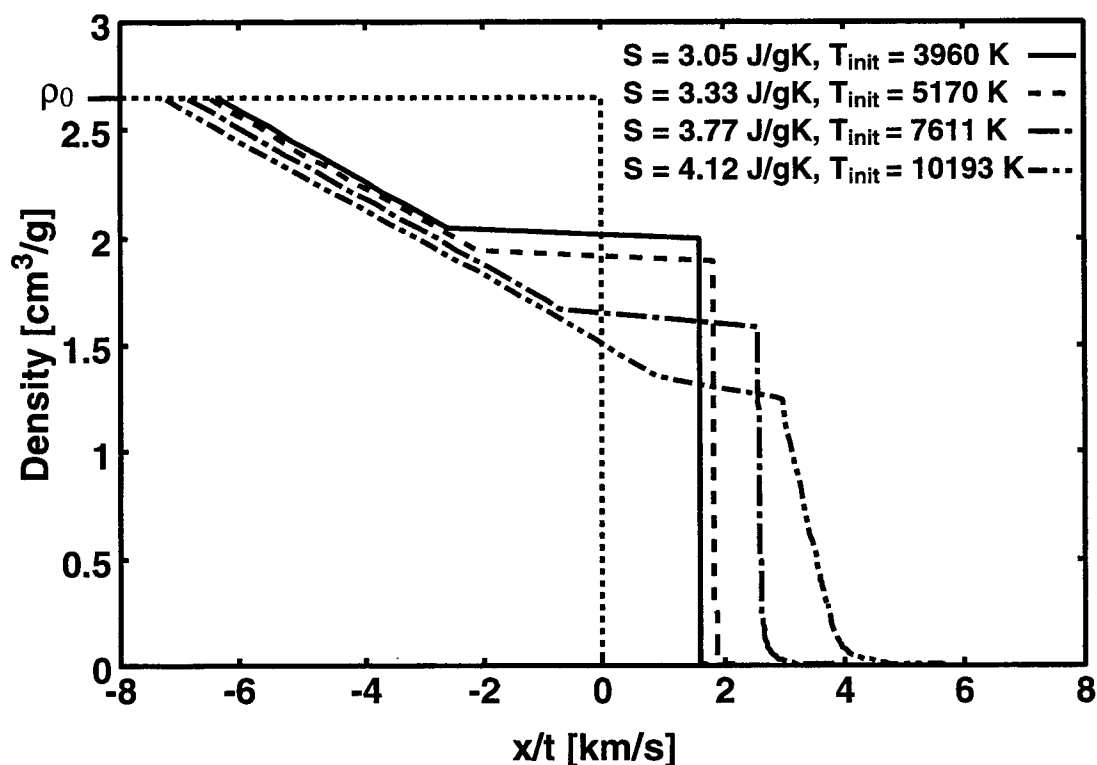


Figure 5. Self-similar solution for adiabatic expansion of aluminum fluid heated isochorically to temperatures T_{init} .

Fig. 5 shows the density profile calculated from eq. (2) using the tabulated equation-of-state data to obtain the values of the entropy for the different initial temperatures (at point A in Fig. 4). For the three lowest initial temperatures, the density decreases on a scale of $\lesssim 10$ nm/ns. Thus, after several nanoseconds, the profile is still steep enough to act as one of the optically sharp interfaces required to produce the observed interference phenomenon.

3.3. Moving shell in front of low-density region

A self-similar rarefaction wave describes the expansion of a semi-infinite, uniformly heated material into vacuum. The condition of uniform temperature can be fulfilled using a thin film of heated material with thickness $d \lesssim 100$ nm.¹⁵ However, in this case the self-similar solution is valid only for times shorter than $t_r = d/c_s(\rho_0)$. At $t = t_r$ the rarefaction wave hits the unperturbed substrate where it is reflected.*

*Also in bulk material the rarefaction wave is reflected at the non-ablating, shock-compressed internal part of the target.

After reflection, the head of the rarefaction wave travels with the local sound velocity towards vacuum or the surrounding air. However, when the plateau is reached it will not travel further because at this point the sound velocity is extremely small. Therefore the plateau remains nearly unperturbed when moving away from the substrate. It follows directly from mass conservation that the density in the region between the substrate and the plateau must decrease. In Fig. 6 the resulting density profile for different stages of ablation is outlined. Numerical gas dynamic calculations¹¹ as well as molecular dynamic simulations¹⁶ confirm this picture.

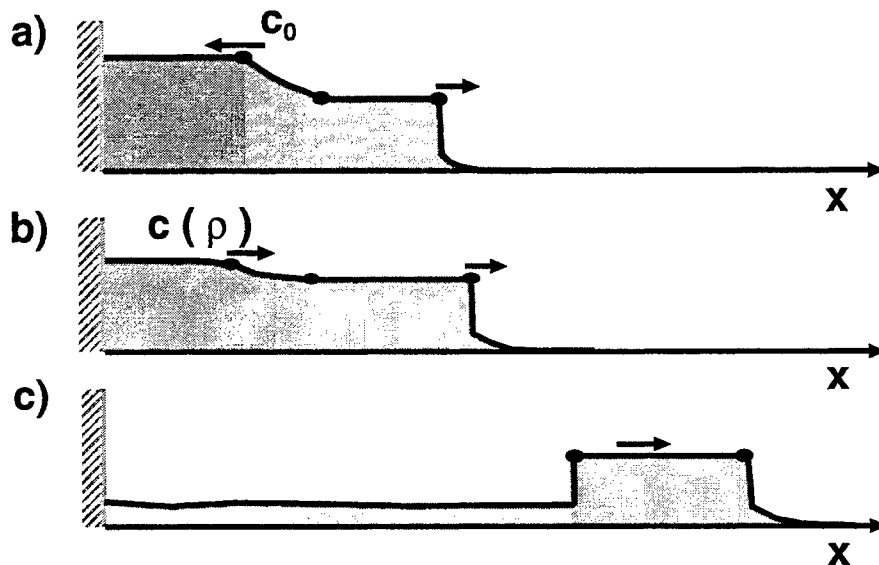


Figure 6. Schematic evolution of the density profile, a) resulting from self-similar solution, b) after reflection of rarefaction wave, c) at the later stage of moving shell in front of low-density region.

The plateau represents a shell of high density in front of a low-density region moving into vacuum or the surrounding air. The thickness of the shell is in the order of tens of nanometers. A laser beam of visible light can therefore pass through the shell. It can also pass through the low-density region between shell and substrate. Thus, all conditions stated at the end of section 3.1 can be fulfilled with the picture of heated material expanding into vacuum: the ablating material can be regarded as transparent because of the low thickness of the shell and the low density between the shell and the substrate. Two optically sharp surfaces are provided (a) by the outer steep density drop occurring already in the self-similar solution and (b) by the cold substrate or the shock-compressed internal part of the target, respectively.

4. LIMITATION OF NEWTON FRINGES

4.1. Experimental Observation

As can be seen from Figs. 2 and 3 bottom right, for silicon and for GaAs, respectively, the appearance of Newton fringes is limited to a certain fluence range. The irradiating laser pulse has a Gaussian profile, thus the snapshots show rings above a certain fluence threshold, and the disappearance of these rings for higher fluences.

The lower limit coincides with the sharp ablation threshold as proved by comparison with the final crater (see Fig. 2). Fig. 7 illustrates the correspondence between the fluence, the Newton rings and the final crater. The bottom

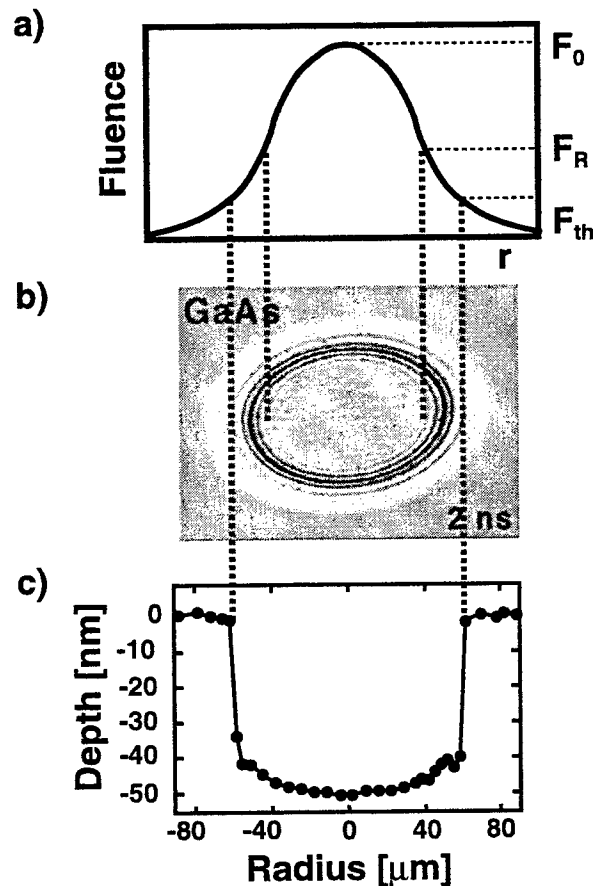


Figure 7. Correspondence between the Newton-ring pattern and the final surface morphology. a) spatial fluence distribution of the pump-pulse, b) transient reflectivity pattern, c) depth-profile of final crater.

picture shows the profile of the ablation crater on GaAs, measured with interference microscopy. The steep walls mark the sharp ablation threshold which was measured to be $F_{th} = 0.25 \text{ J/cm}^2$.

At an upper fluence of approximately $F_R = 0.32 \text{ J/cm}^2$ the rings disappear, as can be seen from the photograph in the center which was taken after excitation with a peak fluence of $F_{max} = 0.47 \text{ J/cm}^2$. This is a rather smooth transition and less sharply defined when compared with the lower limit. Moreover, the upper fluence limit does not correspond to any remaining structure in the final crater.

4.2. Hypotheses for explanation

The lower fluence limit for the observation of Newton fringes coincides with the ablation threshold, i. e. at fluences below this threshold, the solid is heated to temperatures too low for ablation to occur. In the phase diagram the expansion starting from relatively low temperatures occurs on isentropes which do not reach the two-phase region. In a simplified picture one may assume that in this case no transition to the gas-phase is possible and thus the material will finally resolidify. Further studies of the phase transition near threshold and of the resolidification process are needed to clarify the physical reason of the ablation threshold. For the following we consider the isentrope S_1 , reaching the two-phase region at zero pressure (see the sketched phase diagram in Fig. 8), as the lower limit for an expansion isentrope leading to the observation of Newton fringes.

For strong fluences the material is heated up to very high temperatures. In this case the expansion isentrope crosses the two-phase region near the critical point or proceeds above it. In Ref. 17 the possibility of rarefaction

shock that could occur in adiabatic expansion passing above the critical point¹⁸ was discussed. It was left as an open question whether the Newton fringe phenomena can also be explained as an effect of an rarefaction shock. In the following we show that even for lower temperatures than discussed in Ref. 17 the Newton fringes disappear during adiabatic expansion passing the two-phase region near the critical point.

If the expansion isentrope crosses the binodal near the critical point, the drop in sound velocity will not be as sharp as for lower temperatures. The crucial point is the value to which the sound velocity drops. The higher the sound velocity, the smoother the density profile of the self-similar solution, which is taken as a basis of the following discussion. The use of the self-similar solution for times longer than t_r (see section 3.3) is justified for the present discussion, because the outer part of the density profile remains undisturbed for long times up to nanoseconds, conserving the initial profile. A density decrease on a spatial scale of $\gtrsim 100$ nm does not provide an optically sharp surface for visible light, and thus Newton rings can not be observed in this case. An example is the density profile resulting from the highest value of initial temperature shown in Fig. 5, where the density decrease occurs on a scale of ~ 300 nm/ns. We compare the self-similar solutions of several isentropes from Ref. 13,14 for aluminium. As a criterion we define the density drop as “not sharp enough” if it occurs on a self-similar scale of 100 nm/ns. The tabulated data of equation-of-states show that this criterion is rather well defined. The transition from sharp density profile (decrease on a scale of $\lesssim 10$ nm/ns) to a profile with a decrease on a scale of $\gtrsim 100$ nm/ns occurs within two discrete values of entropy. The higher of these values is thus considered as the upper entropy limit for the occurrence of Newton fringes. The corresponding isentrope S_2 is sketched in Fig. 8.

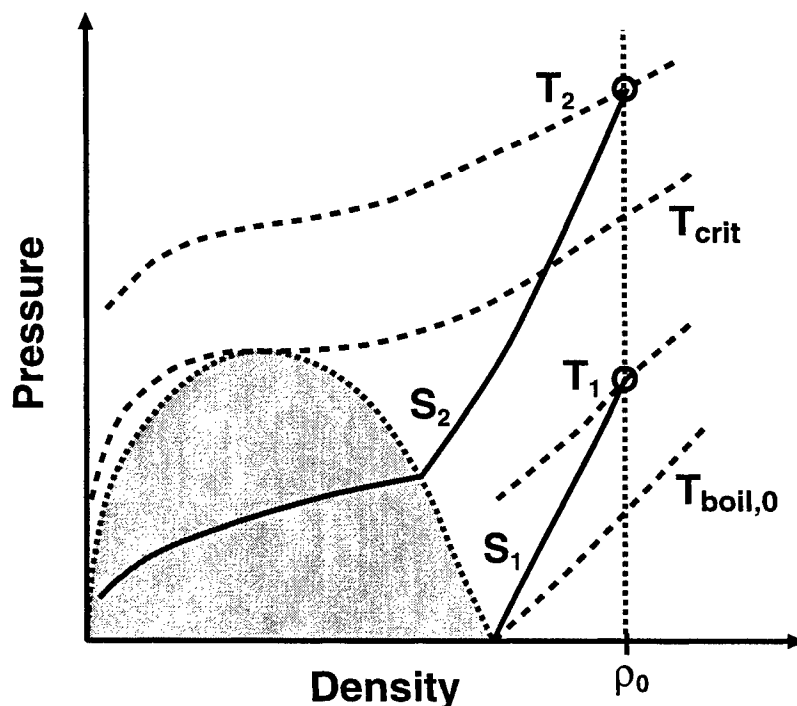


Figure 8. Schematic phase diagram for illustration of the determination of the limiting isentropes S_1 and S_2 and the corresponding initial temperatures T_1 and T_2 , as defined in section 4.2. Also the critical temperature T_{crit} and the normal boiling temperature $T_{boil,0}$ are shown. The two-phase region is shaded; isothermes are shown by dotted lines.

4.3. Support of hypotheses

To support the above discussions we should compare the regime of the two limiting isentropes S_1 and S_2 , defined in the preceding section, with the fluence regime actually found in the experiments.

The expansion on isentropes S_1 and S_2 starts after laser heating to temperatures T_1 and T_2 , respectively, which are marked in Fig. 8. The ratio T_2/T_1 can be compared with the fluence ratio F_R/F_{th} , where F_{th} is the ablation threshold, and F_R is the fluence where the Newton fringes disappear. A fluence ratio F_R/F_{th} leads to a ratio of deposited energy of $\approx Q_R/Q_{th}$ which in turn, for approximately constant heat capacity equals $\approx T_R/T_{th}$. Thus, we have to compare the ratio T_2/T_1 , determined by the criteria in section 4.2, with the experimental ratio F_R/F_{th} in order to support our hypotheses for the nature of the fluence limits. Moreover, it was found from the tabulated equation-of-state data for different materials that the ratio T_2/T_1 may be estimated in most cases by the ratio of critical temperature to boiling temperature at zero pressure $T_{crit}/T_{boil,0}$. This is important as detailed equation of state data are not available for all materials. Table 1 shows the comparison of the experimental fluence range F_R/F_{th} for the observation of

	F_R/F_{th}	T_2/T_1	$T_{crit}/T_{boil,0}$
Silicon	1.5	–	1.4
Graphite	1.3	–	1.35
Aluminum	> 2.3	2.4	2.4
Gold	> 4.3	4.3	3.3

Table 1. Experimental fluence range F_R/F_{th} for the observation of Newton rings, tabulated temperatures T_2/T_1 and the ratio of fundamental constants $T_{crit}/T_{boil,0}$ for four different materials.

Newton rings with the tabulated temperatures T_2/T_1 , where available, and the fundamental constants $T_{crit}/T_{boil,0}$ for different materials.^{13,14,19} For aluminum and gold, the fluence F_R where the interference pattern disappears was not reached in the experiment. The data show that the fluence limits F_R/F_{th} may in fact be estimated by the equation-of-state data, thus our suppositions of section 4.2 are supported. The fundamental constants T_{crit} and $T_{boil,0}$ determine the temperature interval of the two-phase-region and thus the range of occurrence of large drops in sound velocity and in consequence of optically sharp interfaces during expansion of the heated material.

5. SUMMARY AND CONCLUSION

We have presented experimental investigations of ablating surfaces, which were irradiated with a single subpicosecond laser pulse. With help of time-resolved microscopy the behavior of matter on femtosecond to nanosecond timescales was studied with high temporal and spatial resolution. On nanosecond timescales a regular ring pattern was found, identified as Newton fringes. This is a universal feature of the ablating surface of absorbing materials near the ablation threshold.

The phenomenon of an interference pattern was explained by an equation-of-states effect. If the matter is heated to temperatures in the order of the critical temperature, the adiabatic expansion occurs in such a way that the expansion isentrope crosses the two-phase-region well below the critical point. This leads to the formation of two optically sharp surfaces which are responsible for the interference phenomenon.

The observation of Newton fringes is limited to a certain fluence range. The experiments show that the lower fluence limit coincides with the ablation threshold while the upper limit is a rather smooth transition, not related to a final surface modification. We presented suppositions for the explanation of both limits. Comparison of the temperatures determined by our criteria with the fluence regime found in the experiments support our hypotheses. Knowledge of fundamental constants T_{crit} and $T_{boil,0}$ may be used to predict approximately the fluence range for the observation of Newton fringe pattern.

ACKNOWLEDGMENTS

We are greatly indebted to S.I. Anisimov for pointing out the origin of the optically sharp interfaces and valuable advice. We also wish to thank N.A. Inogamov and Yu.V. Petrov for stimulating discussions, B. Proff and M. Bieske for technical support and K. Eibl for careful proofreading of the manuscript.

REFERENCES

1. S. I. Anisimov, A. M. Bonch-Bruевич, M. A. El'yashevich, Y. A. Imas, N. A. Pavlenko, and G. S. Romanov, "Effect of powerful light fluxes on metals," *Sov. Phys. Tech. Phys. [Zh. Tekh. Fiz.]* **11** [36], pp. 945-952 [1273], 1967 [1966].
2. M. C. Downer, R. L. Fork, and C. V. Shank, "Femtosecond imaging of melting and evaporation at a photoexcited silicon surface," *J. Opt. Soc. Am. B* **2**, pp. 595-599, April 1995.
3. C. V. Shank, R. Yen, and C. Hirlimann *Phys. Rev. Lett.* **50**, p. 454, 1983.
4. P. Saeta, J.-K. Wang, Y. Siegal, N. Bloembergen, and E. Mazur, "Ultrafast Electronic Disordering during Femtosecond Laser Melting of GaAs," *Phys. Rev. Lett.* **67**, pp. 1023-1226, August 1991.
5. K. Sokolowski-Tinten, J. Bialkowski, and D. von der Linde, "Ultrafast laser-induced order-disorder transitions in semiconductors," *Phys. Rev. B* **51**, pp. 14186-14198, May 1995.
6. J. A. Van Vechten, R. Tsu, and F. Saris *Physics Letters A* **74**, p. 422, 1979.
7. P. Stampfli and K. H. Bennemann, "Time dependence of the laser-induced femtosecond lattice instability of Si and GaAs: Role of longitudinal optical distortions," *Phys. Rev. B* **49**, p. 7299, 1994.
8. K. Sokolowski-Tinten, J. Bialkowski, A. Cavalleri, M. Boing, H. Schöler, and D. von der Linde *SPIE* **3343**, p. 46, 1998.
9. D. von der Linde and K. Sokolowski-Tinten, "The physical mechanisms of short-pulse laser ablation," *Applied Surface Science* **154-155**, p. 1, 2000.
10. K. Sokolowski-Tinten, J. Bialkowski, A. Cavalleri, D. von der Linde, A. Oparin, J. Meyer-ter-Vehn, and S. Anisimov, "Transient states of matter during short pulse laser ablation," *Phys. Rev. Lett.* **81**, pp. 224-227, 1998.
11. S. Anisimov, N. Inogamov, A. Oparin, B. Rethfeld, T. Yabe, M. Ogawa, and V. Fortov, "Pulsed laser evaporation: equation-of-state effects," *Appl. Phys. A* **69**, pp. 617-620, 1999.
12. L.D. Landau and E.M. Lifschitz, *Course of Theoretical Physics Vol. 5: Statistical Physics*, Pergamon Press, London, Paris, 1958.
13. A. Bushman and V. Fortov *Uspekhi Fizicheskikh Nauk [Sov.Phys.Usp.]* **140** [26], p. 177 [465], 1983.
14. V. Agurejkin, S. Anisimov, A. Bushman, G. Kanel, V. Karyagin, A. Konstantinov, B. Kryukov, V. Minin, S. Razorenov, R. Sagdeev, S. Sugak, and V. Fortov *Teplofiz. Vys. Temp. [High Temp.]* **22**, p. 964 [761], 1984.
15. J. Hohlfeld, J. G. Müller, S.-S. Wellershoff, and E. Matthias, "Time-resolved thermorefectivity of thin gold films and its dependence on film thickness," *Appl. Phys. B* **64**, pp. 387-390, 1997.
16. V. Zhakhovskij, K. Nishihara, S. Anisimov, and N. Inogamov, "Molecular-Dynamics Simulation of Rarefaction Waves in Media That Can Undergo Phase Transitions," *JETP Lett. [Pis'ma v ZhETF]* **71**, pp. 167-172 [241], 2000.
17. N. Bulgakova, "Possibility of rarefaction shock wave under short pulse laser ablation of solids," *Phys. Rev. E* **60**, p. R3498, 1999.
18. Y. Zeldovich *Zh. Eksp. Teor. Fiz. (JETP)* **16**, p. 363, 1946.
19. V. P. Glushko, *Termodinamicheskie svoystva individual'nykh veshchestv (Russian)*, Nauka, Moscow, 1979.

Model for photothermal laser ablation of polymer-like materials

Nikita M. Bityurin *

Institute of Applied Physics RAS, 603600, Nizhny Novgorod, Russia

ABSTRACT

The main feature of polymeric materials is the hierarchy of bonds between molecular groups. There are 'strong' covalent bonds connecting neighbor molecular groups of the same chain, and 'weak' molecular bonds between neighbor groups that belong to different polymer chains. The existing theories of laser ablation of polymers either do not take into consideration this feature (photothermal surface evaporation models) or do not take into account the movement of the interface between condensed and gaseous phases. An important step in this direction has been taken in^{1,2} where the so-called bulk or volume model of laser ablation of polymers has been developed. In this model ablation of organic polymers is described on the basis of photothermal bond breaking within the bulk material. Here a first order chemical reaction is assumed, which can be described by Arrhenius law. Ablation starts when the density of broken bonds at the surface reaches a certain critical value. The position of the interface thereafter is fixed with this critical number. It has been shown, in particular, that the movement of the interface between the condensed and gaseous phases during laser ablation is of great importance. In the present paper we develop this model changing the Stefan-like boundary condition at the ablation interface with the physical Frenkel-Wilson condition, which is more appropriate physically and, on the other hand, more convenient for numerical calculations. According to this model, activation energy for elimination of a short enough polymer chain from the surface is proportional to the sum of the energies of weak bonds connecting this chain with the surface. We compare predictions of this model with the previously derived Stefan-like bulk model and with the predictions of surface photothermal model with respect to kinetics and dynamics of single-pulse laser ablation by nanosecond pulse. The parameters used in numerical calculation correspond to the KrF excimer laser ablation of Polyimide.

Keywords: laser ablation, polymers, modeling

1. INTRODUCTION

In the present communication the model of ablation of polymers and polymer-like materials is formulated. This model takes into account the main feature of this kind of materials, namely, the existence of strong and weak bonds between neighbor molecular groups. This model takes into account also the movement of the interface between gaseous ablation products and condensed material during ablation. A model of such kind was considered in detail in our previous papers^{1,2} where so-called bulk or volume model was introduced. In the present paper we change the Stefan-like condition at the surface with somehow more realistic Frenkel-Wilson condition. The main purpose is to consider how this change influences the main differences of bulk model as compared to the predictions of well-known surface evaporation model which was formulated in Ref.3 and applied to polymer ablation in Refs 4-6. Here only nanosecond ablation is considered. The subpicosecond ablation is considered in detail in the next paper⁷. The terms 'Stefan-like' condition and 'Frenkel-Wilson' approach are used here by analogy with the well-known problems of moving melting front (for a review see⁸).

2. MODELS

In this chapter we discuss ablation governed by the chain breaking process within the bulk of material. This chain breaking process can be induced by either photothermal or photochemical reaction occurring under the effect of laser radiation. Polymeric materials are constituted by long macromolecules consisting of sequences of 'monomers', molecular groups of the same nature. The main feature of polymeric materials is the hierarchy of bonds between molecular groups. There are 'strong', covalent bonds connecting neighbor molecular groups of the same chain and 'weak' molecular bonds between neighbor groups, which belong to different polymer chains. Removal of molecular groups from the surface of material during ablation can proceed through breaking intrachain bonds (covalent). On the other hand, the removal of polymer chain as a whole from the surface is possible as a result of breaking all 'weak' bonds that connect this chain with the surrounding

* E-mail: bit@appl.sci-nnov.ru, phone +7 8312 384389, fax +7 8312 363792

material. Of course, if the chain is long enough, this process is practically unreal, because the sum of 'weak' bonds appears to be greater than the single 'strong' bond. The sum energy of the 'weak' bonds between chain and environment for short enough chains is proportional to its length. If we consider the degradation of polymer by random chain breaking either through photochemical or photothermal reaction, then, after several steps, the averaged chain length would be approximately $\sim 1/n$ where n is the number density of broken bonds. In the surface photothermal model of laser ablation, which is valid for the near-threshold ablation of simple solids, the ablation velocity or the velocity of propagation of ablation front is approximated to be:

$$V_{abl} = V_0 \exp(-E_a / k_B T_s) \quad (1)$$

Here T_s is the value of the temperature at the surface, E_a is the activation energy of removal of molecule (atom) from the surface, and V_0 is of the order of sound velocity, k_B being the Boltzmann constant.

In the considered model, ablation proceeds through removal of short enough polymer chains. Velocity of ablation can be estimated similar to (1) where E_a denotes now the activation energy of removal of short enough polymer chain. As it follows from above, the activation energy is proportional to the averaged length of the chain. The averaged chain length, in turn, is proportional to $1/n_s$, where n_s is the fraction of broken bonds at the surface. In what follows we will use, as a first approximation, formula (1) in which

$$E_a = \bar{E}_m / n_s \quad (2)$$

Here \bar{E}_m reads for the energy of weak bonds per 'monomer'. The expressions (1), (2) now yield:

$$V_{abl} = V_{0m} \exp(-\bar{E}_m / k_B n_s T_s) \quad (3)$$

Expression (3) provides a sharp dependence of ablation rate on the number density of broken bonds at the boundary. In papers^{1,2}, where the bulk or volume model of laser ablation was comprehensively discussed, the Stefan-like boundary condition was employed instead of (3). There ablation starts when the fraction of broken bonds at the surface reaches a certain critical value, n_c . The position of the interface thereafter is fixed with this critical number, i.e. the boundary condition reads:

$$n_s = n_c \quad (4)$$

The difference between the boundary conditions (3) and (4) is similar to the difference between the Stefan and Frenkel - Wilson approaches to the problem of the propagation of the melting front⁸. Thus, the formulation of the physical Frenkel - Wilson condition (3) instead of Stefan-like condition can be considered as the next step in formulation of the bulk or volume model of laser ablation of polymer-like materials.

In the present paper we consider three models of laser ablation of polymer-like materials to single out the difference between them in predictions of ablation kinetics and dynamics.

The first one is the surface photothermal model that provides a good description of kinetics of UV laser ablation of polyimide^{5,6}.

This set of equations consists of the heat diffusion equation that we use in the following form taking into account the temperature dependence of specific heat and thermoconductivity.

$$\frac{\partial T}{\partial t} = V \frac{\partial T}{\partial z} + \frac{1}{\rho c_p(T)} \frac{\partial}{\partial z} (\kappa(T) \frac{\partial T}{\partial z}) + Q \quad (5)$$

Here T is the temperature, ρ is the density, $c_p(T)$ is the specific heat, $\kappa(T)$ is the thermoconductivity, the source term Q in (5) describes heating of material due to absorption of laser radiation. Equations (5) are written in a coordinate system moving with the ablation velocity V and fixed with the ablation front. V obeys the equation (1) where $T_s = T(0, t)$.

In what follows we will use the boundary conditions in a simplified form:

$$\kappa(T) \frac{\partial T}{\partial z} \Big|_{z=0} = \rho \Delta H V \quad T \Big|_{z \rightarrow \infty} = T_{\infty} \quad (6)$$

Here we change the real difference in enthalpy of solid and gas phases by the temperature-independent sublimation 'enthalpy' ΔH .

The intensity distribution within the material $I(z, t)$ is governed by the equation:

$$\frac{\partial I}{\partial z} = -\bar{\alpha} I \quad (7)$$

Here $\bar{\alpha}$ is the effective absorption coefficient which, generally, is not a constant and should be determined from an additional set of equations.

Eq. (7) will be considered together with the boundary condition for laser intensity:

$$I(0, t) = I_0(t) \exp(-\alpha_p h(t)) \quad (8)$$

In (8) $I_0(t)$ is the laser intensity, α_p is the Lagrange absorption coefficient of the plume, $h(t)$ being the ablated depth.

Within the bulk or volume model, laser ablation proceeds through bulk reaction that results in creation of broken bonds. In what follows we consider, similar to^{1,2}, the single-step thermally activated reaction with kinetics equation for a fraction of broken bonds:

$$\frac{\partial n}{\partial t} = V \frac{\partial n}{\partial z} + (1 - n) k_0 \exp(-E_b / k_B T) \quad (9)$$

Here k_0 is a constant. Within the bulk model Eq. (5) is also valid but the source term Q contains, additionally to the surface model, a term that accounts for the thermal effect of the chemical reaction². In this paper we consider two different approaches to the formulation of the bulk model. They differ by the conditions at the surface.

The Stefan-like approach suggests the boundary condition (4). This relation defines the position of the interface, and therefore the velocity V , implicitly. In (4) $n_s = n(0, t)$.

The physical meaning of the interface between gaseous and condensed phase is that the value of thermal conductivity drops sharply across this interface, and the heat flux through the interface can be neglected.

$$\kappa(T) \frac{\partial T}{\partial x} \Big|_{x=0} = 0 \quad (10)$$

The boundary conditions at infinity are obvious:

$$T \Big|_{x \rightarrow \infty} = T_0, \quad n \Big|_{x \rightarrow \infty} = 0 \quad (11)$$

Within the approach investigated in this paper we employ the equation for ablation velocity (3) together with the boundary condition:

$$\kappa(T) \frac{\partial T}{\partial z} \Big|_{z=0} = \rho \frac{\Delta H_m}{n_s} V \quad (12)$$

Here ΔH_m designates the enthalpy of evaporation of weak bonds per 'monomer'.

3. ABLATION BY NANOSECOND PULSES

We suppose that the electronic excitations thermalize on a ps time scale⁹. Thus, with nanosecond pulses we can employ

Eq.(7) with $\bar{\alpha} = \alpha = \text{const}$.

For surface photothermal model we employ Eq. (5) with

$$Q = \frac{\alpha I}{c_p \rho} \quad (13)$$

For both of the bulk models under consideration

$$Q = \frac{\alpha I}{c_p \rho} - \frac{\Delta H_b N_0 (1 - n) k_0 \exp(-E_b / k_B T)}{c_p \rho} \quad (14)$$

Here N_0 is the number density of 'monomers' and ΔH_b is the enthalpy per strong bond between monomers that are broken according to Eq. (9).

Thus, we consider three different models:

- Model I: surface photothermal model within the set of equations (1), (5), (6), (7), (8), (13).
- Model II: bulk photothermal Stefan-like model with the set of equations (4), (5), (7), (8), (10), (11), (14).
- Model III: bulk photothermal model with the set of equations (3), (5), (7), (8), (9), (11), (12), (14).

First we compare ablation kinetics i.e. dependence of ablated depth on fluence per pulse.

We consider the experimental data on mass-loss kinetics of polyimide irradiated by KrF excimer laser¹⁰. These data demonstrate 'Arrhenius tails' near ablation threshold. These tails cannot be explained by bulk models II and III if we assume layer-by-layer ablation as the only reason for mass-loss. However, it has been understood in^{11,2}, that these tails are originated from the depletion of volatile species. These volatile species are resulted from the same bulk reaction (9). It breaks the bonds, destroys polymer chains, and may simultaneously create trapped volatile species.

Below ablation threshold, volatile species result in a mass loss, which requires out-diffusion of trapped species and occurs on the μ s or even ms time scale. As volatile species and broken bonds are produced in a pyrolytic reaction (9), this results in an Arrhenius tail. Above the threshold volatile species leave the material together with the ablation products. When ablation ceases some of the volatile species still exist below the surface and leave the material later. This results in an additional mass loss, M (per unit area), which does not contribute to the ablated (crater) depth. M , which is due to the depletion of species, is proportional to the number of broken bonds left within the material after ablation. Because these species do not diffuse on the ns time scale, their spatial distribution repeats that of the broken bonds and can be calculated as:

$$M = m_v N_0 \int_0^\infty n_b(x) dx, \quad h_M \equiv \frac{M}{\rho} = \frac{m_v}{m_t} \int_0^\infty n_b(x) dx, \quad (15)$$

N_0 is the total concentration of virgin bonds, and m_v is the mass of volatile products produced per broken bond. m_v/m_t is the mass fraction, related to volatile species (per bond). In order to compare the theoretical curves with experimental data on mass-loss kinetics we introduced the "depth" h_M related to M , the ablation depth h and also the total effective "depth" $h + h_M$.

Fig. 1 shows the mass-loss kinetics curve for all three models in comparison with the experimental data of¹⁰ on KrF laser ablation of Polyimide. The parameters used are listed in Table 1. It should be noted that the set of parameters for each model could be changed somehow without damaging the quality of fitting shown in Fig.1. The sets listed in Table 1 provide fitting both of nanosecond ablation kinetics and of pair pulse femtosecond kinetics discussed in⁷. It is seen from these curves that it is really hard to distinguish between the models using only data on ablation kinetics by nanosecond pulses.

Let us now consider the dynamics of ablation, i.e., the time dependence of surface temperature, and ablation velocity. Differences between ablation dynamics predicted by the surface photothermal model and the Stefan-like bulk model are comprehensively discussed in². It has been shown that the main differences are as follows:

- The sharp, singular onset of ablation predicted by model II with pulses well above ablation threshold instead of relatively smooth time dependence of ablation velocity demonstrated by model I.
- With laser pulse with fluence close enough to the ablation threshold, ablation governed by model II starts after laser pulse, whereas according to model I ablation will start no later than the onset of the maximum of surface temperature, which corresponds to the end of the rectangular pulse and occurs even before the end of the pulse for more realistic shape of a laser pulse.

The aim of this communication is to check how these features of bulk model remain for more realistic model III.

In Fig. 2 it is seen that the onset of the laser ablation for the rectangular pulse is sharp enough with model III as well. The surface temperature tends to its stationary value from above in contrast to the prediction of the surface model I. This effect

is more pronounced if we can neglect the absorption by the plume ($\alpha_p = 0$) as it is seen in Fig. 2. Of course, there is no singularity as it occurs with model II. The difference in dynamics is less pronounced if the absorption by the plume is strong enough as it takes place for Polyimide (see Fig. 3 and Table I).

Within the nanosecond time scale the onset of the ablation after the laser pulse is significantly less pronounced in model III than in model II. Thus, it can be seen in Fig. 4 that this feature can hardly be resolved with parameters listed in Table I.

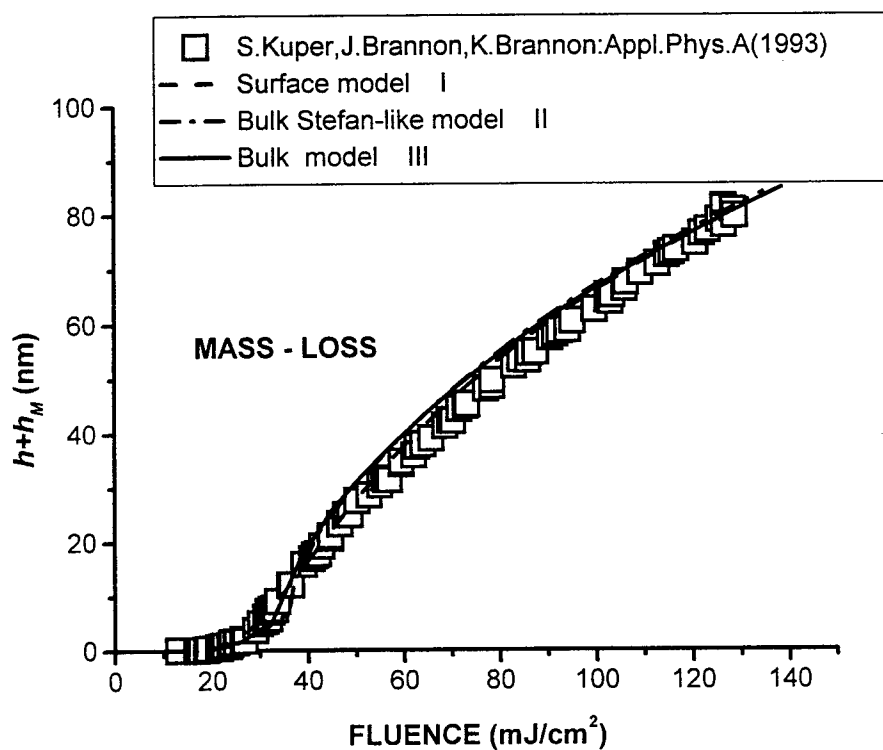


Fig.1. Kinetics of laser ablation of Polyimide by KrF excimer laser. Experimental mass-loss data from¹⁰

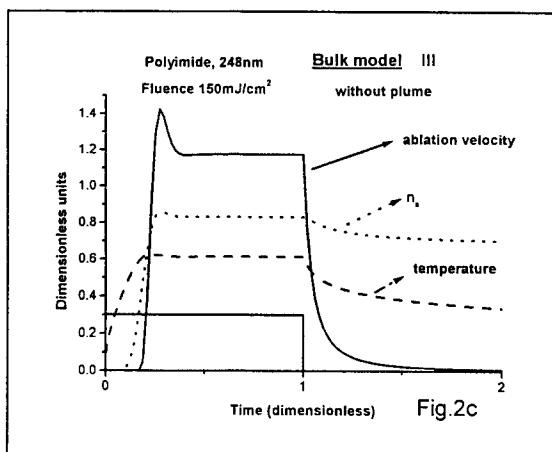
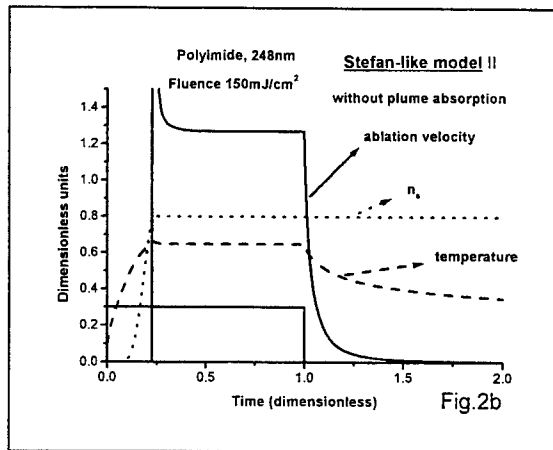
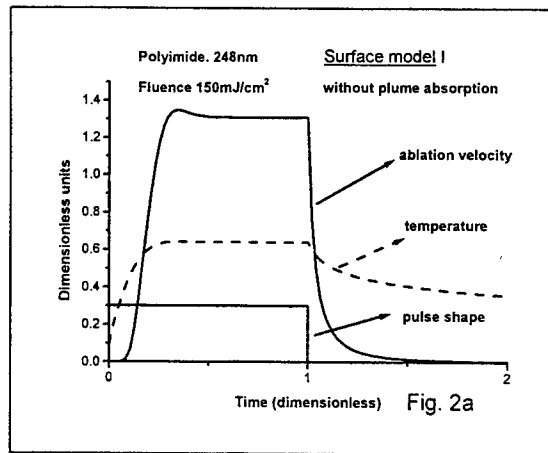


Fig.2. Dynamics of laser ablation for rectangular pulse. Absorption by plume is absent. Pulse fluence is significantly above the threshold.
(a) - surface model I, (b) - Stefan-like model II, (c) - bulk model III.

Table1. Parameters used in calculations.

Parameters	PI $\lambda=248$ nm	Models
Absorptivity	0.9	I+II+III
Absorption coeff. α	$3.2 \cdot 10^5 \text{ cm}^{-1}$	I+II+III
Screening coeff. α_g	$1.4 \cdot 10^5 \text{ cm}^{-1}$	I+II+III
Thermal conductivity κ (W/cm K)	$1.55 \times 10^{-3} (T/T_0)^{0.28}$	I+II+III
Specific heat c (J/g K)	$2.55-1.59 \times \exp[(T_0-T)/460]$	I+II+III
Density ρ	1.42 g/cm^3	I+II+III
Ambient temperature T_0	300 K	I+II+III
Surface preexponential (covalent) V_0	$3 \cdot 10^6 \text{ cm/s}$	I
Surface activation energy (covalent) E_a	1.5 eV	I
Surface enthalpy (covalent) ΔH ()	$0.9 \cdot 10^3 \text{ J/g}$	I
Bulk preexponential k_0	$3.57 \cdot 10^{12} \text{ s}^{-1}$	II+III
Bulk activation energy E_b	1.5 eV	II+III
Bulk enthalpy ΔH_b	$2 \cdot 10^3 \text{ J/cm}^3$	II+III
Fraction of volatile species	0.32	II+III
Critical fraction of broken bonds n_c	0.8	II
Surface preexponential (molecular) V_{0m}	$1.1 \cdot 10^5 \text{ cm/s}$	III
Surface activation energy (molecular) E_m	0.7 eV	III
Surface enthalpy (molecular) ΔH_m	$0.5 \cdot 10^3 \text{ J/g}$	III

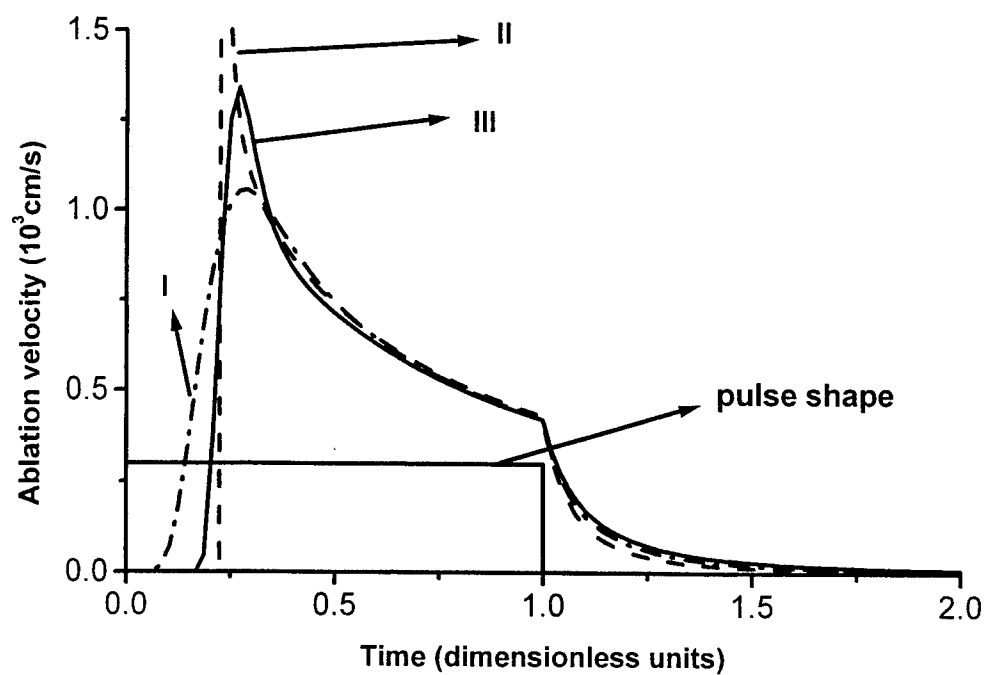


Fig.3. Dynamics of laser ablation with high plume absorption.

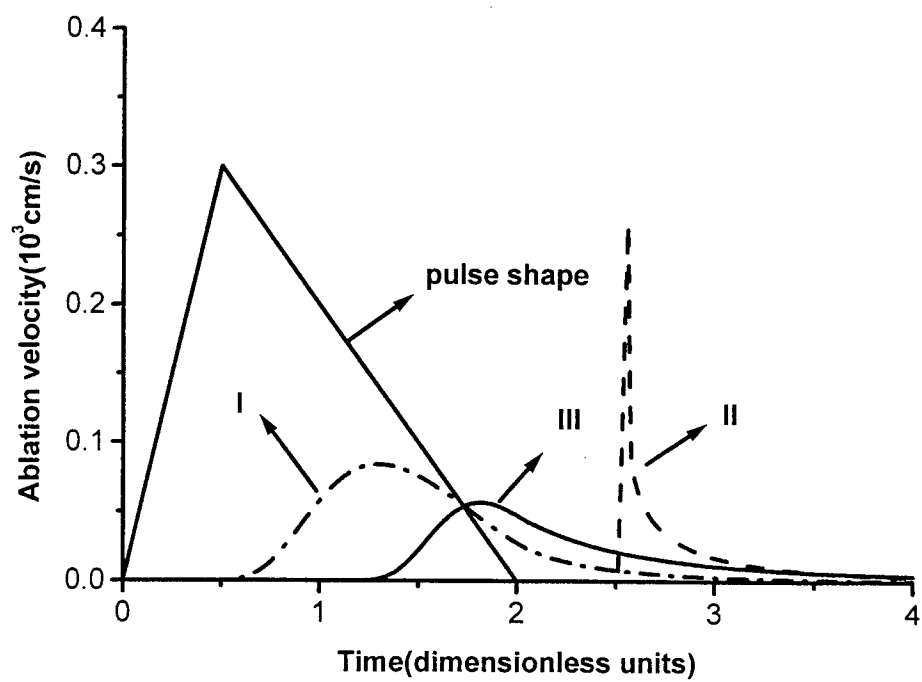


Fig.4. Dynamics of laser ablation with near-threshold fluence.

4. CONCLUSIONS

In conclusion it can be mentioned that the features of ablation dynamics predicted by the bulk model of laser ablation remains in model III. Nevertheless, it should be noted that the smoothening provided by the conditions (3,12) of model III, compared with the Stefan-like model II, makes it questionable to distinguish between the bulk and surface model by experimental data on ablation kinetics and dynamics with nanosecond pulses.

We suggest that it can be done using experimental data on Ultra Short Laser ablation. With subpicosecond pulses we can anticipate that the delay time between the end of the pulse and the start of the developed ablation should be close to the thermal relaxation time for the surface model, whereas for the bulk model it can significantly exceed this relaxation time. In more detail it is considered in the paper⁷ of this issue.

ACKNOWLEDGEMENT

The author thanks Prof. M. Tribelsky for valuable discussion.

REFERENCES

1. N. Bityurin, N. Arnold, B. Luk'yanchuk, D. Bäuerle, "Bulk model of laser ablation of polymers", *Appl.Surf.Sci.*, 127, pp.164-170, 1998.
2. N. Arnold, N. Bityurin, "Model for laser-induced thermal degradation and ablation of polymers", *Appl.Phys. A*, 68, pp.615-625, 1999.
3. S.I. Anisimov, Ya.A. Imas, G.S. Romanov, Yu.V. Khodyko, *Action of high power laser radiation on metals*, Moskva, Nauka, 1970.
4. D. Bäuerle, B. Luk'yanchuk, P. Schwab, X.Z.Wang, E. Arenholz. In *Laser Ablation of Electronic Materials*, Ed. by E. Fogarassy, S. Lazare, E-MRS 4, North Holland-Elsevier, p.39, 1992
5. B.Luk'yanchuk, N.Bityurin, M. Himmelbauer, N.Arnold, UV-laser ablation of Polyimide: from long to ultra-short laser pulses, *Nuclear Instr. and Methods in Physics Research B*. V.122, pp.347-355, 1997..
6. N.Arnold, B.Luk'yanchuk, N.Bityurin, A fast quantitative modeling of ns laser ablation based on non-stationary averaging technique, *Appl.Surf.Sci.*, V. 127-129, pp.184-192., 1998
7. A.Malyshv, N.Bityurin, Laser ablation by ultra-short laser pulses (USLP): surface and bulk models, *Proc.SPIE*, this issue.
8. D. Bäuerle, *Laser Processing and Chemistry*, 3d edition (Springer, Berlin, 2000)
9. J.K.Frisoly, Y.Hefetz, T.F.Deutsch, Time-resolved UV absorption of Polyimide. Application for polymer ablation, *Appl. Phys. B.*, V.52, pp.168-172, 1991
10. S.Kueper., J.Brannon, K.Brannon, Threshold behavior in polyimide photoablation, *Appl. Phys. A.*, v.56, pp.43-50, 1993
11. M. Himmelbauer, N.Bityurin, B.Luk'yanchuk, N.Arnold, and D. Bäuerle, UV-laser-induced polymer ablation: The role of volatile species, *Proc. SPIE*, 3093, p.220, 1997

Infrared free-electron laser photo-ablation of diamond films

J. Sturmann^a, Z. Marka^a, M. M. Albert^a, R. G. Albridge^a, J. M. Gilligan^a, G. Lüpke^a, S. K. Singh^a,
J. L. Davidson^b, W. Husinsky^c and N. H. Tolk^a

^aDepartment of Physics and Astronomy, Vanderbilt University, Nashville, TN 37235

^bDepartment of Electrical Engineering, Vanderbilt University, Nashville, TN 37235

^cInstitut für Allgemeine Physik, Technische Universität Wien, Austria

ABSTRACT

We report first infrared free-electron laser experiments to compare and elucidate the effects of surface-localized vibrational excitation versus bulk vibrational excitation on the ablation of polycrystalline diamond. The measured ablation yield values as a function of laser intensity indicate the existence of two separate thresholds. The lower intensity threshold is identified as the ablation threshold, and the higher intensity threshold is associated with the formation of a plasma plume. The wavelength dependences of both thresholds indicate that the C-H absorption occurring at surfaces and grain boundaries does not play a significant role in the ablation process. However, both thresholds are lower when the laser is resonant with the two-phonon bulk absorption band. These findings are consistent with the model that a rapid laser-induced phase transition to graphite is responsible for the low-intensity ablation of diamond at and above the first threshold.

Keywords: photo-ablation, free-electron laser, phase-transition, diamond, vibrational excitations, impurities, and semiconductors

1. INTRODUCTION

Most infrared laser ablation experiments are performed with Nd:YAG or CO₂ lasers, confining the studies to 1.064 μm and 10.6 μm wavelengths respectively. Free-electron lasers (FEL), unlike conventional lasers, convert the kinetic energy of free relativistic electrons into radiation instead of relying on electron transitions between two bound-state energy levels in an active medium. FELs have the broadest tuning range of all types of lasers and are capable of high power output. The FEL at Vanderbilt University provides a unique opportunity for laser ablation studies in the 2-10 μm region. This wide range tunability makes it possible to perform systematic wavelength-dependent studies of photo-ablation on materials.

IR laser ablation experiments on diamond films offer an excellent opportunity to investigate energy localization in ablation. CVD (chemical vapor deposition) diamond films have two distinct absorption bands close to each other in the spectral region available to us: one represents bulk absorption, the other surface absorption due to hydrogen. The broad two-phonon band peaks around 5 μm , while the vibrational band of the adsorbed hydrogen on surfaces peaks around 3.5 μm . In a CVD diamond film, the absorption coefficient is about 9 cm^{-1} both at 3.5 and 5 μm wavelength. The absorption is weak in both of these absorption bands. In addition, diamond is a very good heat conductor at room temperature. Up to now, no experiment has been done to test the wavelength-dependence of ablation in the range 3 to 5.5 μm . With the choice of this wavelength range for diamond ablation, it is possible to learn whether the resonant excitation of surface-localized hydrogen influences significantly the ablation process compared to resonant bulk excitations.

In laser ablation near the threshold, the energy is delivered to a very small volume of the target material. The laser provides an initial high concentration of energy, but the absorbed energy must remain spatially localized for a sufficient time in order to cause bond breaking and vaporization. A key issue is to understand how it is possible to localize sufficient absorbed energy in various materials. The earliest models for laser ablation focused on the thermal character of ablation. The assumption of vaporization at normal boiling temperature fits the data only of long-pulse (in the order of several hundred microseconds) metal [1] and graphite [2] ablation experiments below the GW/cm^2 intensity range. In ablation with shorter laser pulses in the GW/cm^2 intensity regime, the role of thermal pressure [3] and shock waves [4] in the target material has also been taken into consideration in theoretical treatments. However, the simple thermal model has proven inadequate [5]. Experiments with tungsten and aluminum show that adsorbates can localize the otherwise delocalized excitation of conduction electrons and this way lower the threshold for ion ejection [6].

In many cases, structural modification accompanies ablation. Reif and coworkers [7, 8] first proposed an alternative ablation model based on defect accumulation during the laser pulse. The basic idea in their model is that, as defects accumulate during the laser pulse, a large density of unoccupied surface electronic states could be reached by multi-photon

transitions. A sufficient number of electron-hole pairs could be created. Relaxation of electron-hole pairs to localized excited states could lead to bond breaking through non-radiative transitions. Phase transitions have been shown to be involved in many cases of laser ablation. The most trivial case of that is the melting of metals. The diamond to graphite phase change, induced by near but below bandgap KrF laser (5.0 eV) radiation, was observed before the evaporation of diamond films [9]. Both the rate and threshold of evaporation are related to the purity of the diamond films: the purer the films, the higher the thresholds and the lower the evaporation rates. The classical phase transformation theory is usually not applicable to laser irradiation. The high heating and cooling rates due to the spatial and temporal locality of laser radiation require modification of the classical thermodynamic theory of phase transformation [10].

In this paper we describe wavelength-dependent photo-ablation studies of CVD diamond films in the infrared region. Comparison of ablation thresholds at a surface (C-H stretch) and a bulk (two-phonon) absorption features indicate that the ultimate ablation mechanism is the same for localized and delocalized initial excitations. At all wavelengths, two threshold-like increases in the positive ion yield were found as a function of laser intensity. The first threshold corresponded to the onset of large-scale positive ion ejection (ablation threshold), and the second increase of ion yield coincided with the appearance of UV luminescence, which is attributed to the formation of a plasma plume (plasma threshold). Our experimental data suggests that the onset of photo-ablation at the first threshold is initialized by explosive phase transition from diamond to graphite.

2. EXPERIMENT

The experiments were carried out at the W.M. Keck Free-Electron Laser Center at Vanderbilt University. This free-electron laser [11,12] is capable of operating at wavelengths from 2 μm to 9.8 μm . The typical repetition rate is 30 Hz, the IR macro-pulse energy is around 50 mJ, and the length of the IR pulse is between 2-6 μs . Each macro-pulse consists of 1 ps micro-pulses spaced at intervals of 350 ps. The peak power in a micro-pulse is usually around 6-8 MW, but it can reach 10-20 MW.

For the detection of the ablated particles, a time of flight (TOF) apparatus was used without extraction voltage (Figure 1). The TOF consisted of a detector and a drift tube. In a laser ablation event, both positive and negative ions along with neutral particles are ejected into the gas phase. The experiment was set up to detect positively charged particles among the ablated material. No post-ionization was applied. In order to preserve original velocities, no accelerating field was used, except in auxiliary experiments to estimate kinetic energies. In the TOF apparatus the detector was a chevron assembly of a pair of microchannel plates (MCP) fitted with a co-axial anode. The detector was biased to detect positive ions. The front surface of the chevron was maintained at -2000 V, the rear surface at -200 V, and the anode was at ground potential. Channel plates have direct sensitivity to charged particles and energetic photons. The work function of the channel plates

allow photoelectron production at incident photons having wavelengths shorter than 200 nm (6.2 eV). The drift tube is positioned at a port of the ultra-high vacuum (UHV) chamber at 45-degree angle to the sample normal. The end of the drift tube is at 54 cm from the center of the UHV chamber, where the sample was mounted. The vacuum was maintained in the low 10^{-9} Torr range.

In order to allow sufficient time for the sample to cool between macro-pulse shots, single macro-pulses were gated out from a given FEL pulse train. In the experiments, the laser spot size and the beam attenuation had to be precisely controlled. The beam intensity incident on the sample was varied using a ZnSe Brewster-plate polarizer. Because of fluctuation in the macro-pulse energy, the energy of each macro-pulse was measured. To filter out higher harmonics, a pair of Ge plates mounted at Brewster's angle was placed in the beam. A single plano-convex CaF_2 lens was located

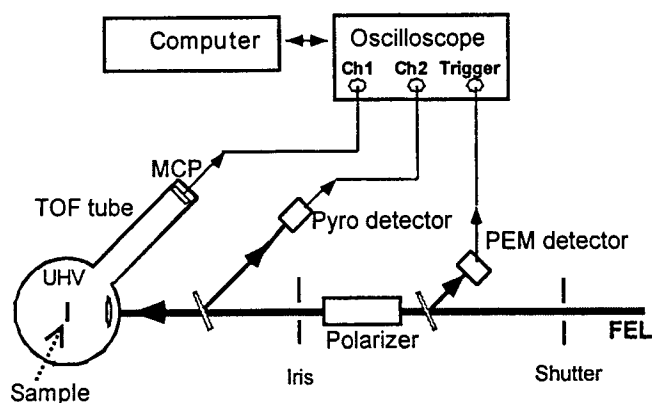


Figure 1 Experimental setup

inside the UHV chamber which was used to focus the laser beam onto the sample with a laser beam spot size of 75 μm . In order to ensure spot-size uniformity at different wavelengths the dispersion in CaF_2 was taken into account.

The TOF spectrum of ejected positive ions and the energy of the corresponding laser macro-pulse were recorded simultaneously with a digitizing oscilloscope. Each TOF signal was recorded for 500 μs with a 1 μs resolution. In the TOF spectra $t=0$ represents the arrival of the leading edge of the macro-pulse to the sample. A fast IR photo-electromagnetic (PEM) detector was used to generate a trigger for the oscilloscope from a small portion of the laser pulse. The energy of the

laser macro-pulses was monitored using another small portion of the beam by a pyroelectric joulemeter. After each change in wavelength the joulemeter was calibrated against a calorimeter. During calibration, the calorimeter was positioned directly in front of the UHV chamber window. To calculate laser power in a micro-pulse, the temporal profile of an average macro-pulse was used. The laser beam is characterized in this paper by its wavelength and peak intensity. The peak intensity is defined as the intensity at the center of a Gaussian laser beam during a micro-pulse.

The samples used in these experiments were polycrystalline intrinsic diamond films, approximately 10 μm thick, deposited on a 500 μm thick silicon substrate. The films were grown using the microwave plasma-assisted chemical vapor-deposition (CVD) process [13]. The grain size in the top layer is typically smaller than 0.5 micron. Fourier transform infrared (FTIR) spectra taken on the samples show the typical features of CVD diamond films. Figure 2 shows the absorption of one representative sample in the studied spectral range. The hydrogen content of the film was high enough to make the C-H vibrational absorption maximum equal to the maximum of the two-phonon absorption. The absorption coefficient is small in this spectral range, such that a film of 10- μm thickness absorbs less than 2% of the incident radiation.

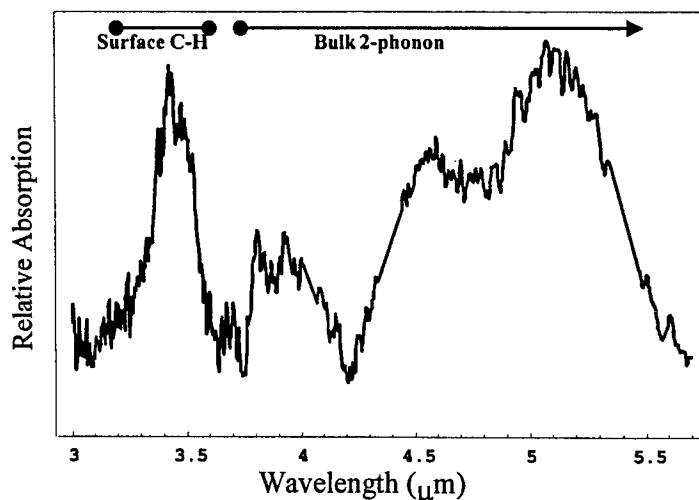


Figure 2 FTIR spectrum of one representative CVD diamond film sample in the studied wavelength range

3. RESULTS

Figure 3 shows time-of-flight spectra at a given laser intensity just barely above the first ablation threshold, where several macro-pulses were incident on the same spot on the sample. The time span between shots was 7-12 seconds, long enough to avoid heat buildup from previous macro-pulses. This series of TOF spectra obtained by repeated FEL macro-pulse shots shows that the diamond target was gradually modified by the laser irradiation. After 10-20 shots on the same spot, the peaks vanished indicating the removal of the film from the substrate. In this case carbon atoms are removed at a rate of few thousand layers per macro-pulse. Above a certain laser intensity corresponding to the second observed threshold, in addition to the two delayed peaks shown in Figure 3 a prompt MCP signal was observed. The leading edge of this peak was within the first 1-3 μs . We attribute this prompt peak to UV photons generated in the ablation plume associated with conventional ablation.

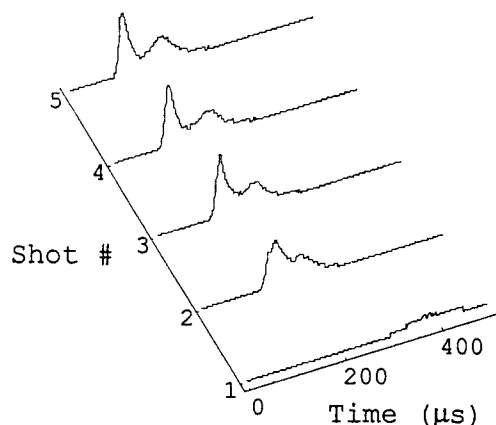


Figure 3 Time of flight spectra for repeated macropulse shots on the same spot slightly above the ablation threshold. The spot diameter was 150 μm , the wavelength was 3.5 μm .

UV arising from an ablation induced plasma plume. Above the plasma threshold intensity, a second increase of ion yield is observed with increasing laser intensity.

Figure 4 shows a typical example of the integrated ablation yield of positive ions as a function of laser micro-pulse intensity. The arrow marks those intensities where UV photons were also emitted. Notably, the onset of UV luminescence corresponds to a second rise in the yield of positive ions. These plots show the existence of two thresholds at all probed wavelengths. Above the ablation threshold, which is the lower intensity threshold of the two observed thresholds, there is a nearly constant ablation yield over a broad range of intensities. As the intensity increases, a second threshold, the plasma threshold, is observed. At the plasma threshold intensity, a prompt signal appears which we attribute to

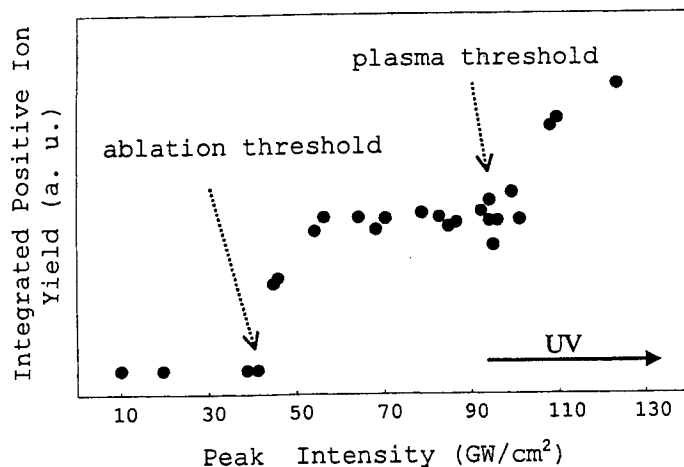


Figure 4 Typical example of positive ion yield as a function of peak laser intensity. These are first macro-pulse shot data taken at $3.9\ \mu\text{m}$ with a spot diameter of $75\ \mu\text{m}$. The arrow indicates the intensities where UV photons are also emitted.

threshold intensities in the region of the C-H absorption peak. By comparing first-shot and second-shot ablation thresholds one finds that second-shot ablation thresholds are slightly lower, and they still reflect the 2-phonon absorption spectrum. In contrast, a significant reduction in the plasma thresholds for the second shots is observed, especially at shorter wavelengths outside the phonon absorption band. Lower second-shot thresholds suggest defect creation or material modification.

4. DISCUSSION

Our data demonstrate the existence of two distinct ablation thresholds for the case of IR diamond ablation. In addition to the first ablation threshold, another threshold, which we associate with plasma-dominated ablation, is observed. At the first ablation threshold intensity there is a steep rise in the ablation yield as laser intensity increases which then remains constant until the onset of plasma dominated ablation. We estimate that in the region between the two ablation thresholds the material removal rate is of the order of thousand monolayers per macro-pulse shot. We have demonstrated that among the ablated material, there are ion clusters consisting of tens of carbon atoms.

The wavelength dependence of ablation thresholds reflects lower thresholds in the two-phonon absorption band. There is no reduction of thresholds, however, in the C-H absorption band despite of the similar low intensity absorption. This suggests that the hydrogen on the surface does not play a significant role in the actual ablation process. C-H vibrations do not couple well to the bulk. It is likely that the spectral bandwidth of the FEL makes vibrational up pumping possible, and hydrogen is removed from the surface even below the temperature required for thermal desorption when irradiated with resonant FEL photons.

The experimental results provide evidence for the modification of sample properties as a result of laser irradiation. TOF spectra of consecutive shots on the same spot on the sample (Figure 3) demonstrate that repeated FEL macro-pulse shots cause gradual changes in the sample. The changes in TOF spectra suggest accumulation of defects and structural imperfections in the CVD diamond film due to prolonged exposure. Gruzdev and Libenson showed that the electric field could be strongly localized at defect sites. Intensity dependent changes in the refractive index of inclusion and host lead to extremely high local amplitudes of the electric field [14]. This involves a threshold behavior for the absorption that cannot be anticipated from the linear absorption properties. All these changes may increase the absorption by orders of magnitude. The absorbed portion of the laser energy may reach a sufficiently high percentage, which is enough to raise the local temperature at the irradiated spot to a point when the diamond begins to graphitize. Earlier experiments indicate that graphitization of diamond accompanies UV [9, 15] as well as IR ablation [16]. Micro-Raman spectra versus number of macro-pulse shots taken around the ablation crater for our samples show the dramatic decrease in the diamond peak at $1332\ \text{cm}^{-1}$ and the appearance of pronounced graphite signatures at $1580\ \text{cm}^{-1}$ and $1350\ \text{cm}^{-1}$.

Preliminary experiments were carried out with a $-200\ \text{V}$ acceleration voltage applied to the drift tube. This value was chosen as a compromise since the $2\text{--}6\ \mu\text{s}$ length of the macropulse strongly limits our mass/charge resolution. These TOF spectra indicate the formation of C_2 and C_3 clusters and also show that the size distribution of ablated particles has a tail that extends to several tens of carbon atoms per electron charge. In addition, we performed experiments at varying retarding potentials. These experiments prove that the kinetic energies of ablated particles reach $200\ \text{eV}$ for laser intensities between the first and second thresholds.

Ablation thresholds and plasma thresholds were determined at several wavelengths. Figure 5 displays the ablation and plasma thresholds as a function of wavelength determined from first and second macro-pulse shots. The wavelength dependence of ablation thresholds generally follows the two-phonon absorption spectrum. Both the ablation and plasma thresholds have a minimum, which coincides with the bulk 2-phonon absorption maximum of the diamond film. Even though the C-H absorption is comparable in magnitude to the 2-phonon absorption, there is no significant reduction in

Above ablation threshold as laser intensity increases, the ejected neutral and charged particles form an increasingly denser cloud above the target surface, and the fraction of ionized particles also increases indicated by the rapidly increasing ion yield (Fig. 3). After the first sharp rise, measured yield intensity curves reach a saturation level. Here the ejected particle cloud reaches a density where the increasing laser intensity contributes more to the increased heating of the particle cloud than to the removal of more material from the sample.

We observed a second increase of the ion yield above the plasma threshold intensity, i.e. the intensity at which UV luminescence appeared in the TOF spectra. We believe that the UV luminescence is the indication of the formation of ablation plasma. The ablation plasma plume can almost completely absorb the incoming IR energy, and convert the absorbed IR energy into visible and UV radiation and into increased kinetic energies of the electrons and ions. The sample is now irradiated by more energetic photons allowing electronic transitions even in the not yet graphitized layers in the sample. These newly opened energy channels make possible the observed increased ablation yields.

In our case, a phase change to graphite is more likely than melting during diamond ablation, since the melting of diamond occurs above the temperature of 3000 K well below what we have calculated for the temperature increase of our irradiated volume [17]. On the other hand, diamond, which is metastable at low pressures, can turn into graphite by overcoming a relatively small activation barrier. The activation energy was measured to be 1.95 eV plus or minus 0.3 eV by Kuznetsov et al. when the diamond was heated in vacuum [18]. However, computer simulations of damage in diamond due to ion impact and its annealing by Saada and coworkers showed that if the vacancy density is sufficient, the activation energy of graphitization can be as low as 0.7eV [19]. In UHV conditions uncatalyzed graphitization occurs at 1800K [20], which is much lower than the melting temperature. Defect-catalyzed graphitization may occur at an even lower temperature of 1100K [21].

We propose a model for IR laser ablation of diamond in which the ablation threshold is related to the threshold for phase transition to graphite. Graphitization may be explained in two ways. One possibility is that the FEL radiation causes non-thermal graphitization. Diamond may overcome the activation barrier by multi-photon absorption of the infrared FEL radiation. However, these experiments provide no evidence for major involvement of a multi-photon process. The other possibility is that the absorption coefficient of CVD diamond changes significantly during an intense FEL macro-pulse, and thereby the local temperature may reach sufficient values for thermal graphitization. It is likely that the intense FEL irradiation creates more defects and changes the electronic and optical properties of the diamond film consequently. The accumulation of defects, in other words gradual change in electronic properties, is supported by the observed evolution of TOF spectra shapes of repeated macro-pulses near the ablation threshold. As soon as graphite regions

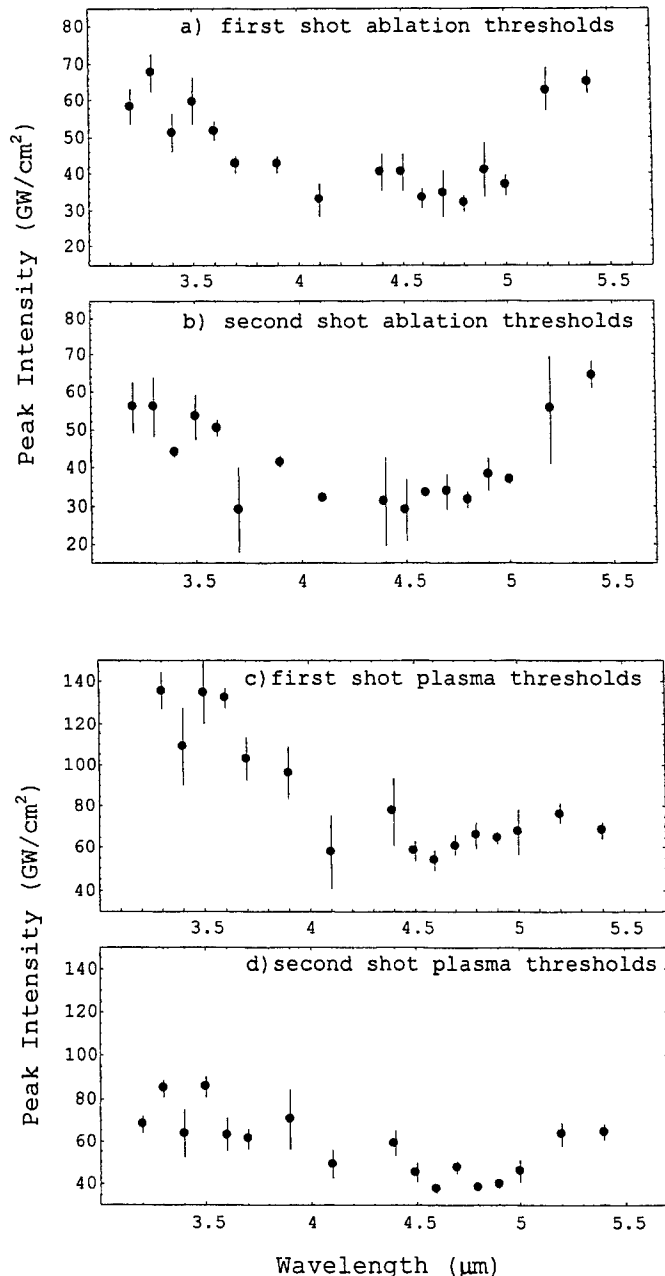


Figure 5 First (a) and second shot ablation thresholds (b) and first (c) and second shot plasma thresholds (d) for a CVD diamond film as a function of wavelength. The diameter of irradiated spot is 75 μm.

are formed, further enhancement of absorption takes place by free carriers in the conduction band of graphite. As a result of the intense laser radiation the graphite phase can progress at a higher rate into the bulk of the diamond than the rate of graphitization due to conventional heating.

If the diamond changes into graphite phase before ablation, a large mechanical stress is created simply due to the density difference of the two phases. Because of its smaller density, graphite occupies roughly 1.5 times the volume of diamond with similar mass. The mechanical stress could lead to the cracking and spallation of the graphite layer. The rapid progression of the graphite phase can result in violent ejection of large clusters due to the rapid volume expansion. This ejection mechanism is similar to the popping of popcorn. At the threshold intensity, *explosive graphitization* may occur in a small central region of the laser spot near the end of the FEL macro-pulse. This explosive process can lead to very high ion kinetic energies as observed in the retarding potential experiments. At only slightly higher laser intensity, the graphitized volume can increase drastically because of the drastic change in absorption properties as a consequence of the largely different electronic properties of graphite compared to diamond.

5. CONCLUSION

We described here the first investigation of CVD diamond film ablation in the IR wavelength range of 3-5.4 μ m. Measured ablation yields as a function of laser intensity indicate the existence of two separate thresholds in case of CVD diamond ablation. The lower threshold intensity is identified as ablation threshold, and the higher threshold intensity is the plasma threshold. Both thresholds have their lowest values when the initial excitation is delocalized bulk two-phonon absorption. The adsorbed hydrogen on the surfaces of the diamond film does not lower the ablation threshold. The evolution of TOF spectra as a result of repeated FEL macro-pulse shots indicates the involvement of laser-induced material modification. Based on our findings we propose that explosive phase transition to graphite leads to the ablation of diamond in the IR region.

6. ACKNOWLEDGMENTS

The authors would like to thank the effort of the staff of the W.M. Keck Free-Electron Laser Center. This project was supported by the Office of Naval Research.

7. REFERENCES

1. V. B. Braginskii, I. I. Minakova and V. N. Rudenko, *Sov. Phys. Tech. Phys.* 12, 753 (1967).
2. P. D. Zavistanos, *GE Rep.* R67SD11 (1967).
3. Y. V. Afanasev and O. N. Krokhin, *Sov. Phys. JETP* 25, 639 (1967).
4. S. S. Penner and O. P. Sharma, *J. Appl. Phys.* 37, 2304 (1966).
5. R. V. Dreyfus, R. Kelly and R. E. Walkup, *Appl. Phys. Lett.* 49, 1478 (1986).
6. H. S. Kim and H. Helvajian, *J. Phys. Chem.* 95, 6623 (1991).
7. J. Reif, H. Fallgren, W. E. Cooke, E. Matthias, *Appl. Phys. Lett.* 49, 770 (1986).
8. J. Reif, H. Fallgren, H. B. Nielsen, E. Matthias, *Appl. Phys. Lett.* 49, 930 (1986).
9. A. Blatter, U. Bögli, L. L. Bouilov, N. I. Chapliev, V. I. Konov, S. M. Pimenov, A. A. Smolin and I. V. Spitsyn, *Proc. of the Second Int. Symp. On Diamond Materials*, Vol. 91-8, 351 (1991).
10. E. N. Sobol, *Phase Transformations and Ablation in Laser-Treated Solids*, Wiley, 1995.
11. C. A. Brau, *Nucl. Instr. and Meth. in Phys. Res., A* 318, 38 (1992).
12. G. S. Edwards, D. Evertson, W. Gabella, R. Grant, T. L. King, J. Kozub, M. Mendenhall, J. Shen, R. Shores, S. Storms and R. H. Traeger, *IEEE J. Sel. Topics Quantum Electron.* 2, 810 (1996).
13. W. Zhu, B. R. Stoner, B. E. Williams and J. T. Glass, *Proceedings of the IEEE*, 79(5), 621 (1991).
14. V. E. Gruzdev and M. N. Libenson, *Laser Damage in Optical Materials: 1994*, SPIE Proc. 2428, 553 (1995).
15. M. Rothschild, C. Arnone and D. J. Erlich, *J. Vac. Sci. Technol. B* 4, 310 (1986).
16. A. Ueda, *Ph. D. Dissertation*, Vanderbilt University, Nashville, TN, 1994.
17. J. Sturmman, *Ph. D. Dissertation*, Vanderbilt University, Nashville, TN, 1999.
18. V. L. Kuznetsov, I. L. Zilberberg, Y. V. Butenko, A. L. Chuvilin and B. Segall, *J. Appl. Phys.* 86, 863 (1999).
19. D. Saada, J. Adler and R. Kalish, *Phys. Rev. B* 59, 6650 (1999).
20. T. Evans, in *Properties of Diamond* Ed. J. E. Field, p.403, Academic Press, UK, 1979.
21. G. S. Woods, *Ph. D. Thesis*, University of the Witwatersrand, South Africa, 1971.

On the mechanism of carbon nanotubes synthesis by laser ablation

A.Gorbunov^{* a}, A.Graff^b, O.Jost^a, W.Pompe^a

^aTechnische Universität Dresden, D-01062 Dresden, Germany

^bInstitute for Solid State and Materials Research Dresden, PF 27 00 16 D-01171 Dresden, Germany

ABSTRACT

Qualitative analysis of the gas-dynamical phenomena by the laser ablation of graphite under conditions of single-wall carbon nanotubes (SWNTs) suggests to reconsider the currently assumed mechanisms of SWNT formation in this technique ("scooter" and other vapor-based ones) and to conclude that it is a form of solid-liquid-solid catalytic graphitization of amorphous carbon or other imperfect carbon forms. The proposed mechanism of melting of catalyst particles followed by precipitation of SWNTs allows to explain the observed dependencies of the SWNT yield on the synthesis temperature and pressure. Critical inspection of the literature data shows that it might also play a role in other physical and chemical deposition techniques of SWNT synthesis (cw-laser, solar furnace, arc-discharge, hydrocarbon decomposition, CO-disproportionalization).

Keywords: carbon nanotubes, graphitization, amorphous carbon, laser ablation

1. INTRODUCTION. REVIEW OF THE EXISTING MECHANISMS

In spite of the enormous progress in the synthesis, theoretical understanding of the catalytic growth of single-wall nanotubes (SWNTs) lags behind [1, 2]. In the first turn, it concerns the more fundamental understanding of nanotube chemistry and kinetics, and primarily the establishment of SWNT growth mechanisms. To make a decisive conclusion on the SWNT formation mechanism, one has to answer the following key questions:

- (a) what is the carbon atom feedstock?
- (b) which role plays the catalyst metal?
- (c) what is the driving force for the elongated structure growth?

Open-edge mechanisms. In the early papers, the growth of the NTs was believed to take place completely in a *vapor phase* through addition of new carbon atoms directly onto an *open edge* of the growing tube, while some form of anisotropy in the C-condensation process was thought to be responsible for growth of elongated carbon structures [3, 4]. More recently proposed "scooter" mechanism of SWNT growth [5, 6] assumes that the chemisorbed metal atom "scoots" around the nanotubes open edge, catalytically annealing the pentagon defects and thus inhibiting closure by partially terminating the dangling bonds and exchanging with incoming carbon atoms. However, molecular dynamics simulations [7, 8] have shown that it is hardly possible that a chemisorbed catalyst atoms are able to preserve the opened SWNTs from closure through incorporation of curvature-inducing defects.

Root growth mechanisms. The competing *root growth* mechanisms assume that the nanotube lengthens with a closed-end, while the catalyst particle remains on the support surface. Carbon atoms are thus supplied from the "root" where the nanotube interfaces with the anchored metal catalyst particle. This mechanism is known since the pioneering works [9] and [10] on the CVD-grown tubular carbon fibers. More recently this mechanism has been considered to be valid for the CVD synthesis of carbon bamboo particles, multi-, and single-wall nanotubes through the metal catalyzed decomposition of certain hydrocarbons at temperatures ranging from 400 - 1100°C [1, 11, 12]. Same as by carbon nanofibers [13], the first step of the CVD reaction involves the absorption and decomposition of hydrocarbon molecules on the surface of transition-metal catalytic nanoparticles. The resulting atomic species dissolve and diffuse to the rear particle faces, and ultimately precipitate at the interface to form a carbon nanostructure. The degree of crystalline perfection of the deposited fiber is dictated by the chemical nature of the catalyst particle, its crystalline orientation, the composition of the reactant gas, and the

^{*}gorbunov@tmfs.mpgfk.tu-dresden.de

temperature. The size of the metal catalyst nanoparticle generally dictates the diameter of the synthesized nanofiber, or multi-walled nanotube.

According to an atomistic model [14], carbon atoms, precipitating from the metal particle, form a graphene sheet that encases the particle in the way the carbon onions do [15]. At the first stage, this graphene sheet will tend to mirror the nanoscale surface roughness of the particle. Simulations show that if the diameter of a single roughness protrusion is small enough, atoms can be preferentially added to the base of such height perturbations, ultimately giving rise to the nucleation of a carbon nanotubes. The encaging the catalyst particles by 10-20 graphitic layers upon cooling below some certain temperature leads to deactivation of their catalytic ability [11, 16, 17].

A similar three-step model [18] is also based on the assumption of the dissolution-precipitation of carbon at a metal catalyst particle. Here, the adsorbed fullerene caps serve as master precursors for the growing nanotubes defining their diameter and chirality. (The cognizance of the interrelation between the pressure dependencies of fullerene and SWNT yields has been also taken in [19]). In this case, the properties of SWNTs should only be defined by the initial fullerene-like carbon clusters initially formed in the vapor and not on the type and composition of the catalyst that is in conflict with the experimental evidence of the same authors [18]. This points to the fact that the nucleation of NTs takes place immediately on the surface of the metal particle with the properties of the SWNTs being defined by the conditions of this surface.

A solid-liquid-solid mechanism of SWNTs growth proposed in this paper allows a consistent explanation for a large number of the experimentally observed facts and dependencies from a single standpoint.

2. EXPERIMENTAL PROCEDURE AND RESULTS

Systematic investigations of the SWNT abundance in the laser-furnace technique have been performed on the setup and under conditions presented in Fig.1. The resulting substance was analyzed by transmission electron microscopy (TEM) (Fig.2) and optical absorption spectroscopy (OAS). In the latter technique, the energy corresponding to the maximum of the most pronounced first absorption band around 0.75 eV is inversely proportional to the mean diameter of SWNTs whereas its amplitude can be considered to be a measure of the *relative* abundance of SWNTs in the laser-ablation soot [22] (Fig.3).

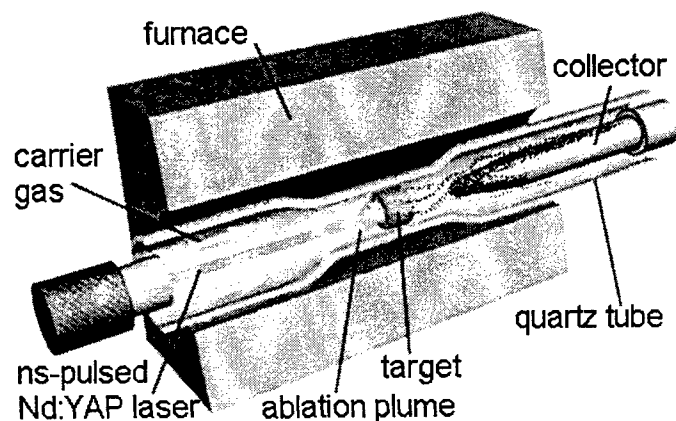


Fig.1. The laser ablation setup used in experiments for synthesis of SWNTs reproduces essential features the one of Ref. 20. The sketch is adapted from Ref.21.

Standard deposition conditions:

furnace tube diameter*	17 mm
pressure P_0	65 kPa
gas flow velocity* V_0	1 cm/s
furnace temperature T_0	1200°C
laser wavelength	1079 nm
laser pulse length τ	15 ns
laser fluence	1.5 J/cm ²
target metal content (at.%)	0.6 Co + 0.6 Ni
* at the target's site	

Qualitatively, the grade of influence of the process variables on the *relative* abundance of SWNTs in the soot Y and on the SWNT diameter \varnothing is presented in Table 1.

First of all the dependence $Y(V_0)$ draws attention. It saturates at low V_0 and sharply decreases at $V_0 > 2$ cm/s. This behavior has driven to a basic conclusion [23] that the nanotube growth time t_{SWNT} is close to the drift time of the reaction products through the hot zone of the furnace t_{drift} which is of the order of few seconds. As a result, one obtains the order of magnitude of the mean SWNT growth rate of a μm length per second. This time correlates by the order of magnitude with that reported for the arc discharge method [24]. By performing the laser-induced luminescence imaging of the carbon-metal targets under the SWNT synthesis conditions, a SWNT growth rate of 0.2 $\mu\text{m/s}$ at $T_0=1000^\circ\text{C}$ have deduced in [25]. The

comparison of this SWNT formation time scale with characteristic times of the individual phenomena taking place during the laser ablation of graphite in the backpressure atmosphere resulted in the following relationship [23]:

$$\tau \ll t_{cond} \ll t_T \ll t_{drift} \approx t_{SWNT}$$

where the upper estimate of the characteristic time of the thermal equalization $t_T < 20$ ms and the carbon condensation time t_{cond} is of the order of tens of μ s. The principal inference that follows immediately from the Eq.1 is that the carbon exists in the form of clusters and large aggregates during most of the SWNT growth. Therefore, all the mechanisms of the SWNT formation which assume the vapor feedstock of carbon atoms cannot be considered as appropriate for the laser ablation SWNT synthesis. As a result, one can make a basic conclusion that the carbon feedstock for the growing SWNTs is the condensed amorphous (as is seen from TEM pictures) carbon and the SWNT growth is a *condensed state* transformation of one solid form of carbon into the other.

process variable	Y	\varnothing
catalyst kind and composition	++	++
catalyst content in target	++	-
furnace temperature T_0	++	++
carrier gas kind	+	+
carrier gas pressure P_0	++	+
carrier gas flow velocity V_0	++	-
laser pulse repetition rate	+	-
laser pulse energy	+	-

Table 1. The grade of the process variables influence on the relative abundance of SWNTs in the soot Y and on the SWNT diameter \varnothing .

++ strong influence
+ certain influence
- no influence

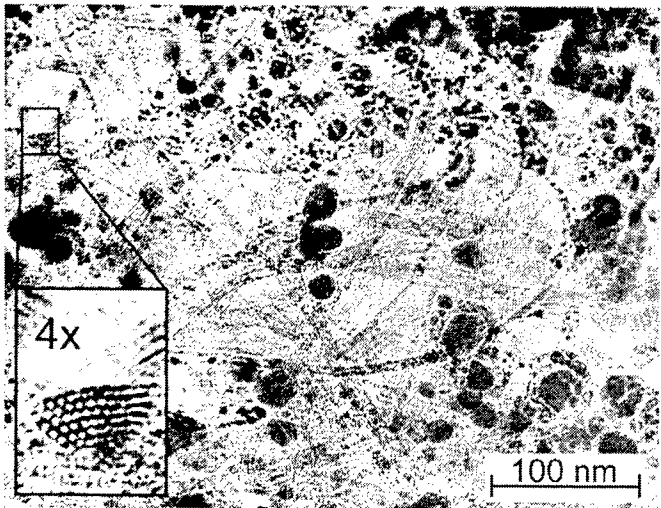


Fig.2. Row soot synthesized under the standard conditions listed in Fig.1. The 4 \times magnified insert demonstrates the packing of SWNTs in a bundle.

A condensed state transformation of a disordered carbon into SWNTs was recently observed in [26], where the carbon nanotubes have been grown without involving any deposition from the vapor phase or chemical reactions. The graphite was first stainless steel ball milled to produce carbon with a highly disordered, nanocrystalline nanoporous structure. The following annealing of this disordered carbon at a temperature of 1400 $^{\circ}$ C resulted in the formation of a number of carbon nanostructures of different morphologies and especially single- and multiwall nanotubes, heterogeneously nucleated by impurity iron particles.

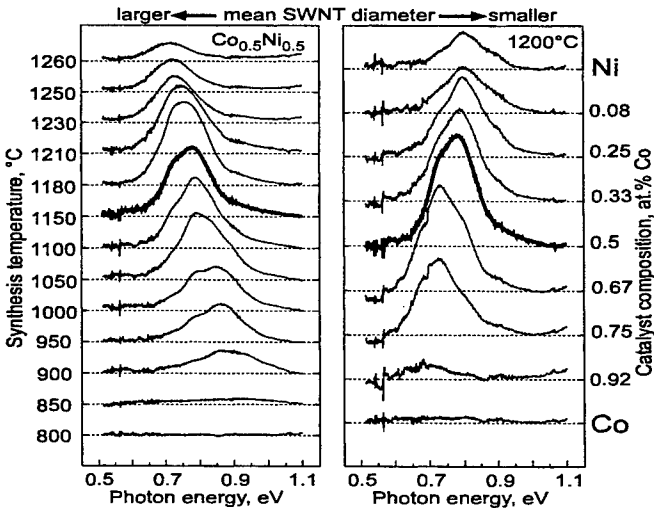


Fig3. Shift of the SWNT absorption band around 0.75 eV as a function of the synthesis temperature T_0 and catalyst composition. The maximum position is inversely proportional to the mean diameter of SWNTs \varnothing . The emphasized curves correspond to $\varnothing = 1.29$ nm

In a similar experiment, we have prepared a SWNT-free laser ablation soot at $T_0 = 700^\circ\text{C}$ and annealed it at 1200°C in the Ar atmosphere. After 1 hour annealing, single and bundled SWNTs along with other fiber-like structures have been detected by a subsequent TEM inspection, which is a direct indication that the growth of SWNTs from the laser ablation soot is also a condensed state process.

3. DISCUSSION. SWNT FORMATION MECHANISM

Catalytic graphitization. A known condensed state reaction of this kind is the catalytic graphitization, which is usually observed at temperatures of $\geq 850^\circ\text{C}$. It is based on the fact that the actual concentration of carbon in the metal-carbon solution should be greater than that in equilibrium with graphite. It involves a group VIII metal or metal-carbon melt dissolving non-graphitic carbon phases and precipitating carbon in form of graphite when cooled, or as a consequence of a supersaturation [27-29]. The metal acts as a transporting medium and the driving force behind the reaction is the free energy difference between the initial and the final forms of carbon.

Molten catalyst particles. As is known, the binary alloy phase diagrams of single-metal catalysts consist of simple eutectics with the stable eutectic temperatures $T_{\text{eut}}(\text{C-Ni}) = 1326.5^\circ\text{C}$ and $T_{\text{eut}}(\text{C-Co}) = 1320^\circ\text{C}$, and a very limited solubility of the metals in the graphitic carbon phase. Nevertheless, there exist strong indications that small catalytical particles involved in the SWNT synthesis are molten even at temperatures far below the equilibrium eutectic one of the corresponding metal-carbon alloy. First, a reduction of the melting temperature in small metal particles becomes significant at $r < 10$ nm. The particles of this size are most common in the SWNT-containing soot found in the experiments. Secondly, the reduction of the melting temperature in an ideal solution is roughly proportional to the mole fraction of the solute. The molten nickel particles 10 - 50 nm in size moving on the surface of amorphous carbon and leaving the graphitic track behind have been observed in Refs. 30- 33 at unusually low temperatures in the range of $600 - 950^\circ\text{C}$ (Fig.4).

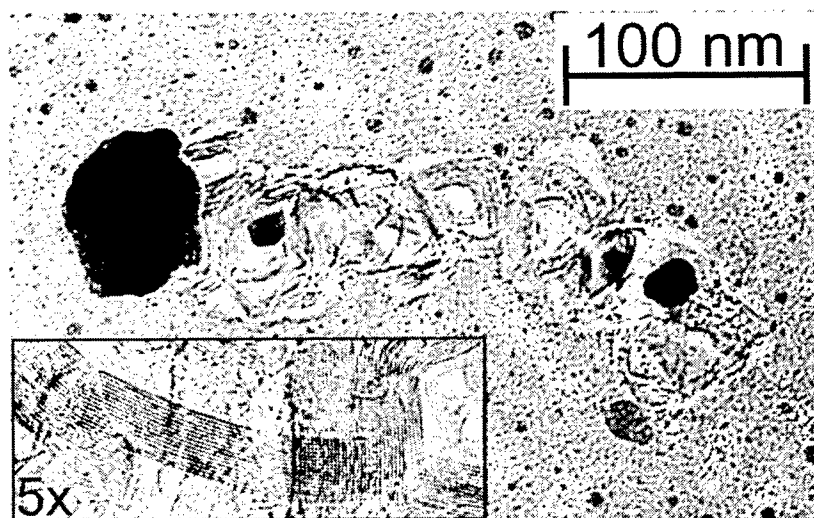


Fig.4. Observation of a liquefied Ni particle moving on the surface of amorphous carbon and leaving the graphitic track behind. The 5x magnified insert shows a fragment of the track with graphitic cage walls having a characteristic layer spacing of 0.335 nm. The photo was taken ca. 10 min after rising the temperature of the TEM sample holder to 800°C .

The encaging and shrinkage of catalytic particles in the soot synthesized at high temperatures (Fig. 2) correlates well with the hypothesis of their molten origin followed by the massive precipitation of the excess carbon upon solidification (cf. Ref.16). By comparing the material amounts in the metal core and the outer carbon shells, one can deduce that the initial carbon concentration in the molten particle was about 50 at.%, same as was estimated in [32]. To compare, a stable 50 at.% concentration in the carbon-nickel melt can be reached first at a temperature well above 3000°C . The dense graphitic cage prevents the further feeding of the amorphous carbon, thus making the particle catalytically inactive.

Mechanism of SWNT nucleation. It follows from the above consideration that the liquefaction of the catalyst particles is the important condition for the SWNT nucleation. In the case of solid catalyst particles, only filamentary carbon structures are known to grow with a rate of up to few tens of nm/s decreasing regularly with increasing particle size [34]. Graphene layers in these carbon structures always nucleate in a parallel direction with any suitable face of the catalyst particles. Consequently, graphitic nanofibers with different crystallographic constitution -tubular, herringbone, or even perpendicularly oriented to the growth axis- can be synthesized depending on the crystallographic orientation of the catalyst particle in respect to fiber axis [9, 10, 35].

Alteration of the carbon precipitation mode with the melting of the catalyst particles is possibly associated with the fact that the higher is the content of C in the melt, the worse is the wetting of graphite by the liquid (Fe, Ni, or Co)-C alloys. At the solubility limit corresponding to the given experiment temperature, the melt does not wet graphite at all [29]. As a consequence, the precipitation of carbon from a strongly supersaturated melt in a form of graphene layers parallel to the surface (as is the case in MWNT synthesis) is no more energetically favorable. To reduce the contact surface as much as possible, the precipitating graphene layers will tend to orient themselves *perpendicular* to the melt surface. According to the negative surface energy balance in the 'system graphite on the supersaturated metal-carbon melt', any local defect of the graphene sheet can cause development of a protrusion followed by nucleation of a nanotube through the mechanism proposed in [14]. Similar mechanism of SWNT nucleation has been proposed in [37], where the SWNT nucleation has been postulated to take place through some molecular oscillations of the precipitated graphitic monolayer on the surface of molten supersaturated metal-carbon droplets.

Therefore, the SWNT growth in the physical synthesis techniques can be considered as a solid-liquid-solid process catalyzed by small nanometer-size metal particles. The natural lower size limitation of the catalyst particles is a single SWNT diameter of about 1.3 nm for the standard synthesis conditions. The observed experimental dependencies reflect the complex interaction of a number of competing processes accompanying the SWNT growth. Generally, it should be noted that the proposed solid-liquid-solid mechanism of the SWNT formation does not seem to be unique to the pulsed laser-oven technique. Critical inspection of the literature data shows that it might also be active in the other PVD (cw-laser, solar furnace, arc-discharge) techniques. The role of the oversaturated fluidized dissolved carbon containing Co particles in carbon nanotube formation through catalytical CO disproportionation has been also considered in [17].

4. CONCLUSIONS

Qualitative consideration of the experimental data on the SWNT yield optimization in a pulsed laser evaporation technique provides a non-contradictory solid-liquid-solid mechanism of the SWNT formation based on the liquid phase graphitization of imperfect (amorphous) forms of carbon. The mechanism consists of the following steps: (1) rapid condensation of the carbon vapor in the form of amorphous carbon and metal catalyst particles; (2) melting of small catalyst metal particles in contact with the amorphous carbon due to its enlarged solubility; (3) the enlarged diffusivity of carbon atoms in the molten metal causes its rapid precipitation in a graphitic form; (4) large contact angle between the supersaturated melt and graphitic carbon prevents orientation of the graphene sheets along the particle's surface and they tend to orient perpendicularly; (5) rolling of the graphene sheets into small tubes is a way to reduce the extra free energy associated with the graphene sheet edges. The proposed mechanism should play a role in the other physical and chemical methods of the SWNT synthesis.

The work was supported by the European Commission (Project IST-10593 SATURN), BMBF (Project 13N7575), DFG (Project PO 392/10-1), SMWK (Project 4-7531.50-03-823-98).

6. REFERENCES

1. T.W.Ebbesen, ed., *Carbon Nanotubes. Preparation and Properties*, CRC Press, Boca Raton, 1997.
2. C.Journet, P.Bernier, "Production of carbon nanotubes", *Appl.Phys. A67*, pp.1-9, 1998.
3. R.E.Smalley, "From dopyballs to nanowires", *Mater.Sci.Eng. B19*, pp.1-7, 1993.
4. E.G.Gamaly, T.W.Ebbesen, "Mechanism of carbon nanotube formation in the arc discharge", *Phys.Rev. B52*, pp.2083-2089, 1995.
5. A.Thess, R.Lee, P.Nikolaev, H.Dai, P.Petit, J.Robert, C.Xu, Y.H.Lee, S.G.Kim, A.G.Rinzler, D.T.Colbert, G.E.Scuseria, D.Tomanek, J.E.Fischer, R.E.Smalley, "Crystalline ropes of metallic carbon nanotubes", *Science* 273, pp.483-487, 1996.
6. R.S.Lee, H.J.Kim, J.E.Fischer, A.Thess, R.E.Smalley, "Conductivity enhancement in single-walled carbon nanotube bundles doped with K and Br", *Nature* 388, pp.255-257, 1997.
7. A.Maiti, C.J.Brabec, C.N.Roland, J.Bernholc, "Growth energetics of carbon nanotubes", *Phys.Rev.Lett.* 73, pp.2468-2471, 1994.
8. J.-C. Charlier, X.Blase, A.DeVita, R.Car, "Microscopic growth mechanisms for carbon and boron-nitride nanotubes", *Appl.Phys. A68*, pp.267-273, 1999.
9. A.Oberlin, M.Endo, T.Koyama, "Filamentous growth of carbon through benzene decomposition", *J.Cryst.Growth* 32, pp.335-347, 1976.
10. G.G.Tibbetts, "Why are carbon filaments tubular?", *J.Crystal Growth* 66, pp.632-638, 1984.

11. N.M.Rodriguez, "A review of catalytically grown carbon nanofibers", *J.Mater.Res.* 8, pp.3233-3250, 1993.
12. A.M.Cassell, J.A.Raymakers, J.Kong, H.Dai, "Large scale CVD synthesis of single-walled carbon nanotubes", *J.Phys.Chem. B103*, pp.6484-6492, 1999.
13. R.T.K.Baker, M.A.Barber, P.S.Harris, F.S.Feates, R.J.Waite, "Nucleation and growth of carbon deposits from the nickel catalyzed decomposition of acetylene", *J.Catal.* 26, pp.51-62, 1972.
14. A.Maiti, C.J.Brabec, J.Bernholc, "Kinetics of metal-catalyzed growth of single-walled nanotubes", *Phys.Rev. B55*, pp.R6097-R6100, 1997.
15. D.Ugarte, "Onion-like graphitic particles", *Carbon* 33, pp.989-993, 1995.
16. D.Zhou, S.Seraphin, S.Wang, "Single-walled carbon nanotubes growing radially from YC₂ particles", *Appl.Phys.Lett.* 64, pp.1593-1595, 1994.
17. A.A.Khassin, T.M.Yurieva, V.I.Zaikovskii, V.N.Parmon, "Effect of metallic cobalt particles on occurrence of CO disproportionation. Role of fluidized metallic cobalt-carbon solution in carbon nanotube formation.", *React.Kinet.Catal.* 64, 63-71, 1998.
18. H.Kataura, Y.Kumazawa, Y.Maniwa, Y.Ohtsuka, R.Sen, S.Suzuki, Y.Achiba, "Diameter control of the single-walled carbon nanotubes", in *Proc. Fullerenes 99*, France, August 1999, Elsevier, in press.
19. M.Yudasaka, T.Komatsu, T.Ichhashi, Y.Achiba, S.Iijima, Pressure dependence of the structures of carbonaceous deposits formed by laser ablation on targets composed of carbon, nickel, and cobalt", *J.Phys.Chem. B102*, pp.4892-4896, 1998.
20. T.Guo, P.Nikolaev, A.Thess, D.T.Colbert, R.E.Smalley, "Catalytic growth of single-walled nanotubes by laser vaporization", *Chem.Phys.Lett.* 234, pp.49-54, 1995.
21. B.I.Yakobson, R.E. Smalley, "Fullerene Nanotubes: C1,000,000 and Beyond", *American Scientist* 85, pp.324-337, 1997.
22. O.Jost, A.A.Gorbunov, W.Pompe, T.Pichler, R.Friedlein, M.Knupfer, M.Reibold, H.-D.Bauer, L.Dunsch, M.S.Golden, J.Fink, "Diameter grouping in bulk samples of single-walled carbon nanotubes from optical absorption spectroscopy", *Appl.Phys.Lett.* 75, pp.2217-2219, 1999.
23. A.A.Gorbunov, R.Friedlein, O.Jost, M.S.Golden, J.Fink, W.Pompe, "Gas-dynamic consideration of the laser evaporation synthesis of single wall carbon nanotubes", *Applied Physics A* 69 [Suppl.], pp.S593-S596, 1999.
24. Y.Saito, M.Okuda, M.Tomita, T.Hayashi, "Extrusion of single-wall carbon nanotubes via formation of small particles near an arc evaporation source", *Chem.Phys.Lett.* 236, pp.419-426, 1995.
25. A.A.Puretzky, D.B. Geohegan, X.Fan, S.J.Pennycook, "Dynamics of single-wall carbon nanotube synthesis by laser vaporization", *Appl.Phys. A70*, pp.153-160, 2000.
26. L.T.Chadderton, Y.Chen, "Nanotube growth by surface diffusion", *Phys.Lett. A263*, pp.401-405, 1999.
27. H.Marsh, A.P.Warburton, "Catalysis of graphitisation", *J.Appl.Chem.* 20, pp.133, 1970.
28. F.J.Derbyshire, A.E.B.Presland, D.L.Trimm, "Graphite formation by the dissolution-precipitation of carbon in cobalt, nickel and iron", *Carbon* 13, pp.111-113, 1975.
29. V.B.Fedorov, M.H.Shorshov, D.K.Khakimova, *Carbon and its interaction with metals*, Metallurgija-Publishers, Moscow, 1978 (in Russian).
30. A.E.Gorodetskij, E.I.Evko, A.P.Zakharov, "Crystallization of amorphous carbon by moving nickel particles", *Fizika Tverdogo Tela* 18, pp.619-621, 1976 (in Russian).
31. R.Lamber, N.Jaeger, G.Schulz-Ekloff, "Electron microscopy study of the interaction of Ni, Pd and Pt with Carbon. I. Nickel catalyzed graphitization of amorphous carbon", *Surf.Sci.* 197, pp.402-414, 1988.
32. O.P.Krivoruchko, V.I.Zaikovskii, "A new phenomenon involving the formation of liquid mobile metal-carbon particles in the low-temperature catalytic graphitization of amorphous carbon by metallic Fe, Co and Ni", *Mendeleev Commun.*, №3, pp.97-100, 1998.
33. E.F.Kukovitsky, S.G.L'vov, N.A.Sainov, "VLS-growth of carbon nanotubes from the vapor", *Chem.Phys.Lett.* 317, pp.65-70, 2000.
34. R.T.K.Baker, P.S.Harris, R.B.Thomas, R.J.Waite, "Formation of filamentous carbon from iron, cobalt and chromium catalyzed decomposition of acetylene", *J.Catal.* 30, pp.86-95, 1973.
35. R.T.K.Baker, M.S.Kim, A.Chambers, C.Park, N.M.Rodrigues, "The relationship between metal particle morphology and the structural characteristics of carbon deposits", in *Catalyst Deactivation*, ed. by C.H.Bartholomew and G.A.Fuentes, pp. 99-109, Elsevier, 1997.
36. H.Kanzow, A.Ding, "Formation mechanism of single-wall carbon nanotubes on liquid-metal particles", *Phys.Rev. B60*, pp.11180-11186, 1999.

Laser ablation of polymers by ultra-short laser pulses (USLP): surface and bulk models

Aleksey Yu. Malyshev^{*}, Nikita M. Biturin^{**}

Institute of Applied Physics, RAS, 603600, Nizhnii Novgorod, Russia

ABSTRACT

In the present communication we consider theoretically the effect of a single UV USLP and two successive UV USLPs on absorbing dielectrics near ablation threshold within the framework of a surface evaporation model and bulk photothermal models, which apply to polymer-like materials.

In the case of pair-pulse ablation we investigate the dependence of the ablated depth on the delay time between USLPs (delay curve). We show that this curve is formed in two possible regimes. It is shown that these regimes influence the shape of the delay curve. We argue that these regimes are the same for the bulk model as well. It means that it is difficult to distinguish between the models investigating only this curve.

We consider possible pump-probe experiment where USLP with the fluence somewhat higher than the ablation threshold is employed as a pump, whereas probe radiation allows to determine the delay time between pump pulse and the start of ablation.

We show that combining the experimental data on determination of delay curve in pair-pulse experiment and the above pump-probe single ablation allows determination of an appropriate model. The results of theoretical modeling are compared with the existing data on time-resolved UV USLP laser ablation experiments.

Keywords: ultra-short laser pulses, bulk model, pump-probe, UV, polymers, modeling

1. INTRODUCTION

Polymeric materials are constituted by long macromolecules consisting of sequences of molecular groups (monomers) of the same nature. The main feature of polymeric materials is the hierarchy of bonds between molecular groups. There are 'strong', covalent bonds connecting neighbor molecular groups of the same chain and 'weak' molecular bonds between neighbor groups which belong to different polymer chains. This feature is taken into account in so-called bulk model of laser ablation of polymers derived in ¹⁻³. In this model ablation of organic polymers is described on the basis of photothermal bond breaking within the bulk of material (random chain breaking). We also consider the surface photothermal model which was investigated in ⁴ for metals. These models were applied for modeling of laser ablation of polymers by nanosecond pulses and gave good results on the prediction of ablation kinetics ^{2,3,5}.

We focus our attention on the ablation with relatively short, namely, subpicosecond or Ultra Short Laser Pulses (USLP). We consider features of single-pulse and pair-pulse ablation by USLP with variable delay between pulses. It is perceived now that the threshold of USLP ablation of transparent dielectrics coincides with the onset of avalanche or multiphoton ionization ⁶. It is not so evident for highly absorbing dielectrics. The ablation threshold fluence can be smaller than that needed for avalanche or step-wise ionization development. In the case of pair-pulse ablation we investigate the dependence of the ablated depth on the delay time between USLPs (delay curve $h(t_d)$). We show that this curve is formed in two possible regimes. These regimes were studied comprehensively in ^{7,8} for the surface photothermal model. It is shown that these regimes influence the shape of the delay curve, whereas the characteristic time scale is governed by the thermal relaxation time. In the present communication we argue that these regimes are the same for the bulk model as well.

Considering single-shot USLP ablation we show that within the bulk photothermal model, in contrast to the surface photothermal one, maximum of ablation velocity does not correspond to the maximum of surface temperature. We obtain that the start of ablation for bulk model has a delay in comparison with the start of ablation for surface model. From this point of view, we consider possible pump-probe experiment where USLP with the fluence somewhat higher than the ablation

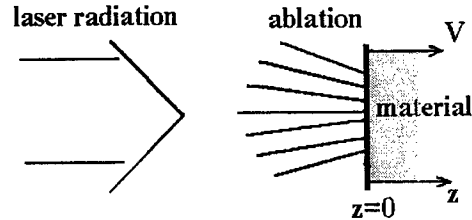
^{*} E-mail: malex@ufp.appl.sci-nnov.ru, phone +7 8312 384503, fax +7 8312 363792

^{**} E-mail: bit@appl.sci-nnov.ru, phone +7 8312 384389, fax +7 8312 363792

threshold is employed as a pump, whereas probe radiation allows to determine the delay time between pump pulse and the start of ablation.

2.MODELS

We consider a one dimensional case. The laser beam propagates in the z-direction and interacts with the surface of material. The ablated surface is placed within the plane $z=0$. We consider two models for description of USLP ablation of polymers: surface photothermal model and bulk photothermal model³.



The set of equations consists of ablation front velocity equations, heat diffusion equation and boundary conditions, and equations for the material response.

Photothermal surface model:

$$V_{abl} = V_0 \exp(-E_a / k_B T_s) \quad (1)$$

Here $T_s = T(0, t)$ is the value of the temperature at the surface, E_a is the activation energy of removal of molecule (atom) from the surface, and V_0 is of the order of sound velocity, k_B being the Boltzmann constant.

$$\frac{\partial T}{\partial t} = V \frac{\partial T}{\partial z} + \frac{1}{\rho c_p(T)} \frac{\partial}{\partial z} (\kappa(T) \frac{\partial T}{\partial z}) + Q \quad (2)$$

Here T is the temperature, ρ is the density, $c_p(T)$ is the specific heat, $\kappa(T)$ is the thermoconductivity, the source term Q in (2) describes heating of material due to absorption of laser radiation. Equation (2) is written in a coordinate system moving with the ablation velocity $V = V_{abl}$ and fixed with the ablation front.

We use the boundary conditions in a simplified form:

$$\kappa(T) \frac{\partial T}{\partial z} \Big|_{z=0} = \rho \Delta H V \quad T_{|z \rightarrow \infty} = T_0 \quad (3)$$

ΔH is the surface sublimation enthalpy.

Photothermal bulk model.

Within the bulk model, laser ablation proceeds through bulk reaction which results in creation of broken bonds. In what follows we consider the single-step thermally activated reaction with the kinetics equation for the fraction of broken bonds:

$$\frac{\partial N}{\partial t} = V \frac{\partial N}{\partial z} + (1 - N) k_0 \exp(-E_b / k_B T) \quad (4)$$

Here k_0 is a constant. Within the bulk model equation (2) is also valid but the source term Q contains, additionally to the surface model, the term accounting for the thermal effect of the chemical reaction.

The boundary conditions at infinity: $N|_{z \rightarrow \infty} = 0$ (5)

The expression for ablation front velocity yields³:

$$V_{abl} = V_{0m} \exp(-E_m / k_B N_s T_s) \quad (6)$$

E_m is the energy of weak bonds per 'monomer', $N_s = N(0, t)$.

Within the approach we employ the equation for ablation velocity (6) together with the boundary condition:

$$\kappa(T) \frac{\partial T}{\partial z} \Big|_{z=0} = \rho \frac{\Delta H_m}{N_s} V \quad (7)$$

ΔH_m is the enthalpy of evaporation of fragments (weak bonds).

The intensity distribution within the material $I(z, t)$ is governed by the equation:

$$\frac{\partial I}{\partial z} = -\alpha I \quad \alpha = \sigma_{12}(n_1 - n_2) + \sigma_{23}n_2 \quad (8)$$

The rate equations of the populations of the energy levels in a medium represented by the three-level model shown in Fig. 1, are as follows:

$$\frac{\partial n_1}{\partial t} = V \frac{\partial n_1}{\partial z} - \frac{\sigma_{12}}{\eta \omega} I(n_1 - n_2) + \frac{n_2}{t_{21}} \quad (9)$$

$$\frac{\partial n_2}{\partial t} = V \frac{\partial n_2}{\partial z} + \frac{\sigma_{12}}{\eta \omega} I(n_1 - n_2) - \frac{\sigma_{23}}{\eta \omega} I n_2 - \frac{n_2}{t_{21}} + \frac{n_3}{t_{32}} \quad (10)$$

$$n_1 + n_2 + n_3 = n_0$$

Equations (9) and (10) ignore stimulated emission as a result of transitions between the second and third levels. As it was discussed in⁸, this model of medium response allows fitting experimental data on pair-pulse ablation of Polyimide.

The heat source term in equation (2) should be overwritten as follows:

- for surface photothermal model:

$$Q = \frac{\eta \omega}{\rho c_p(T)} \left(\frac{n_2}{t_{21}} + \frac{n_3}{t_{32}} \right) \quad (11)$$

- for bulk photothermal model:

$$Q = \frac{\eta \omega}{\rho c_p(T)} \left(\frac{n_2}{t_{21}} + \frac{n_3}{t_{32}} \right) - \frac{L(1-N)k_0 \exp(-E_b / k_B T)}{c_p \rho} \quad (12)$$

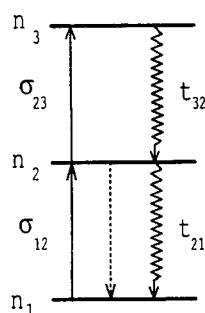


Fig. 1. Scheme of electronic structure of chromophores;
 n_1 , n_2 , and n_3 are populations of the levels; n_0 is the number density of chromophores in the medium; σ_{ij} are the cross sections of the transitions; t_{21} , t_{32} are the nonradiative relaxation times of electronically excited states.

The above set of equations were used to investigate laser ablation kinetics and dynamics by means of numerical modeling. The parameters used in calculations are shown in Table 1. The results of theoretical modeling are compared with the existing data on time-resolved UV USLP laser ablation experiments (ablation of Polyimide by pair UV USLP at the wavelength of a KrF laser).

Table 1. The parameters of models and material used in calculations.

Parameter	Surface photothermal model	Bulk photothermal model
Activation energy (surface) E_a , eV E_m , eV	1.5	0.7
Surface sublimation enthalpy ΔH , J/g	900	500
Surface pre-exponential V_0 , cm/s V_{0m} , cm/s	$3 \cdot 10^6$	$1.1 \cdot 10^5$
Volumetric activation energy E_b , eV		1.5
Volume pre-exponential k_0 , s^{-1}		$3.57 \cdot 10^{12}$
Volumetric reaction enthalpy L , J/cm ³		2000
Ambient temperature T_0 , K	300	300
Parameters PI Kapton TM H 248 nm		Value
Density ρ , g/cm ³		1.42
Specific heat c_p , J/g K	⁵	$2.55 - 1.59 \exp[(T - T_0)/460]$
Thermal conductivity κ , W/cm K	⁵	$1.55 \cdot 10^{-3} (T/T_0)^{0.28}$
Reflection coefficient R		0.1
Absorption coefficient α , cm ⁻¹		$3.2 \cdot 10^5$
Relaxation times of excited states t_{21} , ps t_{32} , ps		30 70
Parameter $s = \sigma_{32}/\sigma_{21}$		1

3. RESULTS AND DISCUSSION

3.1. Pair-pulse ablation.

We consider the process of forming of shape of delay curve in pair-pulse ablation qualitatively. The energy distribution in a medium can be illustrated by the temperature distributions (Fig.2) created by the action of one pulse (zero delay between the pulses) or by two pulses with a delay exceeding the electronic relaxation time in the medium. These distributions are characterized by two important parameters: the characteristic spatial scale of the heated region and the surface temperature. The region heated by one pulse is larger than that produced by the action of two pulses, but the surface temperature is lower.

One can ask in which of these two cases the thickness of the ablated layer will be greater? The answer to this question is not a priori evident. Ablation by ultrashort pulses is determined by the competition between two processes: the conduction of heat and the motion of the ablation front.

If the ablation is fast, the thermal conductivity can be ignored and the result is removal of the heated region as a whole. If the ablation is slow, then during the heat conduction time only a small proportion of the region heated by radiation is removed. It seems natural to consider two regimes of laser ablation by ultrashort pulses:

- *the regime with a characteristic heating scale*, when the thickness of the removed layer is governed by the thickness of the heated region of the material; this is the case of fast motion of the ablation front, compared with the heat conduction process;

- *the regime with insufficient heating*, when the thickness of the removed layer is governed by the surface temperature; this is the case of slow motion of the ablation front, compared with the loss of heat from the absorption region.

We showed that experimental data on 500fs KrF laser ablation of polyimide⁹ can be described as the *insufficient heating regime* with induced bleaching. It is quite evident that for bulk photothermal model we will have the same possible regimes as for the surface model. It is demonstrated in Fig. 3 where the mentioned above experimental data on pair pulse ablation are fitted both by surface photothermal model and by bulk photothermal model. It should be emphasized that the fitting parameters employed are *the same* as for nanosecond pulses. It means that using only data on delay curve it is difficult to distinguish between the models. Really, the delay curve provides the information on the difference in temperature distribution depending on delay time between USLPs because ablation starts after the establishment of the temperature distribution. These differences in temperature distribution are governed by the material response (transient bleaching or darkening). It should be noted that a lot of relaxation times can be involved in transient response of the material. It is very important, however, that delay curve allows determination of thermal relaxation time which actually determines the establishment of the temperature distribution. The delay curve is less sensitive to the model of ablation.

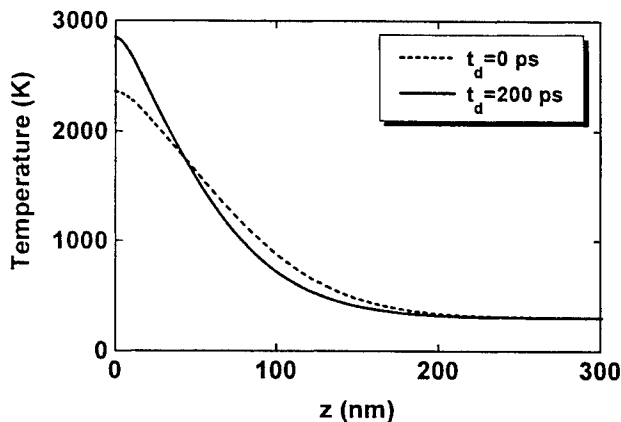


Fig. 2. The dependences of the temperature on the coordinate directed into the material, calculated for $t_2, t_{32} < t < t_T$ and without moving interface (t_T - the characteristic heat conduction time).

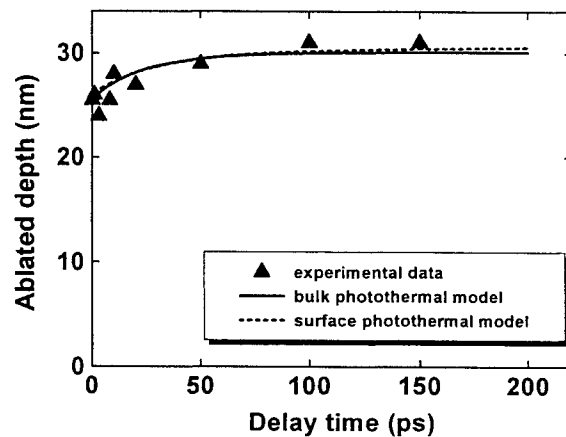


Fig. 3. The comparison of calculated dependences $h(t_d)$ with experimental data⁸ for various ablation models. Single pulse fluence consists of $F_p = 25 \text{ mJ/cm}^2$.

Fig. 4 demonstrates the dependence of delay curve on the fluence of the single pulse (each of pulses). It is seen that an increase in single pulse fluence results in changes in the shape of the delay curve. This corresponds to the transition from the *insufficient heating regime* to the *characteristic scale regime*. In order to characterize this tendency we can consider the

contrast, C , of the delay curve $h(t_d)$ that is the ratio $C = \frac{h(t_d^{\max}) - h(0)}{h(t_d^{\max})}$. It is shown in Fig. 5 that the contrast

monotonically decreased with increasing single pulse for both considered models. It is seen, however, that a decrease in the single pulse fluence leads to a sharp increase in the contrast of the delay curve in the case of bulk model, this dependence being more smooth for the surface model. The low precision of measurement of delay curve contrast nearest the ablation threshold does not permit to distinguish between these models using pair pulse experiments. Thus, we should recognize that there is no significant difference between the models with respect to the pair pulse ablation experiments.

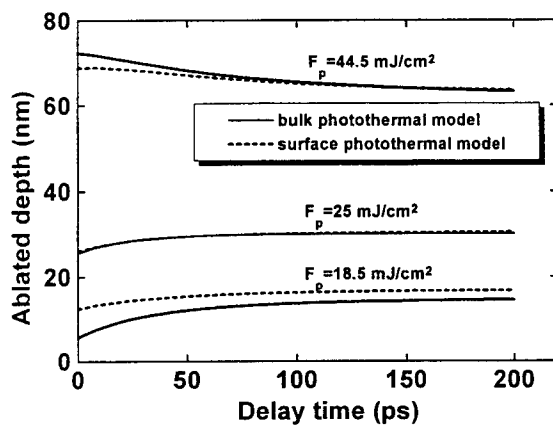


Fig. 4. The dependences of the ablated thickness $h(t_d)$ on the delay time between two ultrashort pulses for various ablation models and pulse fluences.

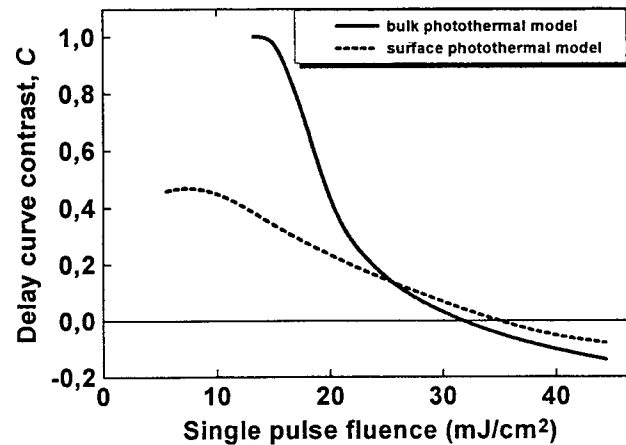


Fig. 5. The dependences of contrast C of delay curve on single pulse fluence for surface photothermal model and bulk photothermal model.

3.2. Ablation by ultrashort single-pulse.

As a rule the integral parameters of laser ablation were investigated, for example, ablated thickness versus laser fluence. The study of this kinetics curve did not permit to determine model of laser ablation of polymer materials. Fig. 6 exhibits kinetics of the single-pulse USLP ablation. The characteristic features are as follows:

- The bulk ablation starts sharply when fluence approaches the threshold value, whereas the surface ablation exhibits the Arrhenius law near ablation threshold.
- After the threshold the kinetics curve is almost linear in the case of surface model and follows more or less square root law investigated in ².

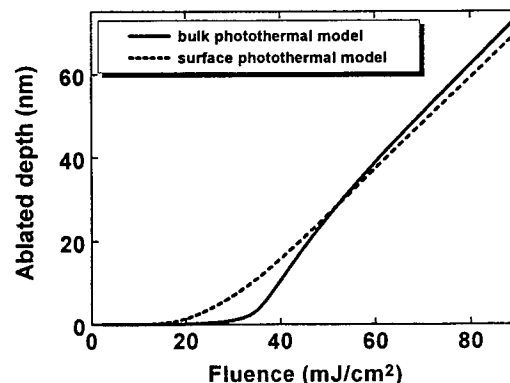


Fig. 6. Ablated depth versus single pulse fluence for two ablation models.

Despite the mentioned above differences, the kinetics curves are too close to each other to be reliably distinguished in experiment. We show that single pulse ablation dynamics permits to distinguish between the two considered models.

In contrast to kinetics curves, the dynamics of laser ablation in both considered cases differ essentially. It is seen from

Fig. 7a that the maximum of ablation velocity for the surface model coincides with the maximum of surface temperature but does not coincide for the bulk model. The start of ablation for the bulk photothermal model is determined not only by surface temperature but also by the density of broken bonds (Fig. 7b). The start of ablation for the surface model is governed by thermal relaxation time. As far as the bulk model is concerned the start of ablation in this case is not governed by thermal relaxation time but rather by the time of thermally activated chemical reaction. The delay time of the start of ablation after the laser pulse for these models is quantitatively different (Fig. 7a). It is a significant feature for the USLP ablation.

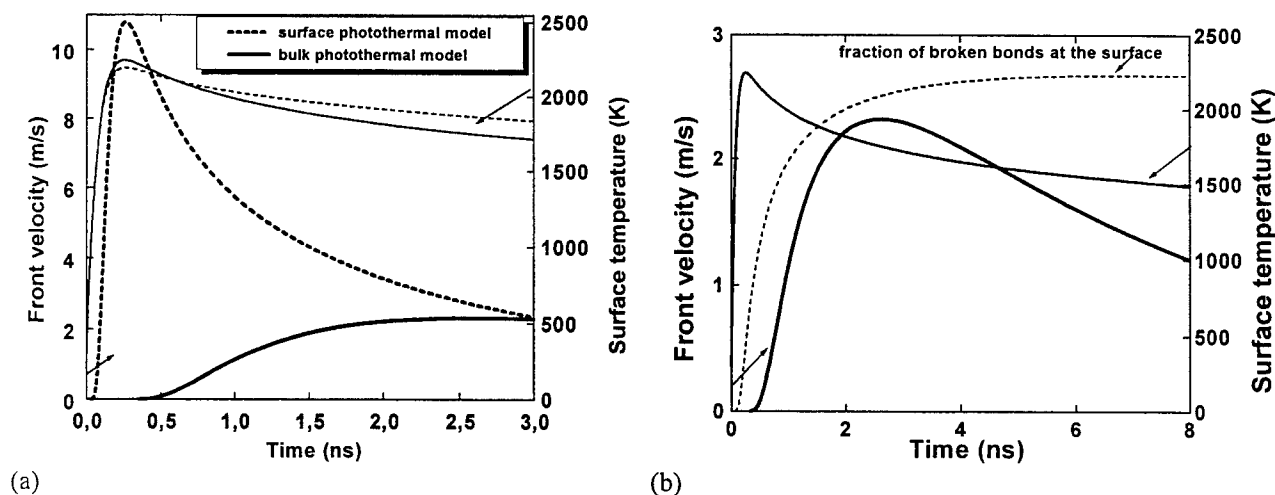


Fig. 7. The dynamics of laser ablation under the effect of single 500 fs laser pulse with fluence $F_p = 50 \text{ mJ/cm}^2$ for two ablation models. (a) Ablation front velocity and surface temperature versus time. (b) Ablation front velocity, surface temperature and fraction of broken bonds versus time (bulk model).

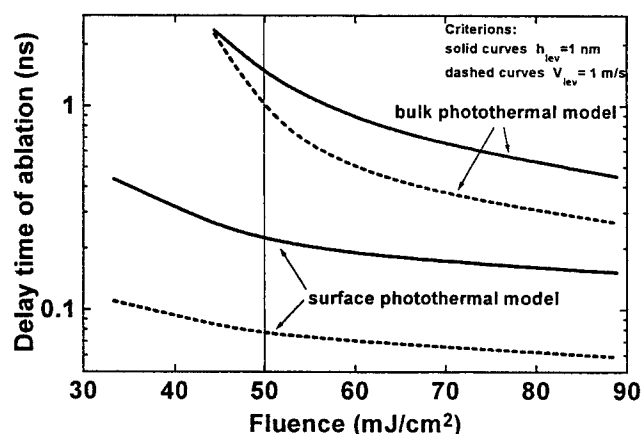


Fig. 8. The dependences of delay time of start of ablation versus pulse fluence for various ablation models and criteria of start of ablation.

We can distinguish between these models using measurements of *this time*. Based on our investigation we suggest the scheme of experiments for determination of model which really describes the laser ablation of given polymeric materials. The thermal relaxation time can be estimated using the pair-pulse experiments⁹. The moment of the start of ablation can be determined by another pump-probe experiment either when the ablation velocity or ablated depth exceeds given level. Fig. 8 shows the dependence of the delay time between the laser pulse and the start of ablation on the laser fluence predicted by both the surface and bulk photothermal models. It is seen that near ablation threshold the differences in delay time predicted by different models are significant and can be experimentally distinguished using, e.g.¹⁰ method. If the time of the start of ablation corresponds to thermal relaxation time then the surface photothermal model is the appropriate model. The other case it is more appropriate to use the bulk photothermal model.

CONCLUSIONS

Two different regimes of laser ablation should be considered to interpret the shape of delay curve for surface photothermal model. These regimes are also relevant to the bulk photothermal model (*insufficient heating regime* and *characteristic scale regime*).

The experimental delay curve⁹ of pair-pulse ablation of Polyimide can be fitted using surface and bulk photothermal models. The *insufficient heating regime* near ablation threshold is more reliable.

Our USLP investigation shows that the start of ablation corresponds to the time of thermal relaxation for the surface photothermal model, whereas for the bulk photothermal model it is determined by an absolutely different time which is not connected with the thermal relaxation. This time is the time of thermally activated chemical reaction. This difference allows to decide which model is more appropriate for description of laser ablation of a polymer.

The pair-pulse experiments do not allow to determine an appropriate model of laser ablation of polymeric materials. It is suggested that combining pair-pulse experiment and the detection of the start of ablation with probe radiation allows determination of an appropriate model (surface or bulk).

REFERENCES

1. N. Bityurin, N. Arnold, B. Luk'yanchuk, D. Bäuerle, "Bulk model of laser ablation of polymers", *Appl.Surf.Sci.*, 127, pp.164-170, 1998.
2. N. Arnold, N. Bityurin, "Model for laser-induced thermal degradation and ablation of polymers", *Appl.Phys. A*, 68, pp.615-625, 1999.
3. N.Bityurin, "Model for photothermal laser ablation of polymer-like materials", *Proc. SPIE*, this issue.
4. S.I. Anisimov, Ya.A. Imas, G.S. Romanov, Yu.V. Khodyko, *Action of high power laser radiation on metals*, Moskva, Nauka, 1970.
5. N. Arnold, B. Luk'yanchuk, N. Bityurin, "A fast quantitative modelling of ns laser ablation based on non-stationary averaging technique", *Appl.Surf.Sci.*, 127, pp.184-192, 1998.
6. B.C. Stuart, M.D. Feit, S. Herman, A.M. Rubenchik, B.W. Shore, M.D. Perry, "Optical ablation by high-power short-pulse lasers", *J.Opt.Soc. Am. B*, 13(2), pp.459-468, 1996.
7. N. Bityurin, A. Malyshev, "UV-laser ablation of absorbing dielectrics by ultra-short laser pulses", *Appl. Surf. Sci.*, 127, pp.199-205, 1998.
8. A.Yu. Malyshev, N.M. Bityurin, "Laser ablation of strongly absorbing dielectrics by pairs of subpicosecond pulses", *Quantum Electronics*, 29 (2), pp.134-138, 1999.
9. S. Preuss, M. Spaeth, Y. Zhang, M. Stuke, "Time resolved dynamics of subpicosecond laser ablation", *Appl.Phys.Lett.*, 62, pp.3049-3051, 1993.
10. A. Rosenfeld, D. Ashkenasi, H. Varel, M. Wähmer, E.E.B. Cambell, "Time resolved detection particle removal from dielectrics on fs laser ablation", *Appl.Surf.Sci.*, 127, pp.76-80, 1998.

Laser ablation of the thin film by thermal tension

E.A.Shakhno

Laser Applications Engineering and Applied Ecology Department,
St.Petersburg Federal Institute of Fine Mechanics (Technical University)

14 Sablinskaya str., 197101, St.Petersburg, Russia

E-mail: veiko@lastech.ifmo.ru

Phone/Fax: +7.812.2333406

ABSTRACT

The process of laser ablation of the thin film in solid or liquid phase in the before-evaporation regime is considered. The physical model of film ablation caused by thermal tension, occurring in the film by its fast laser heating, is proposed. The dependence of velocity of film fragment movement from the substrate surface on laser intensity is defined. The proposed conception of laser film ablation is used to explain the phenomenon of film degradation. The obtained results are in a good agreement with known experimental data.

Keywords: thermal enlargement, compression energy, melting.

1. INTRODUCTION

Laser pulse ablation of thin films is one of the main physical processes occurring by the local laser removal and transfer of films, used by laser technologies of film topology formation¹. Investigation of physical mechanisms and regularities of film ablation is also necessary for prognosis of radiation resistance of covers of optical details. Thin film ablation can occur as by its evaporation, as in solid or liquid phase in the before-evaporation regime. Physical mechanisms of film ablation in the evaporation regime are sufficiently investigated in the main (for instance²). Ablation of thin films in solid and liquid phase by the action of 10^{-8} s excimer laser pulses has been experimentally investigated³. Velocity of film fragment movement from the substrate depending on laser intensity was measured. The main features of before-evaporation ablation of W film turned to be the following. Film ablation begins by intensity value $\varepsilon_1 \approx 50 \text{ mJ/cm}^2$, which is much less than the threshold of melting beginning. Velocity of film fragment movement increases by intensity increasing up to value $\varepsilon_1 \approx 300 \text{ mJ/cm}^2$ (which is the intervening value between the thresholds of film melting and evaporation). By larger intensity values, velocity of film fragment movement decreases by intensity increasing. Such peculiarities of the dependence of the film fragment velocity on laser intensity cannot be explained within the boundaries of the present conception of film ablation in solid and liquid phase.

2. THE MAIN REGULARITIES AND REGIMES OF BEFORE-EVAPORATION FILM ABLATION

Preliminary quantitative analysis of the possible causes of before-evaporation tearing-off of the film² shows, that the main cause of film fragment movement is its exfoliation by thermal enlargement (the maximum value of film fragment velocity by this cause is hundred and more times larger than by other causes). By this, elimination of film adhesion, preceding film fragment movement, can be caused by another reason. The most probable cause of elimination of adhesion of refractory films like W is substrate gasification.

The physical mechanism of film ablation and movement of its fragments from the substrate surface by the action of the laser pulse with energy, that is not sufficient for film evaporation, seems to be following. The absorbing film at the transparent substrate is heating in the irradiated zone. Heat partially transfers to the substrate, its gasification begins, if its temperature at the interface is larger than the temperature of gasification T_0 . In result, film adhesion eliminates and film ablation in the solid phase becomes possible, if absorbed intensity is larger, then the threshold value ε_0 . By laser heating of the film, it enlarges. As the irradiated part of the film lies plane at the substrate interface and is fastened at the boundaries, its size changing is absent and thermal enlargement is transformed to thermal tension, which value is

$$\sigma = E\alpha T \quad (1)$$

E is elasticity module, α is linear expansion thermal coefficient, T is film temperature increasing from its initial value.

Density of the compression energy to volume unit is

$$Q = \frac{\sigma^2}{2E} = \frac{E}{2} (\alpha T)^2 \quad (2)$$

It transforms to the kinetic energy of film fragment movement from the substrate surface. By this the following regimes of film ablation in solid or liquid phase are possible:

1. Laser intensity ε is larger than the threshold of adhesion elimination ε_0 and such, that the film temperature T does not reach the value of melting temperature T_m during the laser pulse action and the compression energy and correspondingly the film fragment velocity V are enough small. By this, the complete tearing-off of the film fragment, occurring by its transfer to the distance, that is about film thickness h , happens after laser pulse finishing, i.e. $\int_0^\tau V dt < h$. In this case, compression energy increases during the whole pulse. The maximum value of fragment velocity corresponds to the pulse finishing.

2. By intensity increasing (film temperature is less than its melting temperature T_m , as in the first regime), fragment velocity increases and it transfers at the distance h in time t_* , which is less, than pulse duration, i.e. $\int_0^\tau V dt > h$. By this, film fragment velocity reaches its maximum value at the moment t_* ($t_* < \tau$).

3. Laser intensity is larger, than the threshold of film melting beginning, but the time of complete separation of the film fragment t_* is less, than the time of its heating to the melting temperature t_H . By this, film separation occurs when it is solid yet, and melting begins after it. Therefore, regularities of film ablation in this regime and the previous one are the same.

4. By intensity increasing, film melting begins before it transfers to the distance h (i.e. $t_H < t_*$). By this, two processes take place additionally:

- film enlargement due to increasing of its volume by melting, that is analogous to thermal enlargement and causes increasing of the compression energy and film fragment velocity;
- melted regions sizes decreasing due to melt transfer under the action of compression tension, causing decreasing of the compression energy and film fragment velocity.

Film fragment velocity is defined by the combined action of the mentioned factors in the moment of complete separation t_* .

All the considered before-evaporation regimes of film ablation are present in the case of refractory films such as W, which thickness is about 10^{-7} m. For films with lower melting temperature or larger thickness, some of the considered regimes can be absent.

Film ablation in these regimes is investigated in detail below. Thermal transfer from the film to the substrate is not taken into account, as it is considerable only before elimination of adhesion and therefore it does not influence the main regularities of the process.

3. FILM ABLATION WITHOUT MELTING BEFORE SEPARATION OF THE FILM FRAGMENT

Let us consider simultaneously two possible extreme cases of film ablation: when adhesion is eliminated only due to compression energy and only for some another reason, for instance due to substrate surface layer gasification. After adhesion elimination, the film compression energy is transformed to kinetic energy

$$Q = \frac{\rho V^2}{2} + Q_0 \quad (3)$$

Q_0 is energy of adhesion elimination per film volume unit (it is zero in the second case). One can define the velocity of fragment movement in the both cases for the 1st, 2nd and 3rd regimes, taking into account the dependence of the film temperature on laser intensity $T = \varepsilon/\rho ch$ (ρ is film density, c is film heat capacity). The results of calculation are given in Table 1.

Table 1. Velocity of film fragment movement without melting before separation.

Regime	I	II, III
Adhesion elimination due to compression energy	$V = \sqrt{\frac{E}{\rho} \frac{\alpha \varepsilon}{\rho ch}}$	$V = \sqrt{\frac{E}{\rho} \frac{\alpha \varepsilon}{\rho ch} \left(\sqrt{\frac{\rho}{E} \frac{8\rho ch^2 \varepsilon}{\alpha \varepsilon_0^2 \tau}} + 1 + 1 \right)}$
Compression energy is not spent for adhesion elimination	$V = \sqrt{\frac{E}{\rho} \frac{\alpha \varepsilon}{\rho ch} \sqrt{1 - \left(\frac{\varepsilon_0}{\varepsilon} \right)^2}}$	$\varepsilon = \frac{\tau \varepsilon_0 V}{2h} \left(\sqrt{\left(\sqrt{\frac{\rho}{E} \frac{\rho ch V}{\alpha \varepsilon_0}} \right)^2 + 1} - 1 \right)$

Calculated values of the threshold intensities separating the regimes are given in Table 2.

Table 2. Threshold intensities.

	Between the I and II regimes, ε_1	Between the III and IV regimes, ε_2
Adhesion elimination due to compression energy	$\varepsilon_1 = \varepsilon_0 + \frac{2h}{\tau} \sqrt{\frac{\rho}{E} \frac{\rho ch}{\alpha}}$	$\varepsilon_2 = \sqrt{\frac{E}{\rho} \frac{\tau \alpha T_m \varepsilon_0}{2h} \left(\frac{\rho ch T_m}{\varepsilon_0} - 1 \right)}$
Compression energy is not spent for adhesion elimination	$\frac{\varepsilon_1/\varepsilon_0}{(\varepsilon_1/\varepsilon_0 - 1)\sqrt{(\varepsilon_1/\varepsilon_0)^2 - 1}} = \frac{\tau}{2h} \sqrt{\frac{E}{\rho} \frac{\alpha \varepsilon_0}{\rho ch}}$	$\varepsilon_2 = \sqrt{\frac{E}{\rho} \frac{\tau \alpha T_m \varepsilon_0}{2h} \left[\sqrt{\left(\frac{\rho ch T_m}{\varepsilon_0} \right)^2 + 1} - 1 \right]}$

4. ABLATION OF THE MELTING FILM

The film fragment begins to melt during its movement before complete separation in the IV regime. Its velocity depending on laser intensity can be estimated by the following way. Let us look through the change of the film tension caused by film enlargement by its melting and by melt transfer by the action of compression tension. There will be considered the one-dimensional case (if irradiated zone at the film surface has a form of a long strip).

Let melting begins in one or several "hot points", forming one or several melting regions in the irradiated zone of the film. We shall consider, that the melted region has initially thickness h and half-width $l|_{t=0} = h$, and then width of the melted region increases by absorbing laser energy increasing. The work of the compression tension can be defined as following:

$$dA = 2\sigma h U dt \quad (4)$$

U is speed of movement of the melted region boundary by the action of compression tension σ . On the other hand, compression tension causes change of the kinetic energy in the melt. Neglecting of melt viscosity:

$$dA = d \left(\frac{2\rho h \bar{U}^2}{2} \right) \quad (5)$$

l is half-width of the melting region, $\sqrt{U_1^2}$ is squared mean of the melt speed at the melted region width. One can obtain it, considering melt speed be linear at the coordinate⁴: $\sqrt{U_1^2} = \sqrt{\frac{1}{l} \int_0^l U_1^2 dx} = \frac{U}{\sqrt{3}}$.

The following differential equation is obtained from (4) and (5):

$$l \frac{dU}{dt} = \frac{3\sigma}{\rho} \quad (6)$$

The half-width of the melt region l decreases due to melt transfer and increases due to melting of solid material, adjoining the melted region:

$$\frac{dl}{dt} = V_m - U \quad (7)$$

The initial conditions to equations (6), (7): $l = h$, $U = 0$ by $t = 0$. $V_m = \frac{L}{2n(\tau - t_H)} \gamma(\tau)$ is speed of the melt boundary transfer by melting without considering of melt transfer, L is the whole width of the irradiated zone of the film, $t_H = \frac{\varepsilon_H}{\varepsilon} \tau$ is the time of melting beginning, n is number of "hot points" at the distance L , $\gamma(t) = \gamma(\tau) \frac{t}{\tau - t_H} = \frac{\varepsilon}{\varepsilon_m - \varepsilon_H} \frac{t}{\tau}$ is ratio of mass of the melted part of the film to whole mass of the film in the irradiated zone at the moment t , which is calculated from melting beginning, $\varepsilon_H = \rho ch T_m$, $\varepsilon_m = \rho ch T_m + \rho h L_m$, L_m is specific melting heat.

The differential equation of change of the half-width of the melted region due to compression action $\Delta = \int_0^t U dt$ one can obtain, integrating the equation (7) and using (6). Value of Δ is connected with compression tension by correlation:

$$\sigma = E \left(\alpha T_m + \delta_L \gamma(t) - \frac{\Delta}{L} \right) \quad (8)$$

δ_L is specific linear enlargement of the material by its melting.

So, the differential equation for change of the compression tension σ is:

$$\sigma'' \left[\frac{\sigma}{E} - \left(\alpha T_m - \frac{h}{L} \right) - \frac{\varepsilon}{\varepsilon_m - \varepsilon_H} \left(\bar{\delta}_L - \frac{1}{2n} \right) \frac{t}{\tau} \right] = - \frac{3E}{\rho L^2} \sigma \quad (9)$$

The initial conditions: $t = 0$, $\sigma = E \alpha T_m$, $\sigma'_t = E \frac{\bar{\delta}_L}{\tau} \frac{\varepsilon}{\varepsilon_m - \varepsilon_H}$. As film melt stops after pulse finishing,

$$\bar{\delta}_L = \begin{cases} \delta_L & \text{by } t \leq \tau - t_H \\ 0 & \text{by } t > \tau - t_H \end{cases}. \text{ Velocity of film fragment movement is defined from the equation (9) as } V = \frac{\sigma(t=t_*)}{\sqrt{E\rho}}.$$

The film fragment velocity was defined from equation (9) by using a numerical method for 10^{-7} m W film irradiated by 10^{-7} s laser pulse. It was shown, that velocity of the film fragment considerably depends on the number of melting regions, i.e. on spatial distribution of laser intensity. Velocity of the film fragment V on laser intensity ε_1 ($\varepsilon_1 = \varepsilon/R$, R is film reflectivity for 193 nm excimer laser), calculated for W film ($h = 10^{-7}$ m) in all considered regimes is given in Fig. 1. The obtained results are in a good agreement with known experimental data³.

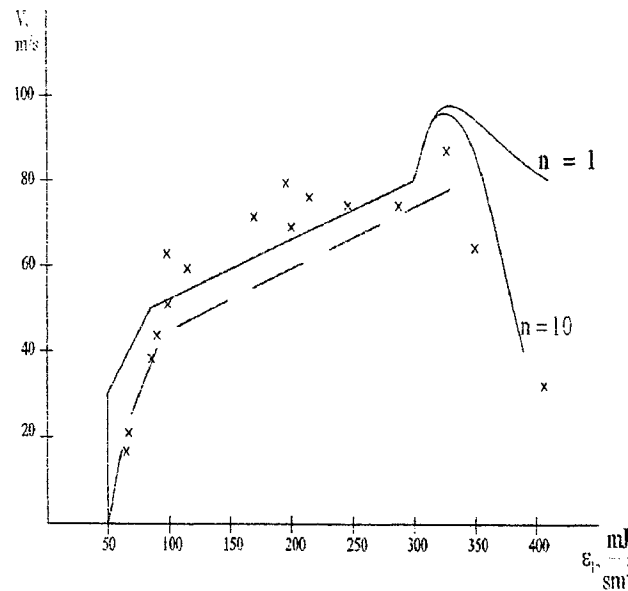


Fig. 1. The dependence of velocity of fragment of W film ($h = 10^{-7}$ m, $\tau = 10^{-8}$ s) on laser intensity

----- elimination of adhesion occurs due to compression energy,

——— elimination of adhesion occurs due to other factors

x experimental data³.

5. FILM DEGRADATION

The considered conception of before-threshold ablation of the film under the action of thermal tension can be used for explanation of the phenomenon of film degradation, i.e. film destruction under the action of many laser pulses, each of them possesses intensity many times less than ablation threshold intensity. Density of compression energy to volume is given by (2). Threshold intensity value ϵ_0 defines the density of compression energy, by which adhesion eliminates in the whole irradiated zone:

$$Q_0 = \frac{E}{2} \left(\frac{\alpha \epsilon_0}{\rho c h} \right)^2 \quad (10)$$

By the action of a series of N pulses, with intensity each of them $\epsilon < \epsilon_0$, the partial adhesion change occurs, it is proportional to $Q(\epsilon)$. In the intervals between the pulses its value decreases due to relaxation. So, adhesion decreases from pulse to pulse, until film ablates after some N -th pulse:

$$Q_0 = N \frac{E}{2} \left(\frac{\alpha \epsilon}{\rho c h} \right)^2 - \frac{q}{h} (N-1) \quad (11)$$

q is relaxation energy per surface unit. One can obtain the dependence of the number of pulses, that is necessary for ablation, on intensity of a single pulse, equating (10) and (11):

$$N = \frac{\epsilon_0^2 - \epsilon_*^2}{\epsilon^2 - \epsilon_*^2} \quad (12)$$

$\epsilon_* = \sqrt{\frac{2qh}{E} \frac{\rho c}{\alpha}}$ is some value, connected with relaxation.

The dependence (12) is in a good agreement with known experimental data. The calculated curve, in which value of ε_* is taken from experimental data⁵, are shown in Fig. 2. The dependence of ε_* on film thickness h also is confirmed: experimental data for Cr films, which thicknesses are $h_1 = 210$ nm and $h_2 = 105$ nm, give value $\varepsilon_*(h_1)/\varepsilon_*(h_2) = 1.6$. The calculated value is $\varepsilon_*(h_1)/\varepsilon_*(h_2) = 1.4$.

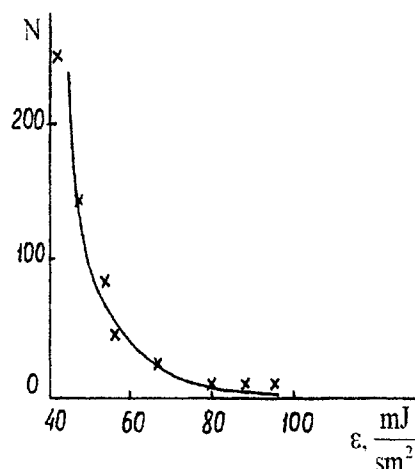


Fig. 2. The dependence of the number of pulses, that is necessary for film ablation in multipulse regime, on intensity of a single pulse.

x experimental data⁵.

6. CONCLUSIONS

The suggested conception of laser ablation of thin films in solid or liquid phase under the action of thermal tension let explain the peculiarities of film ablation in before-evaporation regimes and prognosticate the kinetic parameters of erosion products, defining the conditions of their condensation in the regime of film transfer. The suggested conception of film ablation is used for explanation of the phenomenon of film degradation and let prognosticate the radiation-resistive properties of film covers.

7. ACKNOWLEDGEMENTS

The autor would be like to thank V.P.Veiko and E.B.Jakovlev for useful discussions.

8. REFERENCES

1. V.P.Veiko, S.M.Metev. Laser-assisted microtechnology. Springer-Verlag, Heidelberg, 1994 (first edition), 1998 (second edition).
2. V.P.Veiko, E.A.Shakhno. Laser induced ablation and condensation on to the close-to-target substrate. Proceedings SPIE, v.3093, 1997, p.276-287.
3. Z.Tóth, B.Hopp, Z.Kántor, F.Ignácz, T.Szőrényi, Z.Bor. Dynamics of excimer laser ablation of thin tungsten films as followed by ultrafast photogtaphy. Appl. Phys., v.A 60, 1995, p.431-436.
4. V.P.Veiko, A.I.Kaidanov, E.A.Tutchkova, E.B.Jakovlev. Melt transfer by laser evaporation of metal films. Electronic treatment of materials (Russia), N3, 1983, p.18-21 (in Russian).
5. Z.Tóth. Private information.

Model of laser-induced ablation of solids

Yu.A.Chivel, L.Ya.Min'ko,

Institute of Molecular and Atomic Physics NAS Belarus

70, F.Skaryna av., 22072, Minsk, Belarus

ABSTRACT

The results of a complex study of the ablation of metals when they are acted on by radiation pulses 40-300 ns wide from neodimium laser are presented. Low-thresholds surface ablation has been detected in a number of metals at surface temperatures below the boiling point, before the instant plasma formation, with a burst of particles of the condensed disperse phase and the formation of microstructures with a characteristics size of 1-10 μ m. A description is given of the laser-induced ablation model, based on the purely thermal action of laser radiation and the natural inhomogeneity of solids.

Keywords: Laser ablation, low-threshold, metastable state, pore, particle release.

1. INTRODUCTION

High power pulsed laser ablation has attracted attention in recent time because many types of technological processes are based on laser ablation. Under laser ablation in parallel with material vapour moving from surface the generation of particles of condensed disperse phase takes place. The nano and micron size particles are observed on the early stage of laser-target interaction under the action both high intensity short pulses [1,2] and quasi-continious pulses [3]. The primary mechanism of particles generation is not elucidate. At the present time some mechanisms of particles release are discussed and most of them associate with initiation and break-up of metastable states [4].

Process of high intensive evaporation of solids in noncritical region is certainly accompanied by the occurrence of super heated metastable states. The super heating are caused by recoil pressure lowering relative to saturated vapour pressure under surface temperature and also with the occurrence of temperature maximum in surface region of condensed matter. The magnitude of this maximum depends on the relation between the absorption depth and length of heat effect [5]. For strongly absorbing solids, metals for example, the subsurface maximum temperature is little and metastable state not manifests itself up to $T \sim 0,85 T_{ic}$ [6]. Under the volume absorption of laser radiation the subsurface overheating may be as much as several hundred degree with the metastable state lifetime of hundred nanoseconds [7]. In this case probability of phase explosion significantly increases. Under the surface evaporation the subsurface volume explosion-like phase transition may be occurs on geterogeneous center of boiling. As a heterogeneous centers the structure defects (vacancies, pores etc.), phase inclusions may offer.

In paper [8] the critical analysis of basic thermal mechanisms of particles release was carried out. The conclusion was made that explosion boiling due to homogeneous nucleation when superheating occurs and the surface temperature reaches the region of critical point remains a major mechanism of particulate release at high fluence.

At the same time experimental results of many investigators point of the fact that particle release at the early stage of exposure are recorded at moderate intensity of LR ($\sim 10^6$ - 10^7 W/cm²), even under the action of quasi-continious laser pulses [3]. Furthermore the critical temperatures of most metals under investigation exceed the plasma formation thresholds and frequently compare will ionization potential of metal.

In papers [9,10] on laser action on metals the low-threshold ablation was discovered. The low-threshold ablation may occurs when at the moment of surface destruction the surface temperatures are below boiling point or sublimation point before the moment of plasma formation. It was established the destruction of materials is substantially determined by structural inhomogeneities of solids, generation and structural relaxation of different heterogeneities (pores, vacancies, gas and other inclusions) and due to exclusively thermal action of LR. In article [11] the similar low-energy laser ablation of high-temperature superconductors from solid state is observed, brought on by thermodecomposition of ceramic, gas release and cracks evolution. As shown in paper [12], under intense laser action on solids the defect formation process takes place. Concentration of defect (vacancies clusters, nanopores with diameter $\sim 200\text{\AA}$ run to $10^{19} - 10^{20}\text{cm}^{-3}$). For melted layers the

rapid solidification makes it possible to capture of high concentrations of vacancies, interstitials, pores. By this means, under the intensive action, structural defects not only vanish through the explosion, but occur.

2. EXPERIMENTAL

The investigations were carried in the atmospheric pressure and vacuum $P \sim 10^{-2}$ Torr. We used a neodymium Q-switched laser, generating monopulses of duration ~ 40 ns and 300 ns. The flat targets from aluminium A99, duralumin D16T, zinc, bismuth were used. The control over the surface state under the LR-action carried by measurements dynamic characteristics of the mirror, diffusion, scattering components of reflected LR, surface temperature and the pressure on the surface within the irradiation spot. The surface state before and after the action was studied by means of optical and scanning electron microscope, an X-rays analysis of the target surface was performed. Also the measurements of recoil pulse under the control of surface temperature in preplasma regimes were performed. We used the pendulum method and target with diameter ~ 4.5 mm at irradiative spot diameter ~ 4 mm.

Studies on surface morphology and defect distributions showed that a main defects with density $\sim 10^6 - 10^7 \text{ cm}^{-2}$ are the scratches and species of abrasive, implanting in a surface. The height of relief irregularities $\sim 0.1 - 1 \mu\text{m}$ with period $\sim 10 \mu\text{m}$. Experiments in evaporation regimes was shown that local character of the surface damage is basically determined by nonuniform of LR power distribution rather than defect distribution. This is due to the fact that the defect density is sufficiently large. It was found that the surface temperature run as high as 3000–4000 K (fig.1) up to moment of plasma ignition in the wide range of laser pulse duration ($\tau_{1/2} = 40$ ns–1 ms). The build-up of LR absorption in vapours starts under such temperature level. The transfer of practically transparent

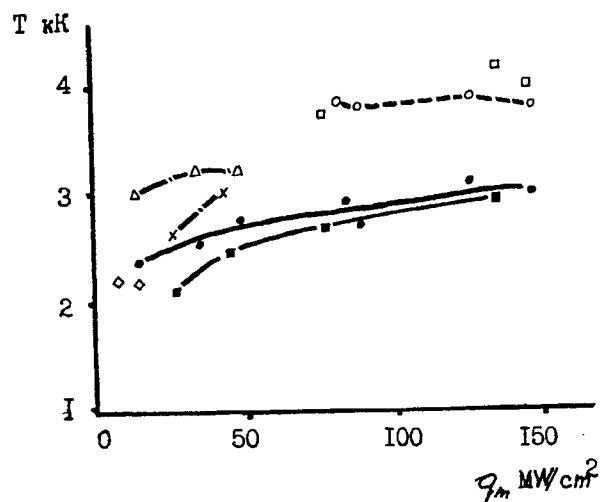


Fig.1. Target surface temperature at the moment of a sharp decrease in the mirror component of reflected LR (•- D16T, ■-Zn, ◇-Bi), maximum surface temperature (◐-D16T, x-Zn), surface temperature at the moment of plasma formation (O-D16T, -Zn) versus maximum LR power density.



Fig. 2. Irradiation spot on the copper surface. ($q_m = 100 \text{ MW/cm}^2$).

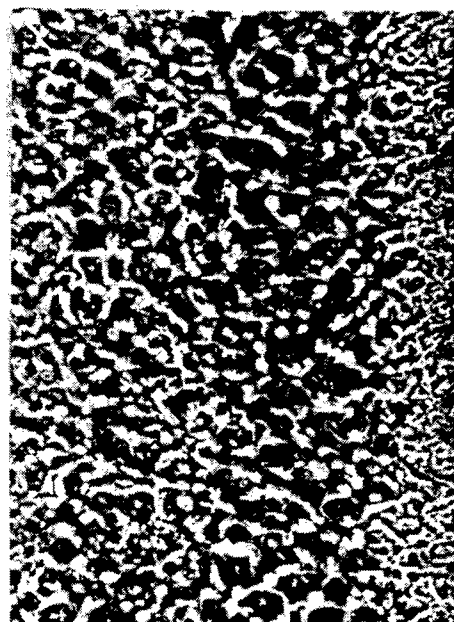


Fig. 3. The structure in laser affected spot on zinc surface ($q_m = 40 \text{ MW/cm}^2$).

vapour to highly absorbing plasma takes place in a time $\sim 10^{-8}$ s ($\tau = 40$ ns) and $\sim 10^{-7}$ s ($\tau = 300$ ns) versus slope of the leading pulse edge.

The particle and desorbed gas release from surface and subsurface are correlated with the emergence of recoil pulse measuring $J \sim 10^6$ N·s at laser pulse duration $\tau \sim 40$ ns. This value agrees well with pulse surface pressure $P \sim 0,5-1,0$ MPa at pulse pressure duration $\tau_{1/2} \sim 40$ ns. The calculated contribution of surface adsorbed gases to recoil is less than 0,1 MPa.

Previously [9] we have set the explosion like destruction of a metal surface in times $\sim 10^{-8}$ s under the action of a pulsed laser before the plasma ignition with the appearance of microparticles and microdefects on the surface with the size $\sim 1-10 \mu\text{m}$ (fig.2). For some materials it takes place at surface temperature below of the boiling point in the temperature range above ~ 2000 K (Fig.1). Only for Zn, the experiments show, the homogeneous volume boiling is probably realized (fig.3). The model of initial destruction of materials under the action of pulsed LR was developed. The destruction was demonstrated to can results from solid state when the porous gas pressure exceed the damage threshold of material and from melted state.

3. MODEL

Consider thermal and hydrodynamic processes in near-surface layer of melted metals on exposure to pulsed ($\tau = 10^{-8} - 10^{-6}$ s) heating by LR ensemble of pores $0,02-1 \mu\text{m}$ in diameter, gas filling of which occur due to the desorption of gas layers, covering the porous wall. The model involves Rayleigh equation, which connect the gas pressure changes with bubble diameter, and the energy equation for gas in bubble.

For materials with melt temperature $T_{\text{melt}} > 2000$ K the pore structure explosion and particle release is quite possible in solid state. Under the laser-heating a subsurface layer of metal $\sim 1 \mu\text{m}$ thick thermostresses is progressing. For example setting at thermal expansion coefficient of aluminium $\sim 2,5 \cdot 10^{-5} \text{K}^{-1}$, we obtain on heating in irradiated spot to $T \sim 10^2$ degree a thermostresses $\sigma = ((\alpha \cdot E)/2(1-\mu)) \Delta T = 10^8 \text{N} \cdot \text{m}^{-2}$. This value exceeds yielding limit for Al. Such stresses are hardly probable through ductility, but it can produce defect formation (pores, cracks). Furthermore, under the gas desorption in pores over the area $\sim 10^3$ K, or heating to such temperature the product of substance decomposition the pressure in pores run to $P \sim 10^7$ Pa and above. For near-surface pore with diameter $\sim 1 \mu\text{m}$ the stresses in thin metal shell ($\delta \ll 1 \mu\text{m}$) may be written as [13] $\sigma_{\pi} = P/2$; $\sigma_{\gamma} = P \cdot R/2$, where R – pore radius. When $P \sim 10^7 - 10^8$ Pa, the stresses run to values $10^7 - 10^8 \text{N} \cdot \text{m}^{-2}$, close to damage thresholds of metals if we take in account of their temperature dependens $\sigma = (1 - T/T_{\text{melt}})$.

On pulsed heating of the easy melt metals ($T_{\text{melt}} < 2000$ K) the dynamics of bubble with desorbed gases in the melt layer of metal is considered.

The basis for description is Rayleigh equation, which connect the gas pressure changes with bubble diameter, and the energy equation for gas:

$$R \cdot \frac{d^2 R}{dt^2} + \frac{3}{2} \left[\frac{dR}{dt} \right]^2 + \frac{4\nu}{3R} \cdot \frac{dR}{dt} = \frac{1}{\rho} \cdot \left[P - \frac{2\sigma}{R} \right]; \quad (1)$$

$$\frac{dP}{dt} + \frac{3 \cdot \gamma \cdot P}{R} \cdot \frac{dR}{dt} = \frac{3(\gamma-1)}{R} \cdot \left[\lambda \cdot \frac{\partial T}{\partial r} \right]_{r=R}; \quad (2)$$

Where R – bubble radius, P – gas pressure, ν – kinematic viscosity, ρ – melt metal density, λ – gas thermal conductivity, γ – specific heat ratio, T – gas temperature. Value $q = \lambda (\partial T / \partial r)$ – density of heat transfer to bubble. From physical consideration, it is clear, that q is formed purely by gas thermoresistance.

Detailed analysis of bubble temperature field in stationary boundary approximation was performed. Considering linear law of liquid temperature rise $T_1 = B \cdot t + T_0$ the relation for bubble gas temperature may be written [14].

$$T = B \cdot \left[t - \frac{R^2 - r^2}{6 \cdot a} \right] - \left[2 \cdot B \cdot \frac{R^3}{a \cdot \pi^3 \cdot r} \right] \cdot \sum_{n=1}^{\infty} \frac{(-1)^n}{n^3} \cdot \exp \left[-a \cdot n^2 \cdot \pi^2 \cdot \frac{t}{R^2} \right] \cdot \sin \pi \cdot n \cdot \frac{r}{R} \quad (3)$$

where a – temperature conductivity, equal for H_2 and N_2 at $P \sim 2 \cdot 10^7$ Pa and $T \sim 10^3$ K the value $0,375 \cdot 10^4 \text{m}^2/\text{s}$, $0,007 \cdot 10^4 \text{m}^2/\text{s}$ accordingly.

Differentiate the expression (3) we obtain

$$\left[\frac{\partial T}{\partial r} \right]_{r=R} = \frac{2 \cdot B \cdot R}{6 \cdot a} \cdot \left[1 - \frac{6}{\pi^2} \cdot \sum_{n=1}^{\infty} \frac{1}{n^2} \cdot \exp \left(-a \cdot \pi^2 \cdot \frac{t \cdot n^2}{R^2} \right) \right] \quad (4)$$

For bubble diameter $\sim 1 \mu\text{m}$ and $t=10^{-8} - 10^{-4}$ s the second member in (4) $\ll 1$. For the density of heat transfer we obtain

$$q = \frac{2 \cdot \lambda \cdot B \cdot R}{6 \cdot a}; \quad (5)$$

As a result the system of equations of bubble dynamic takes the form

$$R \cdot \frac{d^2 R}{dt^2} + \frac{3}{2} \left(\frac{dR}{dt} \right)^2 + \frac{4 \cdot v}{3 \cdot R} \left(\frac{dR}{dt} \right) = \frac{1}{\rho} \left(P - \frac{2\sigma}{R} \right); \quad (6)$$

$$\frac{dP}{dt} + \frac{3\gamma \cdot P}{R} \cdot \frac{dR}{dt} = (\gamma - 1) \cdot C_v \rho_1 B; \quad (7)$$

where ρ_1 – density of deretained gas, equal:

$$\rho_1 = \left(\frac{3A \cdot m}{R_0} \right) \cdot \left(\frac{R_0}{R} \right)^3; \quad (8)$$

m – gas molecule mass, R_0 – initial bubble radius.

The equation system (7) - (8) was solved numerically under initial condition:

$$R(0) = R_0; \quad \left(\frac{dR}{dt} \right)_{t=0} = 0; \quad P(0) = \frac{3(\gamma - 1)C_v \cdot A \cdot m \cdot T_0}{R_0}; \quad (9)$$

$$\left(\frac{dP}{dt} \right)_{t=0} = \frac{3(\gamma - 1)C_v \cdot A \cdot m \cdot B}{R_0}$$

Incorporate in the calculations a temperature dependence of viscosity and surface tension $\sigma \sim \sigma_0 \cdot (1 - T/T_k)^{4/3}$ and $v = v_0 \cdot (1 - \exp E/RT)$; take into account.

4. RESULTS AND DISCUSSION

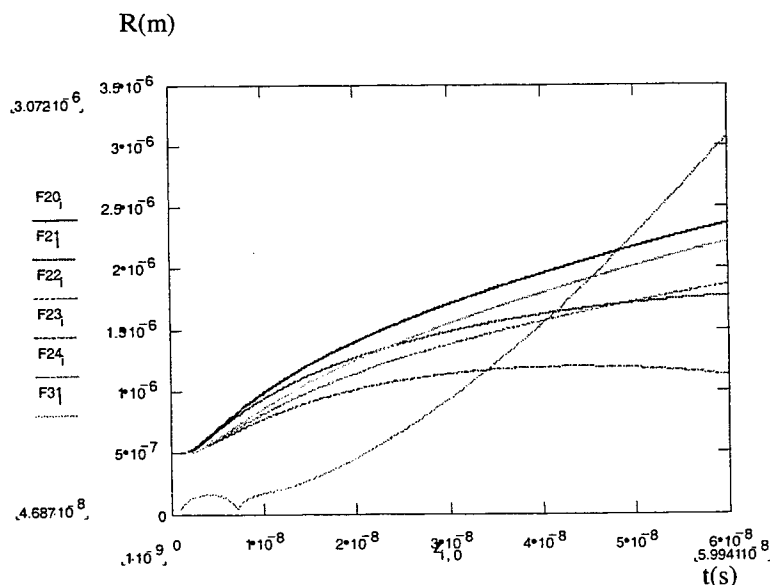


Fig.4. Dynamics of gas bubble in melt layer.

Material: Al, gas H_2 , $R_0 = 5 \cdot 10^{-7} \text{m}$ (1-5), $R_0 = 0.5 \cdot 10^{-7} \text{m}$ (6), $T_0 = 2000 \text{K}$ (1-4, 6), $T_0 = 1000 \text{K}$ (5)

Results of numerical calculations presented at (fig.4) for submicron and micron size pores. The tolerant rise of bubble diameter to value with exceed the melt layer thickness is observed during the length of laser pulse leading edge. The running processes have weak dependence on the sort of gas, because the gas parameters enter into equation in combination $C_v \cdot m$. The surface layer destruction brings into particle release, existance the surface irregularities in the form of microcraters, microparticles with the size $\sim 1 \mu\text{m}$. The calculations of recoil pulse when the particles release from surface are performed. Surface density of pores was taken to be equal $L = 10^6 - 10^7 \text{cm}^{-2}$. Velocity of particles is estimated according the relation $P \cdot V = m \cdot v^2 / 2 + \sigma \cdot S$ where V – bubble volume, S – bubble surface. At pressure $P \sim 10^6 - 10^7 \text{Pa}$ the velocity is found $30 - 200 \text{m} \cdot \text{s}^{-1}$, that agrees well with the results of experimental and

- | | |
|--------------|---|
| 1. _____ | $A=10^{20} \text{ m}^{-2}, B=10^{11} \text{ K/c}$ |
| 2. | $A=10^{20} \text{ m}^{-2}, B=10^{10} \text{ K/c}$ |
| 3. - - - - - | $A=5 \cdot 10^{19} \text{ m}^{-2}, B=10^{11} \text{ K/c}$ |
| 4. - - - - - | $A=5 \cdot 10^{19} \text{ m}^{-2}, B=10^{10} \text{ K/c}$ |
| 5. _____ | $A=10^{20} \text{ m}^{-2}, B=10^{11} \text{ K/c}$ |
| 6. - - - - - | $A=10^{20} \text{ m}^{-2}, B=10^{10} \text{ K/c}$ |

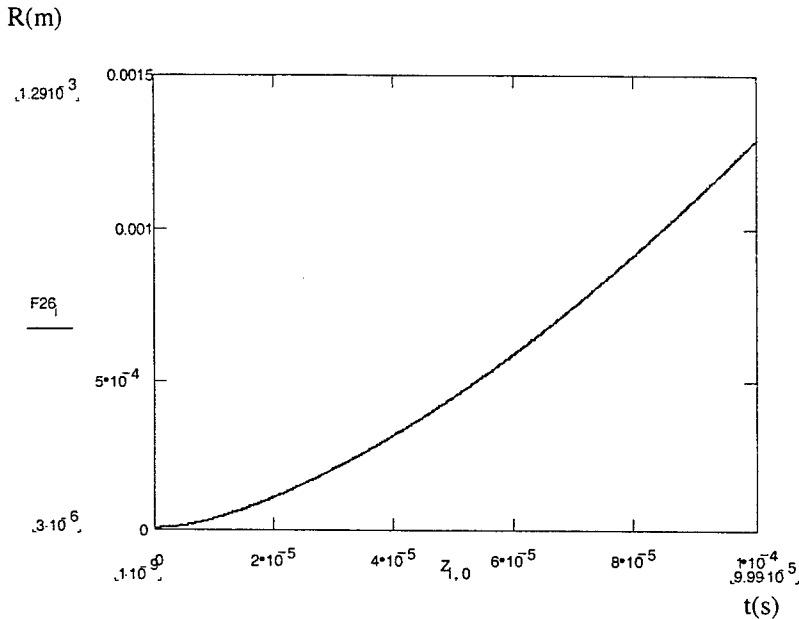


Fig.5. Dynamics of gas bubble in melt layer.

Material: Al, gas H_2 , $R_0=3 \cdot 10^{-6} \text{ m}$
 $A=10^{20} \text{ m}^{-2}, B=2 \cdot 10^7 \text{ K/c}$

diffusion equation for wall of finite thickness L the expression for diffusion time can be obtained $t_0 = L^2 / 6D$.

Diffusion coefficient D in solid metals and melt metals for H_2 and N_2 at 1000-2000K is no more than $10^{-5} \text{ cm}^2 \text{ s}^{-1}$, $10^{-4} \text{ cm}^2 \text{ s}^{-1}$ accordingly. For $L \sim 1 \mu\text{m}$ we obtained $t_{0s} \sim 2 \cdot 10^{-4} \text{ s}$ and $t_{0\text{melt}} \sim 2 \cdot 10^{-5} \text{ s}$. At shorter time the diffusion is negligible.

5. CONCLUSION

The summarize, experiments and numerical simulation of thermophysical and hydrogasdynamic processes in subsurface layer of metals, irradiated by pulsed laser allowed to expose low-threshold character of initial destruction of materials, to establish mechanism responsible for explosive type laser ablation and particles release.

theoretical works [11]. For recoil pulse on square meter $J = m \cdot v \cdot L$ the value was obtained $J \sim 10^{-3} - 10^{-2} \text{ N} \cdot \text{s} \cdot \text{m}^{-2}$, resulting in a surface pressure $P \sim 0,1 - 0,5 \text{ MPa}$, that correlate with experimental results.

In recent time we conduct experiments in circumstances where target is surrounded by high pressure gas [15].

Quasi-continuous laser radiation ($t \sim 10^{-3} \text{ s}$) with power density $2-6 \text{ MW/cm}^2$ exposed the D16T and Zn target in high pressure camera. As the pressure of N_2 increases up to $1,0 - 1,5 \text{ MPa}$ the particles release is missed. The results of numerical calculation according the model in the range of $t = 10^{-4} \text{ s}$ are presented in Fig.5. Pressure in pores has a value $1,0 - 3,0 \text{ MPa}$. The ambient gas pressure like that suppresses the particle release.

Let us consider the factors which to limit the usefulness of this model. The major factor – gas diffusion through the wall of the pores or bubble. From the solution of nonstationary

6. REFERENCES

1. F.P.Gagliano, U.C.Paek, *Appl.Opt.* **13**, pp.274, 1974.
2. L.Ya.Min'ko, Yu.Chivel, *Proc XXI Int. Conf. on Phenomena in Ionized Gases* **1**, pp. 135-136
3. V.K.Goncharov, V.I.Karaban, *Zhurnal Prikladnoi Spektroskopii* **45** 22 (1986)
4. V.P.Skripov, *Metastable Liquids*. Nauka Moscow, 1972
5. S.I.Anisimov, Ya.A.Imas, G.S.Romanov, Yu.V.Hodyko, *High Intensity radiation action on metals*, Nauka Moscow 1970
6. A.A.Samokhin, *Short communication in physics*, FIAN, **4**, pp. 7-10, 1973
7. V.I.Mazhukin, I.V.Gusev, A.V.Shapranov, *Math Modeling* **5**, pp. 30-60, 1993
8. A.Miotello, R.Kelly, *Appl. Phys. Lett* **67**, pp. 3535-3537, 1995
9. L.Ya.Min'ko, Yu.Chivel, *Journal de physique* **4**, pp.175-178, 1994.
10. L.Y.Min'ko, Yu.Chivel, *Izvestia RAS*, **61**, pp.1431-1436, 1997.
11. E.N.Sobol, M.S.Kitai, S.M.Golberg, A.N.Zherikhin, *Appl.Surf.Sci*, **90**, p.235, 1995.
12. V.I.Emel'yanov. *Laser Physics* **2**, pp..389-420, 1992.
13. L.D.Landau, E.M.Lifchitc, *Theory of elasticity*, pp.3-31, Fizmatizdat, M, 1964.
14. A.Karslow, D.Eger."Heat transfer in solids", pp.478, M, 1964.
15. L.Ya.Min'ko, Yu.Chivel, V.I/Nasonov, *Proc.XXIV ICPIG* **2**,pp.91-92, 1999.

Some electromagnetic aspects of high-power laser interaction with transparent solids

Vitali E. Gruzdev*, Mikhail N. Libenson

State Research Center «S.I. Vavilov State Optical Institute»

Birzhevaya Liniya 12, St. Petersburg, 199034, Russia

ABSTRACT

There are considered two effects of nonlinear light propagation that can play important role in initiating of laser-induced damage of transparent materials: self-induced variations of light polarization of focused laser beam and developing of field instability in non-absorbing microinclusions. The effect of self-induced variations of light polarization is considered qualitatively for focused laser beam with arbitrary focal spot. Detailed numerical study of the effect is fulfilled for Gaussian beams of low order. It is shown that any initial light polarization turns into elliptic one with inhomogeneous distribution of polarization-ellips parameters. Developing of field instability in transparent microinclusions is other considered nonlinear effect. It is shown that transparent microinclusion can initiate local field increase accompanied by positive feedback resulting in further field increasing near the inclusion. If the electric field strength exceeds damage threshold during nonlinear evolution in the inclusion then developing of field instability results in damage of microinclusion before electric field reaches certain upper level determined by ionization processes.

Key words: laser-induced damage, transparent materials, nonlinear self-action, field instability, transparent microinclusions

1. INTRODUCTION

Laser-induced damage (LID) of transparent materials presents one of the most actual problems of laser physics, engineering and technology. Its actuality is connected with that LID threshold of optical elements of high-power and high-energy laser systems limits maximum output power or energy of laser pulse. On the other hand, LID threshold determines minimum power or energy of laser pulse required for material processing.

In spite of great success achieved in theoretical and experimental investigation of LID, there are some experimental data [1-4] that has not got adequate explanation and description in the framework of widely accepted thermal model of damage initiating in transparent solids. They cannot be also considered from the viewpoint of influence of self-focusing on field distribution near focal area because self-focusing is excluded by low power of laser radiation and tight focusing [1-4]. Interesting point is that all the mentioned experimental facts are connected with LID study under conditions of strong concentration of laser energy in space (resulting from tight focusing when focal spot size is about few laser wavelengths) and in time (using of femtosecond pulses). According to that, those experimental data can be divided into two partially covering groups: the first of them includes facts connected with LID by nano- and pico-second pulses under conditions of tight focusing, the second group includes facts related to study of LID induced by femtosecond pulses. In both cases there is important feature – LID threshold is about $10^{13} - 10^{14} \text{ W/cm}^2$. That means that laser-induced variations of refractive index are about 0.05 – 0.001 for the most transparent solids [1-4]. Thus, specific conditions of laser action in both cases turn nonlinear electrodynamical effects into important factor of damage initiating because they can take place at high level of nonlinear distortions of refractive index.

Present paper is devoted to consideration of two nonlinear optical effects that can be of great importance for analysis of experimental data of the first group – self-induced variation of light polarization in focal area of tightly focused laser beam and field instability in low-absorbing microinclusion. Importance of those effects is connected with two points. First, they show possible significant variations of value of acting electric field and light polarization in focal area of tightly focused laser beam as compared to linear propagation regime even in case of self-focusing absence. Second, those effects show clearly possible important role of non-thermal effects in initiating of early stage of LID connected with laser-induced ionization and nonlinear absorption.

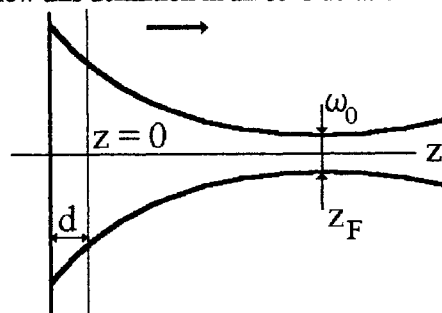
* Phone: (81272) 246-22, Fax (81272) 208-43, E-mail: gru@mailbox.alkor.ru

2. LASER-INDUCED VARIATIONS OF LIGHT POLARIZATION

Light polarization is well known to influence on self-focusing and laser-induced damage threshold [5], rate of multiphoton ionization and other processes of laser-matter interaction [6]. Thus, determining and controlling of polarization of laser beam is of great importance for correct interpretation of experimental data. Experimental and theoretical results show that polarization can change in case of high-power plane wave (self-induced rotation of polarization ellipse [7]) and in case of low-power laser beam propagating in inhomogeneous medium [8-10]. The natural question is what happens to light polarization of tightly focused high-power laser beam propagating in homogeneous isotropic dielectric. In the latter case one should expect variations of light polarization even in homogeneous isotropic transparent medium because laser radiation induces local variations of refraction, and the higher beam power, the more those variations and the larger their gradients. Those laser-induced inhomogeneities of refraction can be considered as locations scattering light. Important difference between this case and linear scattering in inhomogeneous medium is that size and space distribution of laser-induced refraction inhomogeneities are adjusted to space distribution of beam's electric field. Thus, nonlinear laser-induced variations of polarization can be expected to be more effective than that for low-fluence laser beam propagating in inhomogeneous locally isotropic media. As compared with our previous papers [11, 12], we present here brief description of approach and results.

Throughout this paper we consider propagation of laser beam in isotropic homogeneous dielectric. All frequencies of spectrum of laser beam are assumed to be far from any absorption band of the dielectric. Let the beam propagate along z -axis, which is symmetry axis of the beam while x - and y -axes are in transverse plane. Coordinates x and y are in transverse plane (Fig. 1.). Light polarization (i.e., parameters of polarization ellipse) is determined by ratio of two transverse projections of electric-field strength vector E_x/E_y [13]. We follow this definition in all considerations below.

Fig. 1. Geometry of the problem. Input plane is inside dielectric medium at distance d from input surface of the medium (reason for that is considered in the text). Z_F is distance between input and focal planes. ω_0 is beam waist radius (or focal spot radius). Coordinate axes Ox and Oy are in the plane $z=0$. The arrow shows direction of beam propagation.



Sufficient feature of high-power laser beam is that its field can induce variations of refractive index. Dielectric response of considered medium to action of laser-beam electric field includes nonlinear term proportional to the third order of electric field and is described as usually [14]. We assume linear and nonlinear response to be local and do not take into account their dispersion. That is quite correct for quasi-monochromatic beam of moderate power when self-phase modulation does not broaden radiation spectrum much, and generation of higher harmonics can be neglected. We do not consider resonant laser-induced processes (like stimulated scattering or multiphoton absorption) and neglect absorption. Thus, polarization effect under consideration results from pure self-action of laser beam.

In case of quasi-monochromatic approximation (long pulses or continuous radiation) time variation of electric-field strength takes the form $\exp\{-i\omega t\}$. Then space distribution of beam electric field is described by the following equation in the framework of this model [15]:

$$\Delta \vec{E} + k^2 \vec{E} = -\frac{4\pi k^2}{\epsilon_0} \vec{P}_{NL} - \frac{4\pi}{\epsilon_0} \text{grad div} \vec{P}_{NL}, \quad (1)$$

where Δ - is Laplacian second-order differentiation operator, ϵ_0 - is linear constant part of dielectric function. Bearing in mind symmetry properties of nonlinear susceptibility tensor [14], one can deduce the following dependence of nonlinear material response on electric field:

$$\vec{P}_{NL} = \alpha |\vec{E}|^2 \vec{E} + \beta \vec{E}^2 \vec{E}^*, \quad (2)$$

where \vec{E}^* denotes complex conjugated. Coefficients α and β are proportional to nonlinear-susceptibility tensor components and connected with linear n_0 and nonlinear n_2 parts of refractive index [11, 12] in esu units.

In the most studies theoretical description of nonlinear optical phenomena is based on analysis of equations with cubic nonlinear term that is the first right-hand term of equation (1). The second right-hand term in equation (1), to be referred to as gradient nonlinear term throughout this paper, is usually neglected. Cubic nonlinear term describes mutual influence of electric-field projections through their absolute values resulting, in particular, in laser-induced birefringence. Gradient nonlinear term describes mutual influence of the projections through their gradients resulting, in particular, in self-induced variations of polarization in isotropic dielectric. Taking into account only cubic nonlinear term in (1) does not allow correct describing self-induced variations of initial polarization [11, 12]. Thus, presented in this work theoretical analysis of one of nonlinear polarization effects is based on accounting for gradient nonlinear term in (1).

For further analysis one should attach boundary and radiation conditions to obtain its unambiguous solution. Considering the problem in half space $z > 0$ inside the dielectric material (Fig. 1), one can set boundary conditions for all the three projections of electric field if there are given space distributions of transverse projections of electric (E_x and E_y) and magnetic (H_x and H_y) fields at $z=0$ as it was done in [11, 12]. We use linear radiation conditions for setting nonlinear problem and we assume that to be correct for focused laser beam because of the following reason [11, 12]. Nonlinear interaction is concentrated in focal area while tightly-focused laser beam diverges fast and its intensity becomes small enough far from focus to neglect laser-induced variations of refraction at large distances from focal plane. This automatically implies that our consideration must be applied to laser intensity and power below self-focusing threshold. Thus, approximation of weakly nonlinear medium allows to use linear boundary and radiation conditions for setting mathematical problem.

Parameters of polarization ellipse can be calculated from ratio of two transverse projections of electric field [13]. Thus, further analysis is based on asymptotical expansion of exact solutions to (1) with respect to small parameters and calculating the ratio of transverse electric-field projections with bearing in mind perturbation terms of required accuracy. To analyze some properties of solution to (1), we apply perturbation technique and use asymptotical expansions with respect to small "amplitude" parameter

$$q = \frac{n_2}{n_0} \cdot \max |E|^2 \ll 1 \quad (3)$$

and small "diffraction" parameter

$$\frac{1}{p} = \frac{1}{k\varpi_0} \ll 1, \quad (4)$$

where ϖ_0 – is beam waist radius, and refractive index is represented in the form $n = n_0 + n_2 E^2$.

For parameter q to be small, amplitude of electric field must not exceed certain threshold. As it was mentioned, the most natural threshold is that of self-focusing. In case of focal spots with radius about 15 radiation wavelengths or less, self-focusing occurs at input intensity about $I_{SF} \geq 10^{12}$ W/cm² in fused silica and glasses [5]. Thus, considering laser-pulse intensity to be below self-focusing threshold in those isotropic materials, one should put $q \leq 0.0001$. As it was mentioned above, applied approximation is valid only in case of self-focusing absence what implies that power of laser beam P must be below critical power P_{cr} of self-focusing: $P/P_{cr} < 1$. Expressing beam power through laser intensity I and focal spot size as $P = I\pi\varpi_0^2$ and using standard expression for critical power $P_{cr} = c\lambda^2/(32\pi^2 n_2)$ [5], one obtains the following relation:

$$\frac{P}{P_{cr}} = qp^2 < 1, \quad (5)$$

which gives limitation for value of parameter p : $p < 1/\sqrt{q}$. In particular, $p < 100$ for $q < 0.0001$. According to (4) beam focal spot radius must not exceed approximately 15λ . Relation (5) implies also that $qp < 1$. For example, one obtains $qp = 0.01 \ll 1$ for mentioned above values of p and q , and the solution can be presented in the form of asymptotical expansions with respect to small perturbation parameters.

First, we apply expansion with respect to "amplitude parameter" q of the following type:

$$E_j(x, y, z) = e^{ikz} \sum_{m=0} q^m E_{jm}(x, y, z) = e^{ikz} (E_{j0} + qE_{j1} + \dots), \quad (6)$$

where $j=x, y, z$ – denotes number of projection. The first term of (6) satisfies the following linear equation:

$$\Delta E_{j0} + k^2 E_{j0} = 0 \quad (7)$$

to which linear boundary conditions are attached [11, 12]. To describe nonlinear depolarization effect one should take into account the first nonlinear approximation $m=1$ that satisfies the following equations for quasi-monochromatic waves

$$\begin{aligned} \Delta E_{x1} + k^2 E_{x1} = & -4\pi k^2 \alpha \left[E_{x0} |E_0|^2 + \sigma E_{x1}^* E_0^2 \right] \\ & - 4\pi \alpha \left\{ \frac{\partial^2 [E_{x0} |E_0|^2 + \sigma E_{x0}^* E_0^2]}{\partial x^2} + \frac{\partial^2 [E_{y0} |E_0|^2 + \sigma E_{y0}^* E_0^2]}{\partial x \partial y} + \frac{\partial^2 [E_{z0} |E_0|^2 + \sigma E_{z0}^* E_0^2]}{\partial x \partial z} \right\} \end{aligned} \quad (8)$$

$$\begin{aligned} \Delta E_{y1} + k^2 E_{y1} = & -4\pi k^2 \alpha \left[E_{y0} |E_0|^2 + \sigma E_{y1}^* E_0^2 \right] \\ & - 4\pi \alpha \left\{ \frac{\partial^2 [E_{x0} |E_0|^2 + \sigma E_{x0}^* E_0^2]}{\partial x \partial y} + \frac{\partial^2 [E_{y0} |E_0|^2 + \sigma E_{y0}^* E_0^2]}{\partial y^2} + \frac{\partial^2 [E_{z0} |E_0|^2 + \sigma E_{z0}^* E_0^2]}{\partial y \partial z} \right\} \end{aligned} \quad (9)$$

$$\begin{aligned} \Delta E_{z1} + k^2 E_{z1} = & -4\pi k^2 \alpha \left[E_{z0} |E_0|^2 + \sigma E_{z1}^* E_0^2 \right] \\ & - 4\pi \alpha \left\{ \frac{\partial^2 [E_{x0} |E_0|^2 + \sigma E_{x0}^* E_0^2]}{\partial x \partial z} + \frac{\partial^2 [E_{y0} |E_0|^2 + \sigma E_{y0}^* E_0^2]}{\partial z \partial y} + \frac{\partial^2 [E_{z0} |E_0|^2 + \sigma E_{z0}^* E_0^2]}{\partial z^2} \right\} \end{aligned} \quad (10)$$

where $|E_0|^2 = |E_{x0}|^2 + |E_{y0}|^2 + |E_{z0}|^2$, $E_0^2 = E_{x0}^2 + E_{y0}^2 + E_{z0}^2$, $\sigma = \beta/\alpha$.

Equations (8) – (10) are obtained within weak-nonlinear medium approximation and allow analysis of polarization variations within non-paraxial approximation, i.e., for laser beams of arbitrary shape and focusing geometry. Let us consider laser beam with arbitrary space distribution of transverse electric-field projections at input plane. General investigation of solutions to those equations can give exact description of polarization variations but it is rather difficult to obtain exact solution. Nevertheless, some important general properties of the solutions can help to fulfil qualitative analysis of polarization variations without solving the equations. The properties can be derived from integral representation of the solutions: any solution to equations (8) – (10) can be represented in integral form with linear and nonlinear terms [11, 12]. All integrals in the equation represent integral convolutions of certain terms with kernels.

Important point is that all kernels of integral equation (11) depend on $r = \sqrt{(x - x_0)^2 + (y - y_0)^2}$ and are even with respect to transverse coordinates.

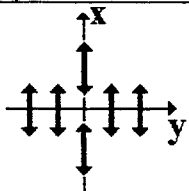
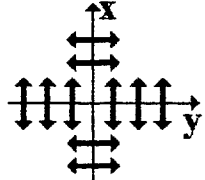
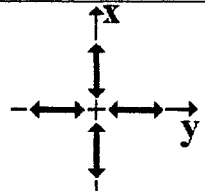
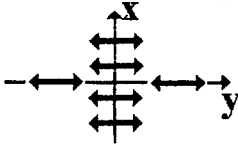
In case of linear polarization, one transverse projection, say, y -projection of electric and x -projection of magnetic field is zero at initial plane. Longitudinal projection appears due to front curvature at input plane and influence of gradient nonlinear terms, and one cannot assume boundary conditions to be zero for the first iteration E_{x0} [11, 12]. The other transverse projection of both electric and magnetic fields appears also due to wave front distortions linear part of which results from non-zero boundary condition [11]. Structure of light polarization depends on parity properties of transverse distribution of input electric and magnetic fields. Let us consider, for example, linearly polarized beam which x -projection of electric field and y -projection of magnetic field have even space distribution at input plane with respect to both transverse coordinates (the first string in Table 1). Then integrating (6) yields even space distribution for E_{x0} because all kernels of corresponding integrals in integral equation are even functions [11, 12]. The first iteration for other transverse projection gives odd dependence on both transverse coordinates. Longitudinal projection is odd too [11, 12]. Thus, in linear approximation, other transverse projection appears due to distortions of wave front. Initial linear polarization turns into elliptic and it stays linear with initial orientation only along two mutually perpendicular symmetry axes passing through beam cross-section center among which one is parallel to the initial direction of electric field.

Let us analyze the second iteration given by equations (8) – (10). The first term in right-hand part of (9) is odd. First-order differentiating of even function $E_{x0} |E_0|^2 + \sigma E_{x0}^* E_0^2$ with respect to both transverse coordinates (the second term) gives odd function in right-hand part of (9). Second-order differentiating of odd function $E_{y0} |E_0|^2 + \sigma E_{y0}^* E_0^2$ (the third term) yields odd function. The last right-hand term of (9) is even with respect to y and odd with respect to x but it is much smaller than the first and the second terms in (9) and can be neglected. Similar qualitative analysis shows that the first three terms in right-hand part of (8) are even functions while the fourth term is even with respect to x and odd with respect to y but its influence can be neglected too. Following integrating of (9) yields odd space distribution of E_{y1} with

small even contribution with respect to y -coordinate what means that $E_y \approx 0$ along coordinate axes. Thus, ratio E_x/E_y is very large along those axes where polarization stays practically the same linear as it is at input plane resulting in formation of cross-shaped polarization structure at focal plane (the first string of Table 1). Elliptic polarization appears between coordinate axes. Results of similar analysis for other three cases of parity of field distribution at input plane (projections E_x and H_y) are presented in Table 1.

Important feature is that depolarization effect resulting from linear diffraction adds to nonlinear depolarization effect. Thus, cross-shaped linear-polarization structure is emphasized by contribution from linear propagation effects. Exactly similar consideration can be done for the case of laser pulse, and all considerations keep their validity for that case too because Green's function of parabolic equation describing pulse propagation is also even with respect to x and y .

TABLE 1. Parity of space distribution of transverse electric-field and magnetic-field projections at input plane and its relation to polarization structure along coordinate axes near focal plane for arbitrary linearly polarized input beam (initial projections are E_x and H_y).

Parity with respect to x -coordinate	Parity with respect to y -coordinate	Distribution of linear polarization along x and y coordinate axes
Even: $E_f(-x)=E_f(x)$ $H_f(-x)=H_f(x)$	Even: $E_f(-y)=E_f(y)$ $H_f(-y)=H_f(y)$	
Even: $E_f(-x)=E_f(x)$ $H_f(-x)=H_f(x)$	Odd: $E_f(-y)=-E_f(y)$ $H_f(-y)=-H_f(y)$	
Odd: $E_f(-x)=-E_f(x)$ $H_f(-y)=-H_f(y)$	Even: $E_f(-y)=E_f(y)$ $H_f(-y)=H_f(y)$	
Odd: $E_f(-x)=-E_f(x)$ $H_f(-y)=-H_f(y)$	Odd: $E_f(-y)=-E_f(y)$ $H_f(-y)=-H_f(y)$	

Similar consideration of beams with initial circular polarization shows absence of any cross-shaped polarization structures at focal plane. No straight connection between polarization structure and parity of transverse distribution of beam electric field is observed. That is connected with symmetry of circular polarization – there is no any selected direction at transverse plane (while in case of linear polarization there are two selected directions – along electric-field vector and perpendicular to it). Nevertheless, general conclusion from qualitative analysis is the same as for linear polarization – circular polarization turns into elliptic one, which dominates initial polarization in focal area. Important qualitative difference between linear and circular initial polarizations is that depolarization of linearly polarized light is less sensitive to laser-induced phase difference between two transverse projections while depolarization of circularly polarized light is extremely sensitive to laser-induced phase shifts. That follows from obvious property of those types of polarization. Really, in case of linear polarization self-induced transverse projection is smaller than initial projection, thus, one axis of polarization ellipse is very small and self-induced phase shift is not critical. In case of initial circular polarization both axes of polarization ellipse are of similar order, and even small phase shifts can result in transformation of initial circle into ellipse.

To do further analytical and numerical calculations easier we apply asymptotical expansion with respect to "diffraction" parameter to each term E_{jm} , $m=0, 1, 2, \dots$, i.e., come to paraxial approximation. Resulting asymptotical series have the following form:

$$E_x(x, y, z) = e^{ikz} \sum_{m=0, n=0} q^m p^{m-n} u_{mn}(x, y, z) = e^{ikz} (u_{00} + \frac{1}{p} u_{01} + qp u_{10} + qu_{11} + \dots), \quad (11)$$

$$E_y(x, y, z) = e^{ikz} \sum_{m=0, n=0} q^m p^{m-n} v_{mn}(x, y, z) = e^{ikz} (v_{00} + \frac{1}{p} v_{01} + qp v_{10} + qv_{11} + \dots), \quad (12)$$

$$E_z(x, y, z) = e^{ikz} \sum_{m=0, n=0} q^m p^{m-n} w_{mn}(x, y, z) = e^{ikz} (\frac{1}{p} w_{01} + qp w_{10} + \dots). \quad (13)$$

Presented asymptotical expansions (11) – (13) allow separate describing of influence of different factors (linear diffraction, nonlinear cubic distortions, nonlinear gradient distortions) on beam propagation. Value of contributions from those factors can be estimated assuming $q=0.0001$ and $p=100$. If the first terms in (11) and (12) are of order of 1 then the second and the third terms in those series are of order of 0.01, the fourth terms are an order of 0.0001. Thus, in case of self-focusing absence, described by presented asymptotical expansions, cubic nonlinear terms show influence of the same order as linear diffraction terms while nonlinear gradient terms are an order of magnitude less than linear diffraction terms. Changes of light polarization of tightly focused laser beam can result from 1) linear diffraction effects [8-10] connected with distortions of input wave front during beam propagation, 2) mutual influence of electric-field projections described by cubic nonlinear term in (1), and 3) from mutual influence of electric-field projections described by gradient nonlinear terms in (1). In case of input elliptic polarization the first two contributions dominate influence of gradient terms, and the latter can be neglected. In case of linear and circular input polarizations the gradient terms must be taken into account to describe depolarization effect because their contribution is of the same order as contributions from diffraction and cubic nonlinearity.

Exact analytical and numerical results can be easily obtained for initial linear polarization by making use of expansions (11) – (13) and equations resulted from them. For example, considering input beam to be TEM₀₀ Gaussian beam, one should set the following conditions at input plane:

$$u_{00}|_{z=0} = E_0 e^{i\phi_0} \exp\left(-k \frac{x^2 + y^2}{2z_c}\right); \quad v_{00}|_{z=0} = 0; \quad w_{00}|_{z=0} = 0. \quad (14)$$

where z_c – is confocal parameter of the beam, E_0 – is amplitude of electric field. Bearing in mind only the first non-zero terms in (11) – (13) describing influence of linear diffraction, cubic and gradient nonlinearities, one obtains the following representation of solutions to (1):

$$E_x \approx e^{ikz} \left(u_{00} + \frac{1}{p} u_{01} + \frac{\alpha}{\epsilon_0} p u_{10} + \frac{\alpha}{\epsilon_0} u_{11} \right), \quad (15)$$

$$E_y \approx e^{ikz} \left(\frac{1}{p} v_{01} + \frac{\alpha}{\epsilon_0} v_{11} \right), \quad (16)$$

Space distribution of parameters of polarization ellipse can be calculated from the ratio $R = |E_y|/|E_x|$ of transverse-projection amplitudes and their phase shift θ_n

$$\frac{E_y}{E_x} = R \cdot \exp(i\theta_n). \quad (17)$$

Significant advantage of paraxial approximation is that corresponding equations can be integrated analytically [11]. Rather long analytical calculations of polarization parameters for expansions (15) – (16) show that they can be represented in the following form [11, 12]:

$$R = x y f(r) \text{ and } \theta_n = \theta(r), \quad (18)$$

where $r^2 = x^2 + y^2$ and

$$R \sim z_c^4 / (z - z_F)^4 \text{ for } (z - z_F) \rightarrow \infty, \quad (19)$$

where $z_c = \pi w_0^2 / \lambda$ – confocal parameter of Gaussian beam, z_F is distance between input and focal planes (Fig. 1). This agrees well with results of qualitative analysis presented in table 1, in particular, with formation of cross-shaped structure

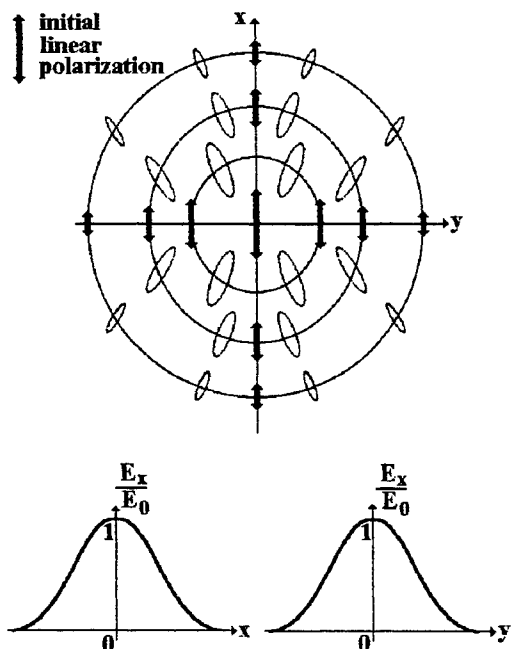


Fig. 2. Space distribution of polarization at focal plane of input Gaussian TEM_{00} beam (field distribution along coordinate axes at initial plane is shown in lower part of this figure) with initial linear polarization along x-axis. Calculated parameters of polarization are shown in the form of linear and elliptic polarizations denoted by arrows and ellipses. There are also shown coordinate axes and circles corresponding to $s^2 = (x^2 + y^2)/w_0^2 = 0.3; 0.7; 1.0$

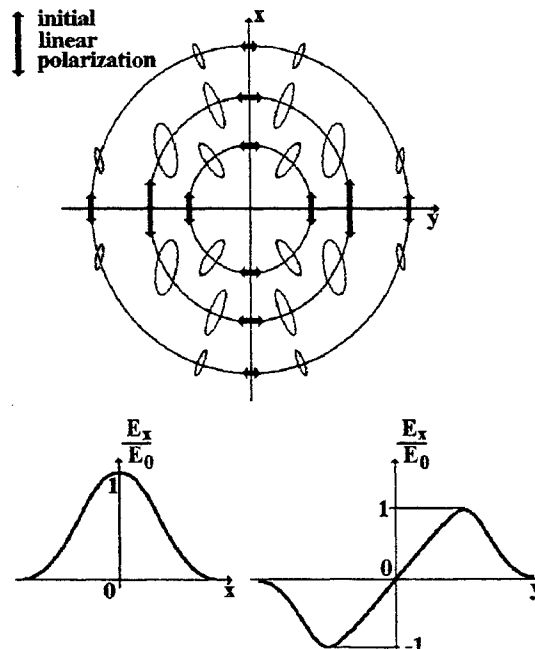


Fig. 3. Space distribution of polarization at focal plane of input Gaussian TEM_{01} beam (field distribution along coordinate axes at initial plane is shown in lower part of this figure) with initial linear polarization along x-axis. Parameters p and q are the same as for Fig. 2. Calculated parameters of polarization are shown in the form of linear and elliptic polarizations denoted by arrows and ellipses. There are also shown coordinate axes and circles corresponding to $s^2 = (x^2 + y^2)/w_0^2 = 0.3; 0.7; 1.0$

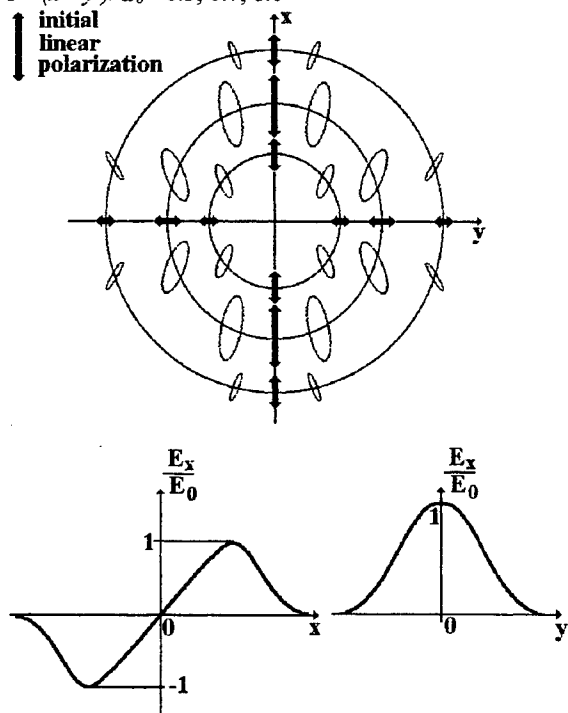


Fig. 4. Space distribution of polarization at focal plane of input Gaussian TEM_{10} beam. All parameters and notations are the same as for Fig. 2 and 3.

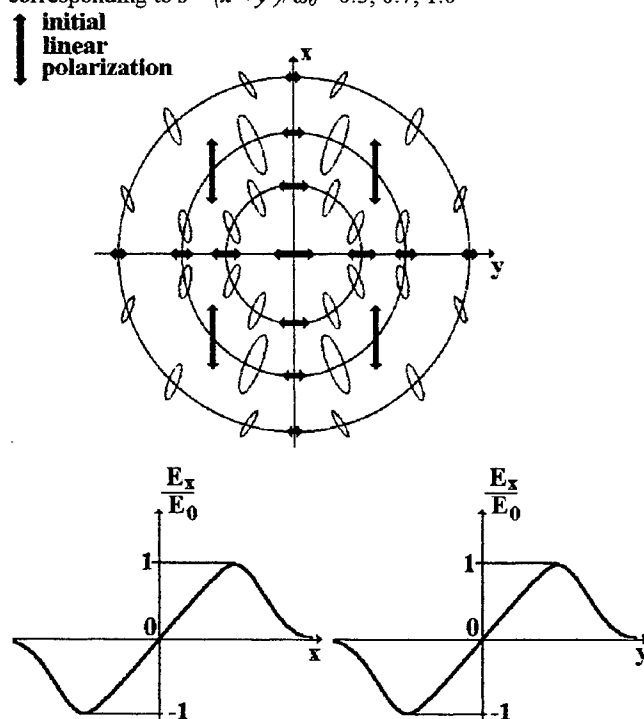


Fig. 5. Space distribution of polarization at focal plane of input Gaussian TEM_{11} beam. All parameters and notations are the same as for Fig. 2 and 3.

along which initial linear polarization conserves. Results of numerical calculation of distribution of polarization ellipses at waist plane illustrate derived regularities (Fig. 2). Calculations are done for the following set of parameters: $p=94$ (corresponding waist (focal) spot radius $\omega_0=15\lambda$, that is $12.8 \mu\text{m}$ for laser wavelength $\lambda=0.8 \mu\text{m}$) and $q=0.0001$ (corresponds to intensity of laser radiation at focus $I=10^{12} \text{ W/cm}^2$). The parameters are chosen so as pulse power to be below self-focusing threshold. Similar calculations have been done for TEM_{01} (Fig. 3), TEM_{10} (Fig. 4) and TEM_{11} (Fig. 5) Gaussian beams. Specific cross-shaped structures in polarization are observed in all those cases with conserving of initial linear polarization along one or other coordinate axis. Interesting feature is that pure laser-induced projection can appear along coordinate axes for beams without radial symmetry, i. e., TEM_{01} , TEM_{10} and TEM_{11} (Figs. 3 - 5). That agrees with data from Table 1 obtained from qualitative analysis within non-paraxial approximation.

3. FIELD INSTABILITY IN TRANSPARENT MICROINCLUSION

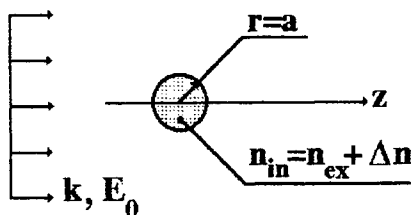
Strong influence of the effects on LID processes through self-focusing or local variations of electric field amplitude due to presence of tiny non-absorbing defects [16] is well known. The problem is that theoretical consideration in [16] was limited by electrostatic case only. We present theoretical model to describe electrodynamical effects induced by transparent inclusions and connected with formation of inclusion eigenmodes [17] resulting in resonant increasing of electric field amplitude inside the inclusions. Combination of resonant properties with nonlinear self-action through laser-induced variation of refractive index can lead to formation of positive feedback. The feedback can result in field instability inside the inclusion. It is shown below that in the most general case the instability comes through the following [16]: field amplitude E_{in} inside the microinclusion tends to some limited value and its derivation with respect to incident field amplitude E_0 tends to infinity while incident field amplitude approaches finite threshold value E_0^* :

$$E_{in} \rightarrow E_{in}^*, \quad \frac{\partial E_{in}}{\partial E_0} \rightarrow \infty \quad \text{with} \quad E_0 \rightarrow E_0^*. \quad (20)$$

According to the definition there is nonstationary development of field structure in the inclusion and near to it. Moreover, absolute value of field amplification in the inclusion is limited. The possible mechanism of this process is as follows. If field and microinclusion parameters are not exactly resonant but do not differ from them very much and light intensity is high enough to induce positive addition to refractive index then light-induced variation of refractive index can result in making conditions for an eigenmode to be formed with pump radiation of near-resonant parameters. Small initial increasing of near-resonant pump field inside the microinclusion is followed by small variation of refractive index. The matter of fact is that pump field induces distribution of refraction index which is adjusted with distribution of eigenmode's field inside the microparticle. This implies increasing of field amplitude inside the particle due to field-induced variation of refractive index. Resonant excitation of the quasi-eigenmode for near-resonant wavelengths results in amplitude increasing inside the microparticle which in turn results in inducing of greater variation of refractive index. Thus, self-induced formation of quasi-eigenmode establishes positive feedback resulting in radiation-induced variation of Q-factor spectrum and resonant increasing of total amplitude and field instability inside the microinclusion if incident pump field amplitude exceeds instability threshold.

General theoretical approach is based on perturbation methods. It is shown below that laser-induced variations of refractive index are small as compared with linear refraction. Thus, field amplitudes can be represented in the form of series with respect to small perturbation to refractive index which is intensity-dependent. Let us consider spherical dielectric microparticle of radius a and refractive index n_{in} which is irradiated by plane linearly polarized wave of amplitude E_0 and wave number k (Fig. 6). We neglect nonlinear properties of the external medium. We suppose that

$$n_{ex} = \text{const}$$



$$n = n_{in} / n_{ex} = 1 + \delta n_0 + \delta n, \quad (21)$$

where $\delta n_0 = \text{const}$ and field-induced addition has the following form for isotropic Kerr-like nonlinear medium:

$$\delta n = n_2 \cdot E_{in}^2, \quad (22)$$

E_{in} is total electric field inside the microparticle. Let us consider a single whispering-gallery mode of the microparticle. According to exact solution of diffraction problem¹⁵ field amplitude inside the particle can be represented in the form of sum of linear term and nonlinear perturbation:

Fig. 6. Geometry of the problem.

$$E_{in} = \sqrt{|E_r|^2 + |E_\theta|^2 + |E_\varphi|^2} \approx E_{in0} + \delta n \cdot E_{in0} S^*(r, \theta, \varphi, x) = S_0 \cdot E_0 \cdot (1 + \delta n \cdot S(r, \theta, \varphi, x)), \quad (23)$$

where E_{in0} is electric field amplitude inside the inclusion in linear approximation (i.e., amplitude of the resonant whispering-gallery mode in linear case), $x = 2\pi a n_{in} / \lambda_0$, $S_0 = \text{const}$ is amplification of field amplitude in linear case, S describes space distribution of laser-induced variations of refractive index.

Equation for real positive value of field amplitude inside the micro particle can be derived from (23) and (22). Maximum value of field amplitude is given by

$$E_{in} = \frac{1}{2n_2 E_0 S_m S_0} \left[1 - \sqrt{1 - 4n_2 S_m S_0^2 E_0^2} \right], \quad (24)$$

where S_m is maximum value of $S(r, \theta, \varphi, x)$. The solution exists under the condition

$$E_{in0} \leq E_{in0}^* = [4n_2 S_m S_0^2]^{-1/2}, \quad (25)$$

where at the edge of solution-existence interval ($E_0 = E_0^*$)

$$E_{in} \rightarrow E_{in}^* = \sqrt{\frac{1}{n_2 S_m}}; \quad \frac{\partial E_{in}}{\partial E_{in0}} \rightarrow \infty. \quad (26)$$

This corresponds to the considered above type of field instability (20). Fig. 7 depicts typical nonlinear behaviour of electric field inside microinclusion.

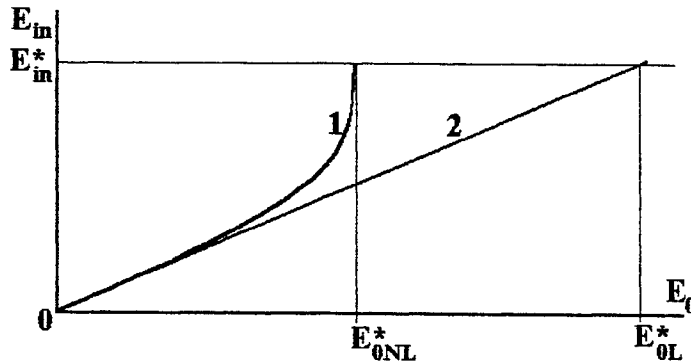


Figure 7. Typical dependence of field amplitude inside microparticle E_{in} on pump field E_0 for nonlinear (curve 1) and linear (curve 2) cases. Slope of the line for linear amplification is determined by quality factor Q_0 of initial microinclusion.

Thus, nonlinear dependence of microparticle refractive index on electromagnetic field amplitude can result in electrodynamic field instability of the determined above type (20). Amplification of field amplitude inside microspherical inclusion which can be estimated through quality factor Q as follows:

$$\left(\frac{E_{in}}{E_0} \right)_{\max} = 1.316 \sqrt{Q} = S_0 (1 + \delta n \cdot S_m) \leq 2 \cdot S_0 \quad (27)$$

Absolute value of instability threshold in microsphere [16] is about 10^6 V/cm what implies laser-induced variation of refraction to be about 1% of initial value.

Let us consider qualitative dependence of electric field amplitude on parameters of the inclusion.

1) $\delta n_0 > 0$; $n_2 > 0$. As it has been shown above, field instability can take place in that case. Such parameters correspond to increasing of particle's quality factor with increasing of field amplitude in it, i.e., action of positive feedback. Field behaviour corresponds to definition of field instability (20) – see curve 1 in Fig. 8. Bearing in mind of higher order terms in perturbation series can allow to describe optical bistability even for considered relation between δn_0 and n_2 .

2) $\delta n_0 > 0$; $n_2 < 0$. Substituting these values of parameters into general relations (23) – (26) one can easily show that field amplitude comes to certain limit which does not depend on amplitude of incident radiation (curve 4 in Fig. 8). Really, it follows from (23) that in case of $n_2 < 0$ solution to (23) has the following form:

$$E_{in} = \frac{\sqrt{1 + 4n_2 S_m E_0^2 (1 + \delta n_0 S_m)} - 1}{2n_2 E_0 S_m} \quad (28)$$

and it is limited by its maximum value reached with $\square_0 \rightarrow \infty$:

$$E_{in}^{**} = \sqrt{\frac{1 + \delta n_0 \cdot S_m}{n_2 \cdot S_m}}, \quad (29)$$

Physical reason for such field behaviour is obvious: laser radiation compensates initial difference of refractive index resulting in "disappearing" of the inclusion. That points at action of negative feedback at all stages of field evolution in considered case.

3) $\delta n_0 < 0$; $n_2 < 0$. This case also corresponds to field stabilization at constant level which does not depend on incident radiation (curve 4 in Fig. 8). Value of the stable amplitude can be estimated in the way as it was done earlier: substituting $-\delta n_0 < 0$ and $-n_2 < 0$ into equation (23) one comes to its solution

$$E_{in} = \frac{-1 + \sqrt{1 + 4n_2 S_m E_0^2 (1 - \delta n_0 S_m)}}{2n_2 E_0 S_m}, \quad (30)$$

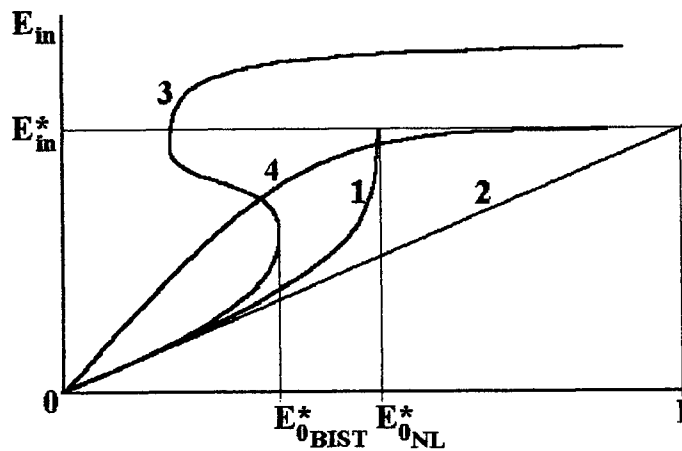


Fig. 8. Dependence of field amplitude inside inclusion on field amplitude of incident radiation for linear (2) behavior, field instability (1), field stabilization (4), and field bistability (3) depending on signs of δn_0 and n_2 .

where it is taken into account the condition $|\delta n_0 S_m| < 1$. Considering field limit for large amplitudes of incident radiation, one obtains the following value:

$$\square_{in} \rightarrow E_{in}^{**} = \sqrt{\frac{1 - \delta n_0 \cdot S_m}{n_2 \cdot S_m}}. \quad (31)$$

Physical reason for such field behavior is connected with increasing of particle relectivity resulting from laser-induced variations of refractive index. That corresponds to action of negative feedback during all stages of field evolution.

4) $\delta n_0 < 0$; $n_2 > 0$. Laser field is bistable inside the particle even in the first approximation of perturbation theory. Really, considered combination of signes results in the following derivative

$$\frac{\partial E_0}{\partial E_{in}} = \frac{(1 - \delta n_0 \cdot S_m) - S_m \cdot n_2 \cdot E_{in}^2}{(S_m \cdot n_2 \cdot E_{in}^2 + (1 - \delta n_0 \cdot S_m))^2}, \quad (32)$$

that turn to zero for

$$E_{in} \rightarrow E_{in}^* = \sqrt{\frac{1 - \delta n_0 S_m}{n_2 S_m}}, \quad (33)$$

what corresponds to $\frac{\partial E_{in}}{\partial E_0} \rightarrow \infty$ while the solution exists only for

$$E_0 \leq E_0^* = [4n_2 S_m (1 - \delta n_0 S_m)]^{-1/2}, \quad (34)$$

4. DISCUSSION OF RESULTS AND CONCLUSIONS

Thus, presented results show that field structure of tightly focused laser beam can vary significantly in focal area at laser intensity close to damage threshold. In particular, polarization of high-power laser beam focused into transparent medium does not stay the same as it is at input plane even for cases of initial linear and circular polarizations. It changes due to influence of both linear diffraction and nonlinear perturbations of wave front. Generalizing obtained results, we can say that any initial polarization turns into elliptic one with complicated space distribution of polarization-ellipse parameters. This follows from equations and qualitative analysis presented in section 2. Because of obvious character of polarization variations the described effect can be referred to as depolarization.

The mechanisms of considered depolarization effect are connected with three factors. 1) Wave front distortions due to linear propagation effects of tightly focused laser beams. 2) Those distortions can result in mutual influence of electric-field projections through cubic nonlinear term leading to increasing of the distortions. 3) Mutual influence of electric field projections described by gradient nonlinear term. One of interesting points is that contributions of all the three factors are of similar order. Thus, neglecting one of them is not correct if others are taken into account. Described effect of self-induced depolarization must be very strong in focal area where both laser intensity and laser-induced refractive-index gradient are maximum. Contribution of gradient nonlinearity is large and can even dominate other contributions in this case. Important factor is also adjustment between space distributions of beam electric field and laser-induced variations of refractive index.

Important feature of described effect for linearly polarized beams is appearing of cross-shaped structures in transverse distribution of elliptic polarization that depends on parity of transverse distribution of input beam (Table 1). At certain parity initial linear polarization can be conserved along one of transverse coordinate axis while pure laser-induced projection of electric field can appear along the other coordinate axis. Polarization is elliptic between coordinate axes, thus, it is possible to separate one or other linear polarization by using of properly oriented polarizers. This can be used for experimental checking of self-induced depolarization effect. In particular, parallel orientation of polarizer and analyzer can result in appearing of cross-shaped distribution of laser intensity for tightly focused TEM_{00} Gaussian beam after it has passed through nonlinear medium placed between the polarizer and analyzer (see Table 1 and Fig. 2). In case of tightly focused TEM_{01} beam, rotation of analyzer from position parallel to polarizer to perpendicular position can result in the following changes in space distribution of transmitted intensity: first, there is bright strip along axis perpendicular to initial polarization plane (see Table 1 and Fig. 3) which becomes less and less bright with rotation of analyzer, and then appears bright strip along axis parallel to initial polarization plane. The reverse order of changes in transmitted intensity can be observed for TEM_{10} beam for the same rotation of analyzer. In case of TEM_{11} parallel orientation of polarizer and analyzer must result in appearing of four bright spots separated by dark cross. Rotation of analyzer to perpendicular position will put out the spots and make the cross bright (Fig. 5 and Table 1).

Important conclusion from presented calculations is that circular polarization changes too as a result of self-depolarization effect. In general case both initial circular and linear polarizations become elliptic in focal area with complicated inhomogeneous space distribution of polarization-ellipse parameters. Qualitative analysis for initial circular polarization does not show any cross-shaped structures like those obtained for linear polarization. In general case, there must be small difference in averaged space distribution of polarization parameters of both linear and circular initial polarizations. That can result in disappearing of polarization dependence for laser-induced damage and self-focusing thresholds with decreasing of focal spot size and increasing of laser intensity at focal plane. Exactly that situation is described in [5] where difference in damage thresholds for linearly and circularly polarized beams tends to zero with decreasing of focal spot radius below 20λ . Thus, absence of polarization dependence of laser damage threshold for small focal spots (geometry of tight focusing) can result from self-induced depolarization effect rather than from disappearing of self-focusing.

Other important effect is field instability in transparent microparticles. The particle can be formed during material manufacturing or can be induced by laser radiation. Laser-induced formation of such particles was observed experimentally in [2]. Mechanism of their influence on LID threshold and initiating of LID is connected with excitation of particle's resonant mode resulting from laser-induced variations of refractive index. Thus, non-absorbing microparticles can initiate LID by increasing of local electric field strength. Characteristic feature of field instability is sharp step in dependence of field amplitude inside the particle on amplitude of incident radiation. Important conclusion

is that not all microparticles are dangerous – some of them induce limited increase of laser intensity and stabilize its value at certain level.

Obtained results must be taken into account for correct interpretation of experimental data on laser-matter interactions within geometry of tightly focused beams. In particular, it is reasonable to expect absence of polarization dependence for high-power laser phenomena such as multiphoton absorption, self-focusing and others observed under action of tightly focused laser beams.

5. ACKNOWLEDGEMENTS

This work is partially supported by INTAS (project 97-02-31777).

6. REFERENCES

1. O.M.Efimov, L.B.Glebov, V.S.Popikov, M.J.Soileau, "The role of laser radiation statistics in the measurements of basic regularities of optical breakdown of glasses", in *Laser-Induced Damage in Optical Materials: 1994*, Proc. SPIE, v. **2428**, pp. 479-483, 1995 (and references therein).
2. O.M.Efimov, O.N.Bosyi, L.B.Glebov, M.J.Soileau, "Mechanisms of multiple shot bulk damage of silicate glasses in conditions of multiphoton absorption and without it", *Laser-Induced damage in Optical Materials: 1994*, Proc. of SPIE, vol. **2428**, pp. 546-552, 1995.
3. R.F.Haglund, Jr., "Mechanisms of Laser-Induced Desorption and Ablation", in «Laser Ablation and Desorption», eds. J.C.Miller and R.F.Haglund, Jr., Boston, Academic Press, 1998, p. 15 - 138.
4. C.B.Schaffer, E.N.Glezer, N.Nishimura, and E.Mazur, "Ultrafast laser induced microexplosions: explosive dynamics and sub-micrometer structures", in *Commercial Applications of Ultrafast Lasers*, Proc. SPIE, v. **3269**, p. 36-45, 1998.
5. M.J.Soileau, W.E.Williams, N.Mansour, E.W.VanStryland, "Laser-induced damage and the role of self-focusing", *Optical Engineering*, v. **28** (10), p. 1133 (1989).
6. B.Rethfeld, A.Kaiser, M.Vicanek, and G.Simon, Proc. SPIE, v. **3343**, p. 388, 1998.
7. P.D.Maker, R.W.Terhune, C.M.Savage, *Phys. Rev. Lett.*, v. **12**, p. 507, 1964.
8. V.S.Liberman, B.Ya.Zel'dovich, *Phys. Rev. A*, v. **46**, p. 5199, 1992.
9. N.D.Kundikiva, B.Ya.Zel'dovich, in *International Trends in Optics and Photonics, ICO IV*, v. 74 of Springer Series in Optical Sciences, Springer Verlag, 1999.
10. N.P.Sadikov, *Sov. Journal of Quant. Electronics*, v. **23**, p. 177, 1996.
11. V. E. Gruzdev, M. N. Libenson, "Propagation of high-power tightly focused laser beams and self-depolarization effect", in *High-Power Laser Ablation-III*, Proc. of SPIE, v. **4065**, pp. 884-895, 2000.
12. V. E. Gruzdev, M. N. Libenson, "Self-depolarization effect of high-power tightly focused laser beams in transparent isotropic materials", in Proc. SPIE, v. **4133A**, 2001 (to appear).
13. R.C.Jones, *J. Opt. Soc. Am.*, v. **31**, p. 488, 1941.
14. F.A.Hopf and G.I.Stegeman, *Applied Classical Electrodynamics*, Volume II: Nonlinear Optics, Vol. 2 in Wiley series in pure and applied optics, A Wiley-Interscience Publ., New York, 1986.
15. M.Born, E.Wolf, *Principles of Optics*, Pergamon Press, New York, 1968.
16. N.Bloembergen, "Role of cracks, pores and absorbing inclusions on laser induced damage thresholds at surfaces of transparent dielectrics", *Appl. Opt.*, v. **12**, pp. 661-664, 1973.
17. V.E.Gruzdev, M.N.Libenson, "Electrodynamic instability as a reason for bulk and surface optical damage of transparent media and thin films", *Laser-Induced Damage in Optical Materials: 1995*, Proc. SPIE, v. **2714**, pp. 595-603, 1996.

Nonequilibrium electron and phonon dynamics in solids absorbing a subpicosecond laser pulse

B. Rethfeld^a, A. Kaiser^b, M. Vicanek^c and G. Simon^c

^a Institut für Laser- und Plasmaphysik, Universität Essen, D-45117 Essen, Germany

^b Max-Planck-Institut für Physik komplexer Systeme,
Nöthnitzer Str. 38, D-01187 Dresden, Germany

^c Institut für Theoretische Physik, TU Braunschweig, D-38106 Braunschweig, Germany

ABSTRACT

We study the temporal evolution of the distribution functions of free electron gas in metals and insulators for the case of irradiation with a laser pulse of moderate intensity. A microscopical description on the basis of time-dependent Boltzmann equations is used. The results show the sequence of excitation and relaxation of the electron gas leading eventually to thermal equilibrium. Due to photon absorption the occupation number of electron gas differs significantly from Fermi distribution. For high enough intensities about damage threshold, the energy exchange between electrons and phonons can be described with the two-temperature model. For low excitations we find a delayed energy transfer from laser-excited electron gas to lattice as compared to the two-temperature model. We obtain fluence-dependent thermalization times of the electron gas. For dielectrics we find that the essential process of free-electron generation is strong-electric-field ionization; no avalanche develops in femtosecond time regime. We propose an extended system of two rate equations taking the effect of energy dependence of impact ionization into account. This averaging approach can reproduce the evolution of free electron density in SiO₂ with reasonable accuracy.

Keywords: femtosecond laser absorption, distribution function, collision integrals, electron-phonon coupling, electron thermalization, ionization processes

1. INTRODUCTION

Ultrashort laser pulses are widely applied in basic research as well as for material processing. The interaction of solids with such pulses involves a number of microscopic processes acting on a subpicosecond time scale. The energy is absorbed mainly by electrons, leading to a transient nonequilibrium of the electron gas with the lattice on a time scale of several picoseconds.¹ Hot electron gas leads to anomalous emission of electrons and thermal radiation,²⁻⁵ and can affect the cold lattice through elastic constants, leading to lattice displacements.^{6,7} Thermal relaxation between electrons and phonons as well as thermalization within the electron gas have been studied both experimentally and theoretically.⁸⁻¹⁴ Dielectrics show strong absorption when being irradiated with intensities above a certain threshold. The abrupt change of the initially transparent material to a strongly absorbing solid with metal-like behavior is known as dielectric breakdown.¹⁵⁻²⁰

For applications as materials processing it may be desired to describe materials response on femtosecond laser irradiation as simple as possible. Applicable descriptions for heat conduction are needed as well as a simple approximation to describe the dielectric breakdown. However, since the governing collision processes occur on the same time scale as they have to be described, averaging descriptions are not applicable from the first and appropriate descriptions have to be chosen carefully. In metals, the delayed energy transfer from the laser absorbing electrons to the initially cold lattice can be included by the well-known two-temperature model.^{21,22} It has to be cleared, how far the two-temperature model provides a proper model on femtosecond time scales, since the thermalization of the electron gas, where electron-electron collisions lead to a Fermi-like distribution occurs on this time scales. Considering dielectrics, the breakdown can be explained by an increasing free electron density reaching critical plasma density. Electrons are transferred from the valence band to the conduction band by microscopic ionization processes. Strong-electric-field ionization (multiphoton ionization and, for higher intensities, tunnel ionization) and electron-electron

E-mail correspondence to brf@ilp.physik.uni-essen.de

impact ionization are two competing processes. The probability of these processes can be described with an expression found by Keldysh.^{23,24} Also there exist approximate equations to describe these ionization processes,^{19,20,25,26} however on femtosecond time scale their applicability is questionable.

We use a kinetic description to understand details of materials behavior under femtosecond laser irradiation. We focus on time dependent behavior as absorption, relaxation within the electron gas (thermalization) and relaxation between electrons and phonons. Each considered process is included by an according collision term in a time-dependent Boltzmann equation. The resulting equation system is solved numerically. This approach allows to investigate the effect of each particular collision process even for highly nonequilibrium electron gas or phonon gas. In our approach, neither relaxation times nor other phenomenological parameters like absorption rate or electron-phonon coupling constant are assumed. Only material parameters describing the crystal at room temperature enter the calculation.

For metals we find that at moderate intensities (from one order of magnitude below damage threshold up to higher intensities) the two-temperature model is applicable while for low intensities the energy transfer from electrons to phonons is delayed by a nonthermalized electron gas. For dielectrics we find that the strong-electric-field ionization is responsible for the generation of a free electron gas. Impact ionization can not be described by simple rate equations when applying a laser pulse of less than 100 fs duration since on femtosecond time scale the energies of the free electrons play an important role. We propose an extension of the simplest rate equation which provides a reasonable approximation of our detailed calculation and allows to calculate qualitatively the evolution of free electron density also on femtosecond time scales.

In the following section we outline the applied model. Results for aluminium are presented in section 3, those for SiO₂ are presented in section 4.

2. MODEL FOR METALS AND INSULATORS

The interaction of electrons and phonons with laser irradiation and among themselves is described with the help of the Boltzmann equation. Since we assume isotropy and do not consider spatial transport in our model, the distribution functions depend only on time and energy.

The system of Boltzmann's equation for the calculation of the distribution functions of electron gas and phonon gas reads

$$\frac{\partial f(k)}{\partial t} = \left. \frac{\partial f(k)}{\partial t} \right|_{\text{1pt-absorb}} + \left. \frac{\partial f(k)}{\partial t} \right|_{\text{el-el}} + \left. \frac{\partial f(k)}{\partial t} \right|_{\text{el-phon}} + \left. \frac{\partial f(k)}{\partial t} \right|_{\text{sefi}} + \left. \frac{\partial f(k)}{\partial t} \right|_{\text{imp}}, \quad (1)$$

$$\frac{\partial g(q)}{\partial t} = \left. \frac{\partial g(q)}{\partial t} \right|_{\text{phon-el}}. \quad (2)$$

Here, $f(k)$ and $g(q)$ are distribution functions of electrons and phonons depending on the modulus of wave vector k and q , respectively. The collision term for the electron occupation number f is composed of collision terms for each considered process. For metals, only processes within the conduction band are considered, described by the first three terms on the right hand side of (1). These are photon absorption by conduction-band-electrons, electron-electron interaction and electron-phonon interaction. For dielectrics two additional terms describing ionization of electrons into the conduction band (strong-electronic-field ionization and electron-electron impact ionization) are added. Fig. 1 shows the considered processes schematically.

The applied collision terms for the description of metals can be found in Ref. 14. For electron-electron interaction we use the same collision term as Sun et al.^{11,27} The matrix element is given by a screened Coulomb integral with a screening length depending on the distribution function according to Ref. 28. Electron-phonon interaction is described by the standard collision term as used by Allen⁸ with a matrix element for electron-phonon interaction in metals as given in Ref. 29. Photon absorption of free electrons requires a third collision partner to provide energy and momentum conservation*, and can be described by a collision integral developed in Refs. 30,31. In metals, photon absorption mediated by electron collisions with an ion core³⁰ are responsible for the absorption. Note, that in our

*Also in classical description an electron, oscillating in the electrical field of the laser, can absorb energy only when being disturbed in its oscillation, i.e. when changing its momentum.

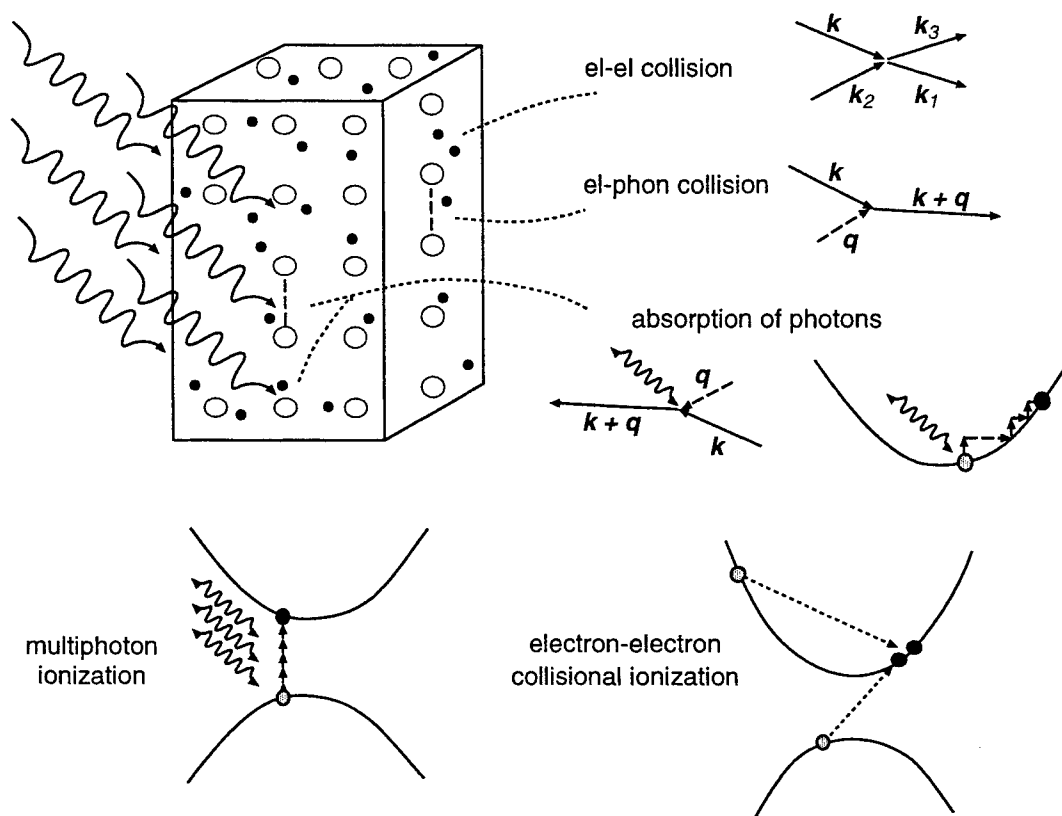


Figure 1. Scheme of a solid irradiated by a laser pulse. We describe transient evolution of the distribution functions of electrons and phonons, respectively, considering the sketched collision processes. Those top right side occur in the conduction band of metals and insulators; the ionization processes in the lower line are considered only in dielectrics.

approach collisions of electrons with fixed ions are assumed to change solely the momentum of free electrons. The energy exchange of free electrons and lattice is described through electron-phonon collisions.

The collision terms for the description of dielectrics are given in Ref. 32. Small changes are performed to the electron-phonon collision term and the photon absorption by free electrons. The latter is in dielectrics mediated by electron collisions with phonons as described in Ref. 31. The matrix element for electron-phonon collisions follows from deformation potential theory.^{33,34} The collision integral for strong-electric-field ionization follows from the work of Keldysh.²⁴ We transform the ionization rate to a complete collision term $\partial f / \partial t|_{\text{seff}}$.^{35,32} One important feature of this collision term is that it represents a δ -function in the case of parabolic dispersion relations in both bands. The collision term for electron-electron impact ionization is composed of the pure electron-electron collision term multiplied by the probability of band exchange.³⁶ The main feature of the impact ionization is that a certain minimum critical energy of the colliding free electron is needed. Requiring momentum conservation, this critical energy is higher than the ionization potential $\bar{\Delta}$. This effective ionization potential $\bar{\Delta}$ is in turn higher than the bandgap Δ because the oscillation energy of free electrons in the electric laser field has to be provided additionally.²⁴

Including momentum conservation for the collision process of impact ionization and the effective ionization potential $\bar{\Delta}$ instead of the bandgap Δ , our model leads to a higher critical energy and therefore a lower probability for impact ionization compared to other approaches.^{19,37}

We assume parabolic energy dispersion of conduction-band-electrons, $\varepsilon(k) = \hbar^2 k^2 / 2m_e$. The valence band is assumed to be always completely filled; we assume a negative parabolic dispersion, $\varepsilon_v(k) = -\hbar^2 k^2 / 2m_e$. Debye's dispersion relation is applied for acoustical phonons, $\varepsilon_{\text{ph}}(q) = v_s q$, where m_e is the effective electron mass and v_s is

the speed of sound. Optical phonons in SiO₂ are described by Einstein's model with a constant frequency.

Taking advantage of the assumed isotropy, the dimensions of the collision integrals can be reduced analytically. After that, a numerical treatment of the equation system (1) and (2) is possible. Thus, we are able to follow the time evolution of the distribution functions $f(\varepsilon(k), t)$ and $g(\varepsilon_{ph}(q), t)$ and observe their changes due to excitation of the electron gas by the laser beam, thermalization of the electron gas by electron-electron collisions and energy exchange between electron gas and phonon gas due to electron-phonon collisions.

3. RESULTS FOR ALUMINIUM

For the calculation of the time evolution of distribution functions in a given metal a few parameters have to be provided. These are the free electron density n , the wave number at Fermi energy, $k_{F,0}$, the number of free electrons per atom, and Debye's wave number which are taken from standard tables.^{38,39} The effective electron mass and the speed of sound are found from comparison of resulting heat capacities with experimental values.⁴⁰ This leads to an effective electron mass of $m_e = 1.45 m_{e,free}$, as also derived in Ref. 41. The phonon heat capacity turned out to be best reproduced applying the sound speed of longitudinal phonons. Thus, only parameters describing the unperturbed solid enter the calculation.

3.1. Excitation of the electron gas by laser irradiation

We assume a laser pulse of rectangular intensity profile with duration $\tau_L = 100$ fs and vacuum wavelength $\lambda = 630$ nm corresponding to a photon energy of $\hbar\omega_L = 1.97$ eV = $0.245 \varepsilon_{Fermi}$. Fig. 2 shows the transient behavior of the occupation number of free electrons for an electric laser field of amplitude $E_L = 1.4 \times 10^8$ V/m, corresponding to an intensity of $I_L = 7 \times 10^9$ W/cm² and an absorbed fluence of $F_{abs} = 0.7$ mJ/cm². This is a weak intensity far below damage threshold ($F_{thresh,abs} = 17$ mJ/cm²).⁴²

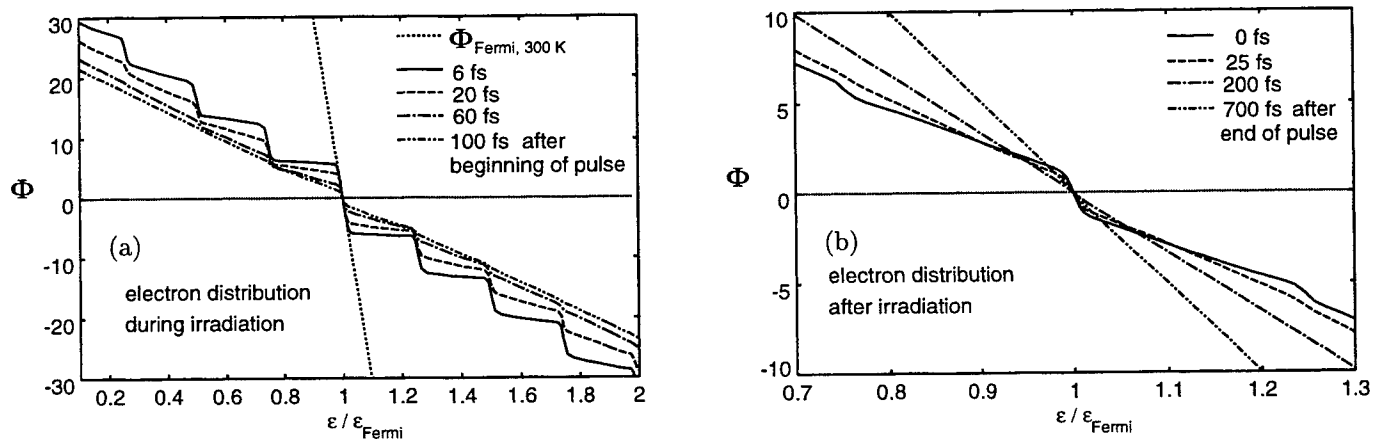


Figure 2. Distribution function of free electrons in aluminium during (a) and after irradiation (b). The quantity Φ , defined by equation (3) is shown as a function of electron energy. A laser pulse with constant intensity of $I_L = 7 \times 10^9$ W/cm² of 100 fs duration and a photon energy of $\hbar\omega_L = 1.97$ eV = $0.245 \varepsilon_{Fermi}$ was assumed.

A function Φ is shown in Fig. 2, which we defined as

$$\Phi(\varepsilon) := -\ln \left(\frac{1}{f(\varepsilon)} - 1 \right). \quad (3)$$

This function increases with increasing f and is especially suitable to visualize the perturbation of the electron gas: In thermal equilibrium, when electrons obey a Fermi-Dirac-distribution, $\Phi(\varepsilon)$ equals $(\varepsilon_{Fermi} - \varepsilon)/(k_B T_e)$. In this

case, $\Phi(\varepsilon)$ is a linear function with a slope proportional to the inverse electron temperature $1/T_e$. Thus, a deviation of the electron gas from thermal equilibrium is directly reflected in a deviation of $\Phi(\varepsilon)$ from a straight line.

In Fig. 2 (a) the strong perturbation of the electron distribution immediately after the begin of irradiation can be seen (solid line). In comparison to the straight line representing the Fermi distribution at 300 K, the absorption of photons lead to a step-like distribution function: Electrons below Fermi energy absorb photons, leading to an increase of the occupation number of electrons with energies up to $\hbar\omega_L$ above Fermi energy. Further absorption of photons by excited electrons lead to an increase of the occupation number for energies up to $2\hbar\omega_L$ above Fermi energy. The occupation number of electrons below Fermi energy decreases at the same rate, reproducing the Fermi edge in steps of $\hbar\omega_L$. A similar step-like electron distribution function for electrons above Fermi energy was found in Ref. 43. Experimentally the first plateau of excited electrons was observed in gold in Refs. 12, and theoretically reproduced in Ref. 44. Our log-like plot of the function $\Phi(\varepsilon)$ defined by (3) has the advantage that not only excited electrons above Fermi energy but also "holes" below Fermi energy can be observed.

Fig. 2 (b) shows the completion of electron thermalization around the Fermi edge after irradiation. A straight line in $\Phi(\varepsilon)$ and thus a Fermi distribution is established quickly after irradiation ended. Now the effect of electron-phonon interaction is also visible: Cooling of the hot electron gas leads to an increasing modulus of the slope of $\Phi(\varepsilon)$, corresponding to lower electron temperatures.

3.2. Absorption and energy exchange between electron gas and lattice

By integrating over the distribution function we find the internal energy of the subsystems at each time step. The increment of internal energy of electrons is given as

$$\delta u_e := u_e - u_e(f_{\text{Fermi},300\text{K}}) = \frac{2}{2\pi^2} \int_0^\infty (f(k) - f_{\text{Fermi},300\text{K}}) \frac{\hbar^2 k^2}{2m_e} k^2 dk . \quad (4)$$

The increment of internal energy of phonons, δu_p , is calculated analogously. The sum of both increments of internal energy gives the total absorbed energy, δu . The constancy of δu after irradiation provides a good check of numerical stability.

Fig. 3 shows the transient behavior of energy increase for the electron gas, the phonon gas and the total absorbed energy, respectively, for the case of excitation with a laser pulse of 100 fs duration and an intensity of $I_L = 7 \times 10^9 \text{ W/cm}^2$. The absorbed energy δu increases linearly during irradiation with constant intensity. In a recent publication¹⁴ we studied the absorption characteristics for different intensities. We found linear absorption corresponding to an exponential absorption profile. Also the strength of absorption compares very well with literature.

The energy increase of the electron gas δu_e follows the total absorbed energy, with a slight decrease due to energy transfer to the phonon gas during the pulse. After irradiation, energy transfer from the electron gas to the phonon gas continues until both systems have the same temperature. Because of the large difference in heat capacity, this corresponds to a much lower internal energy of the electron gas than that of the phonon gas. The absorbed energy δu_e of the laser excited electron gas corresponds to a Fermi distribution at $T_e = 3400 \text{ K}$. As also shown in Fig. 3 the rate of energy transfer from the disturbed electron gas to the phonon gas is essentially the same as the energy transfer rate from a hot electron gas with Fermi-Dirac distribution of the same initial energy, thus a starting temperature of $T_e = 3400 \text{ K}$. We extract an electron-phonon coupling constant α as used in the two-temperature model²¹ and obtain a value of $\alpha = 310 \times 10^{15} \text{ J/Ksm}^3$ for aluminium.

For weak excitations, however, we find that the two temperature model does not hold. In Figure 4 we assumed a laser intensity of $I_L = 5.8 \times 10^8 \text{ W/cm}^2$ leading to an energy increase of $\delta u_e = 5.5 \times 10^7 \text{ J/m}^3$, corresponding to a Fermi distribution at $T_e = 960 \text{ K}$. Figure 4 (a) shows that the initial cooling rate of the laser-heated electron gas is substantially lower than the cooling rate of the corresponding Fermi-distributed electron gas. This is due to the non-equilibrium of the laser-heated electron gas: At $t = 0$ the electron distribution functions interact with a phonon gas of about 300 K. Thus, at this moment the electron-phonon interaction acts on the electron gas in a way that it tends to establish Fermi distribution with 300 K. To this end, electrons above Fermi energy have to be transferred to states below Fermi energy. However, due to the small phonon energy, the phonons are able to act on the electrons only in a small region around Fermi's edge. The maximum phonon energy in the case of aluminium is about $0.08 \varepsilon_{\text{Fermi}}$.⁴⁰ Figure 4 (b) shows three distribution functions of the electron gas: the laser-excited electron gas

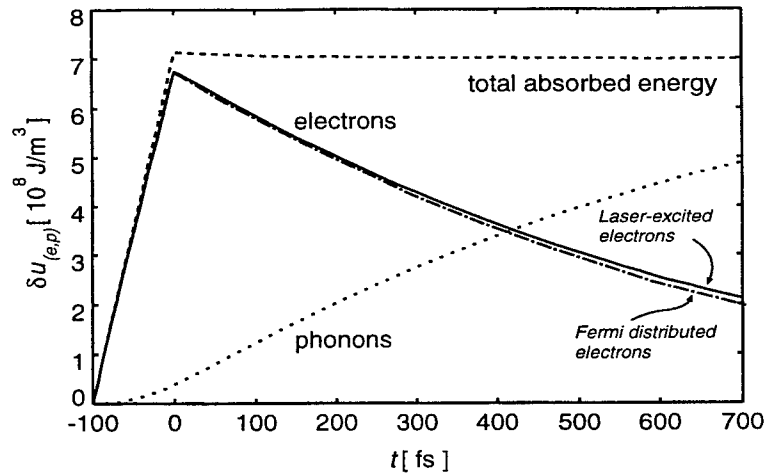


Figure 3. Transient energy increase of electron gas, δu_e , and of phonon gas, δu_p , respectively, and total absorbed energy δu . Additionally the cooling of a Fermi distributed electron gas is shown. The same laser parameters as in Fig. 2 were applied.

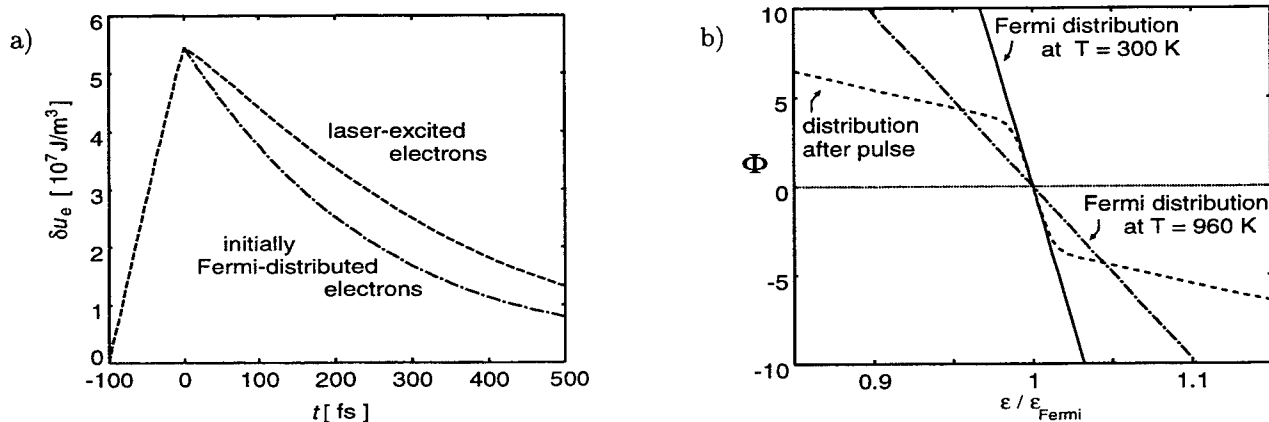


Figure 4. Weak excitations: a) Transient internal energy of laser-excited electron gas and of the corresponding hot Fermi distributed electron gas. b) Distribution function of laser-excited electron gas, the corresponding hot Fermi distributed electron gas and Fermi distributed electron gas at room temperature.

at the end of irradiation, the Fermi distributed electron gas of the same energy, and a Fermi distribution of 300 K. As before, the function $\Phi(\epsilon)$, defined by (3), is shown. In the region of one maximum phonon energy ($0.08 \epsilon_{\text{Fermi}}$) around Fermi energy the laser-excited electron gas shows nearly no deviation from the Fermi distribution at 300 K. Thus, the phonon action on the non-equilibrium electron gas is rather inefficient. In contrast, the corresponding Fermi distribution of a hot electron gas shows a large deviation from the Fermi distribution of 300 K. Therefore here the cooling by the cold lattice is much more efficient. This leads directly to the different cooling rates, i.e. different slopes of energy decay at $t = 0$ in Fig. 4 (a). Such delay of energy transfer to the lattice for a laser perturbed electron gas as compared to the two-temperature model was observed experimentally at low temperatures and for very low intensities.¹³

It is important to note that all intensities studied here are below melting threshold. Thus for laser pulses of moderate intensities about damage threshold and above, we conclude, that the energy exchange between electron gas and phonon gas can be described by the well-known two-temperature model.²¹ Note, that we did not consider

spatial behavior. Experiments indicate an effect of ballistic motion of hot electrons which are present for non-thermal energy distribution.⁴⁵

4. RESULTS FOR SiO₂

The calculations were performed for irradiation on SiO₂ with bulk-like material parameters. Bandgap, deformation potential and phonon energies were given by Arnold and Cartier.³⁷ The laser was assumed to have a wavelength of $\lambda = 500$ nm (photon energy $\hbar\omega_L = 2.48$ eV), an electric field amplitude of $E_L = 1.5 \times 10^{10}$ V/m (corresponding to an intensity of $I_L \sim 10^{14}$ W/cm²) and varying pulse length.

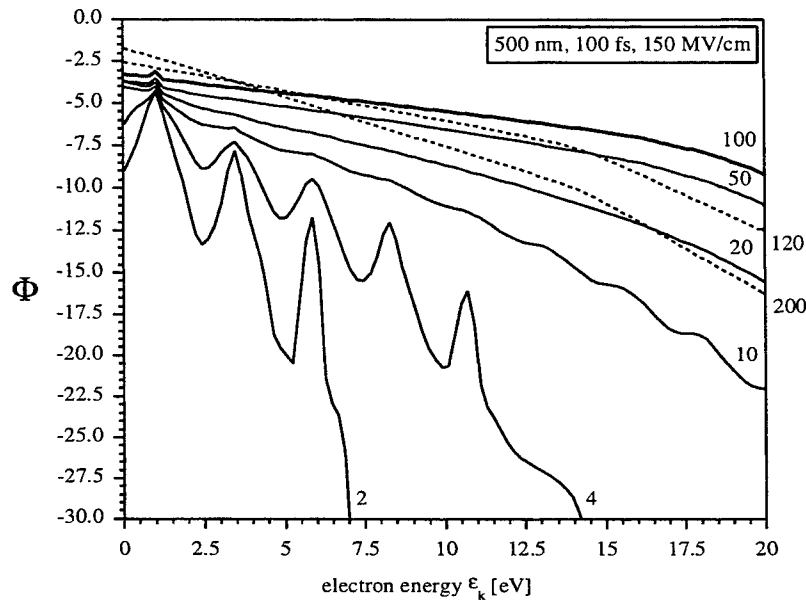


Figure 5. Time evolution of free electron occupation number in SiO₂ irradiated by a laser pulse of constant intensity and 100 fs duration. A log-like plot of occupation number as defined by equation (3) is shown. Solid lines show Φ during irradiation, dotted lines show Φ after the pulse is over. The numbers at the curves denote the time in femtoseconds after irradiation started.

The energy dependent evolution of the occupation number $f(\epsilon)$ of the electrons in the conduction band of SiO₂ is shown in Fig. 5, where the function $\Phi(f)$ defined by (3) is plotted. The numbers at the curves are the time in femtoseconds after irradiation started. The occupation number grows rapidly immediately after the beginning of irradiation. Strong-electric-field ionization leads to a δ -peak in the occupation number at the bottom of the conduction band i.e. for low kinetic energies. Some of these electrons absorb further photons, increasing the occupation numbers at regular distances of one photon energy. The peak-like structure is washed out at later times through relaxation processes (electron-electron and electron-phonon collisions). Strong-electric-field ionization continues during the pulse as well as single-photon absorption so that after several tens of femtoseconds a considerable amount of high-energetic electrons is observable. These high-energetic electrons may perform electron-electron impact ionization leading in turn to an increase of electron occupation number at the bottom of the conduction band. By this, a new excitation cycle may be started. After irradiation ended (dotted lines) impact ionization continues for a while. Now the ionization potential equals the bandgap, thus the critical energy is lower than during irradiation. This can be seen in Fig. 5. Additionally, electron-phonon interaction now leads to cooling of the electron gas, thus to an increasing modulus of the slope of $\Phi(f)$.

4.1. Role of ionization processes

Integrating over the electron distribution function, the density of free electrons may be calculated at each time step. Fig. 6 shows the evolution of the total free-electron density for two different pulse lengths, together with the

contributions of strong-electric-field ionization and impact ionization, respectively.

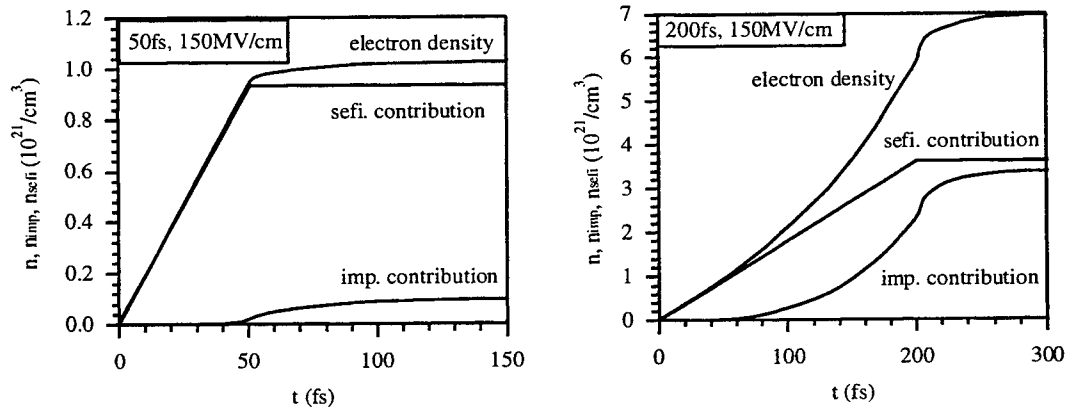


Figure 6. Time dependence of free-electron density and the contributing processes, i.e., strong-electric-field ionization and impact ionization.

For times $\lesssim 50$ fs the electron density increases linearly due to strong-electric-field ionization. Since the rate for strong-electric-field ionization is directly connected with the laser field^{23,32} such linear increase is expected. For impact ionization we expect an exponential increase of the free electron density, because each striking electron shifts a second electron into the conduction band. However, impact ionization becomes important only when a sufficient number of high-energy electrons is present in the conduction band. Therefore, as can be seen in Fig. 6, this process starts much later than strong-electric-field ionization. For very short pulses, free electrons have not enough time during the irradiation to continue absorbing laser energy until they are heated above the critical energy for impact ionization. In this case, the contribution of impact ionization to the electron density is negligible. If the laser pulse length is increased, the number of free electrons created by impact ionization also increases. But only for pulse lengths of 200 fs and more the contribution of impact electrons becomes comparable to the contribution of the strong-electric-field ionization.

In Ref. 32 we have shown that this result holds also for higher electric laser field. Both ionization processes occur at a higher rate for increasing electric field: while impact ionization increases through the avalanche effect of an increased free electron absorption, strong-electric-field ionization is directly connected with the laser intensity. For all applied pulse parameters, strong-electric-field ionization is the main process of free electron generation.

We performed calculations for varying parameters in the pre-breakdown regime.³² A free electron density of $n_c = 10^{21} \text{ cm}^{-3}$ was chosen as damage criterion.^{18,19} This density is somewhat below the critical plasma density, but in a range where calculated damage thresholds depend only weakly on the precise choice of n_c .^{32,40} We obtain damage thresholds of the same magnitude and of the same qualitative dependence on laser pulse duration as experimental results.^{18,46,19,20}

4.2. Description of impact ionization

For pulse lengths in the range of picoseconds, it is commonly assumed that impact ionization grows exponentially and can be described by

$$\partial n_{\text{imp}} / \partial t = \alpha(E_L) n, \quad (5)$$

where α is the so-called avalanche coefficient.^{19,20,37,25} Thus, the total electron density is assumed to change as

$$\frac{\partial n}{\partial t} = \dot{n}_{\text{sefi}}(E_L) + \alpha(E_L) n, \quad (6)$$

with the rate of strong-electric-field ionization $\dot{n}_{\text{sefi}}(E_L)$. For a laser pulse with constant electric field, a constant density increase due to strong-electric-field ionization is expected, which is confirmed by Fig. 6. The density contribution of impact ionization is assumed to grow exponentially. In other words, the *rate* of impact ionization $\partial n_{\text{imp}} / \partial t$

is assumed to be a linear function of the free-electron density n . This is not the case for pulse length below ~ 200 fs as shown by the solid line in Fig. 7 b) and in Ref. 32.

The main reason for the failure of equation (5) is that energy effects are not included in the description of impact ionization. For comparably long pulse durations in the picosecond regime, a stationary shape of distribution function is reached,³⁷ thus justifying an averaging description depending solely on the free-electron density like (5). On this time scale, the necessity for the colliding free electron to have an energy above critical energy can be neglected since the one-photon absorption occurs on a much shorter time scale of about ten femtoseconds (cf. Fig. 5). However, for shorter pulse lengths the shape of the free-electron distribution function changes strongly during irradiation and the probability of one-phonon absorption has to be included.

A first approximation for an equation system considering the energy dependence of impact ionization consists of two equations: one for the density of electrons with kinetic energies below critical energy ε_c , and one for the density of electrons with kinetic energies above ε_c . We denote these densities with $n_<$ and $n_>$, respectively. The equation system reads as follows:

$$\begin{aligned}\frac{dn_<}{dt} &= \dot{n}_{\text{sefi}} + 2 \alpha_{\text{imp}} n_> - S_{\text{seq}} , \\ \frac{dn_>}{dt} &= S_{\text{seq}} - \alpha_{\text{imp}} n_> .\end{aligned}\tag{7}$$

Here, \dot{n}_{sefi} is the rate of strong-electric-field ionization, contributing only to the density of low-energy electrons $n_<$. Impact ionization is described with a coefficient α_{imp} . This process leads to loss of one high-energy electron and gain of two low-energy electrons. The term S_{seq} describes the loss of low energy electrons which, after sequential one-photon absorption, reach energies above critical energy and thus contribute to the density $n_>$.

For the presented case of irradiation of SiO₂ with a laser of 500 nm wavelength and an electric field amplitude of $E_L = 150$ MV/cm, the rate of strong-electric-field ionization \dot{n}_{sefi} can be assumed as constant with a value of $\dot{n}_{\text{sefi}} = 0.0184 \times 10^{21} \text{ fs}^{-1} \text{ cm}^{-3}$ as follows from Fig. 6. Furthermore we assume that (5) can describe the rate of impact ionization also for shorter pulses if considering only those electrons with energy above critical energy as done in Eq. (7). Equation (5) is valid for long pulse lengths. When a stationary shape of free-electron distribution function is reached, the coefficient α_{imp} becomes solely dependent on the electric laser field.³⁷ As a first approximation we apply a constant α_{imp} at constant laser intensity also on shorter time scales and determine its value by the calculated asymptotic behaviour of $\dot{n}(n)$ as $\alpha_{\text{imp}} = 0.007 \text{ fs}^{-1}$.

The term of sequential one-photon absorption S_{seq} may be estimated as follows. Let $W_{1\text{pt}}$ be the probability of one-photon absorption, and ℓ the number of photons a free electron with zero kinetic energy has to absorb to reach critical energy for impact ionization, thus ℓ is the integer above $\varepsilon_c/\hbar\omega_L$. In principle density evolution due to sequential one-photon absorption should be denoted in ℓ equations, each reading $dn_i/dt = W_{1\text{pt}}n_{i-1} - W_{1\text{pt}}n_i$, where n_i is the density of electrons having kinetic energies of $i \times \hbar\omega_L$. In this notation, n_0 is the density of electrons at the bottom of the conduction band, where the strong-electric-field ionization provides a gain of free electrons. Considering only the positive term in the above equations for dn_i/dt and assuming $W_{1\text{pt}}$ as constant we integrate all densities n_i , $i = 0 \dots \ell - 1$ to the density $n_<$; and n_ℓ equals $n_>$. Thus we can approximate the rate for sequential one-photon absorption $dn_>/dt = n_<W_{1\text{pt}}(W_{1\text{pt}}t)^{\ell-1}/(\ell-1)!$. This is an overestimation since we neglected the loss-term in the equations for dn_i/dt and summarize all densities n_i , $i < \ell$ to $n_<$. By this we also disregard the fact that the ionized electrons have low kinetic energies and start the sequential one-photon-absorption at later times $t > 0$. A cruel approach for the term S_{seq} in equation (7) can be chosen as

$$S_{\text{seq}} = \min \left\{ n_<W_{1\text{pt}} \frac{(W_{1\text{pt}}t)^{\ell-1}}{(\ell-1)!} , \dot{n}_{\text{sefi}} + 2 \alpha_{\text{imp}} n_> \right\}\tag{8}$$

to avoid negative densities $n_<$. One can easily see that if S_{seq} equals the second term in (8), the equation system (7) reduces to (6). This case is reached for times $t \gg W_{1\text{pt}}^{-1}$. The probability of one-photon absorption $W_{1\text{pt}}$ can be estimated by the full collision term of electron-phonon-photon absorption which is given in Ref. 32. The approximation reads

$$W_{1\text{pt}} \approx \frac{2\pi}{\hbar\varepsilon_c} \langle M_{ep}^2 \rangle \langle J_{\pm 1}^2 \rangle_\mu ,\tag{9}$$

where $\langle M_{ep}^2 \rangle$ is the average matrix element of electron-phonon interaction which is estimated as 0.07 eV^2 for SiO_2 . $\langle J_{\pm 1}^2 \rangle_\mu$ is an average of Bessel's function with the argument $x_J = e q_D E_L / (m_e \omega_L)$ (with Debye's wave vector q_D) which gives the probability of photon absorption during an electron-phonon collision and can be fitted by the expression $\langle J_{\pm 1}^2 \rangle_\mu \approx (1 - \exp(-x_J/2))^2$. We obtain a probability of one-photon absorption $W_{1pt} \approx 4.3 \times 10^{13} \text{ s}^{-1}$, thus on time scales on the order of $W_{1pt}^{-1} \approx 25 \text{ fs}$ and below the effect of sequential one-photon absorption has to be included in the description and equation system (7) provides a better approximation than (6).

In Fig. 7 we show the solution of the system (7) (dashed lines) in comparison with the detailed microscopical calculation of Section 4.1 (solid lines) and the solution of the simple rate equation (6) (dotted lines). In Fig. 7 a) the

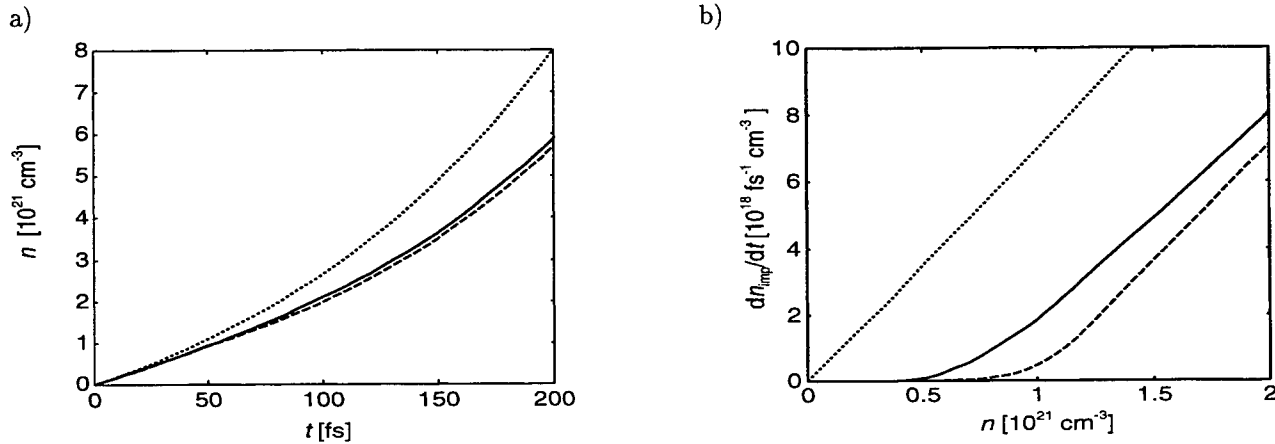


Figure 7. Comparison of the evolution of the free electron density calculated with the full microscopical model (solid lines), the simple rate equation (6) (dotted lines) and the extended system of two rate equations (7) (dashed lines). The left figure a) shows the total free electron density; the right figure b) shows the rate of impact ionization in dependence on the total free electron density.

evolution of total free electron density is shown for the first 200 fs. Since the electric laser field is assumed as constant, shorter pulse lengths are included as cuttings at the corresponding time value. The evolution of electron density and the final value are reproduced by the equation system (7) in very good agreement with the full microscopical calculation. The solution of (7) shows the initial constant increase due to strong-electric-field ionization, as well as the later exponential increase by impact ionization. The simple rate equation (6) overestimates the final free electron density. At the applied laser field, the overestimation is not that striking, since the term (5) is comparatively small in equation (6). The main advantage of the new equation system becomes clear when comparing the density contribution of impact ionization $\partial n_{\text{imp}}/\partial t$. Fig. 7 b) shows the contribution of impact ionization in dependence on the total density for the first $\sim 100 \text{ fs}$ (up to a total free electron density of $n = n_{<} + n_{>} = 2 \times 10^{21} \text{ cm}^{-3}$) for the simple rate equation (5), the new proposed two-equation system (7) and the full microscopical approach of Section 4.1, respectively. The evolution of the impact ionization rate $\alpha_{\text{imp}} n_{>}$ calculated by the equation system (7) is in reasonable agreement with the detailed microscopical calculation of Section 4.1. The main features of initially (for low electron densities) depressed rate and a constant rate only for later times (for higher electron densities) are qualitatively reproduced.

Keep in mind that the new equation system (7) and the rate of sequential one-photon-absorption (8) are first and rather rough approximations. The system (7) represents a possibility to include in a simple equation system the effect of kinetic electron energy and shows therefore, in contrast to (5), the correct behavior of free electron density development also for ultrashort pulse duration. Further studies are needed to confirm the applicability of the proposed equation system (7) for different intensities. The rate S_{seq} according to (8) has to be verified. Moreover the empirical parameters \dot{n}_{sefi} and α_{imp} should be connected with the corresponding full collision integrals to allow their estimation from known material parameters.

5. SUMMARY AND CONCLUSION

We have presented a theoretical model for the calculation of the distribution function of the free electron gas in a solid, irradiated by an ultrashort laser pulse. For the case of a metal we have considered absorption by inverse Bremsstrahlung, electron-electron collisions and electron-phonon coupling. For the case of an insulator two additional processes were included, these are strong-electric-field ionization (multiphoton ionization and, for higher intensities, tunnel ionization) and electron-electron impact ionization. Each microscopical process were considered by corresponding collision terms. No relaxation times or other phenomenological parameters were introduced. The resulting time- and energy-dependent system of equations was solved numerically. We have chosen aluminium as representative of a metal and SiO₂ for modelling of an insulator.

The results show in detail the transient excitation and relaxation of the free electron gas as well as the energy exchange between electrons and phonons. For the case of metals we found that for weak excitations the energy transfer from electron gas to lattice is influenced by the non-equilibrium of the laser-excited electron gas. In contrast, for stronger excitations (about damage threshold and above) thermalization occurs rapidly and electron-phonon coupling can be described by the two-temperature model without modification. For insulators we found, that the main process generating a free electron gas is strong-electric-field ionization. We showed that for irradiation with pulses of less than about 100 fs duration, impact ionization can not be described by simple rate equations. We proposed an extended system of rate equations which considers the energy dependence of impact ionization and thus shows the correct qualitative behavior of ionization rate. Further studies are needed to confirm the applicability of the proposed model for different laser intensities and to verify the applied parameters.

ACKNOWLEDGMENTS

We are grateful to K. Sokolowski-Tinten and D. von der Linde for helpful discussions and valuable suggestions.

REFERENCES

1. S. I. Anisimov, A. M. Bonch-Bruevich, M. A. El'yashevich, Y. A. Imas, N. A. Pavlenko, and G. S. Romanov, *Sov. Phys. Tech. Phys.* **11**, pp. 945–952, January 1967.
2. S. I. Anisimov, V. A. Bendetskii, and G. Farkas *Sov. Phys. Usp.* **20**, p. 467, 1977.
3. J. G. Fujimoto, J. M. Liu, E. P. Ippen, and N. Bloembergen, *Phys. Rev. Lett.* **53**, pp. 1837–1840, 1984.
4. J. P. Girardeau-Montaut and C. Girardeau-Montaut, *Phys. Rev. B* **51**(19), pp. 13560–13657, 1995.
5. M. B. Agranat, S. I. Anisimov, and B. I. Makshantsev, *Appl. Phys. B* **55**, p. 451, 1992.
6. P. Stampfli and K. H. Bennemann, *Phys. Rev. B* **49**, p. 7299, 1994.
7. L. A. Falkovsky and E. G. Mishchenko, *JETP Lett.* **66**(3), pp. 208–213, 1997.
8. P. B. Allen, *Phys. Rev. Lett.* **59**, pp. 1460–1463, September 1987.
9. X. Y. Wang, D. M. Riffe, Y.-S. Lee, and M. C. Downer, *Phys. Rev. B* **50**, pp. 8016–8019, September 1994.
10. S. I. Anisimov and B. Rethfeld, *Proc. SPIE - Int. Soc. Opt. Eng. (USA)* **3093**, pp. 192–203, 1996.
11. C.-K. Sun, F. Vallée, L. H. Acioli, E. P. Ippen, and J. G. Fujimoto, *Phys. Rev. B* **50**, pp. 15337–15344, 1994.
12. W. S. Fann, R. Storz, H. W. K. Tom, and J. Bokor, *Phys. Rev. B* **46**, pp. 13592–13595, 1992; *Phys. Rev. Lett.* **68**, pp. 2834–2837, 1992.
13. R. H. M. Groeneveld, R. Sprik, and A. Lagendijk, *Phys. Rev. B* **45**, pp. 5079–5082, 1992; *Phys. Rev. B* **51**, pp. 11433–11445, 1995.
14. B. Rethfeld, A. Kaiser, M. Vicanek, and G. Simon, *Appl. Phys. A* **69** [Suppl.], pp. S109–S112, 1999.
15. N. Bloembergen, *IEEE J. Quantum Electron.* **QE-10**(3), p. 375, 1974.
16. B. G. Gorshkov, A. S. Epifanov, and A. A. Manenkov, *Sov. Phys. JETP* **49**, pp. 309–314, February 1979.
17. A. A. Manenkov and A. M. Prokhorov, *Sov. Phys. Usp.* **29**, pp. 104–122, January 1986.
18. D. von der Linde and H. Schöler, *J. Opt. Soc. Am.* **B13**, pp. 216–222, January 1996.
19. B. C. Stuart, M. D. Feit, S. Herman, A. M. Rubenchik, B. W. Shore, and M. D. Perry, *Phys. Rev. B* **53**, pp. 1749–1761, January 1996.
20. M. Lenzner, J. Krüger, S. Sartania, Z. Cheng, W. K. Ch. Spielmann, G. Mourou, and F. Krausz, *Phys. Rev. Lett.* **80**(18), p. 4076, 1998.
21. S. I. Anisimov, B. L. Kapeliovich, and T. L. Perel'man, *Sov. Phys. JETP* **39**, pp. 375–377, August 1974.
22. M. I. Kaganov, I. M. Lifshitz, and L. V. Tanatarov, *Sov. Phys. JETP* **4**, pp. 173–178, March 1957.

23. L. V. Keldysh, *Sov. Phys. JETP* **10**, pp. 509–518, 1960.
24. L. V. Keldysh, *Sov. Phys. JETP* **20**, pp. 1307–1314, 1965.
25. A. Tien, S. Backhus, H. Kapteyn, M. Murnane, and G. Mourou, *Phys. Rev. Lett.* **82**(19), p. 3883, 1999.
26. B. C. Stuart, M. D. Feit, A. M. Rubenchik, B. W. Shore, M. D. Perry, *Phys. Rev. Lett.* **74**, pp. 2248–2251, 1995.
27. D. W. Snoke, W. W. Rühle, Y.-C. Lu, and E. Bauser, *Phys. Rev. B* **45**, pp. 10979–10989, May 1992.
28. R. Binder, H. S. Köhler, M. Bonitz, and N. Kwong, *Phys. Rev. B* **55**(8), p. 5110, 1997.
29. N. Ashcroft and N. Mermin, *Solid State Physics*, Saunders College Publishing, 1976.
30. J. F. Seely and E. G. Harris, *Phys. Rev. A* **7**(3), p. 1064, 1973.
31. E. M. Épshtein, *Sov. Phys. Solid State* **11**, pp. 2213–2217, April 1970.
32. A. Kaiser, B. Rethfeld, M. Vicanek, and G. Simon, *Phys. Rev. B* **61**(17), pp. 11437–11450, 2000.
33. J. M. Ziman, *Electrons and Phonons*, Oxford University Press, 1962.
34. D. Arnold, E. Cartier, and D. J. DiMaria, *Phys. Rev. B* **49**, p. 10278, 1994.
35. A. Kaiser, “Energieeinkopplung und -relaxation in Isolatoren bei Bestrahlung mit Subpikosekunden-Laserpulsen.” Diploma Thesis, TU Braunschweig, 1998.
36. B. Ridley, *Quantum Processes in Semiconductors*, Clarendon Press, Oxford, 1993.
37. D. Arnold and E. Cartier, *Phys. Rev. B* **46**, pp. 15102–15115, December 1992.
38. C. Kittel, *Introduction to Solid State Physics*, John Wiley & Sons, 1956.
39. I. S. Grigorev and E. Z. Mejlikhov, “*Fizicheskie Velichini*.” Moskau Energoatomizdat, 1991.
40. B. Rethfeld, *Mikroskopische Prozesse bei der Wechselwirkung von Festkörpern mit Laserpulsen im Subpikosekundenbereich*. PhD thesis, TU Braunschweig, Germany, <http://opus.tu-bs.de/opus/volltexte/2000/118>, 1999.
41. N. W. Ashcroft and J. W. Wilkins, *Physics Letters* **14**, p. 285, 1965.
42. J. Bialkowski, “*Femtosekunden-Laserinduzierter Materialabtrag*.” PhD Thesis, Uni Essen, Germany, 1998.
43. A. V. Lugovskoy, T. Usmanov, and A. V. Zinoviev, *J. Phys. D: Appl. Phys.* **27**, pp. 623–633, 1994.
44. D. Bejan and G. Raseev, *Phys. Rev. B* **55**(7), pp. 4250–4256, 1997.
45. J. Hohlfeld, J. G. Müller, S.-S. Wellershoff, and E. Matthias, *Appl. Phys. B* **64**, pp. 387–390, 1997.
46. H. Varel, D. Ashkenasi, A. Rosenfeld, R. Herrmann, F. Noack, and E. E. B. Campbell, *Appl. Phys. A* **62**, pp. 293–294, 1996.

Formation of electromagnetic shock waves on optical cycle during propagation of femtosecond laser pulses in transparent solids

Vitali E. Gruzdev*, Anastasia S. Gruzdeva
State Research Center «S.I.Vavilov State Optical Institute»
Birzhevaya Liniya 12, St.Petersburg, 199034, Russia

ABSTRACT

There is considered formation of shock electromagnetic waves (SEW) of visible spectral range as possible nonlinear optical phenomenon taking place at laser intensity close to damage threshold induced by femtosecond laser pulses in transparent solids. Main regularities of SEW formation are studied on the basis of 1D model of plane-wave propagation in isotropic dielectric with nonlinear optical response and dispersion. Special attention is paid to influence of color dispersion on SEW formation and propagation. Necessary conditions for appearing of SEW are obtained, in particular, threshold amplitude is estimated. There is presented a model for numerical study of SEW formation and propagation influenced by dispersion of linear and nonlinear parts of effective refractive index. Using the simulation, we studied dynamics of SEW formation on several optical cycles near leading edge of femtosecond laser pulse propagating in transparent medium. Important observed features of SEW are discussed.

Key words: femtosecond laser pulses, transparent materials, shock electromagnetic waves, nonlinear propagation, femtosecond laser-induced damage

1. INTRODUCTION

Two main characteristic features of femtosecond laser pulses make nonlinear processes induced by them very different from similar processes induced by longer pulses: very high laser intensity (damage threshold is above 10^{13} W/cm² [11-17]) and very small pulse duration. Laser-induced variations of refractive index are relatively large at laser intensity close to damage threshold that is a reason to come back to concept of shock electromagnetic waves (SEW) which appeared in high-frequency electrodynamics 45 years ago [1-4] and was not accepted in nonlinear optics [5, 6]. New understanding and models of nonlinear material response [7, 8] allow now more correct consideration of influence of two factors extremely important for SEW appearing – dispersion of linear and nonlinear parts of refractive index and absorption.

Important reason to consider high-power nonlinear propagation of femtosecond pulses and possibility of SEW formation is connected with one of main problems of femtosecond laser-matter interactions that is unclear mechanism of energy transfer from radiation to materials. That is especially true for the case of laser ablation and damage of transparent materials by femtosecond pulses. Any studying of femtosecond laser-matter interactions with transparent materials should start with consideration of nonlinear pulse propagation and accompanying optical phenomena because they determine conditions of energy deposition to electron and phonon systems and, thus, conditions of material modification. In spite of that obvious point many investigators of femtosecond interactions use simple models of pulse propagation (mainly, plane monochromatic wave model) suitable for linear propagation only.

The nonlinear optical phenomenon to be considered in this paper is formation and propagation of shock electromagnetic wave that occurs on optical cycle due to generation of higher harmonics. For the case of positive nonlinear addition to refractive index, brief picture of mechanism of SEW formation is as follows. Radiation-induced nonlinear response of the medium increases refractive index of the medium and results in slowing down the part of optical cycle corresponding to large electric or magnetic field strength (point 1 in Fig. 1). Bottom part of wave profile (2 in Fig. 1) moves with unperturbed speed of light in the material, i. e., faster than top part of wave profile. That process results in distortion of wave profile (Fig. 1) in such a way that top of the profile “falls down” onto the region of the profile where electric-field strength is small and which moves behind the top. That leads to appearing of very abrupt field variation within length much smaller than wavelength what looks like disruption and step of field strength. The step is referred to as SEW front. In general, there is no exact disruption, and structure of SEW front should be studied with taking into account complicated mechanism of dispersion and wave-energy dissipation near SEW front [1-3, 7, 8]. Picture of SEW

* Phone: (81272) 246-22, Fax +7-81272-246-22, E-mail: gru@mailbox.alkor.ru

formation is similar in case of negative field-induced variation to refraction: the top part of wave cycle moves faster and overtakes the nearest bottom part of the profile, then the top part falls onto the forth-going bottom part of wave cycle.

One should distinguish several types of shock waves referred to in literature [1-6, 9, 10]. Historically, SHEW of megahertz frequency range was the first to be revealed in late 50-s and was being intensively investigated in 60-s [1 - 3]. Mechanism of its formation is similar to that described above. Main feature of SHEW of MHz frequency domain is that nonlinear response for electromagnetic pulses of MHz frequency is nonlinear magnetic response in ferromagnetic [1 - 3]. Other type of shock wave that has been studied since late 60-s is self-steepening of slowly-varying amplitude of optical pulse (Fig. 2) [4, 6, 9, 10]. It has been observed for optical pulses propagating in fibers [9] and is now being intensively studied in connection with study of propagation of femtosecond laser pulses [10]. Important feature of self-steepening is dominating contribution of dispersion of linear and nonlinear parts of refractive index in process of its formation [10].

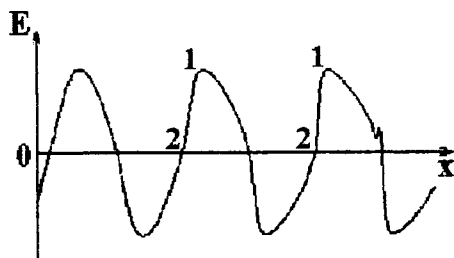


Fig. 1. Sketch of deformation of plane-wave profile during formation of shock electromagnetic wave in nonlinear medium with positive nonlinear addition to refractive index.

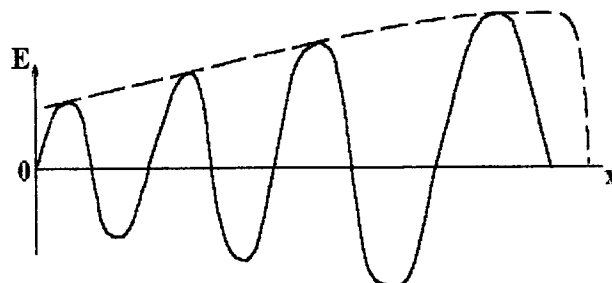


Fig. 2. Sketch of self-steepening process – formation of shock wave for slowly-varying amplitude of laser pulse shown by dashed line.

Self-steepening of laser pulses is not considered below because of the following reason. Self-steepening of pulse envelope is observed in cases when material dispersion plays dominating role and small nonlinear distortions are incubated along long path passed by laser pulse in nonlinear medium. In such conditions threshold of SHEW is much larger than that of self-steepening. In turn, considered SHEW must have smaller threshold and dominate self-steepening in focal area for conditions typical of tight focusing of high-power laser beams in transparent materials [11-17] when laser intensity and laser-induced nonlinear distortions of refraction are large in focal area. On the other hand, path of effective nonlinear interaction in transparent material in this case is much smaller than dispersion length [10] and nonlinear distortions can dominate refractive-index dispersion. The SHEW under consideration is referred to as optical SHEW. Obtained estimation of SHEW threshold shows that this type of SHEW can appear near leading edge of femtosecond laser pulse. Because of that, we start with brief review of experimental facts connected with interaction of high-power femtosecond pulses with transparent materials. Then we consider general concept and specific features of optical SHEW. Key points are consideration of dispersion and absorption influence on SHEW and estimation of threshold for SHEW formation. Modeling of that process is considered also. We conclude with discussion of obtained results.

2. BRIEF REVIEW OF EXPERIMENTAL FACTS

All mentioned below experimental results to be used for estimations are concerned with processes induced by femtosecond laser pulses in transparent wide band-gap materials. *Characteristic parameters of laser radiation* are as follows:

- pulse duration $\tau_p = 900 \text{ fs} - 10 \text{ fs}$ [11 - 17];
 - laser wavelength in vacuum $\lambda_0 = 10.6 \mu\text{m} - \text{IR}$ [12] - $1.06 \mu\text{m}$ - $0.8 \mu\text{m}$ [11, 14] - $0.6 \mu\text{m}$ [17];
 - energy of laser quantum $h\nu$ 0.117 eV - 1.17 eV - 1.55 eV - 2.07 eV;
- | | | | |
|-----------|-------------------------|-------------|---|
| ↓ | ↓ | ↓ | ↓ |
| FE lasers | Nd ³⁺ :glass | Ti:sapphire | |
- type of laser
 - intensity of laser radiation at focal plane 1) for self-focusing and white-light generation $I_{\text{TH}}^* = 10^{12} - 10^{13} \text{ W/cm}^2$ [10, 18], 2) for laser-induced damage and ablation $I_{\text{TH}}^{**} = 10^{13} - 10^{14} \text{ W/cm}^2$ [11 - 17];
 - focal spot radius $r_F = 1 \mu\text{m} - 10^2 \mu\text{m}$ [11 - 17], what allows estimating of beam path s in nonlinear material along which nonlinear interaction is the most effective: $s \approx 2z_c - \pi r_F^2 / \lambda - (10 - 3 \cdot 10^4) \lambda$, typical value of s is $(10 - 100) \lambda$;
 - repetition rate (for multi-pulse damage and ablation) from 10 Hz to 10^9 Hz (pulse trains [12]).

Materials used in experiments are wide band-gap semiconductors and dielectrics which typical band gap is 3 or more times larger than photon energy [11 - 17]: $E_g \geq 3h\nu$. Characteristic value of nonlinear coefficient of refraction is about $n_2 \approx$

$10^{-16} \text{ cm}^2/\text{W}$. Linear constant part of refractive index n_0 for most of considered materials varies between 1.45 and 3. Many of investigated materials are isotropic, for example, fused silica and glasses of various types. Looking through papers with experimental data, one can find that often used material for femtosecond laser-induced damage and ablation is fused silica which parameters are as follows: $E_g = 7.5 \text{ eV}$ [18], $n_0 = 1.45$, $n_2 = 2 \cdot 10^{-16} \text{ cm}^2/\text{W}$, absorption $\alpha \approx 10^{-3} \text{ cm}^{-1}$, group velocity dispersion coefficient $\beta = 385 \text{ fs}^2/\text{cm}$ [10].

For further estimations we can use the following experimental data: length of effective nonlinear interaction path is about 15λ (corresponds to focal spot radius 2.285λ) what is $11.85 \mu\text{m}$ for laser wavelength $0.79 \mu\text{m}$ and $45 \mu\text{m}$ for laser wavelength $3.0 \mu\text{m}$ [12]. For pulse duration 100 fs effective dispersion length in glass BK-7 or fused silica [10] is about 6.5 cm. Thus, the path of effective nonlinear interaction is at least 1000 times less than dispersion length and group velocity dispersion can be neglected in the first approximation. Photon energy is 1.55 eV for the most typical laser wavelength $0.8 \mu\text{m}$. Thus, six photons should be absorbed to ionize a center in fused silica. For wavelength $3.0 \mu\text{m}$ photon energy is 0.413 eV, thus, 20 photons should be absorbed to produce ionization.

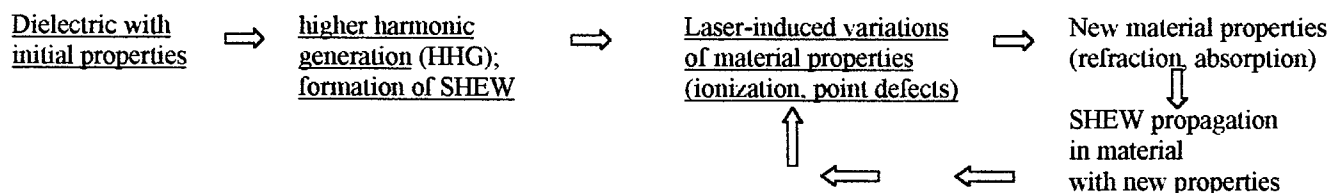
Considering nonlinear optical effects, we concentrate on experimental data connected with effects of nonlinear laser-pulse propagation in transparent media and do not touch results on laser-induced heating and ablation that are considered in other our paper [19]. *Typical regularities of nonlinear femtosecond-pulse propagation in transparent materials* are as follows:

1. Very high damage threshold ($10^{13} - 10^{14} \text{ W/cm}^2$) [11 - 17]. Such thresholds are observed practically for all tested materials, and they vary little for different materials. Laser-induced variations of refraction at laser fluences close to damage threshold are about $\Delta n_{NL} = n_2 I_{TH} \approx 0.1 - 0.01$.
2. White-light generation [10, 18] during propagation of femtosecond laser pulses in transparent materials. Spectrum analysis shows appearing of Stokes and anti-Stokes broadening of central laser line, and anti-Stokes wing of the spectrum of generated white light is about an order of magnitude longer than Stokes wing [18]. White-light generation is observed only for with materials band gap exceeding certain value showing threshold band-gap dependence [18].
3. Thresholds of self-focusing and white-light generation are the same in all transparent materials. [18]. That points at important connection between self-focusing and generation of white light that has not got clear explanation [18].
4. Most femtosecond interactions as well as propagation of femtosecond pulses are accompanied by generation of higher harmonics. In case of isotropic materials the harmonics are odd and can be of very high order (21-st – 27-th harmonics observed in [20]).
5. Detection of laser-induced damage is connected with one of important problems – what process should be taken as a signal of damage onset. Correct investigations [11, 13] shows that bulk laser-induced femtosecond damage of transparent solids includes several stages, each with its characteristic threshold. Formation of plasma comes before irreversible changes take place, and threshold of plasma formation is the lowest among all other thresholds. Next process is formation of invisible single-shot and multi-shot damage which threshold is higher than that of plasma formation. Appearing of visible laser-induced damage and irreversible fall of transparency have the highest threshold that is about 10 times higher than that for plasma formation. Electron plasma can appear at pulse tail and change its propagation sufficiently by specific dispersion [21]. For example, plasma formation results in conical emission effect [21], cut of self-focusing [18].

3. PHYSICAL AND MATHEMATICAL MODEL

2.1. General concept of optical SHEW

In general case, formation and propagation of SHEW is a self-consistent problem because high-power laser beam changes optical properties of the transparent material, where it propagates, and those changes result in variation of beam parameters in self-consistent manner. For example, ionization results in increasing of absorption by free electrons and color centers, while electron plasma also changes dispersion of refractive index. That is illustrated by the following scheme.



Analysis of that self-consistent problem should be based on solution to system of coupled nonlinear equations describing high-power wave propagation (nonlinear wave equation) and material response. Together with usual description of linear and nonlinear optical response, the correct material equations must describe possible phase transitions, laser-induced changes of material structure (e.g., excitation and relaxation of electron plasma and related processes, formation of vacancies and color centers) and variations of optical parameters resulting from those processes. Even deducing of correct material equations presents difficult problem, not to say about solving that system of coupled nonlinear equations.

To start, we reduce self-consistent problem to a couple of independent problems:

- 1) electrodynamical propagation problem - formation and propagation of SHEW in dielectric with constant properties to be studied in this paper;
- 2) interaction problem - processes induced by unperturbed SHEW (which space distribution and time evolution are results of solving of the first problem) in dielectric - to be studied in paper [19].

Several comments should appear in connection with this reducing to independent problems. First, that description can be applied to initial stage of SHEW formation and to a small leading part of laser pulse (first few periods of laser radiation only) where laser-induced variation of material parameters are small enough to be neglected. Duration of leading part of laser pulse to be considered is determined by characteristic time of laser-induced plasma excitation up to the level when it gives sufficient distortions to pulse propagation [21]. That time is about 15-20 fs. Plasma excitation is assumed to be the fastest process, other laser-induced processes of material parameters modification have longer excitation time and their influence on nonlinear processes at leading edge of laser pulse can be neglected. Thus, throughout this paper we consider only few (about 10) first cycles of femtosecond laser pulse.

Second, natural result of such reducing to independent problems is breaking of energy conservation law: energy transferred from SHEW to electrons (ionization and absorption by electrons) and crystal lattice (formation of point defects [19]) is not taken into account within this approximation. Thus, some energy appears in material and leads to its modification while nothing disappears from SHEW. On the other hand, neglecting of energy dissipation at SHEW front results in formation of non-steady SHEW. Two points should be mentioned in this connection: 1) the energy dissipating from SHEW to material is assumed to be small enough at leading part of laser pulse not to influence sufficiently on SHEW propagation; 2) presented consideration is the first approximation to exact solution while calculated in [19] absorption rate will be used to estimate energy dissipation in further approximations.

3.2. Basic equations for description of SHEW formation and propagation

Efficient formation of SHEW can take place at laser intensity close to 10^{13} W/cm², i.e., close to damage threshold. Thus, electric field strength is high enough to induce nonlinear electrodynamic effects in solids. On the other hand, generation of higher harmonics results in significant broadening of radiation spectrum. Thus, even the simplest model of polarization response of considered solid must take into account dispersion of polarization response and nonlinear optical properties. In this paper properties of SHEW and its formation and propagation are studied on the basis of the simplest model of 1D propagation of high-power plane homogeneous wave. Advantages of that 1D model are 1) relatively simple equations describing considered below SHEW allowing to obtain rigorous solutions for some particular cases, 2) possibility to compare obtained results with some rigorous solutions to problems of 1D nonlinear wave propagation and shock wave formation [5 - 9], and 3) relatively low computational resources (in particular, computer memory) required for modelling of SHEW formation.

Nonlinear wave propagation is described by full wave equation including material polarization and linear frequency-independent absorption:

$$\frac{\partial^2 E}{\partial t^2} - c_0^2 \frac{\partial^2 E}{\partial z^2} = -4\pi \frac{\partial^2 P}{\partial t^2} - \frac{4\pi\sigma}{\epsilon_0} \cdot \frac{\partial E}{\partial t}. \quad (1)$$

Wave equation (1) should be coupled with a system of nonlinear equations describing material response P to laser field consisting of fast P_e (electronic) and slow P_i (ionic) components:

$$P = P_e + P_i. \quad (2)$$

Each of them includes linear and nonlinear contributions. Considering input pulse of arbitrary wavelength range that can be close to vibrational absorption band (area of anomalous dispersion of refraction) or electronic absorption band (area of normal dispersion of refraction), one should also take into account frequency-dependent contributions to absorption.

Description of polarization variations in time must give correct dispersion law for both linear and nonlinear parts of

refractive index in all considered spectrum range. One of the simplest models for that is phenomenological model of two parametrically coupled oscillators [7, 22] which gives the same functional form of dispersion as quantum-mechanical three-level model [22]. According to that model, laser-induced variations of polarization have contributions from linear and nonlinear vibrations of electrons and ions and are described by the following four equations:

$$\frac{\partial P_e}{\partial t^2} + \frac{2}{T_e} \cdot \frac{\partial P_e}{\partial t} + \omega_e^2 P_e = \alpha_e E + \beta_e (R_e + R_i) E \quad (3)$$

$$\frac{\partial P_i}{\partial t^2} + \frac{2}{T_i} \cdot \frac{\partial P_i}{\partial t} + \omega_i^2 P_i = \alpha_i E \quad (4)$$

$$\frac{\partial R_e}{\partial t^2} + \frac{2}{T_{e1}} \cdot \frac{\partial R_e}{\partial t} + \omega_{e1}^2 R_e = \gamma_e (P_e + P_i) E \quad (5)$$

$$\frac{\partial R_v}{\partial t^2} + \frac{2}{T_v} \cdot \frac{\partial R_v}{\partial t} + \omega_v^2 R_v = \gamma_v (P_e + P_i) E \quad (6)$$

These equations describe polarization contributions from vibrations of optical electrons (3) and ions (4) excited straightway by laser electric field as well as contributions from secondary vibrations of valence electrons (5) and ions (6) excited by vibrations of electrons and ions. That allows to take into account electronic and electron-vibrational contributions to nonlinear optical response and correct description of Raman and *inertia-free* Kerr nonlinear response. Two-photon absorption is also included into polarization response deduced from (3) – (6). With suitable parameters, dispersion law obtained from (3) – (6) describes real dispersion of linear part of refractive index of transparent materials with accuracy of 0.01% within full transparency band [7]. We do not touch details of two-oscillator model for description of polarization dispersion, which can be found in papers [7, 22].

As it is well known, all processes of SHEW formation and evolution can be divided into two groups – slow processes and fast processes [1, 2]. Characteristic space and time scales for slow processes are much larger than laser wavelength λ_0 in vacuum and laser period T_0 while time and space scales of fast processes are much less than laser period and wavelength. Example of slow process is increasing of intensity of generated higher harmonics in space, slow accumulation of nonlinear distortions connected with generation of higher harmonics resulting in formation of abrupt SHEW front. That process takes from 10 to 100 of T_0 and develops within distances of (10 – 100) λ_0 . Fast processes are connected with SHEW front evolution due to energy dissipation and interplay between higher harmonics which characteristic time is less than $T_0/6$ and space scale is less than $\lambda_0/6$. Making use of (3)-(6), one can estimate what contributions play key role in developing of slow and fast processes. For both processes let us assume all frequencies ω giving sufficient contribution to SHEW formation to be between ionic and electronic absorption bands, i.e., the following condition must be satisfied:

$$\omega_i < \omega < \omega_e, \quad \omega_v < \omega < \omega_{e1}. \quad (7)$$

Applying Fourier integral transformation to (3) – (6), then applying perturbation technique to obtained expressions with respect to small parameters ω/ω_e , ω_i/ω , ω/ω_{e1} , ω_v/ω , and then applying inverse Fourier transformation to obtained perturbation series [7], one can obtain the following expression for polarization:

$$\begin{aligned} P = & \frac{\alpha_e}{\omega_e^2} E - \frac{\alpha_e}{\omega_e^4} \cdot \frac{\partial^2 E}{\partial t^2} + \alpha_i \int_0^t d\tau \int_0^\tau E(\tau') d\tau' - \frac{2\alpha_e}{\omega_e^4 T_e} \cdot \frac{\partial E}{\partial t} - \frac{2\alpha_i \omega_i}{T_i} \int_0^t d\tau \int_0^\tau d\tau' \int_0^{\tau'} E(\tau'', x) d\tau'' + \\ & + \frac{\beta_e \gamma_e \alpha_e}{\omega_e^4 \omega_{e1}^2} \cdot E^3 - \frac{\beta_e \gamma_e \alpha_e}{\omega_e^4 \omega_{e1}^2} \cdot \left(\frac{1}{\omega_e^2} + \frac{1}{\omega_{e1}^2} \right) \frac{\partial^2 E^3}{\partial t^2} + \frac{\beta_e \gamma_e \alpha_i}{\omega_e^2 \omega_{e1}^2} \cdot E^2 \int_0^t d\tau \int_0^\tau E(\tau') d\tau' + \\ & + \frac{\beta_e \gamma_e \alpha_e}{\omega_e^4 \omega_{e1}^2} \cdot \frac{\partial^2}{\partial t^2} \left\{ E^2 \int_0^t d\tau \int_0^\tau E(\tau') d\tau' \right\} \end{aligned} \quad (8)$$

The first, the second and the third terms in (8) give linear contributions to refractive index describing *inertia-free*, normal dispersive and anomalous dispersive contributions respectively. The fourth and the fifth terms describe polarization decay due to absorption corresponding to electron and vibrational transitions respectively. The sixth term gives *inertia-free* nonlinear response, the seventh, the eighth and the ninth terms correspond to nonlinear laser-induced contributions to refractive index describing their normal and anomalous dispersion. Omitted terms describe absorption appearing near vibrational and electronic absorption bands and high-order contributions to linear and nonlinear parts of refractive index. Each term in

(8) can be estimated using the following parameters, corresponding to experimental data for fused silica [7]: $\omega_e=2.096 \cdot 10^{16} \text{ s}^{-1}$, $\omega_i=2.154 \cdot 10^{14} \text{ s}^{-1}$, $\alpha_e=3.862 \cdot 10^{31} \text{ s}^{-2}$, $\alpha_i=2.534 \cdot 10^{27} \text{ s}^{-2}$, $\omega_{ei}=3.0 \cdot 10^{16} \text{ s}^{-1}$, $\omega_{ei}=8.3 \cdot 10^{13} \text{ s}^{-1}$, $\beta_e=2.0 \cdot 10^{43} \text{ esu}$, $\gamma_e=2.9 \cdot 10^9 \text{ esu}$, $\gamma_i=8.0 \cdot 10^3 \text{ esu}$. According to these data [7] omitted terms give about 5% contribution to the value given by (8), and they can be neglected in the first approximation. Among all terms in (8) only the first and the sixth terms give non-dispersive linear part and Kerr electronic nonlinearity of refractive index respectively.

Bearing in mind that possible length of SHEW formation (an order of 100 λ) is much less than dispersion length [10-17] for most focusing geometries of experiments [11-17], one can estimate values of different polarization contributions for "slow" processes. Omitting small terms in (8), one derives the following form of polarization response for "slow" processes:

$$P = \frac{\alpha_e}{\omega_e^2} E - \frac{2\alpha_e}{\omega_e^4 T_e} \cdot \frac{\partial E}{\partial t} + \frac{2\alpha_i \omega_i}{T_i} \int_0^t d\tau \int_0^\tau d\tau' E(\tau'', x) d\tau'' + \frac{\beta_e \gamma_e \alpha_e}{\omega_e^4 \omega_{ei}^2} E^3 + \frac{\beta_e \gamma_e \alpha_i}{\omega_e^2 \omega_{ei}^2} \cdot E^2 \int_0^t d\tau \int_0^\tau E(\tau') d\tau' + \frac{\beta_e \gamma_e \alpha_e}{\omega_e^4 \omega_{ei}^2} \cdot \frac{\partial^2}{\partial t^2} \left\{ E^2 \int_0^t d\tau \int_0^\tau E(\tau') d\tau' \right\} \quad (9)$$

As it was shown in [7], the last two terms in (9) can be neglected for consideration of field evolution within time less than 15 fs from leading edge of femtosecond pulse, what means that near the leading front of femtosecond pulse within 15 fs one can neglect all dispersion terms in material response and consider only *inertia-free* absorption and linear and nonlinear responses in the first approximation:

$$P_{slow} = \frac{\alpha_e}{\omega_e^2} E + \frac{\beta_e \gamma_e \alpha_e}{\omega_e^4 \omega_{ei}^2} E^3 - \frac{2\alpha_e}{\omega_e^4 T_e} \cdot \frac{\partial E}{\partial t} - \frac{2\alpha_i \omega_i}{T_i} \int_0^t d\tau \int_0^\tau d\tau' E(\tau'', x) d\tau'' \quad (10)$$

In particular, estimations of threshold of SHEW formation can be done with neglecting dispersion. For the part of laser pulse which is more than 15 fs far from its leading edge one should take into account at least the last two terms in (9) describing dispersion of nonlinear material response. Thus, SHEW can appear near leading edge of femtosecond pulse where absorption and nonlinear response dominates influence of dispersion.

In case of "fast" processes connected with evolution of SHEW front, general expression (8) can be reduced to the following form by neglecting small contributions:

$$P = \frac{\alpha_e}{\omega_e^2} E - \frac{\alpha_e}{\omega_e^4} \cdot \frac{\partial^2 E}{\partial t^2} + \frac{\beta_e \gamma_e \alpha_e}{\omega_e^4 \omega_{ei}^2} E^3 - \frac{\beta_e \gamma_e \alpha_e}{\omega_e^4 \omega_{ei}^2} \cdot \frac{\partial^2 E^3}{\partial t^2} - \frac{2\alpha_e}{\omega_e^4 T_e} \cdot \frac{\partial E}{\partial t} + \frac{\beta_e \gamma_e \alpha_e}{\omega_e^4 \omega_{ei}^2} \cdot \frac{\partial^2}{\partial t^2} \left\{ E^2 \int_0^t d\tau \int_0^\tau E(\tau') d\tau' \right\} \quad (11)$$

This expression includes two terms (the second and the fourth) describing dispersion of linear and nonlinear responses to be taken into account. Thus, slow process of SHEW formation is dominated by nonlinear Kerr electronic response while dispersion gives only small contributions (about 5% of inertia-free contributions to refractive index) which can be neglected in the first approximation. On the other hand, considering fast process of SHEW front evolution, one should take into account several terms describing dispersion of linear and nonlinear parts of refractive index.

3.3. Estimation of SHEW threshold

Estimating of threshold of SHEW formation is one of key problems because it allows to show applicability of proposed model to real situations. In case of dominating of nonlinear optical response one can neglect dispersion in the first approximation (section 3.2). Then that estimation can be obtained using the following simple consideration of field propagation in nonlinear isotropic medium with positive nonlinear index n_2 .

Let us consider a part of instantaneous profile of electric field with amplitude E_0 , propagating in nonlinear medium (Fig. 3a). Field disruption appears if point 1 of the profile with field value $E_0 - \Delta E$ has overtaken profile's top 2. That is possible because laser-induced addition to refractive index is larger at point 2 than at point 1, so, profile maximum slows down itself.

We consider not moving coordinate system which x-axis coincides with direction of wave propagation. If Δt is duration of moving of point 1 in nonlinear medium then coordinates of points 1 and 2 in the medium are respectively $x_1 - \Delta t \cdot u_1$ and $x_2 = \Delta x + \Delta t \cdot u_2$, where

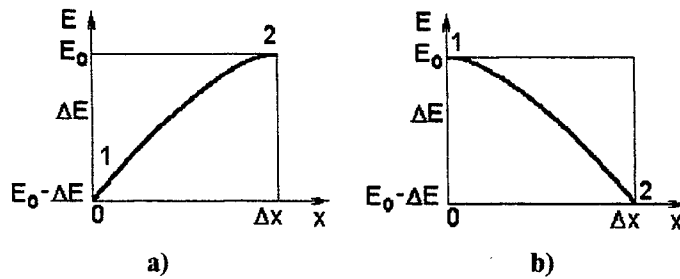


Fig. 3. A part of instant profile of laser wave near its maximum at the beginning of SHEW formation in nonabsorbing dielectric with positive (a) and negative (b) nonlinear coefficient of refractive index.

$$u_2 = \frac{c_0}{n_0 + n_2 E_0^2}, \quad u_1 = \frac{c_0}{n_0 + n_2 (E_0 - \Delta E)^2}, \quad (12)$$

c_0 - is light speed in vacuum, $n_0^2 = \epsilon_0$. According to the mentioned above $u_1 = u_2 + \Delta u$ and $u_1 > u_2$. If field-induced addition to refractive index is smaller than n_0 , we can apply perturbation technique to (12) and take into account only terms linear with respect to ΔE . The coordinates of points 1 and 2 will be the same at some moment $t + \Delta t$: $x_1 = \Delta t \cdot u_1 = x_2 = \Delta x + \Delta t \cdot u_2$. Duration of disruption formation Δt can be estimated from the expression: $1/\Delta t = u/\Delta x$, which implies the following:

$$\frac{1}{\Delta t} = \frac{2n_2 F_0}{n_0 + n_2 E_0^2} u_2 \frac{\partial E}{\partial x}, \quad (13)$$

where $u_2 = c_0 / (n_0 + \Delta n)$ - is speed of profile's maximum and $\Delta E / \Delta x \cong \partial E / \partial x$. Starting at moment t , the maximum have passed distance $s = u_2 \Delta t$ in nonlinear medium by the moment $t + \Delta t$ that gives the following equation for E_0

$$F_0^2 \frac{n_2}{s} - F_0 \cdot 2n_2 \frac{\partial E}{\partial x} + \frac{n_0}{s} = 0. \quad (14)$$

Solution to the equation exists only if the following condition is satisfied

$$\left| \frac{\partial E}{\partial x} \right| \frac{s}{2} \geq \sqrt{\frac{n_0}{n_2}}. \quad (15)$$

This condition shows that field disruption cannot appear at arbitrary point of field profile, for example, at profile's top where derivative $\partial E / \partial x$ is about zero. At the same time the disruption cannot appear far from the top where field magnitude is too small. Integrating of (14) gives estimation for threshold field-amplitude of disruption formation:

$$E_{th} \approx \sqrt{\frac{n_0}{n_2} \left(\exp\left\{ \frac{\Delta x}{s} \right\} - 1 \right)}, \quad (16)$$

where $\Delta x \leq s$. Expression (16) can be rewritten as

$$E_{th}^2 \cdot n_2 = \Delta n_{NL} = I_{th} \cdot \gamma \approx n_0 \cdot \left(\exp\left\{ \frac{\Delta x}{s} \right\} - 1 \right), \quad (17)$$

what implies the following estimation for threshold intensity I_{th} :

$$I_{th} \approx \frac{n_0}{\gamma} \cdot \left(\exp\left\{ \frac{\Delta x}{s} \right\} - 1 \right). \quad (18)$$

For example, disruption threshold is $I_{th} \leq 9.46 \cdot 10^{13} \text{ W/cm}^2$ for $n_0 = 1.41$, $\gamma = 2 \cdot 10^{-16} \text{ cm}^2/\text{W}$ (fused silica), $s = z_c = 15 \lambda_0 \ll L_{DISP}$, $\Delta x = 0.2 \lambda_0$. Confocal parameter corresponds to focal spot radius $d_f = 2.185 \lambda_0 (= 6.555 \mu\text{m}, \lambda_0 = 3.0 \mu\text{m})$.

Similar consideration is valid for negative nonlinear coefficient of refractive index. In this case top of field profile (Fig. 3b) can overtake a part of the profile moving at distance Δx in front of the top, i.e., geometry of this problem is reversed with respect to that depicted in Fig. 3a and point 1 corresponds to profile's. This implies the points 1 and 2 to move with the following speeds

$$u_1 = \frac{c_0}{n_0 - n_2 E_0^2}, \quad u_2 = \frac{c_0}{n_0 - n_2 (E_0 - \Delta E)^2}. \quad (19)$$

Similar consideration shows that disruption threshold can be estimated in the following way:

$$E_{th} \approx \sqrt{\frac{n_0}{n_2} \left(1 - \exp \left\{ -\frac{\Delta x}{s} \right\} \right)} \quad (20)$$

Obtained estimations (16), (18) and (20) show that SHEW can appear at laser intensities ranging between 10^{13} W/cm² and 10^{14} W/cm² that are close to threshold of femtosecond laser-induced damage in transparent materials. That is very pessimistic estimation of SHEW threshold because 1) we considered formation of very hard SHEW corresponding to mesh of $\frac{1}{4}$ of initial optical cycle, 2) the path of nonlinear interaction s can be larger than the value used in numerical estimations. Optimistic estimation of SHEW threshold is about 10^{12} W/cm².

3.4. Influence of color dispersion

Very simple estimation of influence of dispersion on SHEW formation can be obtained in the following way. Let us consider central wavelength of input pulse to be 3.0 μm . Then 15-th harmonic has wavelength 0.200 μm , and it is within transparency band [x]. Refractive index values corresponding to main harmonic and the 15-th harmonic are 1.41925 and 1.55051 respectively [x, xx]. Phase difference between those harmonics appearing during their propagation along x-axis is given by

$$\Delta\varphi = 2\pi \cdot (n_{15} - n_1) \cdot \frac{x}{\lambda_0}, \quad (21)$$

where n_{15} and n_1 are values of refractive index for corresponding harmonics. If phase difference $\Delta\varphi = \pi$ corresponds to dephasing of those harmonics, then distance $x \cong 10\lambda_0$ is required to get dephasing. This rough estimation is close to the value of effective pathway required for SHEW formation that was used in previous section for numerical estimations of SHEW threshold. One can also expect strong influence of laser-induced dispersion resulting from periodic space modulations of refractive index by main harmonic. Analysis of that type of dispersion presents independent problem and will be presented by the authors in a separate paper.

4. SIMULATION OF SHEW FORMATION AND PROPAGATION

4.1. FDTD technique for modeling

More detailed information on SHEW formation and propagation can be obtained from modelling and numerical calculations according to model (1)-(6). The most promising technique for that type of modelling is *finite-difference time domain technique* (FDTD) [24-25]. A very brief description of calculation method used by the authors is given in this section because FDTD has already been described many times [26, 27].

Simulation method used by the authors is based on dependence of field magnitude at fixed time-space point on field magnitudes at previous moments in neighboring points. The dependence is derived from nonlinear differential wave equation (1) by reducing it to a finite-difference equation in traditional way [26, 27]. So, the following updating finite-difference equation is obtained

$$E_x^t = 2E_{x-1}^{t-1} - E_{x-1}^{t-2} + \frac{(c_0 \cdot \Delta t)^2}{(\Delta x)^2} \left(E_{x+1}^{t-2} - 2E_x^{t-1} + E_{x-1}^t - \frac{4\pi}{c_0^2} \left((P_{x-1}^{t-1})^3 - 2(P_x^{t-2})^3 + (P_{x+1}^{t-3})^3 \right) \right), \quad (22)$$

where Δx is period of regular spatial mesh, and Δt is corresponding time increment. The obtained dependence describes field evolution in medium with certain parameters if field source is given. Using of the model (2)-(6) to describe dispersion of refractive index allows to avoid the problem of appearing of field disruptions during SHEW formation because dispersion smoothens the disruptions and makes structure of SHEW front more complicated. The only problem is to take into account enough contributions from higher harmonics that is connected with problem of resolution discussed below.

Similar finite-difference equations can be derived from (3) – (6) and attached to (22) to solve a consequence of coupled equations. Field evolution is observed in the form of animation that can be stopped at any appropriate time. Outgoing waves are described by functions of the following type: $F(x-ct)$ at exit boundary of space grid and $E_s + F(x+ct)$ at entrance boundary. This allows to exclude artificial reflection and calculation mistakes at the boundaries. E_s is source field which is assumed to be as follows $E_s = E_0 \sin(2\pi t / \nu)$. This source describes normal incidence of plane linearly polarized monochromatic wave of amplitude E_0 and frequency ν onto plane surface of considered medium.

For stability of calculations to be obtained the calculation procedure is subjected to the following well-known criterion[28]

$$c \cdot \Delta t < \Delta x, \quad (23)$$

where Δx - is space grid period, and Δt - is corresponding time increment. This allows to exclude increasing of calculation mistakes. In our modeling we chose the ratio $\Delta x / (c \Delta t)$ to be 2 that implies number of time "cells" per laser period to be two times more than number of space "cells" per laser wavelength. Calculation stability was also controlled through energy conservation law by integrating of squared electric field over all calculation mesh and calculating of energy flows.

Space resolution of our calculations varied from 200 to 800 cells of spatial mesh per radiation wavelength in vacuum to give appropriate resolution. Development of field disruptions and SHEW is investigated with resolution 200 cells per wavelength. That resolution was chosen from the following estimations. Minimum number of space cells per wavelength to catch certain harmonic correctly is 5 that correspond to the following points of wave: zero point - point of maximum - zero point - point of minimum - zero point. Thus, space resolution allows to describe correctly harmonics of the order no higher than $200/5=40$, i.e., the first higher harmonic we loose in modeling of SHEW formation and propagation is the 41-st harmonic. Its contribution to total field is similar to accuracy of our calculations (about 0.01% of field amplitude) and it can be neglected. That was also confirmed by calculations with space resolution of 400 cells (catching of upto 80-th harmonic) and 800 cells per wavelength (catching of upto 160-th harmonic). Full length of calculation space is 25 laser wavelengths in vacuum, i.e., 5000 calculation cells for resolution of 200 cells per wavelength.

To determine accuracy of developed simulation model, it has been tested in case of linear light propagation through boundary of two transparent dielectrics with different refractive indexes and plane dielectric layer (Fabri-Perout resonator). Results of calculations are in excellent agreement with well-known theoretical results [29] within accuracy of ($\pm 0.01\%$).

4.2. SHEW formation in transparent solids

First, process of SHEW formation was studied by numerical modelling. Fig. 4 depicts a snapshot of instant field profile in nonabsorbing medium. Appearing and evolution of SHEW is clearly seen from that figure. Large-scale variations of electric field are depicted in Fig. 5 as snapshot of instant field distribution in larger part of calculation mesh. Interesting point is relatively fast decay of total electric-field strength in nonabsorbing (!) medium. That is connected with energy transfer to higher harmonics and energy spreading due to dispersion.

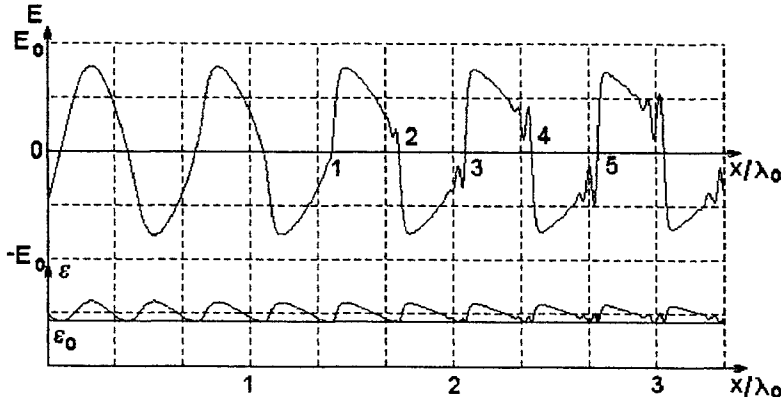


Fig. 4. Evolution of SHEW propagating in non-absorbing dielectric (fused silica, $n_0=1.41$). Points of interest: 1 - appearing of disruption of space derivation of electric-field strength on wave profile (weak SHEW); 2 - formation of disruption of electric-field strength (strong SHEW) and formation of field variations near SHEW front; 3, 4, 5 - developing of SHEW front and formation of high-frequency pulsation near it resulting from higher harmonics generation. Laser-induced variation of dielectric response is shown in the lower part of this figure. Input field amplitude is above damage threshold in order to obtain good illustrative picture with fast SHEW formation (high-frequency pulsations can not be made out in the picture otherwise).

The last question to be considered in this paper is higher harmonic (HH) generation during SHEW formation in transparent materials. Calculations of radiation spectrum are based on straight Fourier transformation of field variations in time for selected space points. For example, Fig. 6 depicts spectrum of SHEW propagating in nonabsorbing dielectric with $\varepsilon_0=1.9881$ after it has passed 6-wavelength path in nonlinear medium (Fig. 6 is related to situation depicted in Fig. 5). One can see only odd harmonics that is characteristic of shock wave of arbitrary nature propagating in material with small energy dissipation and dispersion [1-4, 30, 31]. Characteristic features are also fast decreasing of amplitudes of low-order harmonics with increasing of their order and nonmonotonous decreasing of amplitudes of high-order harmonics - local maxima of harmonics amplitudes appear with period of 6 harmonics (Fig. 6). Spectrum structure has no steady form and varies within whole path of SHEW propagation. General trend of the variations is connected with dominating energy transfer back to main harmonics and fast decay of higher harmonics. Thus, there must be a path of SHEW propagation that

corresponds to the most efficient excitation of higher harmonics.

Fig. 5. SIEW formation and propagation in transparent non-absorbing dielectric (fused silica) with linear dielectric response $\epsilon_0=1.9881$. Grey line in upper part of the figure depicts boundary between vacuum and the dielectric. Resolution 400 calculation cells per laser wavelength.

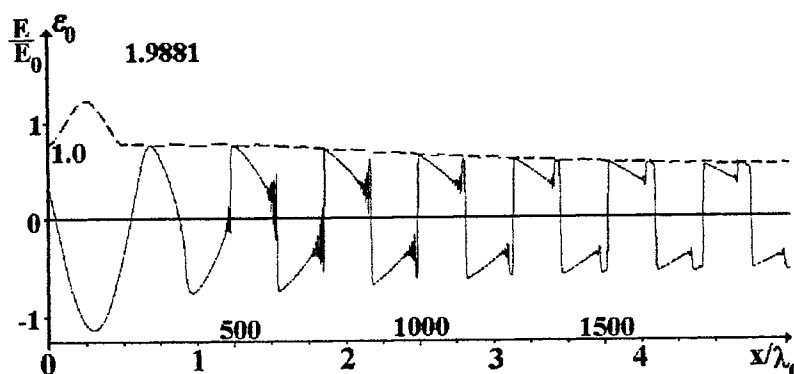
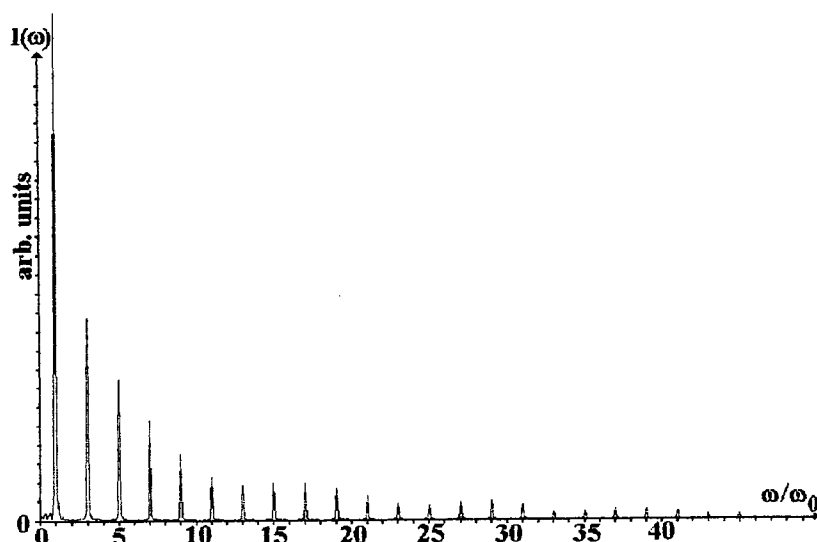


Fig. 6. Spectrum of SIEW propagating in non-absorbing dielectric (fused silica). Obtained after SIEW has passed 6-wavelength distance in the medium. Space resolution of modelling is 200 cells per wavelength, resolution of spectrum calculations is 10% of central frequency ω_0 of input laser pulse. That resolution is kept for all calculated spectra presented below.



5. CONCLUSIONS

Thus, we have shown that SIEW on optical cycle resulting from generation of higher harmonics can appear at certain conditions characteristic of femtosecond pulse propagation in transparent media. SIEW can appear only near leading edge of femtosecond laser pulse where influence of dispersion is minimal. This makes leading-edge form of the pulse of critical importance for process of SIEW formation. Presented results were obtained for rectangular pulses where this problem disappears but it can be critical for pulses with smooth leading front. Important point in this connection is self-steepening process resulting in sharpening of leading front [10] and making it closer to rectangular form. SIEW formation gives one of important examples of processes where exact wave equation (1) must be applied for investigation of nonlinear optical processes because of possible presence of backward moving waves reflected from laser-induced variations of refractive index. Possibly, being based on (1), analysis of high-power nonlinear optical processes induced by femtosecond laser pulses will give better agreement of theoretical results with experimental data.

Important result is also estimation of threshold of SIEW formation. It is interesting that SIEW can appear only at parts of wave front where space derivation of electric-field strength is above certain threshold even if pulse intensity is above SIEW threshold. Estimated SIEW threshold shows that it can appear at laser intensity between threshold of white-light generation and damage threshold. In particular, SIEW can be formed at initial stages of femtosecond laser-induced damage of transparent materials. Important point is that SIEW threshold does not depend straight on laser wavelength while there is strong dependence on refractive index, its nonlinear coefficient and focusing geometry through parameter s .

Important features of SIEW show at least two ways to detect SIEW in experiments. The first of them is connected with specific spectrum structure of HH appearing during SIEW formation (Fig. 6). One can expect appearing of odd harmonics

(in isotropic materials) surrounded by Stocks and anti-Stocks wings at early steps of pulse propagation. Problem of the spectrum registration can be connected with developing of electron plasma which emission spectrum covers SHEW spectrum. Thus, pure SHEW spectrum can hardly be observed at times more than time of plasma formation (about 20 fs) and.

Other way of SHEW detection is connected with frequency shift of low-power probe beam [1-3] resulting from reflection at moving SHEW front. Nature of that shift is similar to well-known Doppler effect and can be calculated for two geometries of probe-beam reflection (Fig. 7) – when the beam propagates in the same direction as SHEW and when the probe beam propagates toward SHEW. In both cases transmitted and reflected parts of probe signal have different frequency shifts. For example, in case of probe beam propagating in the same direction as SHEW one can use the following formula for reflection at moving SHEW front

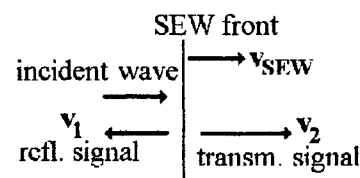
$$\frac{\omega^{refl}}{\omega_0} = \frac{v_2 - v_{SEW}}{v_2 + v_{SEW}} \quad (24)$$

and for transmission through SHEW front:

$$\frac{\omega^{trans}}{\omega_0} = \frac{1 + v_{SEW}/v_1}{1 + v_{SEW}/v_2} \quad (25)$$

where v_1 is light speed for probe signal in front of SHEW, and v_2 is light speed behind the SHEW (Fig. 7). Thus, detection of frequency shift of low-power probe beam reflecting at SHEW front allows both straight detection of SHEW and measurement of its speed. Having information about SHEW speed allows estimating value of field disruption at SHEW front.

Fig. 7. Geometry of low-power probe beam reflection at SHEW front resulting in frequency shift which depends on SHEW speed.



Influence of SHEW can help to explain many observed regularities of nonlinear propagation of femtosecond pulses. In particular, SHEW concept is very promising for theoretical investigation of non-thermal mechanisms of femtosecond laser-induced damage of transparent materials [19]. Generation of higher harmonics of extremely high orders is other promising application of SHEW model. As one can see from estimation (16), the larger laser intensity, the smaller path is required to form SHEW front and to generate HH. Thus, HH can appear even during reflection if laser intensity is much above SHEW threshold what is typical for experiments on HH generation by femtosecond pulses.

6. ACKNOWLEDGEMENTS

Authors wish to thank Prof. M.N.Libenson (S.I.Vavilov State Optical Inst., Russia) and Prof. S.A.Kozlov (State Inst. of Fine Mechanics and Optics, St.Petersburg - Technical University, Russia) for fruitful discussions of various aspects of shock waves. This work was partly supported by INTAS grant 97-31777 and grant of Russian Foundation for Basic Research N 00-02-16716-□.

7. REFERENCES

1. A.M.Beliantsev, A.V.Gaponov, G.I.Freidman, "Structure of shock electromagnetic wave front in transmission lines with nonlinear parameters", URSI Symposium, Delft, Nehterlands, 1965 in *Electromagnetic wave theory*, Pergamon Press, 1967.
2. A.V.Gaponov, L.A.Ostrovsky, M.I.Rabinovich, "Electromagnetic waves in non-linear transmission lines with active parameters", URSI Symposium, Delft, Nehterlands, 1965 in *Electromagnetic wave theory*, Pergamon Press, 1967.
3. G.B.Whiteham, "Nonlinear dispersive waves", *Proc. Roy. Soc., Ser. A*, v. **283**, 1965, p. 238
4. L.A.Ostrovsky, "Propagation of modulated waves in nonlinear dispersive media", URSI Symposium, Delft, Nehterlands, 1965 in *Electromagnetic wave theory*, Pergamon Press, 1967.
5. G.Rosen, "Electromagnetic Shocks and the Self-Annihilation of Intense Linearly Polarized Radiation in an Ideal Dielectric Material", *Phys. Rev.*, v. **139**, N 2A, pp. A539-A543, 1965.
6. F.DeMartini, C.H.Townes, T.K.Gustafson, P.L.Kelley, "Self-Steepening of Light Pulses", *Physical Review*, v. **164**, N

- 2, pp. 312-323, 1967.
7. S.A.Kozlov, S.V.Sazonov, "Nonlinear propagation of optical pulses with a few light oscillation duration in dielectric media", *JETP (Sov. Physics - JETP)*, v. **111**, N 2, pp. 404-418, 1997.
8. N.R.Belashenkov, V.V.Bezzubik, S.A.Kozlov, S.V.Sazonov, "Nonresonant self-action of pulses with a few light oscillation duration", in *Ultrafast Processes in Spectroscopy*, Plenum Publishing Corp., New York, p. 167-170, 1996.
9. J.E.Rothenberg, D.Grischkowsky, "Observation of the formation of an Optical Shock and Waves Breaking in the Nonlinear Propagation of Pulses in Optical Fibers", *Phys. Rev. Letters*, v. **62**, N 5, pp. 531-534, 1989.
10. J.K.Ranka, and A.L.Gaeta, "Breakdown of the slowly varying envelope approximation in the self-focusing of ultra-short pulses", *Opt. Letters*, v. **23**, N 7, pp. 534-536, 1998.
11. C.B.Schaffer, E.N.Glezer, N.Nishimura, and E.Mazur, "Ultrafast laser induced microexplosions: explosive dynamics and sub-micrometer structures", in *Commercial Applications of Ultrafast Lasers*, Proc. SPIE, v. **3269**, p. 36-45, 1998.
12. H.K.Park, R.F.Haglund Jr., "Laser Ablation and Desorption from Calcite from Ultraviolet to Mid-Infrared Wavelengths", *Appl. Phys. A*, v. **64**, pp. 431-438, 1997.
13. C.B.Schaffer, A.Brodeur, N.Nishimura, and E.Mazur, "Laser-induced microexplosions in transparent materials: microstructuring with nanojoules", Proc. SPIE, v. **3616**, 1999, to appear.
14. D.Ashkenasi, A.Rosenfeld, H.Varel, M.Wahmer, E.E.B.Campbell, "Laser processing of sapphire with picosecond and sub-picosecond pulses", *Appl. Surface Science*, v. **120**, pp. 65-80, 1997.
15. E.E.B.Campbell, D.Ashkenasi, and A.Rosenfeld, "Ultra-short-Pulse Laser Irradiation and Ablation of Dielectrics", in *Lasers in Materials*, edited by R.P.Agarwal (Trans Tech Publ., 1998), Ch. 5.
16. R.F.Haglund, Jr., "Mechanisms of Laser-Induced Desorption and Ablation", in *Laser Ablation and Desorption*, eds. J.C.Miller and R.F.Haglund, Jr. (Boston, Academic Press, 1998), pp. 15-138.
17. D.von der Linde, H.Schuler, "Breakdown threshold and plasma formation in femtosecond laser-solid interaction", *JOSA B*, v. **13**, N 1, pp. 216-222, 1996.
18. A.Brodeur, S.L.Chin, "Band-Gap Dependence of the Ultrafast White-Light Continuum", *Phys. Rev. Lett.*, v. **80**, N 20, pp. 4406-4409, 1998.
19. A.S.Gruzdeva, V.E.Gruzdev, "Interaction of shock electromagnetic waves with transparent materials: classical approach", in *Laser Applications to Microelectronic and Optoelectronic Manufacturing-VI*, Proc. SPIE, v. **3933**, 2000 (to appear).
20. A.Bouhal, R.Evans, G.Grillon, A.Mysyrowicz, P.Breger, P.Agostini, R.C.Constantinescu, H.G.Muller, D. von der Linde, "Cross-correlation measurement of femtosecond noncollinear high-order harmonics", *JOSA*, v. **14**, p. 950, 1997.
21. O.G.Kosareva, V.P.Kandidov, A.Brodeur, C.Y.Chien, S.L.Chin, "Conical emission from laser-plasma interactions in the filamentation of powerful ultrashort laser pulses in air", *Opt. Lett.*, v. **22**, N 17, pp. 1332-1334, 1997.
22. S.A.Kozlov, "On classical dispersion theory of high-power light", *Optics and Spectroscopy*, v. **79**, N 2, pp. 198-200, 1995 (translated from Russian *Optika i Spectroscopia*, v. **79**, N 2, pp. 290-292, 1995).
23. R.V.Hohlov, "On the theory of shock radio waves in nonlinear lines", *Radiotekhnika i Elektronika*, N 6, pp. 917-925, 1961 (in Russian).
24. V.E.Gruzdev, A.S.Gruzdeva, "Formation and propagation of shock electromagnetic waves in transparent solids", in *High-Power Ablation II*, Proc. SPIE, v. **3885**, 2000 (to appear).
25. V.E.Gruzdev, A.S.Gruzdeva, "Formation of shock electromagnetic waves during femtosecond pulse propagation in transparent solids", in *Optical Beam and Pulse Propagation*, Proc. SPIE, v. **3927**, 2000 (to appear).
26. K.S.Yee, "Numerical solution of initial boundary value problems in isotropic media", *IEEE Transactions on Antennas and Propagation*, **AP-14**, p.302, 1966.
27. S.J.Yakura, J.T.McGillivray, "Finite-Difference Time-Domain Calculations Based on Recursive Convolution Approach For Propagation of Electromagnetic Waves in Nonlinear Dispersive Media", Final Report PL-TR-97-1170, AF Research Laboratory, Kirtland AFB, NM, 30 October 1997.
28. N.N.Kalitkin, *Numerical Methods*, Nauka Publ., Moscow, 1978, Ch. XIII (in Russian).
29. M.Born, E.Wolf, *Principles of Optics*, 4-th ed. Pergamon Press, N.Y., 1968, Ch.1.6.
30. Ya.B.Zel'dovich, Yu.P.Raizer, *Physics of Shock Waves*, Academic Press, New York, v. I, 1966, v. II, 1968.
31. M.B.Vinogradova, O.V.Rudenko, A.P.Sukhorukov, *Theory of Waves*, Nauka, Moscow, 1990 (in Russian).

The paraxial (2+1)-dimensional self-focusing of extremely short pulses

Mikhail A. Bakhtin, Andrei N. Berkovsky, Sergei A. Kozlov and Yuri A. Shpolyanskiy*

Institute of Fine Mechanics and Optics, 14 Sablinskaya, St. Petersburg, 197101, Russia

ABSTRACT

A new wave equation for the electrical field evolution of intensive femtosecond light pulses in isotropic transparent media is presented. It is demonstrated that a "light bubble" can evolve from a few-optical cycle pulse propagating through a fused silica bulk. The two-octave spectrum supercontinuum is theoretically observed.

Keywords: ultrafast optics, ultrashort pulse, extremely short pulse, paraxial self-focusing, light bubble

1. INTRODUCTION

Recent advances of ultrafast laser technology have provided generation of pulses containing only a few light field oscillations¹. The (1+1)-dimensional dynamics of such extremely short pulses (ESP) in waveguide media has already been investigated². The (2+1)-dimensional nonlinear evolution of ESP in a fused silica bulk is studied in this paper. The ESP self-focusing is illustrated. It is shown that a femtosecond "light bubble" can arise.

2. THE WAVE EQUATION FOR EXTREMELY SHORT PULSES

The complete nonlinear equation for the electromagnetic wave in an isotropic dielectric medium, derived from the Maxwellian set, is

$$\Delta \vec{E} - \frac{1}{c^2} \frac{\partial^2 \vec{E}}{\partial t^2} = \frac{4\pi}{c^2} \frac{\partial^2 \vec{P}_L}{\partial t^2} + \frac{4\pi}{c^2} \frac{\partial^2 \vec{P}_{NL}}{\partial t^2}, \quad (1)$$

where \vec{E} is the electrical field; \vec{P}_L and \vec{P}_{NL} are the medium linear and nonlinear polarization responses, respectively; t is the time; c is the light speed in vacuum. In this paper we restrict ourselves to (2+1)-dimensional ESP dynamics, i.e. consider the Laplasian in the form $\Delta = \frac{\partial^2}{\partial z^2} + \frac{\partial^2}{\partial x^2}$, where z is the propagation direction; x is the transverse axe.

We assume the dependence of the linear refraction index on frequency to be

$$n_L^2(\omega) = N_0^2 + 2N_0a\omega^2 - 2N_0b\omega^{-2}, \quad (2)$$

where N_0 , a and b are empirical constants, permitting to describe both normal and abnormal group-delay dispersion (GDD) within a significant region of the medium transparency band².

The nonlinear polarization response of an isotropic medium with the dominating low-inertial electron nonlinearity can be written in the simplest form

$$\vec{P}_{NL} = \chi E^2 \vec{E} \quad (3)$$

for the case when frequencies in the pulse temporal spectrum are much less than the medium eigenfrequencies. Here χ is the cubic susceptibility concerned with nonlinear refraction index n_2 by the ratio²

$$n_2 = \frac{9\pi\chi}{N_0}. \quad (4)$$

* Correspondence: Email: shpolyan@phd.ifmo.ru

Using the dispersion relation (2) we can construct the linear part of the wave equation to be derived. Doing that and substituting the nonlinear response (3) we have the equation for a linearly polarized ESP:

$$\frac{\partial^2 E}{\partial z^2} + \frac{\partial^2 E}{\partial x^2} - \frac{N_0^2}{c^2} \frac{\partial^2 E}{\partial t^2} + \frac{2N_0}{c} a \frac{\partial^4 E}{\partial t^4} - \frac{2N_0}{c} b E - \frac{2N_0}{c} g E^2 \frac{\partial E}{\partial t} = 0, \quad (5)$$

where $g = \frac{6\pi\chi}{cN_0}$.

Taking a unidirectional approximation^{2,3} we can reduce (5) to the final equation:

$$\frac{\partial E}{\partial z} + \frac{N_0}{c} \frac{\partial E}{\partial t} - a \frac{\partial^3 E}{\partial t^3} + b \int_{-\infty}^t E d\tau + g E^2 \frac{\partial E}{\partial t} = \frac{c}{2N_0} \frac{\partial^2}{\partial x^2} \int_{-\infty}^t E d\tau. \quad (6)$$

To understand the essence of assumptions made let us compare the linear dispersion dependencies of the wave vectors k'_z from (6) and k_z from (5):

$$k'_z(\omega, k_x) = \frac{N_0}{c} \omega + a\omega^3 - \frac{b}{\omega} - \frac{c}{2N_0} \frac{k_x^2}{\omega}; \quad (7)$$

$$k_z(\omega, k_x) = \sqrt{\frac{N_0^2}{c^2} \omega^2 + \frac{2N_0}{c} a\omega^4 - \frac{2N_0}{c} b - k_x^2} \approx k'_z(\omega, k_x) \quad (8)$$

The approximate equality in (8) is performed when

$$\begin{cases} k_x^2 \ll k_z^2 \\ 2c(a\omega^2 - \frac{b}{\omega^2}) \ll N_0 \end{cases} \quad (9)$$

Thus, the unidirectional approximation here is equivalent to the combination of beam paraxial evolution and weak dispersion assumptions.

The ESP spatial-temporal distribution at the medium input is considered to be

$$E(z, x, t)|_{z=0} = E_0 \exp\left(-2 \frac{x^2}{\Delta x^2}\right) \exp\left(-2 \frac{t^2}{\Delta t^2}\right) \cos(\omega_0 t), \quad (10)$$

where E_0 is the peak value of the pulse electrical field; ω_0 is the carrier frequency; Δx is the beam cross-size; Δt is the pulse duration.

3. SELF-FOCUSING OF EXTREMELY SHORT PULSES

Numerical solution of the equation (6) for the input pulse with central wavelength $\lambda_0 = \frac{2\pi c}{\omega_0} = 780 \text{ nm}$; duration

$\Delta t = 10.4 \text{ fs}$; cross-size $\Delta x = 10\lambda_0$ and peak intensity $I = 7 \cdot 10^{12} \text{ W/cm}^2$, propagating in fused silica ($N_0 = 1.447$, $a = 2.47 \cdot 10^{-44} \text{ s}^3/\text{cm}$, $b = 3.4 \cdot 10^{17} \text{ cm}^{-1} \cdot \text{s}^{-1}$, $n_2 = 2.9 \cdot 10^{-16} \text{ cm}^2/\text{W}$)² is given in the Fig. 1. The pulse broadens in time and self-focuses in space under the combined action of dispersion, diffraction and nonlinearity. The self-focusing accumulates the field power in the beam center, thus supporting the self-phase modulation. A beam waist arises in the area of the biggest field value, but collapse does not occur.

The evolution of the pulse with input peak intensity $I = 2 \cdot 10^{13} \text{ W/cm}^2$ is shown in the Fig. 2-4. Other parameters are the same as above. The self-focusing here can be conditionally subdivided into two stages. In the near-input zone ($z < 0.1 \text{ mm}$) the power self-pumping to the beam center also takes place but more effectively to compare to the previous case. The

energy at the distance $z = 0.1 \text{ mm}$ in the beam central longitudinal section in a fused silica bulk (Fig. 3a) is twice as much as in a single-mode fiber of the same material (Fig. 3b). Nonlinear phenomena such as self-steepening (Fig. 3) and corresponding spectral supercontinuum generation (Fig. 4), typically observed in waveguide media at higher input intensities³, can be seen.

Starting from $z = 0.1 \text{ mm}$ the electrical field breaks down and filamentation occurs in the peak intensity area (Fig. 2). A "light bubble" develops from the pulse center. Two low-frequency cycles are isolated at the pulse leading edge. High-frequency components form the pulse tail. Spectrum supercontinuum width has an order of two octaves (Fig. 4).

Further input intensity increase leads to a consecutive splitting of filaments and formation of light structures with several energy emptinesses.

4. CONCLUSION

Thus, the (2+1)-dimensional wave equation for the electrical field evolution of intensive femtosecond light pulses in an isotropic transparent medium is given in the paper. Numerical simulations of the paraxial self-focusing of ESP with the input spectrum within a fused silica normal GDD region are presented. Two different self-focusing pathways are found. There is an input peak intensity range when beam waist arises in the fused silica bulk. A "light bubble" can be formed at higher intensities. It is shown that spectrum supercontinuum generation is more significant in a medium bulk than in a fiber of the same material.

ACNOWLEDGMENTS

The work was supported by the grant RP-2249 of the US Civilian Research and Development Foundation.

REFERENCES

1. Brabec Th., Krausz F., "Intense few-cycle laser fields: Frontiers of nonlinear optics", *Rev. Mod. Phys.* **72**, 2, pp. 545-591, 2000.
2. Bespalov V.G., Kozlov S.A., Oukrainski A.O., Sazonov S.V., Shpolyanskiy Yu.A., "Self-action of femtosecond pulses with continuum spectrum", *Proc. SPIE* **3735**, pp.43-54, 1999.
3. Belenov E.M., Nazarkin A.V., "Nonstationary diffraction effects with propagation of electromagnetic field clot in vacuum", *JETP* **53**, 4, pp. 188-191, 1991.

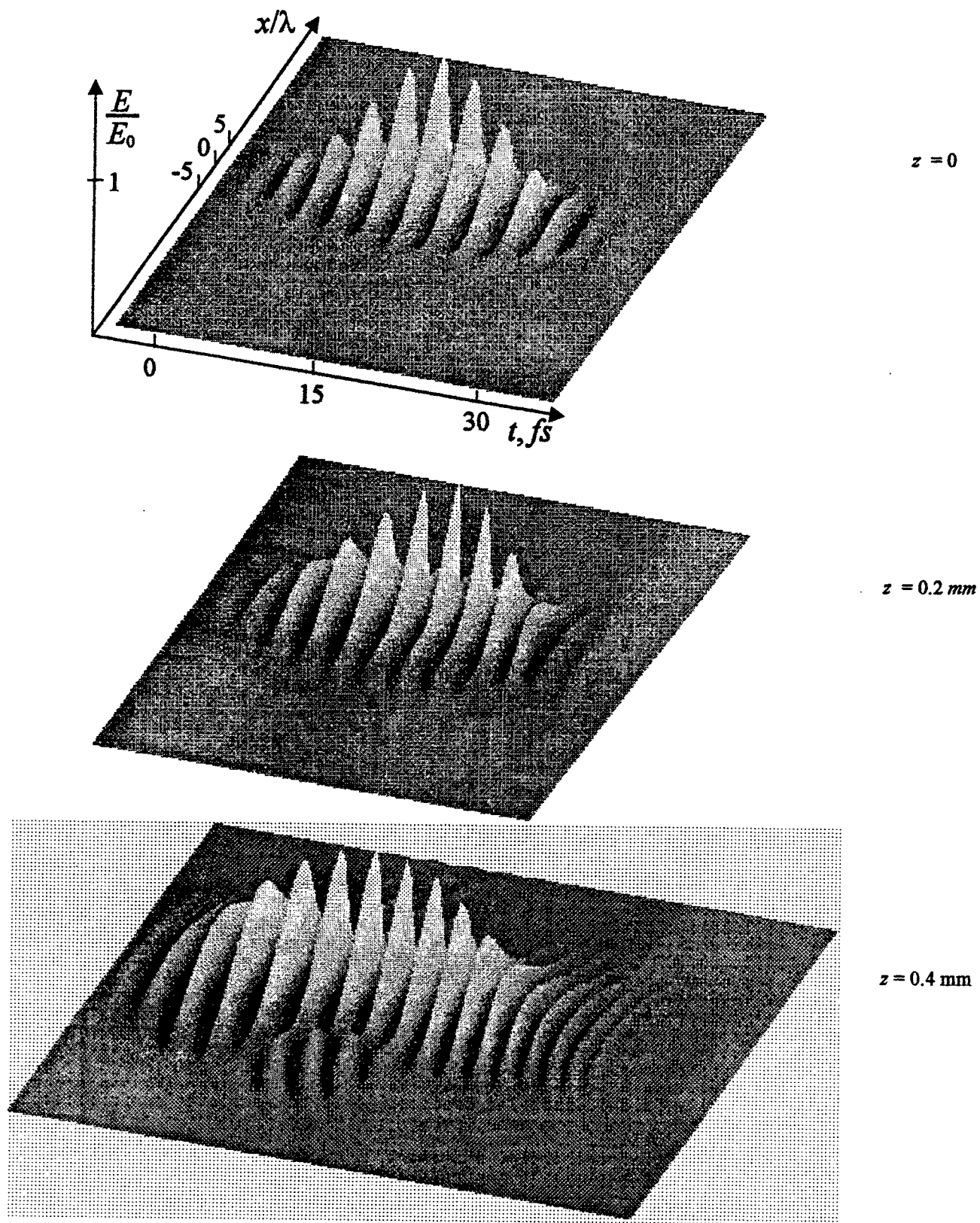


Fig. 1. The electrical field distribution in a fused silica bulk.
 Input pulse parameters are $\lambda_0 = 780 \text{ nm}$; $\Delta t = 10.4 \text{ fs}$; $\Delta x = 10 \lambda_0$; $I = 7 \cdot 10^{12} \text{ W/cm}^2$

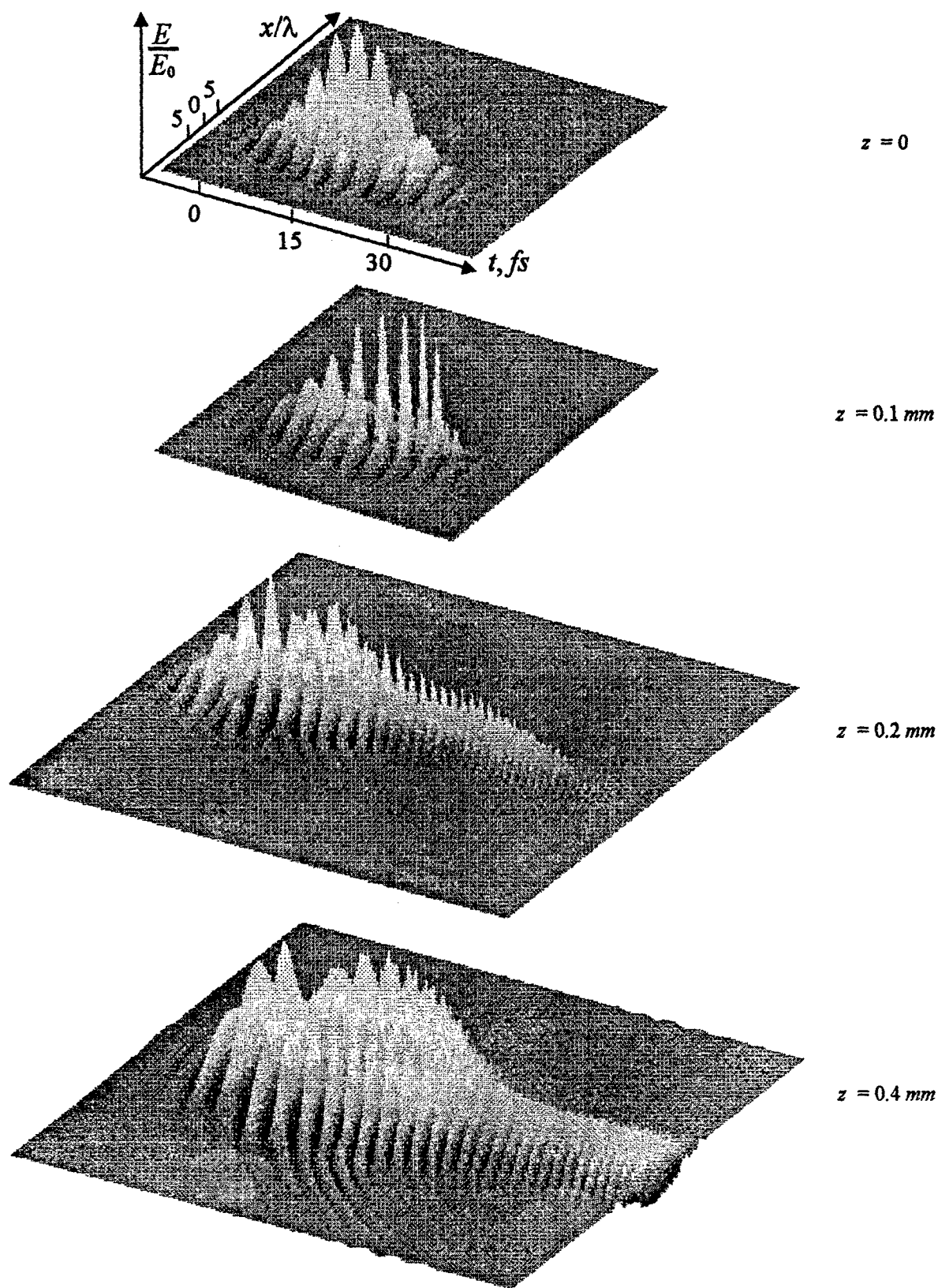


Fig. 2. The electrical field distribution in a fused silica bulk.
 Input pulse parameters are $\lambda_0 = 780 \text{ nm}$; $\Delta t = 10.4 \text{ fs}$; $\Delta x = 10 \lambda_0$; $I = 2 \cdot 10^{13} \text{ W/cm}^2$

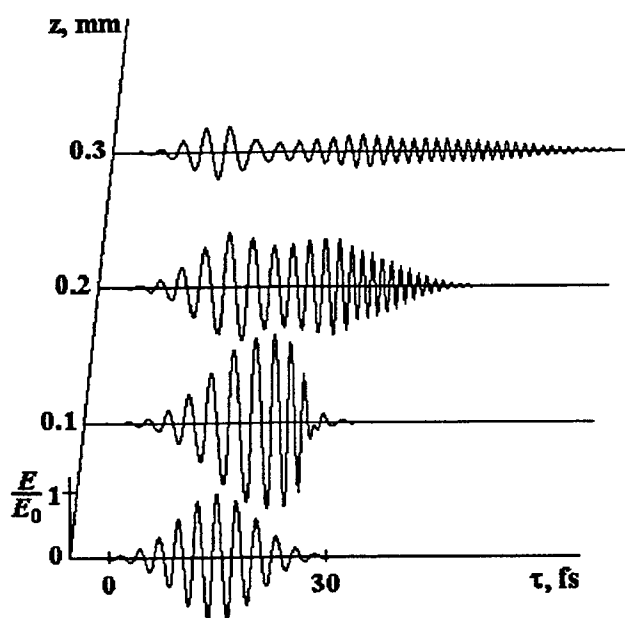


Fig. 3a

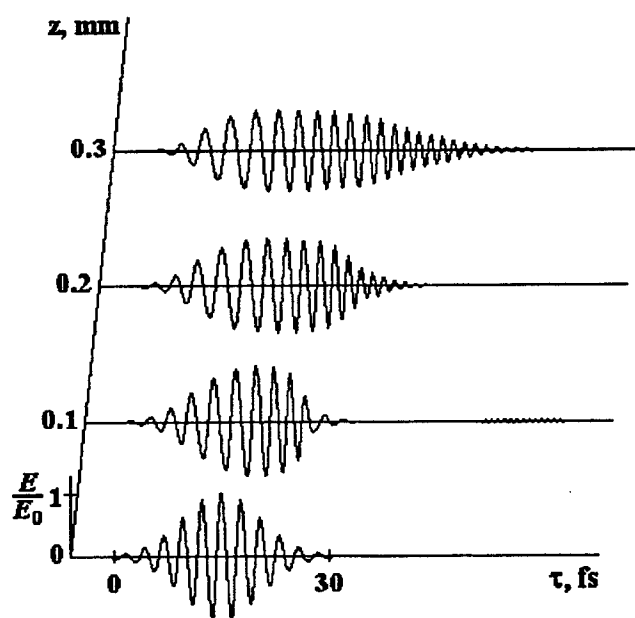


Fig. 3b

Fig. 3. The electrical field profile in the central longitudinal section of a beam, propagating through a) fused silica bulk; b) fused silica fiber. Input pulse parameters are $\lambda_0 = 780 \text{ nm}$; $\Delta t = 10.4 \text{ fs}$; $\Delta x = 10 \lambda_0$; $I = 2 \cdot 10^{13} \text{ W/cm}^2$

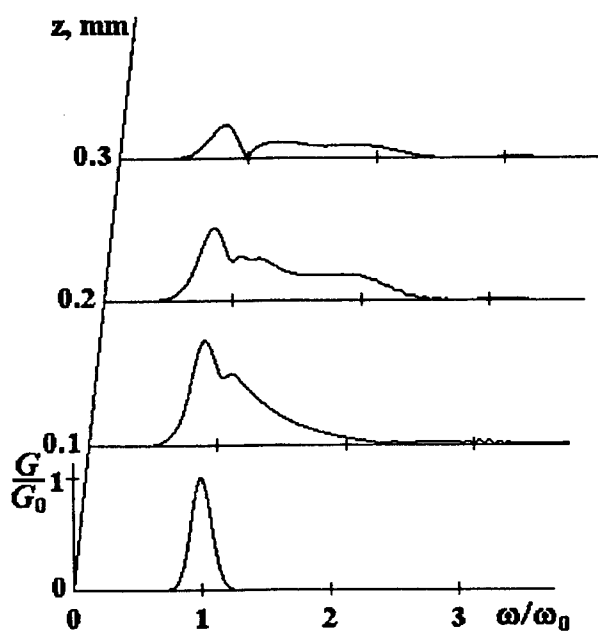


Fig. 4a

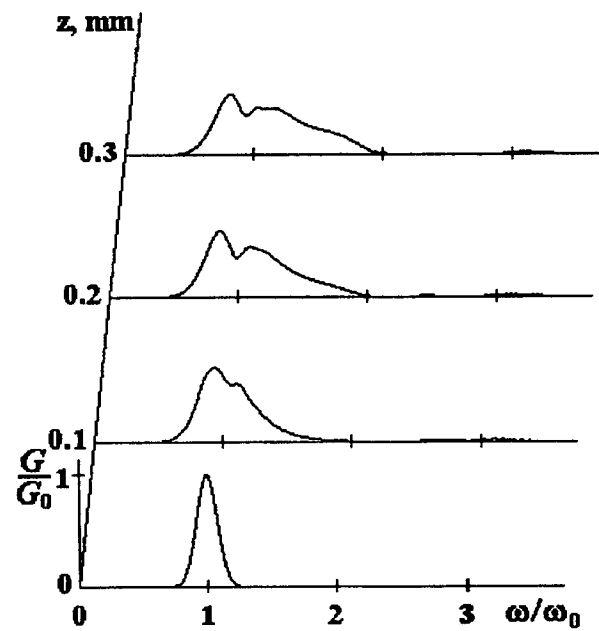


Fig. 4b

Fig. 4. The spectral densities in the central longitudinal section of a beam, propagating through a) fused silica bulk; b) fused silica fiber. Input pulse parameters are $\lambda_0 = 780 \text{ nm}$; $\Delta t = 10.4 \text{ fs}$; $\Delta x = 10 \lambda_0$; $I = 2 \cdot 10^{13} \text{ W/cm}^2$

LINEAR AND NONLINEAR OPTICAL TOOLS TO MEASURE THE DEPHASING TIME OF LOCALIZED SURFACE PLASMON-POLARITONS.

T. A. Vartanyan
State Optical Institute, St. Petersburg 199034, Russian Federation
E-mail: tigran@jamnet.spb.su

F. Träger
Fachbereich Physik, Universität Kassel,
Heinrich-Plett-Str. 40, D-34132 Kassel, Germany
Fax: +49-561-804-4518, E-mail: traeger@physik.uni-kassel.de

KEY WORDS: surface plasmon-polariton, second harmonic generation, autocorrelation function, femtosecond laser pulses

ABSTRACT

Localized surface plasmon-polaritons in small metal particles play an important role in a number of laser-induced surface processes. The intensity and the width of the corresponding resonances are determined by the dephasing time of the plasmon. To get information on the dephasing times, the linear spectroscopy methods are of limited use because of their inability to discriminate between the homogeneous and inhomogeneous line broadening. Consequently, the linear extinction spectra provide only the lower limit of the surface plasmon dephasing time. Nonlinear techniques, such as autocorrelation measurements of second and third harmonic generation employing bandwidth-limited femtosecond pulses and performed with an interferometric accuracy, were intended to give a direct access to the dephasing time of the plasmon excitation. In this contribution, we present the results of the theoretical modeling of the second and third harmonic autocorrelation functions and show that these particular nonlinear techniques suffer from the inhomogeneous broadening to almost the same extent as the linear extinction measurements. Moreover, the general relations between the linear absorption spectrum and second and third harmonic autocorrelation functions produced by an arbitrary inhomogeneous distribution of resonance frequencies are found, provided the resonance itself may be modeled as a slightly anharmonic classical oscillator. Finally, we propose one particular combination of linear and nonlinear results that may help to discriminate between homogeneous and inhomogeneous contributions to the line shape, and analyze the assumptions that lead to the unambiguous determination of the surface plasmon dephasing time.

1. INTRODUCTION

Optical properties of surface plasmon-polaritons in small metal particles earn to them wide spread applications. At the same time, it is the linear optics that provides the main tools for their investigations. A wealth of information on the structural and dynamical properties of free, dissolved or supported metal clusters was obtained via measurements of linear extinction spectra. One of the most severe drawbacks of the linear spectroscopy is its inability to discriminate between homogeneous and inhomogeneous line broadening. Consequently, linear extinction spectra provide only the lower limit of the surface plasmon lifetime, which is of great value for applications as well as for the basic research. Nonlinear techniques, such as autocorrelation measurements of the second and third harmonic generation (SHG, THG) employing bandwidth-limited femtosecond pulses and performed with an interferometric accuracy^{1,2}, were intended to give a direct access to the life-time of the plasmon excitation. In the recent publication³ we have modeled the SHG autocorrelation function (ACF) and shown that this particular nonlinear technique suffers from the inhomogeneous broadening to almost the same extent as the linear extinction measurements. Very similar conclusion was made independently in². Nevertheless, it was speculated that both techniques might be combined to discriminate between the homogeneous and inhomogeneous contributions to the line shape^{2,4}. Some particular assumptions about the functional form of the inhomogeneous distribution were made in both

studies. In this article we are going to analyze the general relations that exist between the linear absorption spectra and SHG (THG) ACF produced by an arbitrary inhomogeneous distribution of plasmon resonance frequencies, the resonance itself being modeled as a slightly anharmonic classical oscillator.

2. LINEAR ABSORPTION SPECTRA

Consider a classical oscillator of eigenfrequency Ω and damping rate Γ . Its behavior under the action of a driven force with an amplitude $\tilde{f}(t)$ and frequency ω is determined by the following equation of motion for the coordinate x

$$\ddot{x} + 2\Gamma\dot{x} + \Omega^2 x = \tilde{f}(t) \exp(-i\omega t) \quad (1)$$

When $\Gamma \ll \Omega$, in the close proximity of the resonance $|\omega - \Omega| \ll \omega + \Omega$, the amplitude of the oscillations is largely enhanced as compared to the nonresonance excitation. If we limit our consideration to this particular region, a simpler version of Eq. (1) may be employed

$$\dot{x} + (i\Omega + \Gamma)x = f(t) \exp(-i\omega t), \quad (2)$$

where $f(t) = i\tilde{f}(t)/(2\Omega)$. This equation holds provided $f(t)$ does not vary too rapidly. If $f(t)$ represents a laser pulse envelope, its duration τ is to be longer as compared to the optical period $2\pi/\omega$.

When the linear spectroscopy is applied to the study of the surface plasmon excitation, one usually measures an extinction spectrum. For small metal particles, this extinction spectrum is dominated by absorption. In this case, the amplitude of the driven force may be regarded as a constant and the normalized spectral line shape $S(\omega)$ gets the Lorentzian form

$$S(\omega) = \frac{\Gamma^2}{(\Omega - \omega)^2 + \Gamma^2}. \quad (3)$$

This profile has a HWHM equal to Γ and, as long as the inhomogeneous width is small compared to Γ , the latter may be obtained directly from the experiment. On the other hand, when the inhomogeneous broadening grows larger, it is to be taken into account explicitly. Let $G(\Omega)$ be the normalized distribution of the eigenfrequencies

$$\int G(\Omega) d\Omega = 1. \quad (4)$$

In the case of the Gaussian distribution with the dispersion Δ around the central frequency Ω_0 it reads

$$G(\Omega) = \frac{1}{\Delta\sqrt{\pi}} \exp\left(-\frac{(\Omega - \Omega_0)^2}{\Delta^2}\right).$$

In general, the spectral line shape may be obtained as a convolution of Eq. (3) with an arbitrary $G(\Omega)$

$$S(\omega) = \int \frac{\Gamma^2 G(\Omega) d\Omega}{(\Omega - \omega)^2 + \Gamma^2}. \quad (5)$$

Now, the width of the line depends on the width of the inhomogeneous distribution as well as on the damping rate. In the extreme case of a very broad inhomogeneous distribution, evaluation of Eq. (5) gives $S(\omega) \propto G(\omega)$ and all information

about the damping rate is lost. Nevertheless, if the dispersion of the inhomogeneous distribution is comparable to the damping rate and the functional form of $G(\Omega)$ is different from Lorentzian and known beforehand, a careful inspection of the spectral line shape will discriminate between the damping rate and the width of the inhomogeneous distribution.

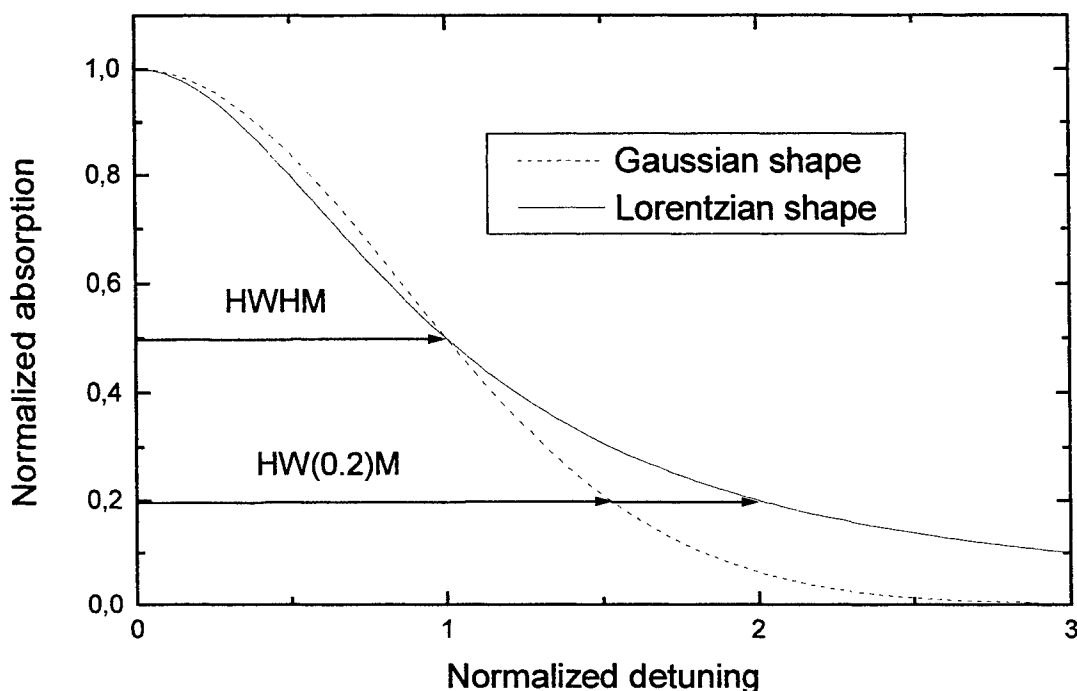


Fig. 1 Comparison between spectral line shapes for Lorentzian and Gaussian profiles. Detuning is normalized to the HWHM. Spectral line shapes are normalized to their maximums.

Figure 1 shows the line shapes of the linear absorption of two different ensembles of oscillators with the Gaussian distribution of resonance frequencies. If $\Delta \ll \Gamma$, inhomogeneous broadening is negligible. Hence, the spectral line shape is Lorentzian. In the other extreme, $\Delta \gg \Gamma$, the line shape is Gaussian. Gaussian and Lorentzian absorption lines with equal HWHM are plotted in Fig. 1. The difference between these two curves becomes evident if one compares their widths at the level of 0.2 of the maximum. We will refer to this width as $HW(0.2)M$. For the Lorentzian $HW(0.2)M$ is twice the HWHM. For the Gaussian, it is much smaller, namely, $\sqrt{\ln 5 / \ln 2} \approx 1.52$ of HWHM. Any number in between 1.52 and 2 obtained in an experiment for a real situation signals of the mixture of homogeneous and inhomogeneous broadening. A nomogram, which enables finding of Δ and Γ separately, provided the ratio of $HW(0.2)M$ to HWHM is known, is plotted in Fig. 2.

It is to be stressed that this method relies heavily on the assumption of the particular functional form of the inhomogeneous distribution $G(\Omega)$. In case $G(\Omega)$ is not Gaussian but rather Lorentzian, the convolution of two Lorentzians will give also Lorentzian and an erroneous conclusion of the absence of inhomogeneous broadening will be drawn. From this point of view, it is of great importance to learn what kind of additional information about the inhomogeneously broadened ensemble of oscillators may be obtained with the aid of nonlinear optical methods.

3. SHG AND THG AUTOCORRELATION FUNCTIONS

Consider first the SHG ACF. In order to describe nonlinear optical phenomena, an anharmonic term is to be included in

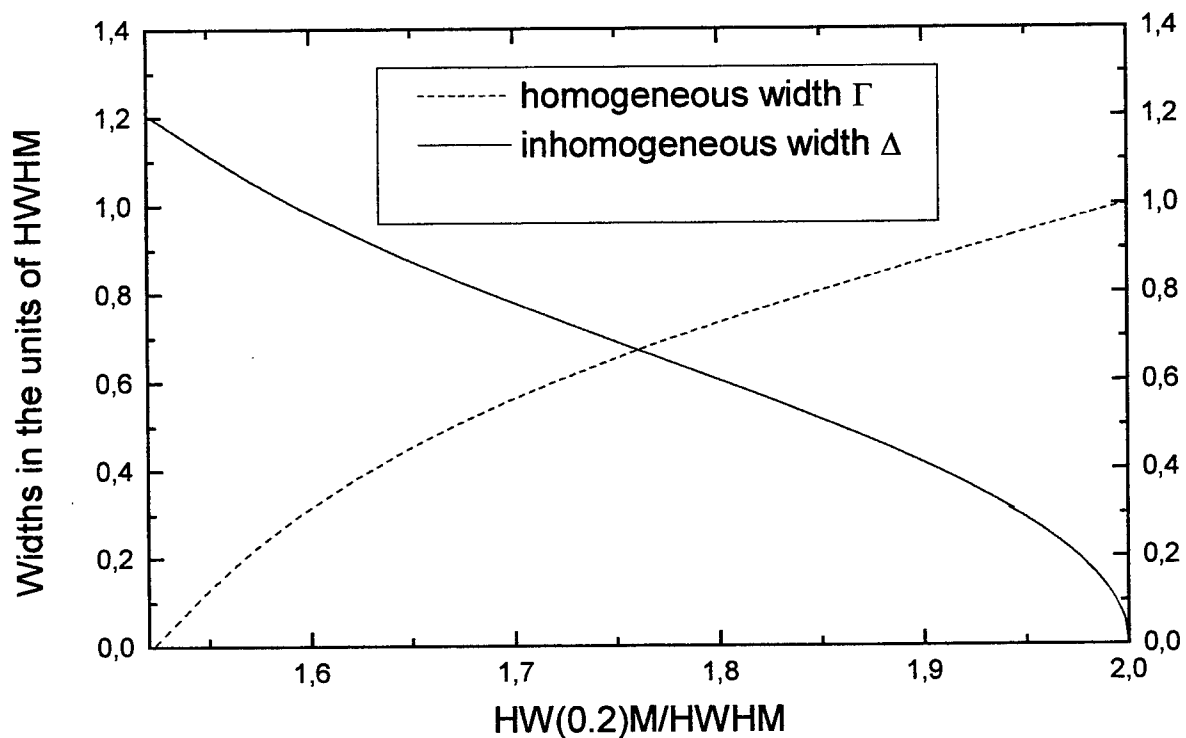


Fig. 2 This nomogram may be used to determine the homogeneous line width and the width of the inhomogeneous distribution provided the ratio of the width at one fifth (HW(0.2)M) and one half (HWHM) of the maximum is known. An inhomogeneous distribution is assumed to be Gaussian.

Eq.(1). Since we are interested in SHG, this term is proportional to x^2 . As the anharmonicity is expected to be small it may be treated as a perturbation. Details of the calculations were published previously³. During the autocorrelation measurements, the system is driven by two identical laser pulses, one of which is delayed by a variable time T with respect to the other. The amplitude of the field exerted on the medium can be written as

$$f(t) = g(t) + \exp(i\omega T)g(t - T), \quad (6)$$

where $g(t)$ represents the time dependent amplitude of one pulse. If the nonlinear medium used for second harmonic generation does not possess resonances at the fundamental and the second harmonic, its nonlinear response is instantaneous. In this case, the amplitude of the light generated at the second harmonic $E(t)$ is given simply by $[f(t)]^2$. The autocorrelation function $S(t)$ describes how the integrated intensity of the second harmonic signal

$$S(t) = \int |E(T)|^2 dt, \quad (7)$$

depends on the time delay T . The temporal profile of $S(T)$ provides in this case a good measure of the duration of the pulse $g(t)$. On the contrary, in the case of the resonant excitation $S(T)$ depends also on the damping rate. Explicit calculations³ give

$$E(t, \Omega) = \int_0^{\infty} \exp\{-[\Gamma + i(\Omega - \omega)]s\} ds \int_0^s f\left(t - \frac{s+r}{2}\right) f\left(t - \frac{s-r}{2}\right) dr, \quad (8)$$

This expression shows the influence of the damping rate on the ACF very clearly. If the damping rate is high as compared to the inverse pulse duration, the outer integration is effectively limited to very small values of s , which, in turn, reduces the inner integration to the term almost equal to $[f(t)]^2$, as in the nonresonant case. If, on the other hand, the damping rate is comparable or smaller than the inverse pulse duration, the outer integration in Eq. (8) extends to rather large values of s , so that the inner integrand represent a product of two functions $f(t)$ taken at different times rather than $[f(t)]^2$. This leads to a better overlap and, as a consequence, to larger values of ACF for the time delays T exceeding the pulse duration. Hence, ACF in this case is expected to be broader in the time domain as compared to that taken with a nonresonant reference.

To account for the inhomogeneous broadening one has to integrate Eq.(8) over the frequency distribution $G(\Omega)$. The result reads

$$\int_0^{\infty} A(s) \exp\{is\omega\} ds \int_0^s f\left(t - \frac{s+r}{2}\right) f\left(t - \frac{s-r}{2}\right) dr, \quad (9)$$

where

$$A(s) = \int_0^{\infty} G(\Omega) \exp[-(\Gamma - i\Omega)s] d\Omega. \quad (10)$$

A straightforward calculation shows that for $s > 0$, which only enters Eq. (10), $A(s)$ is proportional to the Fourier transform of $S(\omega)$ given in Eq.(5)

$$A(s) = \frac{\Gamma}{\pi} \int_0^{\infty} S(\omega) \exp[-i\omega s] d\omega. \quad (11)$$

This last calculation shows that SHG ACF may be computed via Eqs.(7), (9) and (11), provided the linear absorption spectrum is known. That means that, in principle, SHG ACF does not contain any new information about the system as compared to the linear absorption spectrum. This conclusion is drawn here without any particular choice of the functional form of the inhomogeneous distribution of eigenfrequencies and does not depend on it.

The same conclusion is valid for THG ACF. In this case, an anharmonic term is proportional to x^3 . The very similar calculations lead to the third harmonic field

$$E(t, \Omega) = \int_0^{\infty} \exp\{-[\Gamma + i(\Omega - \omega)]s\} ds \int_{-s}^s dv \int_0^s du f\left(t - \frac{s-u+v}{2}\right) f\left(t - \frac{s-u-v}{2}\right) f(t-u), \quad (12)$$

which resembles Eq. (8) for the second harmonic field. As the frequency dependent exponential function enters Eq. (12) just in the same way as in Eq.(8), all steps of computation leading to Eq. (11) may be repeated, so that the temporal profile of the THG ACF will be obtained provided the linear absorption spectrum of inhomogeneously broadened system is known.

Nevertheless, from the experimental point of view measuring of SHG ACF may be desirable in some cases. To understand the reason of that it should be noted that both the linear absorption spectra and ACF are best measured in their respective central parts where the signals are at their maximums. The wings, on the contrary, have a less favorable signal-to-noise ratio. Hence, they are usually less accurately known than the line center. From this point of view, SHG ACF may be regarded as a complementary tool for the linear spectroscopy because its central part is determined by the wings of absorption spectrum. Indeed, according to Eq. (9) the central part of ACF is determined by those values of $A(s)$, which correspond to s in the range from zero to the duration of the pulse. In turn, according to Eq. (11) these values of $A(s)$ samples the whole range of $S(\omega)$ including the wings where the linear spectroscopy data are of the worse quality. Vice versa, the central part of the absorption spectrum gives rise to the values of $A(s)$ in the range from Γ^{-1} to infinity, which, in turn, determines the ill defined wings of ACF.

From this point of view, a combination of linear absorption spectroscopy and SHG or THG autocorrelation data for the determination of the damping rate does make sense. From the analysis presented above it should be clear, however, that the unique determination of the homogeneous and inhomogeneous contributions to the surface plasmon line shape from these combined measurements is possible only in the framework of somewhat arbitrary assumptions about the functional form of the inhomogeneous distribution of eigenfrequencies.

There are several ways to achieve the ultimate goal of an unambiguous determination of the surface plasmon damping rate. First, it is to produce samples with the negligible inhomogeneous distribution or to pick up only one particle and determine its parameters. There were remarkable achievements on this way very recently^{2,5,6,7}. Second, it is to employ more powerful nonlinear methods like photon echoes or spectral hole burning. On the results obtained with use of the last method in the case of supported metal clusters we have reported elsewhere⁸.

Not only the problem of inhomogeneous broadening may be addressed by comparison of the linear and nonlinear properties of the surface plasmon excitations. The universal relation between SHG (THG) ACF and the absorption spectrum obtained in this article is valid only in the framework of the model, in which the surface plasmon is described as a classical slightly anharmonic oscillator. Although this model seems quite reasonable in a view of the recent experimental^{9,10} as well as theoretical results^{11,12}, it cannot be perfect. Hence, a deviation from this relation may serve as a hint for the future refinement of the model.

ACKNOWLEDGEMENT

This work was started during the visit of one of the authors (T.V.) to the University of Kassel and was supported in part by Russian Foundation for Basic Research.

REFERENCES

1. M. Simon, F. Träger, A. Assion, B. Lang, S. Voll, G. Gerber: Chem. Phys. Lett., **296**, 579 (1998)
2. B. Lamprecht, A. Leitner, F.R. Aussenegg: Appl. Phys. B **69**, 223 (1999)
B. Lamprecht, J. R. Krenn, A. Leitner, F. R. Aussenegg: Phys. Rev. Lett. **83**, 4421 (1999)
3. T. Vartanyan, M. Simon, and F. Träger: Appl. Phys. B **68**, 425 (1999)
4. T. Vartanyan, M. Simon, F. Träger: Verhandlungen der Deutschen Physikalischen Gesellschaft, 63 Physikertagung Heidelberg 1999, Frühjahrstagung der Fachgremien, p. 528, Physik-Verlag GmbH, Weinheim 1998.
5. T. Klar, M. Perner, S. Grosse, G. von Plessen, W. Spirke, J. Feldmann: Phys. Rev. Lett. **80**, 4269 (1998)
6. J. Bosbach, D. Martin, F. Stietz, T. Wenzel, F. Träger: Appl. Phys. Lett. **74**, 2605 (1999)
7. F. Stietz, F. Träger: Philosoph. Mag. B **79**, 1281 (1999)
8. F. Stietz, J. Bosbach, T. Wenzel, T. Vartanyan, A. Goldmann and F. Träger: Phys. Rev. Lett., **84**, p. 5644 (2000).
9. M. Schmidt, H. Haberland: Eur. Phys. J. D **6**, 109 (1999)
10. R. Schlipper, R. Kusche, B. V. Issendorff, H. Haberland: Phys. Rev. Lett. **80**, 1194 (1998)
11. A. Doms, P.-G. Reinhard, E. Suraud: Phys. Rev. Lett. **80**, 5520 (1998)
12. F. Calvayrac, A. Doms, P.-G. Reinhard, E. Suraud, C. A. Ullrich: Eur. Phys. J. D **4**, 207 (1998)

Spectral, spatial and polarisation characteristics of harmonics generated at interaction of intense laser radiation with aluminum foils

R. A. Ganeev *, J. A. Chakera, M. Raghuramaiah, A. K. Sharma, P. A. Naik, P. D. Gupta
Centre for Advanced Technology, Indore 452013, India
*NPO Akadempriboir, Academy of Sciences of Uzbekistan, Tashkent 700143, Uzbekistan

ABSTRACT

Investigations on harmonic generation in laser-matter interaction of Nd:glass laser radiation ($I \leq 1.5 \times 10^{15} \text{ W cm}^{-2}$, $\tau = 27 \text{ ps}$) with solid surfaces have been performed. Detailed measurements were made on the intensity of second, third and fourth harmonics, their polarization properties and spectral distribution, as well as dependencies of these characteristics on intensity and polarization of the incident laser radiation. Intensity dependencies of second, third and fourth harmonics for p -polarized laser pump showed a power law scaling of 1.5, 1.8 and 3.8 respectively. Maximal conversion efficiencies for second, third and fourth harmonic generation were observed in the range of 10^{-8} to 10^{-12} . For p -polarized laser radiation, the generation efficiency was more than ten and hundred times higher in comparison to that for the s -polarized radiation for second and third harmonics respectively. Among other features, rotation of second harmonic polarization as a function of laser intensity showed a quite different behavior for p - and s -polarized laser radiation, and the second harmonic observed in the specular reflection direction was red-shifted for laser intensity exceeding $5 \times 10^{14} \text{ W cm}^{-2}$.

Keywords: Harmonic generation, polarization, spectral shift, conversion efficiency

1. INTRODUCTION

Laser-matter interaction at high laser intensities using sub-picosecond and pico-second laser pulses has become a subject of much interest for many scientific investigations and technological applications. One of the most interesting processes involved is harmonic generation as a result of nonlinear optical response of the matter. Harmonic radiation can be useful in a number of applications ranging from plasma diagnostics to atomic physics. The most widely used media for such studies have been gas jets (see, for example ¹⁻³ and references therein). Several groups have reported very high order harmonic generation, e.g. up to 211-th harmonic ⁴ and short wavelength coherent radiation achieved approximately down to 6 nm ^{5,6}. Some attempts have also been made on phase-matched harmonic generation ^{3,7,8} for direct conversion of laser radiation energy into certain high order harmonics.

Another mechanism of generation of harmonic radiation involves oscillations of electron cloud across the solid-vacuum interface during interaction of high intensity laser radiation with solid surfaces. In comparison to the first case, where high order odd harmonics are produced due to nonlinearities of atomic polarizability, high order harmonic generation from solid surfaces is caused due to oscillation of the boundary layer, for example as in a moving mirror model ^{9,10} or impulse-like acceleration of electrons ^{11,12}. Due to lack of inversion symmetry in this case, the usual parity selection rules do not apply. Thus, odd as well as even harmonics are emitted with comparable intensity. Further, recent theoretical and experimental works ^{11,13} also do not show any cut-off on the high order harmonic production.

High harmonics (up to 46th) were first observed in nanosecond experiments using a CO₂ laser ^{14,15}. Both odd and even harmonics were generated via relativistic current associated with the electrons moving back and forth across the solid-vacuum boundary density step. The formation of a steep density gradient in this case is attributed to the action of ponderomotive force, which counteracts the plasma expansion. A thin layer of plasma is formed in which the plasma density drops from solid density to the vacuum over a very small distance. Harmonic generation in this situation is also understood as a result of anharmonic distortion of the laser field upon reflection from a rapidly oscillating surface ^{9,16}. Perturbative methods are inadequate for the treatment of laser-surface plasma interaction at high intensities, but can be used for explanation of generation of low-order harmonics ¹⁰.

A number of theoretical and experimental studies ^{9-13,16-26} have been reported during the last decade on harmonic generation from solid surfaces using picosecond and femtosecond laser pulses. These studies were conducted with pulses varying from tens of femto-second ²⁰ up to 2.5 pico-second ¹³. Most features of the harmonic generation process were same in the above

range of pulse duration. One such feature is a considerably higher efficiency of harmonic conversion for the *p*-polarized radiation as compared to that for the *s*-polarized radiation. Next, a smooth roll-off on the high harmonic intensity was observed. Further, harmonic radiation had the same divergence as that of the incident laser radiation at intensities up to $10^{16} \text{ W cm}^{-2}$, and was observed to be isotropic for $I\lambda^2 > 10^{18} \text{ W cm}^{-2} \mu\text{m}^{-2}$ (here *I* is the laser intensity and λ is the wavelength of the laser radiation). Results were also reported on the measurements of polarization dependence of the harmonic yield, red- and blue- shift of harmonic radiation, and transition from specular to isotropic harmonic emission. These characteristics showed certain differences depending on the pulse duration of the laser used.

Laser pulse duration is an important parameter, which governs mechanism as well as the dynamics of the processes involved in harmonic generation. In this article, we extend the temporal scale of pump source and investigate harmonic generation from the solid surface-vacuum interface using 27 ps Nd:glass laser radiation. We study harmonic generation (up to fourth harmonic), polarization effects (rotation of polarization of both the fundamental and harmonic radiation), spectral, temporal and spatial characteristics of harmonic radiation, and compare these results with those reported for the shorter pulse duration regime.

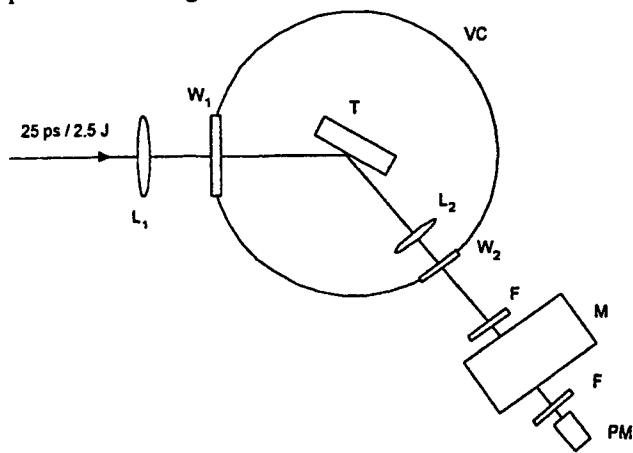


Fig. 1: Experimental setup;

L_1 – focusing lens; L_2 – quartz collimator lens; VC – vacuum chamber; T – target; W_1 , W_2 – input and output quartz windows; F – filters; M – monochromator; PM – photomultiplier

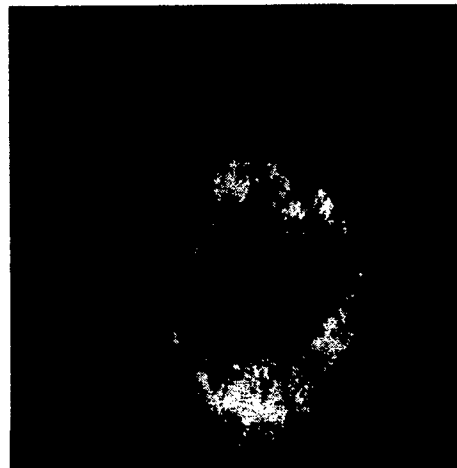


Fig. 2 : Spatial intensity distribution of second harmonic at a laser intensity of $\sim 5 \times 10^{14} \text{ W cm}^{-2}$.

2. EXPERIMENTAL SETUP

A 100 GW Nd: phosphate glass laser chain ($\lambda = 1053 \text{ nm}$) was used for harmonic generation from the surfaces. This laser chain based on MOPA principle, consisted of an active-passive mode locked *Nd:YLF* oscillator, an electro-optic pulse selector, two double-pass amplifiers, two single pass amplifiers, three vacuum spatial filters, and one Faraday isolator to block any back reflected laser beam. A Faraday rotator was also placed at the end of the laser chain to orient the polarization of the output beam in a desired direction. The laser chain provided single laser pulses of energy of 2.5 J in 27 ps (FWHM) with a beam divergence angle of $175 \mu\text{rad}$, beam diameter of 33 mm ($1/e^2$ points) and the M^2 parameter of 4.3. The laser beam was checked for any pre-pulses (due to leakage transmission of the rejected pulses of the mode locked train from the pulse selector) and ASE from the amplifiers. The peak intensity contrast ratio of the former with the main laser pulse was measured to be better than 10^{-5} . Thus pre-pulse intensity was $< 10^{10} \text{ W cm}^{-2}$ at the maximum laser energy. This is below the threshold of plasma formation for picosecond laser pulses. Further, ASE also did not result into any plasma formation as checked by aborting the oscillator operation and firing all the amplifiers stages.

A schematic of the experimental set up is shown in Fig. 1. The laser beam was focused on an aluminum target placed in a

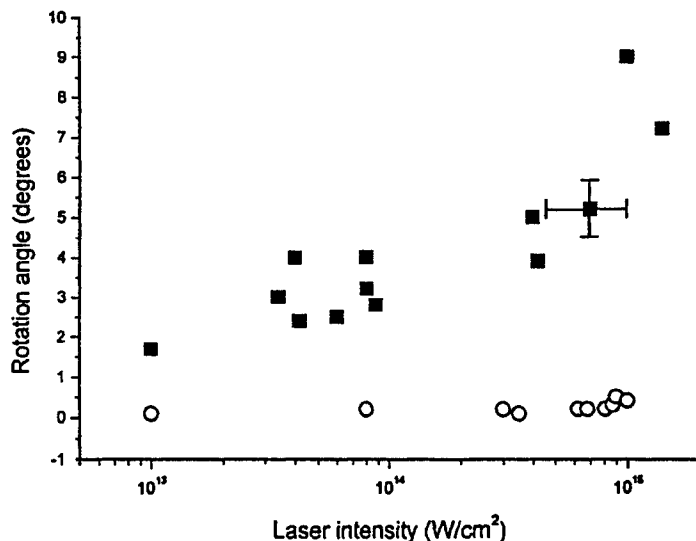


Fig. 3 : Rotation of *s*- polarization (■) and *p*- polarization (○) as a function of laser intensity.

vacuum chamber (5×10^{-5} mbar). The target was prepared by coating 100- μm thick aluminum on optically polished planar glass plates. The laser beam was focused using a 750-mm focal length lens at an angle of incidence of 67.5° on the target. We also measured harmonic yield at 45° and 22.5° angles of incidence. The focal spot on the target was of an oval shape (due to non-normal incidence of the laser beam) with the major and minor dimension of 120 μm and 45 μm respectively. A peak intensity of $\sim 1.5 \times 10^{15} \text{ W cm}^{-2}$ was estimated for the maximum output energy of the laser. The target was rotated about its axis after each shot so that every next pulse of laser radiation interacted with a fresh part of the target. Next, the depolarization factor of the incident radiation was smaller than 10^{-3} . The Faraday rotator was used to change polarization of the incident radiation from *p* to *s* and vice-versa. Reflected fundamental and harmonic radiation were collimated by a quartz lens and dispersed by a monochromator (CVI, model DK480).

Second, third and fourth harmonic radiation were detected by photomultipliers (Philips 2232 for $\lambda=526.5 \text{ nm}$, RCA 4840 for $\lambda=351 \text{ nm}$, and Hamamatsu R166 for $\lambda=263 \text{ nm}$) with rise times $\leq 3 \text{ ns}$. Broadband and interference filters were used to reduce undesirable plasma radiation at other wavelengths from reaching the detector. The temporal profiles of harmonic radiation were measured using Tektronix TDS-360 and Lecroy 9350A oscilloscopes. Appropriate steps were taken to ensure that the photomultipliers operated in linear amplification regime.

3. RESULTS AND DISCUSSION

Most of our studies were performed at 67.5° angle of incidence. First, we measured the variation of second and third harmonic intensity as a function of target position w.r.to the best focus position. It is seen that the intensity ratio of the second and third harmonic radiation is ~ 100 .

Second harmonic emission was observed in the direction of specular reflection for all values of $I\lambda^2$ ranging from $8 \times 10^{12} \text{ W cm}^{-2} \mu\text{m}^2$ to $1.5 \times 10^{15} \text{ W cm}^{-2} \mu\text{m}^2$. No second harmonic emission signal was observed at angles other than the specular reflection direction (checked by placing the collimating lens to collect radiation in directions far from specular) throughout the range of laser irradiation used. The second harmonic signal in the specular reflection direction was fairly strong so much so that a well-collimated second harmonic beam in the direction of specular reflection could be readily observed with unaided eye. These observations are in agreement with earlier published work^{22,24,26,27}. In particular, the specular feature of second harmonic radiation was demonstrated by Marjoribanks *et al*²⁷ in the same range of $I\lambda^2$ from $10^{14} \text{ W cm}^{-2} \mu\text{m}^2$ to $10^{15} \text{ W cm}^{-2} \mu\text{m}^2$ as in our study using pre-pulse free, 1 ps Nd:glass laser pulses.

Some processes lead to the growth of Raleigh-Taylor instabilities distorting the surface of the dense plasma, resulting in broadening of the angular spectrum of the harmonics¹³. Plasma created by pre-pulse is one of the most common situations which may prevent interaction of the intense laser pulse directly with a solid surface. For instance, in the experiments of

Marjoribanks *et al*²⁷, when a pre-pulse of 10^{-4} times the peak intensity was introduced about 1.5 ns before the main pulse, they observed a transition from specular to diffuse harmonic emission for $I\lambda^2$ values in the range of 10^{15} to 10^{16} W cm² μ m². Thus, high background to peak intensity contrast of the laser radiation is a crucial demand for harmonic generation. In accordance to early measurements, the plasma creation threshold on the surfaces for pulses of ~ 10 -ps duration is between 10^{10} W cm⁻² to 10^{11} W cm⁻²³³. Intensity contrast ratio in our laser pulse, as stated earlier, was better than 10^5 . Pre-pulse intensity was below 10^{10} W cm⁻² even at the highest intensity, and the same is below the plasma formation level. Thus in our experiments the laser radiation interacted with a sharp solid-vacuum interface, an inference also supported by the absence of any diffuse emission of harmonic radiation.

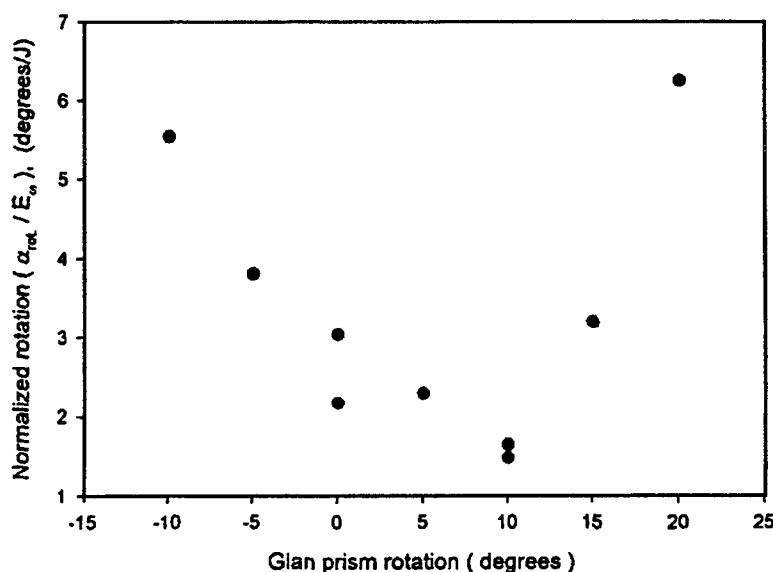


Fig. 4 : Normalized rotation of polarization as a function of Glan prism rotation.

Spatial shapes of reflected laser radiation and second harmonic radiation were registered by a CCD camera in front of the monochromator. The divergence of both the reflected fundamental radiation and the second harmonic radiation were nearly equal. Further, it was observed that as the laser intensity was increased, the spatial intensity distribution of the second harmonic emission changed from the one which is nearly the same as that of the reflected fundamental radiation to a ring-like shape. Fig. 2 shows a typical picture of intensity distribution of the second harmonic radiation observed at a laser intensity of 5×10^{14} W cm⁻².

Temporal characteristics of fundamental radiation and second harmonic were analyzed by streak-camera (with rise time ~ 5 ps) and CCD camera. Pulse duration of second harmonic (23 ps) was close to one of fundamental radiation (27 ps).

Second harmonic conversion efficiency was measured to be 2×10^{-8} at the maximum laser intensity for *p*- polarized radiation, and ~ 10 times smaller for the *s*-polarized radiation. The data can be represented by a power law of the form $I_{2\omega} \propto I_{\omega}^{1.5}$ for *p*-polarization pump, and $I_{2\omega} \propto I_{\omega}^{1.7}$ for *s*-polarization pump. These results are in agreement with the data of Refs.²³ and ²⁴ in studies performed in the picosecond pulse duration regime, where ratio of *p*- and *s*- polarization-induced picosecond second harmonic radiation was observed to vary from 2 to 10. At the same time for short pulses (femtosecond range) this ratio has been reported to be much higher ($\sim 10^3$) (see, for example,²⁸).

The large difference in the ratio of *p*- and *s*- polarization induced second harmonic conversion efficiencies can be understood from rotation of the *s*- polarized fundamental beam due to Faraday rotation. This occurs due to spontaneously generated mega gauss magnetic fields in laser produced plasmas, which becomes important for longer duration laser pulses²⁹. We have performed Faraday rotation measurements for both *p*- and *s*- polarized fundamental beam using the experimental setup²⁹. Laser radiation specularly reflected from the target was analyzed with a Glan prism. The energy of two orthogonal components were measured by a pair of calibrated energy meters. The angle of rotation (α_{rot}) was derived from the relative intensities in the two detectors using the relation $\alpha_{rot} = \arctg (E_{ort} / E_{par})$ where E_{par} , and E_{ort} are the energies of reflected fundamental radiation of the parallel and orthogonal polarizations w.r.to the polarization of the incident

laser beam. Fig. 3 shows the rotation angle as a function of laser intensity for *p*- and *s*- polarized fundamental beam. It is seen that no appreciable rotation occurs for the case of *p*- polarized beam. On the other hand, a rotation of $\sim 9^\circ$ was measured at a laser intensity of $10^{15} \text{ W cm}^{-2}$ for *s*- polarized laser radiation.

In order to confirm that the above stated result is not affected due to any possible contribution of depolarization of the reflected fundamental radiation, measurements were repeated by rotating the Glan prism. Variation of the normalized angle of rotation ($\alpha_{\text{rot}} / E_\omega$, where E_ω is the energy of the fundamental beam) as a function of the rotation angle of the Glan prism is shown in Fig. 4. The minimum value of the normalized rotation is noted to occur at $\sim 10^\circ$ rotation of the Glan prism, which is in agreement with the aforesaid Faraday rotation angle measurement of $\sim 9^\circ$. This confirms that fundamental radiation does not undergo any significant depolarization, and there is a definite Faraday rotation for *s*-polarized fundamental radiation. This is not surprising as a larger polarization rotation angle of $\sim 22.5^\circ$ was reported by Stamper *et al*²⁹ at a similar laser intensity ($10^{15} \text{ W cm}^{-2}$) using longer laser pulses of 100 ps.

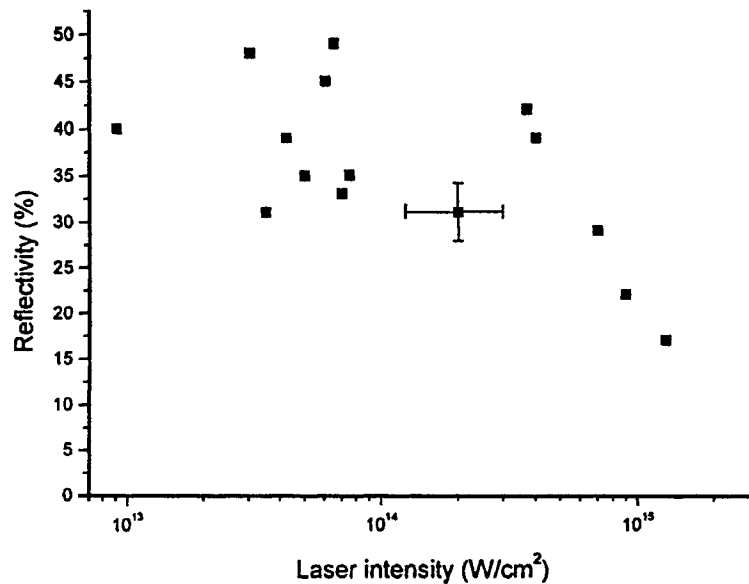


Fig. 5 : Reflectivity of *s*- polarized radiation as a function of laser intensity.

A significant generation of second harmonic radiation by *s*- polarized fundamental radiation can now be explained from the Faraday rotation of the latter. Due to longer pulse duration of 27 ps (in comparison to most of the previous studies up to 2.5 ps pulse duration), the plasma interaction length and hence the Faraday rotation undergone by the fundamental laser radiation increases. Ishizawa *et al*²⁴ observed even a stronger second harmonic generation of *s*- polarized fundamental radiation. The ratio of *p*- and *s*- polarization induced second harmonic yields in their study was ~ 2 . They also attributed this effect to Faraday rotation due to spontaneously generated magnetic fields in the plasma and quantitatively explained the observed ratio of the harmonic yields using the experimental results of Stamper *et al*²⁹ on Faraday rotation using 100 ps laser pulses.

The relative increase in the *s*- polarization induced second harmonic yield with increase in the fundamental laser intensity is also consistent with the observation of increase in Faraday rotation angle with laser intensity. The latter can be explained from the increase in absorption of the laser energy. Fig. 5 shows reflectivity of the *s*- polarized fundamental radiation as a function of laser intensity. It is seen that reflectivity ($\sim 50\%$) at small intensities ($\sim 10^{13} \text{ W cm}^{-2}$) decreases up to $\sim 15\%$ at intensities exceeding $10^{15} \text{ W cm}^{-2}$. This leads to an increase in the spontaneously generated mega gauss level magnetic fields in the plasma, which then results into increase of polarization rotation of the reflected fundamental radiation.

Analysis of the relative contents of parallel and orthogonal polarization components in the harmonic radiation w.r.to the polarization of the driving fundamental radiation can provide interesting information on the plasma processes involved. Earlier experimental studies and theoretical simulations showed that higher harmonics have the same polarization as that of the fundamental beam^{17,18,21,30}. For instance, according to the moving mirror model, the polarization of the incident laser radiation and the harmonics generated should be same. Some polarization selection rules¹⁶ govern that *p*- polarized laser radiation should generate *p*- polarized odd as well as even harmonics. At the same time, odd harmonics of the same polarization and even harmonics of the opposite polarization should be produced by a *s*- polarized fundamental beam.

Variation of the fraction of second harmonic emission in the orthogonal polarization w.r.to laser intensity for *s*- and *p*-polarized fundamental radiation obtained in our study is shown in Fig. 6. It is seen from this figure that for *p*-polarized laser radiation, the second harmonic yield was almost entirely (~ 97 %) of the same polarization as that of the fundamental beam. Further, this behavior did not change with increase in intensity. As opposed to this, for *s*-polarized fundamental beam, more than 30% of the second harmonic radiation at the maximum laser intensity had the opposite (*p*-) polarization. The physical origin of this effect is the rotation of polarization of fundamental beam as stated earlier also. The second harmonic energy versus laser intensity dependence for *s*-polarized laser beam has a greater slope than that for the *p*-polarized beam. This may be understood from the fact that a small rotation of the *s*-polarized fundamental radiation makes an additional contribution to the second harmonic generation.

The difference between *s*- and *p*-polarization induced harmonic generation decreases with increase in intensity. This is due to generation of intense magnetic fields and consequent rotation of the fundamental polarization. One may make a conjecture that at very high laser intensities the harmonic yields for *s*- and *p*-polarization should become nearly equal. For instance, at extremely high intensity of $\sim 10^{19} \text{ W cm}^{-2}$, no difference in harmonic conversion was observed between the two polarization of laser beam¹³. Authors of this work explained the situation by suggesting that the critical density surface got rippled during the interaction with the laser pulse (2.5 ps). Similarly, Losev *et al*²³ and Ishizawa *et al*²⁴ have discussed the occurrence of polarization rotation effects in their experiments using 0.8 ps and 2.2 ps laser pulses. Our studies underline that with the increase of laser pulse duration, there is an increased rotation of the *s*-polarized radiation, which then increases the yield of harmonic conversion at the surface-vacuum interface.

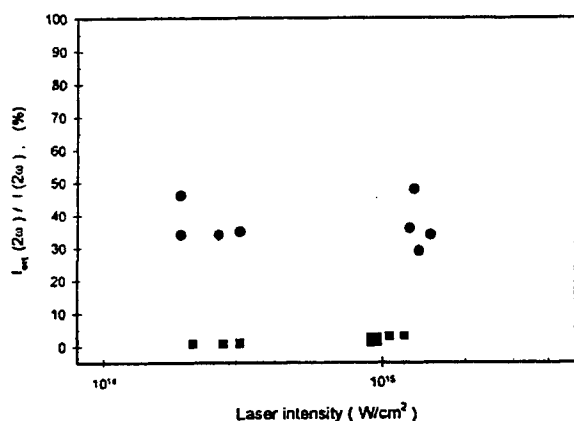


Fig. 6 : Fraction of second harmonic emission intensity in orthogonal polarization for *s*- (•) and *p*- (◻) polarized fundamental radiation.

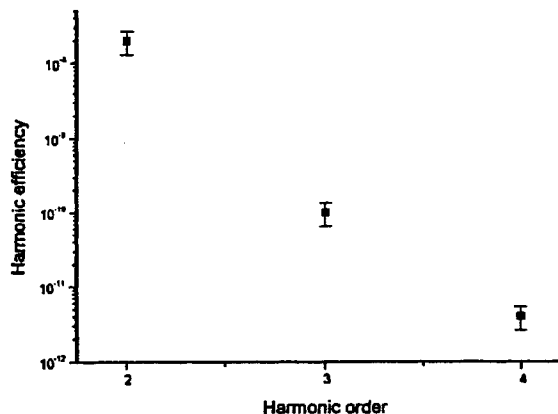


Fig. 7 : Harmonic efficiencies of observed harmonics.

The third and fourth harmonics were also observed in our experiments. The intensity scaling exponent for the two harmonics was 1.8 and 3.8 respectively. Next, the conversion efficiency for third and fourth harmonic for the *s*-polarized fundamental radiation relative to that for the *p*-polarized beam was much smaller in comparison to that for the second harmonic. Specifically, the ratio of third harmonic conversion efficiency for *p*- and *s*-polarizations was observed to be more than 100. This is in line with simulation results¹¹ which predicted that *p*-polarized laser to produce harmonics one to two order of magnitude stronger than that for *s*-polarization. Further, we did not observe any fourth harmonic radiation signal in the case of *s*-polarized laser pump, primarily because the signal in this case was below the detection threshold of our diagnostics system.

Harmonic yield decreased drastically with decrease of angle of incidence (eight-fold drop for 45° respectively to 67.5°). These results are in good coincidence with data of von der Linde *et al*²⁸. Further decrease of angle of incidence (22.5°) led to the growth of harmonic yield. In these experiments we took into account the decrease of interaction area at smaller angles of incidence. Minimum of angular dependence coincided with maximum of reflectance of *p*-polarized radiation and consequently with minimum of resonant absorption.

Conversion efficiencies of various observed harmonics for *p*-polarized pump radiation are plotted in Fig. 7. Maximal

conversion efficiencies for second, third and fourth harmonics were 2×10^{-8} , 10^{-10} , and 5×10^{-12} respectively. It may be noted that conversion efficiency decreases with increase in the harmonic order. This is qualitatively in agreement with the simulation results for $I\lambda^2 = 4 \times 10^{14} \text{ W cm}^{-2} \mu\text{m}^2$ ¹¹. However, our observations are at variance with previously reported results of experiments with picosecond pulse duration^{23,24}. Further, in contrast to experimental results using femtosecond laser pulses on gold surfaces^{21,25}, where conversion efficiency was observed to decrease rather slowly with the order of harmonics (from 10^{-10} to 10^{-13} for second to fifth harmonic), in our case each next higher order harmonic decreased at least 100 times w.r.to the previous harmonic order.

We now analyze our results in terms of the two known mechanisms of harmonic generation occurring in laser irradiation of solid surfaces viz. 1) motion of electrons under the action of optical field at an abrupt plasma-vacuum interface^{9,11,20,31} and 2) the $\mathbf{v} \times \mathbf{B}$ Lorentz force^{11,32}. While it is difficult to attribute all our observation to any one of these mechanisms, main features of the two mechanisms can jointly explain most of our results. Contribution of both the mechanisms can be seen in various aspects of our studies. For instance, while the first mechanism predicts that the energy of various harmonics differ slightly, the second mechanism predicts a large difference between the energy of different harmonics. Thus second mechanism's prediction is closer to our result on harmonic conversion yield. Next, on the basis of the first mechanism, the harmonic energy should be proportional to the laser intensity, i. e the power law exponent is 1. On the other hand, the power law exponent for the second mechanism is predicted to be the order of harmonic.

For *p*- polarized pump radiation, we observed power law exponent of 1.5, 1.8, and 3.8 for the second, third, and fourth harmonics respectively. While the first two are nearly mid-way between the values expected from the two mechanisms, the last one for the fourth harmonic is close to the prediction of the second mechanism. Thus our studies show intermediate results on the scaling behavior of harmonic emission. Next, a comparison may be made on the polarization dependence. First mechanism allows harmonic generation only for *p*- polarization pump. In comparison to this, the second mechanism based on Lorentz force predicts harmonic generation by both *p*- and *s*- polarized laser radiation. Our results on second harmonic generation induced by the *s*-polarized radiation support the $\mathbf{v} \times \mathbf{B}$ mechanism as the observed power law exponent of 1.7 is close to the value of 2 predicted for this mechanism. This result also agrees well with 0.8 ps pulse duration experiments of Losev *et al*²³ who observed a power law exponent of 1.8.

We now come to the spectral characterization of the harmonic radiation. Spectral analysis of harmonic generation from solid surfaces was presented in earlier studies performed using femtosecond pulses^{26,28-33,34}. Both blue- and red-shift of harmonic spectra were observed and this effect was attributed to Doppler shift and anomalous skin effect. We have also performed measurements of spectral shift of second and third harmonics of the *p*- polarized pump radiation. The reflected beam, containing the fundamental frequency and collinearly propagating harmonics, was directed to the monochromator (spectral resolution $\sim 0.05 \text{ nm}$). Output slit of the monochromator was fully opened to permit recording of spectral shift of harmonics and their spectral shape on a CCD camera.

Fig. 8 shows spectrum of second harmonic generated from the surface at a laser intensity of $\sim 10^{15} \text{ W cm}^{-2}$. Also shown in Fig. 8 is the spectrum of the second harmonic radiation generated in a *KDP* crystal. It is seen that second harmonic ($\lambda = 526.5 \text{ nm}$) generated in the *KDP* crystal occurs, within the accuracy of measurements, at the $\lambda_f/2$ position ($\lambda_f = 1053 \text{ nm}$ is the wavelength of the fundamental radiation). Spectral width (FWHM) of the second harmonic radiation in this case was $\sim 0.1 \text{ nm}$. In contrast to this, the spectrum of surface generated second harmonic was broadened and red-shifted w.r.to the second harmonic wavelength of the fundamental radiation.

We investigated red-shift of the second harmonic generated from the solid surface (w.r.to the second harmonic wavelength of Nd:glass laser radiation) as a function of laser intensity. Red-shift increased with laser intensity up to $\sim 0.5 \text{ nm}$ as compared to the peak of second harmonic reference spectrum generated in the *KDP* crystal. A similar red-shift for second harmonic ($\Delta\lambda \sim 1 \text{ nm}$) was observed for 350 fs laser pulses by von der Linde *et al*²⁵ who presented detailed measurements of both red- and blue-shifts of second harmonic. Spectral broadening and shift of the harmonic spectra can be explained from a moving mirror model and self-phase modulation of the input radiation during its propagation through the plasma as discussed in detail by Hansen *et al*²⁶.

Third harmonic spectra showed an uncertain behavior, both in terms of broadening and the nature of spectral shift. There was a considerable shot to shot variation at the same laser intensity so that no definitive conclusion could be drawn on the spectral characteristics of the third harmonic radiation.

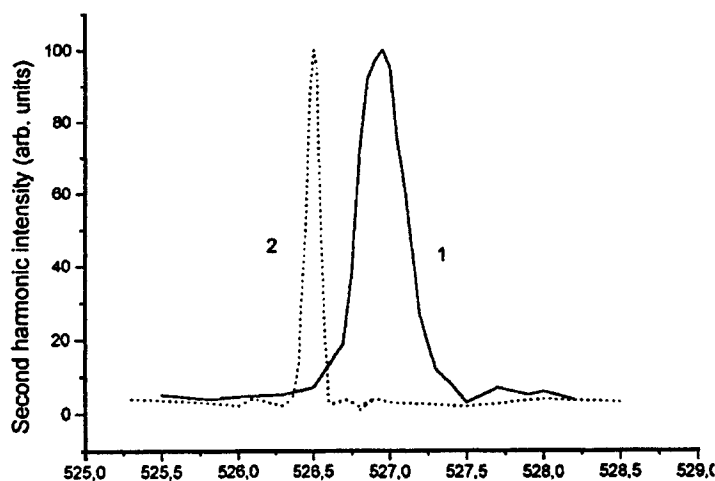


Fig. 8: Spectra of second harmonic generated from the surface (1, $I = 10^{15} \text{ W cm}^{-2}$) and in KDP crystal (2).

Our results on harmonic generation from solid surfaces are broadly in agreement with earlier reported theoretical and experimental investigations performed at large angles of incidence and intensities slightly above $10^{15} \text{ W cm}^{-2}$ where resonance absorption and collisions dominate the absorption process. Occurrence of resonance absorption process²⁶ is generally inferred from various features of the second harmonic generation which include emission of harmonic in the direction of specular reflection, and harmonic wavelength being nearly a factor of two smaller compared to the pump radiation (without considerable spectral shift). Additional features in support of the occurrence of this process are a large value of the ratio of *p*- and *s*- polarization induced second harmonic intensities (tens to hundred times), and the reflectivity being independent of the incident laser intensity.

Except for the observation of dependence of reflectivity on laser intensity, our results are in agreement with the conditions of resonance absorption.

4. CONCLUSION

In conclusions, we have studied harmonic generation from aluminum surface using 27 ps laser radiation at intensities up to $1.5 \times 10^{15} \text{ W cm}^{-2}$. Conversion efficiencies for second, third and fourth harmonics were measured to be 2×10^{-8} , 10^{-10} and 5×10^{-12} respectively. These harmonics were generated by anharmonic motion of electrons on the plasma-vacuum interface. The anharmonicity of such motion is the result of a change in the driving force acting on electrons oscillating in the optical field as they cross from vacuum to dense plasma.

Intensity dependencies of second, third and fourth harmonics showed the power slopes of 1.5, 1.8 and 3.8 respectively. Second harmonic was observed to be confined within a narrow cone in the specular direction, as it was seen by unaided eye. For *p*-polarized laser radiation, the second harmonic efficiency was about ten times higher as compared to that for the *s*-polarized pump radiation. Rotation of second harmonic polarization caused by Faraday effect was observed, and the same could explain the relative yields of second harmonic using *s*- and *p*- polarized pump beam. Detailed measurements of polarization properties and harmonic spectra transformation were performed. Explanations for various observations have been offered, but a more detailed theoretical analysis is necessary for understanding of some peculiarities of the experimental data.

These studies have shown that the main features of harmonic generation from solid surfaces for 27 picosecond laser pump radiation are similar to those observed for the femtosecond laser pulses. Spectral and polarization characteristics of the reflected fundamental radiation and harmonic generation at the surface-vacuum interface have shown that they may serve as a diagnostics for plasma produced by picosecond laser pulses and can be helpful in improving the understanding of the interaction mechanisms of the incident laser radiation with the plasma generated from solid surfaces.

Acknowledgments

Authors would like to thank Dr. D. D. Bhawalkar for support in this work, and one of us (RAG) for his stay with Centre for Advanced Technology. R. A. Ganeev would also like to acknowledge the Third World Academy of Sciences for providing travel support under its Associateship Scheme.

REFERENCES

1. K. J. Schafer and K. C. Kulander, *Phys. Rev. Lett.* **78**, pp. 638-641, 1997.
2. C. Delfm, C. Altucci, F. De Filippo, C. de Lisio, M. B. Gaarde, A.L'Huillier, L. Ross and C.-G. Wahlstrom, *J. Phys. B: At. Mol. Opt. Phys.* **32**, pp. 5397-5414, 1999.
3. M. Schnurer, Z. Cheng, S. Sartania, M. Hentschel, G. Tempea and F. Krausz, *Appl. Phys. B* **67**, pp. 263-270, 1998.
4. J. Zhou, J. Peatross, M. M. Murnane, H.C. Kapteyn and I. P. Christov, *Phys. Rev. Lett.* **76**, pp. 752-756, 1996.
5. I. P. Christov, J. Zhou, J. Peatross, A. Rundquist, M. M. Mumane and H. C. Kapteyn, *Phys. Rev. Lett.* **77**, pp.1743-1747, 1996.
6. S. G. Preston, A. Sampera, M. Zepf, W. J. Biyth, C. G. Smith, J. S. Wark, M. H. Key, K. Bumett, N. Nakai, D. Neely and A. A. Offenberger, *Phys. Rev. A* **53**, pp. 31-47, 1996.
7. Y. Tamaki, J. Itatani, Y. Nagata, M. Obara and K. Midorikawa, *Phys. Rev. Lett.* **82**, pp. 1422-1426, 1999.
8. Y. Tamaki, Y. Nagata, M. Obara and K. Midorikawa, *Phys. Rev. A* **59**, pp. 4041-4050, 1999.
9. S. V. Bulanov, N. M. Naumova and F. Pegoraro, *Phys. Plasmas* **1**, pp. 745-753, 1994.
10. D. von der Linde, and K. Rzazewski, *Appl. Phys. B* **63**, pp. 499-508, 1996.
11. P. Gibbon, *Phys. Rev. Lett.* **76**, pp. 50-54, 1996.
12. P. Gibbon, *IEEEJ. Quantum Electron.* **33**, pp. 1915-1927, 1999.
13. P. A. Norreys, M. Zepf, S. Moustazis, A. P. Fewes, J. Zhang, P. Lee, M. Bakarezos, C. N. Danson, A. Dyson, P. Gibbon, P. Loukakos, D. Neely, F. N. Walsh, J. S. Wark and A. E. Dangor, *Phys. Rev. Lett.* **76**, pp. 1832-1836, 1996.
14. R. L. Carman, D. W. Forslund and J. M. Kindel, *Phys. Rev. Lett.* **46**, pp. 29-33, 1981.
15. R. L. Carman, C. K. Rhodes and R. F. Benjamin, *Phys. Rev. A* **24**, pp. 2649-2659, 1981.
16. R. Lichters, J. Meyer-ter-Vehn and A. Pukhov, *Phys. Plasmas* **3**, pp. 3425-3437, 1996.
17. G. Farkas, C. Toth, S. D. Moustazis, N. A. Papadogiannis and C. Fotakis, *Phys. Rev. A* **46**, pp. 3605-3615, 1992.
18. D. von der Linde, T. Engers, G. Jenke, P. Agostini, G. Grillon, E. Nibbering, A. Mysyrowicz and A. Antonetti, *Phys. Rev. A* **52**, pp. 25-32, 1995.
19. S. Kolhweyer, G. D. Tsakiris, C.-G. Wahlstrom, M. Tilman and I. Mercer, *Opt. Comm.* **117**, pp. 431-436, 1995.
20. D. von der Linde, *Appl. Phys. B* **68**, pp. 315-324, 1999.
21. N. A. Papadogiannis, S. D. Moustazis, P. A. Loukakos and C. Kalpouzou, *Appl. Phys. B* **65**, pp. 339-347, 1997.
22. D. M Chambers, P. A Norreys, A. E. Danger, R. S. Marjoribanks, S. Moustazis, D. Neely, S. G. Preston, J. S. Wark, I. Watts and M. Zepf, *Opt. Comm.* **148**, pp. 289-295, 1998.
23. L. L. Losev and V. I. Soskov, *Quantum Electron.* **28**, pp. 454-460, 1998.
24. A. Ishizawa, K. Inaba, T. Kanai, T. Ozaki and H. Kuroda, *IEEEJ. Quantum Electron.* **35**, pp. 60-66, 1999.
25. N. A. Papadogiannis, P. A. Loukakos and S. D. Moustazis, *Opt. Comm.* **166**, pp. 133-140, 1999.
26. C. T. Hansen, S. C. Wilks and P. E. Young, *Phys. Rev. Lett.* **83**, pp. 5019-5023, 1999.
27. R. S. Marjoribanks, L. Zhao, G. Kulcsar and F. W. Budnik, *Bull. Am. Phys. Soc.*, Denver, pp. 123-127, 1996.
28. D. von der Linde, H. Schuiz, T. Engers and H. Schuler, *IEEE J. Quantum Electron.* **28**, pp. 2388-2401, 1992.
29. J. A. Stamper and B. N. Ripin, *Phys. Rev. Lett.* **34**, pp. 138-143, 1975.
30. A. T. Georges, *Phys. Rev. A* **54**, pp. 2412-2424, 1996.
31. B. Bezzerides, R. D. Jones and D. W. Forslund, *Phys. Rev. Lett.* **40**, pp. 202-206, 1982.
32. S. C. Wilks, W. L. Kruer and W. B. Mori, *IEEE Trans. Plasma Sci.* **21**, pp. 120-127, 1993.
33. T. Engers, W. Fendel, H. Schuler, H. Schuiz and D. von der Linde, *Phys. Rev. A* **43**, pp. 5464-5476, 1991.
34. M. Zepf, M. Castro-Colin, D. Chambers, S. G. Preston, J. S. Wark, J. Zhang, C. N. Danson, D. Neely, P. A. Norreys, A. E. Danger, A. Dyson, P. Lee, A. P. Fewes, P. Gibbon, S. Moustazis and M. H. Key, *Phys. Plasmas* **3**, pp. 3242-3249, 1996.

Non-thermal effects in femtosecond laser damage of transparent materials

Vitali E. Gruzdev*, Anastasia S. Gruzdeva*

State Research Center «S.I. Vavilov State Optical Institute»
Birzhevaya Liniya 12, St. Petersburg, 199034, Russia

ABSTRACT

There are considered non-thermal processes of femtosecond laser-induced damage of wide band-gap transparent materials. Dominating of thermal or non-thermal effects depends on radiation and material parameters among which pulse repetition rate, focal spot size and absorption play key role. Non-thermal mechanisms of damage and ablation can dominate at initiating stage and at low repetition rates (below 10 kHz). They are attributed to nonlinear electrodynamical processes such as higher harmonic generation and formation of shock electromagnetic waves. Considering interaction of shock electromagnetic wave with a particle (single charged particle and a dipole) in potential well, we derive expression for threshold of laser-induced ionization and delocalization. Thermal mechanisms can dominate at later stages of damage and ablation at repetition rates above 10 kHz. There are also discussed after-heating and non-equilibrium non-thermal processes taking place between initiating and thermal stages. There are considered several mechanisms of laser-induced ionization - multiphoton, tunneling, avalanche ionization, also ionization by higher harmonics and by shock-wave front. Estimations of ionization rates show that the latter two mechanisms can dominate at initiating stage of femtosecond damage and determine critically following ionization processes. Obtained results are compared with experimental data.

Key words: femtosecond laser pulses, laser-induced damage, transparent solids, shock electromagnetic waves

1. INTRODUCTION

Great interest attracted by femtosecond laser pulses is connected mainly with possibility to localize laser action in time and in space that corresponds to recent trend to improving of space resolution and quality of laser processing of materials. On the other hand, significant decreasing of pulse duration below 1 ps has resulted in appearing of many experimental data and results that cannot be explained within traditional thermal models of laser-matter interaction. That is especially true for the case of laser interaction with transparent materials.

The most important features of those interactions are extremely small pulse duration and very high damage threshold (10^{13} – 10^{14} W/cm²) [1-6]. Such value of the threshold is observed for many tested materials, and it varies little for different materials. As one can estimate, laser-induced variations of refractive index at laser fluence close to damage threshold are about $\Delta n_{NL} - n_2 I_{TH} \approx 0.05 - 0.01$. In such conditions many nonlinear optical phenomena should be expected to appear before damage starts, for example, generation of higher harmonics, spectral broadening resulting in development of spectral supercontinuum, self-focusing and many other that can occur even at smaller levels of laser-induced variations of refraction. The nonlinear optical effects can play important role in non-thermal processes of initiating of damage and ablation. Influence of electrodynamical effects is illustrated by well-known phenomenon – strong dependence of femtosecond damage on focusing geometry: practically for all materials one cannot observe any significant damage (except formation of color centers [5]) if focal spot size is more than 10 laser wavelengths while strong damage with material removal is observed for tight focusing [3, 4]. On the other hand, thermal effects can also play important role especially for multishot interactions.

Three regimes of femtosecond interactions can be distinguished in this connection: single-shot and multishot damage and ablation at low repetition rate (approximately below 1 kHz) with small linear absorption at input laser wavelength; multishot damage and ablation at high repetition rates (more than 1 kHz) with small linear absorption at input laser wavelength; laser-induced processes in materials with large linear absorption at input laser wavelength. In the first case, non-thermal processes can be expected to dominated at all stages of femtosecond damage and ablation while residual heating can be small. In the second case, non-thermal mechanisms can dominate at initial stage only (within few first shots) while thermal processes play dominating role in incubation effects and formation of ablation crater or damage morphology. The third

*Phonc: (81272) 246-22, Fax (81272) 208-43, E-mail: gru@mailbox.alkor.ru

case of highly absorbing materials is not touched in this paper which general purpose is to consider relation between mentioned thermal and non-thermal effects of femtosecond laser interaction with transparent materials.

To consider areas of dominating thermal and non-thermal mechanisms of femtosecond interactions, we will refer to some experimental data. *Characteristic parameters of laser radiation* are one of the most important among them:

- pulse duration $\tau_p = 500 \text{ fs} - 10 \text{ fs}$ [1 - 11];
- laser wavelength in vacuum $\lambda_0 = 10.6 \mu\text{m} - \text{IR}$ [1, 2, 9] - $1.06 \mu\text{m}$ [11] - $0.8 \mu\text{m}$ [3, 4, 6, 8] - $0.6 \mu\text{m}$ [5];
- energy of laser quantum $h\nu$ 0.117 eV - 1.17 eV - 1.55 eV - 2.07 eV;
- type of laser FE lasers Nd³⁺:glass Ti:sapphire
- intensity of laser radiation at focal plane 1) for self-focusing and white-light generation $I_{\text{TH}}^* = 10^{12} - 10^{13} \text{ W/cm}^2$ [12 - 14], 2) for laser-induced damage and ablation $I_{\text{TH}}^{**} = 10^{13} - 10^{14} \text{ W/cm}^2$ [1 - 11];
- focal spot radius $r_F = 1 \mu\text{m} - 10^2 \mu\text{m}$ [1 - 11];
- repetition rate (for multi-pulse damage and ablation) from 10 Hz to 10^9 Hz (pulse trains [1, 2]).

The most important and characteristic features of femtosecond interactions leading to problems in building their theory are 1) small pulse duration excluding classical thermal mechanisms of laser-induced heating and damage resulting from phase explosion; 2) high radiation intensity which can result in a variety of nonlinear optical processes accompanying laser action on transparent materials and changing its character.

Materials used in considered experiments are wide band-gap semiconductors and dielectrics which typical band gap is 3 or more times larger than photon energy [1 - 11]: $E_g \geq 3h\nu$. Characteristic value of nonlinear coefficient of refraction is about $n_2 \approx 10^{-16} \text{ cm}^2/\text{W}$. Linear constant part of refractive index n_0 for most of considered materials varies between 1.45 and 3. Structure of investigated materials varies from crystal to amorphous solids (glasses). Many of investigated materials are isotropic, for example, fused silica and glasses of various types. Characteristic feature is small absorption α at input laser wavelength that varies from 10^{-2} to 10^{-3} cm^{-1} . Group velocity dispersion coefficient β is about $200 - 500 \text{ fs}^2/\text{cm}$. Heat conductivity of investigated dielectric materials varies from 40 W/(m grad) (crystal Al_2O_3 at $T=300 \text{ K}$) to 1.36 W/(m grad) (fused silica at $T=300 \text{ K}$) depending on structure (crystal or amorphous) of the materials while density and specific heat capacity vary no more than by factor of 2. Looking through papers with experimental data, one can find that often used material for femtosecond laser-induced damage and ablation is fused silica which parameters are as follows: $E_g = 7.5 \text{ eV}$ [14], $n_0 = 1.45$, $n_2 = 2 \cdot 10^{-16} \text{ cm}^2/\text{W}$ [13], absorption $\alpha \approx 10^{-3} \text{ cm}^{-1}$, group velocity dispersion coefficient $\beta = 385 \text{ fs}^2/\text{cm}$ [13], thermal conductivity $k = 1.36 \text{ W/(m grad)}$, specific heat capacity $C = 890 \text{ J/(kg grad)}$, density $2,650 \text{ kg/m}^3$.

For further estimations we can use the following figures resulting from experimental data. First, length of effective nonlinear interaction path can be estimated as beam path s in nonlinear material along which nonlinear interaction is the most effective: $s \approx 2z_c = \pi r_F^2 / \lambda$. For the presented above values of focal spot radius it varies from 10 to $10^4 \lambda$, but in case of tight focusing, the most typical value of s is $(10 - 15)\lambda$. For pulse duration 100 fs effective dispersion length is about several cm in glass BK-7 or fused silica [13]. Thus, path of effective nonlinear interaction is at least 1000 times less than dispersion length, and group velocity dispersion can be neglected in the first approximation. Photon energy is 1.55 eV for the most typical laser wavelength $0.8 \mu\text{m}$. Thus, five photons should be absorbed to produce ionization in fused silica. For wavelength $4.0 \mu\text{m}$ photon energy is 0.31 eV, thus, 25 photons should be absorbed to produce ionization.

Considering a variety of experimental data [1-11, 15, 16 and references therein], one can distinguish three phases of high-power femtosecond laser interaction with transparent solids - initial stage (non-thermal interaction and excitation), intermediate stage (non-equilibrium energy transfer) and final stage (after-heating, diffusion, damage and/or ablation). Non-thermal processes must dominate at the stage of initiating of femtosecond interactions for both single-shot and multi-shot action. Following the scheme of energy transfer from [1, 9], we can say that those processes are connected with initial energy transfer from laser pulse to laser-induced plasma and electronic and vibrational excitations (Fig. 1). Particular mechanisms can be connected with nonlinear electrodynamical processes and straight action of electric field on crystal lattice as they are discussed in section 3. As the most suitable candidate for that we consider generation of higher harmonics that can result in formation and propagation of shock electromagnetic waves (SEW). The processes can also provide sufficient modification of transparent material without heating during single-pulse action, resulting in local excitations [1, 9] leading to phase transition from crystal to amorphous matter [4] and even in total removal of material from focal area [3, 4]. Thus, they are very probable to dominate during whole single-pulse action on transparent materials.

Energy transfer at intermediate stage (Fig. 1) goes through several steps [1, 9] resulting in formation of quasi-equilibrium electron plasma, radiative relaxation, heating and diffusion of electrons and laser-induced defects. The later processes

represent final – thermal – stage of femtosecond action (Fig. 1) when laser-induced electron plasma formed during femtosecond pulse propagation should be considered as a source of heating. In case of multi-shot laser action at high repetition rates, laser-induced defects can be accumulated leading to incubation effects [8] in multi-pulse laser action connected with increasing of linear absorption at input laser wavelength. Total after-heating can be large in that case, and those processes can result in thermal damage or ablation of the material. Thus, final thermal stage of femtosecond interactions can be dominating one for multi-shot ablation with high repetition rate. Considering two limiting cases of femtosecond actions – single-pulse action and multi-shot action at high repetition rate – one comes to conclusion that there must be a critical repetition rate that separates two regimes of femtosecond ablation – thermal and non-thermal. Discussion of those processes and determining of critical value of repetition rate can be found in section 5.

1. Initiating

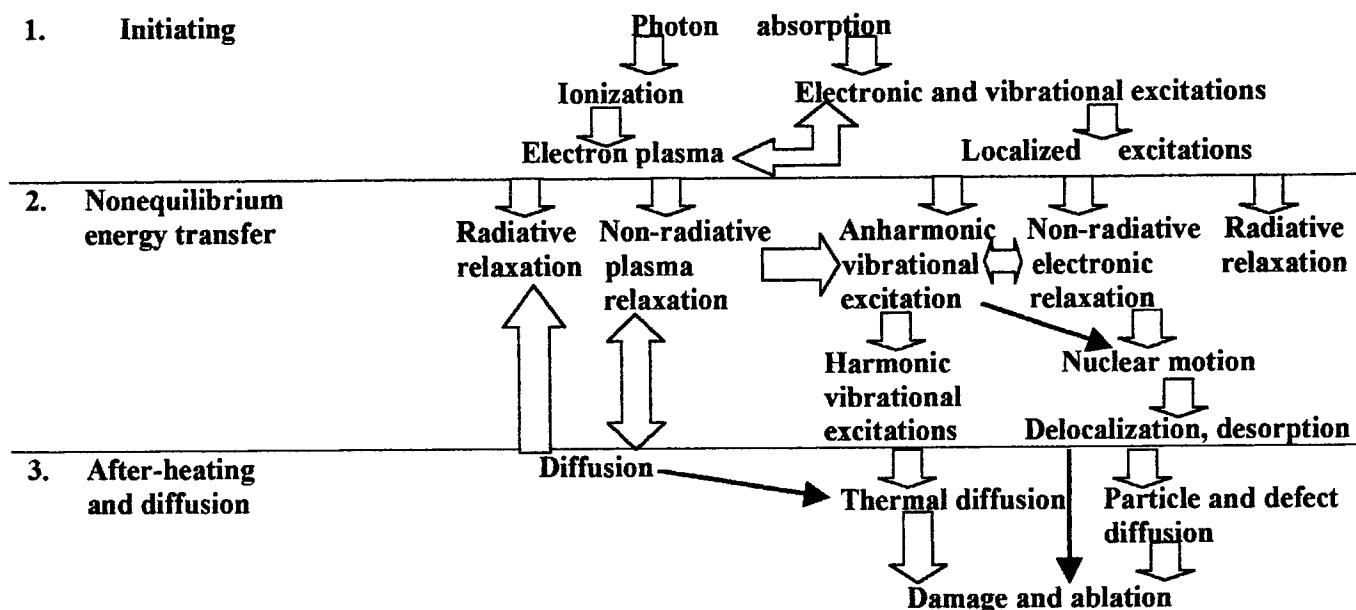


Fig. 1. Energy transformation from absorption to damage and ablation in transparent materials induced by femtosecond laser pulse.

2. NONLINEAR OPTICAL EFFECTS OF FEMTOSECOND PULSE PROPAGATION

Nonlinear optical effects are very natural to be considered as mechanisms of initiating of femtosecond laser interactions. That is connected mainly with their small *inertia* and small pulse duration what makes straight non-thermal energy transfer to localized excitations of crystal lattice more effective than other ways connected with energy absorption by electrons and following thermalization in electron and phonon subsystems.

Effects connected with generation of higher harmonics and formation of abrupt space variations of electric-field strength are the most suitable candidates for being mechanisms of initiating of femtosecond interactions in transparent solids among all possible nonlinear optical processes. Recently authors proposed model of electromagnetic shock wave [17, 18] as that combining both those features. As it was pointed out in [17, 18], SHEW can appear at initial stage of femtosecond interaction and within small leading part of laser pulse (first few periods of laser radiation only) where laser-induced variation of material parameters are small enough to be neglected. Duration of leading part of laser pulse to be considered is determined by characteristic time of laser-induced plasma excitation up to the level when it gives sufficient distortions to pulse propagation [19]. That time is about 15-20 fs. Plasma excitation is assumed to be the fastest process, other laser-induced processes of material parameters modification have longer excitation time and their influence on nonlinear pulse propagation at leading edge of laser pulse can be neglected. Thus, throughout this paper we consider only few (no more than 10) first cycles of femtosecond laser pulse.

Without detailed discussion of SHEW formation and propagation, we briefly describe here several features of SHEW that are important for the discussions below. First, SHEW can appear at laser fluence below damage threshold according to obtained in [17, 18] expression for SHEW threshold

$$E_{th} \approx \sqrt{\frac{n_0}{n_2} \left(\exp\left\{ \frac{\Delta x}{s} \right\} - 1 \right)}, \quad (1)$$

where s is length of path of effective nonlinear propagation in transparent material, Δx is length of mashed part of wave cycle: $\Delta x \leq s$ and $\Delta x \leq \lambda/4$. For example, "pessimistic" estimation of disruption threshold corresponds to mashing of a quarter of optical cycle $\Delta x = 0.25\lambda_0/n_0$ within rather small interaction path $s = z_c = 15\lambda_0$, and it is $I_{th} \leq 1.18 \cdot 10^{14} \text{ W/cm}^2$ for $n_0 = 1.41$, $n_2 = 2 \cdot 10^{-16} \text{ cm}^2/\text{W}$ (fused silica). Confocal parameter corresponds to focal spot radius $r_f = 2.18\lambda_0 (=1.71 \mu\text{m}, \lambda_0 = 0.8 \mu\text{m})$. "Optimistic" estimation gives $I_{th} \leq 6 \cdot 10^{12} \text{ W/cm}^2$ for $s = z_c = 120\lambda_0/n_0$, $\Delta x = 0.1\lambda_0/n_0$ (focal spot radius $r_f = 6.18\lambda_0$).

Formation of SHEW results in appearing of abrupt variation of electric-field strength referred to as SHEW front (Fig. 2, points 1, 2). The front becomes smoother and turns into complicated structure under action of dispersion (Fig. 2).

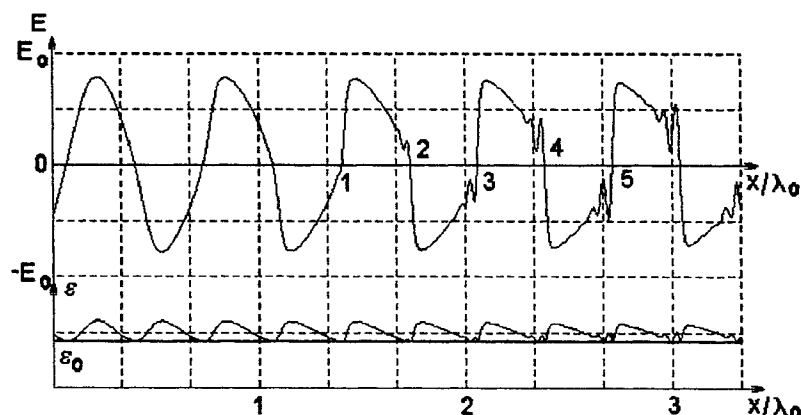


Fig. 2. Formation of SHEW in fused silica (results of FDTD modeling from [17, 18]). 1 – appearing of field disruption, 2 – the disruption turns into abrupt SHEW front, 3, 4, 5 – developing of high-frequency vibrations near SHEW front. Lower part of this figure depicts field-induced variations of dielectric function.

As one can see in Fig. 2, abrupt SHEW front can be approximated by linear dependence on space coordinate for early steps of SHEW propagation while the rest of laser-radiation period looks like unperturbed or lightly perturbed part of a sine. In the first approximation one can neglect field distortions near SHEW front appearing during SHEW propagation and take into account other important SHEW feature – becoming of its front sharper with developing of SHEW. Bearing this in mind, we use below the following approximate description of SHEW (Fig. 3). SHEW front is approximated by linear dependence, and front depth Δ varies from $0.1\lambda_0/n_0$ (weak SHEW describing initial stages of its formation) to $0.01\lambda_0/n_0$ (strong SHEW at late stages of its formation). Other part of wave profile is approximated by sine.

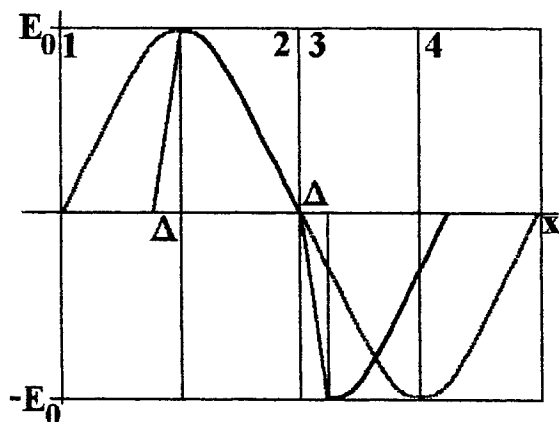


Fig. 3. Approximate description of SHEW for investigation of interactions between SHEW front and transparent material with positive nonlinear coefficient of refractive index (focusing nonlinearity). SHEW is shown by black line while one cycle of harmonic wave is shown by grey line. SHEW fronts of depth Δ appear within the second and the third quarters of initial laser wavelength and are described by linear function. The fronts are considered to move with speed V of SHEW given by (7). Harmonic wave of initial laser frequency is shown with grey for comparison.

Thus, the following description of SHEW electromagnetic field is used: SHEW front appears with approximately linear variations of electric-field strength while field profile is approximately sine between two neighboring SHEW fronts at least at early stages of SHEW formation (Fig. 2). That implies the following description of field variations:

$$E(x, t) = R \cdot (x - V \cdot t), \quad R = \frac{\partial E}{\partial x}; \quad (3)$$

within SHEW front, $E(x, t) = E_0$ before SHEW front where field strength reaches maximum, and $E(x, t) = E_0 (kx - \omega t)$ behind SHEW front where field varies approximately linearly starting with zero. SHEW front described by (3) is assumed to move at speed V that depends on value of electric-field strength E and electric induction D before SHEW front E_1, D_1

and behind it E_2 , D_2 :

$$V = \frac{c_0 \cdot (E_2 - E_1)}{\mu_0 \cdot (D_2 - D_1)} \quad (4)$$

For the case depicted in Fig. 2, one can assume $E_1=0$, $E_2=E_0$ where E_0 is field amplitude. Then, one obtains the following estimation of SHEW speed from (4): $V \cong c_0 E_0 / (E_0 [\varepsilon_0 + \varepsilon_2 E_0^2]) \cong c_0 / n_0^2$. Thus, SHEW moves n_0 times slower than electromagnetic waves forming the SHEW. That implies possible reflection of higher harmonics at SHEW front resulting in complicated interplay between them that cannot be described within approximation of single-direction propagation.

One more important property of SHEW is incubation of its action on crystal particles (e.g., dipoles). As one can see from Fig. 2, that happens due to breaking of symmetry of harmonic waves resulting from formation of SHEW front. Moreover, interaction of SHEW front with a dipole can be especially effective because a sine part of deformed optical cycle forms a dipole, which reaches its maximum value before it begins to interact with SHEW front that can be referred to as "pre-action" of sine part of optical cycle moving before SHEW front.

3. INITIATING OF FEMTOSECOND LASER-INDUCED DAMAGE

As it follows from experimental results, initial stages of femtosecond laser-matter interactions must be managed by fast mechanisms with very small *inertia* because typical pulse duration is less than time of energy transfer from electrons to phonons. The mechanisms must be rather universal, without strong dependence on wavelength if the latter is within transparency band. They must act for pulse duration from several hundreds of femtoseconds to few tens of femtoseconds. The mechanisms must include both effective ionization taking place before irreversible changes of material properties and non-thermal laser-induced damage of transparent materials. We suppose SHEW to be the most suitable nonlinear electrodynamic process for being fast mechanism of initiating of femtosecond damage and desorption. There are two reasons for that connected with *main features of SHEW* [15 - 18]:

- generation of higher harmonics (odd harmonics in isotropic medium) – can result in effective ionization;
- formation of abrupt shock front (can result in straight action on crystal lattice).

General picture of femtosecond laser-matter interactions with participating of SHEW can be as follows. SHEW interaction with transparent materials is dominating mechanism of processes taking place at single-shot as well as at few first shots of low-rate multi-shot interactions. Strong SHEW corresponding to disruption of electric field is formed in case of tight focusing when the pathway of effective nonlinear interaction is small enough for nonlinear distortions to dominate over dispersion. That type of SHEW can damage crystal lattice through removing of ions out of crystal points and formation of point defects, e.g., vacancies. Probably, strong SHEW can produce macroscopic damage of material near focal area. The damage can result from straight action of electric field of SHEW front on dipoles in crystal lattice if amplitude of input wave exceeds certain threshold [15, 16]. In case of not tight focusing only weak SHEW (corresponding to disruption of space derivation of electric field strength) can appear. It is accompanied by higher harmonics generation resulting in ionization and formation of color centers. Macroscopic damage cannot be produced in that case because strong SHEW does not appear due to influence of color dispersion. Important point is that ionization takes place at laser fluence below damage threshold because formation of even weak SHEW is accompanied by generation of HH. Gradient force appearing near SHEW front due to large gradient of laser intensity can be large enough to result in significant pressure what can change conditions of material modification. That phase turns into the next phase of femtosecond interactions dominated by nonequilibrium processes of relaxation, non-diffusion and diffusion motion of SHEW-generated electron plasma and defects, in particular, delocalization of crystal points and even ablation from surface if laser fluence is high enough.

Thus, there can be distinguished the following three mechanisms of initiating of non-thermal interaction of femtosecond laser pulse with transparent materials: ionization, straight action of electric field of SHEW front on crystal lattice, and action of large pressure resulting from large gradient of laser intensity near SHEW front. All the mechanisms are considered below.

3.1. Ionization – competition between several mechanisms

Main mechanisms of ionization treated within traditional approaches are multiphoton [3, 4, 7], avalanche [4, 7] and tunneling [3] ionization. Among them multiphoton ionization is usually taken as the most probable mechanism which is observed in experiments on femtosecond laser-induced damage of solids [3, 4, 7]. That is true in case when nonlinear optical effects are neglected, and laser radiation is described within model of plane harmonic wave. Bearing in mind generation of higher harmonics during pulse propagation and possible formation of electromagnetic shocks, one can add

two more mechanisms of ionization - ionization by higher harmonics and ionization by SHEW front [15, 16]. Multiphoton ionization is considered vs. ionization by higher harmonics and SHEW front in this section.

In the first approximation speed of electron generation dn/dt (ionization rate) can be described by a constant G that depends on material and radiation parameters rather than on electron density [20]:

$$\frac{dn}{dt} = G \propto \frac{\alpha \cdot I}{h\nu}, \quad (5)$$

where α is absorption coefficient dependent on laser intensity I in case of multiphoton absorption:

$$\alpha_{N\text{-photon}} = n' \cdot \sigma_N \cdot I^{N-1}, \quad (6)$$

where n' is density of absorbing particles, σ_N is absorption cross section. In case of one-photon absorption (6) gives linear absorption:

$$\alpha_L = n' \cdot \sigma_1. \quad (7)$$

Expressions (5) – (7) allow to estimate ionization rates for one-photon absorption of N -th order higher harmonic and N -photon absorption. The most optimistic estimations for multiphoton absorption can be obtained for the case $N=3$ because absorption cross-section σ_N decreases fast with increasing of N . On the other hand, it follows from experimental data of Section 1 that three-photon absorption is the lowest-order multiphoton absorption that can take place in wide band-gap materials. According to estimations and numerical results [21] intensity I_{III} of higher harmonics participating in ionization can reach about 10% of radiation intensity I_0 at initial laser wavelength. On the other hand, cross-section for one-photon absorption $\sigma_{1\text{-photon}}$ is about 10^{-16} cm^2 [22] what gives absorption $\alpha_{1\text{-photon}} \cong 10^5 \text{ cm}^{-1}$. Three-photon absorption is given as $\alpha_{3\text{-photon}} = \sigma_3 n' - \delta_3 E^4 n' - \beta E^4$ where $\delta_3 \cong 10^{-54} 1/(\text{cm}^2 \text{ s})$ [22, 23]. Thus, for speed of free-electron generation at laser intensity $5 \cdot 10^{13} \text{ W/cm}^2$ (corresponding field amplitude $E=2 \cdot 10^8 \text{ V/cm}$) one obtains [20]

$$\frac{G_{3\text{-photon}}}{G_{3\text{-harmonic}}} = \frac{\alpha_{3\text{-photon}} I_0}{\alpha_{1\text{-photon}} I_{3\text{-harmonic}}} = \frac{\delta_3 E^4 I_0}{\sigma_{1\text{-photon}} 0.1 I_0} \approx 0.0001 \quad (8)$$

Thus, in presence of SHEW in isotropic dielectric, the lowest order odd harmonic alone produces 10000 times more electrons than 3-photon ionization, i.e., multiphoton ionization gives less than 0.01% of total amount of free electrons. Ratio of ionization speeds decreases with increasing of order of harmonics and multiphoton absorption because probability of multiphoton absorption decreases fast while absorption of HH increases. Thus, ionization by HH is much more effective than multiphoton ionization widely accepted in recent theoretical models [3, 7].

After SHEW front has passed, it can leave point defects, electrons, color centers and other defects [17, 18] which can have energy levels in band gap. That makes possible low-order multiphoton ionization when electron absorbs two – three photons and jumps from valance band to one of intermediate states in band gap, then absorbs two – three photons again and jumps to other intermediate level and so forth until it reaches conduction band (Fig. 4). Probability of such “multi-jump” multiphoton ionization is higher and threshold is smaller than corresponding values for usual multiphoton absorption due to larger absorption cross-section [24]. Several positive feedbacks can appear in this process resulting in blow-up ionization and generation of point defects within focal area [24].

Ionization by HH seems to be the most effective at leading edge of femtosecond laser pulse even if SHEW front does not appear due to strong influence of color dispersion. Ionization rate for ionization through generation of N -th harmonic is proportional to I_0^N because intensity of HH increases as N -th order of input laser intensity I_0 . On the other hand, N -photon absorption has the same dependence I_0^N on input intensity [22] that has been observed in many experiments. Thus, experimental distinguishing of those two processes is not a trivial problem, and the law I_0^N cannot be attributed to N -photon absorption alone.

Other important feature is two- or three-photon absorption of HH with suitable quantum energy. Efficiency of that process is smaller than efficiency of one-photon absorption: M -photon ionization through absorption of HH of N -th order with intensity I_N is proportional to $I_N^M < I_0^{M+N}$. Important point is that in some particular cases ionization by HH can be of small efficiency. That is possible in case when a) there is small energy transfer to HH with photon energy large enough for one-photon ionization; b) two- or three-photon ionization by HH of smaller order is impossible because their intensity is not enough. For example, laser radiation with input wavelength $\lambda_0=4.00 \mu\text{m}$ propagating in fused silica ($E_g=7.5 \text{ eV}$) can result in generation of HH upto 21-st order: $E_g/h\nu_0 \cong 21$. Then rather sharp SHEW front can appear before ionization by 21-st harmonic becomes significant. In such cases one can consider ionization by SHEW front as it was considered in [15, 16]. That process can be considered as simultaneous absorption of several photons of HH (Fig. 5). Simultaneous

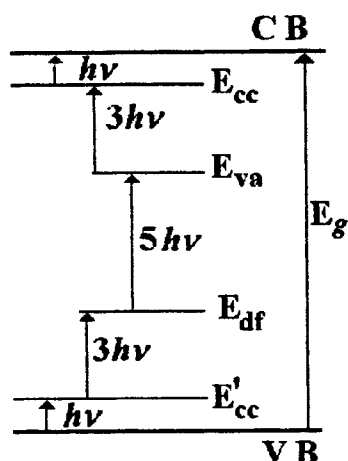


Fig. 4. Energy levels of SHEW-induced defects in band gap and electron transitions between them occurring due to absorption of low-order HH. E_{cc} , E'_{cc} – energy levels of laser-induced color centers, E_{va} and E_{df} – energy levels of laser-induced vacancies and other defects. Energy of main-harmonic photon is $h\nu$.

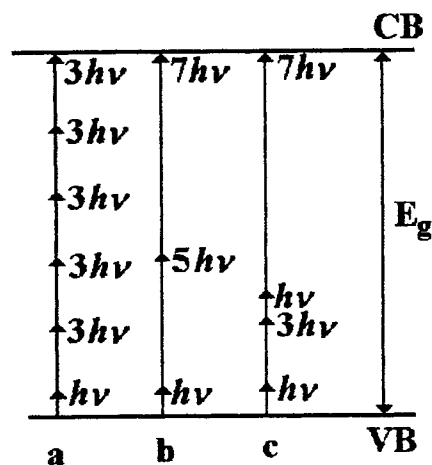


Fig. 5. Scheme of electron transitions through band gap due to simultaneous absorption of several HH of low order. Minimum order of HH required for such transitions is given by (9). Energy of main-harmonic photon is $h\nu$. Probability of multiphoton processes (a, c) increases with decreasing of order of ionization. The highest probability of ionization is reached for the process with all different photons (b in Fig. 5).

absorption of HH with all different frequencies is the most probable process because its total absorption cross section is the largest among all other possible processes with participation of two or more photons with similar quantum energy (Fig. 5). In this case, ionization begins when intensity of HH or certain minimum order exceeds threshold level. Minimum order of HH can be easily calculated as

$$N \geq 2 \sqrt{\frac{E_g}{h\nu_0}} - 1, \quad (9)$$

where ν_0 is central frequency of input laser pulse. For example, $N \geq 8.165$ for considered above example with $\lambda_0 = 4.00 \mu\text{m}$. Thus, SHEW can produce ionization (referred to as straight SHEW-induced ionization) even if each appearing higher harmonic has so small photon energy that cannot ionize the material along through one-photon absorption.

Concluding remarks of this section are about avalanche and tunneling ionization. The first of them can contribute to ionization much more than it is usually assumed because it can have about 10000 times more seed electrons at leading edge of femtosecond pulse appearing due to ionization by HH than due to ionization resulting from multiphoton absorption of photons of input laser frequency. The other type of ionization – tunneling – has not been touched upon in this paper because its probability is usually less than probability of multiphoton ionization except the case of very high damage threshold [3] when tunneling of electrons can take place in very specific conditions that should be discussed in a separate paper.

3.2. Non-thermal damage mechanism

The problem of SHEW interaction with transparent materials is very complicated. Bearing that in mind, we start consideration of this problem with the simplest classical model [15, 16] when electric field of laser radiation is described by classical electrodynamics (that is quite correct for high-power radiation) and motion of structural units of crystal is described by equations of classical mechanics. Advantages of that approach are quite clear:

- 1) obtaining of simple model and equations that can be integrated;
- 2) developing of clear intuitive insight into the problem of SHEW-matter interactions;
- 3) possibility of comparison with similar results for plane harmonic waves [for example, 1, 25].

Considering structural units of ionic crystal [15, 16], one can distinguish two general types of particles – single charges and dipoles. In the simplest model of SHEW interaction with crystal lattice and point defects there should be taken into account the following: 1) action of SHEW electric field described by force $F_{SHEW} = qE$ for each single charge; 2) bonding force appearing due to particle motion in a potential well $U(x)$ and described by force $F_U = -\nabla U$; 3) damping due to energy transfer to surrounding particles described by damping force $F_D = m\gamma dr/dt$ where γ is damping constant. Considering motion of single charge $q = Ne$ consisting of N units of electron charge e , we use the following equation [15, 16]:

$$m \cdot \frac{d^2 \mathbf{r}}{dt^2} = N \cdot e \cdot \mathbf{E} - m \cdot \gamma \cdot \frac{d\mathbf{r}}{dt} - \nabla U \quad (10)$$

where $\mathbf{r}=(x, y, z)$. In case of single free charge (free electron) the latter term in right-hand part of (10) disappears.

Motion of a dipole consisting of two particles with masses m_1 and m_2 with charges of $q=Ne$ should be described by a couple of equations similar to (10) written for each charge forming the dipole. Those equations can be transformed into system of other two equations. The first of them describes motion of mass center of the dipole

$$M \frac{d^2 \mathbf{R}}{dt^2} = N \cdot e \cdot (\mathbf{d}, \nabla) \cdot \mathbf{E} - M \cdot \gamma \cdot \frac{d\mathbf{R}}{dt} - \nabla U, \quad (11)$$

and the second one describes motion of the charges with respect to each other, i.e., variations of dipole momentum:

$$m_{1,2} \frac{d^2 \mathbf{d}_{1,2}}{dt^2} = -m_{1,2} \omega_0^2 \mathbf{d}_{1,2} - m_{1,2} \gamma \cdot \frac{d\mathbf{d}_{1,2}}{dt} + Ne\mathbf{E}, \quad (12)$$

where d is dipole length. Equations (10) - (12) do not include terms describing action of magnetic field that is very small as compared to F_{SHEW} for particle speeds much below speed of light.

Bearing in mind geometry of plane wave (electric-field vector is along y -coordinate axis while the wave moves along x -coordinate axis), one can separate vector equations (10) - (12) and reduce them to simpler form. Then separated equations can be integrated in quadratures for accepted model of SHEW (3). As a result one obtains speed of motion in a certain direction, and kinetic energy transferred from SHEW wave of amplitude E_0 to the particles can be found. In the first approximation damping can be neglected because duration of SHEW-front action is much less than usual value of $1/\gamma$. Then one can obtain expressions for energy transferred from single SHEW front to single free charge $q=Ne$, ion with charge $q=Ne$ in potential well (bonded single charge), and a dipole with momentum $p=d_0(Ne)$ [15, 16]. Those expressions allow calculating of absorption of SHEW energy due to its transfer to particles of crystal lattice and calculation of SHEW amplitude required for moving particles away from their potential wells. The latter problem is of primary interest.

Moving away an electron from its potential well means ionization by SHEW front as it was discussed in previous section and formation of color center. Moving of neutral or charged dipole away from its well means laser-induced delocalization of crystal points and formation of point defect like a vacancy or interstitial [1]. SHEW-induced delocalization of crystal points at surface of material is desorption or ablation [1]. All those processes depend critically on depth of SHEW front Δ .

Equations (10) - (12) allow calculating of threshold SHEW amplitude for corresponding processes: kinetic energy of a particle received from SHEW must be equal to the depth of potential well U_0 for ions at crystal lattice (threshold of laser-induced delocalization) and U_0^e for electron in valence band. Thus, we calculate intensity of laser field at which kinetic energy transferred from single SHEW to the particle front is close to maximum potential energy of bonded particle. The depth of potential well for electron is about band gap (8 eV for fused silica). Potential-well depth for ion at crystal lattice is about $U_0 \approx 0.8$ eV [16]. Using obtained equations and data, one gets the following estimations for SHEW amplitudes:

1) threshold of removing of an ion (N -charged dipole)

$$F_0^* = \frac{\Delta \cdot \sqrt{2M_i(U_0 - W_0^e)}}{Ne \left| \frac{d_0}{\omega_0} \sin\left(\frac{\Delta \cdot \omega_0}{V}\right) - \frac{\Delta^2}{2V} \right|}, \text{ where } U_0 \approx \frac{M_A}{N_A} \int_{T_0}^{T_{mel}} C(T) dt \quad (13)$$

2) threshold of electron removing from potential well (SHEW-induced ionization)

$$E_0^* = \frac{\Delta \cdot \sqrt{2m_e(U_0^e - W_0^e)}}{e \left| \frac{d_0}{\omega_0} \sin\left(\frac{\Delta \cdot \omega_0}{V}\right) - \frac{\Delta^2}{2V} \right|} \quad (14)$$

3) threshold of removing of neutral dipole from potential well

$$E_0^{**} = \frac{\Delta \cdot \omega_0 \sqrt{2M(U_0 - W_0)}}{ed_0 \left| \sin\left(\frac{\Delta \cdot \omega_0}{V}\right) \right|}, \text{ where } U_0 \approx \frac{M_A}{N_A} \int_{T_0}^{T_{mel}} C(T) dt \quad (15)$$

where W_0 and W_0^e are initial kinetic energies of corresponding particles in absence of SHEW, $C(T)$ is heat capacity per kg, $N_A=6.022 \cdot 10^{23}$ 1/mol is Avogadro number, M_A is molecular weight (kg/mol).

One of the most interesting results following from (13) and (14) is that for rather weak SHEW (front depth $\Delta \approx 0.1\lambda$) ionization takes place before delocalization of ions and the latter always take place before neutral dipoles are moved away from their potential wells. SHEW-induced straight ionization and moving a single ion away from its potential well is more effective than moving away an atom because energy transferred from single SHEW front to the ion is about an order of magnitude higher than energy transferred to an atom [15, 16]. But there is an area of SHEW parameters within which removing of dipole from potential well occurs at lower amplitude of electric-field strength than ion delocalization [15, 16].

Other interesting conclusions from (13) – (15) are 1) linear dependence of threshold laser intensity for ionization on band gap, 2) linear dependence of threshold laser intensity for delocalization on molecular weight and specific heat capacity. Using (13) – (15) one can obtain estimations of thresholds for ionization, ion and atom delocalization to be produced by single front of weak and strong SHEW [15, 16]. Those thresholds are much higher than inner atomic electric-field strength and experimentally measured values that points out at limited applicability of classical description to consideration of SHEW-induced processes.

3.3. Action of gradient force

One more important non-thermal effect is connected with action of radiation pressure and gradient force. The latter force appears and grows with appearing of laser-induced variations of refraction and is given by [26]:

$$\vec{f} = -\frac{E^2}{8\pi} \cdot \nabla \varepsilon + \nabla \left(\rho \frac{E^2}{8\pi} \left[\frac{\partial \varepsilon}{\partial \rho} \right]_{T=const} \right) + \frac{\varepsilon\mu - 1}{4\pi c} \frac{\partial}{\partial t} [\vec{E} \times \vec{H}] \quad (16)$$

where ρ is medium density, ε is dielectric function including both linear and nonlinear parts. SHEW model is very promising in this connection too because space variations of laser-induced refraction have very large gradients near SHEW front. Really, accepting dependence of dielectric function on laser field in the form $\varepsilon = \varepsilon_0 + \varepsilon_2 E^2$, one can estimate value of gradient force from (16) as

$$|f| = \frac{E^4}{4\pi \Delta} \cdot \varepsilon_2 + \frac{E^2}{4\pi \Delta} \cdot \rho \cdot \left[\frac{\partial \varepsilon}{\partial \rho} \right]_{T=const} \quad (17)$$

near SHEW front with depth Δ . That force increases much with decreasing of SHEW front depth and can reach values enough for material deformation. Really, assuming SHEW front depth to be $0.05 \lambda_0$ and taking data corresponding to fused silica, one can estimate pressure near SHEW front as 500 atmospheres. That can be of great importance for understanding of mechanisms of femtosecond laser-induced surface evolution, in particular, formation of surface ripple patterns.

3.4. Comparison with experiments

SHEW model is in good qualitative agreement with many peculiarities of femtosecond laser-matter interactions [1 - 11]. Really, very high thresholds of femtosecond damage and ablation are very close to obtained estimation of threshold for SHEW formation [16, 17] what makes proposed model very promising for study of femtosecond laser-induced processes at high laser fluences. Generation of higher harmonics can be a model for description of generation of higher harmonics of very high order (21 – 27 harmonics in UV and X-ray ranges) observed during femtosecond interactions [10].

Important point is also strong dependence of SHEW formation on focusing conditions. Strong SHEW can appear only in case of tight focusing because in that case effective path of SHEW formation is small enough for generated harmonics to have small phase differences due to dispersion. Then harmonics are well synchronized and form sharp SHEW front. Interesting point is that damage is observed in the same conditions when strong SHEW can appear, i.e., in case of tight focusing only [5]. Increasing of focal spot radius results in increasing of the path of SHEW formation, influence of dispersion becomes stronger and abrupt SHEW front can disappear due to large phase differences between different harmonics. In the most optimistic case weak SHEW can appear but it cannot produce damage because there is no large gradient of laser intensity near its front. That corresponds observed formation of color centers only without damage of the material [5]. In that case other nonlinear effects become important, for example, self-focusing and self-defocusing [5].

Sequence of laser-induced processes during femtosecond damage [4] is also in good agreement with proposed picture of SHEW formation. Really, at early stage of SHEW propagation depth of SHEW front is large and the SHEW is weak, thus,

ionization by higher harmonics is much more efficient than delocalization. Increasing of laser fluence results in appearing of strong SHEW that can ionize atoms and ions as well as move single atoms and ions away from their positions in crystal lattice. That results on formation of point defects that are not visible but lead to increasing of scattering [4]. Further increasing of laser fluence makes SHEW so "strong" that density of damaged lattice points becomes large and damaged site becomes visible. Changes of SHEW-induced material structure can vary from appearing of voids (strong SHEW moves away all ions and atoms) to transition from crystal to amorphous structure [3, 4]. Presented model is also in good agreement with absence of thermal damage around ablated and damaged sites because SHEW-induced damage of crystal lattice is very fast process and energy transfer to heat is rather small.

4. NONEQUILIBRIUM PHASE

After laser energy comes to localized excitations (Fig. 1) and electron plasma appears during laser pulse propagation, the processes of non-equilibrium energy transfer start. Description of those processes presents unsolved problem till now. Most recent models for description of those processes are based on Boltzmann's equation [for example, 27] while two important points should be taken into account in this connection. First, appearing of laser-induced defects at the stage of initiating of femtosecond interaction can change crystal lattice in such way that traditional formulation of Boltzmann's equation becomes not valid [28]. Other difficult problem with application of Boltzmann's equation appears in case of amorphous media of glass type, while several approaches to that problem have been developed [28]. Second, Boltzmann's equation becomes not valid in case of strong electron-phonon coupling [28]. Influence of that factor is very difficult to be estimated because there is no reliable data on electron-phonon coupling in dielectrics. Discussion of all those problems cannot be done in the framework of this paper because of its limited volume in spite of clear importance of those questions.

5. THERMAL PROCESSES OF MULTI-PULSE FEMTOSECOND DAMAGE AND ABLATION

After thermalization of energy inside electronic sub-system and relaxation of anharmonic excitations (Fig. 1) the energy is transferred to phonons (thermal relaxation) and photons (radiative relaxation). The first process results in heating of irradiated material after single pulse has gone what is referred to as after-heating. Thermal description of that processes can be applied at time no earlier than characteristic energy thermalization time what is about $10^{-14} - 10^{-13}$ s for electron subsystem and $10^{-12} - 10^{-13}$ s for phonon subsystem. Relaxation time for laser-induced plasma is about $5 \cdot 10^{-9}$ s [4], thus, quasi-equilibrium heated electron and phonon systems co-exist and exchange energy for rather long time. Then, description of crystal heating must be based on model taking into account electron relaxation (both thermal and radiative), electron diffusion and energy exchange between electron and phonon sub-systems. Initial energy comes to this phase of femtosecond interaction from previous non-equilibrium processes and must be described through initial conditions. Possible approach to description of after-heating process can be based on modified two-temperature model [29 - 32] coupled (as it was proposed by Prof. M.N.Libenson) with diffusion equation for electrons [33].

Together with absorption, pulse repetition rate is the most critical parameter for thermal processes. Influence of pulse repetition rate is connected with accumulation of heating from pulse to pulse. It can be illustrated with simple estimations. Considering temperature distribution in focal volume induced by single pulse, one can express temperature as [34]

$$T(\vec{r}, t) = T_0 \cdot F(\vec{r}) \cdot \exp\left(-\frac{t}{\tau}\right) = T_0 \cdot F(\vec{r}) \cdot \exp\left(-f \cdot \frac{a \cdot t}{d^2}\right), \quad (20)$$

where T_0 is maximum temperature, $F(r)$ describes space distribution, $\tau = d^2 / (f \cdot a)$ is characteristic decay time, f is geometry dependent constant factor, a (m^2/s) is thermal conductivity, d is characteristic dimension of heated volume. Approximating focal volume by sphere of radius R equal to focal spot radius, one have $d=R$, $f=\pi^2$. Taking into account data for fused silica ($a=5.766 \cdot 10^{-7} \text{ m}^2/\text{s}$ at room temperature), one obtains then the following estimations:

$\tau=1.757 \cdot 10^{-7}$ sec. for $R=1 \text{ }\mu\text{m}$, $\tau=1.757 \cdot 10^{-5}$ sec. for $R=10 \text{ }\mu\text{m}$, and $\tau=1.757 \cdot 10^{-3}$ sec. for $R=100 \text{ }\mu\text{m}$.

Value of decay time varies a little for different geometries [34] – sphere, cylinder, ellipsoid. Thus, description of focal area as a sphere does not give large error in decay time value. Obtained values of decay time determine critical pulse repetition rates. For example, at 100 kHz repetition rate (time interval between two neighboring single femtosecond pulses is about 10^{-5} s) for focal spot radius $10 \text{ }\mu\text{m}$ one obtains: $T(t=10^{-5} \text{ s}) / T(t=0) = \exp(-1/1.757) \approx 0.66$. Thus, about 66% of thermal energy stays within focal area by the time next pulse arrives, and accumulation of thermal energy can be rather large. Important point is that decay time increases (and critical repetition rate decreases) as R^2 with increasing of focal spot size, and 1 kHz repetition rate can be enough for heat significant accumulation inside focal area at focal spot radius $100 \text{ }\mu\text{m}$.

Significant accumulation of thermal energy during multi-pulse irradiation can result in significant temperature-induced variations of optical parameters, in particular, appearing of positive feedbacks through temperature-induced variations of absorption and refraction [24]. Strong incubation effect can be expected for multi-pulse damage at repetition rates above 1 MHz while incubation effects at low repetition rates can be rather small what has been observed in experiments [6, 8].

6. CONCLUSIONS

Considering of experimental data on femtosecond interactions with transparent materials shows that two types of damage and ablation mechanisms can be distinguished – thermal damage and ablation taking place at multi-shot action with high repetition rates, and non-thermal damage and ablation appearing at single-shot or at low repetition rates. Critical repetition rate determines dominating of one of the mechanisms in formation of ablation crater or damage site and depends on temperature decay time determined by size of focal area and temperature conductivity.

Non-thermal mechanisms should be connected with nonlinear optical processes among which generation of higher harmonics is the most promising. Those mechanisms can dominate at initial stages of femtosecond interaction with no respect to repetition rate. In case of single-shot and low repetition rate interactions they can dominate even in formation of ablation crater. Interaction of electromagnetic shocks appearing on optical cycle due to HH generation can be considered as a possible mechanism of non-thermal damage and ablation. Attractive features of SHEW connected with abrupt SHEW front near that one can expect large laser-induced pressure and damage of crystal lattice due to straight action of electric field of SHEW front. Presented model has good qualitative agreement with many experimental regularities of femtosecond laser-matter interactions.

Multiple-pulse action is accompanied by incubation of SHEW-induced defects resulting in increasing of absorption at input laser wavelength and higher-harmonic wavelengths. Thus, in case of multi-shot femtosecond action with high repetition rate it is possible to distinguish fast mechanisms acting during few first shots and slow mechanisms connected with incubation of laser-induced defects and after-heating produced through absorption by the defects that dominates in formation of ablation crater. This idea is supported by observed morphology of ablation craters formed by multi-pulse radiation at high repetition rates [1, 2].

Presented estimations show that ionization by higher harmonics and by shock front can be dominating mechanisms of ionization at leading part of femtosecond pulse. It can result in more than 100 times higher ionization rate than that resulting from multiphoton absorption. That means, that density of seed electrons for developing of avalanche ionization can be at least 100 times more than it is usually accepted on the bases of model of multiphoton absorption.

7. ACKNOWLEDGEMENTS

Authors wish to thank Prof. M.N.Libenson (S.I.Vavilov State Optical Inst., Russia) and Dr. B.Rethfeld (University of Essen, Germany) for fruitful discussions of various aspects of shock waves and laser-matter interaction. This work was partly supported by INTAS (project 97-31777) and grant of Russian Foundation for Basic Research N 00-02-16716-□

8. REFERENCES

1. R.F.Haglund, Jr., "Mechanisms of Laser-Induced Desorption and Ablation", in *Laser Ablation and Desorption*, eds. J.C.Miller and R.F.Haglund, Jr. (Boston, Academic Press, 1998), pp. 15-138.
2. H.K.Park, R.F.Haglund Jr., "Laser Ablation and Desorption from Calcite from Ultraviolet to Mid-Infrared Wavelengths", *Appl. Phys. A*, v. 64, pp. 431-438, 1997.
3. C.B.Schaffer, A.Brodeur, N.Nishimura, and E.Mazur, "Laser-induced microexplosions in transparent materials: microstructuring with nanojoules", *Proc. SPIE*, v. 3616, 1999, to appear.
4. C.B.Schaffer, E.N.Glezer, N.Nishimura, and E.Mazur, "Ultrafast laser induced microexplosions: explosive dynamics and sub-micrometer structures", in *Commercial Applications of Ultrafast Lasers*, *Proc. SPIE*, v. 3269, p. 36-45, 1998.
5. D.von der Linde, H.Schuler, "Breakdown threshold and plasma formation in femtosecond laser-solid interaction", *JOSA B*, v. 13, N 1, pp. 216-222, 1996.
6. E.E.B.Campbell, D.Ashkenasi, and A.Rosenfeld, "Ultra-short-Pulse Laser Irradiation and Ablation of Dielectrics", in *Lasers in Materials*, edited by R.P.Agarwal (Trans Tech Publ., 1998), Ch. 5.
7. B.C.Stuart, M.D.Feit, S.Herman, A.M.Rubenchik, B.W.Shore, and M.D.Perry, "Nanosecond-to-femtosecond laser-induced breakdown in dielectrics", *Phys. Rev. B*, v. 53, pp. 1749-1761, 1996.

8. D.Ashkenasi, A.Roscnfeld, H.Varel, M.Wahmer, E.E.B.Campbell, "Laser processing of sapphire with picosecond and sub-picosecond pulses", *Appl. Surface Science*, v. **120**, pp. 65-80, 1997.
9. R.F.Haglund Jr., R.Cramer, D.R.Ermer, M.R.Papantonakis, H.K.Park, and O.Yavas, "Vibrational Excitation and Relaxation Processes in Insulators Initiated by Ultrashort, Mid-Infrared Laser Pulses", in *Laser Applications in Microelectronic and Optoelectronic Manufacturing IV*, Proc. of SPIE, v. **3618**, 1999 (to appear).
10. A.Bouhal, R.Evans, G.Grillon, A.Mysyrowicz, P.Breger, P.Agostini, R.C.Constantinescu, H.G.Muller, D. von der Linde, "Cross-correlation measurement of femtosecond noncollinear high-order harmonics", *JOSA*, v. **14**, p. 950, 1997.
11. T.V.Kononenko, V.I.Konov, S.V.Garnov, R.Danielius, A.Piskarskas, G.Tamoshauskas, F.Dausinger, "Comparative study of material ablation by femtosecond and pico/nanosecond laser pulses", *Quantum Electronics*, v. **28**, N 2, pp. 167-172, 1999.
12. R.L.Fork, C.V.Shank, et al, *Opt. Letters*, v. **8**, N 1, p. 1, 1983.
13. J.K.Ranka, and A.L.Gaeta, "Breakdown of the slowly varying envelope approximation in the self-focusing of ultrashort pulses", *Opt. Letters*, v. **23**, N 7, pp. 534-536, 1998.
14. A.Brodeur, S.L.Chin, "Band-Gap Dependence of the Ultrafast White-Light Continuum", *Phys. Rev. Lett.*, v. **80**, N 20, pp. 4406-4409, 1998.
15. A.S.Gruzdeva, V.E.Gruzdev, "Initiating of femtosecond laser-induced damage and ablation of transparent solids by shock electromagnetic waves", in *High-Power Laser Ablation II*, Proc. SPIE, v. **3885**, pp. 358-367, 2000.
16. A.S.Gruzdeva, V.E.Gruzdev, "Interaction of shock electromagnetic waves with transparent materials: classical approach", in *Laser Applications to Microelectronic and Optoelectronic Manufacturing-VI*, Proc. SPIE, v. **3933**, 2000.
17. V.E.Gruzdev, A.S.Gruzdeva, "Formation of shock electromagnetic waves during femtosecond pulse propagation in transparent solids", in *Optical Beam and Pulse Propagation*, Proc. SPIE, v. **3927**, 2000 (to appear).
18. V.E.Gruzdev, A.S.Gruzdeva, "Formation and propagation of shock electromagnetic waves in transparent solids", in *High-Power Laser Ablation-II*, Proc. SPIE, v. **3885**, pp. 346-357, 2000.
19. O.G.Kosareva, V.P.Kandidov, A.Brodeur, C.Y.Chien, S.L.Chin, "Conical emission from laser-plasma interactions in the filamentation of powerful ultrashort laser pulses in air", *Opt. Lett.*, v. **22**, N 17, pp. 1332-1334, 1997.
20. S.A.Akhmanov, V.I.Emelyanov, N.I.Koroteev, V.N.Seminogov, "Action of high-power laser radiation on surface of metals and semiconductors: nonlinear optical effects and nonlinear optical diagnostics", *Sov. Phys. - Uspehi Phisicheskikh Nauk*, v. **147**, N 4, pp.675-745, 1985 (in Russian).
21. A.S.Gruzdeva, V.E.Gruzdev, "Interaction of shock electromagnetic waves with absorbing media", in *High-Power Laser Ablation III*, Proc. SPIE, v. **4065**, 2000 (to appear in this volume).
22. R.H.Pantell, H.E.Puthoff, *Fundamentals of Quantum Electronics*, John Wiley and Sons, Inc., New York, 1969.
23. R.H.Pantell, F.Pradere, J.Hanus, M.Schott, H.E.Puthoff, "Theoretical and Experimental Values for Two, Three and Four Photon Absorptions", *Journal of Chem. Phys.*, v. **46**, p. 3507, 1967.
24. V.E.Gruzdev, A.S.Gruzdeva, V.L.Komolov, and M.N.Libenson, "Laser-induced instability in transparent materials induced by low-absorbing microinclusion" in *Laser-Induced Damage in Optical Materials: 1998*, Proc. of SPIE, v. **3578**, pp. 772-783, 1999.
25. E.Mazur, "Interaction of Ultrashort Laser Pulses with Solids", in *Spectroscopy and Dynamics of Collective Excitations in Solids*, ed. B.Di Bartolo, Plenum, NATO ASI series, 1996.
26. Landau, Lifshits, *Electrodynamics of Continuous Media*,
27. B.Rethfeld, A.Kaiser, M.Vicanek, and G.Simon, "Excitation and relaxation dynamics of electrons and phonons in solids absorbing subpicosecond laser pulses", in *High-Power Laser Ablation II*, Proc. SPIE, v. **3885**, p. 200-211, 2000.
28. O.Madelung, *Introduction to Solid-State Theory*, Springer-Verlag, New York, 1978.
29. S.I.Anisimov, B.Rethfeld, "Theory of ultrashort laser pulse interaction with a metal", in *Nonresonant Laser-Matter Interaction (NLMI-9)*, Proc. SPIE, v.3093, pp.192-203, 1997.
30. B.Huttner, "Short-pulse laser heating of metals: a new approach", in *Nonresonant Laser-Matter Interaction (NLMI-9)*, Proc. SPIE, v.3093, pp. 366-373, 1997.
31. J.J.Klossika, U.Gratzke, M.Vicanek, and G.Simon, "Importance of a finite speed of heat propagation in metals irradiated by femtosecond laser pulses", *Phys. Rev. B*, v. **54**, N 15, pp. 10277 - 10279, 1996.
32. E.I.Levanov, E.N.Sotskiy, "Heat transfer with taking into account heat-flux relaxation" in *Mathematical Modelling: Nonlinear Equations of Mathematical Physics*, eds. A.A.Samarskiy, S.P.Kurdiumov, V.I.Mazhukin, Moscow, Nauka, 1987, pp. 155 - 190 (in Russian).
33. A.S.Gruzdeva, V.E.Gruzdev, "Relaxation processes and formation of thermal shock waves during laser ablation", Proc. SPIE, v. 4065, pp. 200-209, 2000.
34. A.V.Luikov, Y.A.Mikhailov, *Theory of Energy and Mass Transfer*, Pergamon Press, London, 1965.

Investigation of nonlinear optical parameters of metal composites by Z-scan technique

A. I. Ryasnyansky⁺, R. A. Ganeev, Sh. R. Kamalov, M. K. Kodirov⁺, T. Usmanov

NPO Akadempribor, Academy of Sciences of Uzbekistan, Tashkent 700143, Uzbekistan

⁺ Samarkand State University, Samarkand 703004, Uzbekistan

ABSTRACT

Investigations of nonlinear optical parameters of Au, Ag, Pt and Cu colloidal solutions by Z-scan method are presented. Nonlinear refractive indices of these solutions on the wavelength of Nd:YAG laser radiation ($\lambda=1.064$ nm) and its second harmonic ($\lambda=532$ nm) have been measured. Two-photon absorption and nonlinear susceptibilities of these solutions have been studied.

Keywords: Colloidal metals, nonlinear refractive index, susceptibility, nonlinear absorption

1. INTRODUCTION

Investigation of nonlinear refractive indices, two-photon absorption coefficients and nonlinear optical processes connected with self-focusing and self-defocusing of various media is of current interest. The optical nonlinearities of such media are attractive for potential applications in nonlinear optical signal processing and optical devices. Nonlinear refraction of materials is of great interest for a variety of nonlinear optical applications. It should be noted, that although such methods as nonlinear interferometry, degenerate four wave mixing (DFWM) and non-degenerate three wave mixing are very sensitive, there are some problems connected with their application. These techniques require relatively complicated experimental apparatus. Interpretation of measurements of optical nonlinearities of materials are often complicated by the presence or the competition of two or more nonlinear processes. In many cases above mentioned experimental methods cannot separate these nonlinearities. At the same time another technique reported earlier as Z-scan method^{1,2} allows to determine the basic nonlinear optical characteristics caused by different nonlinear processes.

In these papers the new high-sensitive single beam method for determination of nonlinear refraction indices, nonlinear susceptibilities and two-photon absorption coefficients was applied for the first time. This method based on investigation of changes of Gaussian beam intensity profile in the far field during moving of the sample through the focal plane. This process accompanied by changing of power density as the radiation flow remains relatively constant. The main advantage of this method is the fact that for nonlinear optical characteristics determination it is necessary to know only transmission data of the investigated sample. This method is capable to separate the contribution of refractive and absorptive nonlinearities in the case when both two nonlinearities are presented simultaneously.²

Nonlinear optical characteristics of colloidal solutions of metals are under active investigation during last time due to their using as optical limiters of high-power laser radiation. These materials demonstrate high nonlinearities and fast response,^{3,4} especially in the frequency region of surface plasma resonance. Most of nonlinear optical studies of metal colloidal solutions were made using DFWM method. First wave-conjugation experiments in gold and silver colloidal solutions⁵ have shown large reflective index enhancement near the plasma resonance frequency. On the basis of such investigations the range of perspective colloidal solutions was suggested for the optical limiting experiments. Authors of Ref. 6 have shown the connection between small particles associates in metal colloidal solutions and their fractal properties. In Refs. 4,7 it was shown that copper colloidal solution has the considerable value of nonlinear refractive index. The same results have been obtained for silver^{3,8} and gold^{9,10} colloidal solutions.

Nonlinear susceptibilities $\chi^{(3)}$ of silver and gold colloidal solutions were investigated in Refs. 3,8,9. The value of $\chi^{(3)}$ changed from 10^{-11} to 10^{-13} esu depending on fraction of metal particles in composite. At the same time nonlinear optical susceptibilities of silver and gold metal particles were in the range of $(1-5) \times 10^{-8}$ esu and $(2-4) \times 10^{-9}$ esu respectively. A value

of $\chi^{(3)} = 10^{-7}$ esu has been reported in Ref. 11 for copper doped glasses which makes these materials effective for optical limiting.

In this paper, the nonlinear optical parameters of colloidal solutions of various metals (silver, gold, copper and platinum) using Z-scan method were investigated. We measured nonlinear refractive indices, nonlinear optical susceptibilities and nonlinear absorption of such solutions on the wavelength of Nd:YAG laser radiation and its second harmonic ($\lambda=1.064$ nm and 532 nm, $\tau=35$ ps).

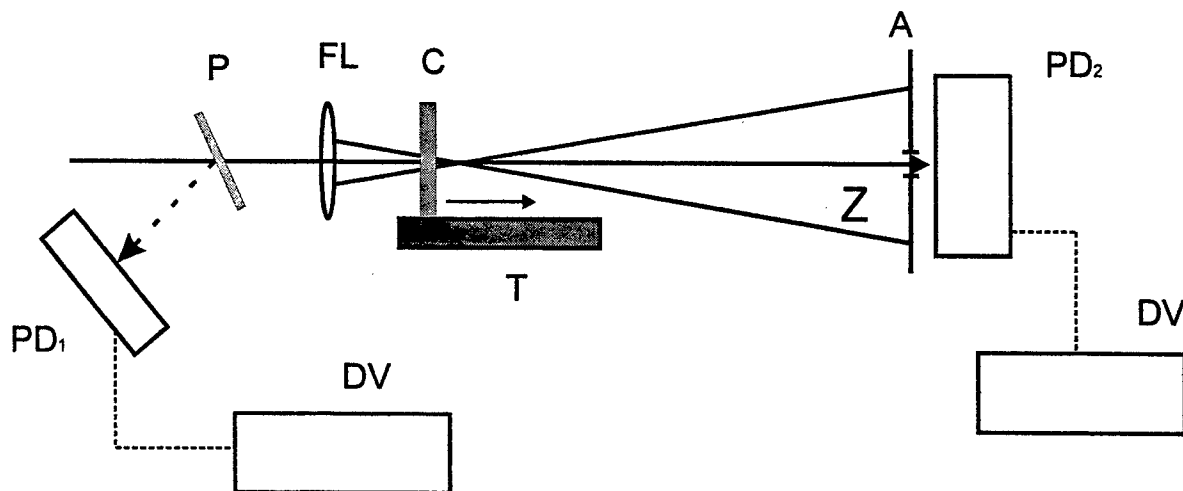


Fig. 1. Experimental set-up: FL – focusing lens; C – cell with colloidal solutions; PD₁, PD₂ – photodiodes; DV – digital voltmeters; A – aperture; T – table; P – glass plate.

2. EXPERIMENTAL SET-UP

In our experiments Nd:YAG laser which generated picosecond pulse train was used. Single pulse ($\tau=35$ ps) extracted from the train was amplified up to 2 mJ. We investigated nonlinear optical characteristics of metal colloidal solutions on the wavelength of Nd:YAG laser radiation (1.064 nm) and its second harmonic (532 nm).

Laser radiation was focused by 25-cm focal length lens (FL, Fig. 1). 5-mm thick quartz cell (C) with colloidal solution moved along Z-axis through the focal point. Spot size of focused radiation was 150 μm , which corresponded to the intensity of $4 \times 10^{11} \text{ W cm}^{-2}$, i. e. it was lower than the threshold of optical damage and multiphoton ionisation of colloidal solution. Using of 15-cm focal length lenses caused an optical ionisation of colloidal solution. Laser radiation had 10% energy fluctuations. Energy of each input pulse was measured by calibrated photodiode (PD₁) FD-24K and digital voltmeter (DV). Calibrated filters were used for laser radiation energy measurements. 1-mm aperture was set-up at the distance of 150 cm from the focusing point which transmitted nearly $S=0.01$ of whole output radiation. Photodiode (PD₂) FD-24K was kept behind this aperture for measurement of output radiation. To avoid non-stability of laser radiation on our results, we used the ratio of transmitted and incident radiation. Experiment set-up with closed aperture ($S=0.01$) allowed to determine the sign and magnitude of nonlinear refraction index (n_2) and nonlinear susceptibility ($\chi^{(3)}$). For measurements of two-photon absorption coefficient (β), the experimental set-up with open aperture was used. To determine the dependence of sample's transmission on the intensity of laser radiation, detector was kept at such distance from the sample that allowed to measure all transmitted radiation. So, decreasing of sample's transmission was attributed to the nonlinear absorption.

To prepare the colloidal gold solution, 30 ml of 1% sodium citrate solution was added to 250 ml of boiling tetrachloroauric acid solution. The mixture was boiled till deep wine red colour was obtained indicating formation of gold colloidal solution. Metal platinum was used to prepare platinum colloidal solution. For this purpose, 0.1 g of platinum was dissolved in HCl and HNO₃ mixture, so that 1 ml of solution contained 1 mg of platinum. To prepare the standard Cu solution we dissolved 4 g of CuSO₄ in one litre of distilled water. In this case 1 ml of solution contained 1 mg of Cu. For preparation of standard Ag solution we dissolved 20 mg of collargolum in 200 ml of bidistilled water and heated this solution at 90 °C.

3. EXPERIMENTAL RESULTS AND DISCUSSION

Optical absorption spectra of metal colloidal solutions have been changed as a result of laser irradiation. In the case of non-aggregated colloidal gold solution the absorption peak was located in the region of 525 nm that coincided with results reported earlier.¹⁰ After irradiation the aggregated colloidal gold absorption peak has moved to $\lambda = 550$ nm. This fact can be explained by aggregation of colloidal gold under the action of radiation. Hydrosol colour during this experiment has changed from wine-red to violet-red. The same picture was observed in the case of other colloidal solutions, particularly in colloidal silver.

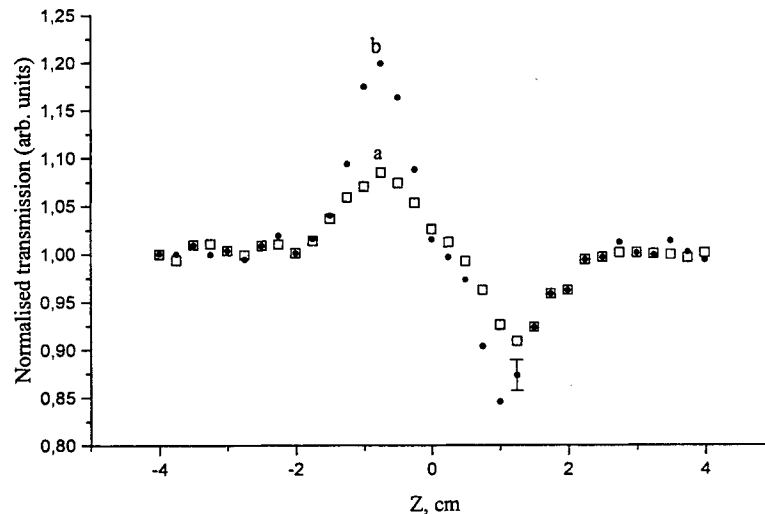


Fig. 2. Normalised transmission as a function of colloidal gold cell position in closed aperture scheme.

Silver colloidal solution is a well-known classical object for optical phenomena investigation. Surface plasma resonance in the case of silver hydrosol is located in the region of 410–420 nm.¹² Silver colloidal aggregation under the action of radiation was observed in Ref. 13. It is also led both to the surface plasma resonance frequency shift to the long-wave spectrum region and to the changes of nonlinear optical properties. Spectral shift observed in our experiments with colloidal silver can be explained by particles aggregation in to the fractal clusters accompanied by dipole-dipole interaction of light induced dipole moments with the surrounded particles.

Metal colloidal solutions were investigated in a number of studies with the purpose to study aggregate's growth under the action of radiation.^{12,14,15} In these papers absorption spectra of solutions were used to determine the changing of particles size. In Refs. 12,13 sharp increasing of particles aggregation under the action of radiation was observed.

Characteristic dependencies of samples transmission (T) in closed aperture scheme as a function of cell position respectively to focal point for $\lambda=1.064$ nm are shown for colloidal gold in Fig. 2,a. The same dependencies were investigated for other metal colloidal solutions. All colloidal solutions had nonlinear refractive indices of positive sign excluding gold solution. The same picture was observed for $\lambda=532$ nm excluding copper colloidal solution, where the nonlinear refractive index has changed its sign from positive to negative (Fig. 3). Observed dependencies can be explained by Kerr-induced nonlinearities, which led to the changing of refractive index in strong electromagnetic field.

Cubic nonlinearities of refractive index (n) which depends on the radiation intensity can be determined as follows²:

$$n = n_0 + 0.5 n_2 |E|^2 = n_0 + \gamma I, \quad (1)$$

where n_0 - linear refractive index, n_2 - nonlinear refractive index, I - radiation intensity, E - electric field of electromagnetic wave.

n_2 and γ are connected with the following relation:

$$\gamma [m^2 / W] = 40 \pi n_2 [\text{esu}] / c [m / s] n_0, \quad (2)$$

where c - light velocity.

Reported earlier investigation of gold aggregates at the wavelength of 532 nm have shown that changes of the refraction index can be due to the different physical mechanisms. Refraction index changes under the action of nanosecond pulses ($\tau=30$ ns) were observed in Ref. 10. This result was attributed to the thermal-induced changing of media density during pulse propagation due to its particular absorption. They could not registered ultra-fast component of n_2 using radiation with pulse duration of 4 ps ($I=10^8 \text{ W cm}^{-2}$). The top limit appreciated by them, for the "fast" component of a nonlinear susceptibility was approximately $\chi^{(3)}=2.9 \times 10^{-14}$ esu while for nanosecond pulses this value was much higher (4.5×10^{-11} esu).

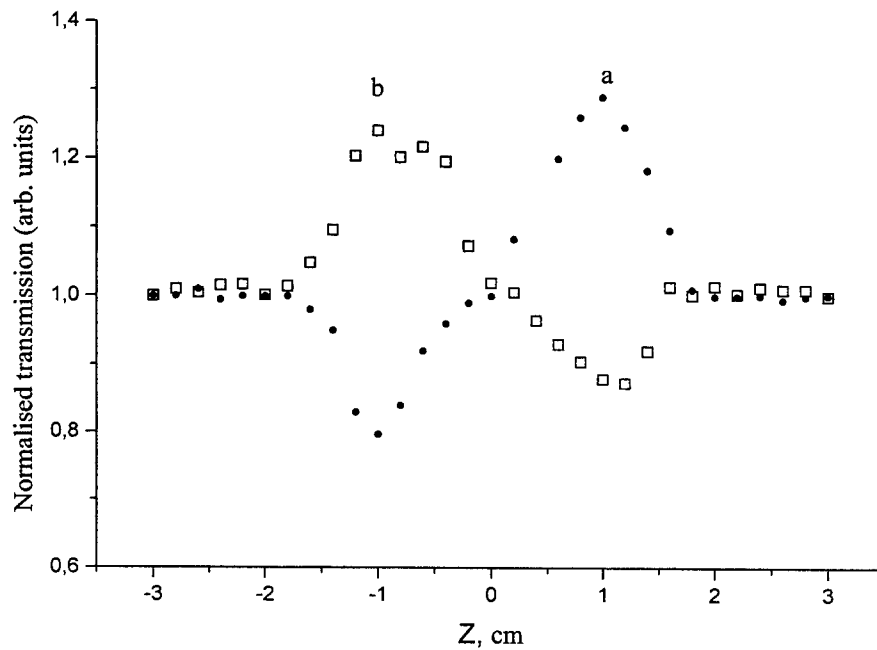


Fig. 3. Normalised transmission as a function of colloidal copper cell position in closed aperture scheme. $a - \lambda=1.064$ nm, $b - \lambda=532$ nm.

In our experiments, power density in the focus has been chosen such a way that there were no optical damage on the cell surface and inside the media volume. For gold solutions we used $I \leq 4 \times 10^{11} \text{ W/cm}^2$. This intensity was below the damage threshold which was estimated as $8 \times 10^{11} \text{ W cm}^{-2}$ (for $\lambda=1.064$ nm).

For calculations of nonlinear-optical parameters of samples we used equations of Z-scan theory:²

$$\Delta T_{pv} = 0.404 (1 - S)^{0.25} |\Delta \Phi_0| \quad (3)$$

and

$$\Delta \Phi_0 = (2 \pi / \lambda) n_2 I L_{\text{eff}}, \quad (4)$$

where ΔT_{pv} – normalised difference between peak-to-value transmission, I – radiation intensity, S – transmission of the aperture, $\Delta \Phi_0$ – phase distortion of radiation passed through the cell, L_{eff} – sample's effective length, that can be determined as follows:

$$L_{\text{eff}} = [1 - \exp(-\alpha L)] / \alpha \quad (5)$$

Here L – length of the sample, α – linear absorption.

Nonlinear refractive indices for colloidal gold were calculated to be $n_2 = -1.82 \times 10^{-14}$ esu for $\lambda = 1.064$ nm and $n_2 = -1.96 \times 10^{-13}$ esu for $\lambda = 532$ nm.

Nonlinear susceptibility of colloidal gold was determined from the equation:¹⁰

$$\chi^{(3)} [\text{esu}] = \gamma [m^2 / W] n_0^2 / 5.26 \times 10^{-6} K^{(3)} \quad (6)$$

(where $K^{(3)}$ – numerical factor, considering as 1) and was calculated to be 1.68×10^{-15} esu for $\lambda = 1.064$ nm, and 1.8×10^{-14} esu for $\lambda = 532$ nm. Obtained value of nonlinear susceptibility for colloidal gold solution for $\lambda = 532$ nm was in a good agreement with the result reported in Ref. 10. For Ag, Pt and Cu solutions the nonlinear susceptibilities were determined by the same way.

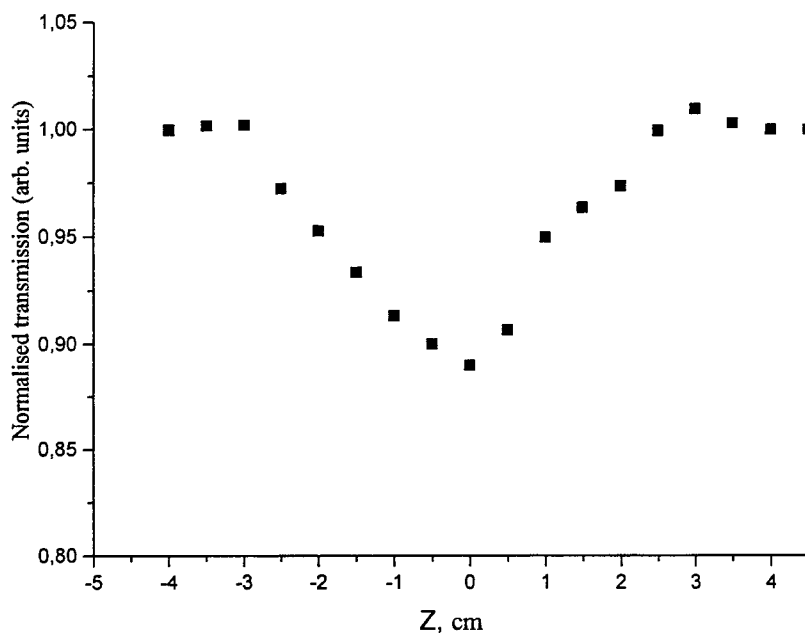


Fig. 4. Normalised transmission as a function of colloidal gold cell position in open aperture scheme.

Calculated results for linear absorption coefficients (α), nonlinear refractive indices (n_2), nonlinear susceptibilities ($\chi^{(3)}$) and two-photon absorption coefficients (β) of investigated colloidal solutions for two wavelengths are presented in Table 1.

Nonlinear refraction in such materials takes place as the result of different mechanisms such as Kerr effect,¹⁶ thermal focusing,¹⁷ population-induced focusing,¹⁸ etc. Taking into account the fact that power density in our experiments was large enough ($4 \times 10^{11} \text{ W cm}^{-2}$), the ratio of aggregate's hyperpolarizability causing Kerr-induced self-focusing and self-defocusing should overlap other two mechanisms.

Nonlinear absorption measurements of investigated solutions have shown, that it took place only for colloidal gold. Fig. 4 shows an open aperture experiments on transition measurements of colloidal gold. One can see the characteristic normalised transmission dependence on the cell position with the respect to focal point.

In our case nonlinear absorption was due to reverse saturable absorption (RSA) as a result of aggregate's excitation into the high-located levels with larger absorption cross-section in comparison with ground levels. It should be noted that samples which show RSA are of great interest for optical limiters elaboration, which can be used for eyes and high-sensitive sensors protection from intense radiation.

Table. 1. Nonlinear optical characteristics of metal colloidal solutions.

Hydrosol	λ , nm	α , cm^{-1}	$n_2 \times 10^{-14}$, esu units	$\chi^{(3)} \times 10^{-15}$, esu units	$\beta \times 10^{-13}$, $\text{cm} \times \text{W}^{-1}$
Au	1064	0.6	-1.82	1.68	9.84
	532	0.94	-19.6	18.1	94
Ag	1064	0.22	3.39	3.12	
	532	0.51	10.2	9.37	
Cu	1064	0.12	4.2	3.86	
	532	0.07	-13.8	12.7	
Pt	1064	0.87	1.13	1.04	
	532	0.23	8.8	8.11	

Two-photon absorption coefficient was determined as follows:²⁰

$$\beta = q_0 / I L_{\text{eff}} \quad (7)$$

and

$$T_0 = q_0^{-1} \times \ln(1 + q_0), \quad (8)$$

where T_0 – normalised transmission minimum in open aperture experiment, q_0 - dimensionless parameter. Two-photon absorption coefficient was calculated to be $9.8 \times 10^{-13} \text{ cmW}^{-1}$ ($\lambda=1.064 \text{ nm}$) and $9.4 \times 10^{-12} \text{ cmW}^{-1}$ ($\lambda=532 \text{ nm}$) for colloidal gold.

Nonlinear absorption of Ag, Pt and Cu colloidal solutions was negligible for $\lambda=1.064 \text{ nm}$. It can be explained by the fact that surface plasma resonance of such materials is located in the UV spectrum region, excluding Cu solutions. An additional studies should be done for clearance of the last fact.

4. CONCLUSIONS

Investigations of nonlinear optical parameters of metal colloidal solutions (Ag, Pt, Au, Cu) are presented. Such media are of great interest due to their possible application in the experiments which include optical modulation and optical limiting of laser radiation. Our Z-scan experiments allowed to measure the third-order nonlinear susceptibilities that cause the refractive index change of such media and also nonlinear refractive indices and nonlinear absorption coefficients. It was shown that Cu, Ag and Pt colloidal solutions had positive value of nonlinear refractive index (for $\lambda = 1.064 \text{ nm}$) but in the case of colloidal gold it had negative sign. The same picture remained on the wavelength of 532 nm excluding Cu colloidal solution for which nonlinear refractive index had changed its sign for negative. It can be explained by the fact that its surface plasma resonance is located in the near IR spectrum region.

Our experiments have shown that nonlinear susceptibilities of investigated solutions have been 4 to 5 orders lower in comparison with nonlinear susceptibilities of metal particles. It should be noted that nonlinear absorption has taken place only in the case of Au colloidal solution (for $\lambda = 1.064$ nm).

5. REFERENCES

1. M. Sheik-Bahae, A.A. Said, E.W. Van Stryland, *Opt. Lett.* **14**, pp. 955-958, 1989.
2. M. Sheik-Bahae, A.A. Said, T.-H. Wei, D.J. Hagan, E.W. Van Stryland, *IEEE J. Quantum Electron.* **26**, pp. 760 - 772, 1990.
3. F. Hache, D. Ricard, C. Flytzanis, U. Kreibig, *Appl. Phys. A.* **47**, pp. 347-354, 1988.
4. L. Yang, K. Becker, F.M. Smith, R.H. Marguder, R.F. Haglund, L. Yang, R. Dorsinville, R.R. Alfano, R.A. Zuhr, *J. Opt. Soc. Am. B.* **11**, pp. 457-467, 1994.
5. D. Ricard, Ph. Roussignol, C. Flytzanis, *Opt. Lett.* **10**, pp. 511-514, 1995.
6. D.A. Weitz, M. Oliveria, *Phys. Rev. Lett.* **52**, pp. 1433-1436, 1984.
7. K. Uchida, S. Kaneko, S. Omi, C. Hata, H. Tanji, Y. Asahara, A.J. Ikushima, *J. Opt. Soc. Am. B.* **11**, pp. 1236-1246, 1994.
8. F. Hache, D. Ricard, C. Flytzanis, *J. Opt. Soc. Am. B.* **3**, pp. 1647-1658, 1986.
9. M. J. Bloemer, J.W. Haus, P.R. Ashley, *J. Opt. Soc. Am. B.* **7**, pp. 790-803, 1990.
10. S.C. Mehendale, S.R. Mishra, K.S. Bindra, M. Laghate, T.S. Dhami, K.S. Rustagi, *Opt. Comm.* **133**, pp. 273-278, 1997.
11. T. Tokizaki, A. Nakamura, S. Kaneko, K. Uchida, S. Omi, H. Tanji, Y. Asahara, *Appl. Phys. Lett.* **65**, pp. 941-945, 1994.
12. S.V. Karpov, A.L. Bas'ko, S.V. Koshelev, A.K. Popov, V.V. Slabko, *Colloidal Journal* **59**, pp. 765-772, 1997.
13. V.V. Slabko, S.V. Karpov, V.I. Zaitsev, A.K. Popov, *J. Phys.: Condens. Matter.* **5**, pp. 7231-7242, 1993.
14. I.Y. Ladyzinsky, *Colloidal Journal* **54**, pp. 80-88, 1992.
15. B.M. Smirnov, *Physical Sciences Uspekhi* **163**, pp. 51-69, 1993.
16. S.R. Mishra, H.S. Rawat, M. Langhate, *Opt. Comm.* **147**, pp. 328-334, 1998.
17. S.R. Mishra, H.S. Rawat, M.P. Joshi, S.C. Mehendale, K.S. Rustagi, *Proc. SPIE* . **2284**, pp. 220-225, 1994.
18. T. Terazima, N. Hirota, *J. Phys. Chem.* **96**, pp. 7147-7154, 1992.
19. L.W. Tutt, T.F. Bogess, *Prog. Quantum Electron.* **17**, pp. 299-312, 1993.
20. C.H. Kwak, Y.L. Lee, S.G. Kim, *J. Opt. Soc. Am. B.* **16**, pp. 600-612, 1999.

Author Index

- Abramova, K. B., 55
 Aksenov, Valerii P., 61, 65, 68, 70
 Albert, M. M., 206
 Albridge, Royal G., 206
 Alexandrov, Alexander P., 74
 Anisimov, Sergey I., 141
 Ašmontas, Steponas P., 18, 87
 Babina, Nadezhda A., 74
 Bagrov, Ig. V., 97
 Baidakova, M. V., 91
 Bakhtin, Mikhail A., 274
 Belousova, Inna M., 97
 Berkovsky, Andrei N., 274
 Bialkowski, Joerg, 186
 Bityurin, Nikita M., 74, 197, 218
 Bivol, Valeriu V., 49
 Bonch-Bruevich, Alexei M., 79
 Boneberg, Johannes, 61, 65, 68, 70
 Brasselet, Etienne, 42
 Bumelienė, S., 87
 Cavalleri, Andrea, 186
 Chakera, J. A., 286
 Chivel, Yuri A., 232
 Coban, A., 49
 Courant, J. L., 28
 David, C., 28
 Davidson, Jeffrey L., 206
 De Giorgi, M. L., 8
 Elia, L., 8
 Fernandez, M., 8
 Flicstein, Jean, 28
 Gaevski, Michael E., 91
 Galstian, Tigran V., 42
 Ganeev, Rashid A., 286, 307
 Gilligan, Jonathan M., 206
 Gobert, Olivier, 153, 178
 Gorbunov, Andre A., 212
 Gradauskas, Jonas, 18, 87
 Graff, A., 212
 Gruzdev, Vitali E., 238, 262, 295
 Gruzdeva, Anastasia S., 262, 295
 Guillonnet, E., 28
 Gupta, Parshotam D., 286
 Hashida, Masaki, 178
 Hirai, Makoto, 172
 Hotta, Eiki, 165
 How Kee Chun, L. S., 28
 Husinsky, Wolfgang, 206
 Jiang, Weihua, 172
 Jost, O., 212
 Jukna, A., 87
 Kaiser, Andreas, 250
 Kaliteevskaya, E. N., 79
 Kaliteevskaya, N. A., 36
 Kamalov, Shavkat R., 307
 Kamanina, Natalie V., 91, 97, 103
 Kitajima, K., 172
 Kodirov, M. K., 307
 Kognovitskii, Sergey O., 91
 Komolov, Vladimir L., 108
 Kozlov, Sergei A., 274
 Krutyakova, V. P., 79
 Kudryashov, Sergei I., 186
 Leggieri, Gilberto, 8
 Leiderer, Paul, 61, 65, 68, 70
 Libenson, Mikhail N., 1, 238
 Lu, Yong F., 115, 141
 Luches, Armando, 8
 Luk'yanchuk, Boris S., 115, 141
 Lüpke, G., 206
 Maisonneuve, D., 28
 Malyshev, Aleksey Yu., 218
 Marka, Z., 206
 Marquez, J., 28
 Martino, Maurizio, 8
 Meynadier, Pierre, 153
 Mikhailova, G. N., 61, 65, 68, 70
 Min'ko, L. Ya., 232
 Muenzer, H. J., 61, 65, 68, 70
 Mukhammedgalieva, Anel F., 127
 Muraviov, Sergey V., 74
 Naik, P. A., 286
 Nesterov, S. I., 91
 Palmier, Jean F., 28
 Paršeliūnas, J., 87
 Perdrix, Michel, 153
 Petite, Guillaume, 153, 178
 Petukhov, V. S., 127
 Pompe, Wolfgang, 212
 Prisacari, A. M., 49
 Przhibel'skii, Sergey G., 108
 Raghuramaiah, M., 286
 Razumova, T. K., 79
 Rethfeld, Bärbel, 186, 250
 Robu, Vitaly S., 49
 Rysanyansky, Alexander I., 307
 Rymalis, M. R., 91
 Sallé, Beatrice, 153
 Seisyan, Ruben P., 36, 91
 Seliuta, Dalius, 18, 87
 Semerok, Alexandre F., 153, 178
 Shakhno, Elena A., 226
 Sharma, A. K., 286
 Shcherbakov, I. P., 55
 Shpolyanskiy, Yuri A., 274
 Simon, Gerhard, 250
 Singh, S. K., 206
 Širmulis, Edmundas, 18
 Smirnov, Valentin N., 108
 Sokolowski-Tinten, Klaus, 186

Sturmann, Judit, 206
Sužiedėlis, Algirdas, 87
Suzuki, Takanori, 172
Temnov, V. V., 186
Tolk, Norman H., 206
Träger, Frank, 280
Usmanov, Timurbek, 307
Valušis, Gintaras, 87
Vartanyan, Tigran A., 280
Vasiliev, B. I., 127
Vicanek, Martin, 250
Vlad, Lyudmila A., 49
von der Linde, Dietrich, 186
Wagner, J.-F., 153, 178
Wang, Zh. Zh., 28
Watanabe, Masato, 165
Yabe, Takashi, 165
Yatsui, Kiyoshi, 172
Zhdanov, Gleb S., 134
Zheng, Y. W., 115
Zhevlakov, Aleksandr P., 97
Zocco, A., 8